

NON-CONTACT MEASUREMENT OF HEART AND RESPIRATION
RATES WITH A SINGLE-CHIP MICROWAVE DOPPLER RADAR

A DISSERTATION

SUBMITTED TO THE DEPARTMENT OF ELECTRICAL ENGINEERING

AND THE COMMITTEE ON GRADUATE STUDIES

OF STANFORD UNIVERSITY

IN PARTIAL FULFILLMENT OF THE REQUIREMENTS

FOR THE DEGREE OF

DOCTOR OF PHILOSOPHY

Amy Diane Droitcour

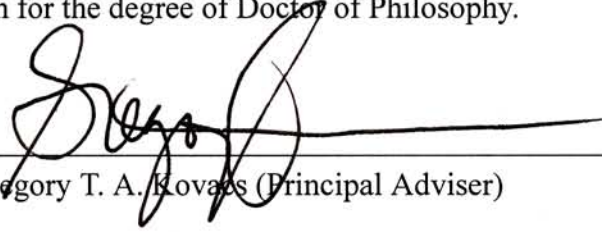
June 2006

© Copyright by Amy D. Droitcour 2006

All Rights Reserved

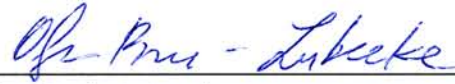
*To my family
whose encouragement and support have made this possible*

I certify that I have read this dissertation and that, in my opinion, it is fully adequate in scope and quality as a dissertation for the degree of Doctor of Philosophy.



Gregory T. A. Kovacs (Principal Adviser)

I certify that I have read this dissertation and that, in my opinion, it is fully adequate in scope and quality as a dissertation for the degree of Doctor of Philosophy.



Olga Boric-Lubecke

I certify that I have read this dissertation and that, in my opinion, it is fully adequate in scope and quality as a dissertation for the degree of Doctor of Philosophy.



Krishna Shenoy

Approved for the University Committee on Graduate Studies.

Abstract

Microwave Doppler radar can be used for non-contact, through-clothing measurement of chest wall motion, from which heart and respiration signatures and rates can be derived in real-time. A heart and respiration rate monitor has been developed based on this principle and the radio electronics have been integrated on a single CMOS chip, making inexpensive mass-production and miniaturization of the system possible. Although there are many potential applications for non-contact monitoring of heart and respiration rates, the fully integrated version focuses on the large and growing home monitoring market.

This dissertation thoroughly explores the design requirements and trade-offs for this system, analyzing the transceiver architecture, circuit specifications, and the effects of phase noise on the system. Non-quadrature 1.6-GHz direct-conversion continuous-wave transceivers have been developed in 0.25- μm CMOS and BiCMOS, and two different 2.4-GHz quadrature direct-conversion continuous-wave radar transceivers with 1-mW transmit power have been fabricated in 0.25- μm CMOS. In a direct-conversion receiver, the phase relationship between the received signal and the local oscillator has a significant effect on the demodulation sensitivity, and the null points can be avoided with a quadrature receiver. The range-correlation effect on residual phase noise is a critical factor when detecting small phase fluctuations with a high-phase-noise on-chip oscillator. Phase noise

reduction due to range correlation has been experimentally evaluated, and the measured phase noise was within 5 dB of predicted values on average.

Data is presented from the method comparison study in which heart and respiration rates measured with the 0.25- μm CMOS quadrature Doppler radar system were compared with those measured with standard techniques on 22 human subjects. Accurate measurement of heart rate at 1 m and accurate respiration measurement at 1.5 m are shown. The data from the method comparison study is used to confirm theoretical estimates of the SNR, to evaluate techniques for combining the quadrature output signals and to evaluate techniques for determining the heart rate from the heart signature. Principal components combining is used to combine the quadrature signals and autocorrelation of the heart and respiration signatures is used to determine the heart and respiration rates.

The current version of the single-chip Doppler radar cardio-respiratory rate detection system can successfully measure heart rate up to one meter and respiration rates up to two meters in most subjects that have been instructed to sit still, and it could be used to monitor sleeping or unconscious persons from a relatively close range, avoiding the need to apply electrodes or other sensors in the correct position and to wire the subject to the monitor. Doppler radar cardiopulmonary monitoring offers a promising possibility of non-contact, through-clothing measurement of heart and respiration rates. A CMOS single-chip version of this technology offers a potentially inexpensive implementation that could extend applications to consumer home-monitoring products, and could enable the use of multiple transceivers to solve some system-level problems. Further advances in the circuit design, system design and signal processing can increase the range and quality of the rate-finding, broadening the potential application areas of this technology.

Acknowledgments

I wish to acknowledge the many people who have helped to make this work possible, by contributing technically, by making my time at Stanford some of the greatest years of my life, and/or by preparing me for my work at Stanford.

First I would like to thank my principal advisor, Professor Gregory Kovacs. He has always been enthusiastic about my research both when talking with me and with others, which has helped to keep me motivated to work on this project. He has helped to make my research focused and practical by redirecting me when I get sidetracked on a tangential or impractical research interest. Finally, he has been a great mentor, encouraging my interests both within and outside of my research.

I would like to thank the examination committee for my special university oral examination, Professors Olga Boric-Lubecke, Krishna Shenoy, and Antony Fraser-Smith. I am especially grateful to Professors Olga Boric-Lubecke and Krishna Shenoy for reading my dissertation. I would like to thank Professor Olga Boric-Lubecke for introducing me to this research project, for her consistent excellent technical advice, for teaching me to write a good research paper, and for encouraging me to publish early and often. Her mentoring is what convinced me to pursue a doctorate and career in research.

Financial support from the Lucent Technologies Bell Laboratories Graduate Research Fellowship and the NASA Center for Space Biological Technologies (John Hines, Program Manager) has made this research possible. I would also like to thank Lucent Technologies and Agere Systems for fabricating the experimental prototypes free of charge.

The tireless and meticulous editing of this document by David Burns has been a fantastic help. I couldn't ask of any more in an editor.

The members of the Stanford Transducers Lab, past and present, have contributed immeasurably to my experience at Stanford. I have also been privileged to work with Valerie Barker, Chris Storment, Tony Flannery, Kristin Gilchrist, Laurent Giovangrandi, Matthew Hills, Omer Inan, Nicole Kerness, Dirk Lange, Janice Li, John Meador, Nathalia Peixoto, Amy Oulette, Tony Ricco, Bob Ricks, Hollis Whittington, and Gaylin Yee. All these people have made working in the lab a lot more fun, and many have provided me with useful advice. Laurent Giovangrandi's expertise in Matlab coding and signal processing has helped me get past a tough spot more than once. I would especially like to thank him for being my consistent companion for coffee breaks and lunches, many of which would have been lonely without him. Janice Li has been a great friend in the lab, sometimes providing technical advice, sometimes letting me vent about my frustrations in the lab, and sometimes just being there to help me get through the low-motivation periods. Bob Ricks gave me advice on designing and debugging the baseband signal conditioning circuits. All these contributions are greatly appreciated.

I would like to thank Sandy Plewa for oiling the gears of the Stanford Transducers Lab throughout my time at Stanford. Without Sandy making sure we had things in stock, expediting the purchasing process, and navigating the Stanford bureaucracy, I think many deadlines would have been missed.

Many people outside the lab have contributed technically to this work. Jenshan Lin, Peggy Gould, and Olga Boric-Lubecke designed the subcircuits of the base station

receiver that were incorporated into this work. Their advice and their circuit design expertise were instrumental in getting the chips to work properly. Victor Lubecke gave me useful technical advice on this project many times, and he also spent significant time helping me to prepare for my first presentations and poster sessions at conferences. Anders Host-Madsen provided me with useful advice and ideas on how to combine quadrature channels in this system. Carsten Metz directed me to papers on the range correlation effect when I thought I was discovering it at Bell Labs, and Mervin Budge (one of the authors of those papers) clarified some of my questions on the topic. David Leeson spent some time giving me advice on the radar cross section problem. I would like to thank all these people for their help

I would like to thank all the subjects of the human testing study for either wanting to advance science or wanting to help me graduate enough to devote an hour of their time to the study.

I have been very lucky throughout my graduate career at Stanford to have many great friends, whose love, support and laughter carried me through the difficult times and made the moments of triumph worth the struggle, and I would like to thank all of them. I would especially like to thank David Barkin, Valeria Bertacco, and John Davis for a great collection of laughs and memories that will always stand out when thinking of my time at Stanford and Nicole Kerness for always being there to chat and for cooking me so many dinners. Many of my friends from Cornell have remained close despite the distance between us now, and I'd like to thank them for still being the same great people although I may only see them once a year. I'd especially like to thank Sarah Calve for being my remote partner in the graduate school experience and understanding the frustration and elation that comes with graduate school research as only another student could.

I dedicate this Dissertation to my family, whose encouragement to always explore my surroundings led to my early interest in science, whose consistent focus on my academic achievement laid the groundwork for the academic success that got me to Stanford, and whose unwavering support has given me the freedom to pursue a doctorate. My mother, Anna Droitcour, was one of the women who paved the way for the women of my genera-

tion to study mathematics, science, and engineering. She always encouraged me to pursue all my interests and she provided such strong support that I'm still held up by it years after her death. My father, Andrew Droitcour, has always encouraged me to be self-sufficient, to be strong and courageous, to think independently, to be realistic, and to be successful,. He has consistently been a good example in all those areas. My stepmother, Judy Droitcour, is a great friend, and I value her place in my family. My brother, Brian Droitcour, has been a lifelong friend, and is part of all my earliest happy memories. His adventurous approach to life continues to inspire me. I went to my Aunt Judy Droitour's doctoral graduation when I was 5 years old, and she got me thinking about research and graduate school at a very early age. My grandfather, Howard Droitcour, was building things with me in his workshop starting as early as I can remember, and his ability and desire to invent has inspired generations of my family to be engineers and innovators. My grandmother, Virginia Droitcour has always been very excited about my accomplishments and is so young at heart, in mind, and in body at 93 that I'm not afraid of growing old. I would like to thank all of my family for their contributions to my success and happiness.

Finally, I would like to thank Scott Castelli for being my best friend and my partner in all aspects of my life. Thanks for sending flowers to my office to cheer me up on the long days, for providing support when I need it most, for being there to celebrate with me, and for making every day a better day.

Contents

Abstract	vii
Acknowledgments	ix
1 Non-Contact Cardio-Respiratory Monitoring	1
1.1 Introduction	1
1.2 Radar Measurement of Physiological Motion	3
1.3 CMOS Radio and Microwave Circuits	4
1.3.1 Advances in the Integration of RF Circuits in CMOS	4
1.3.2 Advantages of Single-Chip Silicon Circuits	5
1.3.3 Challenges Posed by Integration of RF Circuits in Silicon	6
1.4 Motivation for a Single-Chip Radar Cardio-Respiratory Monitor	8
1.4.1 Benefits of Non-Contact Vital Sign Sensors	8
1.4.2 Utility of Heart and Respiration Rate Measurements	8
1.4.3 Safety Considerations	9
1.4.4 Potential Applications of a Single-Chip Doppler Radar Cardio-Respiratory Monitoring System	10
1.5 Contributions to the Art and Science of Non-Contact Cardio-Rerspiratory Monitoring	12
1.5.1 Theory of Doppler Radar for Cardio-Respiratory Monitoring	12
1.5.2 Single-Chip Doppler Radar Design	13
1.5.3 Residual Phase Noise	13
1.5.4 Human Measurement	13
1.5.5 Signal Processing Techniques	14
1.5.6 Future Work and Future Applications	14
1.6 References	14
2 Background	19
2.1 Radar Introduction and History	19
2.1.1 Radar Introduction	19
2.1.2 A Brief History of Radar	21
2.1.3 History of Radar in Physiological Monitoring	22
2.2 Design Choices for Cardiorespiratory Monitoring with Doppler Radar	26
2.2.1 Continuous-Wave Radar vs. Pulsed Radar	27
2.2.2 Comparison of Heterodyne and Homodyne Receivers	31

2.2.3	Single-Channel and Quadrature Receivers	36
2.2.4	Frequency of Operation	40
2.2.5	Antenna Considerations	42
2.2.6	Received Signal Amplitude and Receiver Noise Temperature	44
2.3	Transceiver Design	45
2.3.1	Radio-Frequency Front End	46
2.3.2	Active and Passive Power Dividers	47
2.3.3	Doppler Transceiver Architectures	47
2.4	Conclusions	50
2.5	References	51
3	Physiological Motion and Measurement	55
3.1	Introduction	55
3.2	Heart Motion	55
3.2.1	Location and Gross Anatomy of the Heart	56
3.2.2	Electrical and Mechanical Events of the Heart	58
3.2.3	Surface Motion Due to Heart Function	61
3.2.4	Quantitative Measurements of Chest Wall Motion Due to the Heart	62
3.2.5	Summary of Heart Motion	68
3.3	Circulatory System Motion	68
3.3.1	Location and Structure of Major Arteries and Veins	69
3.3.2	Blood Flow Through Arteries and Veins	71
3.3.3	Surface Motion from Blood Flow	72
3.3.4	Summary of Surface Motion Due to Pulse	75
3.4	Respiratory System Motion	76
3.4.1	Motion Associated with Breathing	76
3.4.2	Chest-Wall Motion Associated with Breathing	79
3.5	Interaction of Respiratory Motion and Cardiac Motion at the Skin Surface ..	79
3.6	Vital Signs and Their Measurement	81
3.6.1	Measuring Vital Signs - Clinical Measurements	82
3.6.2	Commonly Used Alternative Methods for Vital Signs Monitoring	83
3.6.3	Measurement of Heart and Respiratory Surface Motion	86
3.7	Conclusions	91
3.8	References	93

4	Single-Chip Transceivers	101
4.1	Introduction	101
4.2	Base Station Receiver	103
4.3	Subcircuits	105
4.3.1	Introduction	105
4.3.2	Voltage-Controlled Oscillator	106
4.3.3	Mixer	110
4.3.4	Active Balun-Amplifier	119
4.3.5	Low-Noise Amplifier	124
4.3.6	Passive Balun	127
4.3.7	Duplex Switch	129
4.3.8	90° Phase-Shifting Network	130
4.4	Single-Channel Doppler Transceiver Design	135
4.4.1	Hybrid Transceiver	135
4.4.2	Single-Channel Fully-Integrated Transceivers	136
4.5	Quadrature Doppler Transceiver Design	140
4.5.1	Quadrature Architectures	140
4.5.2	CMOS Quadrature 2.4 GHz Transceiver with LNAs	141
4.5.3	CMOS Quadrature 2.4 GHz Transceiver without LNAs	143
4.6	Circuit Characterization	146
4.6.1	Power Consumption	146
4.6.2	Phase Noise	146
4.6.3	1/f Noise Generation	149
4.6.4	Isolation	150
4.6.5	Phase and Gain Balance Between Quadrature Branches	152
4.7	Conclusions	156
4.8	References	158
5	Residual Phase Noise and Range Correlation	161
5.1	Introduction	161
5.2	Range Correlation Theory	163
5.3	Materials and Methods	168
5.3.1	Range Correlation Verification	168
5.3.2	Human Measurements with Different Signal Sources	171
5.4	Results	176
5.4.1	Range Correlation Verification - Results	176

5.4.2	Human Measurement with Different Signal Sources - Results	177
5.5	Discussion	183
5.5.1	Range Correlation Verification - Discussion	183
5.5.2	Human Measurements with Different Signal Sources - Discussion	184
5.6	Conclusions	185
5.7	References	186
6	Human Testing Results	187
6.1	Introduction	187
6.2	Background and Theory	188
6.2.1	Doppler Radar Monitoring of Heart and Respiration	188
6.2.2	Received Signal Power and Radar Cross Section	189
6.2.3	Noise Sources	191
6.2.4	Variation of Signal-to-Noise Ratio with Range and Radar Cross Section	193
6.3	Materials and Methods	198
6.3.1	Experimental Setup	198
6.3.2	Human Subjects	205
6.3.3	Measurements of Human Subjects	207
6.3.4	Analysis of Human Subjects Data	209
6.4	Results	212
6.4.1	Human Subjects Heart and Respiration Signals and Rates	212
6.4.2	Overall Accuracy of Heart and Respiration Rates	220
6.4.3	Signal-to-Noise Ratio vs. Range	230
6.4.4	Signal-to-Noise Ratio vs. Measured Parameters	233
6.5	Discussion	244
6.5.1	Overall Heart and Respiration Rate Measurement Performance	244
6.5.2	Heart Signal-to-Noise Ratio - Discussion	246
6.5.3	Respiration Signal-to-Noise Ratio - Discussion	247
6.5.4	Variation of Signal-to-Noise Ratio with Range	249
6.5.5	Near-Field Antenna Effects	250
6.5.6	Radar Cross Section - Mean-Squared Motion Product	253
6.5.7	Potential Improvements	253
6.6	Conclusions	255
6.7	References	256

7	Signal Processing	259
7.1	Introduction	259
7.2	Background	263
7.2.1	Separating Heart and Respiration Signals	263
7.2.2	Quadrature Theory	266
7.2.3	Techniques for Combining Quadrature Channels	269
7.2.4	Windowing and Resolution	274
7.2.5	Determining Heart Rate from Radar Heart-Motion Signature	278
7.3	Signal Processing Methods	280
7.3.1	Separating Heart and Respiration with Digital FIR Filters	281
7.3.2	Comparison of Methods for Combining I and Q	282
7.3.3	Comparison of Heart-Rate-Finding Methods	284
7.4	Results	286
7.4.1	Separating Heart and Respiration with a Digital FIR Filter	286
7.4.2	Combining Quadrature Channels	291
7.4.3	Heart Rate-Finding	295
7.5	Discussion	298
7.5.1	Separating Heart and Respiration with Digital Filters	298
7.5.2	Combining I and Q	298
7.5.3	Rate Finding	299
7.5.4	Advanced Signal-Processing Techniques	300
7.6	Conclusions	301
7.7	References	302
8	Summary, Outlook and Conclusions	305
A	Medical Glossary	311
B	Quadrature Mixing in Direct-Conversion Receivers	317
B.1	Introduction	317
B.2	Complex Exponentials and Quadrature Mixing	318
B.3	Direct-Conversion Receivers	320
B.3.1	Challenges with Direct Conversion Receivers	321
B.3.2	Direct Conversion Receivers Used in Radar Systems	322
B.4	Image Cancellation	324
B.4.1	Image Frequency	324

B.4.2	Use of Quadrature Mixing in Image Cancellation	324
B.4.3	Quadrature Mixing in Direct Conversion Receivers	328
B.5	References	330
C	Direct Phase Demodulation and DC Offsets	333
C.1	Introduction	333
C.2	Quadrature Receiver Theory	334
C.3	Causes of DC Offsets	337
C.3.1	DC Offset Due to Phase Relationships	337
C.3.2	DC Offset Due to Self-Mixing	338
C.3.3	DC Offset Due to Reflections from Stationary Objects	340
C.4	Effects of DC Offset Removal in a System with Signal Imbalance	342
C.4.1	Theory - Removal of DC without Phase and Amplitude Error	343
C.4.2	Theory - Removal of DC with Phase and Amplitude Error	344
C.4.3	Simulation of Effects of DC Removal	346
C.5	Effects of Signal Imbalance and Gram-Schmidt Technique	349
C.5.1	Causes of Phase and Amplitude Imbalance	349
C.5.2	Effects of Signal Imbalance	349
C.5.3	Gram-Schmidt Technique for Orthonormalization	350
C.5.4	Effects of DC Offset Removal on Gram-Schmidt Technique	351
C.5.5	Effects of Residual Error on Gram-Schmidt Technique	351
C.6	Effects of Zero Crossings	353
C.7	Effects of Adding Offset to Avoid Zero Crossings	355
C.8	Conclusions	357
C.9	References	357
D	Derivation of the Theoretical Signal-to-Noise Ratio	359
D.1	Introduction	359
D.2	Radar Equation	360
D.2.1	Radar Cross Section	363
D.2.2	Reflection and Absorption	367
D.3	Phase-to-Amplitude Conversion	369
D.4	Sources of Noise	372
D.4.1	Residual Phase Noise and Range Correlation	372
D.4.2	Baseband 1/f Noise	376

D.4.3	RF Additive White Gaussian Noise	377
D.5	Variation of Signal-to-Noise Ratio with Range and Radar Cross Section	378
D.6	Near-Field vs. Far-Field Antenna Patterns	380
D.7	References	383
E	Baseband Signal Conditioning	385
E.1	Introduction	385
E.2	Background - Analog Signal Processing	386
E.2.1	Anti-Aliasing Filter	386
E.2.2	DC Blocking	387
E.2.3	Amplification	390
E.2.4	Automatic Gain Control	390
E.2.5	Combined Analog Signal Processing System	393
E.3	Materials and Methods	393
E.3.1	SRS Preamplifier	393
E.3.2	Custom Baseband Signal Conditioning Board	395
E.4	Results	397
E.4.1	Anti-aliasing Filtering	397
E.4.2	DC Blocking and Amplification	399
E.5	Conclusions	401
E.6	References	401
F	Low-IF Architecture	403
F.1	Low-IF Architecture for Doppler Radar Cardiopulmonary Monitoring	403
F.2	References	407
G	Quantitative Measurements of Chest Wall Motion	409
G.1	Quantitative Measurements of Chest Wall Motion Due to Heartbeat	409
G.2	References	412
H	Oscillator Phase Noise Theory	415
H.1	Introduction to Phase Noise	415
H.2	Sources of Oscillator Phase Noise	419
H.3	References	421

I	Analog-to-Digital Conversion	423
I.1	Analog-to-Digital Converter Theory	423
I.2	Analog-to-Digital Conversion Requirements	425
I.3	Analog-to-Digital Converters Used in Doppler Radar Physiological Measurement	426
I.3.1	Digital Oscilloscope	426
I.3.2	16-Bit ADC PCMCIA Card	426
I.4	References	427

List of Tables

Table 2.1.	Information Available from Different Topologies of Radar Transceiver. 21
Table 2.2.	Doppler Radar Measurements of Physiological Motion24
Table 3.1.	Mechanical Events of the Heart59
Table 3.2.	Quantitative Measurements of Chest Wall Motion Due to Heartbeat. Subjects are healthy unless otherwise specified.66
Table 3.3.	Time Delays and Arterial Diameters Associated with Superficial Arterial Pulses74
Table 3.4.	Translations and Rotations of the Heart Between Maximum Inhale and Maximum Exhale.80
Table 3.5.	Techniques for Surface Measurement of Respiration Rate87
Table 3.6.	Techniques for Surface Motion Measurement of Pulse Rate89
Table 4.1:	Measured RF Phase Noise and Calculated Baseband Residual Phase Noise at 50 cm and 1 m for the Different Oscillators Used for Doppler Radar Cardio-Respiratory Monitoring.149
Table 5.1:	Summary of the Heart-Rate Detection Measurement Accuracy.172
Table 6.1:	Measured and Collected Subject Data. “Num” is the 4-digit subject number. “Age” and “Gen” are the subject’s age and gender as reported by the subject. “Ht” and “Wt” are the subject’s measured height in cm and weight in kg, and “BMI” is the subject’s body mass index, calculated as Wt/Ht^2 , with the weight in kg and the height in m. “CB,” “CD,” “WC,” and “CC” are the subject’s chest breadth, chest depth, waist circumference, and chest circumference, all measured at exhale. “HR” and “RR” are the subject’s average heart and respiration rates.206
Table 6.2:	Bland-Altman Data for Each Subject’s Heart Measurement. “Mean” indicates the mean of the difference between the heart rate found with the Doppler system and that found with the ECG. “Std dev” indicates the standard deviation of the difference between the rates. The units are beats per minute.225

Table 6.3:	Bland-Altman Data for Each Subject’s Respiration Measurement. “Mean” indicates the mean of the difference between the respiration rate found with the Doppler system and that found with the respiratory effort belts. “Std dev” indicates the standard deviation of the difference between the rates. The units are breaths per minute.230
Table 6.4:	Doppler Signal-to-Noise Ratio for Each Subject’s Heart and Respiration Measurements.231
Table 6.5:	Statistical Correlation Between Physical Parameters and Doppler Heart Signal-to-Noise Ratios at the Different Ranges. The statistical correlation between the variables is the covariance of the two variables divided by the standard deviation of each variable. The measure ‘r’ is the correlation coefficient, and ‘p’ is the p-value for testing the hypothesis of no correlation. Each p-value is the probability of getting a correlation as large as the ‘r’ value randomly if the true correlation is zero. Correlations with p-values ± 0.10 , are in bold, indicating that there is at least 90% confidence in those correlations.234
Table 6.6:	Statistical Correlation Between Physical Parameters and the Square Root of Doppler Heart Signal-to-Noise Ratios at the Different Ranges. The statistical correlation between the variables is the covariance of the two variables divided by the standard deviation of each variable. The measure ‘r’ is the correlation coefficient, and ‘p’ is the p-value for testing the hypothesis of no correlation. Each p-value is the probability of getting a correlation as large as the ‘r’ value randomly if the true correlation is zero. Correlations with p-values ± 0.10 , are in bold, indicating that there is at least 90% confidence in those correlations.235
Table 6.7:	Statistical Correlation Between Physical Parameters and Doppler Respiration Signal-to-Noise Ratios at the Different Ranges. The statistical correlation between the variables is the covariance of the two variables divided by the standard deviation of each variable. The measure ‘r’ is the correlation coefficient, and ‘p’ is the p-value for testing the hypothesis of no correlation. Each p-value is the probability of getting a correlation as large as the ‘r’ value randomly if the true correlation is zero. Correlations with p-values ± 0.10 , are in bold, indicating that there is at least 90% confidence in those correlations.238

Table 6.8:	Statistical Correlation Between Physical Parameters and the Square Root of Doppler Respiration Signal-to-Noise Ratios at the Different Ranges. The statistical correlation between the variables is the covariance of the two variables divided by the standard deviation of each variable. The measure ‘r’ is the correlation coefficient, and ‘p’ is the p-value for testing the hypothesis of no correlation. Each p-value is the probability of getting a correlation as large as the ‘r’ value randomly if the true correlation is zero. Correlations with p-values ± 0.10 , are in bold, indicating that there is at least 90% confidence in those correlations.239
Table 7.1:	Bland-Altman Statistics for Comparison of Heart Rate Measured with the Doppler Radar System to that Measured with the ECG with Different Methods Used for Combining the I and Q Components of the Doppler Radar Signal. The mean of the difference between the rates from the Doppler and the ECG are the ‘bias’ and the standard deviation of the difference is ‘std.’ The numbers given are the average value of the statistics over 22 data sets at each range. The standard deviation is also given for the bias.291
Table 7.2:	Bland-Altman Statistics for Comparison of Heart Rate Measured with the Doppler Radar System to that Measured with the ECG with Different Methods Used for Combining the I and Q Components of the Doppler Radar Signal on Subsets of the Data. The mean of the difference between the rates from the Doppler and the ECG are the ‘bias’ and the standard deviation of the difference is ‘std.’292
Table 7.4:	Average Signal-to-Noise Ratio for Heart Signals with Each I/Q Combination Method at Each Range on Subsets of the Data. The numbers given in the table are the average value of the statistics over N remaining data sets at each range, and the standard deviation is also provided.293
Table 7.3:	Average Signal-to-Noise Ratio for Heart Signals with Each I/Q Combination Method at Each Range. The SNR is averaged over all 22 data sets, and the standard deviation is also provided.293
Table 7.5:	Bland-Altman Statistics for Comparison of Respiration Rate Measured With the Doppler Radar System to that Measured with the Respiratory Effort Straps with Different Methods used for Combining the I and Q Components of the Doppler Radar Signal. The mean of the difference between the rates from the Doppler and the ECG are the ‘bias’ and the standard deviation of the difference is ‘std.’ The numbers given are the average value of the statistics over 22 data sets at each range. The standard deviation is also given for the bias.294

Table 7.6:	Average Signal-to-Noise Ratio for Respiration Signals with Each I/Q Combination Method at Each Range. The SNR is averaged over all 22 data sets, and the standard deviation is also provided.	294
Table 7.7:	Bland-Altman Statistics for Comparison of Heart Rate Measured with the Doppler Radar System to that Measured with the ECG with Different Methods Used for Rate-Finding of the Doppler Radar Signal. The mean of the difference between the rates from the Doppler and the ECG are the ‘bias’ and the standard deviation of the difference is ‘std.’ The numbers given are the average value of the statistics over 22 data sets at each range. The standard deviation is also given for the bias.	296
Table 7.8:	Bland-Altman Statistics for Comparison of Heart Rate Measured with the Doppler Radar System to that Measured with the ECG with Different Methods Used to Determine the Heart Rate from the Doppler Radar Signal. The mean of the difference between the rates from the Doppler and the ECG are the ‘bias’ and the standard deviation of the difference is ‘std.’ Data sets with Bland-Altman standard deviation greater than 3 or bias magnitude greater than 5 for all combination techniques were eliminated. The numbers given in the table are the average value of the statistics over N remaining data sets at each range. The standard deviation is also given for the bias.	297
Table C.1:	Weighting Values for Scaling Output Signals to Minimize Mean Squared Error Between the Outputs and the Chest Motion Signal.	349
Table C.2:	Weighting Values for Scaling Output Signals to Minimize Mean Squared Error Between the Outputs and the Chest Motion Signal.	357
Table E.1:	Actual Values Used in Sallen-Key Anti-Aliasing Filter, as in Figure E.1. ..	395
Table E.2:	Component Values for DC Block and Amplification Stage Shown in Figure E.2.	396
Table G.1:	Quantitative Measurements of Chest Wall Motion Due to Heartbeat. All subjects are healthy unless otherwise specified.	409

List of Figures

Figure 1.1:	Block diagram of continuous wave radar for measurement of physiological motion. The phase of the reflected signal, $\theta(t)$, is directly proportional to the chest motion, $x(t)$, and is scaled by the wavelength, λ	3
Figure 1.2:	Two on-chip planar spiral inductors in an active balun of the 2.4 GHz radar transceivers. These spirals have outside diameters of 340 μm and 270 μm , and their respective inductances are 8 nH and 4 nH.....	7
Figure 2.1.	Single-antenna radar system block diagram. A radar system consists of a transmitter, an antenna, a receiver, and signal processing hardware. A portion of the transmitted signal is reflected by the target, and a portion of the reflected signal is received by the radar receiver. The received signal is then processed to determine information about the target.....	20
Figure 2.2.	The phase shift of the reflected signal is proportional to the time-varying chest position. A positive value of x corresponds to a retracting chest cavity, or an exhale.....	30
Figure 2.3.	Typical heterodyne receiver architecture. The detector may be a mixer to baseband, a quadrature demodulator, or another type of detector that functions at the intermediate frequency. The RF BPF is a high-quality radio-frequency bandpass filter used to attenuate the image frequency, the LNA is a radio frequency low-noise amplifier, the IF BPF is a high-quality bandpass filter at the intermediate frequency used for channel selection, and the IF Amp is an amplifier at the intermediate frequency. The type of detector varies with the application. The LO is typically tuned to select the desired channel.....	32
Figure 2.4.	Typical homodyne, or direct-conversion, architecture. The RF BPF is a bandpass filter that is sometimes included to attenuate neighboring signals to avoid intermodulation resulting from receiver nonlinearities. The LNA is a low-noise amplifier that increases the receiver noise figure. The local oscillator is at the same frequency as the RF carrier, and when mixed with the received signal after the baseband low-pass filter, the signal is at baseband. The baseband LPF is an anti-aliasing filter that must be applied to the signal before it is digitized.....	33

- Figure 2.5. Simplified Doppler radar system block diagram with signal flow. The oscillator signal, $T(t)$, provides both the transmitted RF signal and the LO signal. The transmitted signal travels a total distance $2d(t)=2(d_0+x(t))$ and becomes the received signal, $R(t)$, which is mixed with the LO and lowpass filtered to give the baseband output, $B(t)$. The target, at a nominal distance d_0 from the antenna, has a periodic displacement $x(t)$. A_R and A_B are the ratios of the received and baseband signal amplitudes to the LO amplitude. The baseband output signal is proportional to the cosine of a constant phase shift determined by the nominal target distance, d_0 , summed with a time-varying phase shift proportional to the time-varying chest motion and with the residual phase noise $\Delta\phi(t)$35
- Figure 2.6. Block diagram of a single-channel CW radar transceiver. The signal source is split into the carrier for the transmitter and the local oscillator, LO. The transmitter couples the output signal to the antenna at the RF_{out} port, and the receiver demodulates the received signal from the RF_{in} port.....36
- Figure 2.7. Block diagram of a quadrature CW radar transceiver. The signal source is split into the carrier from the transmitter and the local oscillator for the receiver. The local oscillator is split with a 90° phase shift between the two LO outputs, and the RF input signal is split with a 0° phase shift. The transmitter couples the output signal to the antenna, and the receivers convert the signal to baseband. The in-phase and quadrature receiver channels each provide an output.37
- Figure 2.8. Block diagram for Doppler radar sensing of chest motion with a quadrature receiver. The oscillator signal provides both the transmitted RF and LO signals, $T(t)$ and $L(t)$. The transmitted signal travels a total distance $2d(t)=2(d_0+x(t))$ and becomes the received signal, $R(t)$. The LO is split into two quadrature LO signals, which have phases $\pi/2$ apart. The received signal is split into signals for the two receiver chains, and each is mixed with the one LO signal and lowpass filtered to give the baseband outputs, $B_I(t)$ and $B_Q(t)$. These two baseband signals can be combined to directly demodulate the phase, or the better of the two signals can be chosen.39
- Figure 2.9. Single-channel transceiver block diagram. This architecture was used in two 1.6-GHz transceivers.48

Figure 2.10.	Quadrature transceiver block diagrams. a) LNAs are to isolate the RCCR phase-shifting circuit and passive baluns are used for single-ended to differential conversion. b) The VCO is coupled directly to the RCCR and active baluns are used to create the differential signal for the mixer. Each configuration was used in a 2.4-GHz transceiver.	49
Figure 3.1:	The location of the heart in the rib cage. The intercostal spaces are indicated by the numbers 1-5. The heart is beneath the sternum and the cartilage of the third, fourth, and fifth ribs. After [94].	56
Figure 3.2:	Diagrammatic section of the heart. The arrows indicate the direction of blood flow. After [135].	57
Figure 3.3:	Exemplary output of an electrocardiogram. Atrial depolarization causes the P wave, ventricular depolarization causes the QRS complex, and ventricular repolarization causes the T wave.....	58
Figure 3.4:	Motion of the left heart through the phases of the cardiac cycle. After [120].	59
Figure 3.5:	During the beginning of systole, the ventricles are contracting, but all the valves in the heart are closed; this is known as the isovolumetric ventricular contraction (1). The pressure in the ventricle increases, and when it is greater than the pressure in the aorta, the aortic valve opens, and ventricular ejection (2) begins. The pressure in the ventricle decreases as blood flows out of it, and when the pressure drops below that of the aortic valve, the aortic valve closes and diastole begins. Since all the valves in the heart are closed and the ventricle is relaxing, this is known as the isovolumetric ventricular relaxation period (3). When the left ventricular pressure drops below that of the atria, the mitral valve opens, and ventricular filling (4) begins. After [135].	60
Figure 3.6:	Interaction of the respiratory and circulatory systems. After [109].	69
Figure 3.7:	Model of the arterial system, showing major arteries. After [131].	70
Figure 3.8:	Diagram of arterial pressure in systole and diastole. During systole, the artery distends, storing blood; during diastole, the artery contracts so blood continues flowing into the arterioles after the aortic valve is closed. After [135].	71
Figure 3.9:	Lee's model of an artery in tissue for analyzing surface motion with radial motion of the vessel wall. After [107].	73

Figure 3.10:	The thoracic wall and body cavities. After [122].	77
Figure 3.11:	Movement of upper, lower, and lowest ribs. After [122].	78
Figure 4.1.	Block diagram of base station heterodyne receiver.	104
Figure 4.2.	DCS 1800 BiCMOS base station receiver chip micrograph [155].	105
Figure 4.3.	VCO circuit diagram with a) BiCMOS and b) CMOS active elements. The BiCMOS RF choke low-pass filters have a 10-pF capacitor and a 20-nH inductor, while the CMOS RF chokes have a 20-pF capacitor and a 20-nH inductor.	109
Figure 4.4.	Single-transistor passive FET resistive mixer. After [163].	111
Figure 4.5.	Circuit diagram of the DCS1800 mixer.	114
Figure 4.6.	Photo of the DCS1800 mixer. The active devices are CMOS transistors.	115
Figure 4.7.	Linearity measurements of the mixer vs. frequency: input IP2 (IIP2), input IIP3 (IIP3), and input 1-dB compression point. This measurement was made with a LO power of 4 dBm while RF power was varied. The IF frequency was maintained at 30 MHz.	116
Figure 4.8.	Balun-amplifier circuit diagrams in a) BiCMOS and b) CMOS.	122
Figure 4.9.	Micrograph of BiCMOS balun-amplifier.	123
Figure 4.10.	LNA circuit diagram in a) bipolar and b) CMOS.	126
Figure 4.11.	Passive balun. The trace inductance and ground inductance were included in the simulation. For the 2.4-GHz balun, the inductors (L) were 5 nH and the capacitors (C) were 0.8 pF.	128
Figure 4.12.	Passive balun a) gain and b) phase bandwidth simulations with inductances of 5 nH and capacitances of 0.8 pF. A sine wave is swept at the input of the balun and the output amplitude and phase are simulated relative to the input. 50-Ω loads are assumed at the output.	129

Figure 4.13.	Passive balun sensitivity to component value accuracy simulation: a) gain vs. capacitor value and b) phase change between input and output vs. capacitor value at a frequency of 2.45 GHz. The value of C in Figure 4.11 is swept and the ratio of the output amplitude to the input amplitude and the phase difference between the input and the outputs are calculated. 50- Ω loads are assumed at the output.	130
Figure 4.14.	Resistor-capacitor-capacitor-resistor network for creating 90° phase shift. ...	131
Figure 4.15.	The a) gain and b) phase of the in-phase (I) and quadrature (Q) outputs of the RCCR with resistances of 65 Ω and capacitances of 1 pF. A sine wave is swept at the input of the network and the output amplitude and phase are simulated relative to the input. 50- Ω loads are assumed at the outputs. .	132
Figure 4.16.	Simulation of RCCR sensitivity to component value: a) gain and b) phase shift between input and output vs. resistor value at 2.45 GHz. The value of C in Figure 4.14 is swept and the ratio of the output amplitude to the input amplitude and the phase difference between the input and the outputs are calculated. 50- Ω loads are assumed at the output.....	134
Figure 4.17.	Block diagram of a single-channel direct conversion Doppler radar transceiver.....	135
Figure 4.18.	Photograph of hybrid Doppler radar transceiver, using individually packaged CMOS mixer and bipolar balun-amplifiers with a commercially available discrete VCO. The MiniCircuits JTOS-1650 VCO has -70-dBc/Hz SSB phase noise at a 1-kHz offset.	136
Figure 4.19.	Micrograph of BiCMOS Doppler radar transceiver.	138
Figure 4.20.	Photo of BiCMOS chip on board.....	138
Figure 4.21.	Micrograph of CMOS Doppler radar transceiver.	139
Figure 4.22.	Photo of printed circuit board with CMOS chip.....	139
Figure 4.23.	2.4-GHz quadrature Doppler radar transceiver architecture with LNAs.	141
Figure 4.24.	Micrograph of the quadrature transceiver with LNAs.....	142
Figure 4.25.	Photograph of the packaged quadrature chip with LNAs on a board.	143

Figure 4.26.	2.4 GHz quadrature Doppler radar transceiver architecture without LNAs.	144
Figure 4.27.	Micrograph of the quadrature chip without LNAs.	145
Figure 4.28.	Photograph of packaged quadrature transceiver without LNAs on a printed circuit board	145
Figure 4.29.	Delay line frequency discriminator method for phase noise measurements.	146
Figure 4.30.	Measured RF phase noise and calculated baseband residual phase noise for CMOS and BiCMOS single-channel chips. The residual phase noise is calculated at a 50 cm range and 1-Hz offset frequency.	147
Figure 4.31.	Measurement of baseband noise due to RF-LO leakage a) varying LO power with RF power fixed at -10 dBm and b) varying RF power with LO power fixed at 0 dBm. Error between repeated measurements was below 2dB.	151
Figure 4.32.	a) Relative amplitude of I and Q outputs and b) phase difference between I and Q outputs of RCCR tester on quadrature chip without LNAs.	153
Figure 4.33.	Test setup for overall phase and amplitude balance measurements.	155
Figure 5.1.	Illustration of the range correlation phase noise filtering effect. Since the transmitted signal is derived from the same source as the received signal, the phase noise on the LO, $s_{\phi}(f_o)$, and the RF input, $s_{\phi, \text{delayed}}(f_o)$, are correlated. When the two signals are mixed, most of the phase noise at baseband is effectively cancelled, leaving only the residual phase noise, $s_{\Delta\phi}(f_o)$	164
Figure 5.2.	Relationship of residual phase noise to target range for a range of RF phase noise values. The values shown are those of the signal sources presented in this chapter, the fully integrated CMOS oscillator, the fully integrated BiCMOS oscillator, the MiniCircuits JTOS-1650 VCO used with the hybrid board, and the HP E433B signal oscillator, which was used as an external source with the CMOS radar chip.	165
Figure 5.3.	RF phase noise vs. range to maintain a constant level of residual phase noise. If a maximum level of residual phase noise and a desired range can be determined for an application, this chart can help determine the oscillator phase noise specification.	166

- Figure 5.4: Setup for the range correlation verification experiment. The chip's RF output was connected to its RF input through a -10-dB attenuator, a phase shifter ($\Delta\phi$) and a cable (td). The baseband noise spectrum was measured with the VSA. Cables of various lengths were connected in place of the cable marked td to change the time delay between the RF and the LO signals. The baseband noise spectrum from 1 Hz to 1 kHz was measured with 1-Hz resolution bandwidth and RMS averaged over 5 measurements....169
- Figure 5.5: Baseband noise spectrum measured for various phase shifts with a 20.9-ns time delay. The time delay through the cables, attenuator, and phase shifter was measured with the HP8714C RF Network analyzer. When the two signals are near in-phase or out-of-phase, the dc voltage at the output is non-zero and the phase-demodulation sensitivity is greatly decreased.170
- Figure 5.6: Heart and respiration activity measurement setup for the hybrid radar board. The baseband output signals were amplified and filtered with SR560 LNAs and then digitized with a Tektronix 3014 digital oscilloscope. A wired finger-pressure pulse sensor was used only as a reference to compare to the heart-rate data obtained with the Doppler radar.173
- Figure 5.7: Heart and respiration activity measurement setup for the 1.6-GHz radar chips. The baseband output signals were amplified and filtered with SR560 LNA's and then digitized with a Tektronix 3014 digital oscilloscope. A wired finger-pressure pulse sensor was used only as a reference to compare with heart-rate data obtained with the Doppler radar.174
- Figure 5.8: Transmitting and receiving patch antennas for 1.6 GHz chips. Each antenna was 2.936 cm by 4.000 cm. Two antennas were used rather than a single antenna and a circulator or power-splitter; the two antennas had 25 dB isolation between them. Each antenna had a 86° by 177° beamwidth and a 50 ohm impedance.175
- Figure 5.9: Frequency response of the twelfth-order elliptic IIR filter used to remove noise and residual respiration information. The fundamental frequency of respiration is usually below 0.4 Hz, while the heart rate is usually above 1 Hz. The cutoff frequencies are 0.9 Hz and 9 Hz.176
- Figure 5.10: (a) Measured phase noise at RF and the -30-dB/decade line used to predict baseband noise. (b) Measured and predicted (5.9) spectral density of phase fluctuation at baseband for time delays of 28.0, 12.6, and 6.2 ns (from top to bottom).178

Figure 5.11:	Heart and respiration activity measured with the signal generator as the source for a) the CMOS chip at a range of 50 cm and b) the hybrid board at a range of 100 cm. The top trace is the analog-filtered raw signal, and the second is the analog-filtered heart signal. The third trace is the heart signal after digital filtering. The bottom trace is the reference obtained from the finger-pressure pulse sensor described in the text. The filtered heart signal was within one beat per minute of the reference 100% of the measurement interval.	180
Figure 5.12:	Heart and respiration activity measured with the hybrid board using the MiniCircuits VCO as the source a) at a range of 50 cm and b) at a range of 100 cm. The top trace is the analog-filtered raw signal, and the second is the analog-filtered heart signal. The third trace is the heart signal after digital filtering. The bottom trace is the reference obtained from the finger-pressure pulse sensor. The filtered heart signal was within one beat per minute of the reference 100% of the measurement interval.	181
Figure 5.13:	Heart and respiration activity measured at a range of 50 cm with a) the 1.6-GHz BiCMOS chip and b) the 1.6-GHz CMOS chip. The top trace is the analog-filtered raw signal, and the second is the analog-filtered heart signal. The third trace is the heart signal after digital filtering. The bottom trace is the reference obtained from the finger-pressure pulse sensor. The filtered heart signal was within one beat per minute of the reference 100% of the measurement interval.	182
Figure 5.14:	Heart and respiration activity measured with the 1.6-GHz CMOS chip at a range of 85 cm rather than 50 cm. The noise is significantly more pronounced than with a 50-cm range, and the accuracy is 63% for the digitally filtered heart signal.	183
Figure 5.15:	Measured oscillator amplitude noise (RF) shown with predicted baseband amplitude noise based on the range correlation effect. The amplitude noise is under -130 dB/Hz at all frequencies, and therefore below the residual phase noise for frequencies of interest.	184
Figure 6.1.	Theoretical model of signal-to-noise ratio vs. range for Doppler radar measurement of a) heart motion and b) respiration motion. See text for details on parametric values.	196
Figure 6.2.	Model of theoretical signal-to-noise ratio vs. radar cross section for an RMS motion of a) 0.3 mm (heart) and b) 2 mm (respiration). See text for details of other parametric values.	197

Figure 6.3.	Block diagram of experimental setup for human subjects method comparison study.	199
Figure 6.4.	Radar system block diagram.	200
Figure 6.5.	Signal processing block diagram. PCA represents principal components analysis, the technique used to combine the I and Q signals. ERC represents equal ratio combining, the technique used to combine the abdominal and chest respiratory effort belts. HPF indicates a highpass filter, LPF indicates a lowpass filter, DC Block indicates the removal of dc offset, "Rate Find" indicates a rate-finding step, "Smooth" indicates a smoothing of the rate, and "R Wave Detect" indicates that the timings of the ECG R waves are found.	203
Figure 6.6.	Data from Subject 4062 at 0.5 m. The top trace is the combined heart signal from the Doppler radar, the second trace is the combined respiration signal from the Doppler radar, the third trace is the ECG, and the bottom trace is the combined respiration signal from the straps.	213
Figure 6.7.	Heart and respiration rates from Subject 4062 at 0.5 m. The mean difference between the ECG heart rate and the Doppler heart rate was 0.030 beats per minute and the standard deviation of the difference was 0.292 beats per minute. The mean difference between the strap respiration rate and the Doppler respiration rate was 0.029 breaths per minute and the standard deviation of the difference was 0.263 breaths per minute.	214
Figure 6.8.	Data from Subject 4062 at 1.0 m. The top trace is the combined heart signal from the Doppler radar, the second trace is the combined respiration signal from the Doppler radar, the third trace is the ECG, and the bottom trace is the combined respiration signal from the straps.	215
Figure 6.9.	Heart and respiration rates from Subject 4062 at 1.0 m. The mean difference between the ECG heart rate and the Doppler heart rate was 2.61 beats per minute and the standard deviation of the difference was 2.195 beats per minute. The mean difference between the strap respiration rate and the Doppler respiration rate was -0.720 breaths per minute and the standard deviation of the difference was 1.769 breaths per minute.	216
Figure 6.10.	Data from Subject 4062 at 1.5 m. The top trace is the combined heart signal from the Doppler radar, the second trace is the combined respiration signal from the Doppler radar, the third trace is the ECG, and the bottom trace is the combined respiration signal from the straps.	217

Figure 6.11.	Heart and respiration rates from Subject 4062 at 1.5 m. The mean difference between the ECG heart rate and the Doppler heart rate was 0.821 beats per minute and the standard deviation of the difference was 1.925 beats per minute. The mean difference between the strap respiration rate and the Doppler respiration rate was -1.144 breaths per minute and the standard deviation of the difference was 1.722 breaths per minute.	218
Figure 6.12.	Data from Subject 4062 at 2.0 m. The top trace is the combined heart signal from the Doppler radar, the second trace is the combined respiration signal from the Doppler radar, the third trace is the ECG, and the bottom trace is the combined respiration signal from the straps.	219
Figure 6.13.	Heart and respiration rates from Subject 4062 at 2.0 m. The mean difference between the ECG heart rate and the Doppler heart rate was 0.786 beats per minutes and the standard deviation of the difference was 3.701 beats per minute. The mean difference between the strap respiration rate and the Doppler respiration rate was -0.306 breaths per minute and the standard deviation of the difference was 3.354 breaths per minute.	220
Figure 6.14.	Bland-Altman plot of heart rate measured with Doppler radar at 0.5 m range and ECG, for all subjects.....	221
Figure 6.15.	Bland-Altman plot of heart rate measured with Doppler radar at 1.0 m range and ECG for all subjects.	222
Figure 6.16.	Bland-Altman plot of heart rate measured with Doppler radar at 1.5 m range and ECG for all subjects	223
Figure 6.17.	Bland-Altman plot of heart rate measured with Doppler radar at 2.0 m range and ECG for all subjects.	224
Figure 6.18.	Bland-Altman plot of respiration rate measured with Doppler radar at 0.5 m range and respiratory effort belts for all subjects.	226
Figure 6.19.	Bland-Altman plot of respiration rate measured with Doppler radar at 1.0 m range and respiratory effort belts for all subjects.	227
Figure 6.20.	Bland-Altman plot of respiration rate measured with Doppler radar at 1.5 m range and respiratory effort belts for all subjects.	228
Figure 6.21.	Bland-Altman plot of respiration rate measured with Doppler radar at 2.0 m range and respiratory effort belts for all subjects.	229

Figure 6.22.	Measured and predicted signal-to-noise ratio vs. range for heart measurements.....	232
Figure 6.23.	Measured and predicted signal-to-noise ratio vs. range for respiration measurements.....	232
Figure 6.24.	a) Scattergram of signal-to-noise ratio vs. chest circumference with a linear regression model for each range. The model for 0.5 m is: $SNR = -16 + 32c$ with R^2 of 0.13. The model for 1.0 m is: $SNR = -17 + 28c$ with R^2 of 0.28. The model for 1.5 m is $SNR = -5.3 + 12c$ with R^2 of 0.22. The model for 2.0 m is: $SNR = -5.9 + 11c$ with R^2 of 0.078. (SNR indicates the signal-to-noise ratio and c indicates the circumference in centimeters.) The chest circumference was measured at a full inhale. b) Grouped bar graph for the same data.....	240
Figure 6.25.	a) Scattergram of signal-to-noise ratio vs. waist circumference with a linear regression model for each range. The model for 0.5 m is: $SNR = -20 + 0.38c$ with R^2 of 0.16. The model for 1.0 m is: $SNR = -12 + 0.23c$ with R^2 of 0.18. The model for 1.5 m is $SNR = -5.6 + 0.13c$ with R^2 of 0.20. The model for 2.0 m is: $SNR = -3.6 + 0.092c$ with R^2 of 0.05. (SNR indicates the signal-to-noise ratio and c indicates the circumference in centimeters.) The waist circumference was measured at a full inhale. b) Grouped bar graph for the same data.....	241
Figure 6.26.	a) Scattergram of signal-to-noise ratio vs. chest depth with a linear regression model for each range. The model for 0.5 m is: $SNR = -17.83 + 1.43d$ with R^2 of 0.15. The model for 1.0 m is: $SNR = -15.87 + 1.15d$ with R^2 of 0.30. The model for 1.5 m is $SNR = -10.08 + 0.74d$ with R^2 of 0.45. The model for 2.0 m is: $SNR = -3.08 + 0.35d$ with R^2 of 0.053. (SNR indicates the signal-to-noise ratio and d indicates the chest depth in centimeters.) The chest depth was measured at a full inhale. b) Grouped bar graph for the same data.	242
Figure 6.27.	a) Scattergram of signal-to-noise ratio vs. height-waist circumference product with a linear regression model for each range. The model for 0.5 m is: $SNR = -11 + 16x$ with R^2 of 0.13. The model for 1.0 m is: $SNR = -7.7 + 10x$ with R^2 of 0.17. The model for 1.5 m is $SNR = -3.2 + 5.6x$ with R^2 of 0.18. The model for 2.0 m is: $SNR = -3.2 + 5.1x$ with R^2 of 0.08. (SNR indicates the signal-to-noise ratio and x indicates the height-waist circumference produce in square meters.) The waist circumference was measured at inhale. b) Grouped bar graph for the same data.	243
Figure 6.28.	Variation of respiration signal-to-noise ratio with gender.	244

Figure 6.29.	Scattergram of error vs. signal-to-noise ratio for heart and respiration. The error is defined as the standard deviation of the difference between the two measurements, and the signal-to-noise ratio is measured on the Doppler signal as described in Section 6.3.4.2. A linear regression is performed on the data; the model for the heart is $E=1.03 - 0.55*SNR$, with R^2 of 0.59. Model for respiration is $E= 2.86 - 0.20*SNR$, with R^2 of 0.42. In these models, E is the error and SNR is the measured signal-to-noise ratio. ...	246
Figure 6.30.	Respiration signal-to-noise ratio vs. range, with measured SNR and the theoretical SNR. The theoretical radar cross section-mean-squared motion product was decreased to a value of 100 mm^4 to match the data as closely as possible.	248
Figure 6.31.	Respiration signal-to-noise ratio vs. range, with measured SNR, corrected for dc-blocking filter attenuation, and the theoretical SNR. The theoretical radar cross section-mean-squared motion product was set to a value of 250 mm^4 to match the data as closely as possible.	249
Figure 6.32.	Theoretical SNR vs. range including near-field effects. The electric fields are calculated as if measured by a point source, with a 27-cm diameter uniformly illuminated circular antenna with a cosine distribution of electric field. At 0.5 m, there is a 1 dB reduction in gain, and at 1.0 m, there is a 0.25 dB reduction in gain. This calculation uses a RCS-RMS motion product of 100 mm^4 . (RCS indicates the radar cross sectional area.).....	253
Figure 7.1:	Sample heart and respiration traces measured with the hybrid radio at a 50 cm range shown in (a) the time domain and (b) the frequency domain. The heart signal was separated from the respiration signal with an analog high-pass filter with a 1-Hz cutoff. The top trace in both the time and frequency domain representations is the superimposed heart and respiration signals, and the bottom trace is the isolated heart signal. Before filtering, the heart signal is approximately 20 dB below the respiration signal, and after the filter, it is about 10 dB above the respiration signal.	261
Figure 7.2:	Comparison of 400-order Kaiser filters with cutoff of 0.9 Hz. The parameter β is varied between 2 and 8, trading off the steepness of the cutoff with the height of the sidelobes. The steeper the cutoff, the higher the sidelobes.	266
Figure 7.3:	Sampling, windowing, and Fourier transformation of a signal.	275

Figure 7.4:	Comparison of rectangular, triangular, Hanning, and Hamming 64 sample window functions in a) time and b) frequency space. The frequency is normalized to f_s/N , where f_s is the sample frequency and N is the number of samples in the window.....	277
Figure 7.5:	Digital signal processing flow.....	280
Figure 7.6:	Frequency response of the digital filter used to isolate the heart signal from the respiration signal. For a 100 Hz sample rate, this 600-order Kaiser filter has the value of β set to 6.5 and a 3-dB cutoff frequency of 0.675 Hz, or 40.5 beats per minute. The amplitude is below 40 dB at frequencies below 0.315 Hz, or 18.9 breaths per minute, and below 60 dB at frequencies below 0.265 Hz, or 15.9 breaths per minute.....	282
Figure 7.7:	Frequency response of the digital filter used to decrease out-of-band noise. For a 100 Hz sample rate, this 20-order Kaiser filter has the value of β set to 6.5 and a 3-dB cutoff frequency of 20 Hz.	282
Figure 7.8:	Time domain data from subject 4062 at a 50-cm range, before and after filtering.....	287
Figure 7.9:	Frequency domain data from subject 4062 at a 50-cm range, before and after filtering. The respiration component is at 0.20 Hz, the heart fundamental is at 0.78 Hz, and the first harmonic of the heart signal is at 1.56 Hz.	288
Figure 7.10:	Time domain data from subject 4665 at a 50-cm range, before and after filtering.....	289
Figure 7.11:	Frequency domain data from subject 4665 at a 50-cm range, before and after filtering. The respiration component is at 0.27 Hz, the fundamental of the heart signal is at 1.12 Hz, and harmonics of the heart signal are at 2.25 Hz and 4.49 Hz.	290
Figure B.1.	Spectra of a real cosine signal and an imaginary sine signal when represented in complex notation.	319
Figure B.2.	For the real signal, $x_r(t)$, to be multiplied by a complex exponential with only a negative frequency component, $l(t)$, the signal must be split and mixed with local oscillator signals to determine the in-phase component, $y_I(t)$, and the quadrature component, $y_Q(t)$. The LO signal on the Q channel is delayed by 90° before mixing. The two components can be summed to create the output: $y(t) = y_I(t) + jy_Q(t)$	320

Figure B.3.	RF and image signals in a heterodyne receiver. When a real signal is mixed with a real cosine signal, and the LO is not in the RF signal band, the RF signal and the image frequency are both mixed to the intermediate frequency. A pre-selection filter that attenuates the image signal must be used to obtain the desired signal without interference from the image. This often requires a high IF, since the image frequency is the RF frequency minus double the IF.	325
Figure B.4.	RF and image signals in an image-reject architecture. When a real signal is mixed with a complex exponential, the RF and image signals continue to occupy separate places in the spectrum.	326
Figure B.5.	Hartley heterodyne image rejection architecture. This design uses quadrature channels, with a 90° phase shift on the quadrature channel before the in-phase (I) and quadrature (Q) channels are summed, eliminating the image signal.	327
Figure B.6.	Weaver heterodyne image rejection architecture. This design uses two downconversions to reach baseband, with a cosine LO used for the two downconversions on the in-phase (I) channel and a sine LO used for both downconversions on the quadrature channel. The two channels are summed to eliminate the image.	328
Figure B.7.	Self-image problem with a direct-conversion receiver. If a quadrature receiver is not used, both the positive and negative frequency components are down-converted to baseband, where they can interfere with each other.	329
Figure B.8.	Avoiding the self-image problem with a quadrature direct-conversion receiver. When the RF signal is mixed with a complex exponential, only the positive or the negative band is converted to baseband, avoiding the interference problem.	330
Figure C.1.	The dc offset due to self-mixing vs. the phase delay in radians. The I signal's dc offset is the solid line, and the Q signal's dc offset is the dotted line.	340
Figure C.2.	Distances to moving and stationary parts of the subject and the chair. ...	341
Figure C.3.	Phases calculated with and without dc offset removed, for a 2.4 GHz carrier.	348

Figure C.4.	Data from subject 4665, showing the I and Q channels, the combined channels using the arctangent technique after the dc offset was removed and the combined channels after the dc value was shifted to avoid zero-crossings. The top four traces are the respiration signal, and the bottom four traces are the heart signal.....	354
Figure C.5.	Phases calculated with dc offset removed and with dc offset shifted to avoid zero-crossings, for a 2.4 GHz carrier.	356
Figure D.1.	Illustration of power, effective radiated power, and power density at various points in the Doppler radar system. P_T is the transmitted power, G is the antenna gain, R is the distance between the target and the antenna, α is the attenuation, σ is the radar cross section, and λ is the wavelength of the RF signal. These equations assume that the target and antenna are sized such that they are in the far-field at the range of measurement.....	362
Figure D.2.	Equivalent circuit representation of the radar equation, after [249].	363
Figure D.3.	Radar cross section of a perfectly conducting sphere as a function of its electrical size, ka . After [249].	365
Figure D.4.	Transmission and reflection coefficients for dry skin in air vs. frequency.	368
Figure D.5.	Percentage of incident power reflecting from and transmitting through biological interfaces at 2.4GHz. The attenuation constant, α , and intrinsic impedance, η , of each material were taken from [250], and the thicknesses and the order of the materials were taken from [252].	369
Figure D.6.	Theoretical axial gain vs. range in the near-field for a 10 cm by 10 cm antenna with a cosine distribution of electric field. At 0.5 m, there is a 0.3 dB reduction in gain.	383
Figure E.1:	Anti-aliasing Sallen-Key lowpass filter configuration.	387
Figure E.2:	DC block and amplification circuit.....	388
Figure E.3:	Automatic gain control using diode voltage drops.	391

Figure E.4:	An automatic gain control (AGC) circuit using an analog to digital converter (8-bit ADC) to coarsely digitize the signal, digital signal processing (DSP) to calculate the amplitude and desired gain, and a digital to analog converter (DAC) to convert the desired gain to a voltage that controls the variable-gain amplifier (VGA).	392
Figure E.5:	Typical signal processing system. The dc portion of the signal is blocked before the fixed amplification. The variable gain amplifier (VGA) fine-tunes the amplification and the anti-alias filter removes out-of-band interference before the analog-to-digital converter (ADC) creates a digital signal for digital signal processing (DSP).	393
Figure E.6:	Configuration of SR560 preamplifiers for single-channel measurements.	394
Figure E.7:	Configuration of SR560 preamplifiers for quadrature measurements.	395
Figure E.8:	Configuration of two polarized capacitors to equal one non-polarized capacitor [264].	396
Figure E.9:	The overall signal conditioning configuration includes differential-to-single-ended conversion, followed by the dc block and fixed-gain stage, followed by the anti-aliasing filter and sometimes a variable gain stage. After signal conditioning, the signal is digitized with an analog-to-digital converter (ADC) and further processed with digital signal processing (DSP). ...	397
Figure E.10:	Simulated (a) and actual (b) frequency response of the Sallen-Key anti-aliasing filter of Figure E.1 with the values given in Table E.1.	398
Figure E.11:	Simulated (a) and measured (b) frequency response of the dc block and 40 dB amplification circuit.	400
Figure F.1:	Block diagram of the creation of the LO for a low-IF receiver for a next-generation Doppler radar cardiorespiratory monitoring system. The LO is the sum of the RF and IF frequencies.	404
Figure F.2:	Low-IF receiver architecture.	405
Figure F.3:	Digital signal processing for low-IF architecture to give baseband I and Q signals.	406

Figure H.1.	RF sideband spectrum, including phase noise and spurious noise. The phase noise spectrum is symmetrical about the oscillation frequency, indicating that phase noise, and not amplitude noise, is dominant in this oscillator. The peaks in the spectrum are spurious noise, indicating modulation by other signals.	416
Figure H.2.	Exaggerated depiction of phase noise in the time domain. The solid line is the perfect sinusoid in Equation H.1 and the dotted line is the sinusoid with phase noise in (H.3).	418
Figure H.3.	Measurement of single-sideband phase noise, $L(f)$	418
Figure H.4.	Example phase noise spectrum: a typical phase noise spectrum will have a $1/f_o^3$ dependence close to the carrier, a $1/f_o^2$ dependence beyond that, and be flat farther from the carrier.	420

Chapter
1

Non-Contact Cardio-Respiratory Monitoring

1.1 Introduction

Non-contact detection and monitoring of human cardiopulmonary activity through clothing and bedding could be a valuable tool in sleep monitoring and home health care applications. Patients with conditions that can be perturbed or worsened by contact sensors include neonates, infants at risk of sudden infant death syndrome, adults with sleep disorders, and burn victims; a non-contact heart and respiration rate monitor could provide vital signs monitoring without affixed electrodes for these patients. Most alternatives to standard heart and respiration monitors require contact and usually accurate control or placement, which may be impossible or undesirable in many situations. Additionally, a non-contact sensor could be used in situations where individuals need to move between measurement stations without the restriction of electrodes, leads, or cuffs; a vital signs monitor that can sense non-contact and through clothing would be ideal in these situations.

Microwave Doppler radar has been used to sense physiologic movement since the early 1970s [24]. The original work was done with bulky, heavy, and expensive waveguide components, limiting its use to research environments. Recent advances in microfabrication and in wireless technology have enabled integration of a Doppler radar transceiver on a single chip that is compact, lightweight, and inexpensively mass-producible. With smaller and less expensive circuitry, microwave Doppler radar measurement of

heart and respiration rates would be welcome in situations where electrode and chest-strap monitors cause discomfort or are difficult to apply. The potential low cost of the fully-integrated version makes home monitoring of infants and adults with sleep disorders or chronic illness an attractive market. Keeping costs down is critical for high-volume consumer markets. Two devices in the consumer home-monitoring market, the Angelcare Baby Nursery SIDS Monitor, which uses an under-the-mattress sensor, and the Sleep-tracker watch, which provides information about the wearer's sleep state, cost \$100 and \$150, respectively. This price range would be targeted for a home heart and respiration rate monitoring system using Doppler radar. Waveguide devices could not be used in this price range, so this market motivates the development of a single-chip version of this device.

Additionally, the use of multiple radar transceivers and MIMO (multiple-input, multiple-output) signal processing shows promise for overcoming problems with the Doppler sensor due to motion artifacts and multiple subjects in a sensing area [40]. This would enable measurements in clinical environments for neonates and burn patients, as well as in spacecraft for astronaut monitoring. The use of many transceivers would require that each transceiver be relatively inexpensive, which the fully-integrated version provides.

The silicon-based radar chips presented in this thesis are direct-conversion Doppler radar transceivers, operating at 1.6 and 2.4 GHz. Each has a single oscillator and output power comparable to the low-end power of consumer radio electronics (under 10 mW). The 2.4-GHz systems use a quadrature receiver to decrease the effects of null points and thus improve on the accuracy of the single-channel 1.6-GHz transceivers. One of the most critical challenges involved in integrating the microwave radar transceiver in a CMOS chip is the notoriously high level of phase noise of CMOS oscillators. Phase noise on the transmitted signal is translated to amplitude noise on the baseband output signal in the radar system. However, range correlation phase noise filtering [4] decreases the effect of phase noise sufficiently for an integrated oscillator to be used successfully in this system.

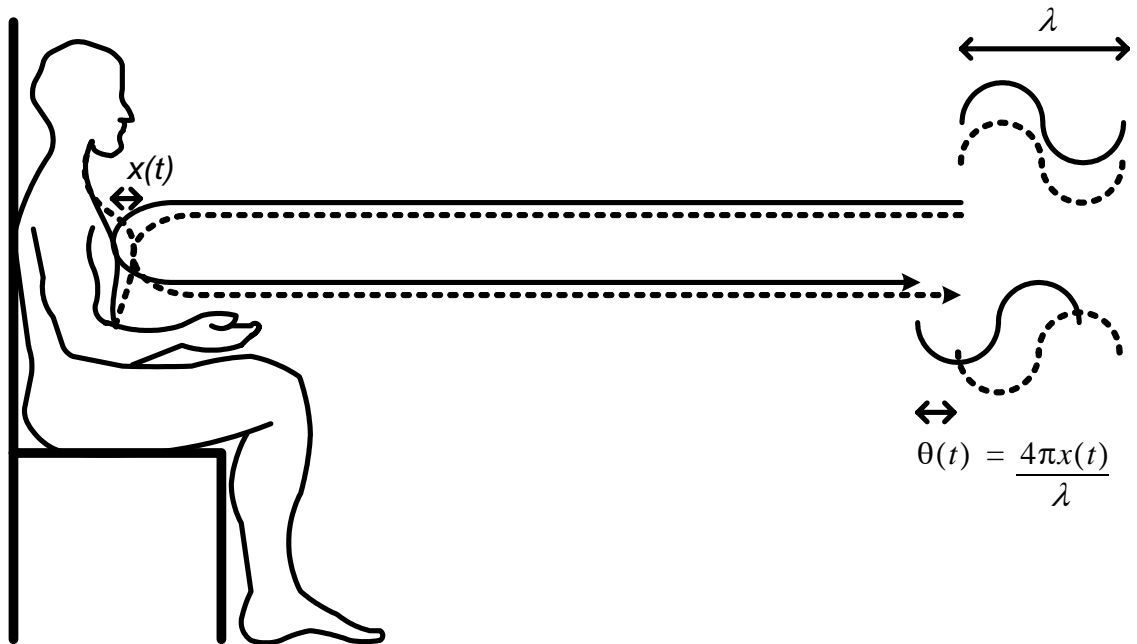


Figure 1.1: Block diagram of continuous wave radar for measurement of physiological motion. The phase of the reflected signal, $\theta(t)$, is directly proportional to the chest motion, $x(t)$, and is scaled by the wavelength, λ .

1.2 Radar Measurement of Physiological Motion

Doppler radar motion sensing systems typically transmit a continuous wave (CW) electromagnetic signal (sometimes frequency modulated) that is reflected off a target and then demodulated in the receiver. According to Doppler theory, a target with a time-varying position but no net velocity will reflect the signal, modulating its phase in proportion to the time-varying position of the target. A stationary person's chest has a periodic movement with no net velocity, and a CW radar with the chest as the target will therefore receive a signal similar to the transmitted signal, with its phase modulated by the time-varying chest position, as shown in Figure 1.1. Demodulating the phase will then provide a signal directly proportional to the chest position, which contains information about movement due to heartbeat and respiration, from which heart and respiration rates can be determined. Non-contact heart and respiration monitors have been developed based on this principle [24]. The peak-to-peak chest motion due to respiration in adults ranges

from 4 mm to 12 mm [9, 21], while the peak-to-peak motion due to the heartbeat is about 0.5 mm [35]. When the wavelength is greater than twice the peak-to-peak motion, the signal can be demodulated by simply multiplying the signal with an unmodulated signal from the same source. When the wavelength is less than twice the peak-to-peak motion, a quadrature receiver is required and more advanced signal processing must be used to accurately demodulate the signal. At 1.6 and 2.4 GHz, the wavelength is 18.75 cm and 12 cm respectively, so the wavelength is much greater than the chest motion for measurements made in this thesis. The tradeoffs with frequency are covered in detail in Chapter 2.

1.3 CMOS Radio and Microwave Circuits

1.3.1 Advances in the Integration of RF Circuits in CMOS

The demand for faster digital processors has driven development of smaller and faster silicon transistors. Thanks in part to these advances, today's bipolar and MOSFET devices are suitable for radio-frequency integrated circuits for wireless applications. BiCMOS technology offers both bipolar and MOSFET devices for circuit design, but the bipolar module increases the number of masks and the process cycle time, and therefore also the cost. The development of RF circuits in CMOS technology is less expensive and affords the opportunity to integrate RF and digital components on a single chip. Once considered unsuitable for RF circuits due to lower transconductance per bias current ratio, the increased device speed of CMOS technology compensates for some of its drawbacks. Designers continue to explore the technology advantages of CMOS, such as higher linearity and lower minimum noise figure than bipolar devices. More expensive substrates, such as GaAs, are sometimes used in high frequency circuits to reduce crosstalk, improve linearity, and reduce noise. However, the GaAs wafers are more expensive, and fabrication costs are greater because there are fewer foundries than there are for silicon and because advances are not made as quickly without the pressure of the large digital circuits market.

1.3.2 Advantages of Single-Chip Silicon Circuits

Single-chip circuits are small and lightweight in comparison to the waveguide microwave devices used in the past for radar systems. Although printed circuit board solutions for microwave designs are now common, the size and weight of the discrete microwave components is significantly greater than a single chip.

The major advantage of using silicon CMOS technology rather than other substrates and/or bipolar devices is the cost savings. Because this technology is used for digital electronics that are pervasive in today's society, modern foundries for chips are plentiful, and competition and high volume have led to cost reductions. The total cost of a chip is the sum of the design costs, the mask costs, the silicon costs and the backend costs. The number of masks and the complexity of processing affect both the wafer cost and yield [11]. The silicon cost is a function of the finished wafer cost, the yield, and the number of possible die per wafer, which depends on the size of the die and the wafer. The finished wafer cost depends on the raw wafer cost, the wafer processing cost, and the wafer test costs. Backend costs include everything after the wafer is probed: dicing, packaging, bonding, trimming, and testing. These are the critical factors in the total cost of a chip. In very high volume products that can be placed in inexpensive packages, the silicon cost is over three quarters of the packaged unit cost [10]. The finished silicon costs are significantly reduced by using a silicon substrate rather than more expensive silicon-germanium (SiGe) or gallium-arsenide (GaAs) substrates, and by using a common process with a low number of process steps, such as CMOS. A CMOS process uses about 30 masks, and adding bipolar devices to the process requires 4-5 additional masks. With 20% more masks and 20% more process steps, the wafer processing cost of a BiCMOS wafer can be roughly estimated to be about 20% more than for a pure CMOS wafer [28]. The cost differences between silicon substrates and GaAs substrates were discussed by Negus and Millicker in [32] in 1993. At that time, GaAs wafers cost between 20 and 50 times more than silicon wafers. In high volume production, the wafer size and yield are more important than the wafer cost, and both favor silicon.

Packaging is often a major factor in cost when reduced parasitic capacitances, resistances, and inductances are required, as is typically the case with radio and microwave circuits. Exposed pad packages, commercially available from Amkor Corporation, are designed for circuits up to 2.4 GHz. The exposed pad, on the back of the package, can be soldered directly to the printed circuit board, reducing the ground loop inductance, which improves performance in high frequency applications [1].

1.3.3 Challenges Posed by Integration of RF Circuits in Silicon

Recent advances in CMOS silicon technology focus on decreasing the cost of digital production, and therefore do not necessarily improve many of the limiting factors for RF electronics. Radio circuits require low noise, high linearity, and good passive components [23]. CMOS devices have excellent linearity, but are plagued with low-quality passive components and high $1/f$ noise.

The passive integrated components required for radio frequency designs are typically compromised by parasitic capacitances, inductances and resistances that are significant at radio frequencies, and they often take up a large percentage of the area on radio frequency die. Inductors are necessary in radio frequency designs, while they are not needed in most analog or digital integrated circuits. Manufacturing repeatability requires the use of on-chip planar spiral inductors, such as those shown in Figure 1.2. Analytical formulas that include parasitics exist for these inductors [30], which enables optimization of their design. However, even with an optimized design, the parasitics have a great effect on these inductors, limiting the achievable quality factor to between 5 and 10. (The quality factor, Q , is defined as the angular frequency multiplied by the ratio of the energy stored to the average power dissipated.) The quality factor for surface-mount discrete inductors is typically twenty or more times higher. A second type of passive component, the on-chip parallel plate capacitor, cannot avoid the substrate acting as an extra plate and therefore adding unwanted parasitic capacitance. Additionally, because the distance between metal layers does not change as technology scales, capacitor size does not scale with transistor size and the capacitors take up a greater proportion of the die area.

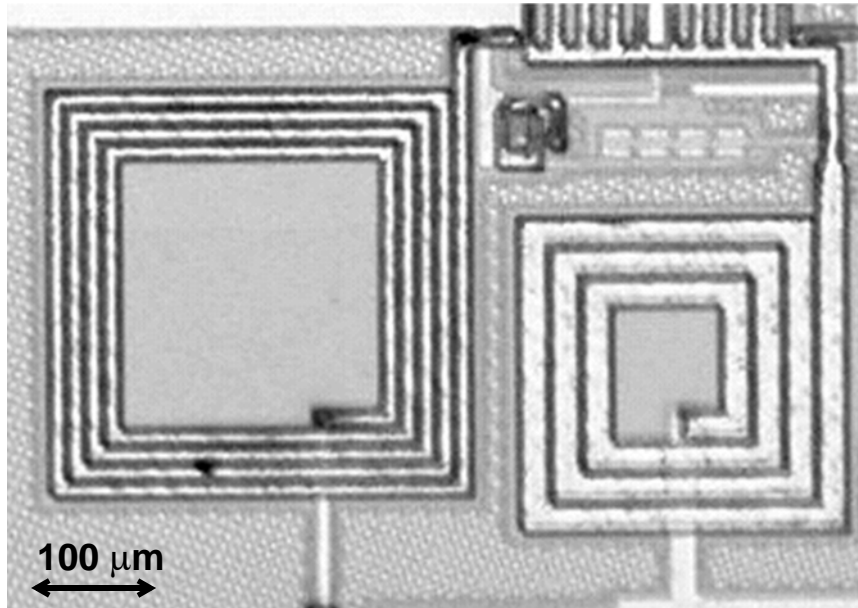


Figure 1.2: Two on-chip planar spiral inductors in an active balun of the 2.4 GHz radar transceivers. These spirals have outside diameters of 340 μm and 270 μm , and their respective inductances are 8 nH and 4 nH.

There is ongoing research in post-processing steps that can improve the quality of passive components [5, 22, 27, 38]. By etching to leave an air gap between the passive device and the substrate, substrate loss in inductors and parasitic capacitance to ground in capacitors can be greatly decreased, improving the quality factor of both types of passive devices. Simply etching the substrate beneath the passive device can be done with a single post-processing step [22] but results in a device that deforms with acceleration and temperature changes in ways that can cause significant changes in its electrical properties [25]. The best solution to ensuring robustness of suspended passive devices when faced with temperature changes and vibrations has not yet been determined, and most proposed solutions to these problems, including various supports and encapsulation, require at least 5 post-processing steps [6, 25], adding significant cost to the CMOS process. However, suspended passive devices may become a viable option in the future, once solutions to these challenges are reached.

The noise in CMOS transistors is dominated by $1/f$ noise from dc to tens of kilohertz [33]. MOSFETs exhibit significantly more $1/f$ noise than bipolar devices do. This noise

affects the radar system in two places: when it is upconverted to oscillator phase noise [23] and on the baseband output of the signal [29, 36]. Oscillator phase noise is the departure of the oscillator's output from a pure spectral tone, and is a particularly important parameter in this application because the desired information is encoded in the phase of the reflected signal. Low-quality passive components degrade the quality of the resonator, that sets the frequency for the oscillator, further increasing oscillator phase noise.

1.4 Motivation for a Single-Chip Radar Cardio-Respiratory Monitor

1.4.1 Benefits of Non-Contact Vital Sign Sensors

Non-contact sensors neither confine nor inhibit the subject with cables, and they do not cause discomfort or skin irritation with electrodes or straps. This makes the sensors more attractive for long-term continuous monitoring. Since the patient is unaware of the measurement, the patient is less likely to alter their respiration because they are being measured, as commonly occurs in face-mask respiration measurements. Additionally, there are no surface loading effects that might reduce the accuracy of the measurement, as has been shown to occur with magnetometer measurements [42].

1.4.2 Utility of Heart and Respiration Rate Measurements

Vital signs, including heart and respiration rates, are recorded regularly in both emergency and clinical situations. Several levels of information can be obtained by measuring the heart and respiration rates. First, the data can be used to verify that the subject is breathing and that the heart is beating. Respiratory rate and pattern are indicators of respiratory physiology, whereas an irregular pulse rate can indicate cardiac abnormality. The rates can be stored over time and trends can be noted, which can provide a valuable diagnostic tool. For example, the amount of increase in heart rate in response to apneic events indicates the level of tissue hypoxia associated with sleep apnea [39], and changes in heart and respiratory rates can indicate the sympathetic and parasympathetic responses to

trauma [13]. Heart-rate variability, which may predict disease states [41], can be assessed, and heart beat-to-beat times can be assessed to determine the presence of cardiac abnormalities such as an irregular beat-to-beat time, which can indicate atrial fibrillation [16]. The shapes of the heart and respiration signatures could potentially be used as an additional diagnostic tool; for example respiratory effort could be measured through the amount of motion.

Many factors add variability to the heart rate, including: circadian rhythm, which varies the heart rate over cycles of five hours or more, temperature regulation, which varies with about twenty-five-second cycles, cardiac sympathetic nervous activity, which varies with about six-second cycles, and synchronization with respiratory rhythm, which varies the beat-to-beat times with each breath [3, 41]. Because of different frequency responses between parasympathetic and sympathetic modulation of the heart, frequency analysis of heart rate variability can determine the balance between the sympathetic and parasympathetic nervous activity. The loss of heart rate variability can indicate severe cardiovascular diseases. Low heart rate variability has been shown to be a prognostic marker for several cardiovascular diseases, including diabetic neuropathy, hypertension, myocardial infarction, and heart failure [41]. Adding storage of heart rate over time and heart rate variability analysis to a Doppler radar heart and respiration rate monitor could provide additional diagnostic capability to the system.

1.4.3 Safety Considerations

An often-cited concern with the use of radar technology for long-term health monitoring is the potential danger that the radiation could pose to patients. However, the single-chip CMOS radar circuits emit radiation at a lower power than most consumer radio devices, and they are well within the FCC guidelines for operation in the 2.4-GHz unlicensed band. The Federal Communications Commission (FCC) Code of Federal Regulations (CFR), Section 15.427 [15] states that the maximum output power in the 2400-2435 MHz unlicensed band is one watt. For antenna gain greater than 6 dBi, the output power must be reduced by 1 dB for every 3 dB that the antenna gain exceeds 6 dBi.

Most consumer wireless devices that operate in this band have radio output powers between 10 mW and 300 mW, with some bluetooth devices transmitting as little as 1 mW. These devices typically have antenna gains near 3 dBi. The radar system developed in this thesis operates with an output power between 1 and 10 mW, at the low end of consumer wireless products, and has an antenna gain of about 6 dBi, about double that of consumer electronics. Given the similarity in the levels of radiation, this monitor poses no greater risk to humans than do 2.4-GHz infant monitors, wireless LAN, or cordless telephones.

1.4.4 Potential Applications of a Single-Chip Doppler Radar Cardio-Respiratory Monitoring System

Due to the sensitivity of this measurement modality to motion artifacts, relatively still subjects, such as hospitalized patients or sleeping subjects, are the most attractive targets. With the less expensive and smaller circuitry provided by silicon CMOS integration of the circuits, microwave Doppler radar could potentially be used in home monitoring, particularly for monitoring of sleep apnea in both infants and adults, where long-term monitoring using chest straps is often prescribed [14, 31]. Other applications include monitoring of astronauts at their sleep stations while in space and clinical patients that are difficult to place electrodes on, such as neonates and burn patients. With data from multiple transceivers and more advanced signal processing, motion artifacts may be removable, which would make the technology practical for additional applications that would benefit from a lightweight monitor that works through clothes, such as continuous monitoring of astronauts and first responders, or use in emergency vehicles or triage situations.

Additionally, the heart rate can be used to estimate energy expenditure [8, 19, 37]. This estimate is very accurate after individual calibration against VO_2 laboratory reading, and is 85% accurate when population-wide calibrations are used [19]. Estimates of energy expenditure are important for studies of obesity [19], dietary recommendations [19], assessment of athletic training [8], assessment of effectiveness of exercise for weight control [8], and for epidemiological studies of physical activity [37].

1.4.4.1 Sleep Disorder Monitoring

Although rates of Sudden Infant Death Syndrome (SIDS) have declined sharply in the past fifteen years, SIDS is still the third leading cause of infant mortality and the leading cause of postneonatal infant mortality [2, 17, 18]. In 2001, 8.1% of all infant deaths were caused by SIDS, affecting 55.5 of every 100,000 live births. Apparent life threatening events (ALTEs), defined as an episode that is characterized by some combination of apnea, color change, marked change in muscle tone, choking, or gagging, are experienced by 2.46 of every 1000 infants [20]. Apnea occurs in approximately 80% of newborns weighing less than 1000 g at birth, and 25% of infants weighing less than 2500 g or with less than 34 weeks' gestation at birth [12, 31]. Although home electronic surveillance does not reduce the risk of SIDS at this time, this may be due to limits of current home-monitoring devices, or high false negative rates. If obstructed breathing, central apnea, bradycardia, or oxygen saturation could be reliably detected, intervention could save infants' lives [18]. The Doppler radar device could detect central apneic events, where there is no respiratory motion, and bradycardia, where the heart rate slows. Doppler radar could be an integral part of a combination of sensors that could provide an accurate home SIDS monitor.

One of every five adults has at least mild Obstructive Sleep Apnea (OSA), and one of 15 has at least moderate OSA [44]. OSA has many negative effects, including excessive daytime sleepiness, increased risk of motor vehicle accidents, hypertension, psychological distress, and cognitive impairment [43, 44]. Apnea is the cessation of airflow for ten seconds or longer, and obstructive sleep apnea is apnea that occurs in spite of respiratory effort. To differentiate between central and obstructive apneic events, measurements of respiratory movement must be made in addition to measurements of airflow [34]. Current laboratory polysomnography is cumbersome, inconvenient and expensive, causing considerable interest in portable monitoring of the condition [34]. A Doppler radar monitoring system could identify respiratory movement, without the difficulties that accompany a full polysomnographic recording.

1.4.4.2 Clinical Applications

In the neonatal intensive care unit, infants often suffer skin damage from adhesive tapes, electrocardiogram electrodes, electroencephalogram electrodes, and transcutaneous monitors, with some lesions leaving scars [7]. Monitoring the cardiac state of burn victims can be challenging because it is sometimes difficult to find enough skin on which to apply an ECG electrode. Sometimes the electrode is stapled to the skin, or to an undebrided burn area [26]. Often esophageal ECG must be used because adequate skin area cannot be located. A wireless heart and respiration rate monitor could fill the needs for both neonates and burn victims, by enabling the monitoring of these vital signs without contacting the skin with ECG electrodes.

1.5 Contributions to the Art and Science of Non-Contact Cardio-Respiratory Monitoring

1.5.1 Theory of Doppler Radar for Cardio-Respiratory Monitoring

Some background on radar systems is presented along with radar system architecture options and tradeoffs in Chapter 2. Radar is introduced and a brief history of radar and its use in physiological monitoring is provided. Then design choices and the system theory required to make the choices is presented, including radar and receiver architecture, frequency, antenna gain, and transmit power. The transceiver design is also presented, including the configuration of the circuit blocks.

Skin surface motion due to heartbeat, pulses, and breathing is described along with techniques for measuring heart beat and respiration from this motion in Chapter 3. Surface motion measurements are compared with traditional methods of monitoring vital signs, and these are compared with Doppler radar measurement of heart and respiratory motion.

1.5.2 Single-Chip Doppler Radar Design

The designs of single-channel and quadrature transceivers are described in Chapter 4. This includes discussion of the technology leveraged from CMOS cellular base station transceiver designs, the design of the subcircuits, and the design of all the radar chips. The critical measurements for each subcircuit are presented along with discussion of how the designs help meet the goals and how designs could be improved in the future. The fabricated circuits are characterized, and their performance is discussed in the context of Doppler radar measurement of heartbeat and respiration.

1.5.3 Residual Phase Noise

One of the biggest challenges involved in using a silicon CMOS radar is the translation of oscillator phase noise, notoriously high in fully integrated CMOS oscillators, to output amplitude noise. When the same source is used for transmitting and receiving, the phase noise of the received signal is correlated with that of the local oscillator, with the level of correlation dependent on the time delay between the two signals. When the delay is small, this effect greatly decreases the noise power at baseband. In a radar application, this time delay is proportional to the target range. Hence, this phase noise reducing effect is known as range correlation [4]. Range correlation is particularly important in measuring chest wall movement since the heart and respiration information is encoded in phase modulations of 0.1 to 10 Hz, where the phase noise is near its peak. This will be discussed in Chapter 5.

1.5.4 Human Measurement

Doppler radar measurements of heart and respiration rates were compared with three-lead ECG measurements of heart rate and respiratory effort belt measurement of heart rate on 22 healthy subjects. This method and results of this measurement are described in Chapter 6. The theory of the variation of the signal-to-noise ratio with range and radar cross section is presented, followed by the actual variation over the 22 subjects.

1.5.5 Signal Processing Techniques

The signal processing techniques used to separate superimposed heart and respiration signals, to combine quadrature channels, and to determine the heart and respiration rates are described in Chapter 7. Although the output signals from each branch of the quadrature receiver theoretically can be combined to make one signal that is proportional to the phase modulation, removal of dc offsets and amplitude or phase imbalance between the two chains will greatly degrade the signal. Given these limitations, the arctangent technique, selection diversity, equal ratio combining, maximal ratio combining, and principal components combining are explored as possible techniques to combine the quadrature channels. Fixed filters can be used to separate the heart and respiration signatures, but then the rates must be found. For the ECG, peak times can easily be detected to determine the rates, but the Doppler signals do not have such a sharp peak, so many methods could be used. The fast Fourier transform, autocorrelation, and peak-finding are explored to find the heart rate.

1.5.6 Future Work and Future Applications

In Chapter 8, areas that could be improved in future versions of the single-chip transceiver are discussed, including architecture, circuit design, and signal processing. The use of multiple transceivers with MIMO signal processing is also discussed. Additional potential applications after MIMO signal processing has been used to remove motion artifacts and detect the cardio-pulmonary activity of multiple people in a measurement area, including emergency, clinical, and continuous monitoring.

1.6 References

- [1] Amkor Technologies, "Amkor ExposedPad L/TQFP Data Sheet," Amkor Technologies, West Chester, PA, Data Sheet DS231E, 2000.
- [2] E. Arias, M. F. MacDorman, D. M. Strobino, and B. Guyer, "Annual summary of vital statistics - 2002," *Pediatrics*, vol. 112, no. 6, pp. 1215-1230, 2003.

- [3] T. G. Buchman, P. K. Stein, and B. Goldstein, "Heart rate variability in critical illness and critical care," *Current Opinion in Critical Care*, vol. 8, no. 4, pp. 311-315, 2002.
- [4] M. C. Budge, Jr. and M. P. Burt, "Range correlation effects on phase and amplitude noise," in *Proceedings of IEEE Southeastcon*, 1993.
- [5] J. Y.-C. Chang, A. A. Abidi, and M. Gaitan, "Large suspended inductors on silicon and their use in a 2 μm CMOS RF amplifier," *IEEE Electron Device Letters*, vol. 14, no. 5, pp. 246-248, 1993.
- [6] Y.-S. Choi, E. Yoon, and J.-B. Yoon, "Encapsulation of the micromachined air-suspended inductors," in *IEEE MTT-S International Microwave Symposium Digest*, 2003, pp. 1637-1640.
- [7] P. B. Colditz, K. R. Dunster, G. J. Joy, and I. M. Robertson, "Anetoderma of prematurity in association with electrocardiographic electrodes," *Journal of the American Academy of Dermatology*, vol. 41, no. 3, pp. 479-481, 1999.
- [8] S. E. Crouter, C. Albright, and D. R. Bassett, Jr., "Accuracy of Polar S410 heart rate monitor to estimate energy cost of exercise," *Medicine and Science in Sports and Exercise*, vol. 36, no. 8, pp. 1433-1439, 2004.
- [9] A. DeGroot, M. Wantier, G. Cheron, M. Estenne, and M. Pavia, "Chest wall motion during tidal breathing," *Journal of Applied Physiology*, vol. 83, no. 5, pp. 1531-1537, 1997.
- [10] S. M. Domer, S. A. Foertsch, and G. D. Raskin, "Model for yield and manufacturing prediction on VLSI designs for advanced technologies, mixed circuitry, and memories," *IEEE Journal of Solid-State Circuits*, vol. 30, no. 3, pp. 286 - 294, 1995.
- [11] J. S. Dunn, D. C. Ahlgren, D. D. Coolbaugh, N. B. Feilchenfeld, et al., "Foundation of RF CMOS and SiGe BiCMOS technologies," *IBM Journal of Research and Development*, vol. 47, no. 2/3, pp. 101-138, 2003.
- [12] A. Erenberg, R. D. Leff, D. G. Haack, K. W. Mosdell, G. M. Hicks, and B. A. Wynne, "Caffeine citrate for the treatment of apnea of prematurity: A double-blind, placebo-controlled study," *Pharmacotherapy*, vol. 20, no. 6, pp. 644-652, 2000.
- [13] P. Fathizadeh, W. C. Shoemaker, C. C. J. Wo, and J. Colombo, "Autonomic activity in trauma patients based on variability of heart rate and respiratory rate," *Critical Care Medicine*, vol. 32, no. 6, pp. 1420-1421, 2004.

- [14] R. Ferber, R. Millman, M. Coppola, J. Fleetham, C. F. Murray, C. Iber, V. McCall, G. Nino-Murcia, M. Pressman, M. Sanders, K. Strohl, B. Votteri, and A. Williams, "Portable recording in the assessment of obstructive sleep apnea," *Sleep*, vol. 17, no. 4, pp. 378-392, 1994.
- [15] Federal Communication Commission, Code of Federal Regulations, Title 47: Telecommunications, Part 15: Radio Frequency Devices, 2000.
- [16] D. L. Gorgas, "Vital signs and patient monitoring techniques," in Clinical Procedures in Emergency Medicine 4th Ed. (J. R. Roberts and J. R. Hedges, Eds.), Philadelphia: Saunders, 2004, pp. 3-28.
- [17] D. L. Hoyert, M. A. Freedman, D. M. Strobino, and B. Guyer. "Annual summary of vital statistics: 2000," *Pediatrics*, vol. 108, no. 6, pp. 1241-1255, 2001.
- [18] C. E. Hunt and F. R. Hauck, "Sudden infant death syndrome," in Nelson Textbook of Pediatrics, 17th Ed. (R. E. Behrman, R. M. Kliegman and H. B. Jenson, Eds.), Philadelphia: Saunders, 2004, pp. 1380-1385.
- [19] R. J. Ianotti, R. P. Clayton, T. S. Horn, and R. Chen, "Heart rate monitoring as a measure of physical activity in children," *Medicine and Science in Sports and Exercise*, vol. 36, no. 11, pp. 1964-1971, 2004.
- [20] U. Kiechl-Kohlendorfer, D. Hof, U. P. Peglow, B. Traweger-Ravanelli, and S. Kiechl, "Epidemiology of apparent life threatening events," *American Academy of Pediatrics Grand Rounds*, vol. 90, no. 3, pp. 297-300, 2005.
- [21] T. Kondo, T. Uhlig, P. Pemberton, and P. D. Sly, "Laser monitoring of chest wall displacement," *European Respiratory Journal*, vol. 10, pp. 1865-1869, 1997.
- [22] C.-Y. Lee, Y.-H. Kao, J.-J. Luo, and K.-M. Chang, "The enhanced Q spiral inductors with MEMS technology for RF applications," in *Proceedings of the Asia Pacific Microwave Conference 2000*, pp. 1326-1329.
- [23] T. H. Lee and S. S. Wong, "CMOS and RF integrated circuits at 5 GHz and beyond," *Proceedings of the IEEE*, vol. 88, no. 10, pp. 1560-1571, 2000.
- [24] J. C. Lin, "Microwave sensing of physiological movement and volume change: A review," *Bioelectromagnetics*, vol. 13, no. 6, pp. 557-565, 1992.
- [25] J.-W. Lin, C. C. Chen, and Y.-T. Cheng, "A robust high-Q micromachined RF inductor for RFIC applications," *IEEE Transactions on Electron Devices*, vol. 52, no. 7, pp. 1489-1496, 2005.

- [26] S. Loo, T. Kuo, G. Waters, M. Muller, and T. L. H. Brown, "A mobile electrode for ECG monitoring," *Burns*, vol. 30, no. 2, p. 203, 2004.
- [27] J. M. Lopez-Villages, J. Samitier, J. Bausells, A. Merlos, C. Cane, and R. Knochel, "Study of integrated RF passive components performed using CMOS and Si micromachining technologies," *Journal of Micromechanics and Microengineering*, vol. 7, pp. 162-164, 1997.
- [28] W. Maly, "Cost of silicon viewed from VLSI design perspective," in *Proceedings of the ACM/IEEE Design Automation Conference*, 1994, pp. 135-142.
- [29] M. Margraf and G. Boeck, "Analysis and modeling of low-frequency noise in resistive FET mixers," *IEEE Transactions on Microwave Theory and Techniques*, vol. 52, no. 7, pp. 1709-1718, 2004.
- [30] S. S. Mohan, M. del Mar Hershenson, S. P. Boyd, and T. H. Lee, "Simple accurate expressions for planar spiral inductance," *IEEE Journal of Solid State Circuits*, vol. 34, no. 10, pp. 1419-1424, 1999.
- [31] National Institutes of Health, "Infantile Apnea and Home Monitoring", *NIH Consensus Statement*, vol. 6, no. 6, 1986.
- [32] K. J. Negus and D. Millicker, "RFICs for reduced size, cost, and power consumption in handheld wireless transceivers," in *Proceedings of the International Conference on Universal Personal Communications*, 1993, pp. 919-925.
- [33] Y. Nemirovsky, I. Brouk, and C. G. Jakobson, "1/f noise in CMOS transistors for analog applications," *IEEE Transactions on Electron Devices*, vol. 48, no. 5, pp. 921-927, 2001.
- [34] B. A. Phillips, M. I. Anstead, and D. J. Gottlieb, "Monitoring sleep and breathing: Methodology; Part I: Monitoring breathing," *Clinics in Chest Medicine*, vol. 19, no. 1, pp. 203-212, 1998.
- [35] G. Ramachandran and M. Singh, "Three-dimensional reconstruction of cardiac displacement patterns on the chest wall during the P, QRS, and T-segments of the ECG by laser speckle interferometry," *Medical and Biological Engineering and Computing*, vol. 27, no. 5, pp. 525-530, 1989.
- [36] W. Redman-White and D. M. W. Leenaerts, "1/f noise in passive CMOS mixers for low and zero IF integrated receivers," in *Proceedings of the European Solid State Circuits Conference*, 2001, pp. 41-44.

- [37] K. L. Rennie, S. J. Hennings, J. Mitchell, and N. J. Wareham, "Estimating energy expenditure by heart-rate monitoring without individual calibration," *Medicine and Science in Sports and Exercise*, vol. 33, no. 6, pp. 939-945, 2001.
- [38] R. P. Ribas, J. Lescot, J.-L. Leclercq, J. M. Karam, and F. Ndagijimana, "Micromachined microwave planar spiral inductors and transformers," *IEEE Transactions on Microwave Theory and Techniques*, vol. 48, no. 8, pp. 1326-1335, 2000.
- [39] H. Saito, M. Nishimura, E. Shibuya, H. Makita, I. Tsujino, K. Miyamoto, and Y. Kawakami, "Tissue hypoxia in sleep apnea syndrome assessed by uric acid and adenosine," *Chest*, vol. 122, no. 5, pp. 1686-1694, 2002.
- [40] D. Samardzija, O. Boric-Lubecke, A. Host-Madsen, V. M. Lubecke, T. Sizer, A. D. Droitcour, and G. T. A. Kovacs, "Applications of MIMO techniques to sensing of cardiopulmonary activity," in *Proceedings of the IEEE/ACEES International Conference on Wireless Communications and Applied Computational Electromagnetics*, 2005, pp. 618-621.
- [41] H. Stauss, "Heart rate variability," *American Journal of Physiology: Regulatory, Integrative, and Comparative Physiology*, vol. 285, no. 5, pp. R927-R931, 2003.
- [42] H. Vermarien and E. van Vollenhoven, "The recording of heart vibrations: a problem of vibration measurement on soft tissue," *Medical and Biological Engineering and Computing*, vol. 22, no. 2, pp. 168-178, 1984.
- [43] A. N. Vgontzas and A. Kales, "Sleep and its disorders," *Annual Review of Medicine*, vol. 50, no. 1, pp. 387-400, 1999.
- [44] T. Young, P. E. Peppard, and D. J. Gottlieb, "Epidemiology of obstructive sleep apnea: A population health perspective," *American Journal of Respiratory and Critical Care Medicine*, vol. 165, no. 9, pp. 1217-1239, 2002.

Chapter
2

Background

2.1 Radar Introduction and History

2.1.1 Radar Introduction

Radar, an acronym for RAdio Detection And Ranging, describes a system that transmits an electromagnetic signal and senses the echo from reflecting objects, thereby gaining information about those objects. The time delay between the transmitted and received signals indicates the distance to the target, the frequency shift of the received signal enables calculation of the target's velocity, and the strength of the signal gives information about the target's radar cross section, which provides information about its size, geometry, and composition. A major advantage of radio and microwave frequency radar systems is that these waves can penetrate through some objects that light cannot penetrate, allowing detection of objects that cannot be seen. However, radar systems developed for different applications may operate at many different frequencies, varying from a few MHz to optical frequencies.

As shown in Figure 2.1, a radar system typically consists of a transmitter, an antenna, a receiver, and signal processing hardware and/or software [74]. The transmitter creates a waveform and amplifies it to the required transmission power. A directional antenna both concentrates the beam in the direction of the target and enables determination of the direction of the target; electronically tunable antenna arrays are often used for this purpose. The receiver converts the signal from the transmission frequency to either an intermediate frequency or baseband, separates the signal from both noise and interferers, and amplifies the signal enough for digitization and/or display. Signal processing is used to reject clutter and

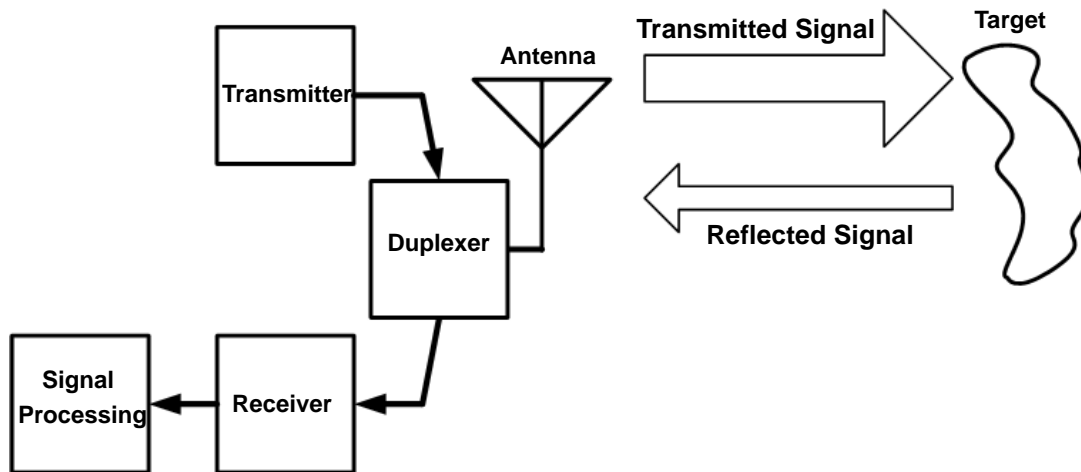


Figure 2.1. Single-antenna radar system block diagram. A radar system consists of a transmitter, an antenna, a receiver, and signal processing hardware. A portion of the transmitted signal is reflected by the target, and a portion of the reflected signal is received by the radar receiver. The received signal is then processed to determine information about the target.

out-of-band noise, while passing the desired signal, and to derive information from the signal.

Depending on the radar system hardware and the type of signal sent, it may be possible to detect the range and/or angle to the target, the size and shape of the target, and the linear and/or rotational velocity of the target [74]. Depending on which of these parameters is most important to sense, as well as the range to and the nature of the target, different radar topologies may be used. A pure continuous-wave (CW) system can readily detect moving targets via the Doppler shift of the received signal, although it cannot detect the range; CW systems are commonly used when the rotational velocity of the target needs to be detected. Police radar systems typically sense the speed of cars with pure CW radar systems because they are difficult to detect and interfere with [71]. Frequency-modulated continuous-wave (FMCW) radar systems can detect both the range to and the velocity of the target. Altimeters and Doppler navigation devices use FMCW radar systems [71]. Pulsed radar allows transmitting and receiving to occur at different times, and it is used when the return signal is much smaller than the transmitted signal and therefore difficult to

sense the received signal in the presence of the transmitted signal. Pulsed radar is also useful when the peak power of the transmitted signal needs to be much higher than the average power [74]. There are three major groups of pulsed radar: pulse compression radar, moving target indicator (MTI) radar, and pulse Doppler radar. The information that can be sensed with radar systems, how it is detected, and the system topology requirements are listed in Table 2.1.

Table 2.1. Information Available from Different Topologies of Radar Transceiver.

Information	Method of Determination	Required Topology
Range	Time Delay	Any but CW; must have sufficient range resolution
Velocity	Doppler Shift	Any; pulsed systems must have sufficient velocity resolution
Angle	Direction of Reflection	Any; must have directive receiving antenna (or antenna array)
Size and Shape	Received Power	Any but CW; must be high resolution
Radial Velocity	Doppler Shift and Time Delay	CW

2.1.2 A Brief History of Radar

Radar systems were originally developed for military applications including surveillance and weapon control. Radar now has many civil applications, including navigation of aircraft, ships, and spacecraft, remote sensing of the environment (including weather), and law enforcement.

The use of electromagnetic waves was pioneered by Maxwell, who developed the equations governing electromagnetic waves in 1864, and Hertz, who first demonstrated the transmission and reflection of radio waves in 1886 [67]. The use of reflected electromagnetic waves to detect objects was not explored until the 1920s, when the Doppler effect, which was described by Christian Andreas Doppler in 1842 [53], was used to detect moving objects. During this period, Dr. A. Hoyt Taylor of the Naval Research Laboratory developed a radar for ship tracking that was first installed on a ship in 1937 [74]. In 1924, Sir Edward Victor Appleton used what is now known as FMCW radar to prove the exist-

ence of and measure the distance to the ionosphere. The ionosphere is considered the first object detected by radar [67]. Sir Robert Alexander Watson Watt of Britain developed a radar system to detect storms while working at the British Meteorological Office. In 1935, Sir Watt developed a radar system for detecting enemy aircraft before they were visible, and he received a patent for the first pulsed radar system [67]. By 1939, Britain had a chain of radar stations along its coasts to detect enemy arrivals by air and by sea, which was instrumental in the second world war [67]. During World War II, imaging radars and sweep displays were developed [74].

After the war was over, civilian uses of radar began to proliferate. In the 1950s, the first weather imaging radar systems were developed. In the 1960s, a network of Doppler weather radar systems, known as NexRad, was installed to observe rainfall rate, mean radial velocity, and the spread in wind speed [73]. In the 1960s, the Federal Aviation Administration began to build radar systems for air route surveillance. More recently, airborne weather avoidance radar has used Doppler information to indicate turbulence, windshear and downbursts to commercial airline pilots. Wind profiling uses FMCW radar to detect both the velocity and the location of the wind shifts [73].

Continuous-wave (CW) radar systems are blind to stationary or slow-moving clutter, detecting only the moving objects. This makes them useful for detecting low-flying aircraft, which are lost in clutter with pulsed radar systems. The low-altitude Hawk radar system, first developed in the 1960s, uses CW radar to detect moving targets amidst clutter [71]. CW radar systems are commonly used for target illumination, such as in semi-active radar-homing air-to-air missiles. Additionally, continuous-wave radar has a low probability of detection since it has a very narrow bandwidth.

2.1.3 History of Radar in Physiological Monitoring

Since CW radar systems are well-suited for measuring motion near stationary clutter, these systems are a natural choice for measuring motion due to heartbeat and respiration. Microwave Doppler radar monitoring of respiratory and cardiac movements was first

demonstrated in the late 1970's, when respiration [57, 58] and heart beats [59] were measured separately, with a breath-hold required for the heart measurement [59]. X-band sweep oscillators were used, with horn antennas directing the microwave energy toward the upper torso of the subjects. Lin, in [57], measured a non-anesthetized rabbit's respiration from 30 cm. In [58], the same system was used with an apnea-detector circuit, and was tested on a rabbit and two cats, all of which were anesthetized and intubated. Both hyperventilation and apnea were induced in the animals, and both states were clearly detected by the microwave monitor. Microwave apexcardiography was demonstrated by Lin, et al. in [59]; a continuous-wave 2-GHz microwave antenna was placed 3 cm above the apex, and the precordial motions were easily detected.

From the mid-1980's through the late 1990's, radar transceivers were developed that incorporated analog and digital signal processing to separate the small heart signal from the much larger respiration signal, so the subject did not need to hold his/her breath for the heart rate to be measured, and heart and respiration could be measured simultaneously [50, 51, 52, 54, 72]. These transceivers were used for the detection of heart and respiration rates of persons in rubble, persons behind walls, and olympic athletes. Chan and Lin [50] combined analog amplification and filtering for separation of heart and respiration signatures with 8-bit digitization and digital signal processing to detect heart and respiration rates. An automatic clutter-cancellation circuit was developed by Chuang, et al., facilitating measurement of the heart and respiration signatures through seven layers of brick [52] and through ten feet of rubble [51]. Heart and respiration rates of athletes were successfully detected at ranges exceeding 10 m by Greneker et al [54]; at 100 m, the limit was moving background clutter, not the system sensitivity. A quadrature receiver was used to avoid phase-demodulation null points by J. Seals, et al. [72].

Recently, Matsui, et al. have proposed Doppler radar vital signs monitoring to detect hypovolemic states and shock in persons under rubble or in biochemical hazard conditions that could pose danger to health care providers [61, 62]. Hypovolemic rabbits and rabbits in shock could be reliably distinguished from the control rabbits based on the Doppler radar information by using linear discriminant analysis on the heart and respiration rates.

The hypovolemic rabbits have higher heart and respiration rates. Matsui, et al. have also estimated arterial blood pH without contact using Doppler radar heart and respiration rate monitoring coupled with an infrared thermographic temperature measurement and an exhaled gas (CO and CO₂) analyzer [64]. This measurement was successful at estimating blood pH using linear regression analysis on hypovolemic rabbits.

There has been additional recent work in connecting this technology to the existing wireless communications infrastructure [48, 49, 60]. A modified wireless LAN PCMCIA card was used to detect heart and respiration by Boric-Lubecke, et al. [49], and a module that combines the transmitted and reflected signals from any wireless communication device, such as a cordless telephone, was used to detect heart and respiration by Lubecke et al. [60]. Using this technology to directly connect Doppler measurement of heart and respiration rate to health care providers has been proposed [48].

Additionally, ultra wideband radar has been used for measurement of heart and respiration rates. Using 0.4-W pulses and a 1-GHz central frequency, heart rates were detected through 1 m of air and a 0.4-m brick wall [55] and respiration was measured at up to 5 m [65].

The works are described briefly in Table 2.2 with the year of publication, reference, description and results.

Table 2.2. Doppler Radar Measurements of Physiological Motion

Year	Reference	Description	Results
1975	Lin [57]	X-band sweep oscillator, rectangular horn antenna	Respiration measured on rabbit and human at 30-cm range
1977	Lin et al. [58]	Microwave apnea detector proposed for low-birth-weight infants 3 mW at 30 cm, 3 cm by 3 cm horn	Respiration measured on cats and rabbit at 30-cm range Detection of apnea and hyperventilation
1979	Lin et al. [59]	“Apexcardiography” heart measurements made while breath held Signal amplitude and phase vary with antenna location	Heart measurement made 3 cm from apex

Table 2.2. Doppler Radar Measurements of Physiological Motion

Year	Reference	Description	Results
1986	Seals et al. [72]	Analog signal processing separates heart and respiration signs Digital rate detection algorithm 10-GHz and 3-GHz quadrature radar systems	Measured heart and respiration simultaneously with digital rate detection algorithm
1987	Chan and Lin [50]	Heart and respiration separated with analog and digital signal processing: amplification, filtering, 8-bit ADC sampled at 80 Hz 10.5-GHz, 10-mW, horn antenna a few cm from subject	Heart and respiration obtained simultaneously at 5-7-cm range
1990	Chuang et al. [52]	Heart and respiration for detecting victims in clutter 10-GHz system does not penetrate wet bricks, but 2-GHz system does. Automatic clutter cancellation algorithm introduced	Successful measurement with subject both face-up and face-down, through 4 to 7 layers of brick, with 2-GHz and 10-GHz radar systems
1997	Greneker [54]	0.6-m dish aimed at subject's thorax 24-GHz, 30-mW output signal, 40-dB antenna gain	Heartbeat and respiration measured at ranges exceeding 10 meters
2000	Chen et al. [51]	Life-detection system for victims under rubble or behind barriers including 6' of steel, bricks, and cinder blocks Heart and respiration were measured.	450-MHz signal penetrates deepest into concrete rubble without metal 1150-MHz signal penetrates rubble with metallic wire mesh
2001	Arai [46]	1.2-GHz, 70-mW quadrature superheterodyne receiver operates CW and pulsed CW system used to detect breathing, pulse used to detect location in 1.5-m rubble.	Breathing identified through rubble and collapsed house
2002	Lubecke et al. [60]	Add-on module uses signals from existing wireless devices to measure heart and respiration rates	Heart and respiration were measured with a 2.4-GHz cordless phone and a 2.4-GHz signal generator
2003	Boric-Lubecke et al. [49]	Modified wireless LAN PCMCIA cards are used to sense heart and respiration rates	Heart and respiration were obtained successfully at 40 cm
2004	Matsui et al. [61, 62]	Determining hypovolemic and shock states using linear discriminant analysis. Heart and respiration rates of hypovolemic rabbits 1215 MHz, 70-mW output power	Linear discriminant analysis effectively predicted hypovolemic state of 10 rabbits.
2004	Ossberger et al. [65]	Ultra wideband pulse radar Wavelet signal processing	Respiration measured at 1-5 m and through a wall at 85 cm

Table 2.2. Doppler Radar Measurements of Physiological Motion

Year	Reference	Description	Results
2005	Immoriev and Sakov [55]	Ultra wideband radar, 1-GHz central frequency	Measured respiration through 1-m air and 0.4-m brick wall on one subject.
2005	Matsui et al. [63]	Used 1215-MHz radar to detect RR-intervals well enough for heart-rate-variability studies	Detect peaks from Doppler radar signal to measure heart rate variability on one subject.
2006	Matsui et al. [64]	Used 1215-MHz radar, infrared thermography, and exhaled CO/CO ₂ analyzer to estimate blood pH	Significant correlation of measured and calculated blood pH on rabbits.

2.2 Design Choices for Cardiorespiratory Monitoring with Doppler Radar

When monitoring motion due to heartbeat and respiration with Doppler radar, the associated noise is primarily residual phase noise and baseband noise. The receiver should maximize the ability to discriminate between the physiological signals and these noise sources. In a Doppler radar for monitoring cardiopulmonary motion, there are trade-offs between several parameters, including signal-to-noise ratio, cost, weight, size, and bandwidth, which need to be weighed when making design choices at all levels of system architecture. This chapter explores the trade-offs presented in various system architecture choices, provides justification for the choices made, and describes the choices that were selected for experimental evaluation.

The first architectural decision is the radar configuration. The two main categories are pulsed and continuous wave, each of which has advantages and disadvantages for different applications. For Doppler cardiopulmonary monitoring, measurement of motion is critical and measurement of the range to the target is not; therefore a continuous-wave radar topology is chosen, as discussed in Section 2.2.1. Next the receiver architecture must be determined; the choice is between a heterodyne receiver with an intermediate frequency stage and a homodyne receiver that converts the signal directly to baseband. Factors in the choice of receiver for an integrated design include filtering requirements,

circuit complexity, die size and noise levels; these correspond to trade-offs between cost and signal quality. The homodyne receiver is the simplest and least expensive architecture, and this was chosen in spite of some of the challenges it poses, as described in Section 2.2.2. The third design choice is the detector portion of the receiver architecture. A quadrature receiver provides an improvement in phase demodulation over a single-channel receiver at the price of additional die size (which corresponds to a cost increase) and increased power consumption. The trade-offs are described in detail in Section 2.2.3, and both receiver topologies are explored in this work.

After the topology is determined, the frequency and power of the transmitted signal need to be selected, as well as the antenna. The optimal frequency of operation of the transceiver is explored in Section 2.2.4. While operating within FCC regulations, trade-offs include reflectance, signal-to-noise ratio, production cost and antenna size. The choice of an antenna is discussed in Section 2.2.5 and the choice of transmit power is discussed in Section 2.2.6.

2.2.1 Continuous-Wave Radar vs. Pulsed Radar

A continuous-wave radar system transmits and receives a very narrow bandwidth signal. A pulsed radar system switches between transmitting and receiving, and the signal has a somewhat wider bandwidth because of the pulses. This section describes the trade-offs between these topologies and why a CW radar was chosen for Doppler radar cardiorespiratory monitoring. Then the theory of CW radar monitoring is introduced to set the stage for other architecture choices.

A continuous-wave radar has a simple topology, consisting of a signal source that can be used for both transmitting and receiving and either a heterodyne or homodyne receiver [71]. Since the CW system constantly transmits and receives, there is no need for a transmit/receive switch, as is required in a pulsed radar system. The extremely narrow-band nature of the CW radar means that the filters at each stage of the receiver can be quite simple. Finally, the signal processing is straightforward if velocity or displacement

information is desired. The main system-level advantage of a pure CW radar system is that it can unambiguously measure the velocity of targets which are at any range and moving at any velocity; pulsed and other modulated systems have some ambiguity in both range and velocity measurements.

The biggest problems with CW radar are linked to its nature of constantly transmitting and receiving, which results in the inability to separate reflections temporally. A portion of the transmitted signal leaks from the transmitter to the receiver, either through coupling between the transmit and receive circuitry, or directly through the antenna(s) [70]. Additionally, clutter reflects some of the signal and its noise sidebands back to the receiver, adding to the signal power at the transmit frequency due to leakage. These unwanted signals result in a dc offset and low-frequency noise if they are not eliminated before the signal is detected.

A transceiver with a pulse repetition period longer than the round-trip signal path length transmits a burst of energy and then listens for echoes between transmissions. This means that leakage from the transmitter and strong echoes from short-range clutter are separated temporally from the weaker echoes of long-range targets; this is the main advantage of pulsed radar over CW radar. However, in Doppler monitoring of heart and respiration motion, the target is typically at the same or shorter range than the nearest clutter, so that the pulsed radar system's advantage is limited to the elimination of leakage. Another major advantage of pulsed radar is the ability to instantaneously measure target range, but since range measurements do not aid in Doppler monitoring of heart and respiration motion, this is not a factor in this application. The increased complexity of a pulsed radar over a continuous-wave radar does not result in a commensurate increase in benefits. For these reasons, a continuous-wave radar system is used in this work.

A continuous-wave (CW) radar topology is the simplest radar topology for two reasons: a single oscillator can be used for both the transmitter and the receiver, and the extremely narrow signal bandwidth avoids interference and eases filtering requirements. A pure CW radar system can measure targets at any range (subject to the signal-to-noise ratio) that are moving at any velocity (subject to the receiver bandwidth) without ambigu-

ity, unlike pulsed or modulated systems that have limited velocity resolution. Additionally, since the peak power of solid state transmitters is not much greater than their average power, the potential benefits of a pulsed radar are diminished when it is used in an integrated circuit. CW radar systems cannot detect range without modulation, and when modulated, the same range ambiguities found in pulsed radar systems are present.

When the goal of the measurement is target motion rather than distance to the target, a pure CW radar system is ideal. When the CW signal is directed at a target, it is reflected and frequency-modulated by the target motion. If the target is moving at velocity $v(t)$ in m/s, the frequency of the reflected signal is shifted by an amount known as the Doppler shift:

$$f_d(t) = \frac{2f}{c}v(t) = \frac{2(v(t))}{\lambda} \quad (2.1)$$

where f_d is the Doppler shift frequency in Hz, f is the transmitted frequency in Hz, c is the signal propagation velocity in m/s, t is the elapsed time in seconds, and λ is the wavelength of the transmitted signal in meters [71]. When the target undergoes a periodic movement $x(t)$ with no net velocity, the Doppler shift of the reflected signal can be better described as a phase modulation,

$$\theta(t) = \frac{2f}{c}(2\pi x(t)) = \frac{4\pi x(t)}{\lambda}. \quad (2.2)$$

When a person's chest is the target, as shown in Figure 2.2, the phase is modulated in direct proportion to the chest displacement. When the phase is demodulated, the resulting signal is proportional to the time-varying chest position, from which the heart and respiration rates can be determined.

Neglecting amplitude variations, a CW radar typically transmits a single tone signal,

$$T(t) = \cos(2\pi ft + \phi(t)) \quad (2.3)$$

where f is the oscillation frequency and $\phi(t)$ is the phase noise of the oscillator. Phase noise is described in more detail in Appendix H, but it is considered here as a random fluctuation in the signal's phase. If the transmitted signal is reflected by a target at a nominal

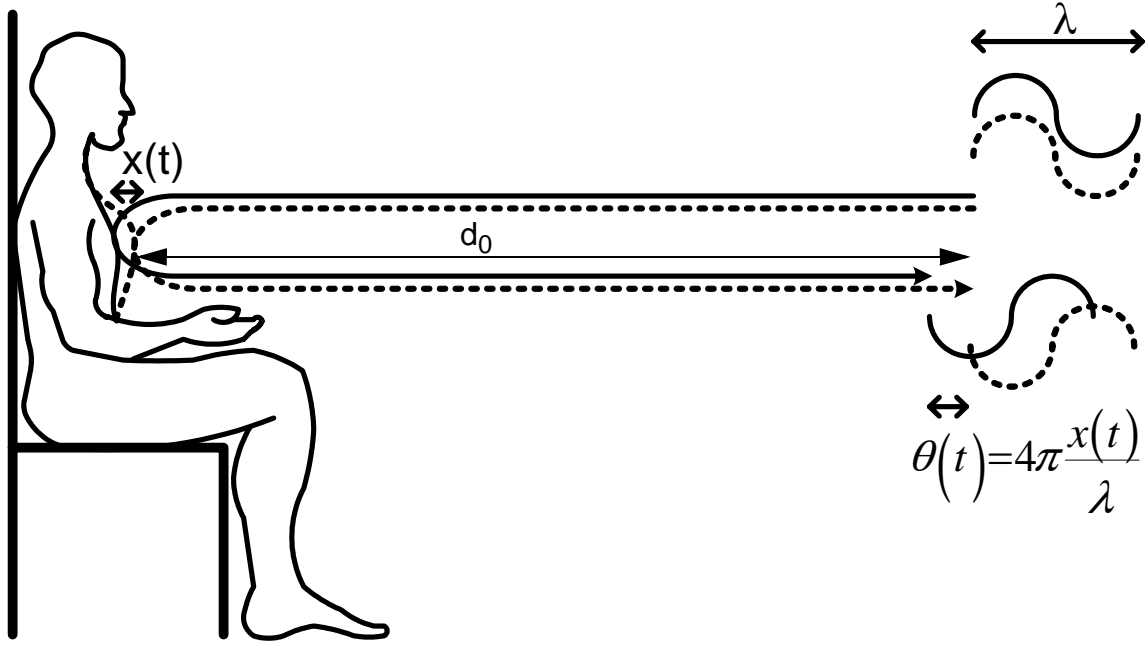


Figure 2.2. The phase shift of the reflected signal is proportional to the time-varying chest position. A positive value of x corresponds to a retracting chest cavity, or an exhale.

distance d_0 having a time-varying displacement given by $x(t)$, the distance between the transmitter and target is $d(t) = d_0 + x(t)$. The time delay between the transmitter and target is the distance traveled by the signal, $d(t)$, divided by the signal's propagation velocity, c . Since the chest moves while the signal is traveling, the distance between the antenna and the chest at the time of reflection is $d\left(t - \frac{d(t)}{c}\right)$. Therefore, the round-trip time delay in seconds, t_d , is:

$$t_d = \frac{2d\left(t - \frac{d(t)}{c}\right)}{c} = \frac{2\left(d_0 + x\left(t - \frac{d(t)}{c}\right)\right)}{c}. \quad (2.4)$$

The signal at the receiver, $R(t)$, is a time-delayed version of the transmitter signal, with its amplitude reduced by A_R :

$$R(t) = A_R \cos\left[2\pi f(t - t_d) + \phi(t - t_d) + \theta_0\right]. \quad (2.5)$$

Several factors affect the value of the constant phase shift, θ_0 , such as the phase shift at the reflection surface (near 180°) and any time delay between the transmitter and antenna

and between the antenna and the mixer. Substituting for t_d using (2.4), the received signal is:

$$R(t) = A_R \cos \left[2\pi f t - \frac{4\pi d_0}{\lambda} - \frac{4\pi x\left(t - \frac{d(t)}{c}\right)}{\lambda} + \phi \left(t - \frac{2d_0}{c} - \frac{2x\left(t - \frac{d(t)}{c}\right)}{c} \right) + \theta_0 \right], \quad (2.6)$$

where the wavelength is $\lambda = c/f$. Assuming that $(d(t))/c$ in the $x(t - (d(t))/c)$ term is negligible because the chest moves with a period $T \gg d_0/c$, and assuming that the $\frac{2x(t - (d(t))/c)}{c}$ term is negligible in the phase noise term, since $x(t) \ll d_0$, the received signal can be approximated as:

$$R(t) \approx A_R \cos \left[2\pi f t - \frac{4\pi d_0}{\lambda} - \frac{4\pi x(t)}{\lambda} + \phi \left(t - \frac{2d_0}{c} \right) + \theta_0 \right]. \quad (2.7)$$

The received signal is similar to the transmitted signal with amplitude A_R , with a time delay determined by the nominal target range, d_0 , and with its phase modulated by the periodic motion of the target, $x(t)$. To determine the motion signature, the phase needs to be demodulated or otherwise detected in the receiver to detect the motion.

2.2.2 Comparison of Heterodyne and Homodyne Receivers

The simplest phase detector involves mixing the received signal with a signal at the same frequency as its carrier, so that the RF frequency is converted directly to baseband. This type of receiver is known as either direct conversion or homodyne. (Homodyne is sometimes used to describe a system where the local oscillator is synchronized in phase with the incoming carrier [45].) A heterodyne receiver instead mixes the received signal with a local oscillator (LO) signal at a different frequency, so the information is modulated on a non-zero intermediate frequency (IF) rather than being converted directly to baseband. The heterodyne receiver has been the most commonly used radio receiver for over 50 years, because tuning can be accomplished by varying the frequency of the LO, so that the IF gain and filtering stages can consist of high quality fixed-frequency components. This section introduces the heterodyne and direct-conversion architectures, describes why

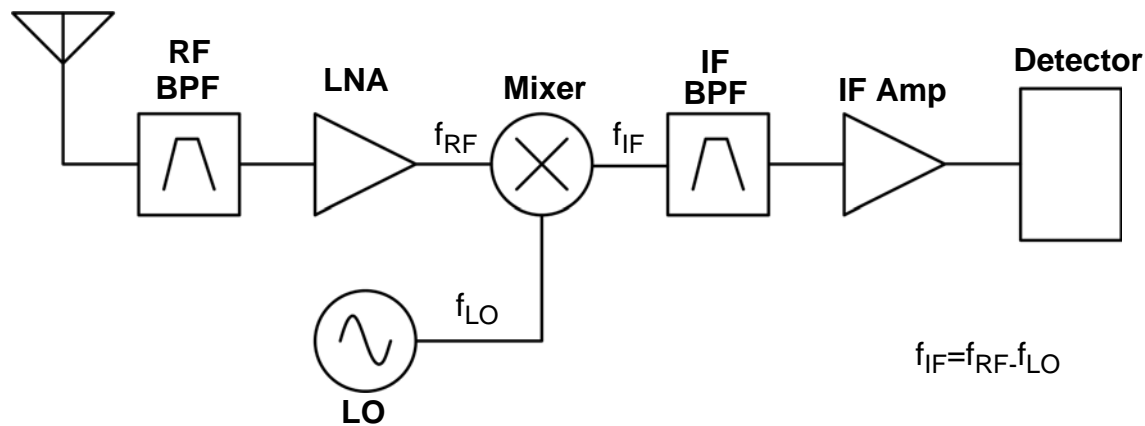


Figure 2.3. Typical heterodyne receiver architecture. The detector may be a mixer to baseband, a quadrature demodulator, or another type of detector that functions at the intermediate frequency. The RF BPF is a high-quality radio-frequency bandpass filter used to attenuate the image frequency, the LNA is a radio frequency low-noise amplifier, the IF BPF is a high-quality bandpass filter at the intermediate frequency used for channel selection, and the IF Amp is an amplifier at the intermediate frequency. The type of detector varies with the application. The LO is typically tuned to select the desired channel.

the direct-conversion architecture is chosen for Doppler radar cardiorespiratory monitoring, and introduces the theory for Doppler radar monitoring with a CW system and a direct-conversion receiver.

In a heterodyne receiver, the input signal is amplified and filtered at RF, then mixed to an intermediate frequency (IF) where it is amplified in a tuned IF stage and filtered with high-quality fixed bandpass filters before the signal is detected (which may involve mixing to baseband). The receiver's basic architecture is shown in Figure 2.3. The RF bandpass filter, or preselector, is designed to eliminate the image frequency, the undesired signal capable of producing the same IF as the desired signal produces when mixed with the LO. The low noise amplifier (LNA) decreases the receiver noise figure by increasing the signal power at the input before the rest of the receiver adds noise. The signal is then mixed with the LO to downconvert it to the intermediate frequency. The IF bandpass filter is used to isolate the desired channel from neighboring channels, so it is generally a high-quality complex filter. The IF amplifier is often a gain-controlled amplifier that adjusts the signal to the appropriate amplitude for the detector. The detector varies depending on the modulation scheme and the type of information that is modulated. It may

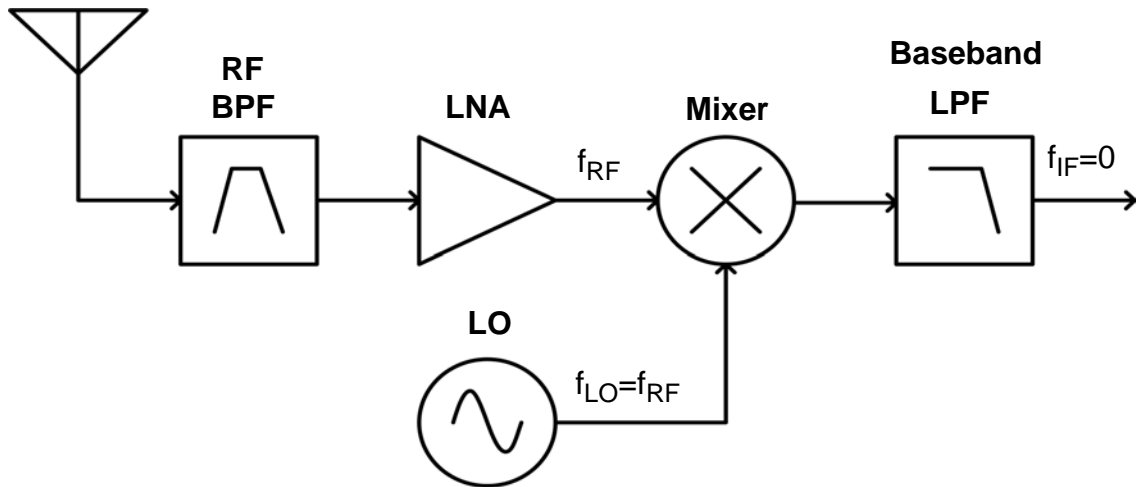


Figure 2.4. Typical homodyne, or direct-conversion, architecture. The RF BPF is a bandpass filter that is sometimes included to attenuate neighboring signals to avoid intermodulation resulting from receiver nonlinearities. The LNA is a low-noise amplifier that increases the receiver noise figure. The local oscillator is at the same frequency as the RF carrier, and when mixed with the received signal after the baseband low-pass filter, the signal is at baseband. The baseband LPF is an anti-aliasing filter that must be applied to the signal before it is digitized.

consist of downconversion to baseband, a differentiator, an envelope detector, a phase-locked loop, or other topologies.

In a homodyne receiver, as shown in Figure 2.4, the received signal is sometimes bandpass filtered to remove noise and amplified with an LNA to decrease the receiver noise figure. The signal is then mixed with an LO at the same frequency as its carrier, converting the signal to baseband. Depending on the modulation of the signal, this may complete the demodulation, or an additional detector may be required. In a homodyne system, both sidebands of the signal are converted to the same frequency space at baseband. Because this problem is analogous to the image frequency problem in a heterodyne receiver, it is known as the self-image problem. This is discussed in more detail in Appendix B.

A homodyne receiver is selected for this application due to its simplicity and its straightforward use as a phase detector. Theory for Doppler radar monitoring using a CW radar with a homodyne receiver is outlined below, and shown in Figure 2.5. The information about the periodic target motion can be readily demodulated if this signal is multiplied

by a local oscillator (LO) signal that is derived from the same source as the transmitted signal in a direct-conversion architecture. Because the phase noise of the received signal is correlated with that of the LO, ignoring amplitude variations, the LO signal is expressed by:

$$L(t) = \cos(2\pi ft + \phi(t)). \quad (2.8)$$

When the received and LO signals are mixed and the output is low pass filtered the resulting baseband signal is:

$$B(t) = A_B \cos\left[\theta + \frac{4\pi x(t)}{\lambda} + \Delta\phi(t)\right], \quad (2.9)$$

where

$$A_B = A_R \sqrt{G_{RX} G_{CL}} \quad (2.10)$$

is the baseband amplitude with G_{RX} the receiver gain and G_{CL} the mixer conversion gain,

$$\Delta\phi(t) = \phi(t) - \phi\left(t - \frac{2d_0}{c}\right) \quad (2.11)$$

is the residual phase noise and

$$\theta = \frac{4\pi d_0}{\lambda} - \theta_0 \quad (2.12)$$

is the constant phase shift dependent on the nominal distance to the target, d_0 . Figure 2.5 shows a simplified block diagram and the signal flow of a Doppler radar system used to detect periodic target motion.

If $x(t) \ll \lambda$ and θ in (2.12) is an odd multiple of $\pi/2$, the small angle approximation is valid, and the baseband output is approximately:

$$B(t) \approx A_B \left(\frac{4\pi x(t)}{\lambda} + \Delta\phi(t) \right). \quad (2.13)$$

In this case, the optimum phase demodulation sensitivity is achieved, and the baseband output is proportional to the periodic chest displacement, $x(t)$, summed with the residual phase noise.

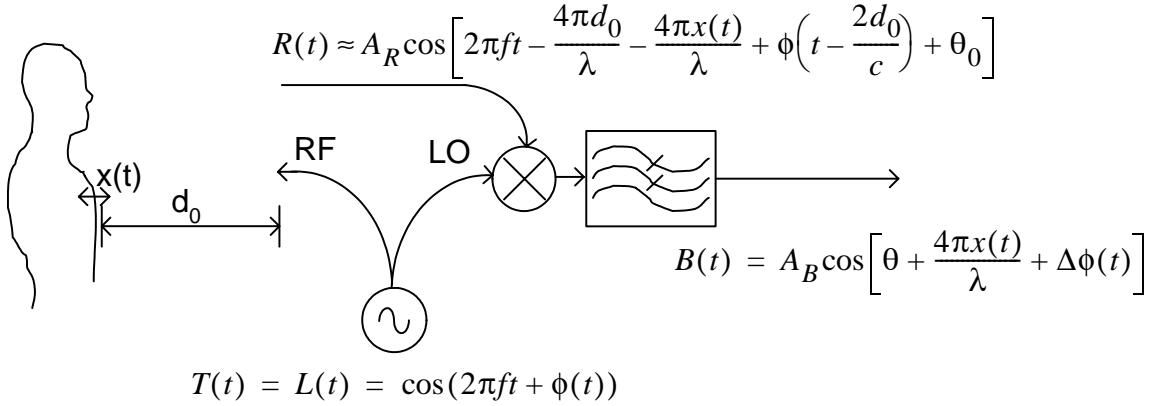


Figure 2.5. Simplified Doppler radar system block diagram with signal flow. The oscillator signal, $T(t)$, provides both the transmitted RF signal and the LO signal. The transmitted signal travels a total distance $2d(t)=2(d_0+x(t))$ and becomes the received signal, $R(t)$, which is mixed with the LO and lowpass filtered to give the baseband output, $B(t)$. The target, at a nominal distance d_0 from the antenna, has a periodic displacement $x(t)$. A_R and A_B are the ratios of the received and baseband signal amplitudes to the LO amplitude. The baseband output signal is proportional to the cosine of a constant phase shift determined by the nominal target distance, d_0 , summed with a time-varying phase shift proportional to the time-varying chest motion and with the residual phase noise $\Delta\phi(t)$.

When θ is an integer multiple of π , the output is approximately:

$$B(t) \approx A_B \left(1 - \left[\frac{4\pi x(t)}{\lambda} + \Delta\phi(t) \right]^2 \right). \quad (2.14)$$

In this case, the baseband output is no longer linearly proportional to the time-varying displacement, and the sensitivity is decreased. This null point occurs when the LO and the received signal, $T(t)$ and $R(t)$, are either in phase or 180° out of phase. Since the variable part of θ is dependent only on the distance to the target, d_0 , there is a null point every quarter wavelength from the radar. At a frequency of 2.4 GHz, these null points occur every 3 cm, and therefore can be difficult to avoid due to variations in the positions of the transceiver and the subject. These null points can be avoided with a quadrature receiver, as shown in the next section.

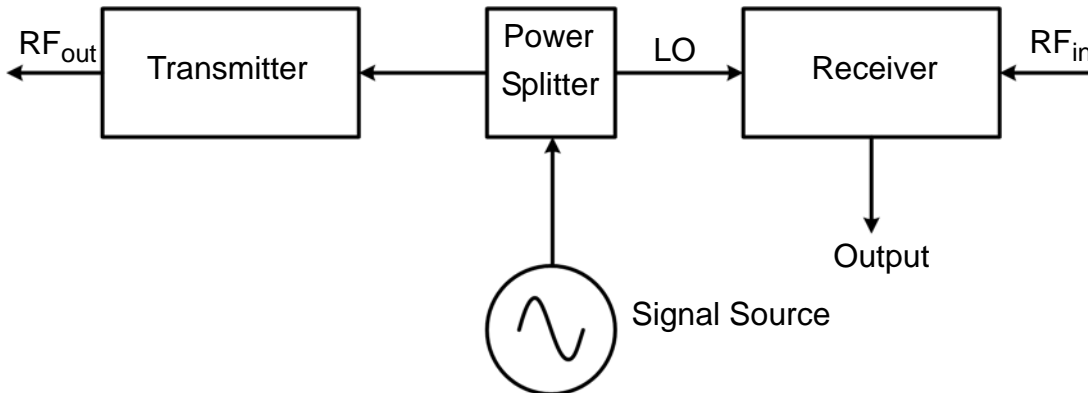


Figure 2.6. Block diagram of a single-channel CW radar transceiver. The signal source is split into the carrier for the transmitter and the local oscillator, LO. The transmitter couples the output signal to the antenna at the RF_{out} port, and the receiver demodulates the received signal from the RF_{in} port.

2.2.3 Single-Channel and Quadrature Receivers

As discussed in detail in Appendix B, communications direct-conversion receivers need quadrature receivers to avoid the self-image problem. Additionally, quadrature receivers can avoid the phase demodulation null points as in (2.14) with range that makes heart rate detection less accurate at some ranges. However, a quadrature receiver requires two receiver chains, which leads to increased power consumption and requires more die area, which makes an integrated receiver more expensive to fabricate. This section assesses the necessity, benefits, and costs of a quadrature receiver over a single-channel receiver. A single-channel continuous-wave direct-conversion transceiver is shown in Figure 2.6 and a quadrature continuous-wave direct-conversion transceiver is shown in Figure 2.7.

Because the spectra of the heart and respiratory motion are encoded on the RF signal as a phase, and not an amplitude, modulation, the spectrum is symmetrical about the carrier. Therefore, when the signal is converted to baseband, the self-image problem does not apply. Therefore, it is possible to use a single-channel homodyne receiver without self-image distortion. The main challenge is that the phase demodulation accuracy varies with the range to the target; in the null points, the signal is difficult to detect accurately. As

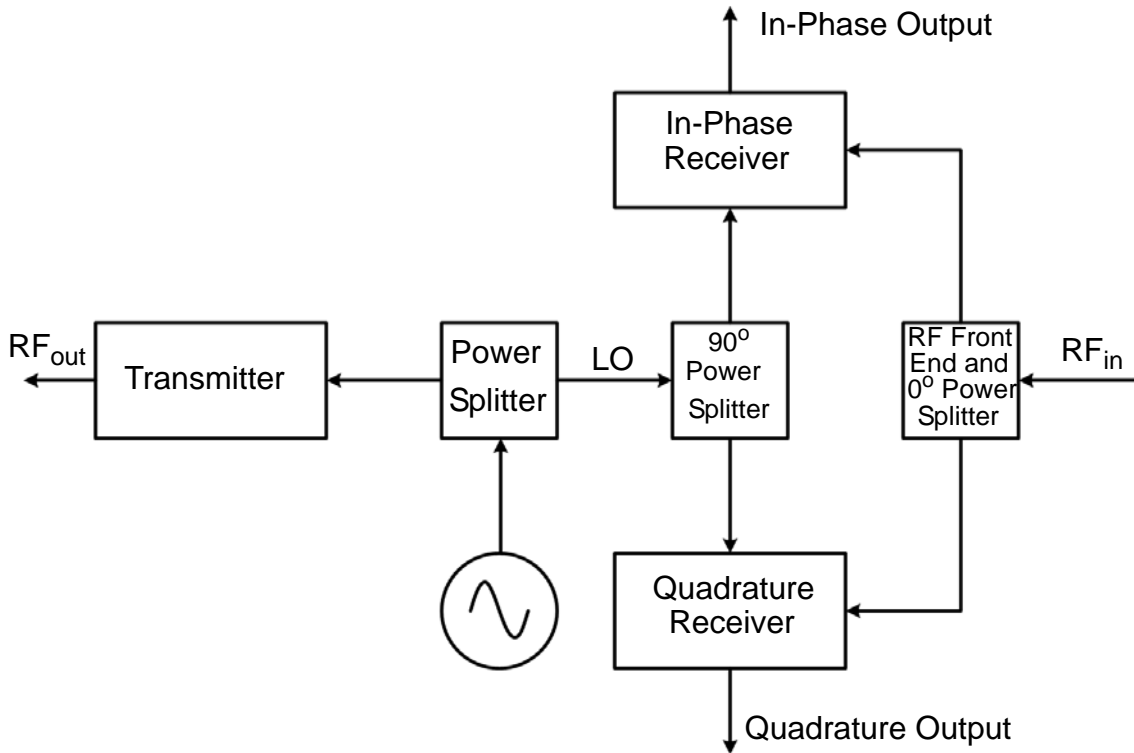


Figure 2.7. Block diagram of a quadrature CW radar transceiver. The signal source is split into the carrier from the transmitter and the local oscillator for the receiver. The local oscillator is split with a 90° phase shift between the two LO outputs, and the RF input signal is split with a 0° phase shift. The transmitter couples the output signal to the antenna, and the receivers convert the signal to baseband. The in-phase and quadrature receiver channels each provide an output.

shown in the previous section, at the optimal phase demodulation point, the baseband signal is approximately directly proportional to the chest motion (2.13), and at the phase-demodulation null point the baseband signal is proportional to the square of the motion. A quadrature receiver offers the opportunity to avoid phase demodulation null points. By choosing the larger of the two signals, which should be closer to the optimal phase demodulation point, through direct phase demodulation, or by combining the signals with another technique. Direct phase demodulation theoretically results in an output that is independent of the target range, but faces practical problems from gain and phase balance in the quadrature receiver chains as well as from dc offset removal in the baseband signal conditioning.

A quadrature receiver, as shown in Figure 2.7, has two receiver chains with LO phases 90° apart to insure that at least one of the outputs is not in a null point. A quadrature receiver can also be used to directly demodulate the phase, as shown below and in Figure 2.8. The two LO signals have phases that differ by $\pi/2$:

$$L_I(t) = \cos\left(2\pi ft + \phi(t) + \frac{\pi}{4}\right) \quad (2.15)$$

and

$$L_Q(t) = \cos\left(2\pi ft + \phi(t) - \frac{\pi}{4}\right) = \sin\left(2\pi ft + \phi(t) + \frac{\pi}{4}\right) \quad (2.16)$$

Therefore, the two receiver output channels will be:

$$B_I(t) = A_B \cos\left[\theta + \frac{\pi}{4} + \frac{4\pi x(t)}{\lambda} + \Delta\phi(t)\right] \quad (2.17)$$

and

$$B_Q(t) = A_B \cos\left[\theta - \frac{\pi}{4} + \frac{4\pi x(t)}{\lambda} + \Delta\phi(t)\right] = A_B \sin\left[\theta + \frac{\pi}{4} + \frac{4\pi x(t)}{\lambda} + \Delta\phi(t)\right] \quad (2.18)$$

These signals are shown in the quadrature block diagram of Figure 2.8.

When $\theta + \pi/4$ is an integer multiple of π , the I signal will be at a null point (2.14). However, $\theta - \pi/4$ will be an odd multiple of $\pi/2$, and the Q signal will be at an optimum phase-demodulation point. When selecting the best signal with quadrature demodulation, the worst case occurs when θ is an integer multiple of π , so that both $\theta + \pi/4$ and $\theta - \pi/4$ are odd multiples of $\pi/4$ and neither receiver chain is at an optimum phase demodulation point. At this point, the baseband outputs are:

$$B_I(t) = B_Q(t) \approx \pm A_B \left[\frac{1}{\sqrt{2}} - \frac{1}{\sqrt{2}} \left[\left(\frac{4\pi x(t)}{\lambda} + \Delta\phi(t) \right) + \left(\frac{4\pi x(t)}{\lambda} + \Delta\phi(t) \right)^2 \right] \right]. \quad (2.19)$$

As long as $x(t) \ll \lambda$, the linear term is much larger than the squared term, and the chest motion signal can still be accurately detected.

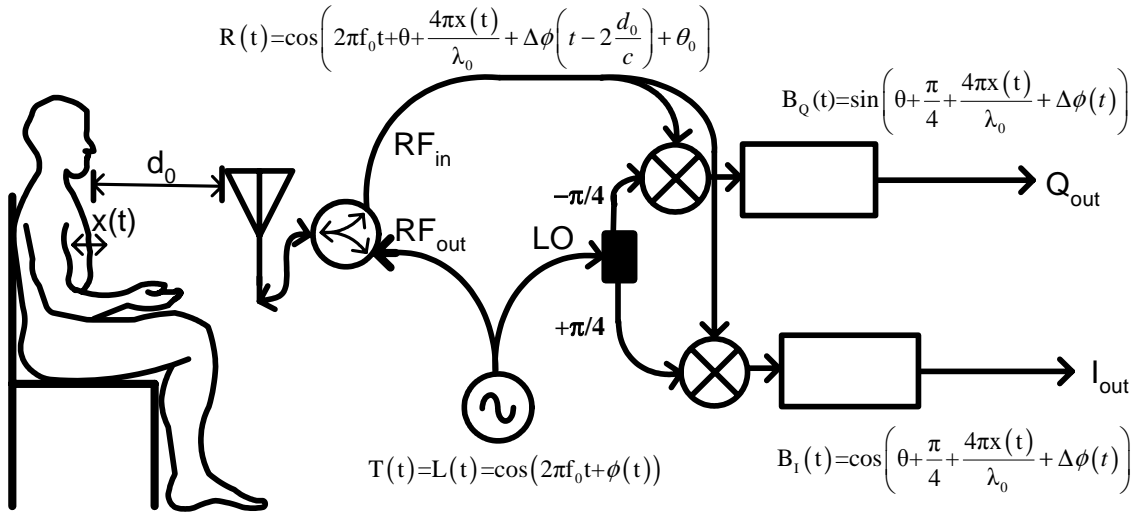


Figure 2.8. Block diagram for Doppler radar sensing of chest motion with a quadrature receiver. The oscillator signal provides both the transmitted RF and LO signals, $T(t)$ and $L(t)$. The transmitted signal travels a total distance $2d(t) = 2(d_0 + x(t))$ and becomes the received signal, $R(t)$. The LO is split into two quadrature LO signals, which have phases $\pi/2$ apart. The received signal is split into signals for the two receiver chains, and each is mixed with the one LO signal and lowpass filtered to give the baseband outputs, $B_I(t)$ and $B_Q(t)$. These two baseband signals can be combined to directly demodulate the phase, or the better of the two signals can be chosen.

Generally, the term closest to the optimal phase demodulation point should have the greatest amplitude after the dc offset is removed. If the dc offset is not removed, the signal closest to the optimal point should have the smallest dc offset. However, other causes of the dc offset make the amplitude method a superior technique for selecting the better channel, although significant gain imbalance between the signals could pose a problem with the amplitude method.

Another approach that takes advantage of the quadrature receiver requires more signal processing than the above-mentioned approach. It involves calculating the phase by processing the signals with the following equation:

$$\theta(t) = \text{atan}\left(\frac{B_Q(t)}{B_I(t)}\right) = \text{atan}\left(\frac{A_B \sin\left(\theta + \frac{\pi}{4} + \frac{4\pi x(t)}{\lambda} + \Delta\phi(t)\right)}{A_B \cos\left(\theta + \frac{\pi}{4} + \frac{4\pi x(t)}{\lambda} + \Delta\phi(t)\right)}\right) \quad (2.20)$$

$$\theta(t) = \theta + \frac{\pi}{4} + \frac{4\pi x(t)}{\lambda} + \Delta\phi(t) \quad (2.21)$$

This method directly demodulates the phase, and does not rely on the small angle approximation, making it more robust. However, the removal of dc offsets in analog signal conditioning or the presence of undesired dc offsets can adversely affect the ability to use this method, as discussed in detail in Appendix C. Chapter 7 compares channel selection, direct phase demodulation, principal components analysis, and three diversity combining techniques for taking full advantage of a quadrature receiver after dc offsets have been removed.

Both single-channel receivers and quadrature receivers are used in this work to examine the trade-offs between demodulation accuracy and size, complexity, and power dissipation. For direct phase demodulation, techniques to correct amplitude and phase imbalance between the receiver chains and the effects of removing the information near dc through dc blocking are both assessed in Appendix C.

2.2.4 Frequency of Operation

One of the most important features of Doppler radar monitoring of heart and respiration motion is that the RF signal can penetrate clothing or bedding with minimal reflection, and have a large reflection at the air/skin interface. These properties are frequency dependent but occur at most microwave frequencies; the signal reflects at the air/skin interface less as the frequency decreases, and has more significant reflections from clothing or bedding as the frequency increases. However, these features are preserved at all microwave frequencies.

An important feature in frequency choice is the resolution. The signal-to-noise ratio is dependent on the wavelength of the carrier, λ , mostly because the amount of phase modulation in radians is:

$$\frac{4\pi x(t)}{\lambda}, \quad (2.22)$$

where $x(t)$ is the chest motion. The higher the frequency, the shorter the wavelength, and therefore the greater the phase modulation. If the phase noise is the same across different frequencies, increasing the frequency increases the signal-to-noise ratio.

Another important factor for single-chip radar transceiver design is the device speed of inexpensive fabrication technologies, since cost savings is the most important reason to develop this technology on a single chip. CMOS technology is the least expensive for mass production of chips, and the high end of frequency is limited by the advances in the technology. The 5 GHz band has been used for CMOS implementations of wireless LAN transceivers, and frequency bands as high as 60 GHz are being explored in CMOS RF research [68]. However, this work was done in 0.25- μm CMOS, which has a transistor frequency of 25 GHz. A general rule of thumb is that a RF system must operate 8-10 times below the transistor frequency, so 3 GHz was the upper limit in this technology.

The choice of an unlicensed band is important for FCC compliance, and also in order to have a range of commercially available antennas to choose from. The FCC unlicensed bands at RF and microwave frequencies are: 902 - 928 MHz, 2.4 - 2.4835 GHz, 5.725 - 5.875 GHz, 24.0 - 24.25 GHz, and 57 - 64 GHz. Transceivers used in this work operate at 1.6 GHz and at 2.4 GHz. The 1.6 GHz transceivers leverage technology developed for a DCS1800 base station receiver, which has a 1.8-GHz RF signal and a 1.6-GHz LO. Custom antennas were developed for this operation frequency. Later versions of this transceiver were redesigned to operate at 2.4 GHz, where commercially available antennas were used. This was the highest frequency unlicensed band at which the 0.25- μm technology could operate.

A higher frequency also means that the same antenna gain can be obtained with a physically smaller antenna. The maximum directivity that can be obtained from an antenna with aperture area A is:

$$D_{max} = \frac{4\pi A}{\lambda^2}, \quad (2.23)$$

so that as λ decreases, the area can decrease for constant directivity. Since the far field begins at a range $R_{far-field}$, where

$$R_{far-field} = \frac{2l^2}{\lambda} \quad (2.24)$$

and where l is the maximum dimension of the antenna. If the antenna area A equals l^2 , then

$$R_{far-field} = \frac{D_{max}\lambda}{2\pi}. \quad (2.25)$$

This implies that for a given directivity, the distance to the far field region is directly proportional to the wavelength, so that as the frequency increases, the antenna gets smaller, and the far-field limit moves closer to the antenna. When the far-field limit is closer to the antenna, it is easier to avoid null points in the antenna beam caused by near-field effects.

At frequencies high enough that the $x(t) \ll \lambda$ assumption is no longer valid, there are no phase-demodulation optimal or null points, and direct phase demodulation is required. This means that a quadrature receiver must be used and the problems with dc-offsets and amplitude and phase imbalance must be resolved.

These trade-offs indicate that a higher frequency is generally better, as long as a radio frequency or microwave system can be successfully fabricated at this frequency in inexpensive technology.

2.2.5 Antenna Considerations

The choice of whether to use a highly directive, a wide-beam, or an omnidirectional antenna requires consideration of trade-offs between size and directivity. Generally, the higher the directivity of an antenna, the larger its area. An antenna with a larger size has a larger region that is near-field, in which the antenna pattern is not constant over varying range. A highly directive antenna could focus on only the desired target. This would enable increased selectivity (the sensitivity to alternate targets would be greatly reduced) and would also decrease the sensitivity to clutter, since less clutter would be in the

antenna's beam. However, if the beam is focused to cover only a small area on the subject's chest, it may be difficult to ensure that beam is on the appropriate part of the subject [76]. Additionally, in applications where the subject may move during monitoring, a highly directional antenna would need to track the subject's motion to avoid losing contact. It is possible to increase selectivity with broad-beam antennas by using several transceivers [69]. Finally, a large antenna has some drawbacks of its own; it makes the entire system less portable and it may intimidate subjects.

Another important question is whether to use separate antennas for transmitting and receiving, or to use a single antenna for both transmitting and receiving with a ferrite circulator to provide isolation between the transmitted signal and the received signal. Antennas are generally larger and more massive than drop-in circulators. The price of an additional commercially made antenna is similar to the price of an on-board circulator. However, patch antennas developed on printed circuit boards could decrease the cost of mass-produced items. Drop-in circulators are specified to provide between 20 and 26 dB of isolation, and antenna spacing and design affects the isolation between the antennas.

Using two antennas leads to a bistatic radar system, which may affect the radar cross section of the target. However, as long as the two antennas are kept near each other this effect will be minimal [75]. If the antennas are near each other, care must be taken to minimize leakage between the two antennas. When the antennas are spaced and angled appropriately, the dominant source of leakage generally is backscatter from nearby clutter, which is unavoidable [47].

Another important consideration for connecting antennas to the transceiver is the minimization of the path length to and from the antenna. Keeping the antenna electrically close to the RF_{out} and RF_{in} ports of the transceiver chip is an important consideration. Because the residual phase noise is proportional to the square of the one-way path length, minimizing the length the signal travels within the radar transceiver system is critical for minimizing the adverse effects of oscillator phase noise. If printed-circuit-board antennas are placed on the same board as the radar chip, this path length would be minimized.

A antenna gain between 5 and 10 dBi has been determined to be a good compromise between size and directivity. At 2.4 GHz, this antenna is about 10 cm on a side. At this frequency, one antenna and a ferrite circulator uses less space than two antennas, and this method was selected for this work.

2.2.6 Received Signal Amplitude and Receiver Noise Temperature

The amplitude of the received signal was ignored in the theoretical calculations in the previous section, but it is an important factor in determining the signal-to-noise ratio of the signal after it has been downconverted to baseband. The received signal power, P_R (mW), is calculated with the radar equation as a function of the transmitted power, P_T (mW), the antenna gain, G , the radar cross section of the target, σ (m²), the wavelength of the radio signal, λ (m), and the range to the target, R (m). The radar equation is derived in Appendix D, and given in the following equation.

$$P_R = \frac{P_T G^2 \sigma \lambda^2}{(4\pi)^3 R^4} \quad (2.26)$$

The radar cross section is the only term that is determined by the target and not by the radar transceiver. It is a measure of how well the target reflects the transmitted radar signals in the direction of the radar receiver, and it depends on the target's projected cross section, reflectivity, and the directivity of the reflected signal. The radar cross section is also described in more detail in Appendix D. When measuring a person, calculation of the projected cross section requires including the whole person as well as the bed or chair on which they are sitting. However, for physiological motion measurement, the area undergoing motion determines the radar cross section; the stationary part of the body is considered to be clutter. This value is challenging to determine, as the radar cross section of the parts of the body that move with physiological motion varies from person to person and with the angle of the antenna.

The dominant RF noise at the input to the receiver is thermal noise; thermal noise is zero-mean, has a gaussian distribution, and does not vary with frequency. This is additive to the RF signal. The thermal noise power is expressed by:

$$P_{N, thermal} = 4kTB , \quad (2.27)$$

where k is Boltzman's constant, T is the receiver temperature in K, and B is the bandwidth in Hz. The transmitted signal power and antenna gain should be chosen so that the received signal power at the desired target ranges is well above the RF thermal noise level.

The signal power at baseband is also proportional to the transmitter power, as described in Appendix D,

$$S_B = \frac{2P_T G_{CL} G_{RX} G^2 \sigma^2}{4\pi R^4} x^2(t), \quad (2.28)$$

where G_{RX} is the gain or loss between the antenna and the mixer's RF input, G_{CL} is the conversion gain of the mixer (power gain), and $x^2(t)$ is mean-squared chest motion. In this application, $1/f$ noise from the mixer and from the baseband signal conditioning circuitry dominates the baseband noise spectrum. The transmitted power must be high enough that the baseband signal power is well above the baseband noise level.

The third type of noise is residual phase noise, and when residual phase noise is dominant, it is not possible to improve the SNR by increasing the transmit power. Ideally, the received signal power and baseband signal power are high enough that only residual phase noise is of concern, as long as the transmitted power level is still both safe and legal. With this system, 1 mW transmit power puts us in this regime.

2.3 Transceiver Design

A transceiver design is typically broken down into sub-circuit blocks such as oscillator, LNA, and mixer. In order to leverage RF CMOS design techniques developed for communication circuits, common blocks are used. A critical step in the transceiver design is determining which blocks are necessary in the transmitter and receiver. Because a rela-

tively low-power transmitter is desired, a power amplifier is not necessary between the oscillator and the antenna. The receiver front end is the first receiver section; RF receivers typically have a LNA and filtering capability. The benefit of these circuits in a Doppler radar transceiver is explored in Section 2.3.1. Since the same source is being used for the transmitter and the receiver, the output from the source is split into transmit and receive signals, which can be achieved with either a passive power divider or an active one, as discussed in Section 2.3.2. After the RF front end, the signal is downconverted to baseband with a mixer. RF input matching and RF-LO isolation is improved through the use of a balanced mixer, which requires differential inputs at both the RF and LO inputs. Differential mixer inputs require additional signal splitting as does the 90° power splitter in the quadrature receiver. Both types of signal dividers can be achieved actively or passively. These topological differences and subcircuits are discussed in Section 2.3.3.

2.3.1 Radio-Frequency Front End

Although low-noise amplification of the received signal is used in most radio receivers to reduce the receiver noise figure, it is not commonly used in CW radar receivers. In CW radar systems, noise due to leak-through from the transmitted signal and reflections from clutter typically exceeds the noise contributed by the receiver, so that a low-noise amplification typically does not improve the signal-to-noise ratio. Since an LNA consumes power and die area there is no reason to include it in a CW receiver. Also, since this system is designed such that RF thermal noise is not the dominant noise source on the demodulated signal, as discussed in Section 2.2.6, an LNA will not improve the overall SNR because an LNA only improves the SNR if receiver thermal noise is dominant.

Homodyne systems use front-end filtering to eliminate large signals that might cause distortion in the mixer, with second-order intermodulation products (IP2) causing additional dc offsets. If the dc offsets are being removed with a method such as filtering, which removes general dc offset rather than just those from reflections of the transmitted signal, dc offsets due to intermodulation will not cause an irresolvable problem. In this work, a filter is used to remove dc offset in the baseband signal conditioning, described in Appen-

dix E, so the filter is not required. If this dc offset is not removed in analog processing in future work, a front-end filter should be considered.

2.3.2 Active and Passive Power Dividers

An active balun can provide phase and amplitude balance over a wider bandwidth than a passive balun, and it can also provide some amplification and isolation, which a passive balun cannot [66]. A passive balun, by its nature, consumes no power. In this work, active baluns were used when amplification and/or isolation were desired; the narrow-band nature of the heart-monitoring application does not require phase and amplitude balance over a wide bandwidth. Because the system is not limited by receiver noise, the choice between active and passive baluns does not affect the SNR through differences in additive noise.

When the signal is split into the transmit RF signal and the receiver LO, the phase relationship between the two signals is unimportant. Therefore, an active circuit can be used if gain is desired, but otherwise, if the antenna input and the receiver LO input have the same impedance, the signal can just be applied to both inputs and will be divided equally between them.

When a 90° shift is required, most solutions are passive using resistors and capacitors, and sometimes a polyphase oscillator is used to create the quadrature phase directly. This system uses a monophasic oscillator and a passive 90° phase shifter.

2.3.3 Doppler Transceiver Architectures

The final architectures for the single-channel and quadrature transceivers are shown in Figure 2.9 and Figure 2.10, respectively. Both types of transceivers use a voltage-controlled oscillator (VCO) to generate both the transmitted signal and the local oscillator. The subcircuits in these architectures are discussed in more detail in Chapter 4.

The single-channel receiver uses three active baluns, first to split the RF output and local oscillator signals and then to convert the single-ended LO and RF input signals into

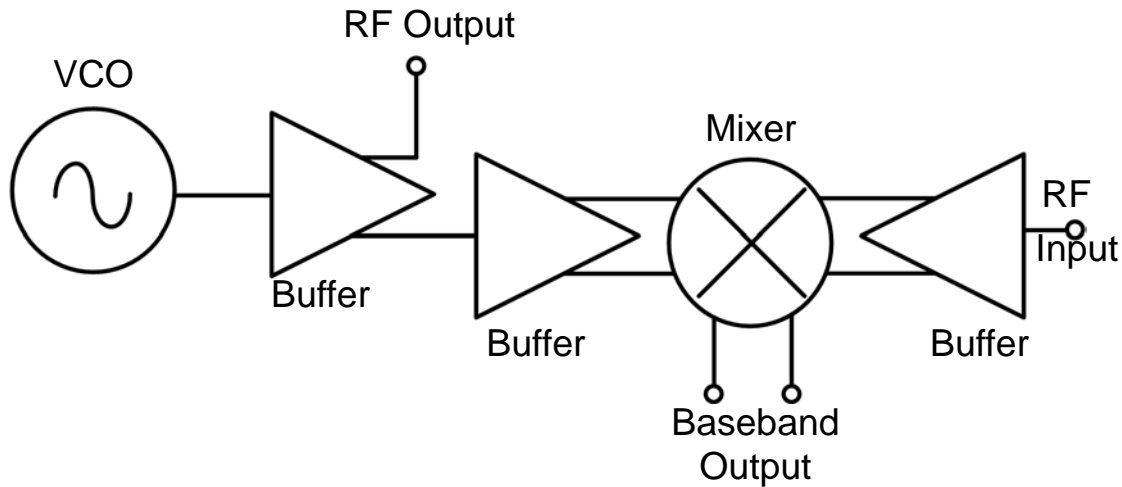


Figure 2.9. Single-channel transceiver block diagram. This architecture was used in two 1.6-GHz transceivers.

the differential signals required by the double-balanced mixer. Active baluns are used in the LO because the LO power needs to be amplified to drive the mixer properly. Isolation is required on the RF side to prevent antenna loading from affecting the oscillator.

Two different quadrature transceiver architectures have been developed. The first, shown in Figure 2.10a, uses low-noise amplifiers (LNAs) to isolate the resistor-capacitor-capacitor-resistor (RCCR) circuit, which provides the 90° phase difference between the I and Q LO channels. Passive baluns are used to perform the single-to-differential conversion for the LO, since the LNAs have already amplified the LO sufficiently to drive the mixer. Active baluns are used for the RF input.

Figure 2.10b shows a second quadrature architecture. This design uses a direct input to the RCCR, without an active stage for isolation between the VCO and the 90° power divider. Active baluns provide amplification, isolation, and single-ended to differential conversion between the RCCR subcircuits and the mixers. They also provide amplification and single-ended to differential conversion for the RF input signal. The RF input signal is not divided with a balun, the active baluns have identical input impedances so that the signal can be applied to both inputs and the RF power is divided equally between the receiver chains. In both of the quadrature designs, a voltage-controlled oscillator

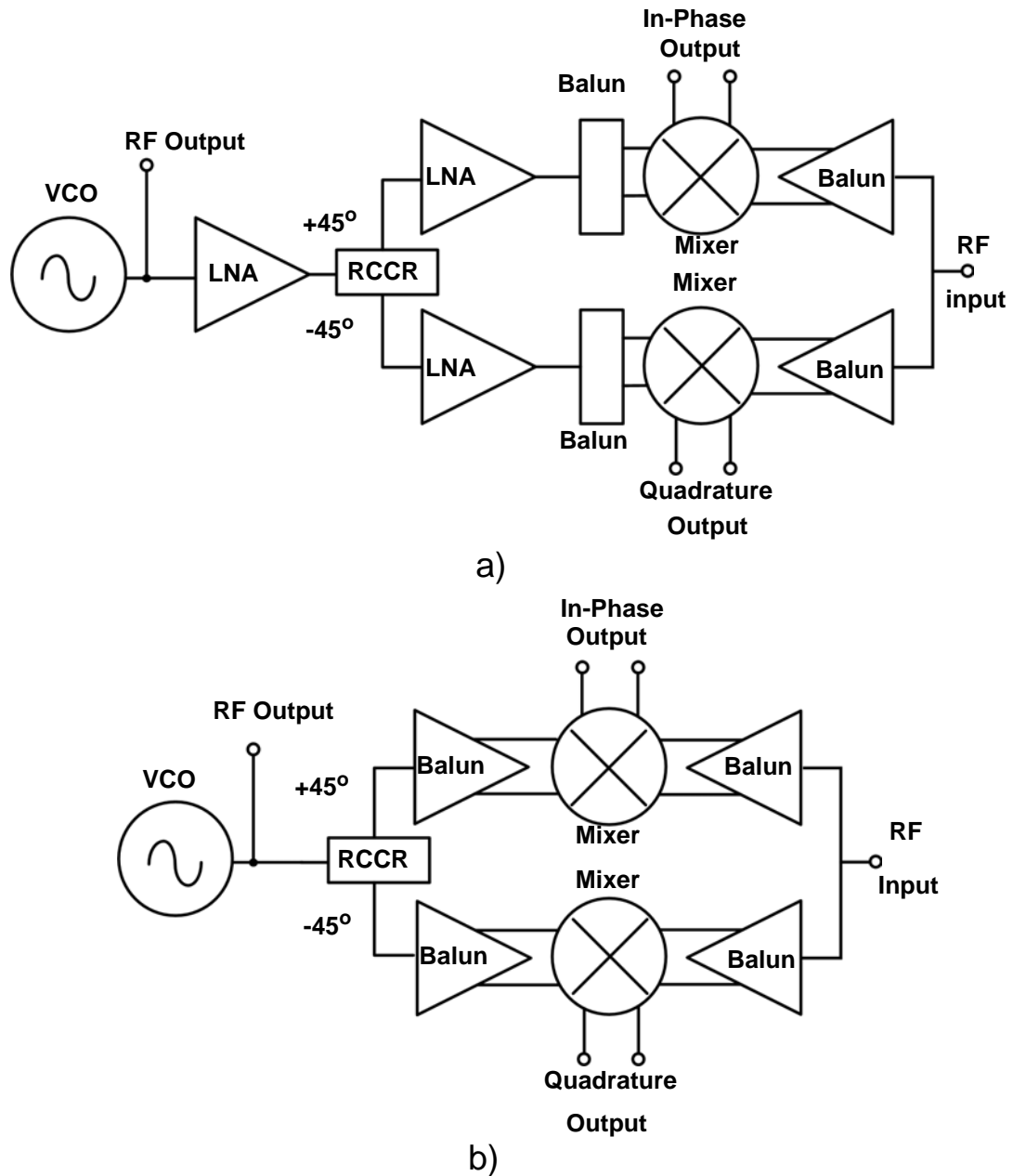


Figure 2.10. Quadrature transceiver block diagrams. a) LNAs are to isolate the RCCR phase-shifting circuit and passive baluns are used for single-ended to differential conversion. b) The VCO is coupled directly to the RCCR and active baluns are used to create the differential signal for the mixer. Each configuration was used in a 2.4-GHz transceiver.

(VCO) is couples to a passive 90° phase shifter that works optimally at only one frequency.

2.4 Conclusions

A continuous-wave direct-conversion radar transceiver was chosen for this work. The increased complexity of a pulsed radar over a continuous-wave radar does not result in a commensurate increase in benefits for Doppler measurement of heart and respiration. Similarly, a direct-conversion receiver was chosen due to its simplicity, low power consumption, and low fabrication cost compared to a heterodyne receiver. However, due to challenges with dc offset removal while preserving the sub-Hz respiration signal, a heterodyne receiver with an IF low enough to be directly digitized as described in Appendix F may be considered for future work.

A quadrature receiver can be used to avoid null points, thereby improving the repeatability of measurements, as null points can be difficult to avoid due to variations in the relative position of the subject and the transceiver. With quadrature outputs, the better of the two outputs can be chosen or the two outputs can be combined using direct phase demodulation or another combining technique. When the two outputs are combined, dc offset removal and gain and phase imbalance between the two outputs can cause some distortion of the signal. These issues will be explored in detail in Appendix C. While quadrature receivers pose great benefits over single-channel receivers in phase demodulation accuracy, they consume more power and more die area, making them more expensive to fabricate. These trade-offs were explored experimentally, as discussed in Chapter 4. The benefits of the quadrature receiver outweigh the increased power and cost for most applications.

Frequencies of 1.6 GHz and 2.4 GHz were used in this work; as technology progresses, higher frequency unlicensed bands will be explored since higher frequencies enable use of smaller antennas and improve the SNR when a quadrature receiver is used.

Antennas with a gain of 6 to 8 dBi were chosen as a general-use antenna, although specific applications of Doppler heart and respiration rate monitoring could dictate the use of different antennas. Whether a bistatic antenna setup is preferable over a single antenna and a circulator again depends on the application and the frequency of operation, since a

bistatic setup may be less expensive but bigger. As the operation frequency increases, the antennas become smaller and the size variation between the methods decreases.

2.5 References

- [45] A. A. Abidi, "Direct-conversion radio transceivers for digital communications," *IEEE Journal of Solid State Circuits*, vol. 30, no. 12, pp. 1399-1410, 1995.
- [46] I. Arai, "Survivor search radar system for persons trapped under earthquake rubble," in *Proceedings of the Asia Pacific Microwave Conference*, 2001, pp. 663-668.
- [47] D. S. Banks, "Continuous wave (CW) radar," *Electronic Progress*, vol. 17, no. 2, pp. 34-41, 1975.
- [48] O. Boric-Lubecke and V. M. Lubecke, "Wireless house calls: Using communications technology for health care monitoring," *IEEE Microwave Magazine*, vol. 3, no. 3, pp. 43-48, 2002.
- [49] O. Boric-Lubecke, G. Atwater, and V. M. Lubecke, "Wireless LAN PC card sensing of vital signs," in *Proceedings of IEEE Topical Conference on Wireless Communications Technology*, 2003, pp. 206-207.
- [50] K. H. Chan and J. C. Lin, "Microprocessor-based cardiopulmonary rate monitor," *Medical and Biological Engineering and Computing*, vol. 25, no. 9, pp. 41-44, 1987.
- [51] K.-M. Chen, Y. Huang, J. Zhang, and A. Norman, "Microwave life-detection systems for searching human subjects under earthquake rubble or behind barrier," *IEEE Transactions of Biomedical Engineering*, vol. 47, no. 1, pp.105-114, 2000.
- [52] H.-R. Chuang, Y.-F. Chen, and K.-M. Chen, "Microprocessor-controlled automatic clutter-cancellation circuits for microwave systems to sense physiological movements remotely through the rubble," in *Proceedings of the Instrumentation and Measurement Technology Conference*, 1990, pp. 177-181.
- [53] I. M. Coman, "Christian Andreas Doppler -- the man and his legacy," *European Journal of Echocardiography*, vol. 6, no. 1, pp. 7-10, 2005.
- [54] E. F. Greneker, "Radar sensing of heartbeat and respiration at a distance with applications of the technology," in *Radar 97 Conference Proceedings*, 1997, pp. 150-154.

- [55] I. Y. Immoreev and S. Samkov, "Short-distance ultrawideband radars," *IEEE Aerospace and Electronic Systems Magazine*, vol. 20, no. 6, pp. 9-14, 2005.
- [56] J. C. Lin, "Microwave sensing of physiological movement and volume change: A review," *Bioelectromagnetics*, vol. 13, no. 6, pp. 557-565, 1992.
- [57] J. C. Lin, "Non-invasive microwave measurement of respiration," *Proceedings of the IEEE*, vol. 63, no. 10, p. 1530, 1975.
- [58] J. C. Lin, E. Dawe, and J. Majcherek, "A noninvasive microwave apnea detector," in *Proceedings of the San Diego Biomedical Symposium*, 1977, pp. 441-443.
- [59] J. C. Lin, J. Kiernicki, M. Kiernicki, and P. B. Wollschlaeger, "Microwave apexcardiography," *IEEE Transactions on Microwave Theory and Techniques*, vol. 27, no. 6, pp. 618-620, 1979.
- [60] V. Lubecke, O. Boric-Lubecke, and E. Beck, "A compact low-cost add-on module for Doppler radar sensing of vital signs using a wireless communications terminal," in *The IEEE Microwave Theory and Techniques Symposium Digest*, 2002, pp. 1767-1770.
- [61] T. Matsui, T. Ishizuka, B. Takase, M. Ishihara, and M. Kikuchi, "Non-contact determination of vital sign alterations in hypovolemic states induced by massive hemorrhage: an experimental attempt to monitor the condition of injured persons behind barriers or under disaster rubble," *Medical and Biological Engineering and Computing*, vol. 42, no. 6, pp. 807-811, 2004.
- [62] T. Matsui, K. Hagiwara, T. Ishizuka, B. Takase, M. Ishihara, and M. Kikuchi, "A novel method to prevent secondary exposure of medical and rescue personnel to toxic materials under biochemical hazard conditions using microwave radar and infrared thermography," *IEEE Transactions on Biomedical Engineering*, vol. 51, no. 12, pp. 2184-2188, 2004.
- [63] T. Matsui, I. Arai, S. Gotoh, H. Hattori, B. Takase, M. Kikuchi, and M. Ishihara, "A novel apparatus for non-contact measurement of heart rate variability: a system to prevent secondary exposure of medical personnel to toxic materials under biochemical hazard conditions, in monitoring sepsis or predicting multiple organ dysfunction syndrome," *Biomedicine and Pharmacotherapy*, vol. 59, suppl. 1, pp. S188-S191, 2005.
- [64] T. Matsui, H. Hattori, B. Takase, and M. Ishihara, "Non-invasive estimation of arterial blood pH using exhaled CO/CO₂ analyzer, microwave radar, and infrared thermography for patients after massive hemorrhage," *Journal of Medical Engineering and Technology*, vol. 20, no. 2, pp. 97-101, 2006.

- [65] G. Ossberger, T. Buchegger, E. Schimback, A. Stetzler, and R. Weigel, "Non-invasive respiratory movement detection and monitoring of hidden humans using ultra wideband pulse radar," in *Proceedings of the International Workshop on Ultrawideband Technologies*, 2004, pp. 395-399.
- [66] David N. Pozar, Microwave and RF Design of Wireless Systems, New York: Wiley, 2001.
- [67] "Radar in the twentieth century," *IEEE Aerospace and Electronic Systems Magazine*, vol. 15, no. 10, pp. 27-46, 2000.
- [68] B. Razavi, "A 60 GHz direct-conversion CMOS receiver," in *IEEE International Solid State Circuits Conference Digest of Technical Papers*, 2005, pp. 400-401.
- [69] D. Samardzija, O. Boric-Lubecke, A. Host-Madsen, V. M. Lubecke, A. D. Droitcour, and G. T. A. Kovacs, "Applications of MIMO Techniques to Sensing of Cardiopulmonary Activity," in *Proceeding of IEEE/ACES Conference on Wireless Communications and Applied Computational Electromagnetics*, 2005, pp. 618-621.
- [70] W. K. Saunders, "Post-war developments in continuous-wave and frequency-modulated radar," *IRE Transactions on Aerospace and Navigational Electronics*, vol. ANE-8, no. 1, pp. 7-19, 1961.
- [71] W. K. Saunders, "CW and FM Radar," in Radar Handbook, 2nd ed., (M. I. Skolnik, Ed.). San Francisco: McGraw-Hill, Inc., 1990, pp. 14.1 - 14.45.
- [72] J. Seals, S. R. Crowgey, S.M. Sharpe, "Electromagnetic vital signs monitor" Georgia Tech Research Institute Biomedical Division, Atlanta, GA, Final Report Project A-3529-060, 1986.
- [73] R. J. Serafin, "Meteorological radar," in Radar Handbook, 2nd ed. (M. I. Skolnik, Ed.), San Francisco: McGraw-Hill, Inc., 1990, pp. 23.1 - 23.33.
- [74] M. I. Skolnik, "An Introduction to Radar," in Radar Handbook, Second Edition (M. I. Skolnik, Ed.), San Francisco: McGraw-Hill, Inc., 1990, pp. 1.1 - 1.21.
- [75] M. I. Skolnik, "An analysis of bistatic radar," *IRE Transactions on Aerospace and Navigational Electronics*, vol. ANE-8, pp. 19-27, 1961.
- [76] H. Vermarien and E. van Vollenhoven, "The recording of heart vibrations: a problem of vibration measurement on soft tissue," *Medical and Biological Engineering and Computing*, vol. 22, pp. 168-178, 1984.

Chapter
3

Physiological Motion and Measurement

3.1 Introduction

For Doppler radar to detect heart and respiration rates, it must detect motions that occur due to periodic physiological events, including heartbeat, arterial pulsation, and breathing. These motions are concentrated in the thorax, where the lungs and heart lie, but also include the abdomen, which moves in respiration, and superficial pulses, which are present at many points in the body. A review of surface motion due to heartbeat, respiration, and arterial and venous pulsations is given in Sections 3.2 to 3.5. Vital signs, including heart and respiration rates, are recorded in patients in both emergency and clinical situations. Currently available techniques for measuring heart and respiration rates are discussed in Section 3.6, including commonly used clinical measurements, alternative measurements, and measurements of heart and respiration motion through motion at the skin surface. Doppler radar measurement of these motions is reviewed and compared to other methods for measuring heart and respiration rates. Medical terms are described in Appendix A.

3.2 Heart Motion

The heart drives blood through the lungs and to tissues throughout the body. When the heart contracts to generate the pressure that drives blood flow, it moves within the chest cavity, hitting the chest wall, and creating a measurable displacement at the skin surface.

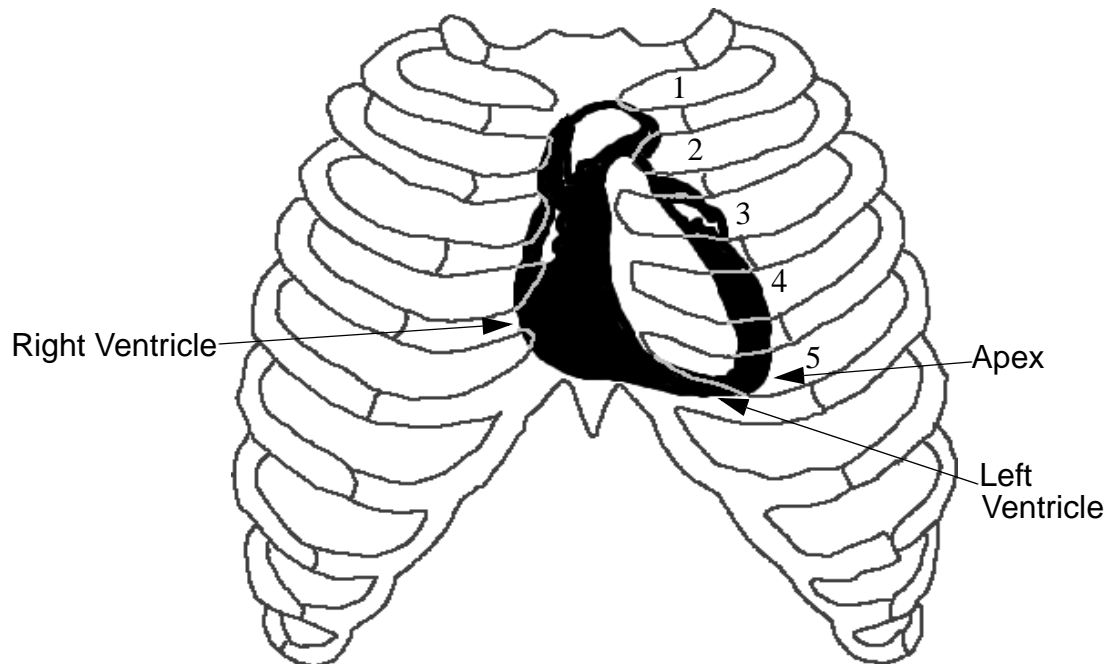


Figure 3.1: The location of the heart in the rib cage. The intercostal spaces are indicated by the numbers 1-5. The heart is beneath the sternum and the cartilage of the third, fourth, and fifth ribs. After [94].

This section describes the location and anatomy of the heart, the electrical and mechanical events that cause contraction, the motion of the heart during contraction, and how that motion affects chest wall motion.

3.2.1 Location and Gross Anatomy of the Heart

The heart is located in the middle of the thorax, between and partially overlapped by the lungs. The sternum covers the front of the heart, as do the cartilages of the third, fourth and fifth ribs as shown in Figure 3.1. Two-thirds of the heart is to the left of the midline. The heart rests on the diaphragm, tilted forward and to the left, so the apex is forward of the rest of the heart. Motion of the apex can be felt at the fourth or fifth intercostal space, near the left midclavicular line [132].

The left side of the heart pumps blood to the organs and tissues, while the right side of the heart pumps blood to the lungs. A diagrammatic section of the heart is shown in

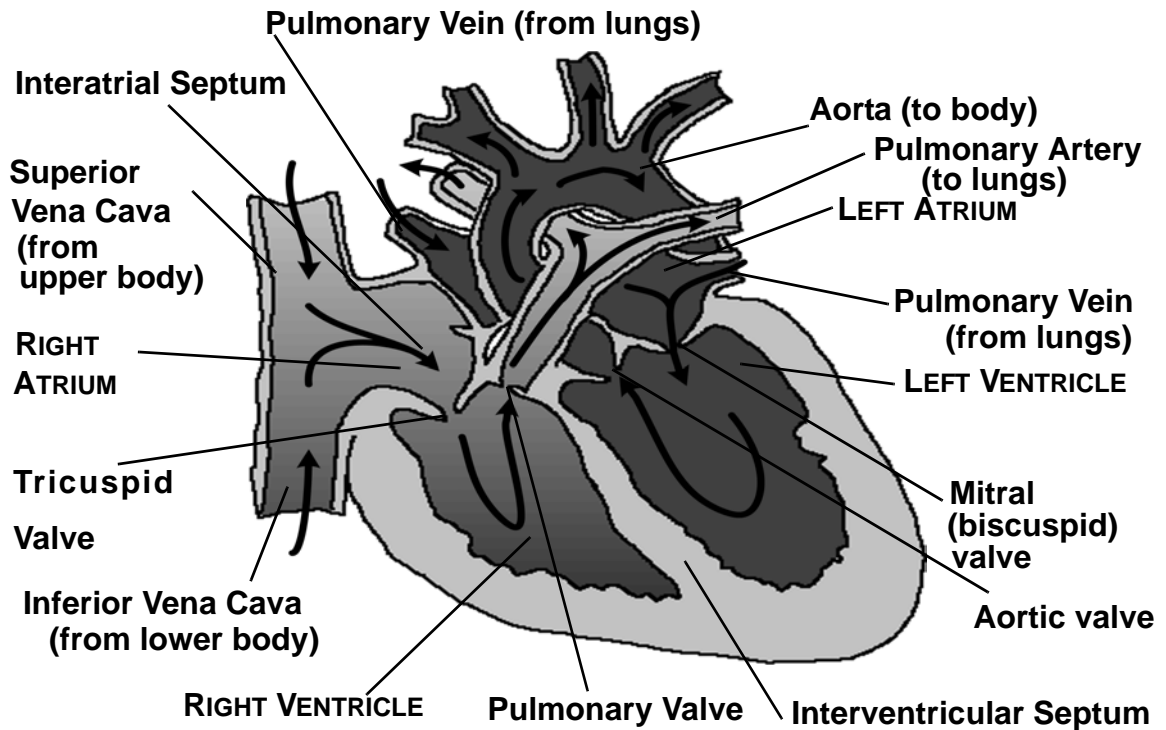


Figure 3.2: Diagrammatic section of the heart. The arrows indicate the direction of blood flow. After [135].

Figure 3.2. The vena cava, carrying blood from the peripheral tissues, enters at the upper right of the heart, into the right atrium. Blood from the right atrium enters the right ventricle, directly beneath the sternum, when the tricuspid valve opens. When the right ventricle contracts, the pulmonary valve opens, and blood exits from the top of the right ventricle in the front of the heart and into the pulmonary artery, which takes blood to the lungs, where gas exchange removes carbon dioxide from and introduces oxygen to the blood. Blood from the lungs returns to the heart through two pulmonary veins, which enter the left atrium at the top and back of the heart, along the midline of the thorax. When the mitral valve is open, blood from the left atrium enters the left ventricle. When the left ventricle contracts, the aortic valve opens and blood exits from the top of the heart into the aorta, which begins the system of arteries that deliver blood to the tissues of the body, where it provides nutrients and oxygen to and removes waste products from the tissues.

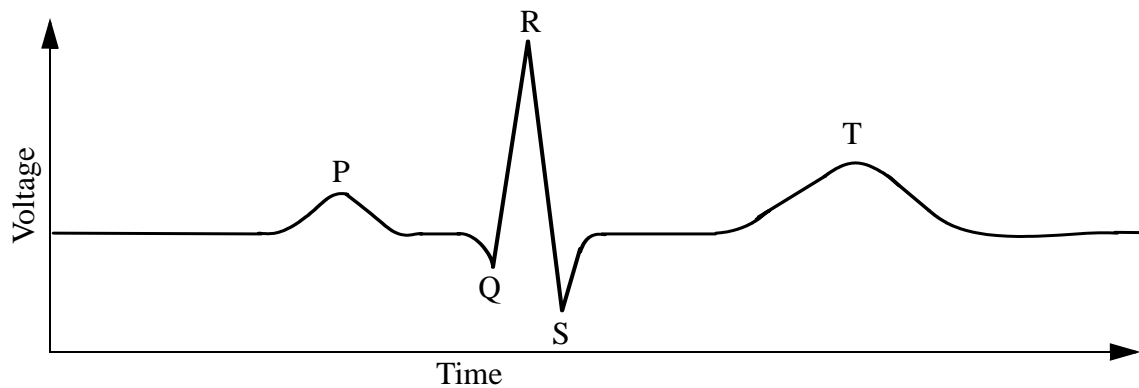


Figure 3.3: Exemplary output of an electrocardiogram. Atrial depolarization causes the P wave, ventricular depolarization causes the QRS complex, and ventricular repolarization causes the T wave.

3.2.2 Electrical and Mechanical Events of the Heart

The heart's beating is synchronized by electrical impulses that originate as the depolarization of the pacemaker cells in the right atrium. The heart's conduction system transmits the electrical impulses such that both atria contract at about the same time, followed by both ventricles. The electrocardiogram, or ECG, uses electrodes on the chest and the limbs to measure the electrical current generated in the extracellular fluid by changes in membrane potential across many cells in the heart. It displays waveforms generated by the atria and the ventricles, as shown in Figure 3.3. The P wave shows current flow during atrial depolarization, which triggers the atria to contract. The QRS complex shows ventricular depolarization, which triggers the ventricles to contract. The T wave shows ventricular repolarization; atrial repolarization occurs at the same time as the QRS complex, so it is not visible in the ECG. The use of multiple combinations of recording locations on the limbs and the chest delivers information about different areas of the heart; the shapes and sizes of the P and T waves and the QRS complex vary with electrode placement.

The depolarization of the heart begins a cycle of atrial and ventricular contractions that cause chest-wall motion, which is measurable by motion sensors such as Doppler radar. The motion of the left side of the heart is shown in Figure 3.4, the phases of this cycle are

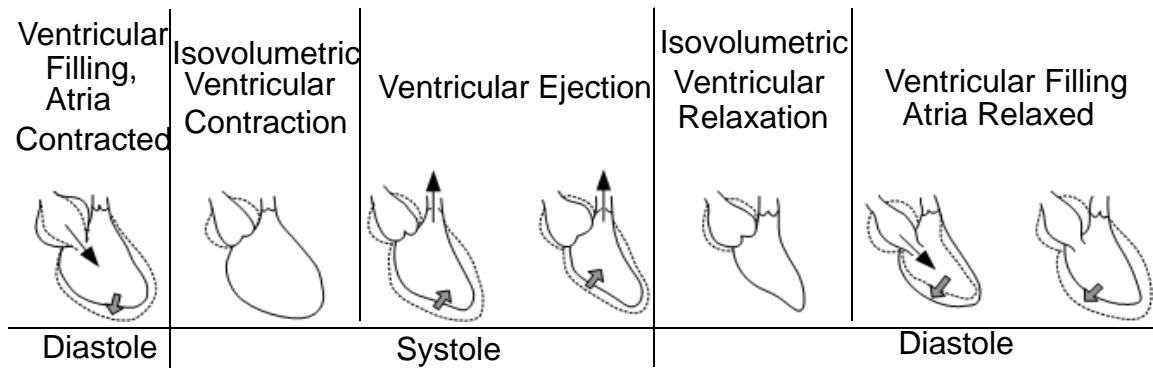


Figure 3.4: Motion of the left heart through the phases of the cardiac cycle. After [120].

outlined in Table 3.1, and the pressures and volumes in the left side of the heart during these cycles are illustrated in the Wiggers diagram in Figure 3.5. During systole, the contracting ventricles eject blood, and during diastole, the relaxed ventricles fill with blood. In systole, when the ventricles initially contract, the ventricular pressure is still below that of the aorta so that the aortic valve is closed, and the ventricle maintains constant volume in isovolumetric ventricular contraction. Once the ventricular pressure is greater than the aortic pressure, the aortic valve opens, and ventricular ejection begins. When the ventricles stop contracting, they maintain a constant volume while the atrial pressure is less than the ventricular pressure in isovolumetric ventricular relaxation. Once the AV valve opens, the ventricle begins to fill with blood from the atrium; this initial filling is passive, with the atria relaxed. Then the atrial contraction starts and fills the ventricle until ventricular pressure is greater than atrial pressure, and then the AV valve closes [80].

Table 3.1. Mechanical Events of the Heart

Mechanical Event	Systole or Diastole	Atria	Ventricles	AV Valves	Aortic and Pulmonary Valves	Stage, Fig.3.5
Isovolumetric Ventricular Contraction	Systole	relaxed	contracted	closed	closed	1
Ventricular Ejection	Systole	relaxed	contracted	closed	open	2
Isovolumetric Ventricular Relaxation	Diastole	relaxed	relaxed	closed	closed	3
Ventricular Filling, atria relaxed	Diastole	relaxed	relaxed	open	closed	4
Ventricular Filling, atria contracted	Diastole	contracted	relaxed	open	closed	4

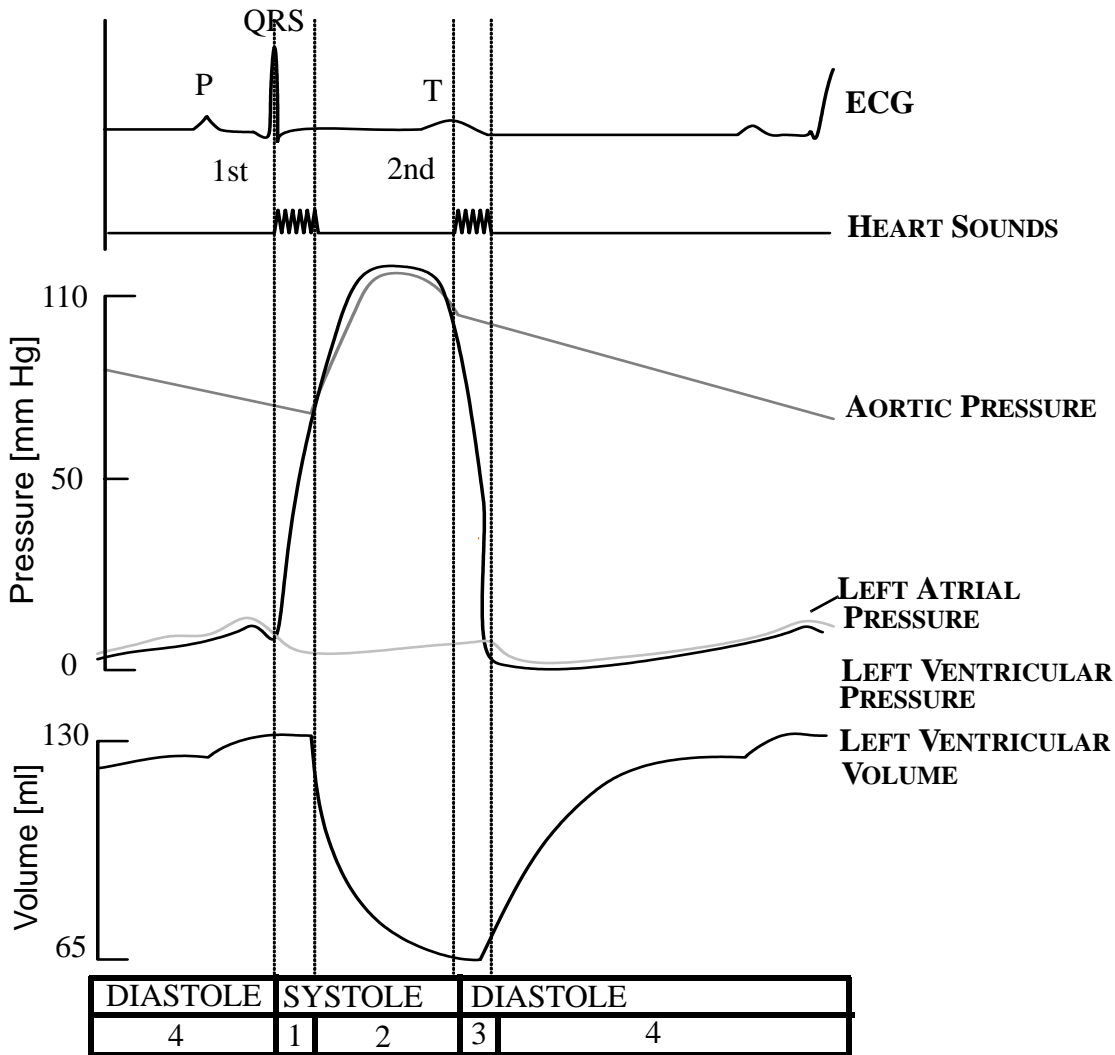


Figure 3.5: During the beginning of systole, the ventricles are contracting, but all the valves in the heart are closed; this is known as the isovolumetric ventricular contraction (1). The pressure in the ventricle increases, and when it is greater than the pressure in the aorta, the aortic valve opens, and ventricular ejection (2) begins. The pressure in the ventricle decreases as blood flows out of it, and when the pressure drops below that of the aortic valve, the aortic valve closes and diastole begins. Since all the valves in the heart are closed and the ventricle is relaxing, this is known as the isovolumetric ventricular relaxation period (3). When the left ventricular pressure drops below that of the atria, the mitral valve opens, and ventricular filling (4) begins. After [135].

3.2.3 Surface Motion Due to Heart Function

The non-contact Doppler radar system operates at frequencies where it detects primarily skin surface motions as was discussed in Chapter 2. Changes in the shape and volume of the heart during systole move the ribs and soft tissue near the heart, causing the chest to pulse with each heartbeat. This section explores how heart motion translates to both palpable and visible motions. The next section discusses actual measurement of skin surface motion, including a discussion of the measurement techniques.

The contraction and relaxation of the left ventricle causes a larger chest motion than other heart actions in healthy subjects. During isovolumetric contraction, the heart normally undergoes a partial rotation in a counter-clockwise (when facing the patient) direction, causing the lower front part of the left ventricle to strike the front of the chest wall [85]. The left ventricle also shortens as it contracts, making the heart more spherical, increasing its diameter and further adding to the impulse on the chest wall [90]. The peak outward motion of the left ventricular impulse occurs either simultaneously with or just after the opening of the aortic valve (just before the upstroke of the carotid pulse); then the left ventricular apex moves inward [85, 89]. The left ventricular motion causes the chest to pulse outward briefly, and the adjacent chest retracts during ventricular ejection [95]. This impulse occurs at the lowest point on the chest where the cardiac beat can be seen, and it is normally above the anatomical apex, in the fourth and fifth intercostal spaces in the left mid-clavicular line [81]. In healthy patients, this is usually the point of maximal impulse (PMI). It is typically palpable as a single brief outward motion, but it may not be palpable in as many as half of normal subjects over 50 years of age; obese, muscular, emphysematous, and elderly persons may have weakened or undetectable pulsations [85]. Some studies found a second outward movement at the apex: the pre-ejection beat [89].

There are also more gradual motions in the left parasternal region of the chest. There is an outward motion of the apex with left ventricular diastolic filling and an outward motion of the left parasternal region at the third intercostal space due to bulging of the left atrium at the end of systole [85, 89]. An increase in pulmonary blood flow can cause a prominent

systolic pulsation in the second intercostal space to the left of the sternum, caused by the closure of the pulmonic valve [85]. Because left parasternal motion is smaller than apex motion and occurs over a wide area of the praecordium rather than at a localized point, it is more difficult to palpate, although this motion is present in all healthy persons. Gillam, et al. [95] found that the left parasternal portion of the chest wall moves outwardly during early systole, followed by retraction in late systole in most normal subjects, but in some subjects, only the retraction occurs. Surface vibration from sounds measured in a stethoscopic exam cause negligible motion compared to the gross surface displacements caused by the heart striking the chest wall and the expansion and contraction of the heart [81]. Motion of the right ventricle is not generally palpable in healthy patients.

Mechanical circuits have been proposed as models for the chest wall, but vibration measurement in soft tissues is not a well studied topic. There have been no thorough studies on how the heart striking the inside of the chest wall couples to motion on the skin surface [136]. Some quantitative measurements have been made of the chest displacement, but there are no known studies of how these vary over age or body type. Not all the published measurements have taken into account how their measurement device loads the chest and alters the measurement [136].

3.2.4 Quantitative Measurements of Chest Wall Motion Due to the Heart

Many techniques for quantitatively measuring the gross displacement of the chest wall have been applied, including the impulse cardiogram [89, 95], a single point laser displacement system [79, 128], structured lights and the Moiré Effect [84], laser speckle interferometry [125, 134], a capacitance transducer [126], a magnetic displacement sensor [115, 116], and a phonocardiographic microphone [101]. The average displacement measured at the point of maximum displacement with each of these techniques is shown in Table 3.2. A table that shows all the measurements made in these studies can be found in Appendix G.

The impulse cardiogram has been used to make quantitative measurements of chest motion due to heartbeat at the apex by Deliyannis, et al. [89] and at the left parasternal region by Gillam, et al. [95]. This impulse cardiogram consisted of a metal rod supported by springs that is affixed to the chest wall in order to measure chest-wall motion. Displacement of the rod interrupts a beam of light on a photoelectric cell, which varies resistance in an electrical current. In measurement of normal subjects, Deliyannis, et al. [89] found that the largest impulse cardiogram measured had an amplitude of one centimeter. Gillam, et al. measured an average left parasternal deflection of 3.6 mm in 14 normal subjects [95]. The outward movement did not last longer than two-thirds of systole in any of the normal subjects. In six of the subjects, an outward movement due to the atrial beat was detected with a maximum pulse amplitude of 5 mm. In all the normal subjects, the apical impulse displacement was larger than the left parasternal displacement.

Ramachandran, et al. [126] used a capacitance transducer to measure out-of-plane chest wall motion on five subjects. The subjects were asked to hold their breath during the measurement in order to isolate heart-related movement. A maximum displacement of 0.04 mm was measured at the apex during the T wave.

Magnetic displacement sensors were used to measure chest wall pulsation by Mohri, et al. in two studies [115, 116]. A small magnet was placed on the skin at the measurement site, and a magnetic sensor determined changes in the magnetic field. The field sensor has an amorphous wire core as a component in a bridge circuit to sense changes in the magnetic field as the magnet moves while close to the core. The sensor with two cores has a 9-mm linear range and 1 μm resolution [116], while the sensor with the star-shaped core has a 20-mm linear region and 0.2 μm resolution [115]. The maximum measured chest displacement for the one subject in [115] was 0.21 mm, while in [116] a healthy subject had a maximum displacement of 0.035 mm, and an overweight subject had a maximum chest displacement of 0.012 mm.

Ikegaya, et al. [101] used phonocardiographic microphones to measure the motion of the chest wall in one subject. The microphones were calibrated to account for the coupling between the chest wall and the microphone using calculated chest wall impedance. The

amount of measured motion in this study depended on the amount of force applied to the chest. When a mass of 100 grams was applied, the chest motion was measured to be 0.05 mm, and when a mass of 200 grams was applied, the chest motion was 0.08 mm.

Berson and Pipberger [83] placed a lamp on the chest and used a detector with a photo-potentiometer to measure the chest motion, in three dimensions: normal to the chest, left-to-right, and head-to-foot. The three 30-40 year old males subjects each held their breath while they were measured at three different points - the apex, the fourth intercostal space to the left of the sternum, and the fifth intercostal space to the right of the sternum. Normal measurements at the apex ranged from 0.10 mm to 0.84 mm, and the magnitudes of the displacements in directions other than normal to the chest wall were comparable with those normal to the chest wall.

Single point laser displacement has been used to measure chest wall displacement [79, 128]. Aubert, et al. [79] used an infrared (850 nm) laser displacement measuring system and found a 0.6 ± 0.2 mm displacement at the point of maximal impulse at the apex on five normal male subjects, 20-40 years old. Ronaszeki, et al. [128] used a similar system to measure the apex motion in sixteen men, but the absolute displacement was not recorded. In the one shown data plot, a scale bar is given, and the measured peak-to-peak distance was 1.25 mm.

Brandt, et al. [84] evaluated chest wall motion with structured lights and the Moiré effect. This technique gives a contour map of distance from the source, so that the difference in plots must be assessed in order to determine the relative displacement. These images were recorded on one subject in [84]; the amplitude of the maximum displacement was estimated to be 1.7 mm, and the diameter of the quasi-spherical displaced area was about 8 mm.

Ramachandran and Singh [125] used laser speckle interferometry to measure displacement of the chest wall due to cardiac action on ten healthy men of different builds. A thin layer of paint was applied to the chest to enhance reflectivity, and the seated subject was asked to hold his breath during recording. Since the scan time for the 3-D image was long

compared to a cardiac cycle, the measurement was synchronized with the ECG so the scan could be performed over several cardiac cycles. The maximum displacement was over the apex and the left ventricle during the QRS wave, or ventricular contraction, 0.57 ± 0.11 mm at the apex and 0.53 ± 0.10 at the left ventricle. The largest significant displacement during the P wave, when the atria contract and the ventricles fill was above the left ventricle, 0.45 ± 0.07 mm. The largest significant displacement during the T wave, when the ventricles begin to refill was at the apex, 0.45 ± 0.03 mm. No assessment of how the build of the subject affected the measurements was given.

Singh and Ramachandran [134] used a similar technique to measure the in-plane cardiac displacement pattern of the area over the heart. The in-plane motion is expected to be much less than the motion perpendicular to the chest plane. Again, the cardiac movement was isolated by each subject holding his breath, and the exposure of the laser light was synchronized with the ECG so different phases of the cardiac cycle could be measured when the scan time was greater than the cardiac cycle length. The maximum in-plane displacement was 0.09 mm, measured at the apex during the QRS complex. Right ventricular in-plane motion was also at its maximum during the QRS complex, with a displacement of 0.07 mm. In-plane motion would not be measured by Doppler radar if it is pointed perpendicular to the chest, but it could be measured from the side.

While these studies are useful for getting an idea of how much the chest wall moves with heart beat, they leave many areas open to future research. First, none of these studies indicated the error due to the measurement, only the variation between subjects, so the accuracy of the data is unclear. Second, the number of subjects is small in all of these studies, with 20 being the greatest number of subjects, and some only giving quantitative data for a single subject. None of these studies compared males and females, and those that compared a healthy subject with an overweight subject or cardiac patient only used one of each, which does not provide reliable information about how body shape or heart condition affects the chest wall motion due to heartbeat. Third, in measurements that involved a sensor sitting on the chest, the sensor may have affected the chest motion, making those measurements unreliable. In [101], doubling the weight of the phonographic microphone

sensor increased the measured motion by 60%, indicating that the pressure applied to the chest in contacting measurements can significantly affect the measurement. The only non-contact measurements of out-of-plane chest wall displacement due to the motions of the heart that had more than one person in the study were those using infrared laser displacement [79] and laser speckle interferometry [125]. They both found the maximum displacement to be over the apex, and approximately 0.6 mm. Fourth, none of the studies explored how the position of the subject affected the chest wall motion due to heartbeat. The subject position affects how easy it is to palpate motion at the chest wall, so the position likely also affects the amount of chest wall motion without pressure as well.

Table 3.2. Quantitative Measurements of Chest Wall Motion Due to Heartbeat. Subjects are healthy unless otherwise specified.

Reference	Measurement Method	Subject(s)	Location on Chest	Position	Maximum Displacement [mm]
Aubert, et al., 1984 [79]	Infrared Laser Displacement	N=5 male age 21-40 years	Apex	lying in left lateral decubitus	0.6 ± 0.2
Berson and Pipberger, 1966 [83]	3-D Lamp-Photopotentiometer	N=3 male age 30-40	Apex	not specified	0.37 ± 0.41
Brandt, et al., 1986 [84]	Moiré Structured Lights	N=1 gender unspecified	Apex	left lateral supine	1.7
Deliyannis, et al., 1964 [89]	Impulse Cardiogram	N=1 gender not specified	Apex (PMI)	propped up in bed at a 45° angle	10
Gillam, et al., 1964 [95]	Impulse Cardiogram	N=20 14 males 6 females age 5-52 years	Left Parasternal Area, PMI	lying on a couch in a semi-recumbent position	3.6 (mean)

Table 3.2. Quantitative Measurements of Chest Wall Motion Due to Heartbeat. Subjects are healthy unless otherwise specified.

Reference	Measurement Method	Subject(s)	Location on Chest	Position	Maximum Displacement [mm]
Ikegaya, et al. 1971 [101]	Calibrated Phonocardiographic Microphone mass 100g	N=1 male	Apex	supine	0.05
	Calibrated Phonocardiographic Microphone mass 200g	N=1 male	Apex	supine	0.08
Mohri, et al., 1987 [115]	Magnetic Displacement Sensor	N=1 male 22 year old	Apex	not specified	0.21
Mohri, et al., 1985 [116]	Magnetic Displacement Sensor	N=1 male 22 year old	Apex	not specified	0.035
Ramachandran and Singh, 1989 [125]	Laser Speckle Interferometry	N=10 Varying build male	Apex QRS	seated	0.568 ± 0.11
Ramachandran et al., 1991 [126]	Capacitance Transducer	N=5 gender not specified	Apex T	supine	0.04
Ronaszeki et al., 1990 [128]	Linear Laser Displacement	N=1 male	Apex	left lateral decubitus	1.2
Singh and Ramachandran, 1991 [134]	Laser Speckle Interferometry (In Plane)	N=1 male	Apex QRS	not specified	0.09

The values of motion at the skin surface due to heartbeat are expected to vary widely between individuals due to physiological difference, age differences, and body shape differences. It is expected that the amount of chest motion due to the heartbeat changes with age, since the amount of and speed of the motion of the heart within the chest changes with age. Yip, et al., [140] found the expected amplitude of motion of the mitral valve along the long axis of the heart was expected to be 1.49 cm at age 20 and 1.22 cm at age

84. The expected velocity was 7.48 cm/s at age 20 and 5.22 cm/s at age 84. Owen [123] found that displacement of the septum decreased with age, but displacement of the left lateral wall and the posterior wall of the heart stayed constant between ages 49 and 73. Arcem, et al. [78] found that the absolute diastolic displacement of annular sites in children increased significantly with increasing body weight (which is expected since the size of the heart and thorax is increasing), but the percent displacement was inversely proportional to body weight.

3.2.5 Summary of Heart Motion

As the heart beats and drives blood into the arteries it rotates and its size changes, causing motion of the chest wall that can be detected at the skin surface, both by palpation and with non-contact sensors. The greatest motion occurs at the 4th and 5th intercostal space when the left ventricle strikes the chest wall as it contracts. More gradual motions due to filling of the heart occur in the left parasternal region. The maximum motion detected at the apex with non-contact sensors has an average of 0.6 mm, and this value is expected to vary widely over population due to differences in physiology, health, fitness and age. However, this average motion is sufficient to provide detection with a Doppler radar system.

3.3 Circulatory System Motion

Blood vessels carry blood from the heart to the tissues and back, as shown in Figure 3.6. The blood is moved through the body by the pumping of the heart, the recoil of the arteries, the compression of veins by skeletal muscle, and the negative pressure in the thorax during inspiration. Blood pulses through the distensible arteries, which expand when the heart pumps blood into them during systole and contract during diastole, when the aortic valve is closed. As the arteries expand and contract, the skin above them moves; the skin surface motion is most prominent above superficial arteries. The following sections describe the location and structure of the arteries and veins, how they distend as the

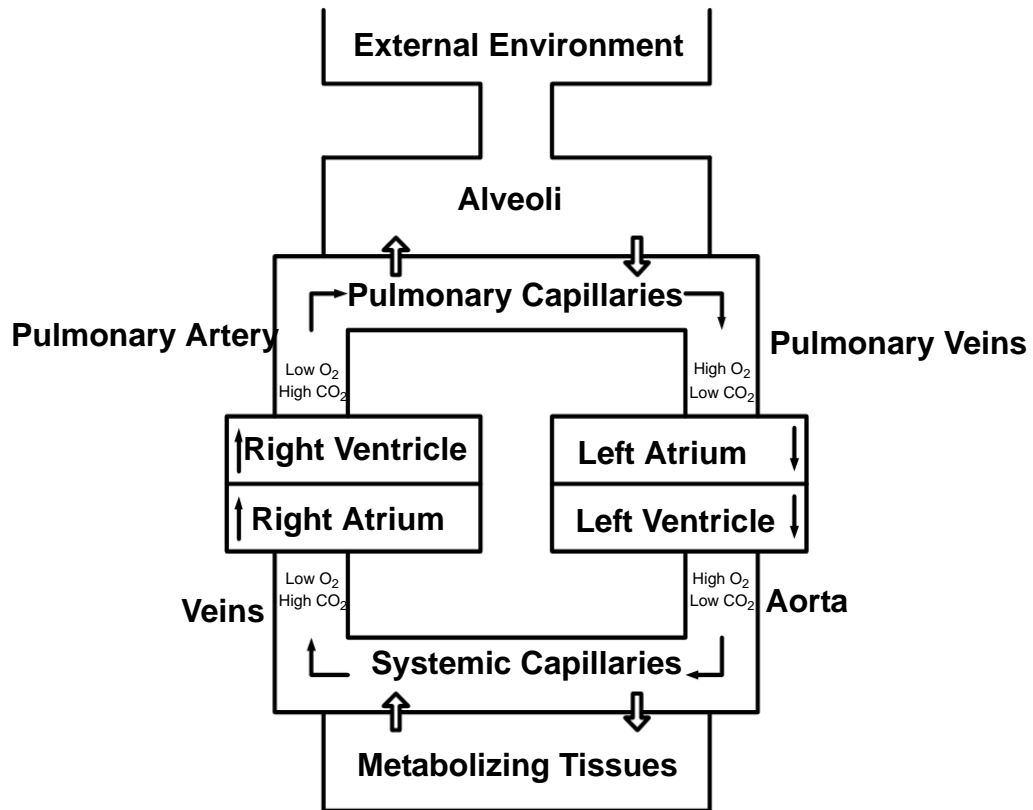


Figure 3.6: Interaction of the respiratory and circulatory systems. After [109].

pressure of the blood in them varies during the cardiac cycle, and how this distension affects the skin surface motion.

3.3.1 Location and Structure of Major Arteries and Veins

The diameter of the arterial vessels progressively decreases from the aorta to the capillaries, as shown in the model of the arterial system in Figure 3.7. When arteries are near the skin surface, their pulses are palpable and sometimes visible. The main superficial arteries are: the carotid artery in the neck, the brachial artery at the elbow, the radial artery in the wrist, the femoral artery in the upper thigh, the popliteal artery in the back of the knee, the posterior tibial artery in the inside ankle, and the dorsalis pedis artery on the top of the foot.

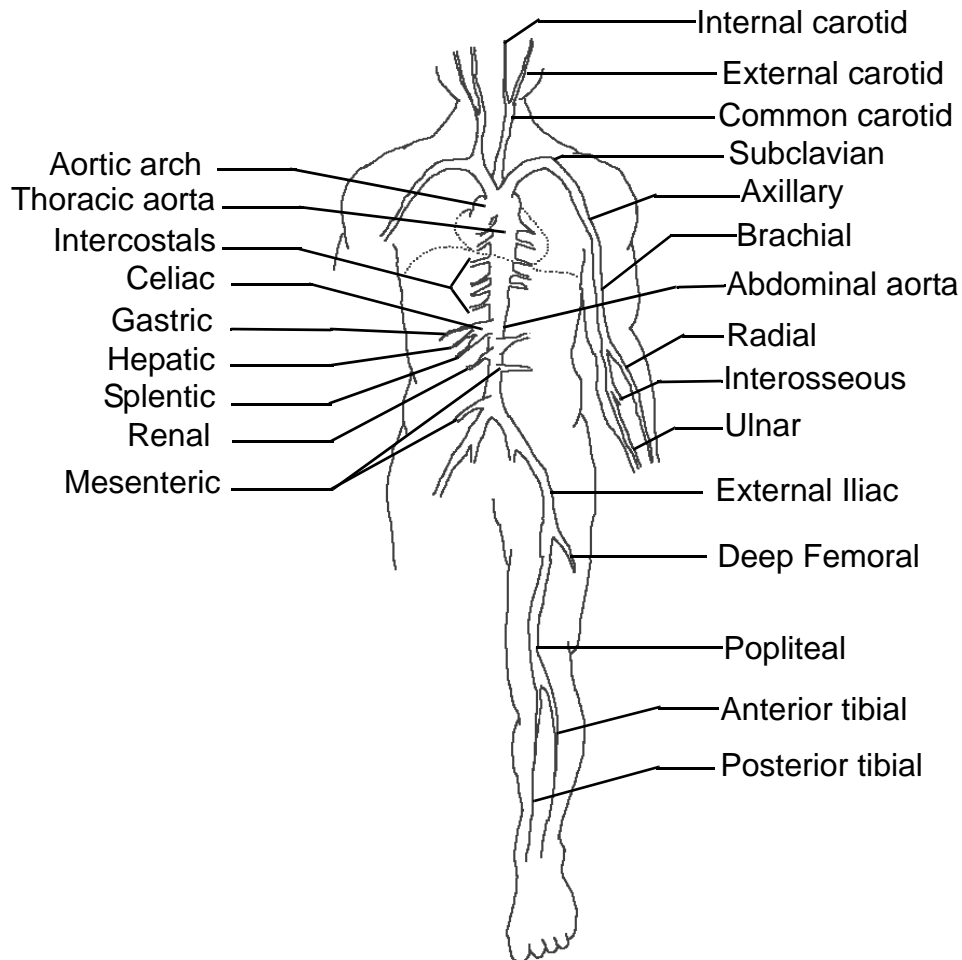


Figure 3.7: Model of the arterial system, showing major arteries. After [131].

Elastic arterial tissue enables arteries to accept blood from the heart in impulses while delivering blood to capillaries by gradually stretching and recoiling. As shown in Figure 3.8, during systole, when the heart pumps blood into the aorta, only one third of the stroke volume (the volume of blood which leaves the left ventricle) leaves the arteries; the other two thirds of the blood distends the arteries, raising the arterial pressure. During diastole, when the heart is filling with blood, the stretched arterial walls begin to return to their non-stretched shape, continuing to push blood into the arterioles as the arterial pressure falls. Larger, more central arteries dilate more than peripheral arteries, which are less distensible. Older people have less distension in their arteries than children do, because arteries become more rigid over time [121].

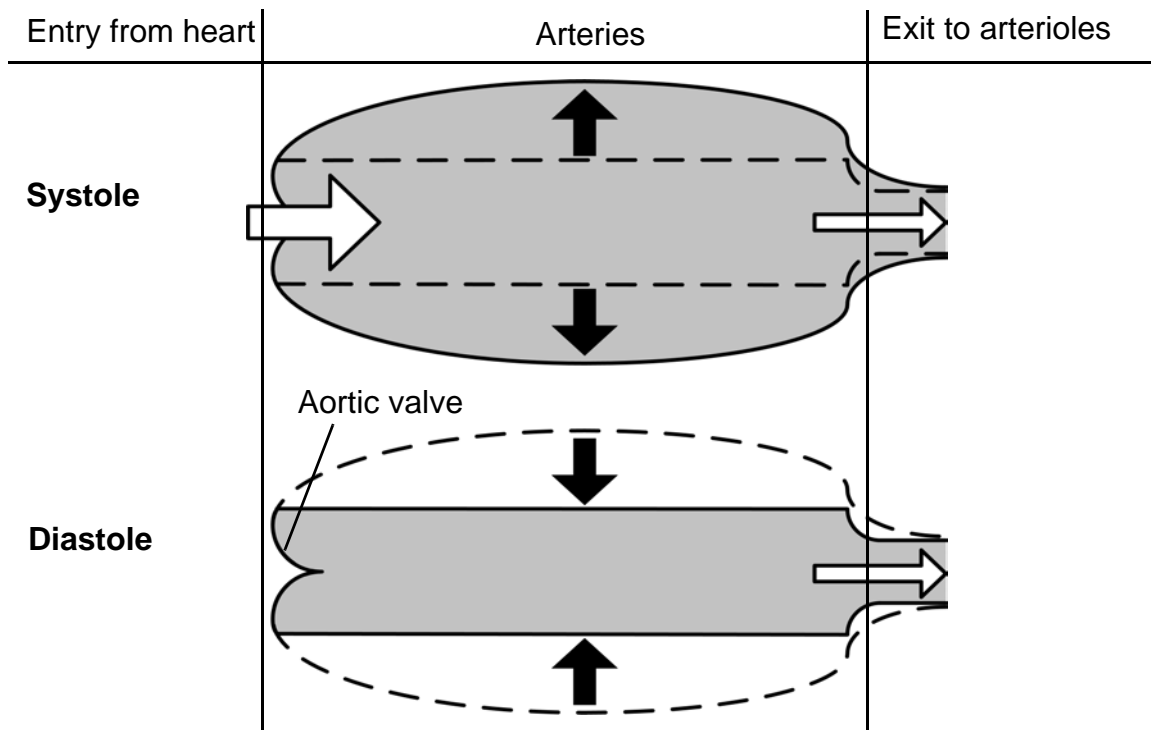


Figure 3.8: Diagram of arterial pressure in systole and diastole. During systole, the artery distends, storing blood; during diastole, the artery contracts so blood continues flowing into the arterioles after the aortic valve is closed. After [135].

Veins have much thinner walls than arteries because the blood in the veins is under lower pressure. Veins have little elastic tissue, and therefore are not distensible like arteries. They can accommodate large volumes of blood with minimal pressure changes, and they lie flat when they are not full and they become cylindrical as they fill with blood. Valves in veins prevent backflow as blood is pumped against gravity by skeletal muscles.

3.3.2 Blood Flow Through Arteries and Veins

With each ventricular contraction, the heart ejects a surge of blood into the aorta, leading to flow, pressure, and diameter waves as the blood propagates through the body. Flow waves are the changes of the velocity of blood flowing through the arteries. The blood velocity varies 70-90% from its mean velocity, which decreases as the arteries get further from the heart [121]. Pressure waves are the increase in pressure that propagates from the aorta through the other arteries in body. In the large arteries, the pressure fluctuation is as

much as 300% of the mean pressure, while in the peripheral arteries the fluctuation is 40-80% of the mean pressure [121]. Propagating changes in arterial diameter, or diameter waves, result from the stretching of the compliant arteries caused by the change in pressure. The larger, more central elastic arteries dilate more than the peripheral arteries, which are less distensible. The carotid artery typically has a 8-15% variation in diameter, while the radial artery typically has a 1.6% variation in diameter [86, 117].

3.3.3 Surface Motion from Blood Flow

Lee [107] presents a simple model of an artery in the center of a cylinder of a homogeneous, isotropic, elastic solid tissue, and derives an expression coupling the arterial wall motion with surface motion, as is shown in Figure 3.9. Lee postulates that the volume expansion at the skin surface must be equal to the volume expansion at the vessel wall, due to the incompressibility of tissue. Therefore the size of the appendage and the change in the cross-sectional area of the vessel determine the amount of motion at the surface. The change in the area of the artery is determined by its distensibility, which is influenced by several factors, including how close the artery is to the heart, the size of the artery, and the age of the subject. This model is an oversimplification, however; the arteries most frequently palpated are the superficial arteries, as listed in Table 3.3. When the artery is not in the center of the limb, the arterial expansion is not a bulging of the entire limb, but rather a pulsation of the area of the surface of the limb closest to the artery.

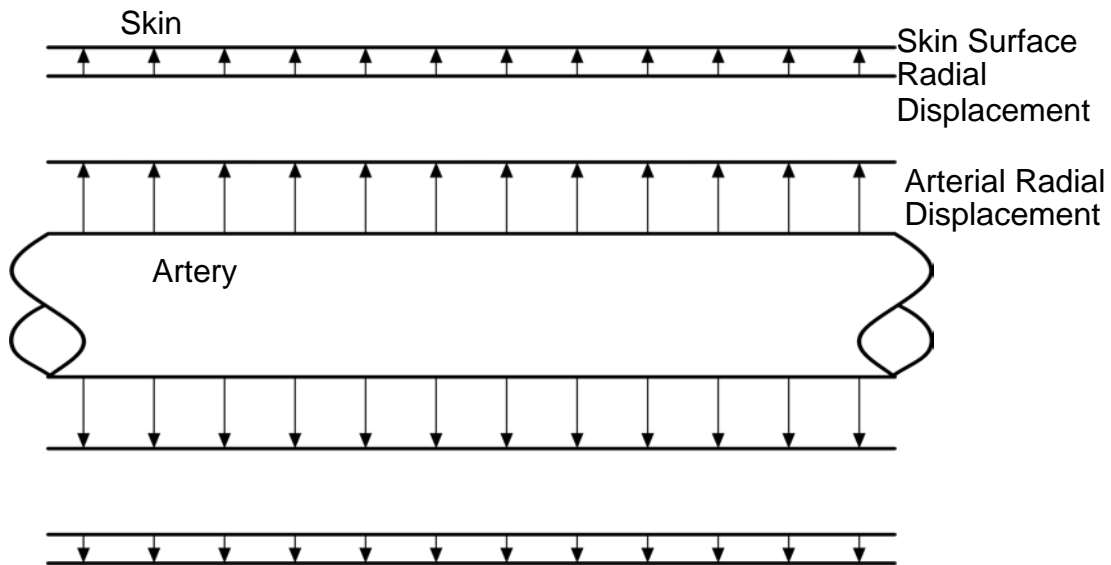


Figure 3.9: Lee's model of an artery in tissue for analyzing surface motion with radial motion of the vessel wall. After [107].

Hong and Fox [100] used optical interferometry to measure the velocity of skin above superficial arteries and the time delay between the R wave of the electrocardiogram and the pulse, as is shown in Table 3.3. Although the velocity measurements indicate that there is detectable motion due to pulse at the skin surface, they did not quantitatively measure the displacement. In addition to the pulse points measured by Hong and Fox, visible pulsations are available at the aortic artery (in the 2nd right intercostal space at the suprasternal notch) and at the pulmonic artery (in the 3rd left intercostal space) [81].

Mohri et al. [115] used a small magnet placed on the chest skin surface and a magnetic field sensor with two micron resolution to measure the blood vessel displacement at the skin surface, as described in Section 3.2.4. They found that the carotid artery produced a skin displacement of 0.06 mm while the jugular vein produced a skin displacement of 0.01 mm. In [116], the same authors measured the carotid artery to produce a skin displacement of 0.05 mm, the radial artery to produce a skin displacement of 0.03 mm, the finger pulse to produce a skin displacement of 0.01 mm, and the jugular vein to produce a skin displacement of 0.005 mm. However, this is a contacting measurement, and the measurement may have been affected by the presence of the magnet. The same sensors were used to measure chest wall motion due to the heart in Section 3.2.4, and they measured the chest

wall motion to be twenty times less than that measured with non-contact techniques. In [116], the arterial motion was similar in amplitude to the heart motion.

Table 3.3. Time Delays and Arterial Diameters Associated with Superficial Arterial Pulses

Arterial Pulse	Location	Delay (sec) from R wave [100]	Arterial Diameter (mm)	Percentage Variation in Diameter (%)	Surface Motion [mm]
Carotid	neck	0.15	6.1 [102]	10.13 [86] 14 [102]	0.06 [115] 0.05 [116]
Digital	finger				0.01 [116]
Radial	wrists	0.20	2.36 [117]	1.6 [117]	0.03 [116]
Brachial	inside of elbows	0.17	3.1 [102]	7.83 [86]	
Femoral	upper thighs	0.17	7.1 [102]	7.69 [86] 7 [102]	
Popliteal	back of knees	0.24		9.10 [86]	
Posterior Tibial	inside ankles	0.28		7.24 [86]	

The jugular vein is covered by a muscle, and is usually not visible as a discrete structure, but its pulsations are transmitted to the skin of the neck, where they are usually visible. The jugular venous pulse has two peaks and two troughs, distinguishing it from the carotid arterial pulse, which has a single upstroke. The venous pulses are typically quite distinct when the patient is at a 45-degree or greater angle, but are not typically visible in upright healthy subjects [85].

The measurements that have been made indicate that there is measurable motion at the skin surface at superficial pulse sites. This motion may be measurable by Doppler radar, and measurement of the amount of surface motion due to pulse is an interesting area for future research that has not been thoroughly explored. It is expected that motion due to arterial pulsation is less than that due to heartbeat.

Although there is no significant change in left ventricular ejection volume with age, the arterial pressure wave varies greatly with age. With age, arterial wall thickness increases, arterial diameter increases, and arterial distensibility decreases [102]. In [114], the arterial wall rigidity was expressed as:

$$\alpha = 0.421 + (0.0602 \times age). \quad (3.1)$$

This indicates that pulses will be smaller and more difficult to measure in older subjects. The data provided by Meinders and Hoeks [114] indicates that the change in cross sectional area of the artery with a pulse is 50% less for 60-70 year-olds than it is for 20-30 year-olds. A decrease in the amount of change in diameter of the arteries would decrease the amplitude of skin surface pulsations. A decrease in the amplitude of skin surface motion with age would reduce the signal-to-noise ratio in measurement of pulse with Doppler radar, as the SNR of Doppler radar is proportional to the amount of motion at the skin surface.

3.3.4 Summary of Surface Motion Due to Pulse

The skin surface moves measurably due to arterial pulsations at locations where the artery is near the skin surface. This motion does not necessarily occur at the same time as the maximum chest wall motion due to the heart beat. The delay between the R-wave, which causes ventricular contraction, and the posterior tibial pulse is approximately 0.26 seconds [100]. This delay from the chest wall motion to the motion at the furthest pulse points from the heart could cause some spreading in time of the heart signal when measured by Doppler radar, since it integrates over all motion. However, according to Mohri et al, [115] the chest displacement is 4 times that of the largest carotid pulse, and therefore the much smaller pulse should not cause a major problem.

Although the relationship of skin surface displacement due to pulse and age has not been published, increases in arterial rigidity with age are well proven, and they cause decreased change in cross sectional area with increasing age. Therefore, it is expected that any skin surface motion due to arterial pulses will decrease as the age of the measurement subject increases.

This section has focused on motion at the superficial pulse sites, which most likely create the largest displacement of arterial pulses. However, other areas of the body likely also pulse at the heart rate, although with a smaller amplitude. Ko, et al. [103] use interfer-

ometric holograms to measure cerebral pulsations on the scalps of patients with incomplete skulls. In the process, they also noticed motion at the eyes at the pulse rate. The amplitude of the pulsations was not provided.

3.4 Respiratory System Motion

For gas exchange to occur in the lungs, air with carbon dioxide needs to be removed from the lungs and air with oxygen needs to be inspired. In respiration, muscles contract to generate changes in thorax volume, which create pressure differences between the thorax and the external environment, causing air to move in and out of the lungs, from areas of high pressure to areas of low pressure. The motions of the thorax and the abdomen cause significant displacements at the skin surface that are measurable with Doppler radar, allowing non-contact measurement of respiration rates. This section describes the motion associated with breathing, and how this motion affects the skin surface's motion.

3.4.1 Motion Associated with Breathing

Figure 3.10 shows the location of the muscles associated with breathing, the lungs, and the ribs. As the diaphragm contracts, its dome descends into the abdominal cavity, causing the thorax to elongate and increase in volume, and pushing the abdominal viscera out against the compliant abdominal wall. In normal inspiration the diaphragm extends 1-2 cm into the abdominal cavity. In deep inspiration the diaphragm can descend as much as ten centimeters; at this point the abdominal wall is stretched to its limit of compliance, and the abdominal pressure increases, limiting the downward motion of the diaphragm. When abdominal displacement is prevented, for this or any other reason, further contraction of the diaphragm causes the lower ribs to elevate, further decreasing the thoracic pressure [127].

The external intercostal muscles contract simultaneously with the diaphragm for inspiration. If the diaphragm contracted alone, the decrease in pressure would pull the rib cage downward and inward, decreasing the amount of air inspired. Contraction of the external

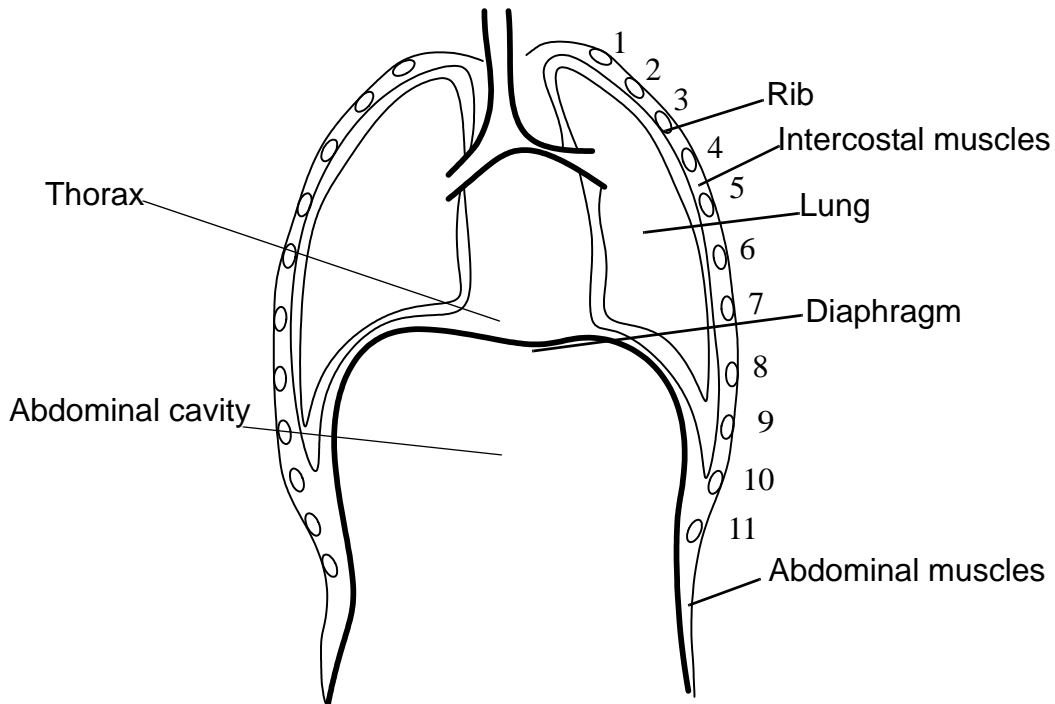


Figure 3.10: The thoracic wall and body cavities. After [122].

intercostal muscles pulls the ribs upward and outward, further increasing the volume of the thorax and preventing the collapse of the ribcage. If the external intercostals contracted by themselves, the decrease in pleural pressure would cause the flaccid diaphragm to be displaced into the thorax rather than leading to inspiration. Joint action by the external intercostal muscles and the diaphragm is required for inspiration [112, 113].

There are three types of rib movement at different points in the rib cage: the “pump-handle” motion of the upper ribs, the “bucket-handle” motion of the lower ribs, and the “caliper” motion of the lowest ribs, as shown in Figure 3.11. The dominant motion of the upper ribs is rotation upward around their long axis, known as “pump-handle” motion. The lower ribs connect to the spine differently than the upper ribs, so that they can glide as well as rotate. The combination of this motion and the rotation keeps the front of the rib at approximately a constant location, and the ribs effectively rotate upward while fixed at the front and the back in a “bucket-handle” motion. The lowest ribs are not connected to the sternum, and are known as floating ribs. These ribs tend to flare open and

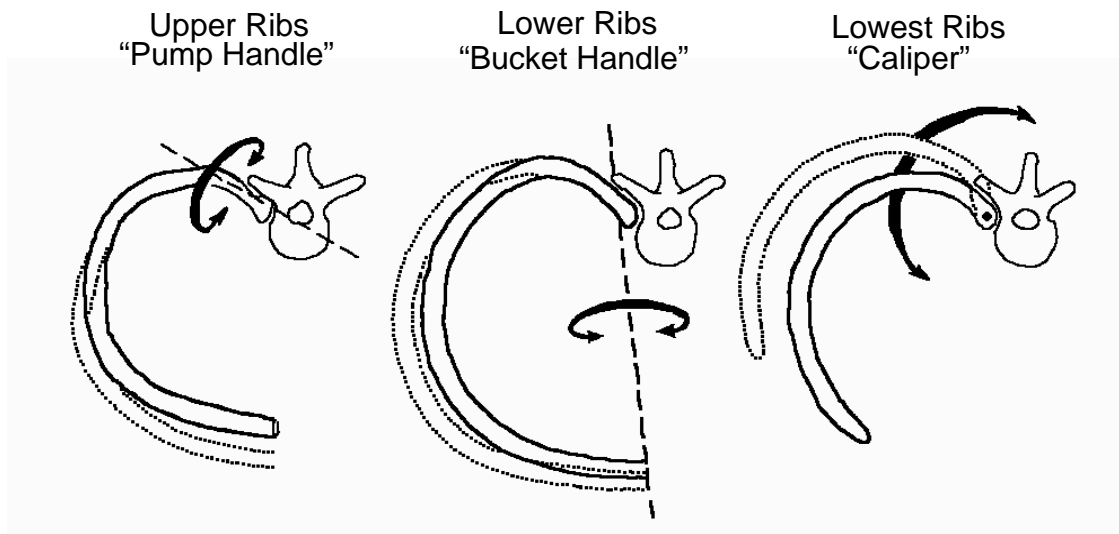


Figure 3.11: Movement of upper, lower, and lowest ribs. After [122]

backward, rotating around their connection with the spine in a “caliper” motion. Since the ribs increase in size and curvature as they go downward, at any given horizontal cross-section, the diameter increases as the ribs hinge upward [122].

During normal quiet breathing, no muscles contract for expiration; the elastic recoil of the alveoli is sufficient to decrease the alveolar volume. During exercise, speech, singing, coughing, or sneezing, muscles are required for expiration. The abdominal wall muscles contract, increasing abdominal pressure and pushing the contents of the abdomen up against the relaxed diaphragm, pushing the diaphragm into the thorax. Contraction of the abdominal muscles also depresses the lower ribs and pulls down the lower ribs, further decreasing the volume of the thorax. The internal intercostal muscles also contract in expiration, depressing the upper rib cage [122]. Contraction of the external intercostal muscles raises and enlarges the rib cage, further increasing the volume of the thorax. Muscles in the abdominal wall are muscles of deep expiration: contraction of these muscles increases the abdominal pressure, elevating the diaphragm and depressing the ribs. Contraction of the internal intercostals pulls the ribs downward, decreasing the volume of the thorax for active expiration [122].

3.4.2 Chest-Wall Motion Associated with Breathing

The chest surface motion associated with breathing is the combination of the abdominal and rib cage movements was described in the previous section. Kondo, et al. [104] present MRI data indicating a linear correlation between cross-sectional area of the thorax, displacement of the diaphragm, displacement of the rib cage, and lung volume. Wilson, et al. [137] present data showing that the pump-handle angle varies from 20° to 30° on the third rib, and from 30° to 37° on the seventh rib. This motion caused the rib radius to vary from 10.6 to 10.8 cm at rib three, and to vary from 137 to 142 mm at rib seven. DeGroot, et al. [88] measured the chest motion in the front/back, left/right, and up/down directions at thirty-six points. The largest motions were the sternum, which moved forward 4.3 mm with inspiration, and the navel, which moved forward 4.03 mm with inspiration. Kondo, Uhlig, et al. [105] measured the relationship between tidal volume and abdominal wall linear displacement with a laser displacement measuring device; they found the abdomen distended 4 mm with a 400 mL inspiration, and 11 mm with an 1100 mL inspiration. They also showed a 12-mm abdominal displacement during spontaneous breathing in another subject. Overall, there is a 4 mm to 12 mm radial expansion of the thorax during breathing, depending on individual physiology and how much air is inspired.

3.5 Interaction of Respiratory Motion and Cardiac Motion at the Skin Surface

Many studies have shown that motion of the lungs and diaphragm due to respiration move and deform the heart [111, 119, 133]. However, apparently no studies have been performed on the interaction of respiratory and cardiac motion at the chest's surface. In the studies of chest wall motion due to the heart described in Section 3.2.3, the subjects were holding their breath during the measurements, so it is not known how the respiratory motion of the heart affects the chest wall motion due to the heart.

The motion and deformation of the heart due to respiration has been measured with magnetic resonance imaging (MRI) and coronary angiography, in order to create models

so that MRIs of the heart can be performed without the patient needing to hold his or her breath. Results from some of these measurements are summarized in Table 3.4. Results indicate that the feet-to-head motion of the heart is roughly linear with the diaphragm motion in the same direction, but some subjects had a good degree of hysteresis in this motion [119]. In [119], the heart moved from 12 to 24 mm due to respiratory motion in ten healthy volunteers. In [111], combined rotations and translations led to a 22.5 ± 4.5 mm total displacement of the apex of the left ventricle in the eight healthy subjects. The heart also rotated 3.8 ± 1.9 degrees, and the left ventricle deformed up to 4 mm due to respiration.

Table 3.4. Translations and Rotations of the Heart Between Maximum Inhale and Maximum Exhale.

Source	Total Left Ventricle Displacement [mm]	Translation Cranio-Caudal [mm]	Translation Antero-Posterior [mm]	Translation Right-Left [mm]	Rotation CC [°]	Rotation AP [°]	Rotation LR [°]
[133] 10 patients	--	4.9 ± 1.9	1.3 ± 1.8	0.4 ± 2.0	-0.7 ± 1.5	1.2 ± 1.3	-1.5 ± 0.9
[111] 9 patients	11.3 ± 7.0	8.3 ± 3.9	1.5 ± 1.6	-1.4 ± 2.1	-0.7 ± 1.7	2.7 ± 3.1	-1.4 ± 2.1
[111] 8 volunteers	22.5 ± 4.5	16.4 ± 4.5	7.1 ± 3.1	3.8 ± 1.3	-0.6 ± 3.5	3.8 ± 1.9	-0.5 ± 1.8
[111] 9 patients & 8 volunteers	17.3 ± 8.1	12.1 ± 5.8	4.1 ± 3.7	2.0 ± 2.1	-0.7 ± 2.6	3.2 ± 2.6	-1.0 ± 1.9

Rosa [129] studied how the acceleration of the skin surface as measured with a vibrocardiogram was affected by respiration by taking measurements during normal respiration, full inspiration breath hold, and full expiration breath hold. They found the acceleration patterns that corresponded to ventricular contraction to be much more reproducible in during the breath hold measurements than with normal respiration, indicating that the rotary heart movements and respiratory displacement of the heart distort the skin surface motion [129].

The translation, rotation, and deformation of the heart due to respiration certainly affect how the heart's motion interacts with the chest wall at different points in the respira-

tory cycle. The studies of chest wall motion due to the heart beating in Section 3.2.4 all required the subject to hold his/her breath. There are no known studies of skin surface chest motion due to beating of the heart during respiration or at different levels of inspiration. This provides an interesting area for future research. Since the contraction of the left ventricle causes the largest motion at the chest wall in healthy subjects, a 4 mm deformation of the left ventricle likely changes the motion due to heartbeat at the skin surface. Additionally, a 2 cm motion of the heart could affect what part of the heart causes the largest skin surface motion, changing the relationship of the peak due to the Doppler signal.

For estimating the signal-to-noise ratio of the Doppler radar system, as in Appendix D, the integral of the mean-squared motion in the direction of the antenna over the cross-sectional area of the chest is required. This value is then multiplied by factors for directivity of the reflected radar signal and reflectivity of the chest. The breathing motion could affect the area and the directivity of the heart signal, the RMS motion from the heart at the skin surface, and even which part of the heart is causing the maximum chest motion.

3.6 Vital Signs and Their Measurement

Vital signs include pulse rate, respiration rate, blood pressure and temperature [97]. These are recorded in all patients regularly in both clinical and emergency situations, because they can indicate the severity of an illness, and changes in their values can be an early warning sign of a changing physiological condition. In some conditions, it is desirable to continuously monitor select vital signs. Since heart and respiration rates can be measured with Doppler radar, this section focuses on these two vital signs. Since this technology would compete primarily with non-invasive measurements of these rates, only non-invasive alternative measurements are discussed.

3.6.1 Measuring Vital Signs - Clinical Measurements

3.6.1.1 Respiratory Rate and Patterns

Most studies indicate 16 to 24 breaths per minute is a normal adult respiratory rate, but some studies indicate that rates as low as 8 breaths per minute are normal [97]. Respiratory rate, pattern, effort and volume of respiration together are a strong indicator of respiratory physiology. The respiratory rate is typically measured through observation and/or palpation of the chest, with the patient unaware that the breathing is being observed. An accurate reading requires counting for a full minute, because the rates are so low [97]. The measurement of respiratory rate by different examiners can vary significantly [91], and if the patient realizes that their respiration is being monitored, they may change their breathing rate and pattern [97].

3.6.1.2 Pulse Rate

The pulse is examined to establish cardiac rate and rhythm, and the pattern of the palpation can be used for further diagnosis of cardiac and circulatory disease. The normal resting heart rate in adults is 50 to 90 beats per minute [97]. A heart rate outside the normal range can indicate either a cardiac abnormality or another condition that causes abnormal heart rate. An irregular pulse is usually indicative of a cardiac abnormality. The amplitude and contour of the pulse, such as a small, weak pulse, a large bounding pulse, or an irregularly shaped pulse can be indicative of a pathophysiologic state [97].

The clinician can measure the rate, rhythm, pressure, and upstroke of the pulse at the bedside with any timepiece that measures seconds. The clinician typically measures the radial pulse at the wrist with the tips of the first and second fingers. Pulses are also palpated at the carotid, brachial, femoral, posterior tibial, and dorsalis pedis arteries. If no abnormalities are present, the rate is typically obtained by counting for 15 seconds and multiplying the number of pulses by 4 [97].

When continuous monitoring is required over a long period, a bedside cardiac monitor is often used to monitor heart rate and rhythm. A bedside cardiac monitor is typically a

3-lead electrocardiogram [96]. The positive electrode is typically pasted in the V1 position between the 4th and 5th ribs on the left side of the sternum, the negative electrode is placed at the right shoulder, and a ground electrode is placed at the left shoulder [96]. Depending on the symptoms and diagnosis of the patient, a 5 or 12 lead electrocardiogram is sometimes used at the bedside. Sometimes, a fingertip pulse oximeter is used to measure heart rate as well as oxygenation.

Bedside cardiac monitors are only useful for patients confined to a bed or a chair since the electrodes are affixed to the patient and are attached to the monitor via cables. The electrodes can irritate the skin of some patients, and poor electrode contact or patient movement can cause artifacts in the electrocardiogram signal [96].

The twelve-lead electrocardiograph is the gold standard for cardiac monitoring [96]. Six of the leads are placed in the frontal plane of the body and six are placed in the horizontal plane of the chest, along the fourth or fifth intercostal space. Each of the leads indicates a different path of electrical depolarization, and different combinations of leads are required to detect different disease states. Any lead will indicate the heart rate and rhythm, but more leads are required to determine the presence or absence of hypertrophy, ischemia, or necrosis, for example.

Since the ECG signal measured at the chest surface is under 2 mV, it is important to optimize the skin-electrode interface. Any hair present needs to be shaved, and the skin needs to be cleansed with alcohol and abraded, as the top layer of skin can be a source of high resistance. Loose electrodes can cause artifacts that simulate disease states. The most commonly used electrodes are pre-gelled disposable silver/silver chloride electrodes [99].

3.6.2 Commonly Used Alternative Methods for Vital Signs Monitoring

Methods of measuring vital signs typically used in the emergency vehicle and in the clinic are not ideal for all situations. The standard measurements require contact with the subject, and either require the presence of a medical professional or that the subject be

wired to the monitor. Alternative techniques for measuring vital signs have been developed to meet different needs.

3.6.2.1 Respiration

There are three methods by which respiration can be measured: measurements of airflow, measurement of respiratory movement and effort, and measurement of oxygen saturation. Direct measurements of airflow typically involve the use of face masks, which can change the subject's respiration, but provide information about the total volume. Indirect measurements of airflow, such as a thermocouple or capnography, have less adverse effects. Measurements of respiratory movement have been common indirect measurements of airflow since Konno and Mead's two-degree-of-freedom model of chest wall motion was introduced in the 1960s [106]. This model indicates that ventilation can be derived from measurement of the rib cage and abdomen displacements, but recalibration is required when the subject varies his posture. McCool, et al.'s three-degree-of-freedom model works accurately as posture varies without requiring recalibration [112]. Peripheral tissue oxygenation is measured with a pulse oximeter; this provides an indication of the efficacy of respiration, but does not provide the respiration rate.

Thermocouples and capnography are two indirect measurements of airflow that do not require a face mask and provide respiration rate, but not volume of airflow. Thermocouples infer airflow by changes in temperature in front of the nose and/or the mouth: exhaled air is warm, and inhaled air is cool [124]. Capnography, the measurement of expired carbon dioxide, is used to assess airflow in some sleep laboratories. Inhaled air contains negligible amounts of carbon dioxide, while exhaled air contains 6-7% CO₂. An infrared analyzer can be placed in front of the nose and/or mouth to detect airflow by changes in the CO₂ concentration [124].

Plethysmography is the measurement of changes in volume of organs or other body parts. For respiratory plethysmography, measurements are typically made with bands around the chest and the abdomen. These bands typically measure changes in diameter, circumference, or cross-sectional area of the thorax by changes in impedance or with

strain gauges. In respiratory inductance plethysmography, wire coils stitched to elastic bands are placed around ribcage and abdomen, and the inductance of the coils is measured. These measures a complex function of cross-sectional area and circumference [98]. Impedance plethysmography, involves placing electrodes on the skin and measuring changes in the impedance between the electrodes with respiration [77, 98, 108, 138].

Strain gauges can be placed on the abdomen and rib cage wall to monitor the distension of the abdominal and thoracic cavities, and thereby assess respiratory changes [92]. These devices are easy to use, though do not lend to an estimation of respiratory volume.

Pulse oximetry is used for the chronic assessment of oxygenation. The absorption of light passing through the ear or the finger is related to the amount of oxyhemoglobin in the tissue it passes through. The device eliminates the constant absorption due to the tissue, and measures only the absorption of the arterial blood. Pulse oximetry measures the oxygen saturation of arterial blood. It can be used to measure respiratory disturbance, but does not measure airflow, respiratory movement or respiration rate. [124]

3.6.2.2 Pulse Rate

The heart rate is typically measured via its electrical impulses. The Polar strap is a commonly used exercise heart rate monitor. It measures a bipolar electrocardiogram with an elastic chest strap. At each R-wave, it wirelessly transmits a pulse to a receiver. This device works well during activity, but does not give the information of a true electrocardiogram [130]. If the skin under the electrodes is not moistened, the signal can be inaccurate. The receiver uses the pulse timings to calculate the rate.

The pulse oximeter, as described in the previous section, can be used to measure the pulse rate. Although its primary purpose is to measure oxygen saturation of arterial blood, it also measures a variable absorption due to the change in blood volume with each pulse. Because they have this information, most pulse oximeter displays also include the pulse rate [139].

3.6.3 Measurement of Heart and Respiratory Surface Motion

Surface motion measurement is by definition non-invasive, which makes such measurements convenient for home-monitoring and long-term monitoring. Some measurements are non-contact and non-invasive, and these can be used without the knowledge of the subject, with reduced risk of the measurement device affecting the parameter being measured. However, these measurements do not necessarily measure the same parameters as gold-standard measurements. Surface motion measurement of the heart measures physical motion, which is different than the electrical signal provided by the electrocardiogram. Surface motion measurement of respiration measures the motion of the abdominal wall and rib cage, but does not directly measure the airflow. Doppler radar measurement of heart and respiration is also a measurement of surface motion and is discussed in this section followed by other methods.

3.6.3.1 Radar Measurement of Physiological Motion

According to Doppler theory, as presented in Chapter 2, a continuous wave radar with a stationary person's chest as the target should receive a signal similar to the transmitted signal with its phase modulated by the time-varying chest position and a received power determined by the radar system properties, the environment, and the area of the moving part of the body. When the phase is demodulated, the chest displacement over time can be inferred, from which heart and respiration rates can be determined. Analog and digital signal processing remove noise and interference, separate the heart and respiration signals, determine the heart and respiration rates, and prepare the signal for display. Previous work in microwave monitoring of heart and respiration is described in detail in Chapter 2, Section 2.1.3. This system works from a distance, non-contact, and through clothing. It does not require contact with the subject or that the subject be wired to a monitor. Because it is a motion sensor, it does require that the subject be still. It will measure and motion within the antenna beam, and with a single transceiver it cannot distinguish between motion from two different sources.

3.6.3.2 Surface Motion Measurement of Respiration Rate

Two main surface measurements of respiration rate exist: measuring the circumference or area of the thorax and abdomen, or measuring the linear displacement of the thorax or abdomen. Both types of measurements are listed in Table 3.5. Some of the circumference measurements were described in Section 3.6.2.1. Inductance plethysmography uses bands around the chest and abdomen that vary in inductance as the bands are stretched, and piezoelectric strain gauge straps emit a voltage when the chest changes in circumference. Strain gauges measure the deformation of the chest.

Table 3.5. Techniques for Surface Measurement of Respiration Rate

Technique	Description	Circumference or Linear Displacement?	Contact or Non-Contact?	Pros and Cons?
Doppler Radar	Radar signal is directed at subject's chest; linear motion of entire chest is measured.	Linear	Non-Contact	Subject can remain clothed and unwired. Artifacts due to subject motion.
Impedance Plethysmography [98, 138]	Injects small amounts of electrical current into subject to measure the subject's impedance changes with respiration	Thoracic impedance (indirectly Circumference)	Contact	Can make a cross-sectional "slice" image of subject. May require many electrodes. May suffer from interference.
Inductance Plethysmography [98, 108, 138]	Band worn around chest wire coils stitched into the elastic band change inductance as circumference changes	Circumference and Area	Contact	Measures a complex function of circumference and cross-sectional area. Displacement in transducer bands can lead to inaccuracies.
Magnetometer [108, 110]	Transmitter and receiver coils on chest, abdomen, and back measure changes in displacement	Linear	Contact	Sensor can also be used to monitor changes in body position.
Strain Gauges [92, 108]	Strain gauges placed on chest measure changes in circumference	Circumference	Contact	Displacement of body movements influences signal quality. Overstretching or understretching the gauges can affect accuracy.

Table 3.5. Techniques for Surface Measurement of Respiration Rate

Technique	Description	Circumference or Linear Displacement?	Contact or Non-Contact?	Pros and Cons?
Laser Displacement [104, 105]	Laser pointed at chest measured the change in linear displacement	Linear	Non-Contact	Subject cannot be clothed.
Linearized Magnetometer [98]	One coil is driven to make a weak magnetic field; receiving coils determine their position in the field	Linear	Contact	Rotational motion of coils creates an artifact.

In [105], a laser sensor was used to measure anteroposterior chest wall motion. This is a non-contact measurement, offering no resistance to respiration and no tactile stimuli, which should ensure a noninvasive measurement of respiration that does not alter the respiratory pattern. The laser monitor measures the distance between the chest wall and the sensor, and obtains a respiratory waveform by plotting the change in distance over time. The laser monitor can track rapid changes in lung volume with almost no lag. They propose a monitor with multiple laser sensors so that they can monitor multiple points on the chest, and better model the volumes of respiration.

In magnetometer measurements, one coil is driven by an oscillator to produce a weak magnetic field, while other coils are attached to the skin on the thorax and abdomen. The coils on the skin pick up the magnetic field and can determine their position in the field. Magnetometers are susceptible to rotational movement, which creates artifacts [98]. Magnetometers were used to measure the antero-posterior motion of the rib cage and abdomen [98], and to measure displacement between the abdomen and the sternum [110]. In [110], two transmitter coils operating at two different frequencies are placed near the spine at the sternal level and on the abdomen. Two receiving coils are also placed on the body: one tuned to both frequencies is placed on the sternum to measure the sternal-umbilical displacement and the rib cage antero-posterior displacement. The other is tuned only to the frequency of the abdominal transmitter and measures the anterior-posterior abdominal displacement. With these three measurements, after calibration, respiratory volume can be estimated using a three-degree-of-freedom model.

3.6.3.3 Surface Motion Measurement of Pulse Rate

The two methods of measuring the pulse rate through body surface movement are global measurement of the chest wall and measurement of a small surface on the chest wall or at a pulse point. Either the chest wall motion resulting from the heart beating against the chest wall or the surface motion resulting from arterial and venous pulses can be measured. Mechanocardiography is an all-encompassing term for the measurement of the motion or vibration of the chest wall due to the heart. Several of the techniques in Section 3.2.4 could be used for vital sign measurement, as well as several additional techniques that are discussed in this section.

Table 3.6. Techniques for Surface Motion Measurement of Pulse Rate

Technique	Description	Contact or Non-Contact?	Global or Small Area?	Pros and Cons
Doppler Radar	Radar signal is directed at subject's chest; linear motion of entire chest is measured.	Non-Contact	Global	Subject can remain clothed and un-wired. Artifacts due to subject motion.
Apexcardiography [82, 85]	Measures chest wall displacement at the apex relative to the rest of the chest	Contact	Small Area	Difficult to place correctly.
Kinetocardiogram/ Impulse Cardiogram [82, 85]	Measures chest wall displacement relative to the laboratory coordinate system	Contact	Small Area	Reading closely resembles palpation.
Cardiokymogram (Displacement Cardiograph) [93]	A coil that is part of a tuned circuit is placed near the chest of the patient; as the coil's environment changes the output frequency changes	Non-Contact	Global (depends on size of coil)	Measures superposition of heart motion and chest wall motion.
Laser Displacement System [79, 128]	Laser beam is pointed at chest; displacement is measured	Non-Contact	Small Area	Not affected by loading. Clothing must be removed.
Ballistocardiogram/ Seismocardiogram [118, 87]	Accelerometer is attached to the chest	Contact	Small Area	Measures acceleration rather than displacement.

Apexcardiography is the measurement of chest motion at the apex relative to the rest of the chest wall. Positioning the apexcardiograph transducer typically requires repeated exploration of the apical area, and this degrades the reproducibility of the measurement. Only the apex impulse measurements can be made with regularity [82]. Apexcardiography represents the displacements for the precordium overlying the apex of the heart, caused by left-ventricular movement. The apexcardiogram measures the movement of the chest wall, and is indicative of the pulsation of the entire left ventricle. Its contour differs from that perceived in palpation [85].

The kinetocardiogram measures chest wall displacement at a single point (typically the apex) similar to the apexcardiogram. The difference is that the kinetocardiogram measures relative to an external fixed laboratory coordinate system, not relative to the rest of the chest. These reading most closely resemble the movements detected by palpation [82]. The kinetocardiogram records the motion of specific points on the chest wall relative to a fixed point in space, and its contour is similar to that perceived by palpation [85].

The displacement cardiograph, also known as the cardiokymograph, consists of a coil that is part of a tuned circuit oscillator and is placed between 5 and 15 mm from the subject's chest wall. Changes in the environment of the coil by changes in the location and volume of the chest due to the heart beating and respiration changes the loading of the coil, and therefore the frequency of oscillation. This frequency is compared with that of a reference frequency, and the difference is converted to an output voltage. The field created by the coil penetrates tissue, so that motion of the heart itself is sensed as well as chest-wall motion. The system is much more sensitive to chest-wall motion than the heart motion, but the heart motion is greater. The output of this system is qualitative because of the superposition of the heart motion and chest motion. The cardiokymograph can detect heart motion in patients for whom the apexcardiograph is not detectable, including patients with emphysema, and others in which no apical impulse can be palpated [93].

The laser displacement system, as described in Section 3.2.4, points a laser beam at the chest wall and measures the displacement. This required the subject to be unclothed since the laser cannot penetrate clothing.

The ballistocardiograph, also known as the seismocardiograph, consists of an accelerometer strapped to the subject's chest, but is not a quantitative measurement of displacement [118, 87]. It can be used to sense the heart rate but needs to be placed on the area of the chest that is moving.

Doppler radar simultaneously measures heart and respiration rates. In order to measure the heart rate, it is necessary to use filters to attenuate the respiration signal relative to the heart signal so that the heart signal is dominant. This measurement is non-contact and works through clothing. No other respiration measurements are non-contact and operate through clothing. The cardiokymograph could theoretically operate through clothing but it needs to be placed very close to the chest.

3.7 Conclusions

With each heart beat, the heart undergoes a partial rotation and an expansion, which causes it to strike the chest wall during left ventricular contraction. This contact with the chest wall causes an impulse to occur at the apex, in the 4th or 5th intercostal space, resulting in a total displacement estimated to be about 0.6 mm as measured with non-contact laser measurements of multiple subjects. The expansion and contraction of the heart also leads to a slower pulsation of the left parasternal area of the chest wall with every heart beat. There is also skin-surface motion at the heart frequency due to pulsing of superficial arteries. The pulsation of the arteries is delayed from that at the chest wall by 0.15 to 0.28 seconds, and the greatest arterial displacement at the carotid artery is estimated to be about one fourth that at the chest. Motion from the veins at the skin surface may be measurable in supine subjects, but not in upright subjects.

The motion at the skin surface has been measured with a variety of contacting and non-contacting techniques. Many of the contacting measurements of chest motion require careful placement at the apex for accurate readings and may be difficult to place correctly. Subjects cannot wear clothing during the non-contact laser measurements since the laser cannot penetrate clothing. For the 1-D laser measurements, aligning the laser at the apex

may be a challenge. The Doppler radar measurement of heart motion does not require careful aiming of the antenna since it uses a broad beam, and it can operate through most normal dry clothing. It does suffer from motion artifacts while the subject is moving, but these disappear as soon as the subject is still again. The laser displacement measurements are useful as a research tool, since they can provide quantitative information about the amount of chest-wall displacement. However, because of risks associated with lasers, the importance of alignment, and the inability to penetrate clothing, the laser sensor could not be used as a heart rate monitor.

The electrocardiogram is the gold standard for measurement of the heart. It measures the electrical activity of the heart rather than its motion, and can therefore be used for a wide range of diagnostic activities. When only the heart rate is being monitored, a three-lead ECG is typically used. The main drawbacks are that some subjects have adverse reactions to the electrodes and the electrode gel, that artifacts occur if the electrodes are not properly applied, and that the patient must be wired to the monitor, limiting his/her ability to move about. Although Doppler radar is a less accurate measurement of heart rate than the three-lead ECG, it may be a better choice in applications where accuracy is not of utmost importance and in chronic applications where it is important to avoid sensitivity to electrodes and frustration with being wired to a monitor.

With each inhalation and exhalation, the chest and abdomen expand and contract. The peak-to-peak motion perpendicular to the chest wall is estimated to be between 4 and 12 mm. Respiration rate is often measured by chest motion with a variety of plethysmographic methods, including straps that sense the change in chest circumference, electrode systems that sense the change in chest impedance, and strain gauges that measure the distortion of the chest shape. All these measurements of chest motion require contact with the subject and having the subject wired to the monitor. The non-contact measurements of respiration are the laser monitor and the Doppler radar monitor. As with the heart measurements with these systems, the laser monitor cannot operate through clothing like the Doppler radar monitor, and has safety issues that would not make it as good a choice as the Doppler radar monitor for measurement of heart and respiration rates.

When calculating the signal-to-noise ratio for the Doppler radar system, the integral of the mean-squared physiological motion with the desired period over the chest area, multiplied by the directivity of the reflected signal towards the antenna and the reflectivity of the chest is desired. This factor is challenging to compute; even if a mapping of motion over the chest was obtained, the factor for the directivity would depend on the angle of the antenna to the chest. For the heart signal, the amount of motion, the timing of the motion, and the directivity could change significantly during respiration. Additionally, these values will likely vary widely from person to person. Because this value cannot be precisely calculated with currently available information, RMS motion and the chest area in motion is estimated from the data in this chapter. The RMS motion is estimated to be 0.3 mm for heart and 2 mm for respiration. The area in motion is estimated to be 10 cm² for the heart and 50 cm² for the respiration. These values are assumed to be linearly superimposed for the purposes of estimating the signal-to-noise ratio.

Future research could include a three dimensional model of skin surface motion due to heartbeat and respiration based on known physiology. This would enable accurate calculation of the integral of RMS motion over the area of the body, and would enable accurate calculations of the signal-to-noise ratio of the output of the Doppler radar cardiopulmonary monitor from different angles to the body.

3.8 References

- [77] R. D. Allison, E. L. Holmes, and J. Nyboer, "Volumetric dynamics of respiration as measured by electrical impedance plethysmography," *Journal of Applied Physiology*, vol. 19, pp. 166-173, 1964.
- [78] O. X. Arcem, O. A. Knudson, M. C. Ellison, P. Baselga, D. D. Ivy, C. DeGroff, and L. Valdes-Cruz, "Longitudinal motion of the atrioventricular annuli in children: Reference values, growth-related changes, and effects of right ventricular volume and pressure overload," *Journal of the American Society of Echocardiography*, vol. 15, no. 9, pp. 906-916, 2002.

- [79] A. E. Aubert, L. Welkenhuysen, J. Montald, L. de Wolf, H. Geivers, J. Minten, H. Kesteloot, and H. Geest, "Laser method for recording displacement of the heart and chest wall," *Journal of Biomedical Engineering*, vol. 6, no. 2, pp. 134-140, 1984.
- [80] E. H. Awtry and J. Loscalzo, "Structure and function of the normal heart and blood vessels," in *Cecil Essentials of Medicine, 5th ed.*, (C. C. J. Carpenter, R. C. Griggs, and J. Loscalzo, Eds.), New York: W. B. Saunders Company, 2001, pp. 21-29.
- [81] E. H. Awtry and J. Loscalzo, "Evaluation of the patient with cardiovascular disease," in *Cecil Essentials of Medicine, 5th ed.*, (C. C. J. Carpenter, R. C. Griggs, and J. Loscalzo, Eds.), New York: W. B. Saunders Company, 2001, pp. 30-42.
- [82] W. H. Bancroft Jr. and E. E. Eddleman Jr., "Methods and physical characteristics of the kinetocardiographic and apexcardiographic systems for recording low-frequency precordial motion," *American Heart Journal*, vol. 73, no. 6, pp. 756-764, 1967.
- [83] A. S. Berson and H. V. Pipberger, "Measurement of chest wall vibrations due to the activity of the heart," *Journal of Applied Physiology*, vol. 21, no. 2, pp. 370-374, 1966.
- [84] C. M. Brandt, H. Annoni, J. Harthong, J. M. Reiner, and R. Krauskopff, "Evaluation of chest wall distortion related to cardiac activity by structured lights: A study of the apical impulse by the Moiré Technique," *Acta Cardiologica*, vol. 41, no. 3, pp. 207-213, 1986.
- [85] E. Braunwald and J. K. Perloff, "Physical examination of the heart and circulation," in *Heart Disease: A Textbook of Cardiovascular Medicine*, (E. Braunwald, D. P. Zipes, and P. Libby, Eds.), New York: W. B. Saunders Company, 2001, pp. 45-81.
- [86] C. M. Buntin and F. H. Silver, "Noninvasive assessment of mechanical properties of peripheral arteries," *Annals of Biomedical Engineering*, vol. 18, no. 5, pp. 549-566, 1990.
- [87] R. S. Crow, P. Hannan, D. Jacobs, L. Hedquist, and D. M. Salerno, "Relationship between seismocardiogram and echocardiogram for events in the cardiac cycle," *American Journal of Noninvasive Cardiology*, vol. 8, no. 1, pp. 39-46, 1994.
- [88] A. DeGroot, M. Wantier, G. Cheron, M. Estenne, and M. Pavia, "Chest wall motion during tidal breathing," *Journal of Applied Physiology*, vol. 83, no. 5, pp. 1531-1537, 1997.

- [89] A. A. Deliyannis, P. M. S. Gillam, J. P. D. Mounsey, and R. E. Steiner, "The cardiac impulse and the motion of the heart," *British Heart Journal*, vol. 26, pp. 396-411, 1964.
- [90] W. Dressler, "Pulsations of the chest wall," *Archives of Internal Medicine*, vol. 60, p. 225-239, 1937.
- [91] Z. V. Edmonds, W. R. Mower, L. M. Lovato, and R. Lomeli, "The reliability of vital sign measurements," *Annals of Emergency Medicine*, vol. 39, no. 3, pp. 233-237, 2002.
- [92] P. J. Fadel, S. M. Barman, S. W. Phillips, and G. L. Gebber, "Fractal fluctuations in human respiration," *Journal of Applied Physiology*, vol. 97, pp. 2056-2064, 2004.
- [93] T. R. Fenton and R. Vas, "Measuring characteristics of the displacement cardiograph," *Medical and Biological Engineering*, vol. 11, no. 5, pp. 552-558, 1973.
- [94] A. Flint, Practical Treatise on the Diagnosis, Pathology, and Treatment of Diseases of the Heart, Philadelphia: Blanchard Lea, 1859.
- [95] P. M. S. Gillam, A. A. Deliyannis, and J. P. D. Mounsey, "The left parasternal impulse," *British Heart Journal*, vol. 26, pp. 726-736, 1964.
- [96] A. L. Goldberger, Clinical Electrocardiography: A Simplified Approach, Chicago: Mosby, 1999.
- [97] D. L. Gorgas, "Vital signs and patient monitoring techniques," in Clinical Procedures in Emergency Medicine: 4th ed., (J. R. Roberts and J. R. Hedges, Eds.), Philadelphia, : Saunders, 2004, pp. 3-28.
- [98] H. R. Gribbin, "Using body surface movements to study breathing," *Journal of Medical Engineering and Technology*, vol. 7, no. 5, pp. 217-223, 1983.
- [99] Z. Hillel and D. M. Thys, "Electrocardiography," in Miller's Anesthesia, 6th ed., (R. D. Miller, Ed.), Philadelphia: Elsevier, 2005, pp. 1389-1414.
- [100] H.-D. Hong and M. D. Fox, "No touch pulse measurement by optical interferometry," *IEEE Transactions on Biomedical Engineering*, vol. 41, no. 11, pp. 1096-1099, 1994.
- [101] K. Ikegaya, N. Suzumura, and T. Funada, "Absolute calibration of phonocardiographic microphones and measurements of chest wall vibration," *Medical and Biological Engineering and Computing*, vol. 9, no. 6, pp. 683-692, 1971.

- [102] T. Kawasaki, S. Sasayama, S.-I. Yagi, T. A., and T. Hirai, "Non-invasive assessment of the age related changes in stiffness of major branches of the human arteries," *Cardiovascular Research*, vol. 21, no. 9, pp. 678-687, 1987.
- [103] K. Ko, R. Erickson, T. Schmidt, J. Webster, "Holographic interferometry of cerebral pulsations," *Surgical Neurology*, vol. 63, no. 2, pp. 118-122, 2005.
- [104] T. Kondo, I. Kobayashi, Y. Taguchi, Y. Ohta, and N. Yanagimachi, "A dynamic analysis of chest wall motions with MRI in healthy young subjects," *Respirology*, vol. 5, no. 1, pp. 19-25, 2000.
- [105] T. Kondo, T. Uhlig, P. Pemberton, and P. D. Sly, "Laser monitoring of chest wall displacement," *European Respiratory Journal*, vol. 10, pp. 1865-1869, 1997.
- [106] K. Konno and J. Mead, "Measurement of the separate volume changes of rib cage and abdomen during breathing," *Journal of Applied Physiology*, vol. 22, no. 3, pp. 407-422, 1967.
- [107] J.-S. Lee, "On the coupling and detection of motion between an artery with a localized lesion and its surrounding tissue," *Journal of Biomechanics*, vol. 7, no. 5, pp. 403-409, 1974.
- [108] T. L. Lee-Chiong, Jr., "Monitoring respiration during sleep," *Clinics in Chest Medicine*, vol. 24, no. 2, pp. 297-306, 2003.
- [109] M. G. Levitzky, *Pulmonary Physiology*, San Francisco: McGraw Hill, 1999.
- [110] F. D. McCool, J. Wang, and K. L. Ebi, "Tidal volume and respiratory timing derived from a portable ventilation monitor," *Chest*, vol. 122, no. 2, pp. 684-691, 2002.
- [111] K. McLeish, D. L. G. Hill, D. Atkinson, J. M. Blackall, and R. Razavi, "A study of the motion and deformation of the heart due to respiration," *IEEE Transactions on Medical Imaging*, vol. 21, no. 9, pp. 1142-1150, 2002.
- [112] P. T. Macklem, "The Act of Breathing," in *The Thorax*, (C. Russo, Ed.), New York: Marcel Dekker, Inc., 1995, pp. 445-456.
- [113] P. T. Macklem, D. Gross, A. Grassino, and C. Roussos, "Partitioning of inspiratory pressure swings between diaphragm and intercostal/accessory muscles," *Journal of Applied Physiology*, vol. 44, no. 2, pp. 200-208, 1978.
- [114] J. M. Meinders and A. P. G. Hoeks, "Simultaneous assessment of diameter and pressure waveforms in the carotid artery," *Ultrasound in Medicine and Biology*, vol. 30, no. 2, pp. 147-154, 2004.

- [115] K. Mohri, T. Jinnouchi, and K. Kawano, "Accurate mechanocardiogram sensors using amorphous star-shaped core multivibrator combined with a magnet," *IEEE Transactions on Magnetics*, vol. MAG-23, no. 5, pp. 2212-2214, 1987.
- [116] K. Mohri, T. Kondo, H. Sugino, J. Yamasaki, K. Yoshino, "Non-contact linear displacement sensors using amorphous-core multivibrators for mechanocardiography," *IEEE Transactions on Magnetics*, vol. MAG-21, no. 5, pp. 2071-2073, 1985.
- [117] V. Mooser, J.-D. Etienne, P.-A. Farine, P. Monney, F. Perret, M. Cecchini, E. Gagnebin, C. Bornoz, Y. Tardy, M. Arditi, J.-J. Meister, C.-E. Leuenberger, E. Saurer, E. Mooser, B. Waeber, and H. R. Brunner, "Non-invasive measurement of internal diameter of peripheral arteries during the cardiac cycle," *Journal of Hypertension*, vol. 6, suppl. 4, pp. S179-S181, 1988.
- [118] P. Mounsey, "Precordial ballistocardiography," *British Heart Journal*, vol. 19, pp. 259-271, 1957.
- [119] K. Nehrke, P. Bornert, D. Manke, and J. C. Bock, "Free-breathing cardiac MR imaging: Study of implications of respiratory motion - initial results," *Radiology*, vol. 220, no. 3, pp. 810-815, 2001.
- [120] L. H. Opie, "Mechanisms of cardiac contraction and relaxation," in Heart Disease: A Textbook of Cardiovascular Medicine, (E. Braunwald, D. P. Zipes, and P. Libby, Eds.), New York: W. B. Saunders Company, 2001, pp. 443-478.
- [121] M. F. O'Rourke, R. Kelly, and A. Avolio, The Arterial Pulse, Philadelphia: Lea and Febiger, 1992.
- [122] D. G. Osmond, "Functional anatomy of the chest wall," in The Thorax, (C. Russo, Ed.), New York: Marcel Dekker, Inc., 1995, pp. 413-444.
- [123] A. Owen, "Effect of increasing age on diastolic motion of the left ventricular atrioventricular plane in normal subjects," *International Journal of Cardiology*, vol. 69, pp. 127-132, 1999.
- [124] B. A. Phillips, M. I. Anstead, and D. J. Gottlieb, "Monitoring sleep and breathing: methodology; Part I: Monitoring breathing," *Clinics in Chest Medicine*, vol. 19, no. 1, pp. 203- 212, 1998.
- [125] G. Ramachandran, M. Singh, "Three-dimensional reconstruction of cardiac displacement patterns on the chest wall during the P, QRS, and T-segments of the ECG by laser speckle interferometry," *Medical and Biological Engineering and Computing*, vol. 27, no. 5, pp. 525-530, 1989.

- [126] G. Ramachandran, S. Swarnamani, M. Singh, "Reconstruction of out-of-plane cardiac displacement patterns as observed on the chest wall during various phases of ECG by capacitance transducer," *IEEE Transactions on Biomedical Engineering*, vol. 38, no. 4, pp. 383-385, 1991.
- [127] J. R. Rodarte and F. R. Shardonofsky, "Respiratory system mechanics," in Textbook of Respiratory Medicine, 3rd ed., (J. F. Murray and J. A. Nadell, Eds.), New York: W.B. Saunders Company, 2000, pp. 91-117.
- [128] A. Ronaszeki, A. E. Aubert, and H. de Geest, "Laser apexcardiogram in healthy young men: a comparative study with the conventional method," *Acta Cardiologica*, vol. 45, no. 3, pp. 203-210, 1990.
- [129] L. M. Rosa, "The 'displacement' vibrocardiogram of the precordium in the low frequency range," *American Journal of Cardiology*, vol. 4, no. 2, pp. 191-199, 1959.
- [130] M. Scanlon, "Acoustic monitoring of first responder's physiology for health and performance surveillance," *Proceedings of the SPIE*, vol. 4708, pp. 342-353, 2002.
- [131] B. W. Schaff and P. H. Abbrecht, "Digital computer simulation of human systemic arterial pulse wave transmission: A nonlinear model," *Journal of Biomechanics*, vol. 5, no. 4, pp. 345-364, 1972.
- [132] R. C. Schlant, M. E. Silverman, and W. C. Roberts, "Anatomy of the heart," in The Heart, Arteries, and Veins, (J. W. Hurst, R.C. Schlant, C. E. Rackley, E. H. Sonnenblick, and N. K. Wenger, Eds.), San Francisco: McGraw Hill, 1990, pp. 14-35.
- [133] G. Shechter, C. Ozturk, J. R. Resar, and E. R. McVeigh, "Respiratory motion of the heart from free breathing coronary angiograms," *IEEE Transactions on Medical Imaging*, vol. 23, no. 8, pp. 1046-1056, 2004.
- [134] M. Singh and G. Ramachandran, "Reconstruction of sequential cardiac in-plane displacement patterns on the chest wall by laser speckle interferometry," *IEEE Transactions on Biomedical Engineering*, vol. 38, no. 5, pp. 483-489, 1991.
- [135] A. Vander, J. Sherman, and D. Luciano, Human Physiology: The Mechanisms of Body Function, Seventh Edition, San Francisco: McGraw Hill, 1998.
- [136] H. Vermarien and E. van Vollenhoven, "The recording of heart vibrations: a problem of vibration measurement on soft tissue," *Medical and Biological Engineering and Computing*, vol. 22, no. 2, pp. 168-178, 1984.

- [137] T. A. Wilson, K. Rehder, S. Krayner, A. Hoffman, C. G. Whitney, and J. R. Rodarte, "Geometry and respiratory displacement of human ribs," *Journal of Applied Physiology*, vol. 62, no. 5, pp. 1872-1877, 1987.
- [138] G. K. Wolf, J. H. Arnold, "Noninvasive assessment of lung volume: Respiratory inductance plethysmography and electrical impedance tomography," *Critical Care Medicine*, vol. 33, no. 3 (Suppl.), pp. S163-S169, 2005
- [139] M. W. Wukitsch, M. T. Petterson, D. R. Tobler, and J. A. Pologe, "Pulse oximetry: Analysis of theory, technology, and practice," *Journal of Clinical Monitoring and Computing*, vol. 4, no. 4, pp. 290-301, 1988.
- [140] G. W. Yip, Y. Zhang, P. Y. Tan, M. Wang, P.-Y. Ho, L.-A. Brodin, and J. E. Sanderson, "Left ventricular long-axis changes in early diastole: impact of systolic function on diastole," *Clinical Science*, vol. 102, no. 5, pp. 515-522, 2002.

Chapter
4

Single-Chip Transceivers

4.1 Introduction

Single-chip Doppler radar transceivers can provide measurement of heart and respiration rates without heavy, bulky, and expensive waveguide and discrete microwave components. By leveraging subcircuit designs developed for cellular base station radio-frequency integrated circuits (RFICs), such transceivers have been fabricated in both silicon CMOS and silicon BiCMOS processes [149, 159, 160]. These transceivers used modified versions of fully-integrated subcircuits that were developed for the 1800-MHz Digital Cellular System (DCS1800) and the 1900-MHz Global System for Mobile communications (GSM1900) standards. This chapter describes both the base station receiver and radar transceiver integrated circuits, emphasizing the technology leveraging that facilitated the development of the single-chip radar transceiver.

The Digital Cellular System (DCS) standard is a modification that provides additional bandwidth to the Global System for Mobile communications (GSM) standard. Since the base station handles multiple channels simultaneously, it requires a higher dynamic range than a mobile receiver. The dynamic range is limited by the receiver noise figure, which determines the lowest receivable signal power, and linearity, which determines the highest receivable signal power. Base station radios typically use high performance but costly GaAs technology and have a low level of integration with many off-chip RF passive components. The cost of base station receivers can be greatly reduced by developing highly integrated receivers in low-cost silicon technology that meet base station specifications.

Realizing the base station receiver in low-cost silicon technology presents challenges due to phase noise in the LO and due to noise figure and nonlinearities in the RF path. Therefore, the oscillator and the LO path circuits were optimized for phase noise performance and the RF amplifiers and mixer were optimized for linearity and noise figure.

As shown in Appendix D, the main noise sources for the signal-to-noise ratio of a Doppler radar system used for cardio-respiratory sensing are residual phase noise, baseband $1/f$ noise, and dc offsets due to self-mixing and reflections from clutter. To lower residual phase noise, the oscillator should be optimized to minimize RF phase noise and other subcircuits need to have sufficiently low residual phase noise that they do not further degrade the phase noise of the LO and received signal. To minimize baseband $1/f$ noise and dc offsets, the receiver should be optimized to reduce the generation of $1/f$ noise at its baseband output, provide good LO-RF isolation to minimize self-mixing, and have a high second-order intermodulation product (IP2) to eliminate large dc offsets from the squaring of the desired signal and other large signals. In the following sections, the base station subcircuits are assessed in how well they meet the requirements for Doppler radar cardio-respiratory monitoring.

A problem unique to Doppler radar cardiopulmonary monitoring is that of phase-demodulation null points, which depend on the phase relationship between the LO and the received signal. This problem can be mitigated by using a quadrature receiver, which provides two receiver chains with a 90° difference in their LO phases. Quadrature receivers developed for this purpose are discussed in this chapter. By either selecting the output closest to the optimal phase demodulation point or by intelligently combining the two outputs, phase-demodulation null points can be avoided.

In this work, a single-channel hybrid Doppler transceiver has been developed that combines individually packaged base station mixer and buffer test circuits and a commercial off-the-shelf voltage-controlled oscillator on a printed circuit board [152]. Single-channel transceivers were then fabricated in monolithic silicon in both CMOS and BiCMOS processes [153]. Finally, Doppler radar transceivers with quadrature receivers were developed in silicon CMOS, using two receiver architectures [154]. The single-chan-

nel transceivers were developed to operate at the DCS1800 LO frequency of 1.6 GHz, while the quadrature transceivers were developed to operate in the 2.4 GHz unlicensed band, which required the retuning of narrowband subcircuits. For each architecture, the Doppler radar transceivers, block diagrams, circuit schematics, fabrication, and packaging are discussed. Basic circuit characterization, including measurements of phase noise, isolation, linearity, and $1/f$ noise generation, are provided.

4.2 Base Station Receiver

Advances in silicon technology have made it possible to realize fully integrated 0.25- μm BiCMOS and CMOS receivers for DCS1800 base stations, meeting very stringent performance requirements for phase noise, linearity, and noise figure [149, 155, 158]. These radios use a heterodyne or direct IF sampling architecture, as shown in Figure 4.1.

The received RF input signal (RF_{in}) is amplified with a low noise amplifier (LNA) in order to maximize the signal-to-noise ratio. The receiver has the flexibility to use an external LNA when the antenna is far from the receiver or an on-chip LNA (LNA1) when the antenna is close to the receiver. A duplex switch is used to select between these options. LNA1 is optimized to minimize noise figure rather than to maximize gain. After the duplex switch, signals from either source are amplified by another LNA (LNA2) which is optimized for high linearity. The post-LNA image filtering is off-chip, so that filters with different specifications can be used depending on the intermediate frequency (IF). The receiver must function with IFs up to 300 MHz (the DCS1800 base station receiver IF is 170 MHz). A passive inductor-capacitor (LC) balun is used to split the single-ended filtered RF input signal into the differential signal required by the double-balanced mixer. The voltage-controlled oscillator (VCO) is on a separate chip, and is phase-locked to a crystal oscillator to provide a local oscillator (LO) signal at the correct frequency. The LO balun-amplifier amplifies the LO in order to provide the mixer with high LO drive and converts the single-ended LO input to the differential signal required by the mixer.

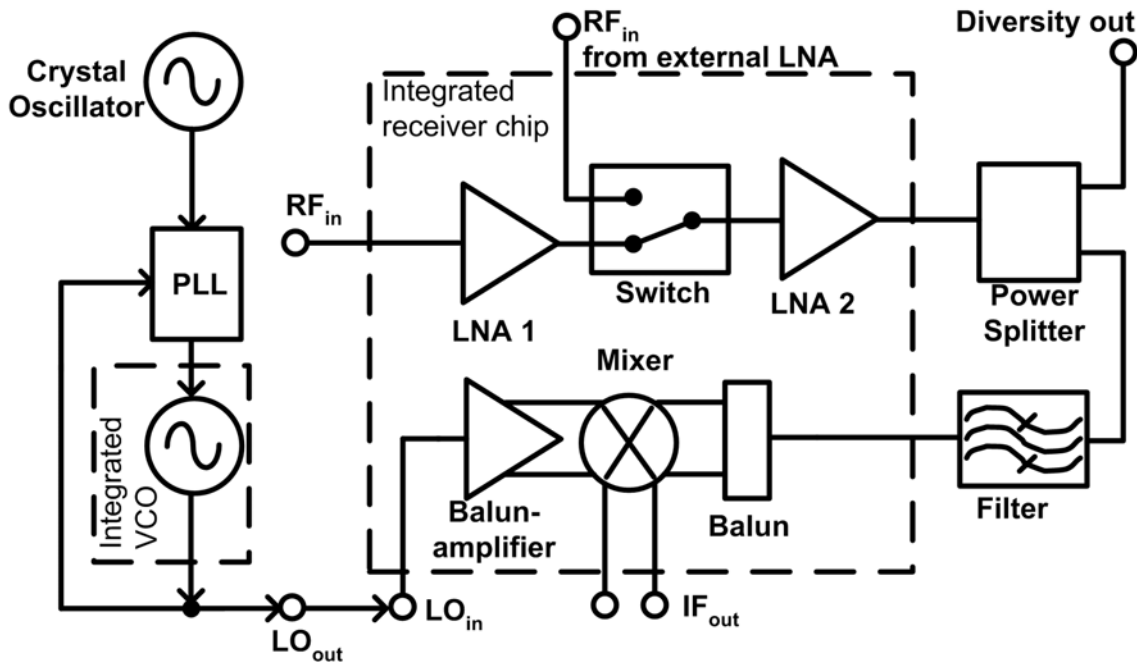


Figure 4.1. Block diagram of base station heterodyne receiver.

Receiver chips and VCOs have been fabricated using Agere Systems 0.25 μm CMOS and BiCMOS processes [149, 155]. Both processes offer 5 metal levels, with a 3 μm thick top level metal providing inductor quality factor (Q) between 8 and 10. Since inductor Q affects oscillator phase noise, it is important to maximize this factor. Both receiver chips have a die size of 3.5 mm by 3.5 mm, and were packaged in Amkor exposed pad TQFP-48 packages [144], which have a 7 mm by 7 mm body size. The bipolar VCO die was 1.4 mm by 2.0 mm, and the CMOS VCO die was 1.2 mm by 1.1 mm, and both were packaged in Amkor exposed pad SSOP-16 packages, which have a 3 mm by 5 mm footprint [145]. The exposed pad packages have a backside ground pad that provides a RF ground with low parasitic inductance. With several bondwires connected from the chip ground directly to the backside ground pad, the total grounding inductance is reduced to below 1.0 nH. A micrograph of the BiCMOS receiver chip is shown in Figure 4.2.

The BiCMOS version of the receiver used a bipolar balun-amplifier and bipolar LNAs, and a CMOS mixer and switch [155], while the CMOS receiver used only CMOS subcircuits [149]. Both a bipolar and a CMOS VCO were also fabricated, and because

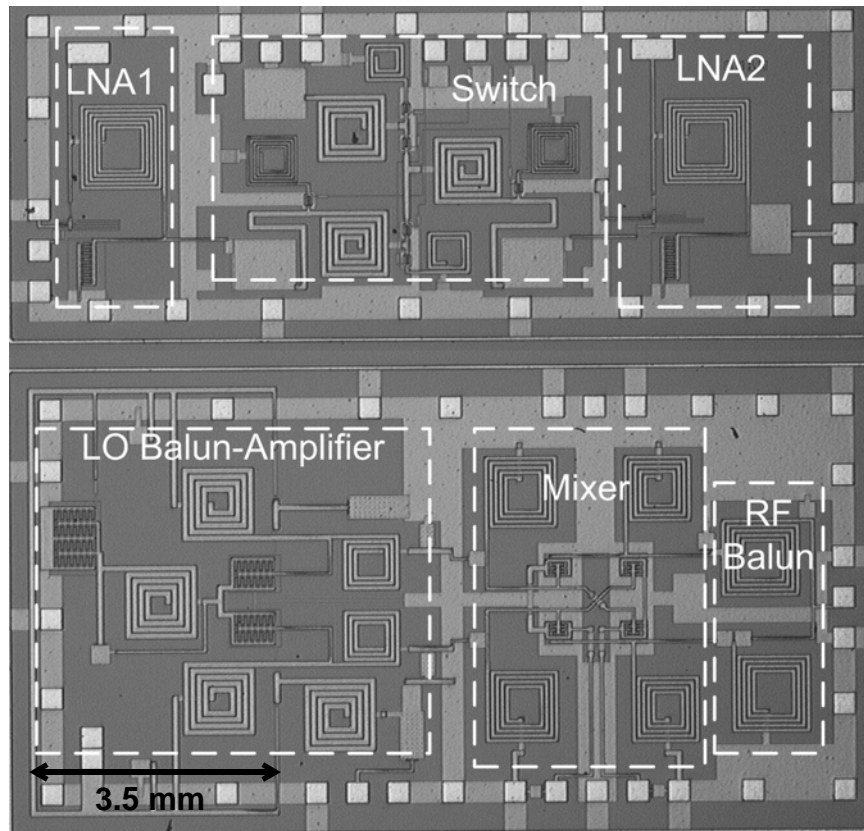


Figure 4.2. DCS 1800 BiCMOS base station receiver chip micrograph [155].

bipolar devices have lower $1/f$ noise than MOSFET devices, the bipolar VCO has 12 dB lower phase noise than the CMOS version [152]. The CMOS versions of the other subcircuits were comparable in performance to the bipolar versions. The subcircuits and a summary of their performance in relation to the base station requirements are discussed in Section 4.3.

4.3 Subcircuits

4.3.1 Introduction

The subcircuits presented in this section were designed for DCS1800 base stations, and were leveraged for the Doppler radar transceivers presented here. Each subcircuit is discussed, including its design, how it met the base station specifications, how well it per-

forms for the Doppler radar transceiver, and how modifications (if any) were made for Doppler radar. Narrow-bandwidth subcircuits were retuned for the 2.4-GHz transceivers. Additionally, the phase-shift network used to divide the LO signal into the quadrature LO signals required for the quadrature transceiver is introduced.

4.3.2 Voltage-Controlled Oscillator

4.3.2.1 Phase Noise Requirements

Phase noise is the challenging specification for voltage-controlled oscillators designed to meet Global System Mobile communications (GSM) requirements. This is due to in-band blocking requirements, which are more stringent for base station receivers than for mobile device receivers. The DCS1800 micro base station requires phase noise at and 800-kHz offset to be below -131 dBc/Hz, and the normal base station requires phase noise below -138 dBc/Hz at the same offset frequency [158].

As shown in Appendix D, residual phase noise is one of the limiting factors when developing a Doppler radar system. Since the motion signal is modulated on the carrier as a phase modulation, phase noise manifests itself as amplitude noise on the output. The residual phase noise level, $S_{\Delta\phi}(f_o)$, is directly proportional to the RF phase noise, $S_{\phi}(f_o)$:

$$S_{\Delta\phi}(f_o) = S_{\phi}(f_o) \left[4 \sin^2 \left(2\pi \frac{Rf_o}{c} \right) \right], \quad (4.1)$$

where f_o is the offset frequency, R is the target range, and c is the signal velocity.

For the VCO, both the base station and the Doppler transceiver require the lowest possible phase noise. Specifications for GSM oscillators are set at offsets from 600 kHz to 3 MHz, while the Doppler radar transceiver is most focused on phase noise at offsets from 0.3 to 3 Hz. No studies on minimizing the phase noise of integrated VCOs at such close-in frequencies have been published, and it is not clear if the phase noise at these frequencies can be further reduced through design variations. However, very-close-in phase noise is generally proportional to $1/f_o^3$, which is generally also true at frequencies near and below 1 MHz where the GSM phase noise specifications lie.

The phase noise performance of integrated VCOs is typically limited by the quality factor (Q) of the on-chip resonator [167]. This is affected by the Q of the inductors in the resonator, as well as by the value of negative resistance in the oscillator that cancels any undesired resistance in the resonator due to its imperfect quality so that the oscillation will not be damped. A larger negative resistance leads to a higher resonator Q that increases the resonator energy, making the oscillation easier to start, increasing the output power, and improving the phase noise performance. Phase noise is discussed in more detail in Appendix H.

4.3.2.2 Bipolar VCO

The bipolar VCO was designed for low phase noise and high output power at the DCS1800 LO frequency of 1.6 GHz. A circuit schematic of the VCO is shown in Figure 4.3a. The common-base configuration with a feedback inductor at the base terminal generates a broadband negative resistance. The transistor size is optimized for high negative resistance at the oscillation frequency. The transistor is biased in a nonlinear mode so it is saturated for part of the cycle to increase the harmonic content of its oscillation, which gives the output waveform a steeper slope at the zero crossing. As discussed in Appendix H, a steeper slope at zero crossing reduces the sensitivity of the phase of the waveform to noise, which decreases the phase noise of the oscillator. The oscillation frequency is determined by the series LC resonator at the emitter, which includes a varactor for frequency tuning [158]. The varactor in the LC resonator is the base-collector junction diode of a transistor with an emitter area of $384 \mu\text{m}^2$ and a zero-bias junction capacitance of 37 pF. Lowpass LC filters consisting of 20-nH series inductors and 10-pF shunt capacitors were used as RF chokes in all three bias lines. The oscillator output is at the transistor's collector, and the series capacitor at the output prevents the base bias voltage from propagating to the next stage in the receiver. Saturation of the transistor limits the output amplitude.

The bipolar chip is 1.4 mm by 2.0 mm, fabricated in $0.25 \mu\text{m}$ BiCMOS [158]. The inductor Q was 8.9, 7.1, and 6.7 for the 5-nH, 3-nH, and 20-nH inductors, respectively.

The close-in phase noise of RF outputs was measured using an HP E5500 Phase Noise Measurement System with the FM discriminator technique and a 24-ns delay line. The VCO dissipates 40 mW, with -80-dBc/Hz phase noise at a 10-kHz offset and -132-dBc/Hz phase noise at a 800-kHz offset, meeting the GSM micro base station requirement [158]. The phase noise spectral density at a 1-Hz offset is +52 dB/Hz [152].

4.3.2.3 CMOS VCO

The common-gate MOSFET VCO is similar in design to the bipolar VCO, but uses a loop resonator rather than a series resonator and uses a current mirror to set the gate voltage rather than using a separate bias. The circuit schematic is shown in Figure 4.3b. An n-type MOSFET is biased in a common-gate configuration with a feedback inductor at the gate terminal to generate a negative resistance when looking from the source. The resonator is the LC loop at the source, with a series capacitor and varactor in parallel with an inductor. The RF output is connected to the drain terminal, and the drain bias is isolated with an RF choke. The transistor was optimized for high negative resistance. Multiple gate fingers were used in the device layout to minimize the gate parasitic capacitance. The oscillation frequency is determined by the LC loop, which includes a varactor so that the frequency can be tuned. The varactor is a MOSFET with the drain and source connected together, with $W \times L$ of $1 \mu\text{m} \times 2 \mu\text{m}$. A lowpass LC filter with a 20-nH inductor and a 20-pF capacitor is used as an RF choke, similar to that of the bipolar version.

As in the bipolar version, the phase noise is reduced by having a large negative resistance. The device is driven into deep saturation during oscillation, so that the steepness of the waveform at the zero-crossings reduces the sensitivity of the phase to noise. The FET is $0.32 \mu\text{m} \times 1.36 \mu\text{m}$. The CMOS chip is 1.2 mm x 1.1 mm on a 0.25- μm CMOS process. The 10-nH feedback inductor has a Q of 7 at 1.6 GHz. The phase noise was measured on an HP E5500 Phase Noise Measurement System using the FM discriminator technique. The phase noise is -134 dBc/Hz at 1900 kHz and -150 dBc/Hz at 3 MHz, meeting the DCS1800 micro base station requirement. The phase noise spectral density at 1-Hz offset is +64 dB/Hz [152].

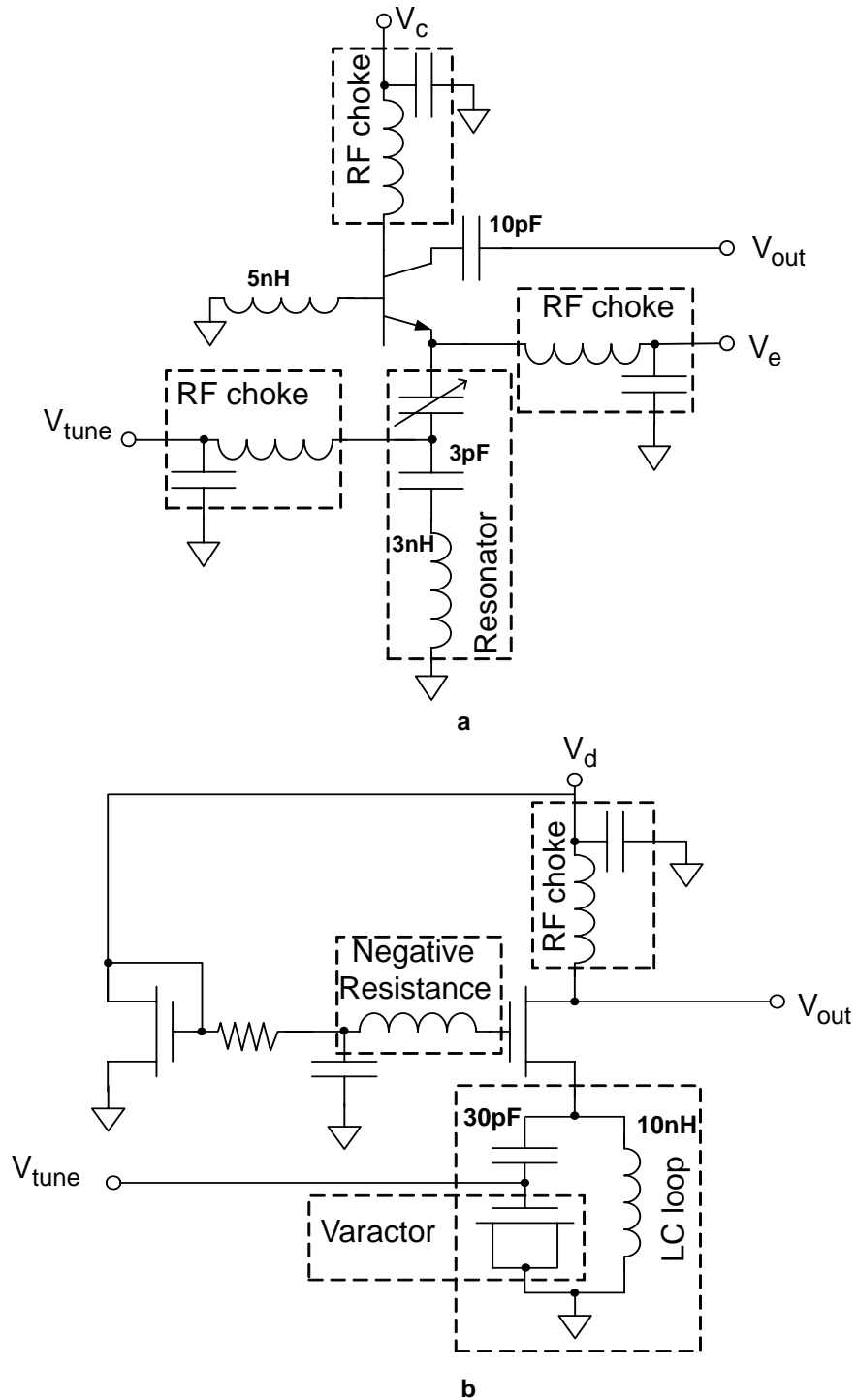


Figure 4.3. VCO circuit diagram with a) BiCMOS and b) CMOS active elements. The BiCMOS RF choke low-pass filters have a 10-pF capacitor and a 20-nH inductor, while the CMOS RF chokes have a 20-pF capacitor and a 20-nH inductor.

Re-tuning the CMOS VCO to 2.4 GHz required changing the values of the resonator elements to an inductance of 20 nH and a capacitance of 3.5 pF. The negative resistance inductor is 10 nH and the RF choke inductor remained 20 nH.

4.3.3 Mixer

4.3.3.1 Goals for the Base Station Receiver Mixer

GSM base station receivers have much tighter intermodulation and blocking requirements than mobile stations, so receiver linearity was an important specification in the base station design. Receiver nonlinearity is typically dominated by the mixer and the low noise amplifier (LNA). Maximizing the linearity of the LNA requires lowering the gain, which puts tighter noise figure requirements on the rest of the receiver including the mixer, which was required to have a noise figure below 8 dB [156]. The mixer needs to have high linearity, and was required to have an input third order intermodulation product (IIP3) between 15 and 20 dBm, depending on the front-end architecture [156].

Most integrated mixers for mobile communications have used variations on double-balanced Gilbert cell mixers [156]. These mixers have a relatively high noise figure (typically over 10 dB), and a nonlinearities that cause an input IP3 below 10 dBm [156]. The Gilbert cell so this topology was unsuitable for the DCS1800 base station receiver, so a double-balanced resistive ring mixer was used.

4.3.3.2 Mixer Topologies and Trade-Offs

The passive resistive FET mixer is the best topology for distortion performance, and requires only moderate LO power [164]. Resistive FET mixers use the time-varying channel resistance of an FET for frequency conversion. A single-FET mixer is shown in Figure 4.4. The LO is applied to the gate and no dc bias is applied to the channel, and the LO voltage modulates the depth of the depletion region, which varies the channel resistance so that the FET serves as a gate-voltage-controlled resistor [162]. When the RF signal is used to apply the drain-source current, the drain-source voltage is the RF current

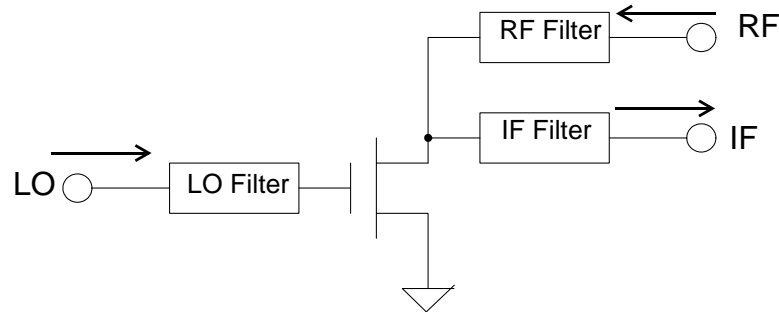


Figure 4.4. Single-transistor passive FET resistive mixer. After [163].

multiplied by the channel resistance. Since the channel resistance of FETs is nearly linearly proportional to the gate voltage at small signal voltages, this produces a very linear mixer, with the output voltage proportional to the multiplication of the LO and RF signals. Filtering is required to separate the RF signal from the IF signal, since both are at the transistor drain. Also, to prevent the LO from leaking to the RF via gate-drain capacitance, either the RF or the IF matching circuit must provide a short at LO frequencies. The gate-drain capacitance is larger when the drain is not biased [162]. If the LO is applied as a square wave, the RF is multiplied by a square wave with values ± 1 , which, after filtering, multiplies the RF signal by the LO fundamental frequency to generate the IF output [162]; but if the LO signal is smaller, there will be less harmonic content. Because of their linearity, FET resistive mixers have much lower levels of intermodulation than diode or active FET mixers [162]. The conversion loss and required LO power of resistive FET mixers are generally comparable to that of diode mixers [162].

The lowest distortion levels in resistive FET mixers are achieved with GaAs MESFET and silicon MOSFET devices; other heterojunction FETS have greater channel nonlinearities and therefore higher levels of distortion [164]. Silicon devices have the most linear channel resistance, so the silicon MOSFET devices are ideal for mixers operating at sufficiently low RF and LO frequencies for the transistors to switch completely. Because silicon has a lower mobility than GaAs, the devices must be larger to achieve the desirable channel conductance. Parasitic capacitances and resistances are also greater in MOSFETs than in many other types of FETs [164].

At frequencies near and above 2 GHz, balanced FET resistive mixers are used to avoid high levels of LO-to-RF coupling [162]. Balanced mixers provide inherent port isolation, rejection of amplitude-modulated LO noise, and rejection of certain spurious responses and intermodulation products [162]. In a double-balanced ring mixer, all the nodes in the ring are at virtual ground points of the LO signal. The IF connection nodes are at virtual ground points of the RF signal and the RF nodes are at virtual ground points of the IF signal [162]. The transistor gates are at virtual ground points of both the RF and the IF signals. Therefore, the RF, IF, and LO are all inherently isolated, so that the filtering required for isolation the single-FET mixer in Figure 4.4 is not required in the double-balanced mixer. A perfectly balanced mixer would eliminate all second order nonlinearities, but phase and gain imbalances caused by parasitic capacitances and inductances in real mixers cause some second-order effects [141]. The mixer's bandwidth is limited primarily by the RF, IF, and LO baluns.

Most literature indicates that passive FET mixers do not create flicker noise at baseband and that the noise generated in the channel of a resistive FET is entirely thermal in origin so that its noise figure is equal to its conversion loss [162]. Diode mixers suffer from shot noise, and active FET mixers, such as the Gilbert cell mixer and its variants, have significant $1/f$ noise, which increases the noise figure. However, recent literature indicates that resistive FET mixers introduce some $1/f$ noise, and that any dc offset produced at the IF increases the level of $1/f$ noise [161, 168].

Generally, $1/f$ noise in FETs can be modeled as fluctuations in channel resistance [161]. Therefore, both ac and dc currents create $1/f$ noise. All semiconductor resistances fluctuate in this manner, with the cause of the fluctuation varying with the device technology [161]. In active mixer topologies, the $1/f$ noise generation is dominated by the dc bias current. In a passive resistive FET mixer, variations in the channel resistance add $1/f$ noise to the output even when there are no dc offsets. Also, LO self-mixing creates a dc current, which causes $1/f$ noise [161].

A balanced structure has high LO to RF isolation, which suppresses both the down-conversion of LO amplitude noise and self-mixing, which leads to a dc current that causes

1/f noise generation. However, parasitic elements between the drain elements on the two transistors used in the balanced mixer cause imperfect cancellation of LO leakage [161]. Also, with a direct-conversion radar, there will be RF-LO leakage through the circulator, creating additional dc offset.

4.3.3.3 DCS1800 Base Station Mixer

A passive resistive FET mixer was developed for the DCS1800 base station. The double-balanced mixer employs a ring configuration, as shown in the circuit diagram in Figure 4.5. The gates of the FETs are driven by the LO signals in antiphase, so that a diagonal pair of resistors is conducting at any point in time. When the transistors are operated as ideal switches, the output is effectively the RF signal multiplied by a square wave with amplitude ± 1 . This results in a linear multiplication, but adds a significant harmonic content to the output, as the square wave has harmonic content at all the odd multiples of its fundamental frequency. When the gate voltage amplitude is lower, the conversion gain is decreased, but the harmonic content is also decreased [166].

The size of the NMOS devices was chosen for a $50\text{-}\Omega$ match at the IF port so that no on-chip matching networks were required [156]. Wide metal feeds for the gate, drain, and source were used so that the mixer can handle large ac signals and minimize both terminal-to-terminal and substrate-to-terminal parasitic capacitance. A total device gate width of $240\text{ }\mu\text{m}$ is arranged in 8 groups of 15 fingers to minimize the polysilicon gate access resistance [156]. Each parasitic capacitance within the 120 finger NMOS device is less than 25 fF. Parasitic circuit resistance is minimized by using a thick inductor metal for all circuit connections, inductors, and device access.

NMOS rather than PMOS devices were used for improved conversion loss. The cross-connected gates of the LO lead to excellent LO to IF isolation, but have poor LO matching. A $250\text{-}\Omega$ shunt and a high pass LC matching network improved the match to $50\text{-}\Omega$. The shunt decreased the Q of the matching network, so that the match would be more broadband. RF to IF isolation depends on the phase and amplitude balance of the RF baluns; a high level of isolation requires exact symmetry in the RF, LO, and IF circuit

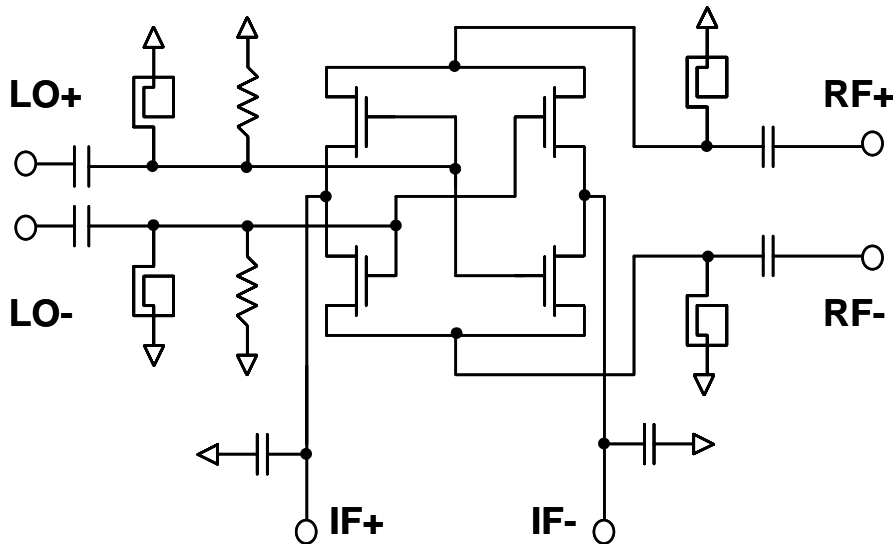


Figure 4.5. Circuit diagram of the DCS1800 mixer.

paths. The highpass LC matching network has series capacitors at the mixer input, which block any dc offset from the previous stage. The series resistance of these capacitors is minimized by arraying small value metal-insulator-metal (MIM) capacitors. The circuit components are widely spaced in the layout to minimize degradation in port-to-port isolation due to capacitive and inductive cross-coupling, as can be seen in the micrograph of the mixer, shown in Figure 4.6.

The mixer is broadband and can operate with RF signals up to 2500 MHz and with IF signals from dc to 300 MHz. It has an IP3 of 19.5 dBm and a conversion loss of 5.8 dB with a 14-dBm LO power gradually degrading to 6.9 dB with a 4-dBm LO power [156]. This gradual decrease in conversion loss indicates that small variation in LO power should not have major effects on the IF power. The RF to IF isolation was 29.5 dB and the LO to IF isolation was 43 dB with 14 dB LO power. Measurements of the linearity of the mixer are shown in Figure 4.7. The LO power level was 4 dBm as the RF power was varied. Frequency spacing between the two tones was 30 MHz for all measurements. The IIP2 was 24 dBm at 2.2 GHz and was 19 dBm at 2.4 GHz.

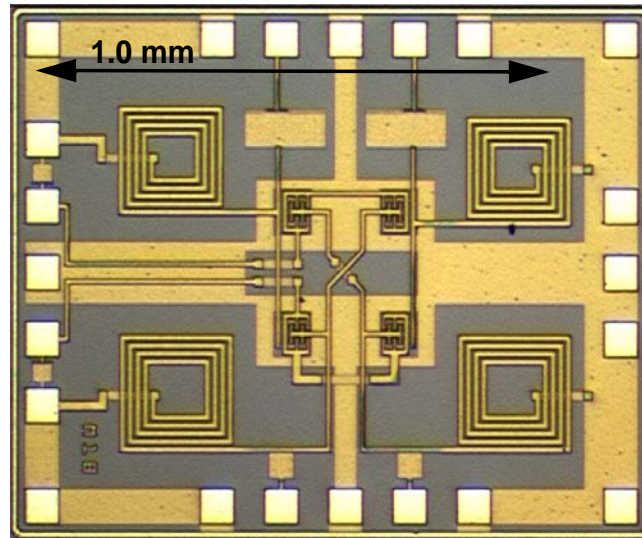


Figure 4.6. Photo of the DCS1800 mixer. The active devices are CMOS transistors.

4.3.3.4 Goals for the Doppler Radar Mixer

As shown in Appendix D, baseband $1/f$ noise created by the mixer can be a dominant noise source for Doppler radar monitoring of chest wall motion. Use of a passive mixer minimizes $1/f$ noise, which is caused by fluctuations in the channel resistance of CMOS devices. If the $1/f$ noise is not minimized, it can be the limiting factor in the Doppler monitoring system.

The effects of nonlinearity deserve a closer analysis, which requires determining the output as a function of the input. The output is

$$f[x(t)] = (K_0 + K_1[x(t)] + K_2[x(t)]^2 + K_3[x(t)]^3 + \dots), \quad (4.2)$$

where the input is $x(t)$. The second order nonlinearity causes the $K_2[x(t)]^2$ output term. For direct conversion receivers, problematic second order nonlinearities are caused by two strong signals, $\cos(\omega_1 t)$ and $\cos(\omega_2 t)$, within the preselection filter's bandwidth that

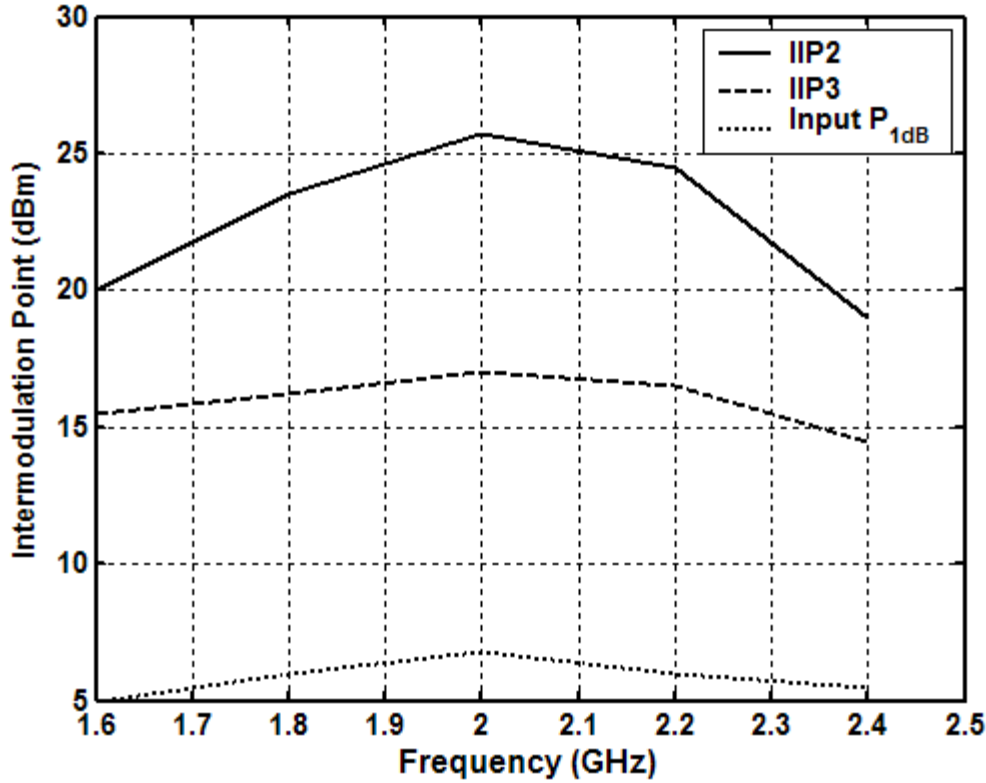


Figure 4.7. Linearity measurements of the mixer vs. frequency: input IP2 (IIP2), input IIP3 (IIP3), and input 1-dB compression point. This measurement was made with a LO power of 4 dBm while RF power was varied. The IF frequency was maintained at 30 MHz.

differ in frequency by less than the signal bandwidth [147]. The second order nonlinearity causes both a dc term and a baseband component:

$$[\cos(\omega_1 t) + \cos(\omega_2 t)]^2 = 1 + 0.5 \cos(\omega_1 t) + 0.5 \cos(\omega_2 t) + \cos(\omega_1 t + \omega_2 t) + \cos(\omega_1 t - \omega_2 t) \quad (4.3)$$

where the dc term is 1 and the baseband term is $\cos(\omega_1 t - \omega_2 t)$. Because the two interfering signals are separated by an amount less than the signal bandwidth, they create a tone in the baseband output signal.

However, in a Doppler cardio-respiratory monitoring system, the output signal is extremely narrow band, and the baseband component caused by two strong interfering signals is not an issue. The dc term adds to dc offsets from other sources, and therefore does

not have a major effect on the receiver if dc offsets are being removed in analog signal processing.

Another source of interference due to second-order intermodulation in a direct-conversion receiver is a single strong interferer with modulation, $a(t)\cos(\omega t + \phi(t))$. When this signal is squared by a second-order nonlinearity, it can result in a beat signal at baseband:

$$[a(t)\cos(\omega t + \phi(t))]^2 = \frac{a^2(t)}{2}[1 + \cos(2\omega t + 2\phi(t))] \quad [147]. \quad (4.4)$$

The baseband term is $\frac{a^2(t)}{2}$. When a signal has envelope modulation,

$$a(t) = A_c(1 + m(t)), \quad (4.5)$$

and

$$\frac{a^2(t)}{2} = \frac{A_c^2}{2}[1 + 2m(t) + m^2(t)]. \quad (4.6)$$

As above, the dc term is dealt with along with other dc offsets, but if $m(t)$ and $m^2(t)$ are in the signal bandwidth, they will interfere with the desired signal. The amount of interference in this case depends not only on the power of the interfering signal, but also on its modulation scheme [147]. Also, amplitude modulation noise on the interfering signal causes amplitude noise at baseband. Because the interfering signal is squared, there is no time delay between the two signals and residual phase noise from that signal is not a factor.

Isolation between the LO and the RF input signals is also important because leakage between the LO and the RF ports in a direct-conversion receiver can lead to large dc offsets. Noise figure is not a critical measurement, since the additive gaussian noise at RF is not a limiting factor.

4.3.3.5 Potential Improvements to the Doppler Radar Mixer

Since the base station mixer was designed for a heterodyne receiver with a 170 MHz IF, 1/f noise was not of critical importance and IP3 rather than IP2 was maximized to meet

linearity specifications. FET resistive mixers exhibit lower $1/f$ noise than diode or active mixers [164], and therefore they are a good choice for the direct-conversion Doppler transceiver. However, the $1/f$ noise could be improved over that of the base station mixer through optimization of this mixer topology.

PMOS devices have lower $1/f$ noise than NMOS devices by about an order of magnitude, especially at low gate voltages [165]. The dominant cause of $1/f$ noise in MOS transistors is trapping and detrapping of carriers at the silicon-silicon dioxide interface [165]. The difference in $1/f$ noise between NMOS and PMOS transistors can be explained by the differences in the effective masses of the hole and the electron, and by differences in the barrier heights for holes and electrons. The effective mass of a hole is 10 to 20 times greater than that of an electron, and the hole barrier is 4.7 eV while an electron's barrier is 3.1 eV. Both the electron's lower mass and lower barrier voltage make it easier for an electron to be trapped or detrapped than a hole [165]. Therefore, PMOS devices have less channel resistance fluctuations than NMOS devices. Developing the mixer with PMOS transistors could further reduce the $1/f$ noise.

Larger MOS transistors, typically used to improve linearity in resistive FET mixers, generally result in larger overlap capacitances, which lead to larger RF drain currents and therefore more $1/f$ noise [168]. The trade-off between the linearity and $1/f$ noise should be assessed in the context of device size when a dedicated direct-conversion mixer is developed.

The DCS1800 mixer was designed to optimize third-order intermodulation (IP3) rather than second-order intermodulation (IP2), which is more relevant in the Doppler radar application. Ideally, when a balanced nonlinear circuit has differential inputs and outputs, it displays no second-order distortion [141]. However, offsets and mismatches cause imbalances which lead to proportional second-order nonlinearities [141]. Any dc offset at the output of a circuit that is directly coupled to the input of the following circuit degrades the following circuit. Therefore, decoupling capacitors should be used between all stages where mismatched dc offsets could cause problems. Within the circuit, dc offsets often come from mismatches between transistors, which can be lowered by decreasing the

surface area occupied by the circuit [141]. Even with dc offsets, the IP2 is directly proportional to the square of the IP3 [141]; therefore, maximizing the IP3 is beneficial as long as it does not come at the expense of greatly increased offsets. The DCS1800 mixer had decoupled inputs, so that dc offsets from previous stages would not affect the linearity of the system. The maximization of IP3 implies that the IP2 will be proportionally high. Although the circuit is compact, an optimized layout may further decrease the IP2.

Resistive FET mixers have both higher linearity and lower $1/f$ noise than the commonly used Gilbert cell mixers, and therefore this is the desired topology for the mixer in a Doppler radar cardio-respiratory monitor. However, the optimization of the circuit elements for $1/f$ noise and IP2 could lead to a better mixer for this application. Since this mixer is very broadband, it operates with RF and LO signals up to 2500 MHz. Therefore, no tuning was necessary for operation at 2.4 GHz

4.3.4 Active Balun-Amplifier

In the base station, the active balun-amplifier connects the single-ended output of the VCO to the differential LO input of the mixer. The balun-amplifier provides both the appropriate LO power and the balanced LO signal to the mixer. Additionally, the narrow-band nature of the active balun filters harmonics on the LO signal. An active balun's dynamic range is typically limited by nonlinearities. When linearity is increased through the use of larger transistors, increases in parasitic capacitance limit the signal balance.

The entire receiver chain needs to have an input IP3 (IIP3) greater than -17 dBm. Therefore the active balun - mixer - passive balun combination needs to have IIP3 between 15 and 25 dBm [155]. Both imbalances between the differential outputs of the active balun and coupling between the LO and RF ports decrease the linearity of the mixer. Since the resistive mixer requires a high LO drive, the LO balun must include gain, and therefore must be active. A high output 1-dB compression point is required in the active balun because a high LO drive improves the mixer's linearity. To maintain LO signal purity and meet GSM blocking requirements, the LO balun-amplifier needs to have

low residual phase noise. This type of noise adds to the oscillator phase noise entering the mixer, and therefore needs to be far below the VCO phase noise to avoid degrading the LO signal.

In the radar system, the active balun-amplifier is used as a signal splitter and as a single-to-differential converter. When used as a signal splitter, the phase and amplitude balance is unimportant, but when used as a single-to-differential converter, the balance between the two outputs is critical because phase and/or amplitude imbalance in the signals leads to LO to RF coupling in the mixer, which results in an increase in dc offsets and in $1/f$ noise.

Emitter-coupled pairs of bipolar transistors and source-coupled pairs of field effect transistors, also known as differential pairs, are two of the most widely used two-transistor subcircuits in integrated analog circuits. Differential inputs and outputs are desirable in many types of analog circuits [157]. With slight modifications, one of these transistor pairs can be used to convert between single-ended and differential signals. By setting one of the inputs to analog ground, a single-ended to differential converter can be realized. At high frequencies, however, it is a challenge to maintain phase and amplitude balance while facing the effects of parasitic capacitances and inductances.

4.3.4.1 Bipolar Balun-Amplifier

Figure 4.8 a shows the circuit schematic of the BiCMOS balun-amplifier. It is a differential pair amplifier with a single-ended input and a balanced output. A large impedance is desired looking into the current source from the emitter-coupled node to avoid output signal imbalance due to parasitic capacitances. A large bias current improves linearity in the amplifier, and this requires a large biasing transistor. At high frequency, the biasing transistor's parasitic capacitance reduces the current source impedance and adversely affects the output signal balance. A resistor cannot be used to isolate the biasing transistor because it causes a large voltage drop at high current. Since this is a narrow-band application, a parallel LC band-stop resonator can be inserted between the emitter-coupled node and the current source. This increases the impedance looking into the current source at the

resonant frequency without creating dc voltage drop (except the small drop across the relatively small parasitic series resistance in the inductor). Parasitic inductance at the differential-pair emitters was included in the design simulation since the output signal balance is so sensitive to this node. The parasitic inductance at each emitter was estimated to be 0.1 nH based on the length of the interconnect. DC-blocking capacitors of 10 pF were placed at the input and output. Input and output matching is achieved with low-pass LC networks at both the input and outputs. In addition to the matching function, the low-pass effect helps eliminate interference and LO harmonics. The main benefit of using bipolar transistors rather than CMOS transistors is the lower $1/f$ noise, which leads to lower residual phase noise.

A micrograph of the bipolar balun-amplifier is shown in Figure 4.9. The chip size is 1.8 mm x 1.6 mm. The LO balun-amplifier operates at frequencies up to 2 GHz, and the gain is about 6 dB at both outputs [149]. This chip can be biased with a voltage from 1.5 V to 5 V with phase and amplitude balance error within 5° and 2 dB [149]. With a 5 V supply, the bias current is 65 mA and the circuit has phase and amplitude balance error less than 2° and 1.2 dB, respectively. The noise figure varies between 5.6 dB and 5.9 dB across the voltage range [149]. The 1-dB compression point is at 5 dBm and the input IP3 is 16.6 dBm with a 5 V supply, and is greater than 13 dBm at supply voltages between 1.5 V and 5 V.

At 1.6 GHz, the residual phase noise is better than -155 dBc/Hz at a 100-kHz offset and above, ensuring that the VCO phase noise will not be degraded [149]. For the Doppler radar, a closer phase noise measurement is required; at a 10-Hz offset, the residual phase noise is -125 dBc/Hz. The residual phase noise levels are well below that of the voltage controlled oscillator, so it will not contribute to LO phase noise. At the output $P_{1\text{dB}}$ power level, the amplifier provides 25 and 43 dB suppression of the second and third harmonics, respectively. The output balance is not sensitive to the transistor sizes in the emitter-coupled pair, but is sensitive to mismatches in the output passive components.

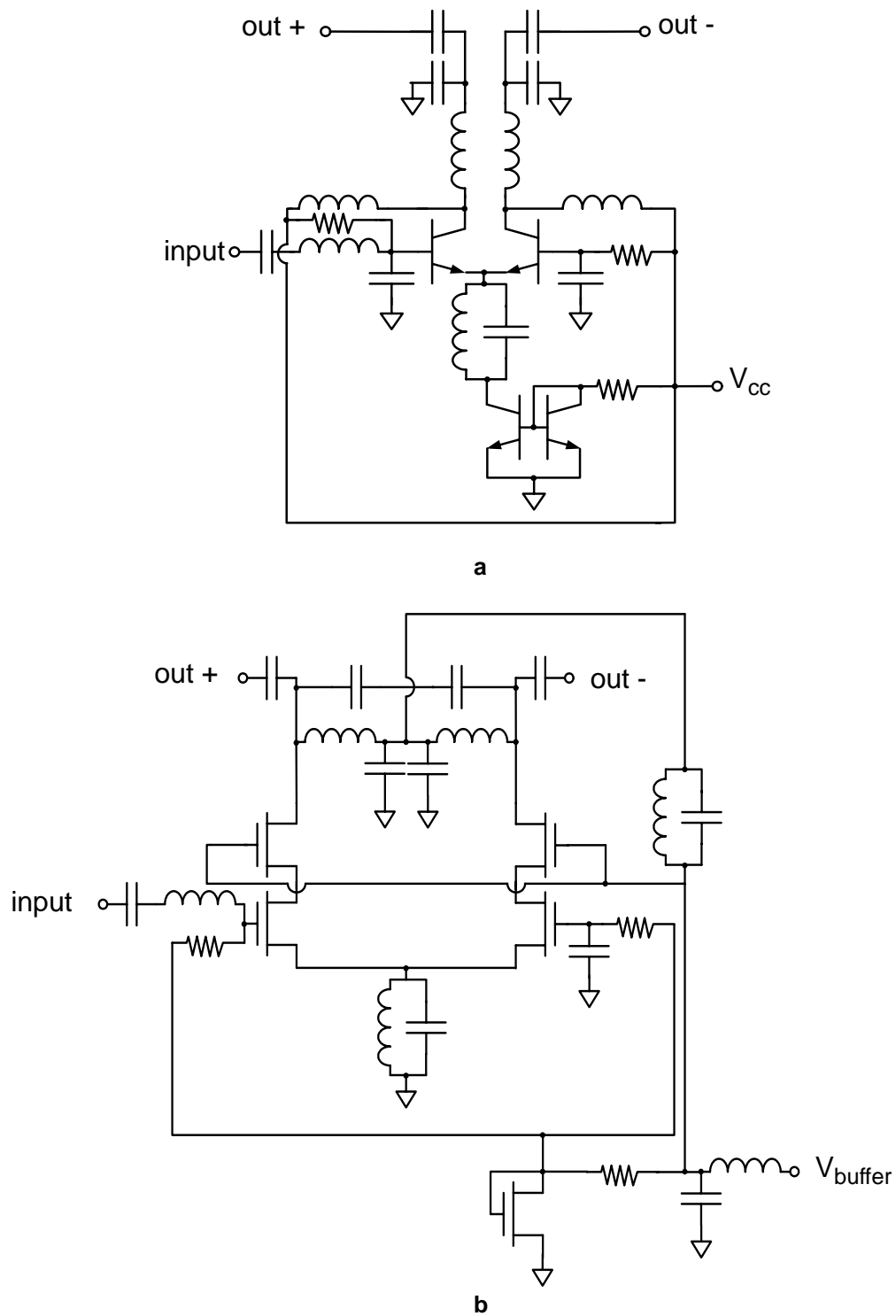


Figure 4.8. Balun-amplifier circuit diagrams in a) BiCMOS and b) CMOS.

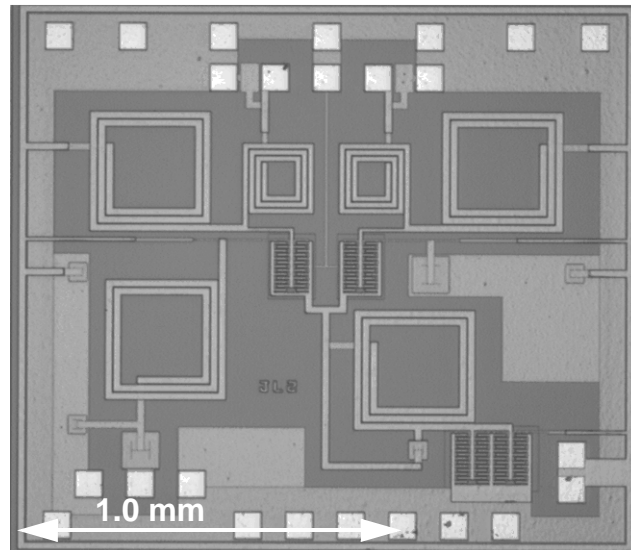


Figure 4.9. Micrograph of BiCMOS balun-amplifier.

4.3.4.2 CMOS Balun-Amplifier

A circuit schematic of the CMOS balun-amplifier is shown in Figure 4.8b. The CMOS balun-amplifier is similar to the bipolar balun-amplifier, but the collector-source bias is removed from the source-coupled node and a current mirror is used to set the gate voltage. Additionally, large resistors were added at the gates of the source-coupled transistors and the current mirror transistor to improve RF isolation. This is acceptable in CMOS, where there is no current at the gate, but not in bipolar, when the base current is non-zero and a large voltage drop would result. Since the current source is removed from the source-coupled node, there is enough power supply overhead for a cascode, which provides good isolation and makes impedance matching easier. An LC resonator at the coupled-source node and an output impedance matching network enhance the common mode rejection ratio, improving the 180° phase balance between the two outputs. An additional resonator was used to isolate the current source from the RF signal at the output when biasing the drains of the cascode transistors. The input and output are ac coupled, and the amplifier provides 15 dB of gain. The balun-amplifier consumes 15 mW with a 3V supply.

The CMOS balun-amplifier was re-tuned to 2.4 GHz by re-tuning the two resonators. The resonator inductors are 4 nH and the capacitors are 1 pF. Output matching was retuned, with 0.25-pF capacitors positioned between the output nodes. The input matching includes an 8-nH inductor.

4.3.5 Low-Noise Amplifier

In the base station receiver, as in most radio receivers, the LNA amplifies the received signal while adding a minimal amount of noise to minimize the noise figure of the entire receiver. However, in the base station receiver, the linearity of the LNA is also important. A low noise figure is required for receiver sensitivity, but a high linearity is necessary to prevent interference. Bipolar amplifiers require low bias current for low-noise performance and high current for high linearity; therefore in the BiCMOS base station receiver, gain, noise figure, and linearity are optimized by performing the amplification in two stages. The first low-noise amplifier tries to minimize the noise figure while maximizing gain; the second one sacrifices gain and noise figure slightly to minimize the nonlinearities. However, in CMOS, low noise and high linearity can be achieved simultaneously, allowing one LNA design to be used for both amplification stages.

The LNA was not used in the single-channel transceivers, but was used in one version of the quadrature transceiver. The quadrature transceiver with LNAs used the LNAs primarily for isolation of the phase-shift network and for amplification of the LO. Therefore, noise figure and linearity were not critically important steps for the Doppler transceiver's LNAs.

4.3.5.1 Bipolar LNA

The bipolar LNA circuit diagram is shown in Figure 4.10a. The single-stage, common-emitter configuration was chosen for the best linearity and noise figure. Two common-emitter stages have a lower noise figure and a higher IP3 than a cascoded stage, which is commonly used when gain and blocking are more important than noise figure and IP3 [146]. A degeneration inductance at the emitter improves the input and output

return loss, while increasing IP3. The package parasitic inductance was included in the degeneration inductance during design [150]. The device size was selected for input match at the design frequency and for gain. The emitter size is $49.9 \mu\text{m}^2$ for the 1800 MHz LNA. This allowed the elimination of on-chip input impedance matching, which improved the noise figure by avoiding loss at the input to the amplifier [150].

The bipolar LNA that was optimized for noise figure has a gain of 11.3 dB, a noise figure of 1.85 dB, a 1-dB compression point of -9 dBm, and an input IP3 of 3.7 dBm. The LNA that was optimized for linearity has a gain of 12.3 dB, a noise figure of 2.08 dB, a 1-dB compression point of -3 dBm, and an input IP3 of 10.7 dBm.

4.3.5.2 CMOS LNA

A single-stage, common source configuration was chosen for linearity and good noise figure in the CMOS version of the LNA. The CMOS LNA circuit diagram is shown in Figure 4.10b. The device size was chosen for optimum linearity and noise figure at the design frequency, while maintaining the requisite gain. This resulted in a gate size of $170 \mu\text{m}^2$ [149]. A series on-chip inductor is used for input matching. Degeneration inductance at the source terminal improves linearity and reduces input and output return losses. A current mirror with a smaller transistor size is used to set the gate bias voltage. With a 3-V bias, a 28-mA bias current provides the best linearity and noise figure, but the amplifier can be biased at a lower current with minimal current degradation. With half the drain current, the input IP3 is lowered by about 1 dB, and the noise figure is increased by 0.2 dB [149].

A noise figure of 2.1 dB was achieved with 21 dB of gain. At 1.8 GHz, the third order intercept point is 1 dBm at the input and 22 dBm at the output, and 1-dB compression occurs at +4.2 dBm [149]. The CMOS LNA was re-tuned to 2.4 GHz by adjusting the gate size for linearity and noise figure and by adjusting the series inductor for input matching.

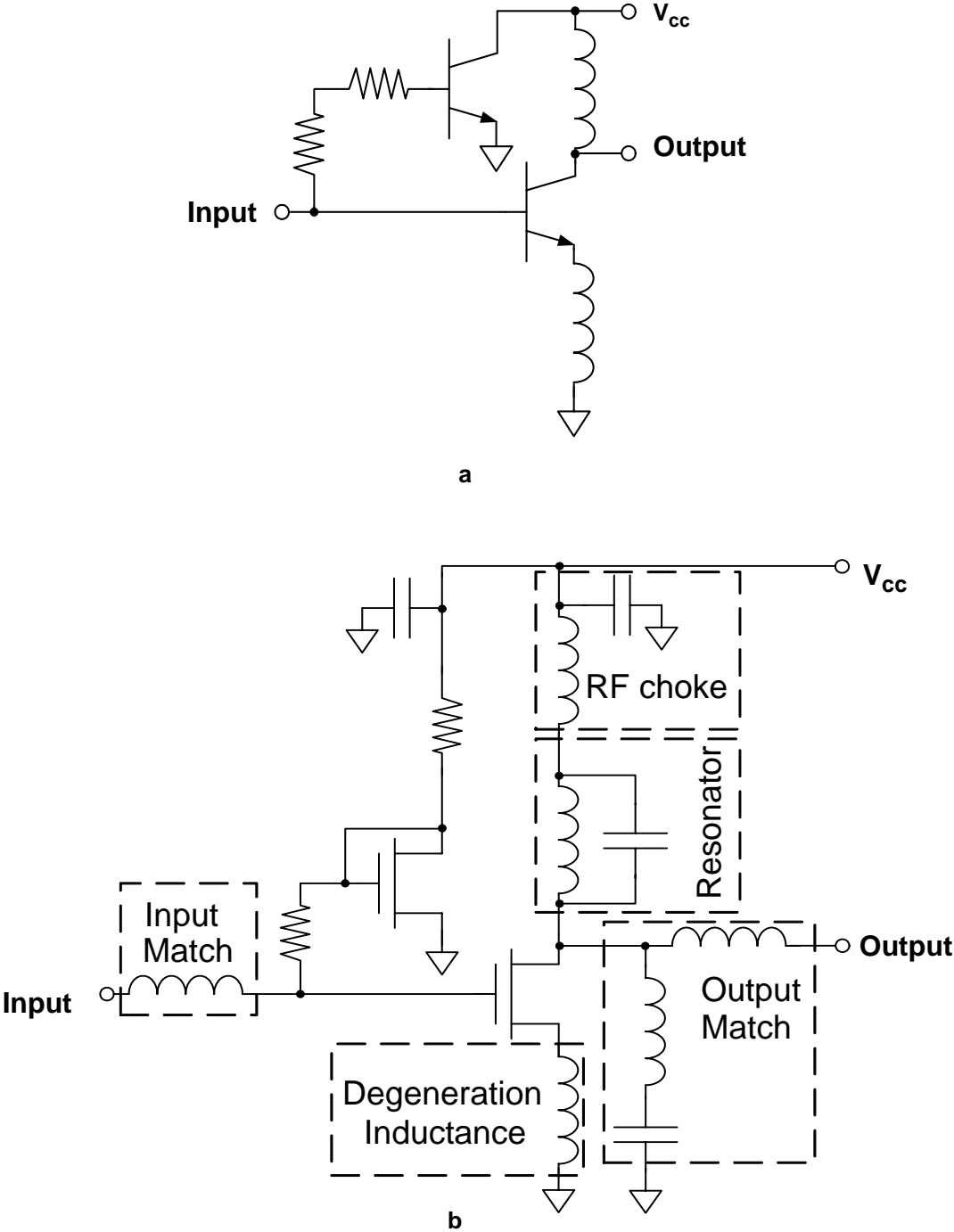


Figure 4.10. LNA circuit diagram in a) bipolar and b) CMOS.

4.3.6 Passive Balun

A double-balanced mixer requires a differential input. The RF input from the antenna is single-ended, as is the LNA output, and the signal needs to be converted to a balanced signal before the mixer. A passive balun is used to convert a single-ended signal to a differential signal when gain is not required. The phase and gain balance of the component performing this function is important, as the level of the double-balanced mixer's rejection of second-order nonlinearities depends directly on the balance of its inputs. At low frequencies this is typically performed with a center-tapped transformer, and at higher frequencies with transmission line techniques. A passive balun also can be designed with lumped elements, as it was in this work.

The passive balun combines a pi-network impedance transformation and a T-network impedance transformation in parallel. It transforms the two parallel 50- Ω impedances to two parallel 100- Ω impedances, to provide an overall 50- Ω impedance at the input that avoids reflections at the design frequency. Matching the input impedances maximizes transmission while minimizing reflection, thereby minimizing the mismatch loss. The pi and T networks have wider bandwidth than an equivalent L network [148] by transforming to an intermediate impedances between stages. The pi and T networks also provide the benefit of a -90° and a $+90^\circ$ phase shift at the design frequency, providing the differential signal required by the mixer.

The LC balun design is shown in Figure 4.11. The 0.1-nH ground inductance and the 0.2-nH trace inductance that were included in the simulation are included in the figure. For the final design, the inductors were 5 nH and the capacitors were 0.8 pF. The bandwidth is indicated in the simulation results shown in Figure 4.12, where the balun outputs were simulated over a range of input frequency. Figure 4.12a shows the simulated amplitude of the two outputs over frequency. There is a 1-dB amplitude difference over a 400 MHz bandwidth, with the amplitudes identical at 2.3 GHz. Figure 4.12b shows the difference between the phases of the two outputs and the phase of the input. There is a 1° phase imbalance over a 400-MHz bandwidth, and the phases are $+90^\circ$ and -90° at 2.3 GHz.

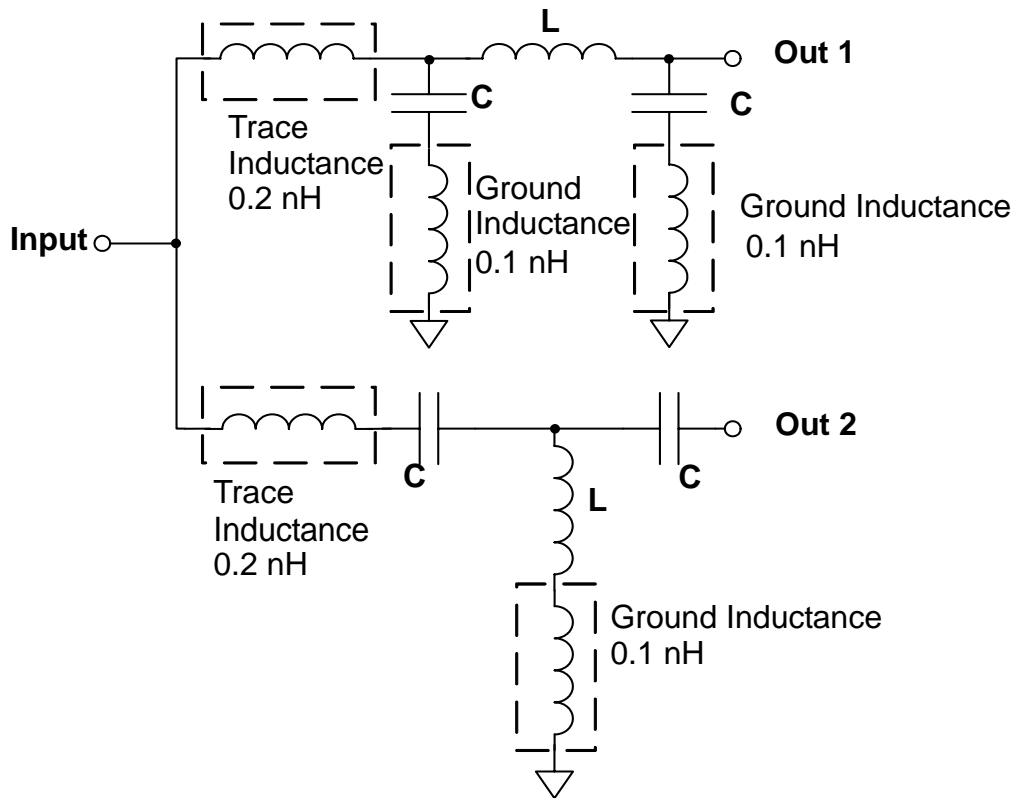


Figure 4.11. Passive balun. The trace inductance and ground inductance were included in the simulation. For the 2.4-GHz balun, the inductors (L) were 5 nH and the capacitors (C) were 0.8 pF.

The sensitivity of the passive balun's phase and amplitude balance to component values was simulated by varying the capacitance while keeping the inductance at 5 nH, while a 2.45 GHz signal was applied at the input. The results of the simulation are shown in Figure 4.13. Figure 4.13a shows the gain of the two outputs from the input. The amplitude balance is within 1 dB over a 25% change in capacitance. Figure 4.13b shows the relative phase shift between the input and the output; the phase balance is within 1 degree for a 15% change in capacitance.

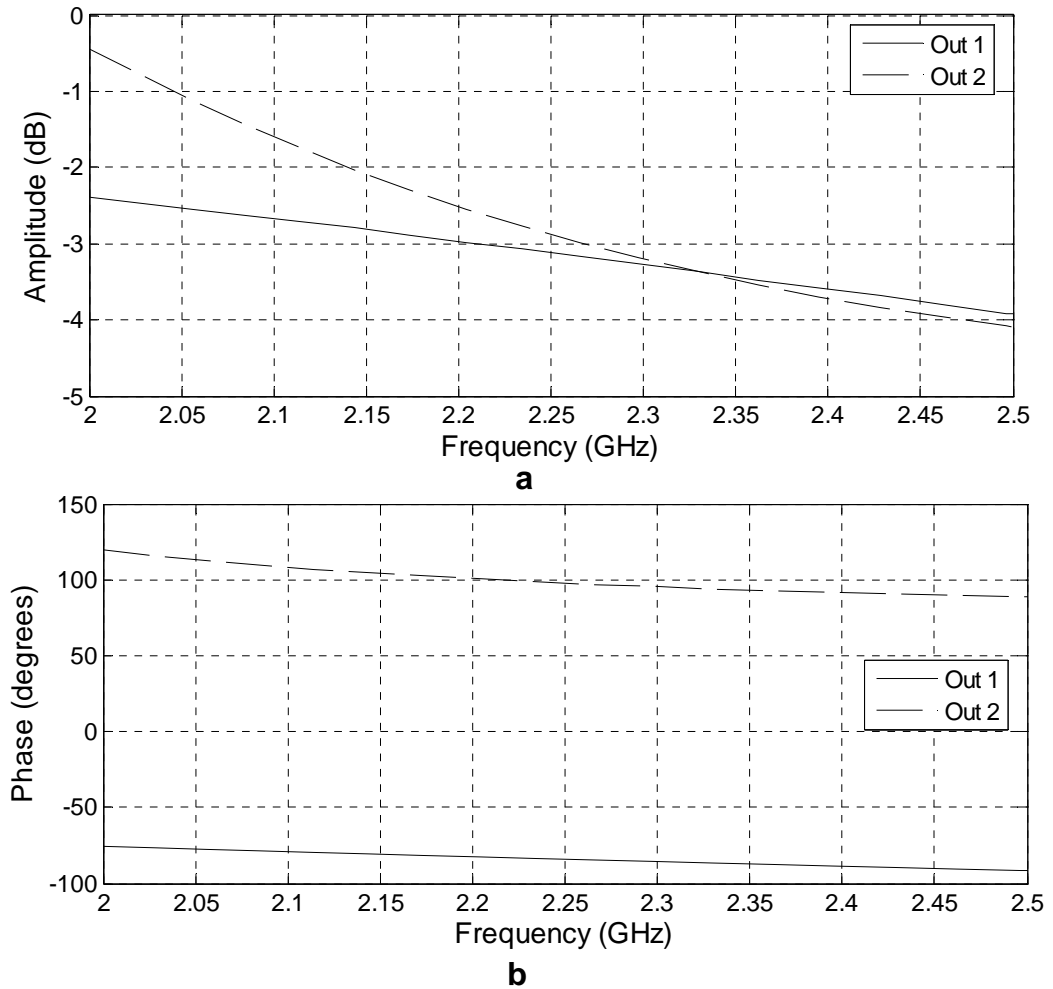


Figure 4.12. Passive balun a) gain and b) phase bandwidth simulations with inductances of 5 nH and capacitances of 0.8 pF. A sine wave is swept at the input of the balun and the output amplitude and phase are simulated relative to the input. 50- Ω loads are assumed at the output.

4.3.7 Duplex Switch

The duplex switch is used to switch between the on-chip LNA and external LNA. Since the switch is not used in Doppler radar architectures, it is not discussed in this work.

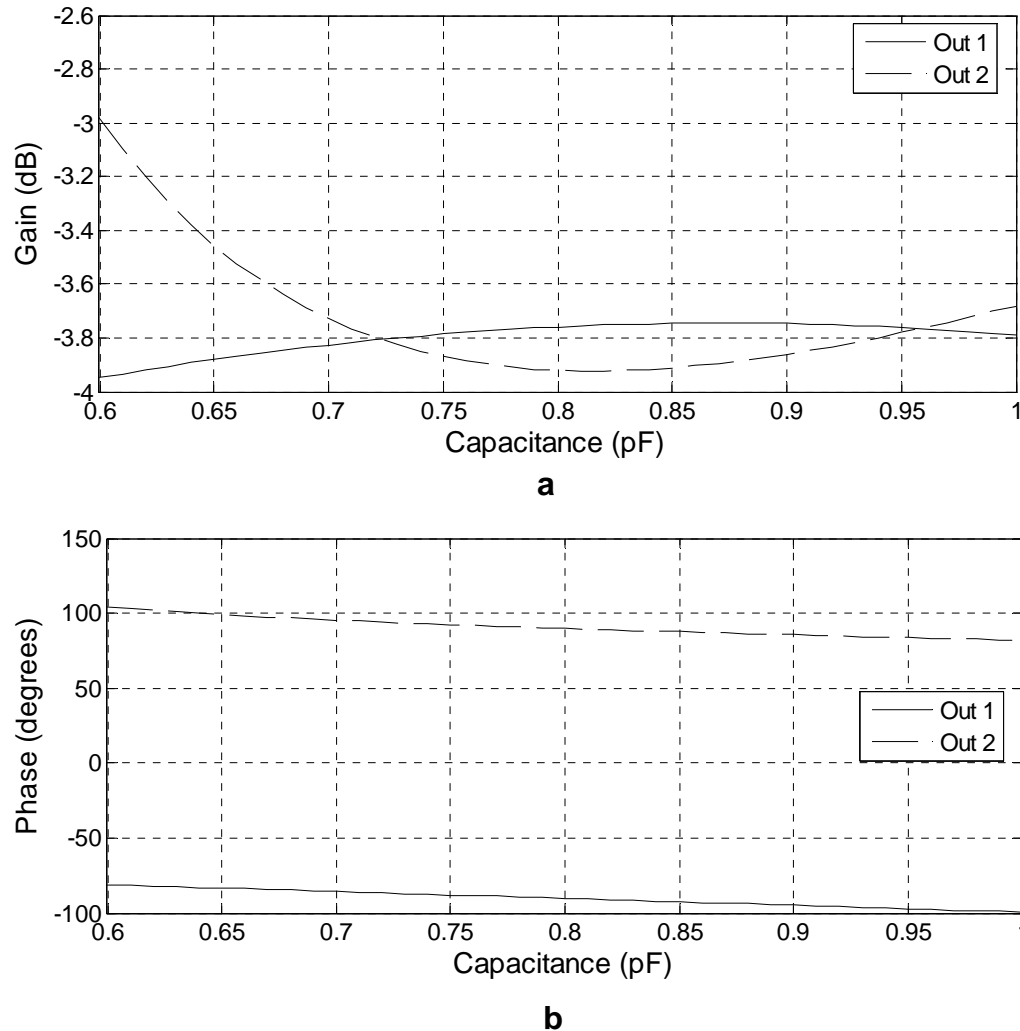


Figure 4.13. Passive balun sensitivity to component value accuracy simulation: a) gain vs. capacitor value and b) phase change between input and output vs. capacitor value at a frequency of 2.45 GHz. The value of C in Figure 4.11 is swept and the ratio of the output amplitude to the input amplitude and the phase difference between the input and the outputs are calculated. $50\text{-}\Omega$ loads are assumed at the output.

4.3.8 90° Phase-Shifting Network

Creating quadrature local oscillator signals requires either a phase shifter or an oscillator designed with quadrature outputs. When leveraging technology from base station receiver sub-circuits that provide a single-phase oscillator, a phase-shifter must be used. The phase and amplitude need to be well-balanced, especially if direct phase demodula-

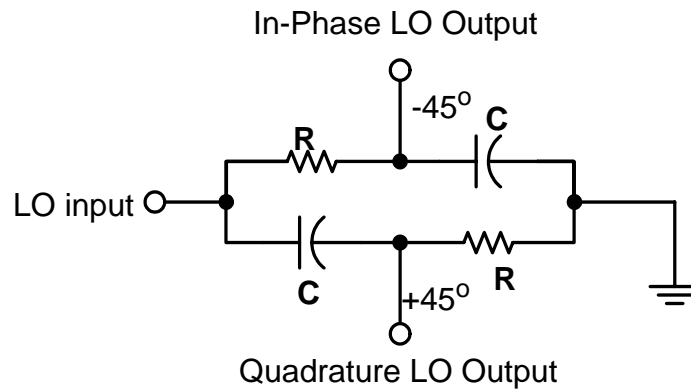


Figure 4.14. Resistor-capacitor-capacitor-resistor network for creating 90° phase shift.

tion is desired, as phase and amplitude imbalances can cause significant errors when the quadrature outputs are combined.

A phase shift network can convert a single-phase LO signal to a quadrature one. The phase-shift network shown in Figure 4.14 comprises a series resistor and capacitor in parallel with a series capacitor and resistor, and is therefore referred to as an RCCR [169]. The end of the two parallel branches is grounded, so that when outputs are tapped between the series elements in each branch, the phase is shifted by -45° in the resistor-capacitor branch and by $+45^\circ$ in the capacitor-resistor branch. When the time constant is equal to the period of the LO signal, the amplitudes of the in-phase and quadrature outputs are equal.

Since the unlicensed ISM band is 2.4 to 2.483 GHz, the narrow-band components were designed to operate in the middle of the band at 2.44 GHz. Therefore, $65\text{-}\Omega$ resistors and 1-pF capacitors were used in the RCCR.

With this type of phase-shifting network, inaccurate values of the resistors and capacitors can cause errors in the quadrature phase and amplitude balance. Additionally, if the operating frequency is not that which the RCCR was designed for, there will be quadrature errors. Figure 4.15a shows how the amplitude balance varies with frequency. At 2.45 GHz, the $65\text{-}\Omega$ and 1-pF RCCR is balanced ideally. At 2.2 GHz, the amplitude of the in-phase output is 1 dB greater than that of the quadrature output. As shown in

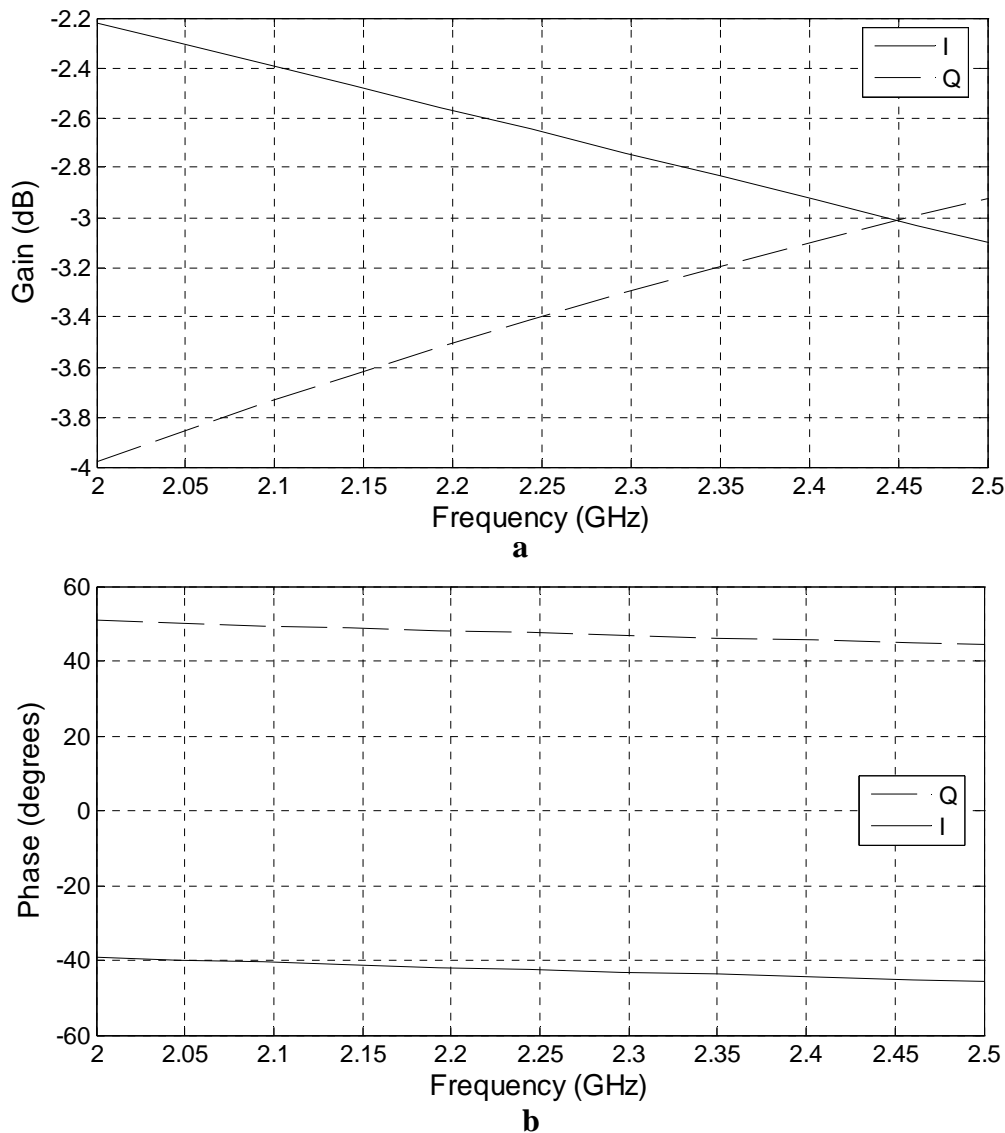


Figure 4.15. The a) gain and b) phase of the in-phase (I) and quadrature (Q) outputs of the RCCR with resistances of 65Ω and capacitances of 1 pF . A sine wave is swept at the input of the network and the output amplitude and phase are simulated relative to the input. $50\text{-}\Omega$ loads are assumed at the outputs.

Figure 4.15b, the phase difference between the outputs remains constant at 90° over this frequency range although the phases at the two outputs are $+45$ and -45 only at the design frequency of 2.45 GHz . A 1-dB decrease in LO power will increase the conversion loss (and therefore decrease the IF power) by less than 0.2 dB .

After integrated circuit fabrication, the passive component values do not always match those they were designed for. To assess the effects of such errors, the value of the resistors was swept while keeping the capacitors at 1 pF with a 2.45-GHz input signal. The outputs are shown in Figure 4.16. A 10% variation in the resistor value results in a 1-dB amplitude mismatch between the I and Q outputs. The phase balance remains at 90° as long as both resistors and both capacitors are the same value. The amplitude balance, however, varies with the frequency of operation and the absolute values of the components.

Abidi, in [142], suggests alternative phase-shift network topologies that improve the quality of quadrature when component values cannot be accurately designed. In future iterations of this design, these techniques will be considered.

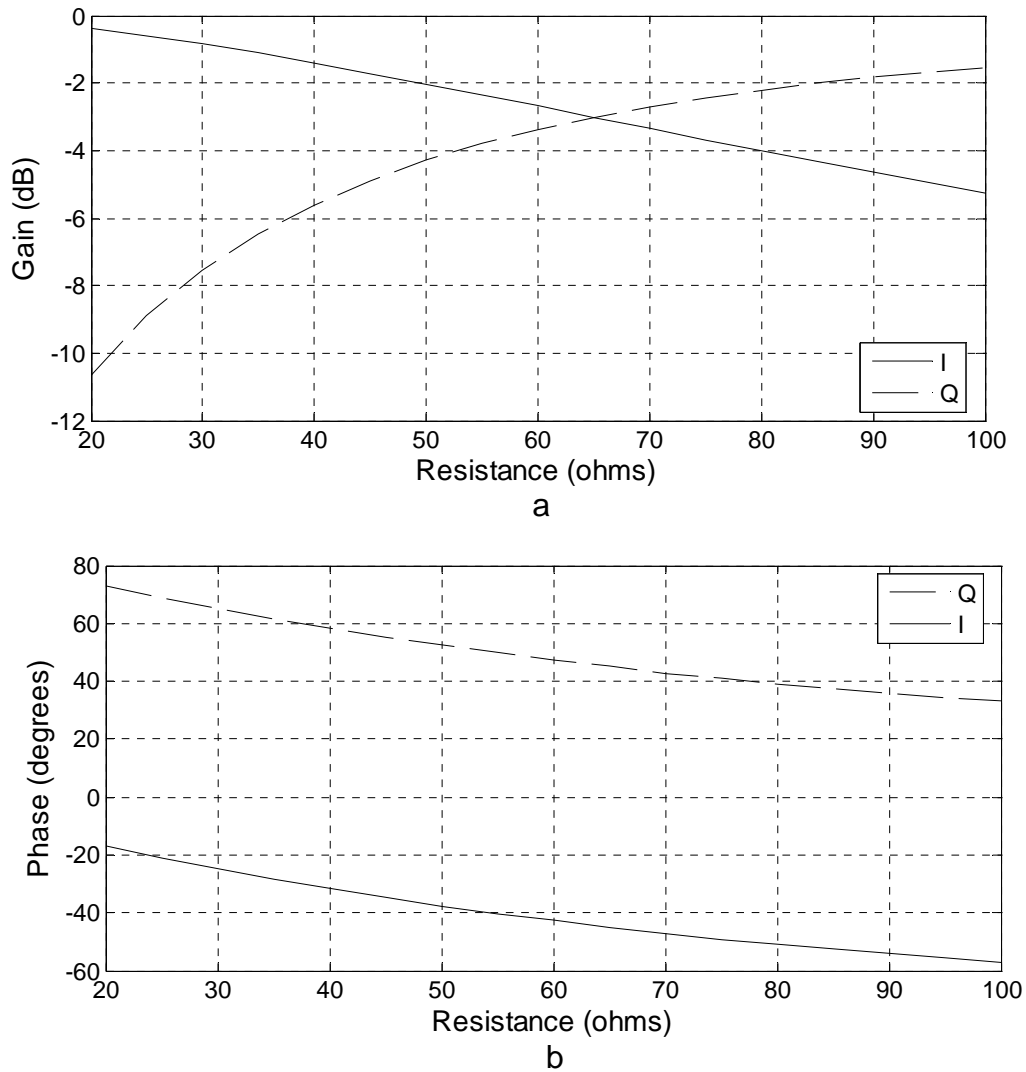


Figure 4.16. Simulation of RCCR sensitivity to component value: a) gain and b) phase shift between input and output vs. resistor value at 2.45 GHz. The value of C in Figure 4.14 is swept and the ratio of the output amplitude to the input amplitude and the phase difference between the input and the outputs are calculated. 50- Ω loads are assumed at the output.

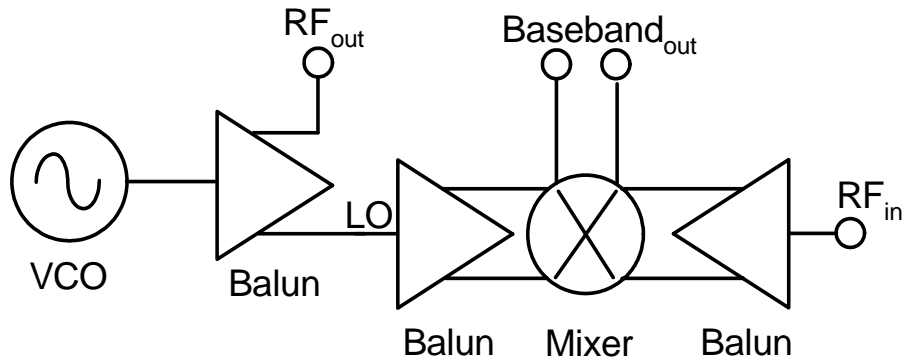


Figure 4.17. Block diagram of a single-channel direct conversion Doppler radar transceiver.

4.4 Single-Channel Doppler Transceiver Design

A block diagram of the single-channel Doppler radar transceiver is shown in Figure 4.17. It uses one balun-amplifier to split the VCO signal into the transmitted signal (RF output) and the LO, making it a transceiver rather than a receiver. Two additional balun-amplifiers split the single-ended LO and RF input signals into the differential signals required by the double-balanced mixer. Since noise figure is not a limiting factor, the Doppler radar can use a balun amplifier rather than a LNA - passive balun combination at the RF input port. Because the RF input signal and the LO are generated by the same source, this is a homodyne architecture. The resistive ring mixer is particularly well suited to direct conversion architectures because it is passive and therefore minimizes baseband $1/f$ noise.

4.4.1 Hybrid Transceiver

Initially, the individual building blocks of the base station receiver were designed, fabricated, packaged, and tested individually. They were packaged in Amkor SSOP-16 exposed pad packages with 3 mm by 5 mm footprints [145]. As shown in Figure 4.18, the individually packaged bipolar balun-amplifiers and the CMOS mixer were placed on a printed-circuit board with a commercially available VCO to make a Doppler radar trans-

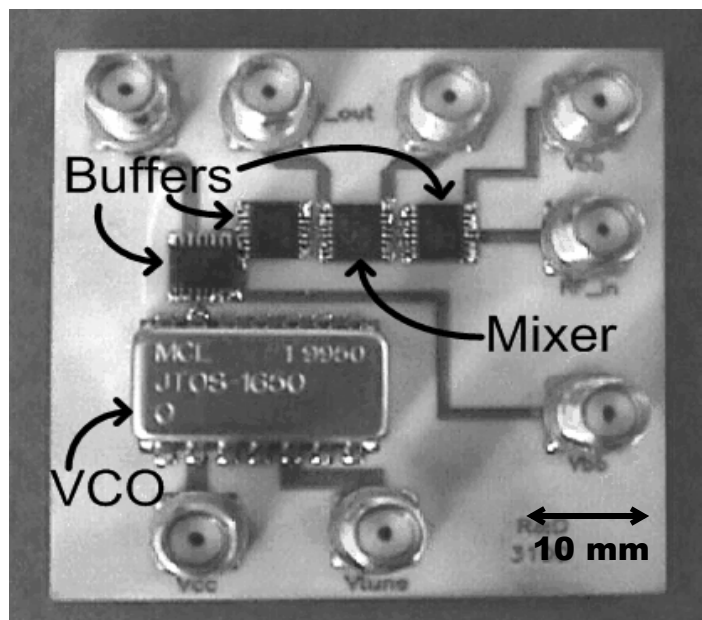


Figure 4.18. Photograph of hybrid Doppler radar transceiver, using individually packaged CMOS mixer and bipolar balun-amplifiers with a commercially available discrete VCO. The MiniCircuits JTOS-1650 VCO has -70 -dBc/Hz SSB phase noise at a 1-kHz offset.

ceiver using the architecture of Figure 4.17 [151]. The MiniCircuits JTOS-1650 VCO has -70 -dBc/Hz SSB phase noise at 1-kHz offset. This hybrid radar operates in the DCS1800 band. The circuit was built on a Rogers RO-4003 (Rogers Corporation, Rogers, CT) substrate with a dielectric constant of 3.38 and a thickness of 0.5 mm. SMA connectors are used for the inputs, outputs, and dc bias. The RF signals are routed via $50\text{-}\Omega$ lines, which are 1.1 mm wide on this material. The RF traces between the components are short enough compared to the wavelength that they need not be $50\text{-}\Omega$. The board dimensions are 50 mm by 50 mm.

4.4.2 Single-Channel Fully-Integrated Transceivers

4.4.2.1 Introduction

The architecture of Figure 4.17 was also used in two fully integrated chips which were fabricated using the Agere Systems $0.25\text{-}\mu\text{m}$ CMOS and BiCMOS processes and pack-

aged in the same exposed pad package as used for the base station receiver chips [144], described in Section 4.2. The Doppler radar transceivers are fully integrated, including all passive components, and inductor Q is below 10. Both transceivers operate at 1.6 GHz, the DCS1800 LO frequency, for which the VCO and the balun-amplifier were designed. The mixer is broadband, and can accommodate 1.6-GHz signals at its RF port as well as at its LO port and output baseband signals at its IF port. The CMOS and BiCMOS designs are presented below.

The Rogers RO-4003 material (Rogers Corporation, Rogers, CT) was used for these circuit boards; it has a well-controlled dielectric constant of 3.38. A 0.51-mm board thickness was selected as a compromise between stiffness and trace width.

4.4.2.2 BiCMOS Transceiver

The BiCMOS chip was integrated using the bipolar VCO, bipolar balun-amplifiers, and the CMOS mixer. This chip operates at 1600 MHz, the same frequency as the LO for DCS1800 base station receivers for which the VCO was originally designed. A micrograph of the chip is shown in Figure 4.19, and a photograph of the packaged chip on the printed-circuit board is in Figure 4.20. The fabricated BiCMOS chip is 3.75 mm by 3.75 mm.

4.4.2.3 CMOS Transceiver

The CMOS transceiver used the same CMOS mixer as the BiCMOS transceiver, along with the CMOS versions of the balun-amplifier and VCO. The CMOS transceiver operates at 1600 MHz, as does the BiCMOS chip. A micrograph of the CMOS Doppler transceiver chip is shown in Figure 4.21. The die is 3.75 mm by 3.75 mm. Fabrication and design rules were identical to those for the BiCMOS version of the chip. The CMOS circuit includes an external LO option so that a signal source other than the on-chip voltage-controlled oscillator can be used for measurements. A photo of the packaged CMOS chip on the board is shown in Figure 4.22.

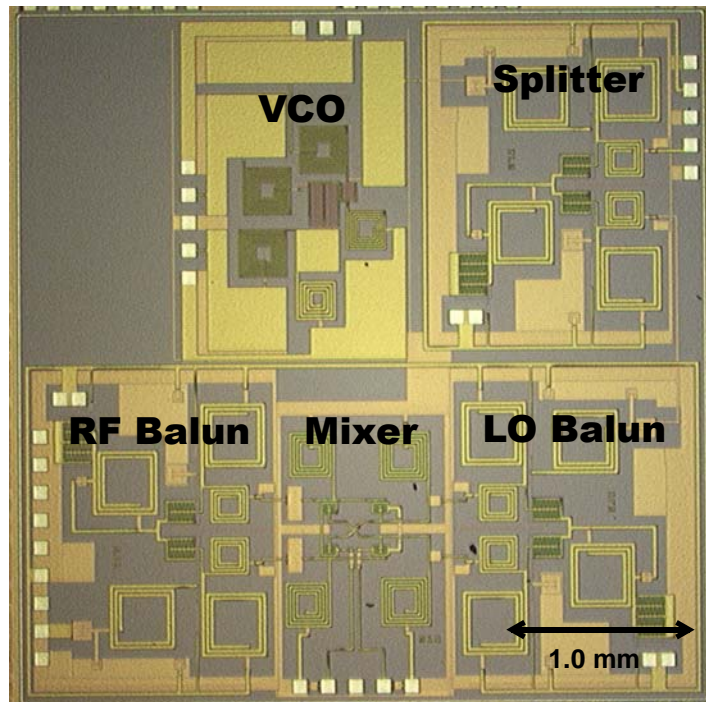


Figure 4.19. Micrograph of BiCMOS Doppler radar transceiver.

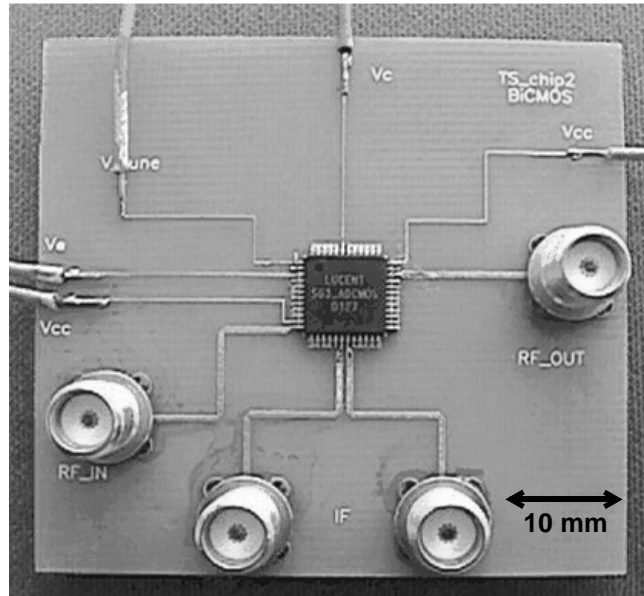


Figure 4.20. Photo of BiCMOS chip on board.

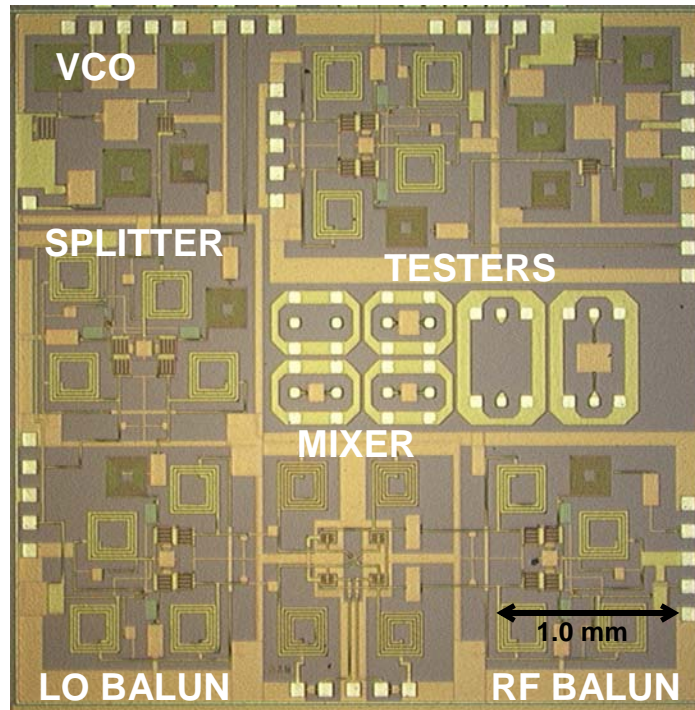


Figure 4.21. Micrograph of CMOS Doppler radar transceiver.

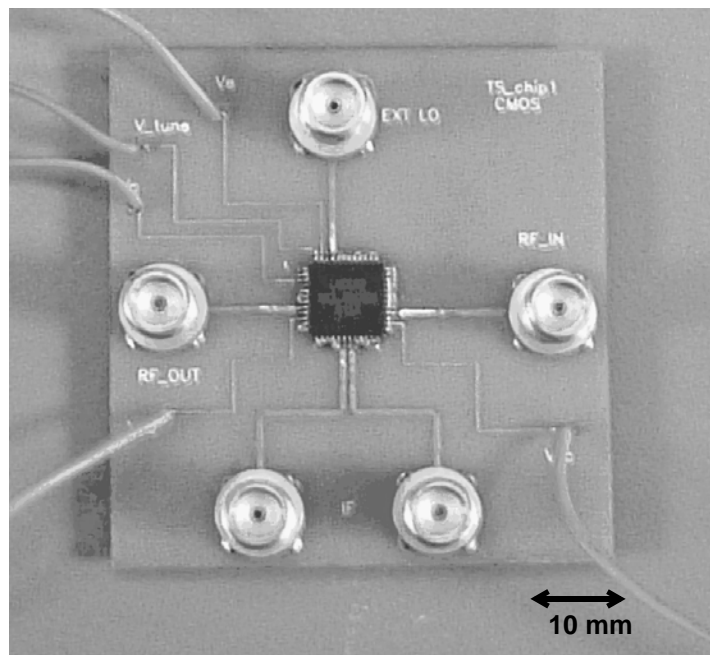


Figure 4.22. Photo of printed circuit board with CMOS chip.

4.5 Quadrature Doppler Transceiver Design

4.5.1 Quadrature Architectures

Two different architectures with quadrature receivers were developed. The first uses low-noise amplifiers to isolate the phase-shifting network, and passive baluns to convert each single-ended LO to a differential LO as required by the circuit. The second architecture uses active baluns to provide both isolation and the single-ended to differential conversion, thereby saving both die area and power consumption. Both of these transceivers operate in the 2.4-GHz unlicensed band, which required re-tuning of narrowband DCS1800 sub-circuits designed for 1.6 GHz and 1.8 GHz including the voltage-controlled oscillator (VCO), the passive balun, the balun-amplifier, and the low-noise amplifier (LNA) from the original digital cellular system (DCS) subcircuits. Both architectures were fabricated in 0.25 μm CMOS.

The quadrature architecture with LNAs was developed initially, and the quadrature architecture without LNAs provided some refinements from the original design. Since the RF additive noise is not a limiting factor in this system, noise factor is not a critical parameter. This eliminates the need for an LNA at the RF input. The performance-limiting factors in the system are the oscillator phase noise and $1/f$ noise at the mixer output. The $1/f$ noise at the mixer output is increased by nonlinearity in the receiver chain that causes dc offsets. Minimizing second-order nonlinearities requires maximizing gain and phase balance at the mixer's inputs and this was better provided by an active balun than a passive balun. Additionally, simulations indicate that the LNA isolating the VCO from the RCCR was not necessary, so that was eliminated in the architecture without LNAs. These modifications provided a transceiver chip that used marginally less die area and consumed significantly less power than the architecture with LNAs.

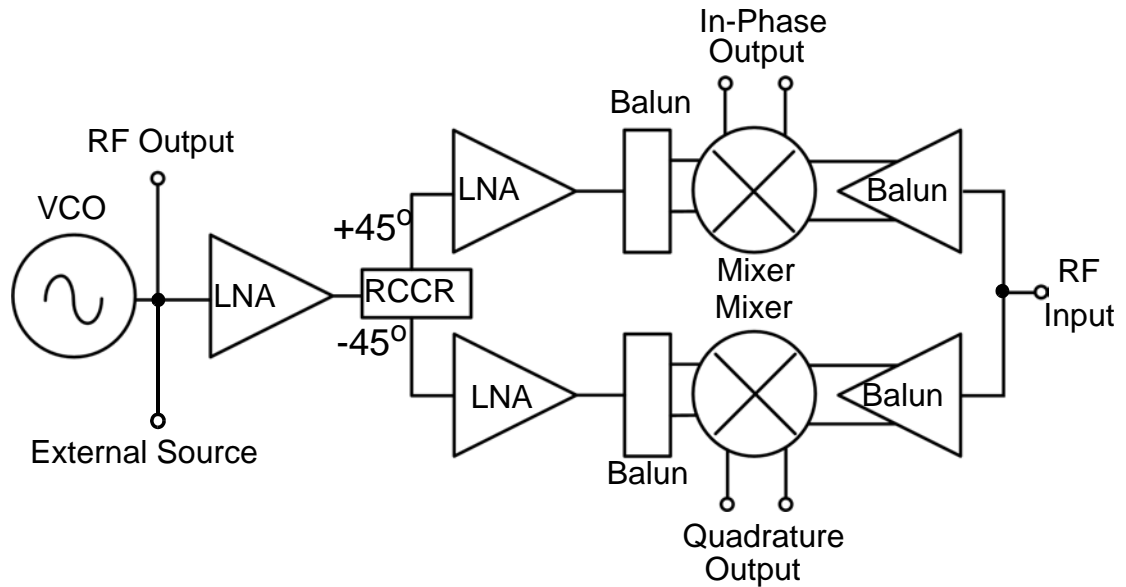


Figure 4.23. 2.4-GHz quadrature Doppler radar transceiver architecture with LNAs.

4.5.2 CMOS Quadrature 2.4 GHz Transceiver with LNAs

The architecture of the quadrature transceiver with LNAs is shown in Figure 4.23. The voltage-controlled oscillator (VCO) provides both the RF output signal and the local oscillator (LO). An external source port provides the option of bypassing the on-chip VCO for testing purposes, or for using a phase-locked loop to control the oscillator frequency. The oscillator signal is split into the RF output signal that drives the antenna and the LO signal that is used for demodulation. The VCO is isolated from the phase-shift network with an LNA, which also amplifies the LO. The LO is then split into two quadrature LO signals for I and Q receiver chains. The quadrature LO signals are created with a passive resistor-capacitor-capacitor-resistor network (RCCR) which provides a $+45^\circ$ phase shift to one LO output and a -45° phase shift to the other LO output. Additional LNAs amplify each of these signals to provide isolation between the in-phase (I) and quadrature (Q) receiver chains, and then a passive inductor-capacitor (LC) balun transforms the single-ended LO into the differential LO required by the double balanced mixer. The RF input signal is passively divided in two for the in-phase (I) and quadrature (Q) channels by applying the

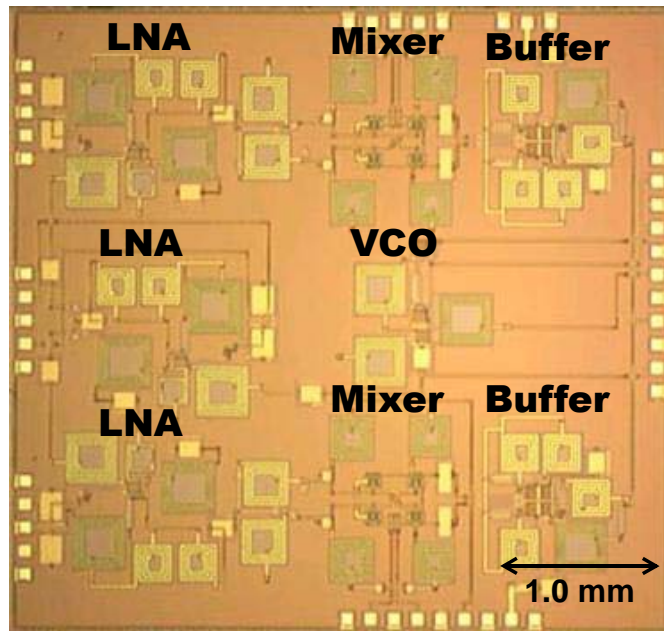


Figure 4.24. Micrograph of the quadrature transceiver with LNAs.

signal to two parallel inputs with equal input impedances. Active buffer amplifiers convert single-ended RF signals to differential signals that feed the mixer.

The chip was fabricated using an Agere 0.25- μm CMOS process with five metal levels. An inductor Q between 5 and 10 was obtained using the 3- μm thick top metal level. The chip is 4.0 mm x 4.2 mm, and is packaged in an Amkor TQFP-48 exposed-pad package [144]. The radio dissipates 190 mW, and provides 3 dBm RF output power at 2.3 GHz. With an external source, the chip can be used in the frequency range of 2.2 to 2.5 GHz.

The circuit was laid out so that the two receiver chains were symmetrical, with no trace on one chain significantly longer than one on the opposite chain to avoid any phase shifts. This symmetry can be seen in the chip micrograph of the Doppler radar transceiver, shown in Figure 4.24. Each subcircuit has separate biases.

The printed circuit board was made on Rogers 4003 (Rogers Corporation, Rogers, CT) dielectric material with a dielectric constant of 3.38. Its size was 75 mm by 85 mm, and a photo of the chip on the printed circuit board is shown in Figure 4.25.

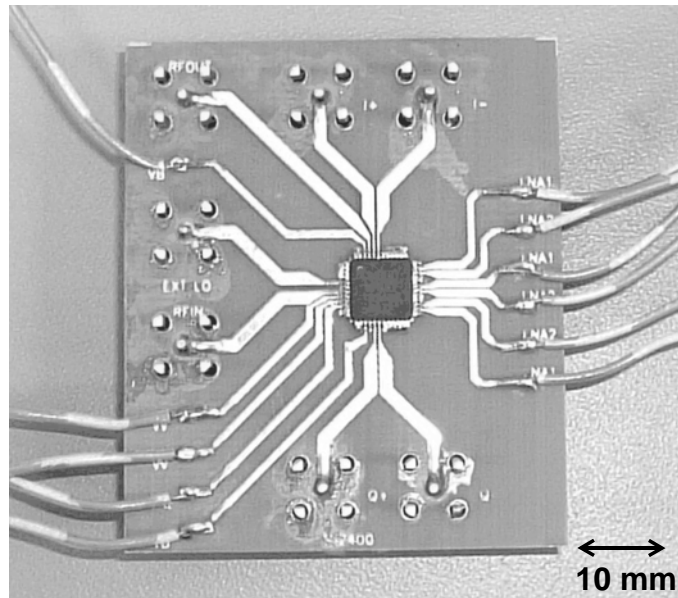


Figure 4.25. Photograph of the packaged quadrature chip with LNAs on a board.

4.5.3 CMOS Quadrature 2.4 GHz Transceiver without LNAs

A block diagram of the quadrature CMOS microwave radio without LNAs is shown in Figure 4.26. This transceiver is similar to the previous architecture, but the LNA before the RCCR was eliminated and the LNA-balun combination between the RCCR and the mixer was replaced with an active balun. These changes provided some advantages: the active balun draws lower power than the LNA, so the power consumption is reduced. Secondly, the active balun provides phase and amplitude balance over a wider bandwidth than the passive balun, which decreases second-order intermodulation if the passive element values are not accurate or the oscillator frequency is not accurate.

The signal source is a voltage-controlled oscillator (VCO), which delivers a signal to the RF output port and provides the local oscillator (LO). The next block in the LO path is a passive resistor-capacitor network (RCCR), which is used to split the LO signal into the I and Q channels. In each receiver chain, the LO is amplified and converted from a single-ended signal to a differential signal with an active balun-amplifier. The RF input

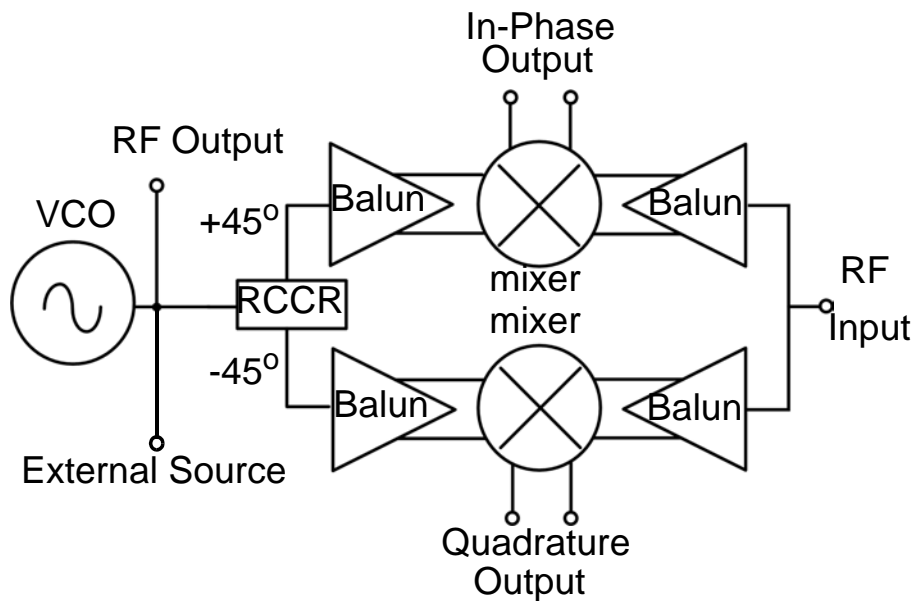


Figure 4.26. 2.4 GHz quadrature Doppler radar transceiver architecture without LNAs.

signal is divided into the two receiver chains, and each chain also has an active balun-amplifier for single to differential conversion. The double-balanced ring mixer is fully passive; use of a balanced mixer minimizes even-order distortion, which is especially important in a direct-conversion architecture, as even-order distortion creates interference at the baseband signal. A passive mixer is used to minimize $1/f$ noise, which can be limiting in homodyne systems where the signal frequencies are near zero.

The chip was fabricated with the same Agere Systems $0.25\ \mu\text{m}$ CMOS process as the other CMOS chips. A micrograph of the receiver chip is shown in Figure 4.27. The chip has a size of 4.3 mm by 3.8 mm, and is packaged in an Amkor exposed pad TQFP-48 package, which has a 7 mm by 7 mm body size. The printed circuit board was made on a Rogers 4003 substrate (Rogers Corporation, Rogers, CT), 20 mil thick with a dielectric constant of 3.38. This board was 56 mm by 90 mm. A photograph of the chip on the board is shown in Figure 4.28. When biased at 3V, this chip consumes 100 mW.

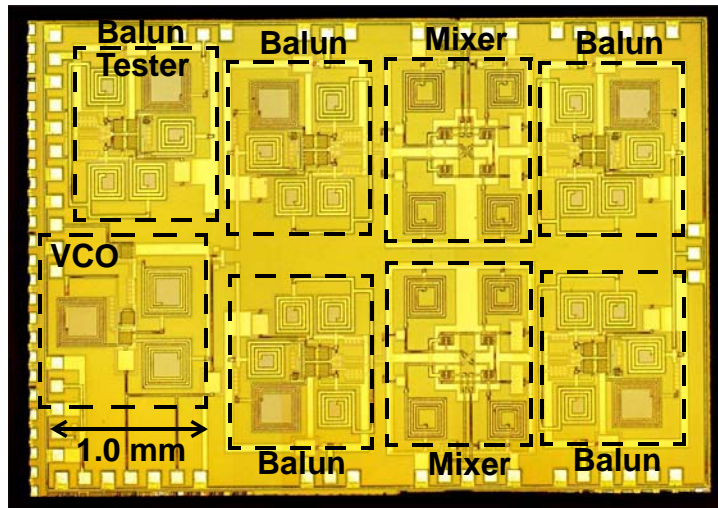


Figure 4.27. Micrograph of the quadrature chip without LNAs.

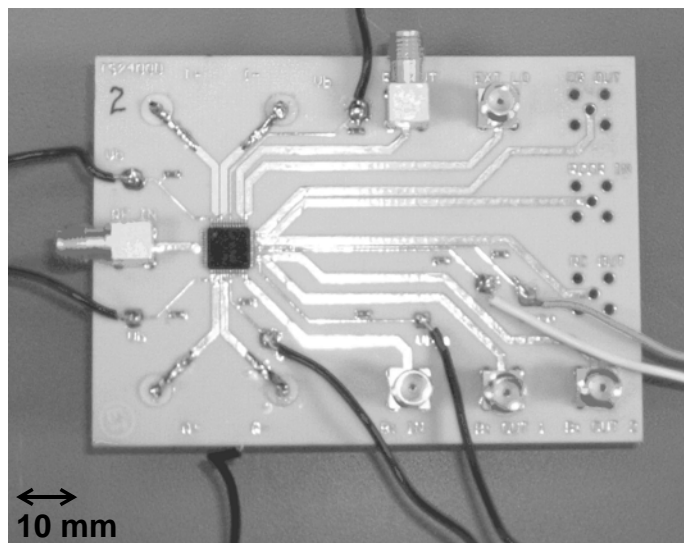


Figure 4.28. Photograph of packaged quadrature transceiver without LNAs on a printed circuit board

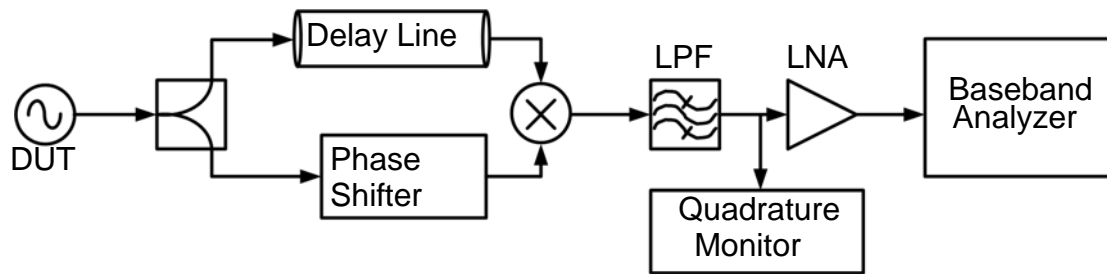


Figure 4.29. Delay line frequency discriminator method for phase noise measurements.

4.6 Circuit Characterization

4.6.1 Power Consumption

The quadrature chip with the LNAs consumes a total of 190 mW when with a 3V bias: 40 mW from the VCO, 15 mW from each of the two buffers and 40 mW from each of the three LNAs. This quadrature chip without LNAs consumes a total of 100 mW with a 3V bias: 40 mW from the VCO and 15 mW from each of the 4 buffers.

4.6.2 Phase Noise

The delay line/mixer frequency discriminator method is used with the Agilent E5500 phase noise measurement system to measure phase noise. A block diagram of this method is shown in Figure 4.29. This method does not require a reference source phase to be locked to the source under test, which makes it useful for measuring free-running oscillators that may drift quickly. A wideband delay line is created with a coaxial cable. This system converts frequency fluctuations to phase fluctuations, and then converts the phase fluctuations to voltage fluctuations [143].

A delay line causes a fixed time delay between the nominal signal and the delayed signal. Variations in the frequency of the signal change the amount of phase delay between the nominal and delayed version of the signal. The mixer then acts as a phase detector, transforming the instantaneous phase fluctuations to voltage fluctuations. When the two

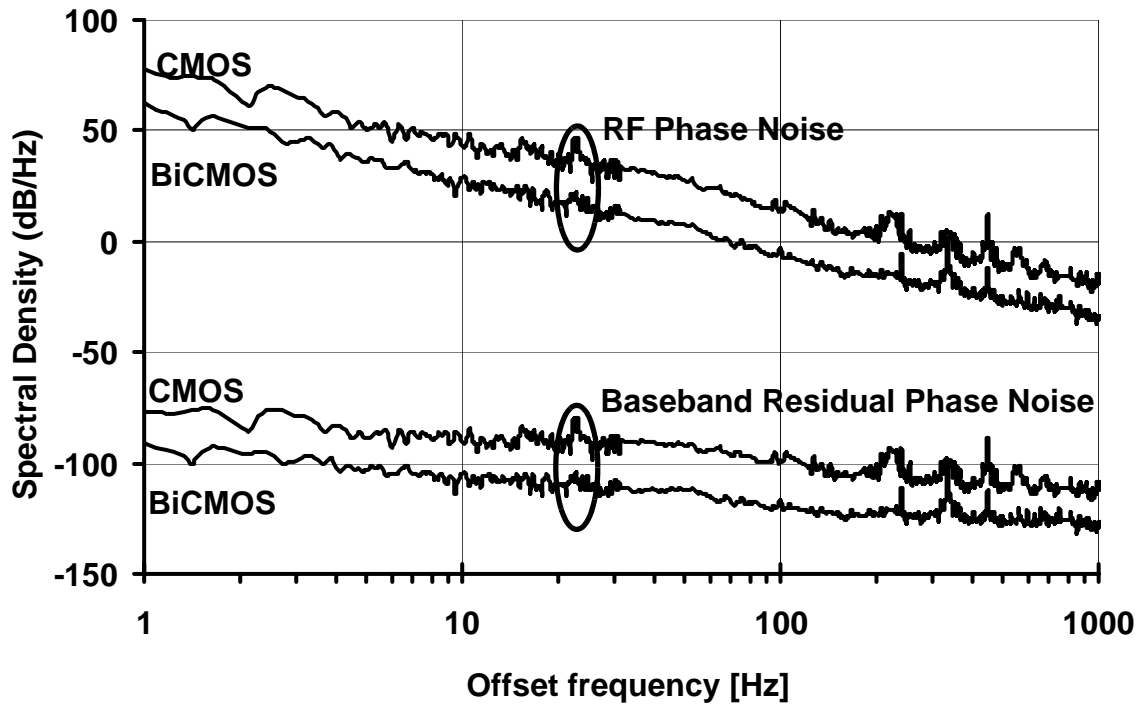


Figure 4.30. Measured RF phase noise and calculated baseband residual phase noise for CMOS and BiCMOS single-channel chips. The residual phase noise is calculated at a 50 cm range and 1-Hz offset frequency.

input signals are near 90° out of phase, the voltage fluctuations approximate the phase fluctuations. The voltage fluctuations are then measured with the baseband analyzer and converted to phase noise units.

The phase noise spectral density of the CMOS and BiCMOS single-channel chips are shown for offset frequencies from 1 Hz to 10 kHz in Figure 4.30. The CMOS chip has about 12-dB higher phase noise than the BiCMOS chip. The single-sideband phase noise of the CMOS chip with an external source (HP E4433B) measured with a spectrum analyzer (HP 8563E) is -80 dBc/Hz at 10 Hz, verifying that residual phase noise of the CMOS balun-amplifier does not degrade the RF output.

As discussed in Section 4.3.2, residual phase noise is directly proportional to RF phase noise at any given offset frequency. However, since the RF phase noise, which has a $1/f_o^3$ slope close-in, is multiplied by a factor of f_o^2 to calculate the baseband residual phase noise, the residual phase noise has a $1/f_o$ slope. The measured RF phase noise and

the calculated baseband residual phase noise at a 50 cm target range is also shown in Figure 4.30. The values at an offset frequency of 1 Hz, where the heart signal power spectrum lies, are given in Table 4.1.

Table 4.1: Measured RF Phase Noise and Calculated Baseband Residual Phase Noise at 50 cm and 1 m for the Different Oscillators Used for Doppler Radar Cardio-Respiratory Monitoring.

Oscillator	Distance (cm)	Measured RF Phase Noise at 1Hz Offset (dBc/Hz)	Calculated Baseband Residual Phase Noise at 1 Hz Offset (dB/Hz)
Hybrid	50	$+20 \pm 1.9$ N=2,	-134
	100		-128
BiCMOS	50	$+52 \pm 1.4$ N=2	-102
	100		-96
CMOS	50	$+64 \pm 1.6$ N=3	-90
	100		-84
HP E433B Signal Generator	50	-77 ± 0.4 N=2	-231
	100		-225

4.6.3 1/f Noise Generation

As discussed in Section 4.3.3, the level of 1/f noise at the output of the mixer is important for a direct-conversion system. Because the resistive FET mixer is passive, there is no 1/f noise generated when signals are not being mixed. However, if the signals are mixed to baseband, it is impossible to differentiate residual phase noise from 1/f noise generated by the mixer. Therefore, two low-noise signal generator sources are used, and their frequencies are selected to mix to an IF frequency that is sufficiently above baseband so that residual phase noise can be differentiated from 1/f noise. The literature indicates that the 1/f noise is proportional to the leakage from the LO to the RF inputs and vice versa, as well as due to any dc offset created by self-mixing due to leakage [161]. This technique isolates the LO and RF noise due to leakage. The LO drive power is varied during this measurement to determine if the 1/f noise is decreased with increasing LO drive, so that the CMOS transistors are switching on and off rather than acting as linear variable resistors.

This measurement was performed with a RF and LO frequency of approximately 2200 MHz, giving an IF frequency of about 240 Hz. INA105 instrumentation amplifiers were

used to convert the differential IF signals to single-ended. The baseband noise power spectral density was measured with the vector signal analyzer with a resolution bandwidth of 300 mHz over a 100mHz to 1 kHz bandwidth. Ten measurements were RMS averaged to give the traces shown in Figure 4.31. The baseband noise measurement is shown with fixed RF input power of -10dB with LO power varying from +10 dBm to -10 dBm in Figure 4.31a, and with fixed 0-dBm LO power and RF input power varying from 0 dBm to -40 dBm in Figure 4.31b. The power spectral density at 1 Hz was measured to be between -84 and -102 dBm for all measured combinations of RF and LO power.

4.6.4 Isolation

Measurements of isolation between the RF and LO ports of the mixer require use of a mixer test-circuit rather than the chip because the active baluns provide additional isolation. Transformers can be used to convert the outputs of the network analyzer to the differential inputs of the mixer. Measurements were made in all combinations between the RF, LO, and IF ports of the mixer with the HP8417C Network Analyzer. Typical values for the isolation were 44 dB for the RF - LO isolation, 26 dB for the LO - IF isolation, and the 38 dB for the RF - IF isolation.

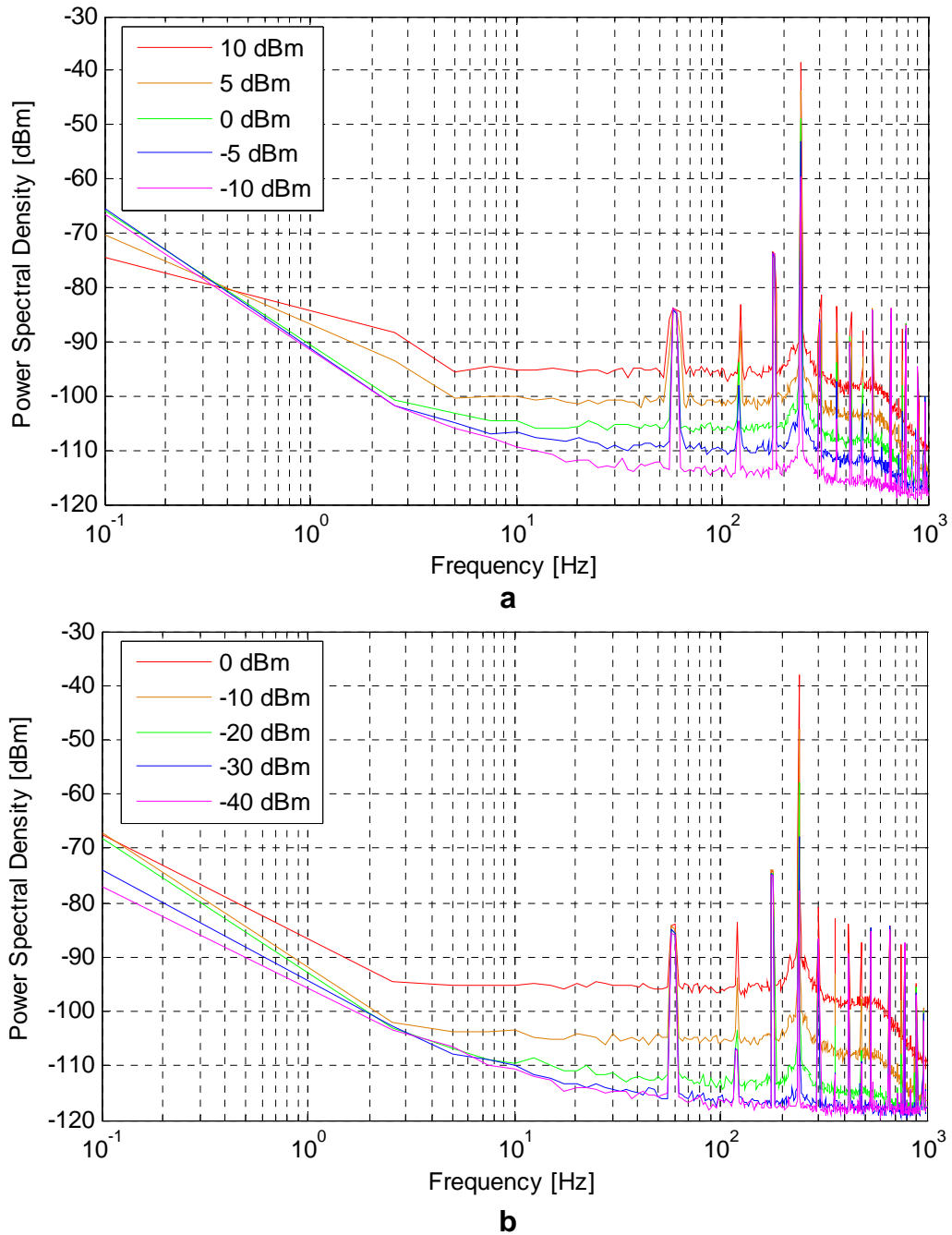


Figure 4.31. Measurement of baseband noise due to RF-LO leakage a) varying LO power with RF power fixed at -10 dBm and b) varying RF power with LO power fixed at 0 dBm. Error between repeated measurements was below 2dB.

4.6.5 Phase and Gain Balance Between Quadrature Branches

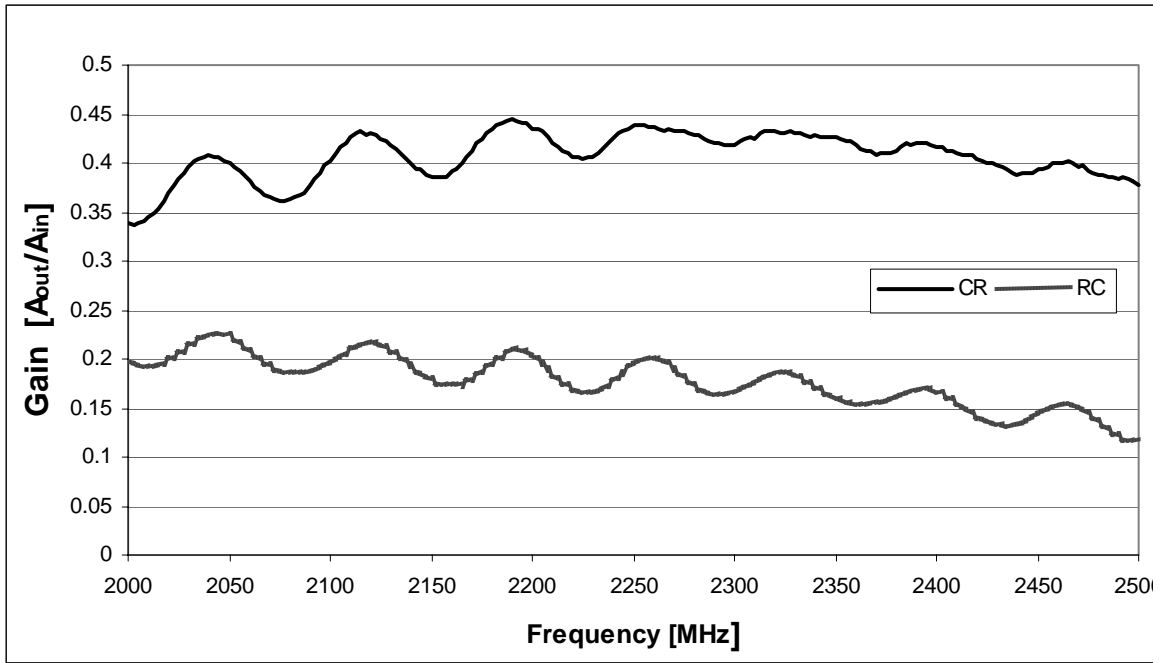
Phase and amplitude imbalance between the two receiver chains were induced by the RCCR circuit and mismatches between RF components, baseband components, and the ADC in each receiver chain. In Section 4.6.5.1, the mismatch introduced by the RCCR has been assessed through measurements of isolated RCCR testers. In Section 4.6.5.2, the phase and gain imbalance for the whole receiver is assessed.

4.6.5.1 RCCR Testers

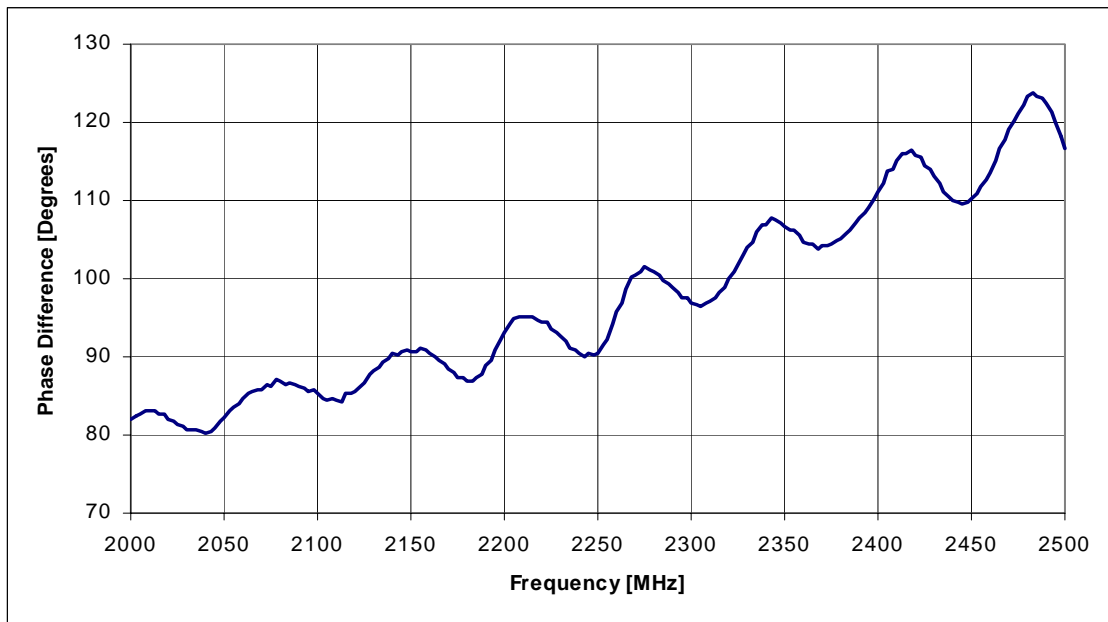
Measurements of the phase and gain balance of the RCCR test circuit were made with an HP8417C Network Analyzer. It was calibrated for transmission measurements from 2000-2500 MHz immediately before testing. The RF output of the network analyzer was attached to the input of the RCCR tester. The RF input of the network analyzer was either attached to either the CR output or the RC output of the RCCR tester. The tester output that was not attached to the network analyzer input was terminated with 50- Ω .

Measurements performed on the RCCR tester on the chip without LNAs are shown in Figure 4.32. The gain to each output is shown and the phase difference between the two outputs is shown for one tester that had typical values. The desired measurements are for equal amplitude on the two outputs and a 90° phase difference. At 2.2 GHz, the measured phase error is 3° and the amplitude imbalance is 3.3 dB on this tester. Over the three testers measured, at 2.2 GHz the phase error was $5 \pm 25^\circ$ and the amplitude error was 1.96 ± 0.26 .

In simulation, the phase difference between the outputs was constant, not increasing with frequency as seen in the measured data. The gain was expected to be matched at 2300 MHz, but is matched at a frequency below 2000 MHz. The 3-dB gain imbalance in the LO will produce a difference the mixer conversion loss of the I and Q channels of less than 1 dB. This lack of correspondence between the measurements and simulation is likely due to the resistor and capacitor values on the chip differing from those in the design and simulation.



a



b

Figure 4.32. a) Relative amplitude of I and Q outputs and b) phase difference between I and Q outputs of RCCR tester on quadrature chip without LNAs.

4.6.5.2 Transceiver Phase and Amplitude Balance Measurements

The overall phase difference between the I and Q channels was measured by using two signal generators as the external LO and the RF input, and looking at IF frequencies below 50 Hz. The voltage amplitude relationship between I and Q was measured by comparing the magnitude of the signals, and the cross correlation of the two signals was used to determine their phase relationship. This data was collected with an oscilloscope directly from the chip, and the phase error on a typical chip was found to be 27° while the voltage amplitude ratio was 2.1. When the same parameters were measured on the same chip after the signals were digitized, the phase error was 7° , and the voltage amplitude imbalance ratio was determined to be 2.8.

The test setup is illustrated in Figure 4.33. Two signal generators, the Marconi 2051 and the Marconi 2031, were used as the RF input and the external LO for the 2.4 GHz quadrature chip. The RF input was set at a -10-dBm power and with a 2200-MHz signal and the external LO was set at 0-dBm with a 2200-MHz signal. All four outputs were connected to a National Instruments BNC110 breakout box with 12" BNC cables. The breakout box was connected to a National Instruments DAQCard 6036E PCMCIA card analog-to-digital converter, which was inserted in a PC running MATLAB data acquisition software. The MATLAB software filtered the data, determined its frequency and amplitude, and found the phase difference between I+ and I-, Q+ and Q-, I+ and Q+, and I- and Q-. It removed any dc offset, converted the differential signals to single-ended signals, and compared the phase between the two. The VCO was not biased, but all four buffers were biased at 3V.

The software acquired the data, then applied an FIR low-pass filter which passed 50 Hz but cut off above 200 Hz. Any dc offset was removed, and the frequency was determined via the FFT. The amplitudes were found by subtracting the maximum from the minimum. Then the phase relationships were determined. The differential signals were combined to have just I and Q signals, and the phase difference between the I and Q sig-

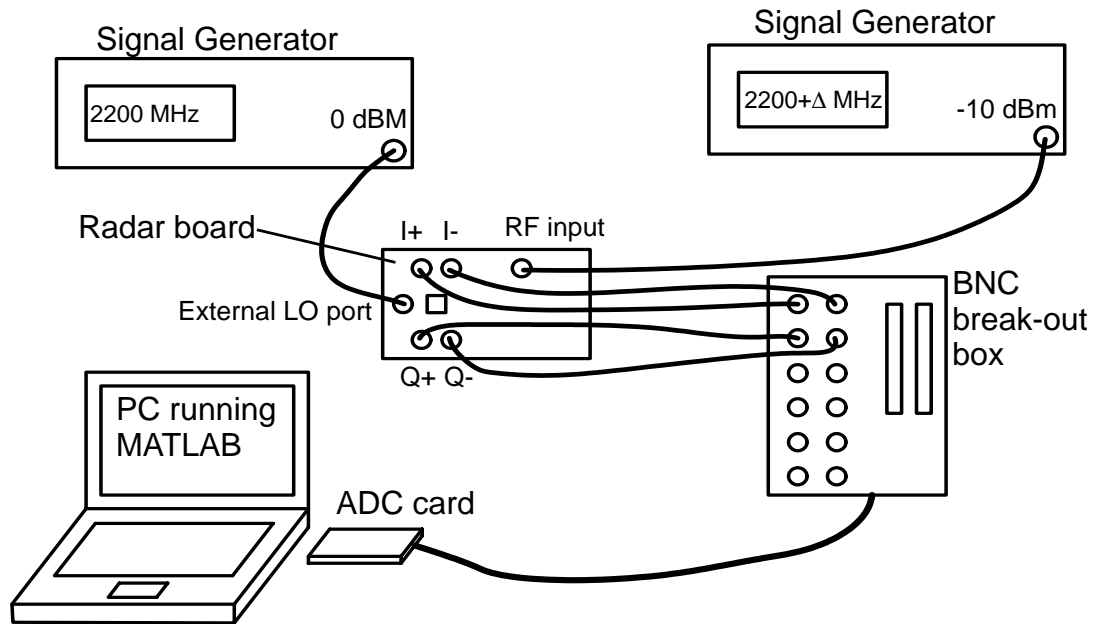


Figure 4.33. Test setup for overall phase and amplitude balance measurements.

nals was determined. The phase difference was found by the peak of the cross correlation between the two signals.

The phase difference was $88.3^\circ \pm 1.2^\circ$, and the amplitude difference was 2.78 ± 0.05 times. These measurements were made over 100 1-second intervals with a time span of 169 seconds (the time span was longer than 100 seconds because the processing took longer than the acquisition), and the measurement was repeated on this chip and baseband board combination three times, with IF frequencies of 2.3 Hz, 1.1 Hz, and 1.6 Hz. The measurement was repeated including the baseband signal conditioning board described in Appendix E. For the chip-board combination that was used for human subjects testing, the phase difference was $117^\circ \pm 1.9^\circ$ and the amplitude difference was 2.66 ± 0.2 times. These measurements were made over 100 1-second intervals with a time span of 169 seconds.

These measurements also were made on the nine possible permutations of three chips and three boards. The phase difference from all these systems was $117.2^\circ \pm 1.2^\circ$ and the amplitude difference was 2.65 ± 0.04 times.

4.7 Conclusions

In this work, three single-channel Doppler radar transceivers and two quadrature Doppler radar transceivers have been developed for use in monitoring of heartbeat and respiration. The single-channel transceivers are a hybrid transceiver on a board with a commercially available VCO and individually packaged components, a fully integrated CMOS transceiver, and a fully-integrated BiCMOS transceiver. The quadrature transceivers were both developed in CMOS; one used LNAs to isolate and amplify the LO signals, and the other used active balun amplifiers for this purpose.

The performance of the CMOS and BiCMOS versions of the single-channel transceivers was similar, other than the phase noise, which was about 12 dB lower in the BiCMOS version. Since residual phase noise is one of the limiting factors and residual phase noise is directly proportional to oscillator phase noise, the BiCMOS chip will have a higher signal-to-noise ratio than the CMOS chip when used for heart and respiration monitoring. The quadrature transceiver without LNAs consumes 47% less power than the quadrature transceiver with LNAs, but otherwise the two receivers had similar performance. The quadrature receivers provide the ability to avoid phase demodulation null points. However, imperfect phase and amplitude balance between the quadrature channels creates challenges when performing direct phase demodulation. In Chapter 7, real-time digital signal processing techniques are presented that can be used to combine I and Q signals with phase and amplitude imbalance. It is shown that using combined I and Q signals improves the accuracy with which the heart and respiration rates can be detected compared to the single-channel transceivers.

The transceiver that is used for human subjects testing as described in Chapter 6 is the quadrature receiver without LNAs. This transceiver uses a single VCO, which was optimized for phase noise performance, for both the transmitted signal and the LO. A RCCR resistive-capacitive phase shifting circuit is used to create the quadrature LO signals. Active balun-amplifiers (buffers) are used to amplify the LO signals to sufficiently high power to drive the mixer, and to convert the LO to the differential signal that is required by

the double-balanced mixer. Each RF signal is also amplified and converted from single-ended to differential with a buffer. The RF and LO signals are mixed with a double-balanced resistive FET ring mixer. This double-balanced mixer consumes no DC power, is very linear, produces a low level of $1/f$ noise, and has a low level of RF-LO coupling.

The limiting noise factors of the Doppler radar cardiopulmonary monitoring system, as discussed in Appendix D, are baseband residual phase noise and $1/f$ noise at baseband. Residual phase noise at baseband is directly proportional to VCO phase noise, and provides motivation for minimizing oscillator phase noise. The $1/f$ noise is generated by the mixer, and the larger the dc offsets, the greater the noise generated by the mixer. Additionally, dc offsets are difficult to remove while passing the sub-Hertz respiration signal, so by minimizing the dc offsets the requirements on the baseband signal conditioning and/or the ADC can be relaxed. These two facts motivate the minimization of dc offsets. One cause of dc offsets is receiver nonlinearities, so improving the linearity of the receiver can improve system performance. Finally, minimizing phase and amplitude imbalance between the quadrature receiver chains facilitates direct phase demodulation, which optimizes the detection of chest motion.

There are several potential improvements in the transceiver design. First, the mixer could be further optimized for $1/f$ noise by using PMOS rather than NMOS transistors and could also be optimized to minimize second-order nonlinearities, which affect this system more than third-order nonlinearities. Second, the RCCR phase-shift network could be replaced with a different passive network that would provide more robust phase and amplitude balance, as the RCCR's phase and amplitude balance is dependent on accurate component values that cannot be easily controlled in a fully integrated device. Third, the VCO could be phase-locked to a low-phase noise reference, reducing the phase noise significantly.

4.8 References

- [141] A. A. Abidi, "General relations between IP₂, IP₃, and offsets in differential circuits and the effects of feedback," *IEEE Transactions on Microwave Theory and Techniques*, vol. 51, no. 5, pp. 1610-1612, 2003.
- [142] A. Abidi, "Direct-conversion radio transceivers for digital communications," *IEEE Journal of Solid-State Circuits*, vol. 30, no. 12, pp. 1399-1410, 1995.
- [143] Agilent Technologies, "Agilent E5505A Phase Noise Measurement System User's Guide," Agilent Technologies, Santa Rosa, CA, Manual Part Number E5505-90003, June 2004.
- [144] Amkor Technologies, "Amkor ExposedPad L/TQFP Data Sheet," Amkor Technologies, West Chester, PA, Data Sheet DS231E, 2000.
- [145] Amkor Technologies, "Amkor ExposedPad SOIC/SSOP," Amkor Technologies, West Chester, PA, Data Sheet DS571G, 2005.
- [146] C. Baringer and C. Hull, "Amplifiers for wireless communications," in RF and Microwave Circuit Design for Wireless Communications (L. E. Larson, Ed.), Boston: Arctech House pp. 345-395, 1996.
- [147] E. E. Bautista, B. Bastani, and J. Heck, "A high IIP₂ downconversion mixer using dynamic matching," *IEEE Journal of Solid State Circuits*, vol. 35, no. 12, pp. 1934-1941, 2000.
- [148] L. Besser and R. Gilmore, Practical RF Circuit Design for Modern Wireless Systems, Volume I: Passive Circuits and Systems, Boston: Arctech House, 2003.
- [149] O. Boric-Lubecke, J. Lin, P. Gould, "DCS1800 base station receiver integrated in 0.25 μm CMOS," in *IEEE MTT-S International Microwave Symposium Digest*, vol. 2, 2002, pp. 1049-1052.
- [150] O. Boric-Lubecke, J. Lin, T. Ivanov, and R. H. Yan, "Si-MMIC BiCMOS low-noise, high linearity amplifiers for base station applications," *IEEE Asia-Pacific Microwave Conference*, 2000, pp. 181-184.
- [151] A. D. Droitcour, O. Boric-Lubecke, V. M. Lubecke, J. Lin, "A microwave radio for Doppler radar sensing of vital signs," in *IEEE MTT-S International Microwave Symposium Digest*, vol. 1, 2001, pp. 175-178.

- [152] A. D. Droitcour, O. Boric-Lubecke, V. Lubecke, J. Lin, and G. T. A. Kovacs, "0.25 μm CMOS and BiCMOS single-chip direct-conversion Doppler radars for remote sensing of vital signs," in *International Solid-State Circuits Conference Digest*, vol. 1, 2002, p. 348.
- [153] A. D. Droitcour, O. Boric-Lubecke, V. M. Lubecke, J. Lin, G. T. A. Kovacs, "Range correlation and I/Q performance benefits in single-chip silicon Doppler radars for non-contact cardiopulmonary monitoring," *IEEE Transactions on Microwave Theory and Techniques*, vol. 52, no. 3, pp. 838-848, 2004.
- [154] A. Droitcour, O. Boric-Lubecke, V. M. Lubecke, J. Lin, G. T. A. Kovacs, "Chest motion sensing with modified silicon base station chips," *IEICE Transactions on Electronics*, vol. E87-C, no. 9, pp. 1524-1531, 2004.
- [155] P. Gould, J. Lin, O. Boric-Lubecke, C. Zelle, Y. J. Chen, and R. H. Yan, "0.25 μm BiCMOS receivers for normal and micro GSM900 and DCS1800 base stations," *IEEE Transactions on Microwave Theory and Techniques*, vol. 50, no. 1, pp. 369-376, 2002.
- [156] P. Gould, C. Zelle, J. Lin, "CMOS resistive ring mixer MMICs for GSM 900 and DCS 1800 base station applications," in *IEEE MTT-S International Microwave Symposium Digest*, vol. 1, 2000, pp. 521 - 524.
- [157] P. R. Gray and R. G. Meyer, Analysis and Design of Analog Integrated Circuits, 3rd ed., New York: Wiley, 1993.
- [158] J. Lin, "An integrated low-phase-noise voltage controlled oscillator for base station applications," in *IEEE International Solid State Circuits Conference Digest*, vol. 1, 2000, pp. 423-433.
- [159] J. Lin, O. Boric-Lubecke, P. Gould, C. Zelle, Y. J. Chen, and R. H. Yan, "3V GSM base station receivers using 0.25 μm BiCMOS," in *IEEE International Solid State Circuits Conference Digest*, 2001 pp. 416-417.
- [160] J. Lin, C. Zelle, O. Boric-Lubecke, P. Gould, and R. H. Yan, "A silicon MMIC active balun/buffer amplifier with high linearity and low residual phase noise," in *IEEE MTT-S International Microwave Symposium Digest*, 2000, pp. 1289-1292.
- [161] M. Margraf and G. Boeck, "Analysis and modeling of low-frequency noise in resistive FET mixers," *IEEE Transactions on Microwave Theory and Techniques*, vol. 52, no. 7, pp. 1709-1718, 2004.
- [162] S. A. Mass, "Mixers for Wireless Applications," in RF and Microwave Circuit Design for Wireless Communications (L. E. Larson, Ed.), Boston: Artech House, 1996, pp. 225-283.

- [163] S. A. Maas, Microwave Mixers, Second Edition, Boston: Arctech House, 1993.
- [164] S. Maas, "Mixer technologies for modern microwave and wireless systems," in *Proceedings of the Gallium Arsenide Application Symposium*, 2002, pp. 245–248.
- [165] K. K. O, N. K. Park, D.-J. Yang, "1/f noise of NMOS and PMOS transistors and their implications to design of voltage controlled oscillators," in *Proceedings of the Radio Frequency Integrated Circuit Symposium*, 2002, pp. 59-62.
- [166] J. Pihl, K. T. Christensen, and E. Bruun, "Direct downconversion with switching CMOS mixer," in *Proceedings of the IEEE International Symposium on Circuits and Systems*, vol. 1, 2001, pp. 117-120.
- [167] J. J. Rael and A. A. Abidi, "Physical processes of phase noise in differential LC oscillators," in *Proceedings of the IEEE Custom Integrated Circuits Conference*, 2000, pp. 569-572.
- [168] W. Redman-White and D. M. W. Leenaerts, "1/f noise in passive CMOS mixers for low and zero IF integrated receivers," in *Proceedings of the European Solid State Circuits Conference*, 2001.
- [169] G. D. Vendelin, et al., Microwave Circuit Design Using Linear and Nonlinear Techniques, New York: Wiley, 1990.

Chapter

5

Residual Phase Noise and Range Correlation

5.1 Introduction

The Doppler radar heart and respiration monitoring system transmits a continuous-wave (CW) signal, which is reflected off the subject and then demodulated in the receiver. In accordance with Doppler theory, when the subject has no net velocity but the chest and pulse points move with respiration and heartbeat, the phase of the reflected signal is modulated proportionally to the time-varying position of the body's surface. Demodulating the phase then gives a signal directly proportional to the body motion. Since the body motion contains information about the movement due to heartbeat and respiration, heart and respiration signatures and rates can be determined from the demodulated signal.

Since the heart and respiration information is encoded in the phase of the signal, the phase noise of the transmitted signal can be a limiting factor in the system. In the direct-conversion radar receiver, the same source is used for the transmitted signal and the local oscillator signal in the receiver, which means the received signal is a time-delayed version of the local oscillator signal. Therefore, the phase noise of the received signal is correlated with that of the local oscillator, with the level of correlation dependent on the time delay between the two signals. When the two signals are mixed, the correlated portion of the phase noise effectively cancels, leaving a residual phase noise spectrum at baseband that is far below the phase noise spectrum at RF. In a radar application, this time delay is the time it takes the signal to travel to the target and back, which is proportional to

the target range. Hence, this residual-phase-noise reducing effect is known as range correlation [170, 171]. Range correlation is particularly important when measuring the motion due to the heartbeat and respiration since the information is encoded in phase modulations of 0.1 to 10 Hz, where the phase noise is near its peak [172]. The radar transmits the signal:

$$T(t) = \cos(2\pi ft + \phi(t)) \quad (5.1)$$

where f is the oscillation frequency, t is the elapsed time, and $\phi(t)$ is the phase noise of the oscillator. Phase noise is described in more detail in Appendix H, but it can be considered here as a random fluctuation in the signal's phase. If the transmitted signal is reflected by a target at a nominal distance d_0 that has a time-varying displacement given by $x(t)$, the received signal is approximately:

$$R(t) \approx \cos\left[2\pi ft - \frac{4\pi d_0}{\lambda} - \frac{4\pi x(t)}{\lambda} + \phi\left(t - \frac{2d_0}{c}\right) + \theta_0\right], \quad (5.2)$$

where the wavelength is $\lambda = \frac{c}{f}$ and θ_0 is the constant phase shift due to reflection at the body surface. The received signal is similar to the transmitted signal with a time delay determined by the nominal distance to the target, d_0 , and with its phase modulated by the periodic motion of the target, $x(t)$. The information about the periodic target motion can be demodulated if this signal is multiplied by a local oscillator (LO) signal that is derived from the same source as the transmitted signal. Ignoring amplitude variations, the LO signal is expressed by:

$$L(t) = \cos(2\pi ft + \phi(t)). \quad (5.3)$$

The phase fluctuations of the LO due to oscillator phase noise are correlated to those of the received signal.

When the received and LO signals are mixed and the output is lowpass filtered the resulting baseband signal is:

$$B(t) = \cos\left[\theta + \frac{4\pi x(t)}{\lambda} + \Delta\phi(t)\right], \quad (5.4)$$

where

$$\Delta\phi(t) = \phi(t) - \phi\left(t - \frac{2d_0}{c}\right) \quad (5.5)$$

is the residual phase noise and

$$\theta = \frac{4\pi d_0}{\lambda} - \theta_0 \quad (5.6)$$

is the constant phase shift dependent on the nominal distance to the target, d_0 . As discussed in Chapters 2 and 7, this baseband signal can be demodulated and processed to be:

$$B(t) \approx \frac{4\pi x(t)}{\lambda} + \Delta\phi(t) \quad (5.7)$$

with a single-ended receiver, or

$$\theta(t) = \theta + \frac{\pi}{4} + \frac{4\pi x(t)}{\lambda} + \Delta\phi(t) \quad (5.8)$$

with a quadrature receiver and direct phase demodulation. In both cases, the desired signal that is proportional to the chest signal is summed with the residual phase noise.

5.2 Range Correlation Theory

Range correlation theory describes how to calculate the residual phase noise spectrum, and it was first proposed to explain why CW radar systems were not swamped by ground clutter noise [174]. Since the transmitted signal and the local oscillator (LO) are derived from the same source, and the received signal is a time-delayed version of the transmitted signal with a phase modulation, the phase noise on the received signal is correlated with that of the LO. When these two signals are mixed, the correlated portion of the phase noise effectively cancels, leaving only the residual phase noise at baseband. This is illustrated in Figure 5.1. The amount of correlation is determined by the time delay between the LO and the received signal: the greater the time delay, the less correlated the phase noise on the RF and LO signals, and the higher the baseband residual phase noise. Since this time delay is proportional to the target range, the target range determines the level of phase noise reduc-

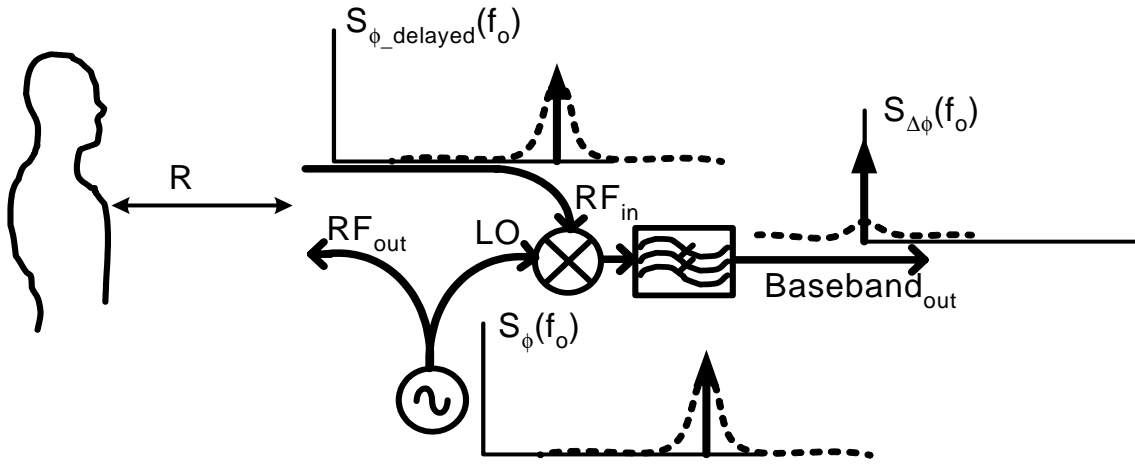


Figure 5.1. Illustration of the range correlation phase noise filtering effect. Since the transmitted signal is derived from the same source as the received signal, the phase noise on the LO, $S_{\phi}(f_o)$, and the RF input, $S_{\phi_delayed}(f_o)$, are correlated. When the two signals are mixed, most of the phase noise at baseband is effectively cancelled, leaving only the residual phase noise, $S_{\Delta\phi}(f_o)$.

tion provided by the range correlation effect. The dependence of the amount of correlation between the signals on range gave the range correlation effect its name [170].

According to [170], the baseband noise spectral density, $S_{\Delta\phi}(f_o)$, can be calculated from the RF phase noise spectral density, $S_{\phi}(f_o)$, and the target range, R :

$$S_{\Delta\phi}(f_o) = S_{\phi}(f_o) \left[4 \sin^2 \left(2\pi \frac{Rf_o}{c} \right) \right] \quad (5.9)$$

where f_o is offset frequency. At values relevant for radar monitoring of heart and respiration, Rf_o/c will be on the order of 10^{-9} , so the small angle approximation is valid, and range correlation will cause the baseband noise spectrum to increase proportionally to the square of the target range, R , and the square of the offset frequency, f_o :

$$S_{\Delta\phi}(f_o) \approx S_{\phi}(f_o) \left[16\pi^2 \frac{R^2 f_o^2}{c^2} \right]. \quad (5.10)$$

The relationship between the baseband residual phase noise, the RF phase noise, and the target range is illustrated in Figures 5.2 and 5.3. Figure 5.2 displays the relationship between residual phase noise and target range for four RF phase-noise values. The resid-

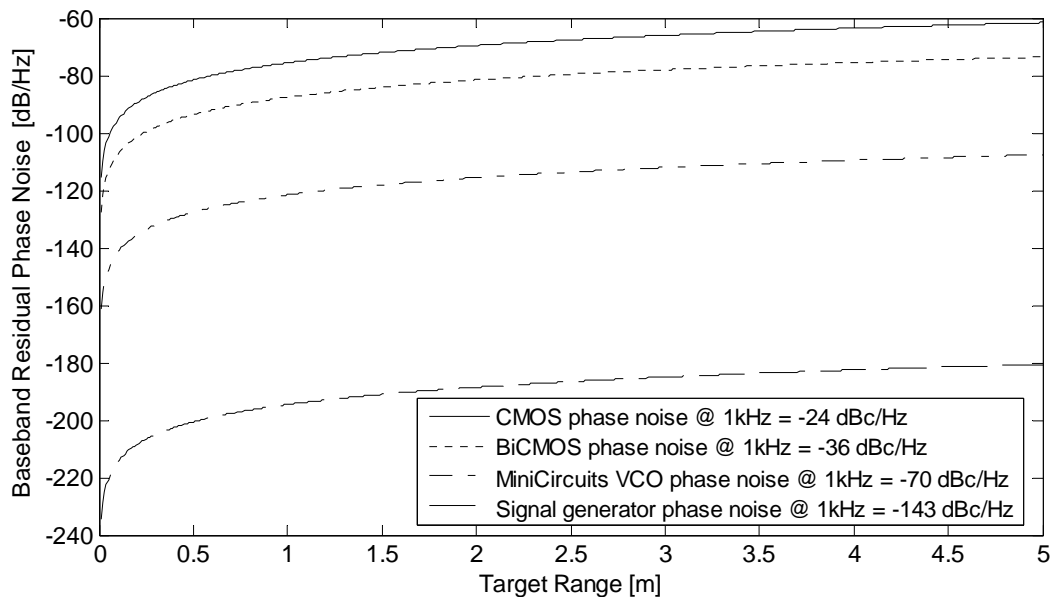


Figure 5.2. Relationship of residual phase noise to target range for a range of RF phase noise values. The values shown are those of the signal sources presented in this chapter, the fully integrated CMOS oscillator, the fully integrated BiCMOS oscillator, the MiniCircuits JTOS-1650 VCO used with the hybrid board, and the HP E433B signal oscillator, which was used as an external source with the CMOS radar chip.

ual phase noise increases with the square of the range. Therefore, when the range increases from 0.5 m to 2.0 m, the phase noise is expected to increase by 12 dB. Figure 5.3 illustrates the relationship between RF phase noise and target range while maintaining four constant residual phase-noise levels. To maintain a constant level of the residual phase noise when increasing the range (which would be necessary to maintain a minimum signal-to-noise ratio when residual phase noise is the dominant noise source), the oscillator phase noise must decrease. Therefore, the range requirements and noise level limits for a given application set the required oscillator phase noise specification, which determines the technology requirements.

The close-in RF phase noise spectrum of almost all oscillators has a -30 -dB/decade slope [172, 173]. Range correlation effectively multiplies the phase noise spectrum by that of a filter with a $+20$ -dB/decade slope (because the range correlation effect is proportional to the square of the offset frequency), so the resulting baseband noise spectrum is expected

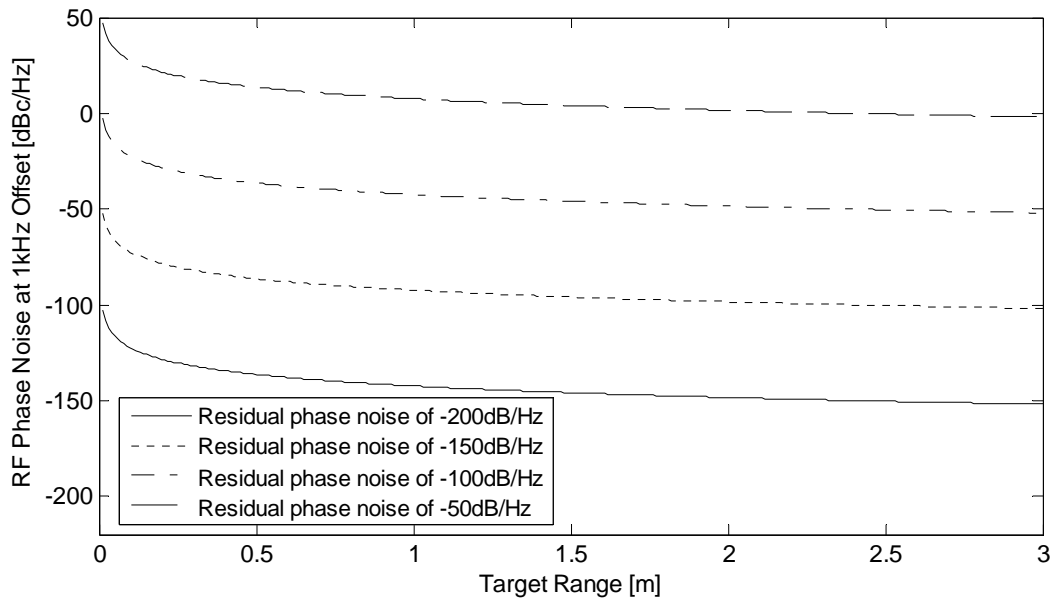


Figure 5.3. RF phase noise vs. range to maintain a constant level of residual phase noise. If a maximum level of residual phase noise and a desired range can be determined for an application, this chart can help determine the oscillator phase noise specification.

to have a -10 -dB/decade slope. For a 50-cm range and an offset frequency of 1 Hz, the residual phase noise is decreased by 154 dB.

In [175], Shrader and Gregers-Hansen recommend increasing the single sideband power spectral density of the phase noise value by 6 dB before applying the range correlation filtering effect. This accounts for a 3 dB increase because both sidebands of noise affect clutter residue and another 3 dB increase because the oscillator contributes noise during both transmitting and receiving. The first 3 dB factor would not be present if an intermediate frequency was used, as in a heterodyne receiver. Both of these factors of two are represented in (5.9).

Because there is no carrier at dc, residual phase noise needs to be expressed as a spectral density, in dB/Hz, rather than as a single-sideband phase noise in dBc/Hz. The dB/Hz units are the ratio of the spectrum in $\text{radians}^2/\text{Hz}$ to $1 \text{radian}^2/\text{Hz}$. As shown in Appendix H, when the phase deviation due to phase noise is small (with a quiet oscillator or at a high offset frequency), $S_\phi(f_0)$ is 3 dB greater than $L_\phi(f_0)$ since it includes both sidebands. When

the phase deviation is high, the phase noise is causing the signal frequency to vary over a bandwidth greater than 1 Hz, and the phase noise spectral density can be greater than 0 dB. For calculating the level of residual phase noise, the spectral density should be used.

Since the residual phase noise appears as additive noise on the baseband signal, as shown in (5.4), the phase noise reduction due to the range correlation effect is particularly important. If two different oscillators with uncorrelated phase noise were used for transmitting and receiving, it would be impossible to detect the small phase variations created by heart motion, unless the phase noise level was extremely low in both oscillators.

The relationship of the residual phase noise spectrum to the baseband noise level is discussed in detail in Appendix D, Section D.4.1. The RMS phase deviation is calculated as the integral of the residual phase noise over the bandwidth that is passed by the filters:

$$\Delta\phi_{RMS} = 4\sqrt{2}\pi\left(\frac{R}{c}\right)\sqrt{S_{\phi}(1)\ln\left(\frac{f_{max}}{f_{min}}\right)} \quad (5.11)$$

where R is the range to the target, c is the propagation velocity, $S_{\phi}(1)$ is the RF phase noise at a 1-Hz offset, and f_{max} is the highest frequency and f_{min} is the lowest frequency passed through the filters.

The noise power at baseband from residual phase noise can be calculated from the mean-squared phase deviation with the following equation:

$$N_{RPN,B} = \frac{2P_T G_{CL} G_{RX} G^2 \sigma_c \lambda^2 \overline{(\Delta\phi(t))^2}}{(4\pi)^3 R^4} \quad (5.12)$$

where P_T is the transmitted power, G_{CL} is the mixer conversion loss, G_{RX} is the receiver gain, G is the antenna gain, σ_c is the clutter radar cross section, and λ lambda is the wavelength.

Combining (5.11) and (5.12), the baseband noise is:

$$N_{RPN,B} = \frac{P_T \sigma_c G_{antenna}^2 G_{RX} G_{CL}}{\pi f^2 R^2} S_{\phi}(1) \ln\left(\frac{f_{max}}{f_{min}}\right). \quad (5.13)$$

Range correlation has a much less significant effect on amplitude noise. The range correlation effect on amplitude noise is described in [170] as follows:

$$S_{AA}(f_o) = S_A(f_o) \left[4 \cos^2 \left(\frac{2\pi R f_o}{c} \right) \right] + 2R_A(t_d) \delta(f_o) \quad (5.14)$$

where $S_A(f_o)$ is the spectrum of the amplitude noise and term in brackets accounts for the effects of range delay. R_A is the autocorrelation of the amplitude noise, and for gaussian white amplitude noise, $R_A(t_d)$ is much less than one, and the second term is negligible. Since, as described above, $R f_o / c$ is very small, the small angle approximation applies, and Equation 5.14 can be approximated as:

$$S_{AA}(f_o) \approx 4S_A(f_o) \quad (5.15)$$

For small $R f_o / c$, and Gaussian white amplitude noise, range correlation results in an amplitude gain of 6 dB [170].

5.3 Materials and Methods

5.3.1 Range Correlation Verification

When range correlation theory was proposed by Budge and Burt [170], it was not experimentally verified. An experiment was designed to verify the residual phase noise theory at offset frequencies and time delays relevant to Doppler monitoring of heartbeat and respiration. The expected effect of range correlation on baseband residual phase noise for different offset frequencies and time delays was estimated using (5.9) and phase noise data obtained from the quadrature CMOS chip. The range correlation theory was verified by measuring the baseband noise spectrum at the I/Q output with varying delay between transmitter and receiver, and comparing the measured results with the predicted values.

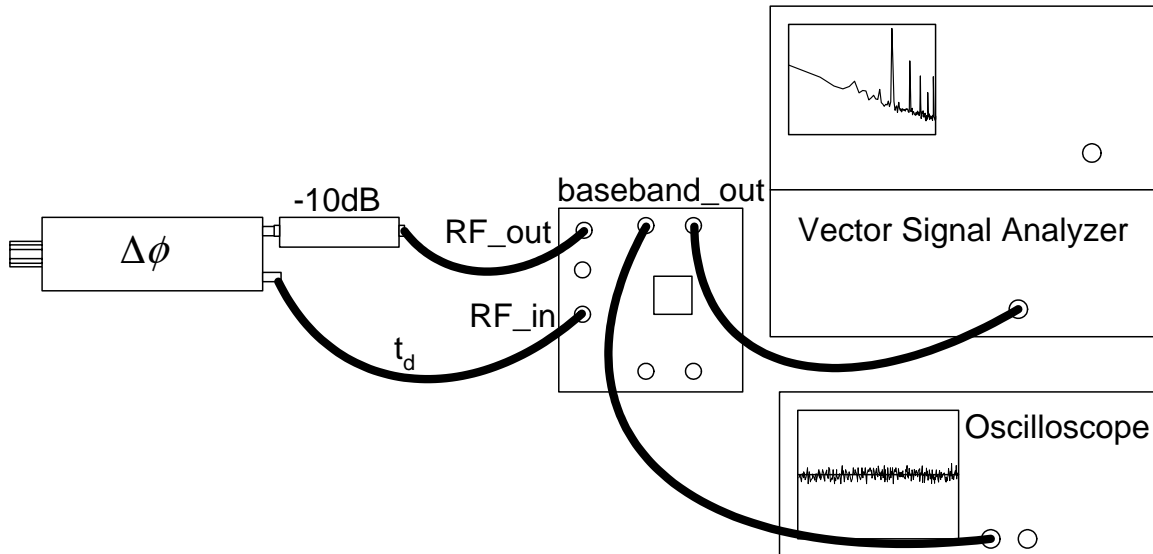


Figure 5.4: Setup for the range correlation verification experiment. The chip's RF output was connected to its RF input through a -10-dB attenuator, a phase shifter ($\Delta\phi$) and a cable (t_d). The baseband noise spectrum was measured with the VSA. Cables of various lengths were connected in place of the cable marked t_d to change the time delay between the RF and the LO signals. The baseband noise spectrum from 1 Hz to 1 kHz was measured with 1-Hz resolution bandwidth and RMS averaged over 5 measurements.

The setup of this experiment is shown in Figure 5.4. The RF output of the chip was connected to the phase shifter input through a 30-cm SMA cable and a 10 dB attenuator. The 10 dB attenuator was used to reduce VCO loading by the phase shifter. An SMA cable connected the phase shifter output to the RF input of the chip. The length of this cable, marked t_d in Figure 5.4, was varied to change the time delay between the RF and LO signals. The baseband output of the chip was measured with a HP89410A vector signal analyzer. To ensure consistent measurements, the RF and LO signals were kept in quadrature (θ in (5.6) is an odd multiple of $\pi/2$) so that the maximum phase to voltage sensitivity is maintained. To find this point, a Pasternack phase shifter (PE8442) was used to tune the phase relationship until the dc component of the baseband signal, as viewed on an oscilloscope, was zero. All unused RF connectors were terminated with $50\text{-}\Omega$ loads. The baseband noise spectrum from 1 Hz to 1 kHz was measured with a 1 Hz resolution bandwidth and RMS averaged over five measurements. The baseband noise spectrum measurements were converted to a phase noise equivalent by calculating the ratio of the

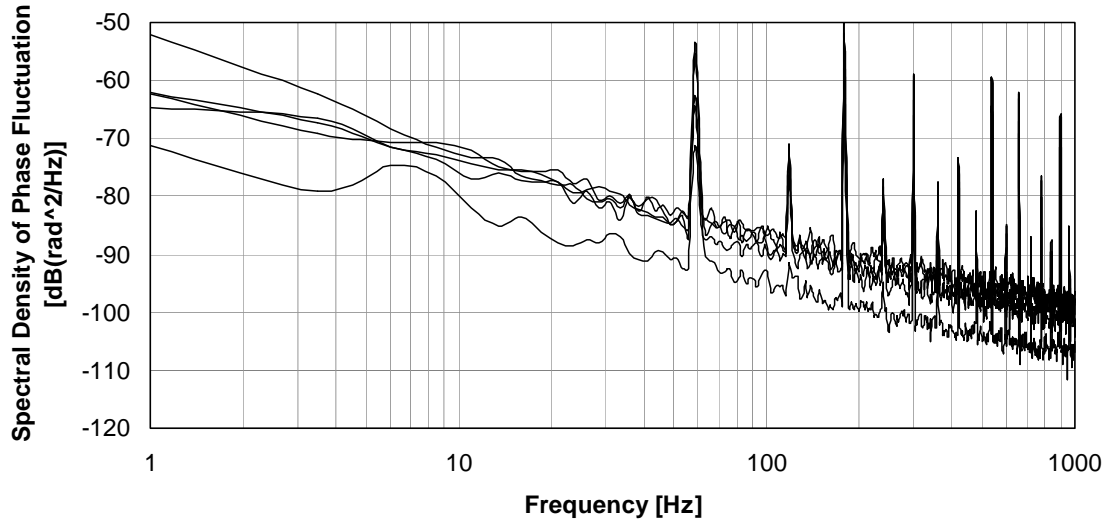


Figure 5.5: Baseband noise spectrum measured for various phase shifts with a 20.9-ns time delay. The time delay through the cables, attenuator, and phase shifter was measured with the HP8714C RF Network analyzer. When the two signals are near in-phase or out-of-phase, the dc voltage at the output is nonzero and the phase-demodulation sensitivity is greatly decreased.

measured noise power to the power a 30 kHz IF signal would have with the same RF and LO power. This was then converted to spectral density of phase fluctuation, $S_{\Delta\phi}(f_o)$, by multiplying by 2 [176]. The time delay and loss through the cables, attenuator, and phase shifter was measured with a HP 8714C RF Network Analyzer, and the loss was taken into account when calculating the equivalent IF power.

To show the importance of tuning the phase relationship so the RF and LO signals are in quadrature, the baseband noise plots are shown with the phase tuned to different positions in Figure 5.5. When the RF and LO signals are either in phase or 180° out of phase, the phase demodulation sensitivity is reduced, and the residual phase noise can appear much lower than it does when the signals are in quadrature. Figure 5.5 shows a 10 dB reduction in the measured residual phase noise due to this effect. In order to compare results for various time delays in range correlation measurements, it was important to ensure that all measurements were made at the optimum-phase-sensitivity demodulation point. It may seem that using this effect to decrease the residual phase noise would be beneficial. However, since the chest motion is encoded as a phase modulation, as the

phase-to-voltage sensitivity decreases, the baseband signal will decrease with the noise, and no benefit can be derived from this effect.

Figure 5.5 also shows that the measurement in the 1 Hz to 10 Hz decade was very noisy, because that with the 1-Hz resolution bandwidth there are only 10 points in that portion of the spectrum. The measurements selected for the range correlation verification were chosen based on a slope that was consistent with the rest of the data. The variation in the power spectral density of the traces with dc values near zero was within ± 3 dB, of the best-fit line for any individual measurement. The expected slope is -10 dB/decade, which is consistent with the measured slope.

5.3.2 Human Measurements with Different Signal Sources

To test the performance difference in the measurement of heart and respiration rates due to varying levels of residual phase noise, vital signs data were collected with the following three radar devices:

- 1) 1.9-GHz hybrid board with +20 dB/Hz phase noise spectral density at 1 Hz offset,
- 2) 1.6-GHz BiCMOS chip with +52 dB/Hz phase noise spectral density at 1 Hz offset,
- 3) 1.6-GHz CMOS chip with +64 dB/Hz phase noise spectral density at 1 Hz offset.

All measurements were made with similar output power, under 10 mW. The hybrid radar, described in detail in Chapter 4, uses a Minicircuits JTOS-1650 VCO as its signal source and individually packaged buffers and mixer. A HP E433B signal generator was also used as a source for some measurements to provide a very low level of source phase noise; the signal generator's phase noise was -53 dBc/Hz at a 1-Hz offset. To show the effects of varying residual phase noise on signal quality, signals obtained with chips with different levels of oscillator phase noise and with the target at a varying range were examined. The phase noise and predicted residual phase noise at 1- and 10-Hz offsets are shown for each measurement in Table 5.1.

Table 5.1: Summary of the Heart-Rate Detection Measurement Accuracy.

Figure	Chip	Fit Measured Phase Noise [dB/Hz]		Target range [cm]	Predicted Baseband Noise [dB/Hz]		Heart Measurement Accuracy [%]
		1 Hz	10 Hz		1 Hz	10 Hz	
5.11a	CMOS, SG as source	-53	-84	50	-207	-219	100
5.11b	Hybrid - SG as source	-53	-84	100	-201	-213	100
5.12a	Hybrid	+20	-11	50	-134	-156	100
5.12b	Hybrid	+20	-11	100	-128	-150	100
5.13a	BiCMOS	+52	+21	50	-102	-114	100
5.13b	CMOS	+64	+33	50	-90	-102	98
5.14	CMOS	+64	+33	85	-85	-97	63

Figure 5.6 shows the experimental setup used to make measurements with the hybrid board. A MiniCircuits power splitter, part ZFSC-2-2500, provided 17 dB of isolation between input and output signals. A commercially available Antenna Specialists ASPPM2988 1900 MHz patch antenna with 65° by 80° beam width was used. These measurements were performed on a single subject in an anechoic chamber at Lucent Technologies' Bell Laboratories in Murray Hill, NJ. The subject was seated fully clothed, facing the antenna, and breathing normally. A wired finger-pressure pulse sensor (UFI-1010 pulse transducer) was used during the measurements to provide a reference signal for heart activity. The baseband signals were filtered with a series of Stanford Research Systems SR560 Low-Noise Preamplifiers. The baseband signal was initially filtered with a 12-dB/decade highpass filter with a 0.03-Hz cutoff frequency and amplified 37 dB and then was filtered with a 6dB/decade bandpass filter that passed 0.03 Hz to 10 Hz, to remove the dc component and minimize out-of-band noise and aliasing error. The respiration signal was clearly visible after this filtering stage, but it could be better resolved with an additional low-pass filter to attenuate the heart signal. The heart signal was isolated using two consecutive 6-dB/decade 1-Hz to 3-Hz bandpass filters, and this

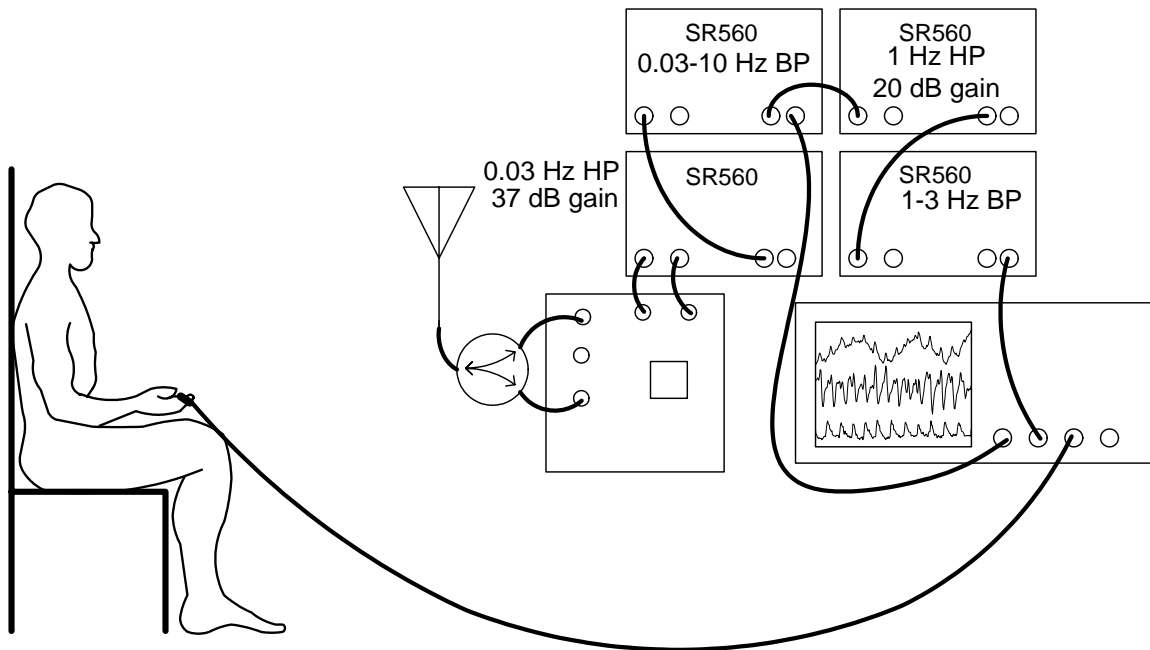


Figure 5.6: Heart and respiration activity measurement setup for the hybrid radar board. The baseband output signals were amplified and filtered with SR560 LNAs and then digitized with a Tektronix 3014 digital oscilloscope. A wired finger-pressure pulse sensor was used only as a reference to compare to the heart-rate data obtained with the Doppler radar.

signal was amplified an additional 20-dB. The first filtering stage provided most of the amplification, which was adjusted to produce the clearest output signal. The signal was then digitized at 25 samples per second with the digital oscilloscope.

The measurement setup for the measurements with 1.6-GHz chips was similar to that of the hybrid board, with the exception of the use of two custom 1.6-GHz patch antennas rather than a power splitter and a commercially available patch antenna, and slightly different analog filtering with the series of Stanford Research Systems SR560 Low-Noise Preamplifiers, as shown in Figure 5.7. The antennas are shown in Figure 5.8. Each antenna has a 50- Ω input impedance and a 86° by 177° beam width. The two antennas were placed 4 cm apart to obtain greater than 25 dB isolation between them. As with the hybrid board, the heart signal was separated with analog filters before it was digitized. The first stage of analog filtering blocks the dc offset with a 0.03 Hz 12-dB/decade highpass filter, avoids aliasing and removes out of band noise with a 10-Hz 12-dB/decade lowpass

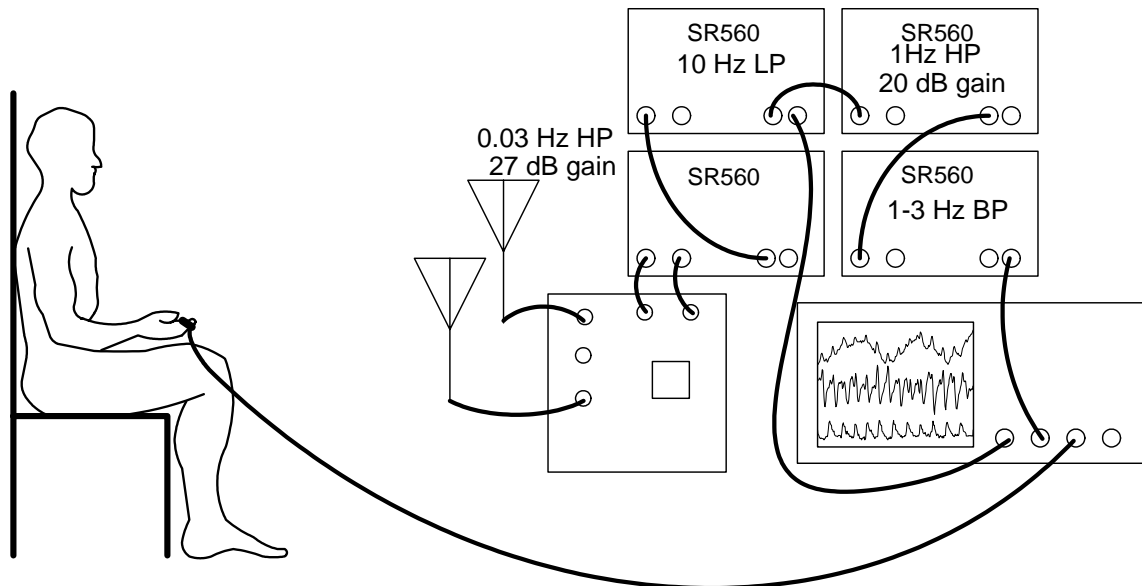


Figure 5.7: Heart and respiration activity measurement setup for the 1.6-GHz radar chips. The baseband output signals were amplified and filtered with SR560 LNA's and then digitized with a Tektronix 3014 digital oscilloscope. A wired finger-pressure pulse sensor was used only as a reference to compare with heart-rate data obtained with the Doppler radar.

filter, and amplifies the signal by 27 dB. The output from these analog filters includes both respiration and heart information. This signal is then passed through a 1 Hz, 12 dB/decade highpass analog filter followed by a 1-3 Hz, 6-dB/decade bandpass analog filter and amplified by 20 dB to isolate the heart movement from the respiration movement.

After digitization, the signals were processed with custom MATLAB signal processing software. The heart signal was filtered with a twelfth-order elliptic IIR bandpass filter, passing 0.9 to 9 Hz and blocking below 0.8 Hz and above 10 Hz, as shown in Figure 5.9, to separate the heart signal from any noise and any residual respiration information. Then the signal was windowed with a 4-second rectangular window, and an 8192-point power spectral density was taken. The heart rate was calculated as the greatest local maximum between 0.7 Hz and 2 Hz for each window. The rate for the reference was found with the same technique, but the reference was not filtered first. The signal accuracy was calculated as the percentage of windows for which the heart rate was within 1% of the reference rate, and the rate was calculated at each sample, every 0.04 seconds, over the 10-second measurement interval.

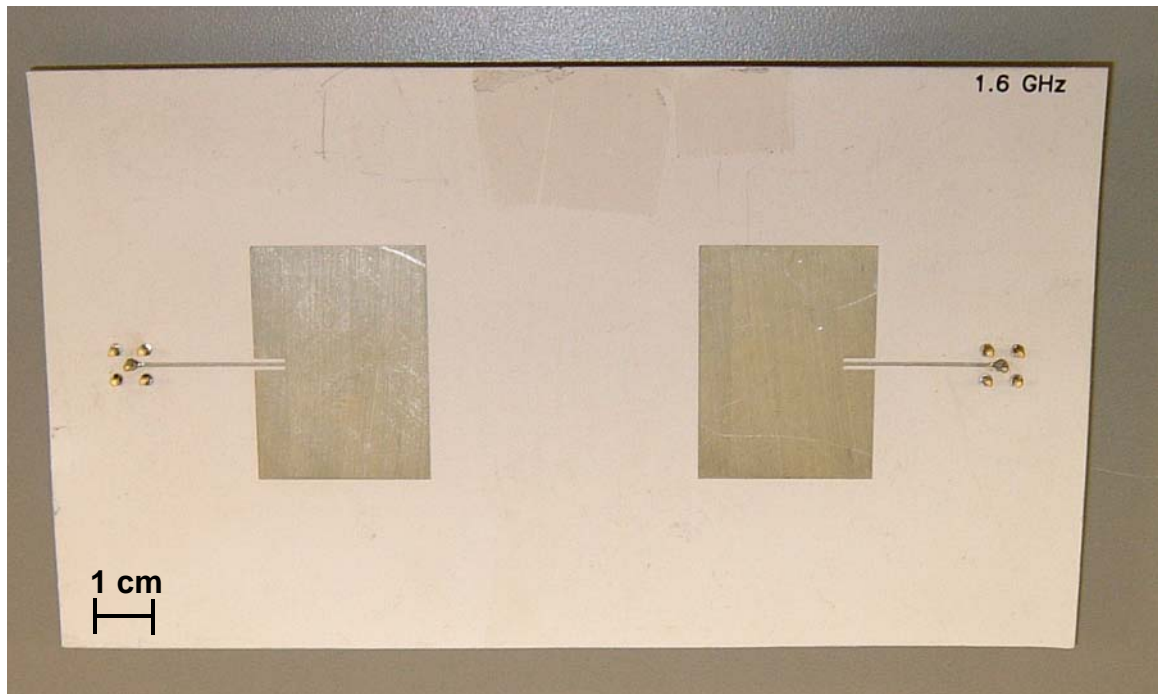


Figure 5.8: Transmitting and receiving patch antennas for 1.6 GHz chips. Each antenna was 2.936 cm by 4.000 cm. Two antennas were used rather than a single antenna and a circulator or power-splitter; the two antennas had 25 dB isolation between them. Each antenna had a 86° by 177° beamwidth and a 50 ohm impedance.

According to range correlation theory (5.9), to operate at a greater range, a lower phase noise source is needed to achieve the same residual phase noise. Otherwise, with the same source, as range increases, the amount of noise at baseband will also increase. For example, at 85 cm, the increase in distance 1.7 times will result in a 4.6 dB increase in residual phase noise. Therefore, a source with at least 4.6 dB lower phase noise would be required to achieve the same results, assuming that residual phase noise is still the limiting factor. If the same source is used, the increase in residual phase noise is expected to adversely affect the heart rate measurement detection accuracy. As range increases, there is an additional factor of free space loss and therefore a lower power received signal when the distance is increased, which will affect the output signal if residual phase noise is not the dominant noise source. The effect of changing target range was evaluated using the 1.6-GHz CMOS chip at an 85-cm range, as well as the hybrid board at a 100-cm range.

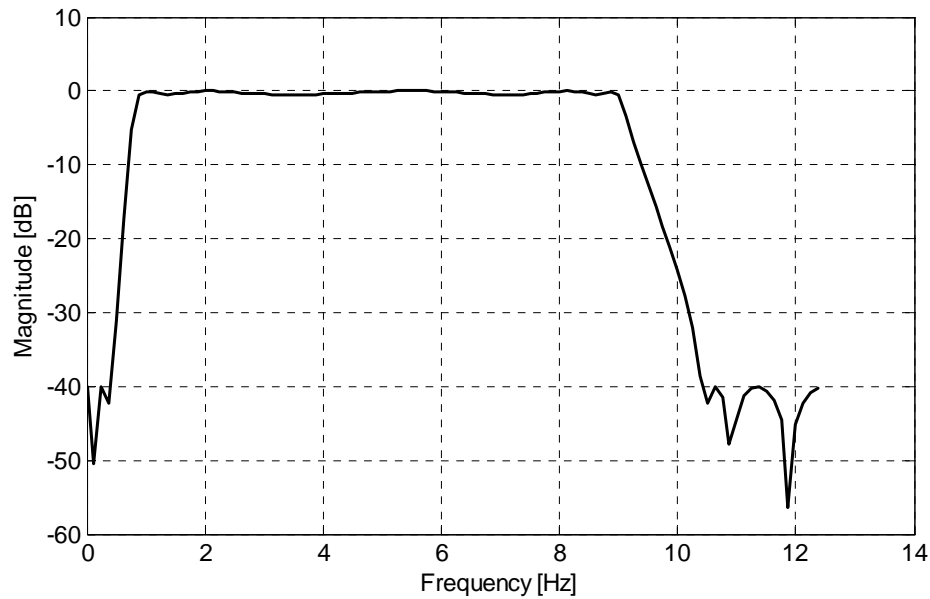


Figure 5.9: Frequency response of the twelfth-order elliptic IIR filter used to remove noise and residual respiration information. The fundamental frequency of respiration is usually below 0.4 Hz, while the heart rate is usually above 1 Hz. The cutoff frequencies are 0.9 Hz and 9 Hz.

5.4 Results

5.4.1 Range Correlation Verification - Results

The measured phase noise and the -30-dB/decade slope line used to predict the baseband noise are shown in Figure 5.10a for offset frequencies from 1 Hz to 1 kHz. The predicted and measured phase fluctuation spectral density are plotted in Figure 5.10b for delays of 6.2, 12.6, and 28.0 ns. On average, the measured values were within 5 dB of the predicted values. Departures from the theoretical noise level included spikes at 60-Hz and its harmonics. The signals matched within 3 dB between 1-Hz and 10-Hz, and above 100-Hz, the signals with 6.2-ns and 12.6-ns delays hit the noise floor of the VSA at that resolution bandwidth, so they could not be accurately measured. The signals had similar slope to the theoretical estimates between 10 Hz and 100 Hz, but were generally below the theoretical estimate in the region, other than the 60-Hz spur. The baseband phase noise

was reduced by 148 to 136 dB at 1 Hz for the time delays from 6.2 to 28.0 ns, which correspond to ranges from 0.93 to 4.2 m.

5.4.2 Human Measurement with Different Signal Sources - Results

The results of measurements with the four sources - signal generator, Minicircuits VCO, BiCMOS integrated VCO, and CMOS integrated CMOS - are shown in this section. The results are described in the text, shown for ten-second measurement intervals in the figures, and summarized in Table 5.1. The accuracy is described as the percentage of the rates calculations in the measurement interval that the Doppler heart rate was within 1% of the pulse sensor. The rate was calculated in 4 second windows every 0.04 second.

The measurements with the lowest residual phase noise are those made with the signal generator rather than the VCO operating as the source. A measurement using the external source on the 1.6-GHz CMOS chip at a 50-cm range is shown in Figure 5.11a. There is very little noise visible on the heart signal, and the calculated rate is within 1% of the reference rate for 100% of the 10-second measurement interval. The heart rate averages 84 beats per minute. A measurement made with the signal generator as the external oscillator on the hybrid board at a 100-cm range is shown in Figure 5.11b. As in Figure 5.11a, the signal is very clear, and the calculated heart rate is within 1% of the reference rate for all of the measurement intervals. The heart rate averages 86 beats per minute.

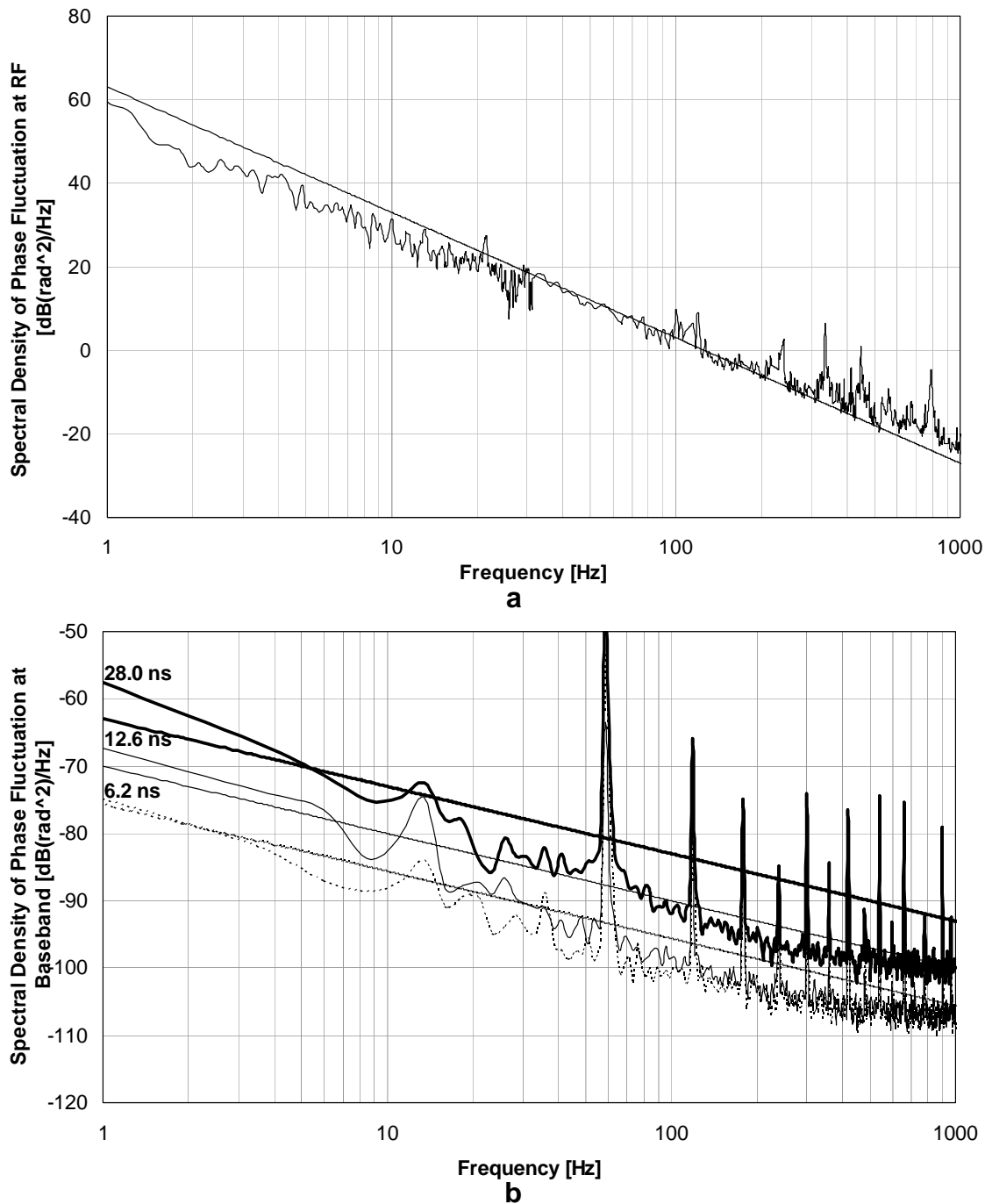


Figure 5.10: (a) Measured phase noise at RF and the -30-dB/decade line used to predict baseband noise. (b) Measured and predicted (5.9) spectral density of phase fluctuation at baseband for time delays of 28.0, 12.6, and 6.2 ns (from top to bottom).

The VCO on the hybrid board has 53 dB greater phase noise than the signal generator, but at a 50 cm range, the heart signal is still clear enough that the calculated rate matches the reference within 1% for all measurement intervals. This signal is shown in Figure 5.12a. The heart rate averages 83 beats per minute. Figure 5.12b shows a signal measured with the hybrid board at a 100 cm range. This signal, with 6 dB greater calculated residual phase noise, is visibly noisier than the signal measured at 50 cm. However, the noise level is still low enough that simple signal processing gives a heart rate within 1% of the reference for 100% of the measurement intervals. The heart rate averages 77 beats per minute.

Figure 5.13a shows data from the 1.6-GHz BiCMOS chip, which has -72 dBc/Hz phase noise at a 10 kHz offset, 12 dB lower than the CMOS chips. After digital filtering, the heart signal from the BiCMOS chip was within 1% of the reference for 100% of the measurement intervals. The heart rate averages 85 beats per minute. In Figure 5.13b the digitally filtered heart signal from the 1.6 GHz CMOS chip was within one beat per minute of the reference 98% of the time. These measurements were made near the optimum phase demodulation point. The heart rate averages 82 beats per minute. The signal from the CMOS chip is visibly noisier than that of the BiCMOS chip.

The effect of changing target range was evaluated using the 1.6-GHz CMOS chip at a range of 85 cm, and the data are shown in Figure 5.14. In this case, the heart rate accuracy dropped to 63% from the 98% accuracy measured at a 50 cm range. The heart rate averages 84 beats per minute.

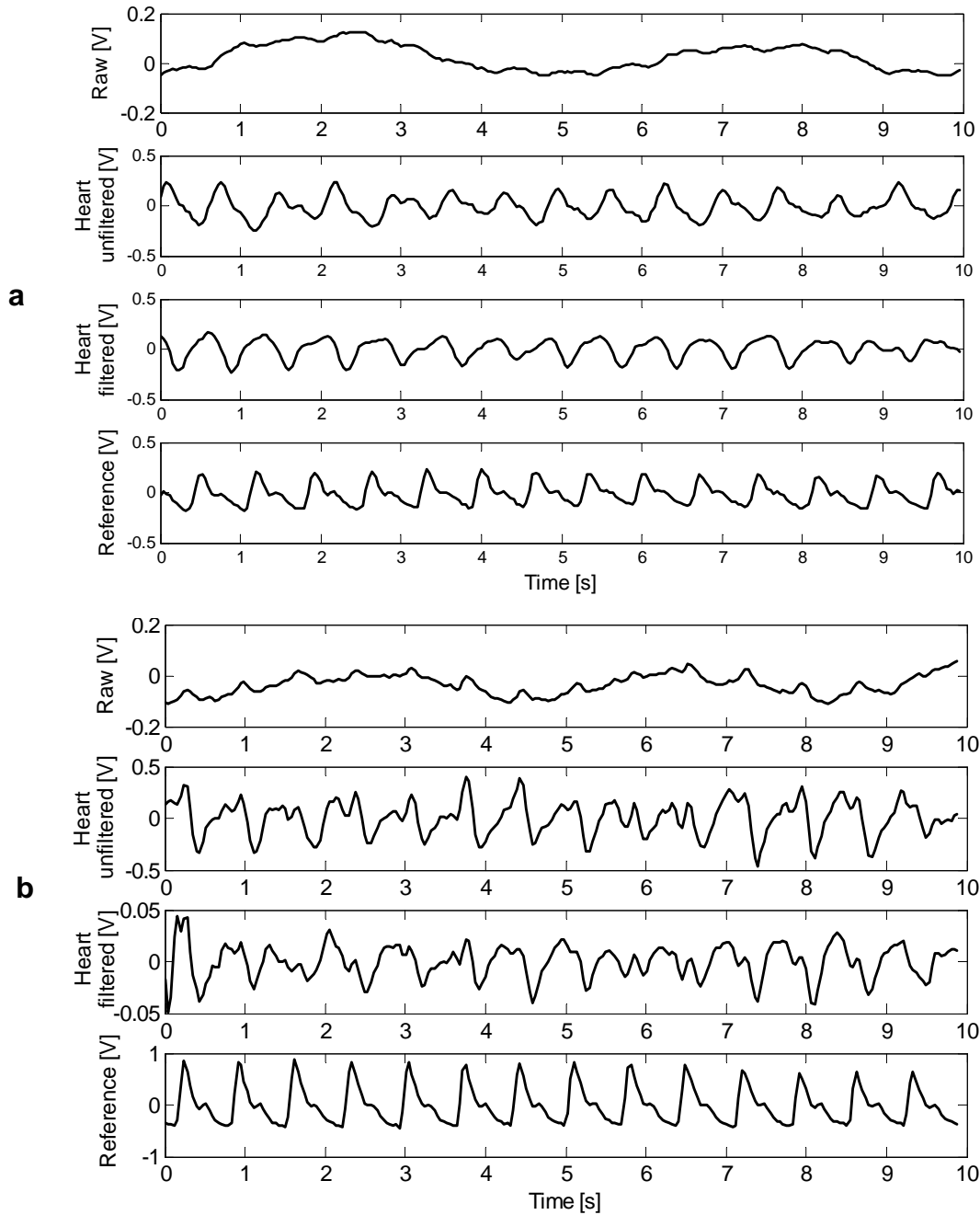


Figure 5.11: Heart and respiration activity measured with the signal generator as the source for a) the CMOS chip at a range of 50 cm and b) the hybrid board at a range of 100 cm. The top trace is the analog-filtered raw signal, and the second is the analog-filtered heart signal. The third trace is the heart signal after digital filtering. The bottom trace is the reference obtained from the finger-pressure pulse sensor described in the text. The filtered heart signal was within one beat per minute of the reference 100% of the measurement interval.

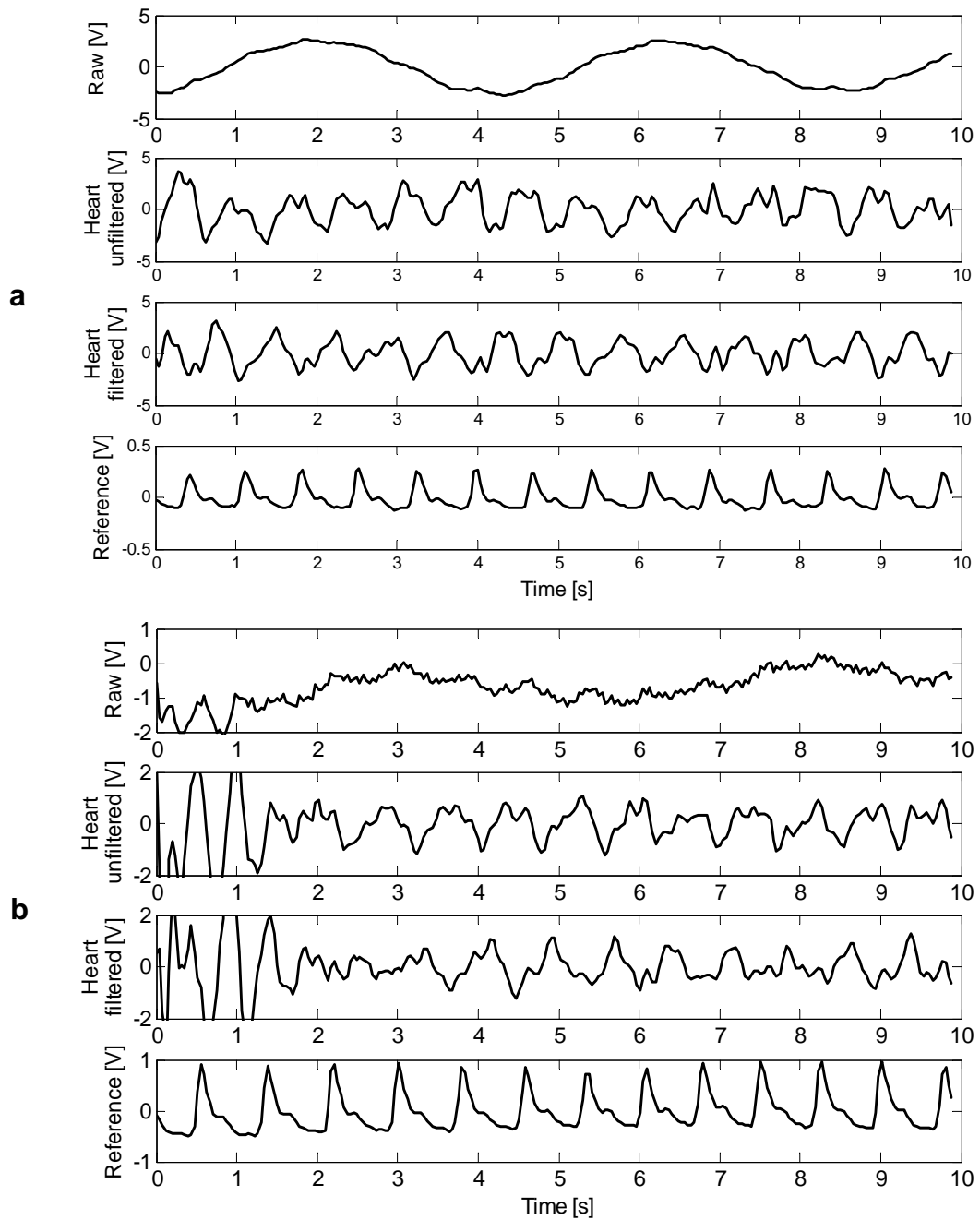


Figure 5.12: Heart and respiration activity measured with the hybrid board using the MiniCircuits VCO as the source a) at a range of 50 cm and b) at a range of 100 cm. The top trace is the analog-filtered raw signal, and the second is the analog-filtered heart signal. The third trace is the heart signal after digital filtering. The bottom trace is the reference obtained from the finger-pressure pulse sensor. The filtered heart signal was within one beat per minute of the reference 100% of the measurement interval.

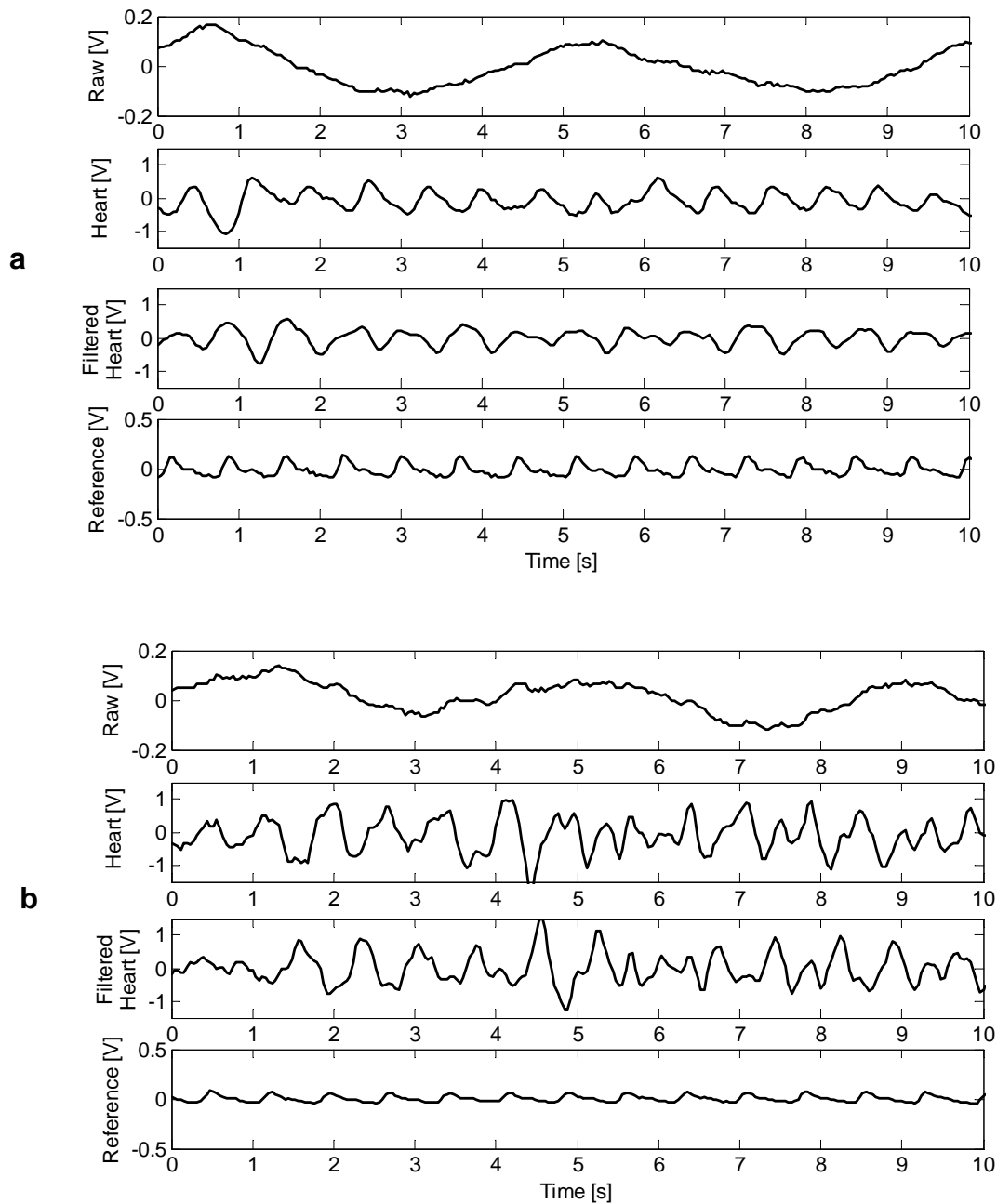


Figure 5.13: Heart and respiration activity measured at a range of 50 cm with a) the 1.6-GHz BiCMOS chip and b) the 1.6-GHz CMOS chip. The top trace is the analog-filtered raw signal, and the second is the analog-filtered heart signal. The third trace is the heart signal after digital filtering. The bottom trace is the reference obtained from the finger-pressure pulse sensor. The filtered heart signal was within one beat per minute of the reference 100% of the measurement interval.

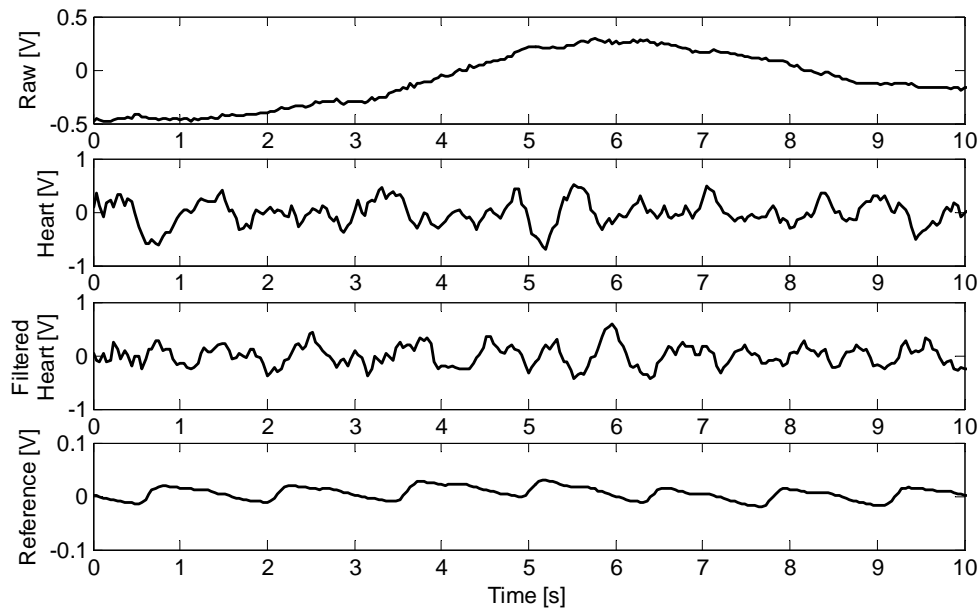


Figure 5.14: Heart and respiration activity measured with the 1.6-GHz CMOS chip at a range of 85 cm rather than 50 cm. The noise is significantly more pronounced than with a 50-cm range, and the accuracy is 63% for the digitally filtered heart signal.

5.5 Discussion

5.5.1 Range Correlation Verification - Discussion

The measured baseband noise spectral density was in the same range as that predicted based on the previously measured phase noise and range correlation theory. The measured baseband noise increased as the time delay increased and had approximately a -10 dB/decade slope, as was predicted. Some variation in the measurement may be due to the RF and LO signals not being exactly in quadrature and affecting the phase demodulation sensitivity (Figure 5.5). The signals were estimated to be in quadrature by the baseband signal having zero dc offset, so they should be near to quadrature. The phase noise was not measured at the same time as the baseband noise spectrum, and this may be another cause for some of the discrepancy between the predictions and measured results.

The amplitude noise of the oscillator, measured with the HP E5500 system, is shown in Figure 5.15, along with the predicted amplitude noise at baseband after range correla-

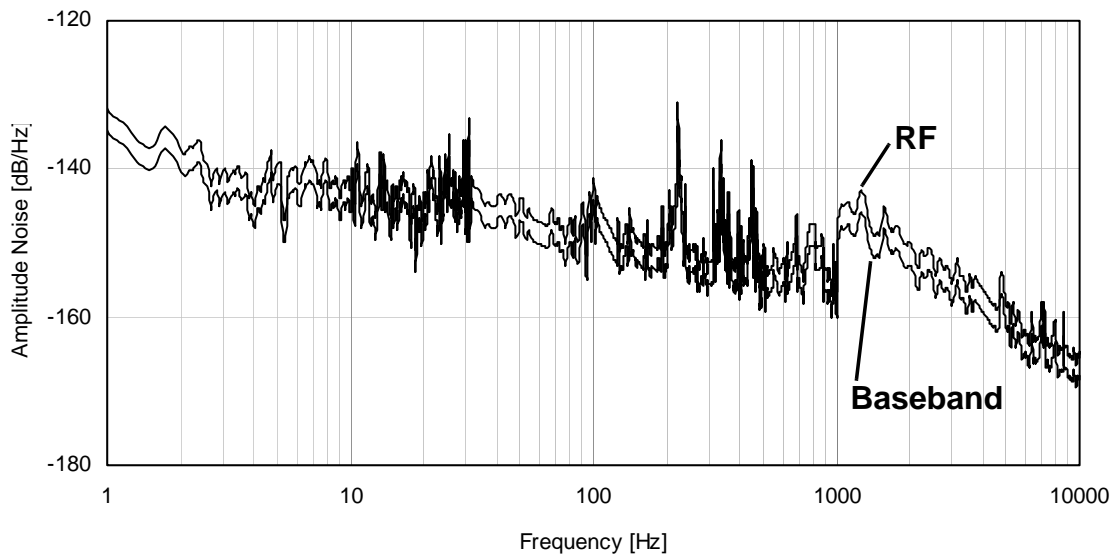


Figure 5.15: Measured oscillator amplitude noise (RF) shown with predicted baseband amplitude noise based on the range correlation effect. The amplitude noise is under -130 dB/Hz at all frequencies, and therefore below the residual phase noise for frequencies of interest.

tion [170]. Amplitude noise was under -130 dB/Hz, and therefore below the phase noise for frequencies under 10 kHz, even after range correlation. Since the amplitude noise is significantly lower than the phase noise for all frequencies of interest, it does not affect the accuracy of heart rate measurements.

5.5.2 Human Measurements with Different Signal Sources - Discussion

The 1.6-GHz BiCMOS chip has about 12-dB lower phase noise than the CMOS chips, and thus, using this chip, it is possible to obtain a clearer signal and to achieve a higher accuracy than with the CMOS chip. Using an external source with over 100-dB less phase noise than BiCMOS oscillator improved the signal quality, but since the CMOS chips could detect the heart rate with high accuracy, it is not necessary to use high quality oscillators for this application at a range of 50 cm. Applications requiring greater range may require low-phase noise oscillators.

The residual phase noise first became visible when the calculated residual phase noise at 1 Hz was -128 dB/Hz, with the hybrid board at a range of 100 cm. The residual phase noise began to adversely affect signal accuracy when the calculated residual phase noise at 1 Hz was -102 dBc/Hz, with the CMOS chip at a range of 50 cm. When the 1 Hz residual phase noise values are greater than this, the detection of heart signals is adversely affected. As discussed in Chapter 2 and Appendix D, when the residual phase noise levels are low, the limiting factor is not residual phase noise, but rather baseband $1/f$ noise as the signal level is decreased with free-space loss.

The difference in the heart rate accuracy obtained with different levels of oscillator phase noise and with different target range suggests that residual phase noise is a limiting factor in this measurement system when a free-running on-chip VCO is used. Because the phase noise is such a critical factor, the range correlation theory is important to consider in system engineering of a Doppler radar for vital signs measurement. It highlights the advantages of minimizing oscillator phase noise and of minimizing time delays. Keeping the antenna electrically close to the transceiver and keeping the target as close to the antenna as possible can reduce time delays, improving system performance. When building a prototype monitoring device, time delays should be minimized.

The variation of the SNR of the heart signal with range with a CMOS oscillator is explored in more detail in Chapter 6. Residual phase noise is the limiting factor and the SNR is calculated over 90-second measurement intervals averaged over 22 different subjects, and measured at ranges from 0.5 to 2.0 m.

5.6 Conclusions

Residual phase noise can be a limiting factor in single-chip Doppler radar. The residual phase noise depends on both target range and oscillator phase noise. Free-running CMOS oscillators with -60 dBc/Hz phase noise at a 10-kHz offset were found to be adequate for heart rate detection at distances up to 50 cm; in the measurement shown in this chapter, the heart rate measured with the Doppler radar matched that of the reference 98%

of the measurement interval. Measurements made with a fully-integrated CMOS oscillator with approximately the same level of phase noise are shown in Chapter 6. Experimental verification of the range-correlation effect, which determines the level of residual phase noise, was presented, and the measured baseband noise spectrum agreed with theoretical values with an average of 5 dB.

5.7 References

- [170] M. C. Budge, Jr. and M. P. Burt, "Range correlation effects on phase and amplitude noise," in *Proceedings of the IEEE Southeastcon*, Charlotte, NC, 1993.
- [171] M. C. Budge, Jr. and M. P. Burt, "Range correlation effects in radars," in *Proceedings of the IEEE Radar Conference*, 1993.
- [172] T. H. Lee and A. Hajimiri, "Oscillator phase noise: A tutorial," *IEEE Journal of Solid State Circuits*, vol. 35, no. 3, pp. 326-336, 2000.
- [173] D. B. Leeson, "A simple model of feedback oscillator noise spectrum," *Proceedings of the IEEE*, vol. 54, pp. 329-220, 1966.
- [174] R. S. Raven, "Requirements on master oscillators for coherent radar," *Proceedings of the IEEE*, vol. 54, no. 2, pp. 237-243, 1966.
- [175] W. W. Shrader and V. Gregers-Hansen, "MTI radar" in Radar Handbook, 2nd ed. (M. I. Skolnik, Ed.), San Francisco: McGraw-Hill, Inc., 1990.
- [176] G. D. Vendelin, A. M. Pavio, U. L. Rohde, E. L. Rohde, Microwave Circuit Design Using Linear and Nonlinear Techniques, New York: Wiley, 1990.

Chapter
6

Human Testing Results

6.1 Introduction

Doppler radar measurements of heart and respiration rates were compared with three-lead ECG measurements of heart rate and respiratory effort belt measurements of respiration rate on 22 healthy subjects wearing T-shirts. This work was performed under Stanford protocol number 2899, approved by the Stanford University Internal Review Board in August 2005. A CMOS single-chip Doppler radar with a free-running oscillator and a quadrature receiver was used with custom baseband signal conditioning hardware and custom Matlab signal processing software to measure heart and respiration rates from a distance of 0.5 to 2.0 m. Signals from the three-lead ECG and the respiratory effort belts were digitized simultaneously with the Doppler radar output signals and used to find heart and respiration rates which were compared with the rates from the Doppler system using the Matlab software.

The primary objective of this study was to determine whether the Doppler radar heart and respiration rate monitor can detect heart and respiration rates of non-stressed subjects with sufficient accuracy to replace traditional contact measurements in a well-controlled environment. Secondary objectives included obtaining data at varying distances to verify the theoretical estimate of signal-to-noise ratio vs. range and determining how the subject's body shape affects the accuracy and signal-to-noise ratio of the measurements.

Section 6.2 offers some system background and theory and shows how the theoretical signal-to-noise ratio varies with range and radar cross section. Section 6.3 discusses the single-chip Doppler radar, the baseband signal conditioning, and the digital signal processing used for this experiment. It also provides the details of the experimental setup and

protocol and the data analysis methods. Section 6.5 presents the results of the system over all subjects for each range, the signal-to-noise vs. range, and the signal-to-noise vs. body type. These results are discussed in the Section 6.6 and Section 6.7.

6.2 Background and Theory

6.2.1 Doppler Radar Monitoring of Heart and Respiration

The system theory for Doppler radar monitoring of heart and respiration is provided in detail in Chapter 2. In this system, the same oscillator is used to provide the local oscillator and the transmitted signal. A portion of the transmitted signal is reflected by the subject back towards the radar receiver with its phase modulated by physiological motion. The received signal with physiological motion data is:

$$R(t) \approx A_{RF} \cos \left[2\pi ft - \frac{4\pi d_0}{\lambda} - \frac{4\pi x(t)}{\lambda} + \phi \left(t - \frac{2d_0}{c} \right) + \theta_0 \right], \quad (6.1)$$

where A_{RF} is the amplitude, f is the carrier frequency, t is time, d_0 is the nominal range to the target, λ is the wavelength, $x(t)$ is the physiological motion, $\phi \left(t - \frac{2d_0}{c} \right)$ is the phase noise of the received signal, and θ_0 is a constant phase shift.

A higher power signal is reflected by stationary objects and parts of the body, known as clutter. The received signal from clutter is:

$$R_c(t) \approx A_c \cos \left[2\pi ft - \frac{4\pi d_0}{\lambda} + \phi \left(t - \frac{2d_0}{c} \right) + \theta_0 \right], \quad (6.2)$$

where A_c is the amplitude of the received signal with clutter.

The signal is demodulated by mixing with the LO. The signal at baseband is:

$$B(t) = A_b \cos \left[\frac{4\pi d_0}{\lambda} + \frac{4\pi x(t)}{\lambda} + \Delta\phi(t) - \theta_0 \right], \quad (6.3)$$

where A_b is the amplitude of the baseband signal and $\Delta\phi(t)$ is the residual phase noise, the phase noise that remains after mixing with a LO from the same source.

6.2.2 Received Signal Power and Radar Cross Section

The radar equation is used to estimate the received signal power in a radar system; this can help determine the system's theoretical limits. The estimated received power is based on the transmitted power, the range to the target, and the properties of the transmit antenna, target, receive antenna, and receiver. When measuring motion due to heart and respiration with a Doppler radar transceiver, the residual phase noise will be the limiting factor in some cases; otherwise the limiting factor will usually be receiver sensitivity and the received signal power. When the same antenna is used for transmitting and receiving, the gain is the same for both antennas, and the radar equation is:

$$P_R = \frac{P_T G^2 \sigma \lambda^2 e^{-2\alpha R}}{(4\pi)^3 R^4}, \quad (6.4)$$

as derived in Appendix D, where P_R is the received power, P_T is the transmitted power, σ is the radar cross section, G is the antenna gain, λ is the wavelength of the transmitted signal, R is the range to the target and α is the atmospheric absorption coefficient.

For the ranges used in this method comparison study, the atmospheric attenuation term has a negligible effect and can be dropped, so that the received power is:

$$P_R = \frac{P_T G^2 \sigma \lambda^2}{(4\pi)^3 R^4}. \quad (6.5)$$

To determine the signal power at baseband, the RF signal power, the mixer conversion loss or gain, the receiver gain, and the amount of phase modulation must all be considered. As calculated with the phase-modulation link equation in Appendix D, the signal at baseband is:

$$S_B = \frac{2P_T G^2 G_{CL} G_{RX} \sigma \overline{x^2(t)}}{4\pi R^4}, \quad (6.6)$$

where G_{CL} is the conversion loss of the mixer, G_{RX} is the receiver gain, and $\overline{x^2(t)}$ is the mean squared motion due to either heart and /or respiration.

For radar monitoring of heart and respiration rate, the radar cross section and the mean squared motion are the only values in the baseband signal power expression (6.6) that are not clearly defined. These values are expected to vary greatly from person to person. However, to estimate the baseband signal power, it is necessary to obtain a rough estimate of the product of the radar cross section and the mean-squared physiological motion. Since there is not a defined area of the target that moves a specific amount, it is not straightforward to calculate these values separately; the desired value is actually the integral of the mean-squared motion over the area of the body, multiplied by factors for the body reflectivity, the directivity of the reflected signal, and the amount of motion that is in the direction of the antenna.

The reflectivity is the amount of the intercepted power that is reflected rather than absorbed. Approximately 51% of the incident signal is reflected at the air-skin interface, as is calculated in Appendix D.

The directivity is the ratio of the scattered power back towards the antenna to the power that would have back-scattered had the target been an isotropic radiator. This is difficult to calculate for this physiological motion measurement, as it will vary with individual physiology and shape, as well as orientation with respect to the antenna.

As described in Appendix D, estimates of the radar cross section of a large man are between 0.2 to 0.9 m². A literature survey did not locate values for the radar cross section of the fraction of the area moving due to heart and respiration. It is expected that the area moving due to respiration is about 1% of the total area, and that the area moving due to heart is about 20% of the area moving due to respiration.

As discussed in detail in Chapter 3, the estimated RMS motion at the location of and in the direction of maximum motion is 0.3 mm for the pulsations of the heart and 2 mm for the chest motion due to respiration. The maximal motion occurs over a very small area on the body surface, with a lesser motion occurring over a larger area of the body. Additionally, this motion is generally not exactly in the direction of the antenna, and the antenna is likely not positioned such that the reflected signal's highest power is back toward the

antenna. If the areas that are moving are 1 cm^2 associated with the heart and 50 cm^2 for respiration, the product of the area moving at the maximum RMS motion and the mean-squared motion is 0.009 cm^4 for the heart and 2.0 cm^4 for the respiration. The RMS motion and RCS product can be assumed to be the values presented above, multiplied by a factor of 0.05 for the directivity, and a factor of 0.5 for the reflectance of the body. This leaves an estimated RCS-RMS motion product of about 2.25 mm^4 for the heart and 500 mm^4 for the respiration. These estimates are used in the estimates of the SNR. In Section 6.5.6, values of the RCS-RMS motion product will be back-calculated from the measured SNR data.

The stationary part of the body and the surrounding environment are considered when estimating the radar cross section of the clutter. This radar cross section is more straightforward to calculate since it is not restricted to an area of motion and therefore does not depend on the physiology of the subject. A clutter radar cross section estimate of 0.5 m^2 will be used in these calculations.

6.2.3 Noise Sources

After the signal has been demodulated to baseband, there are three main sources of noise: residual phase noise from the oscillator, downconverted RF additive white gaussian noise (AWGN) from the front end of the receiver, and baseband $1/f$ noise from the mixer and baseband circuits. To combine these, the signal power at baseband must be determined, as well as the noise power due to each of these sources. The SNR calculations are made at the output of the mixer, where the signal has been converted from a phase-modulated signal at RF to a baseband amplitude signal. Because the noise sources are uncorrelated, when they have been converted to their baseband values, their powers are additive. In this section, each of these noise sources will be converted to their baseband values so they can be combined and used to calculate the system signal-to-noise ratio.

6.2.3.1 Residual Phase Noise and Range Correlation

The baseband noise spectral density, $S_{\Delta\phi}(f_o)$, can be calculated from the RF phase noise spectral density, $S_{\phi}(f_o)$, with the target at a given range, R , and offset frequency, f_o :

$$S_{\Delta\phi}(f_o) = 2S_{\phi}(f_o) \left[4 \sin^2 \left(2\pi \frac{Rf_o}{c} \right) \right], \quad (6.7)$$

where c is the propagation velocity of the signal [182]. At values relevant for radar monitoring of heart and respiration, Rf_o/c will be on the order of 10^{-9} , so the small angle approximation is valid. This approximation shows that range correlation causes the baseband noise spectrum to increase proportionally to the square of the target range, R , and the square of the offset frequency, f_o . Additionally, delays between the oscillator and the antenna and between the antenna and the receiver, combined as t_d , must be included in the range correlation equation when the delay is on the order of the range, as it is in radar monitoring of heart and respiration. With the small angle approximation and delay included, the phase noise spectral density can be calculated as:

$$S_{\Delta\phi}(f_o) \approx 2S_{\phi}(f_o) \left[16\pi^2 \frac{\left(R + \frac{ct_d}{2} \right)^2 f_o^2}{c^2} \right]. \quad (6.8)$$

In Appendix D, the noise at baseband due to residual phase noise is derived using the phase modulation link equation, and assuming the RF phase noise has a -30dB/decade slope at the offset frequencies of interest. The baseband noise power from residual phase noise is:

$$N_{RPN, B} = \frac{P_T G^2 G_{RX} G_{CL} \sigma_c}{\pi f^2} S_{\phi}(1) \ln \left(\frac{f_{max}}{f_{min}} \right) \frac{\left(R + \frac{ct_d}{2} \right)}{R^4}, \quad (6.9)$$

where f is the RF signal frequency, f_{max} and f_{min} are the maximum and minimum frequencies of the baseband bandpass filter, σ_c is the radar cross section of the clutter, and $S_{\phi}(1)$ is the 1-Hz intercept of the phase noise spectrum.

6.2.3.2 Baseband 1/f Noise

In this application, 1/f noise at the mixer output and in baseband signal-conditioning circuits dominates the baseband noise spectrum. Choosing a mixer that minimizes 1/f noise, such as a passive mixer, and minimizing the input-referred 1/f noise added by the baseband filtering and amplifying stages will minimize the amount of baseband noise. When 1/f noise dominates, the baseband receiver noise can be approximated as:

$$N_{\frac{1}{f}, B} = \int_{f_{min}}^{f_{max}} P_{1/f}(1) f^{-1} df = P_{1/f}(1) \ln\left(\frac{f_{max}}{f_{min}}\right), \quad (6.10)$$

where $P_{1/f}(1)$ is the noise power in a 1-Hz bandwidth centered at 1 Hz.

6.2.3.3 RF Additive White Gaussian Noise

The dominant RF noise at the input to the receiver is thermal noise, which is zero-mean, has a gaussian distribution, and does not vary with frequency, e.g. white noise. This is additive to the RF signal. The thermal noise power at RF is expressed by:

$$P_{N, thermal} = 4kTB, \quad (6.11)$$

where k is Boltzman's constant, T is the absolute temperature, and B is the bandwidth.

In Appendix D, the RF noise after conversion to baseband is calculated to be:

$$N_{RF, B} = 8G_{CL}G_{RX}(NF)(kTB), \quad (6.12)$$

where G_{CL} and G_{RX} are the mixer conversion gain and the receiver gain, and NF is the noise figure of the receiver.

6.2.4 Variation of Signal-to-Noise Ratio with Range and Radar Cross Section

Because the baseband 1/f noise, RF additive white noise, and residual phase noise are uncorrelated, the noise powers simply add when combined. Therefore, the signal-to-noise ratio for the system is:

$$\frac{S_B}{N_B} = \frac{S_0}{N_{1/f, B} + N_{RF, B} + N_{RPN, B}}. \quad (6.13)$$

This can be expanded to:

$$\left(\frac{S_B}{N_B}\right) = \quad (6.14)$$

$$\frac{\frac{P_T G^2 G_{RX} G_{CL} \sigma_c}{2\pi R^4} \overline{x^2(t)}}{P_{\frac{1}{f}}(1) \ln\left(\frac{f_{max}}{f_{min}}\right) + 8G_{RX} G_{CL} (NF)(kTB) + \frac{P_T G^2 G_{RX} G_{CL} \sigma_c}{\pi f^2} S_\phi(1) \ln\left(\frac{f_{max}}{f_{min}}\right) \left(\frac{\left(R + \frac{ct_d}{2}\right)^2}{R^4}\right)}$$

This is equivalent to:

$$\left(\frac{S_B}{N_B}\right) = \frac{\frac{P_T G^2 G_{RX} G_{CL} \sigma_c}{2\pi R^4} \overline{x^2(t)}}{2\pi \left(N_{\frac{1}{f}, B} + N_{RF, B}\right) R^4 + 2 \left(\frac{P_T G^2 G_{RX} G_{CL} \sigma_c}{\pi f^2} S_\phi(1) \ln\left(\frac{f_{max}}{f_{min}}\right)\right) \left(R + \frac{ct_d}{2}\right)^2} \quad (6.15)$$

When residual phase noise is dominant, the signal-to-noise ratio will be inversely proportional to $\left(R + 0.5ct_d\right)^2$, and when either the baseband noise or the RF additive white gaussian noise is dominant, the signal-to-noise ratio will be inversely proportional to R^4 . If one noise source is not dominant for all ranges, the residual phase noise will be dominant close to the target, and the baseband or RF noise will be dominant further from the target.

The signal-to-noise ratio is plotted in Figure 6.1 for a transmit power of 0 dBm, an antenna gain of 6 dBi, a receiver gain of 6 dB, a conversion gain of -3 dB, a radar cross section-mean-squared motion product of 2.25 mm^4 for the heart and 500 mm^4 for respira-

tion, a $1/f$ noise power of -130 dBm/Hz at 1 Hz referred to the mixer output, a bandwidth from 0.6 to 10 Hz for the heart, and 0.01 to 10 Hz for respiration, a receiver noise figure of 6 dB, a RF noise temperature of 300 K, a 5 -ns delay, and a phase noise of 64 dB/Hz at the 1 -Hz intercept. This plot indicates that with calculated values of RF noise and measured values of phase noise and baseband noise, the baseband noise dominates over the RF noise, but the residual phase noise dominates over both with the CMOS transceiver.

When looking at the results of the human subjects study, it is possible to confirm that the residual phase noise is the dominant noise source because it is inversely proportional to $(R + 0.5ct_d)^2$, where R is the range to the target, c is the signal's propagation velocity in air, and t_d is the time delay between the chip and the antenna. If baseband noise or RF noise were dominant, the SNR would fall off with R^4 .

The theoretical SNR equation also indicates that the signal-to-noise ratio should be linear with the radar cross section of the target, and that the changes in the radar cross section of the target should not affect the dominant type of noise, as shown in Figure 6.2. (Changes in the radar cross section of the clutter could change the dominant noise type, however.) The radar cross section for both heart and respiration motion is expected to vary from subject to subject, and likely also with orientation with respect to the antenna.

These SNR calculations assume the signal is at the optimal phase demodulation point. This gives the best-case signal-to-noise calculation for a single-channel receiver. For the quadrature receiver, if the signal is determined by choosing between the I and Q signals, the signal power and the residual phase noise power would be cut in half. This does not affect the signal-to-noise ratio if residual phase noise is dominant, but does affect the SNR if either RF amplitude noise or mixer baseband $1/f$ noise is the dominant noise source. If the I and Q signals are combined, the baseband noise from the filtering and amplifying stages is added before the combination takes place. If baseband noise is not the dominant noise source, then after the I and Q signals are combined the signal-to-noise ratio would be similar to that of the single-channel receiver at the optimal phase demodulation point. If the baseband noise is dominant, the SNR would be decreased by a factor of two.

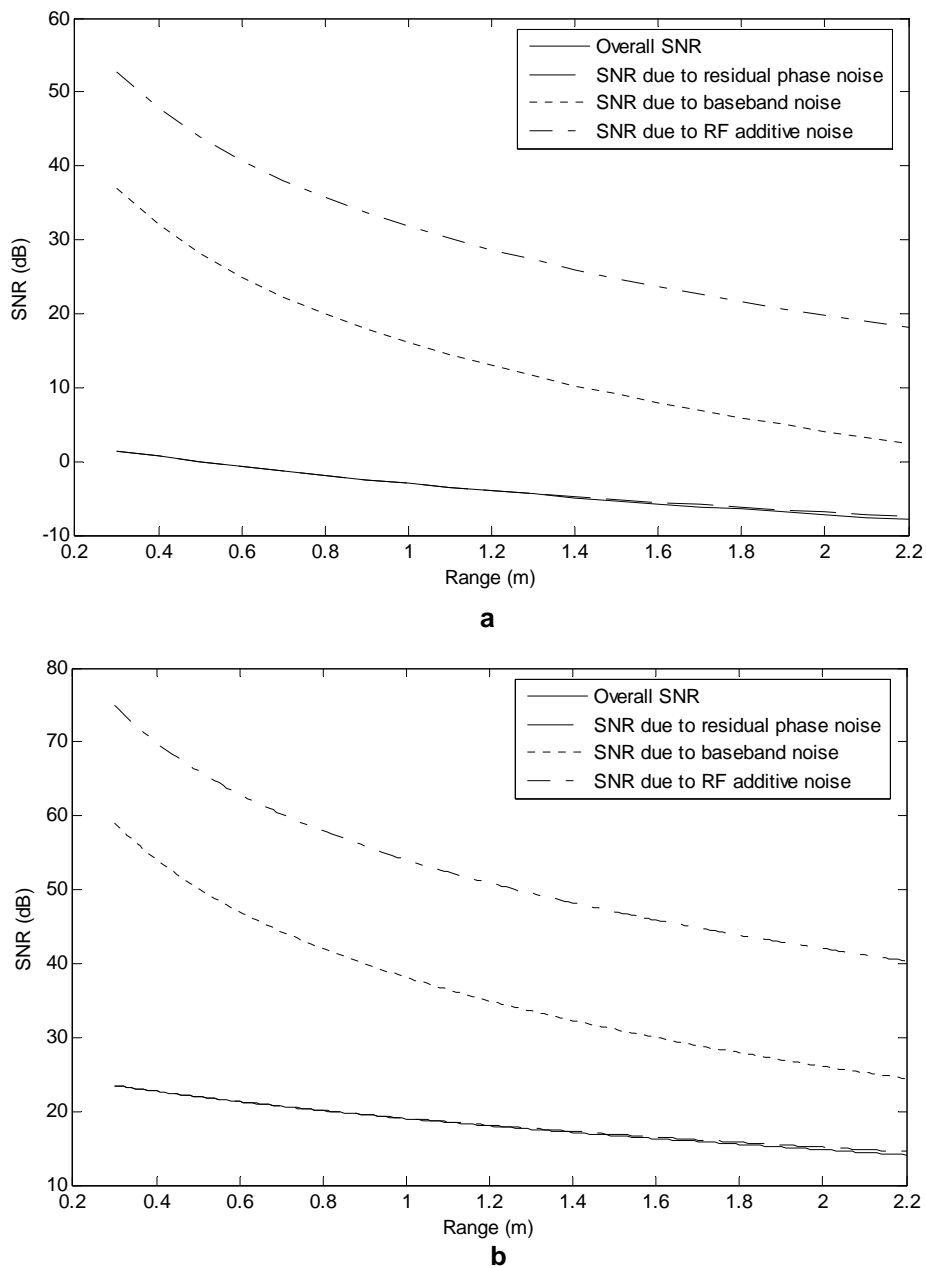


Figure 6.1. Theoretical model of signal-to-noise ratio vs. range for Doppler radar measurement of a) heart motion and b) respiration motion. See text for details on parametric values.

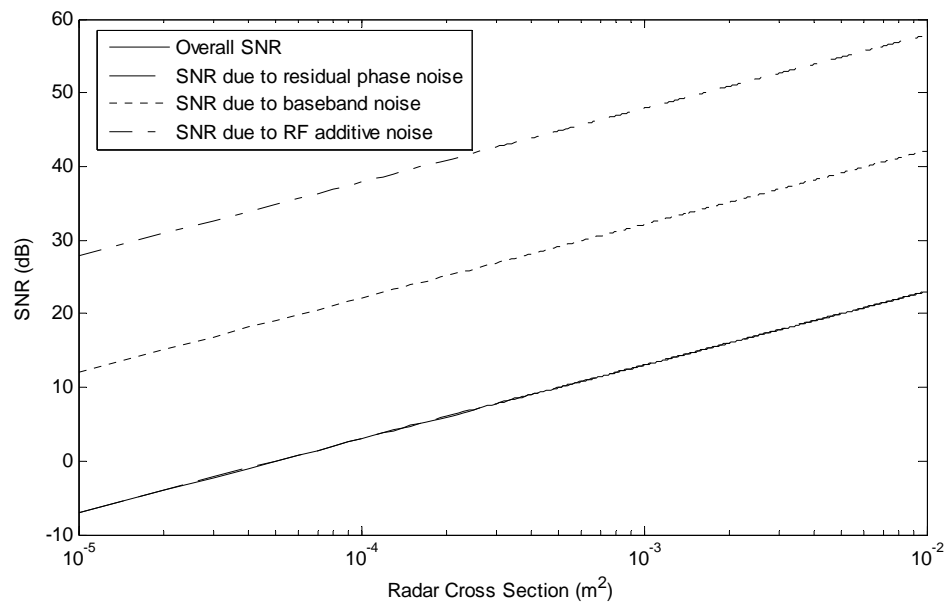
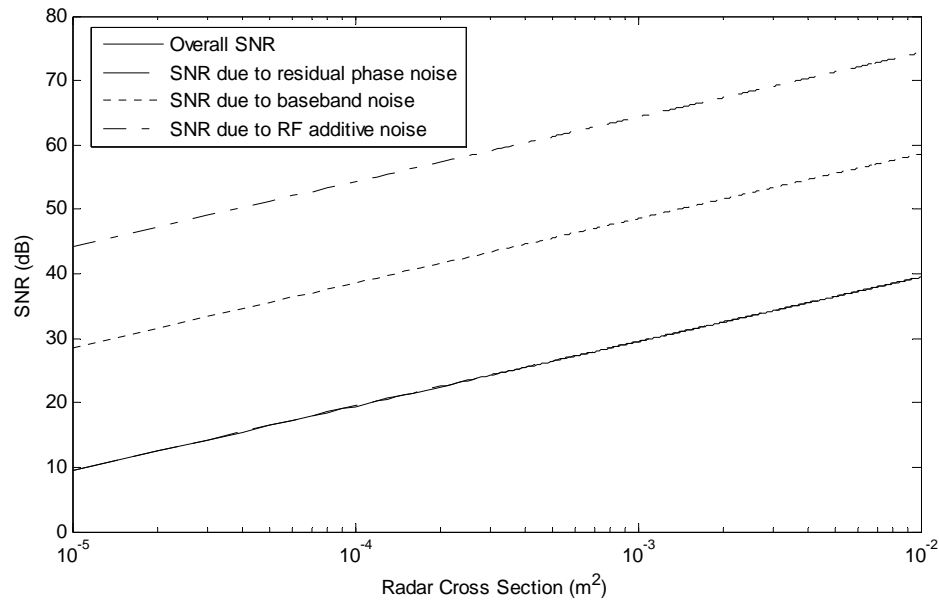
**a****b**

Figure 6.2. Model of theoretical signal-to-noise ratio vs. radar cross section for an RMS motion of a) 0.3 mm (heart) and b) 2 mm (respiration). See text for details of other parametric values.

6.3 Materials and Methods

Section 6.3.1 will introduce the experimental setup, including the human testing protocol, the Doppler radar measurement system, the digital signal processing used on the collected data, and the control measurements. Section 6.3.2 will describe the 22-subject population used in the human testing experiment. Section 6.3.3 will describe all the measurements of the human subjects body shape and size. Finally, Section 6.3.4 will describe the techniques used to analyze the data, including Bland-Altman analysis for method comparison studies, the calculation of the signal-to-noise ratio, and the correlation coefficient and linear regression techniques used to evaluate the relationship between the SNR and the measured subject parameters.

6.3.1 Experimental Setup

6.3.1.1 Experimental Procedure

This work was performed under Stanford protocol number 2899, approved by the Stanford University Internal Review Board in August 2005. After obtaining informed consent, the administrator asks the subject whether he/she has any diseases or disorders relating to or affecting the heart or respiratory system, whether he/she has a pacemaker or neurostimulator, and if a female, whether she is pregnant. If the subject answered yes to any of these questions, he/she would have been excluded from the study, but no exclusions were necessary. Each subject was given a new T-shirt to wear for the duration of the measurements if he/she was not already wearing a T-shirt, and was provided with a private area to change into this T-shirt. The administrator of the measurement asked the subject his/her age and gender and then measured the subject's weight, height, and thorax dimensions. Thorax dimensions were measured both at full inhale and full exhale, and included chest circumference, waist circumference, chest breadth, and chest depth.

The ECG electrodes were affixed to the subject's left and right upper arms and left abdomen, and the piezoelectric respiratory effort belts were affixed on the subject's abdomen and chest. The subject was then asked to sit in a chair for the measurements, and the

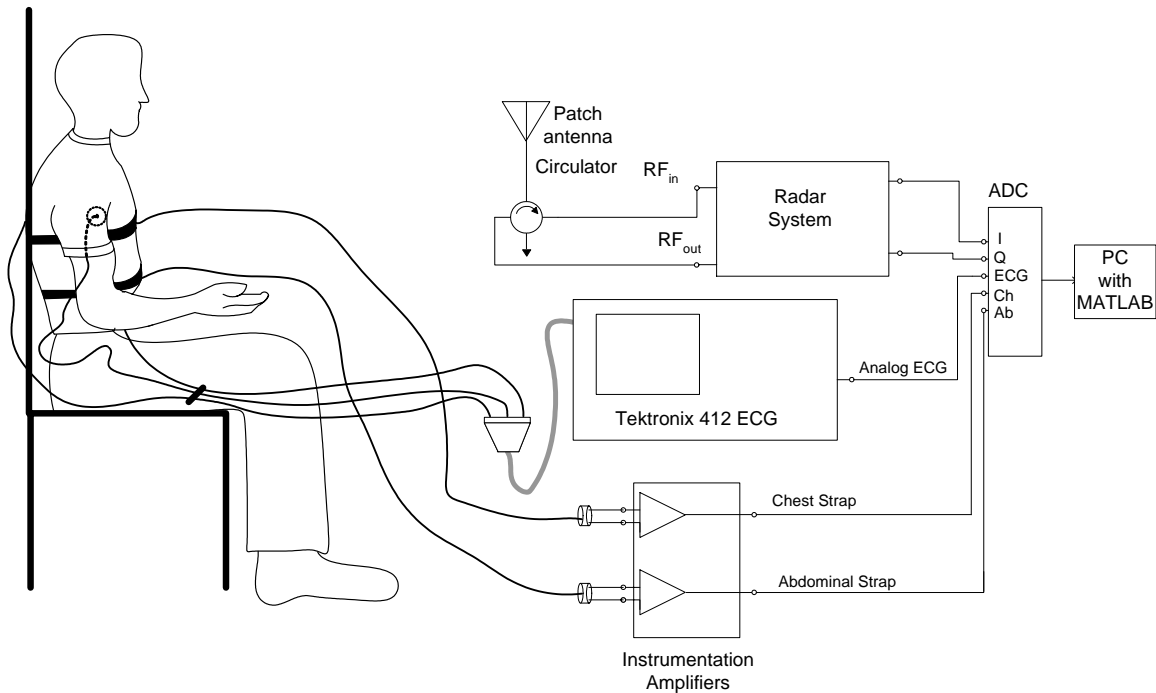


Figure 6.3. Block diagram of experimental setup for human subjects method comparison study.

antenna height was adjusted to be approximately level with the subject's sternum. The subject was asked to remain still, to refrain from scratching, talking, and any other motion for the duration of each measurement if possible. Each measurement had a 90-second duration. Two measurements were made at each range; ranges were 0.5 m, 1.0 m, 1.5 m, and 2.0 m. The subject's chair was not moved and the equipment, all on a cart, was moved to vary the range. The range was measured with a measuring tape from the subject's sternum to the antenna. Additionally, after two measurements at the 0.5 m range, the administrator asked the subject if he/she was comfortable holding his/her breath for a portion of the measurement. If the answer was yes, the subject was instructed to breathe normally for the first 15 seconds of the measurement, after which the subject was instructed to hold his/her breath when ready. The subject was instructed to end the breath hold whenever breath-holding became uncomfortable or when instructed to do so. The administrator timed the breath hold, and instructed the subject to end the breath hold after 30 seconds if the subject was still holding his/her breath at that time.

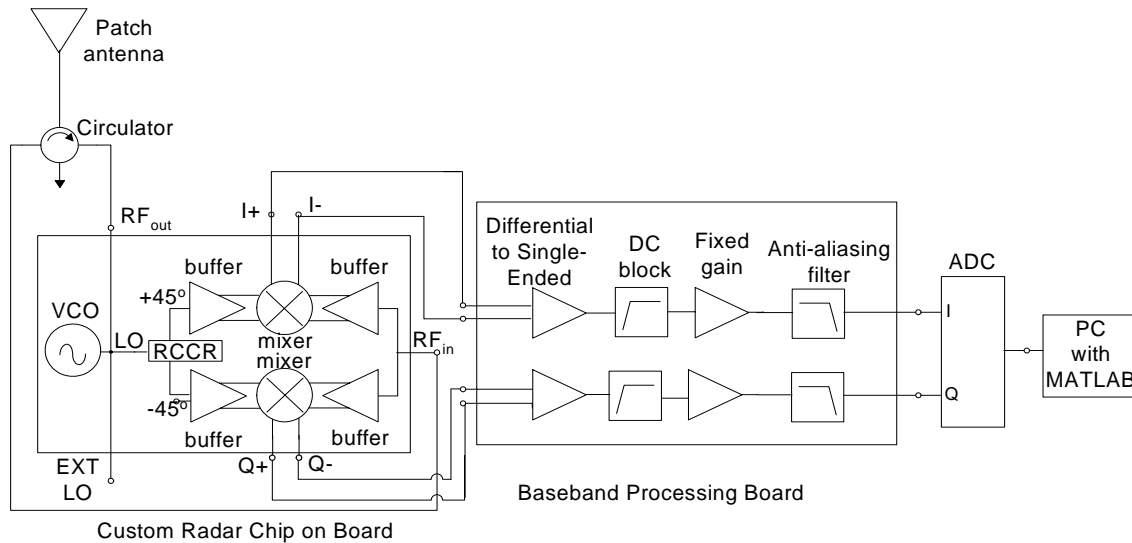


Figure 6.4. Radar system block diagram.

When the measurements were completed, the subject was instructed to remove the reference sensors. Then the subject was provided with a private area to change back into his or her shirt if necessary.

6.3.1.2 Doppler Radar System

The radio frequency radar electronics are on the single chip described in Chapter 4, operating at 2.2 GHz, and baseband electronics are on a printed circuit board. A commercially available antenna designed for use in the bands of operation was used, and the effective isotropic radiated power of 6 mW is similar to or lower than that used in many wireless consumer electronics products operating in this band, including wireless network cards, cordless telephones, and video infant monitors, and well below the FCC limit for consumer electronics devices in this band.

Figure 6.4 shows a block diagram of the radar system. The microwave portion consists of the on-chip radio, a circulator, and an antenna. The antenna used is an Antenna Specialists ASPPT 2988 patch antenna, with 60° by 80° beamwidth and 6 dBi gain. The antenna is used in conjunction with a Pasternack PE8401 circulator to isolate the received signal from the transmitted signal. The baseband portion of the system, described in detail in

Appendix E, consists of two channels, each with a differential-to-single-ended converter followed by a dc-blocking amplification and filtering stage and an anti-aliasing low-pass filter. Each baseband channel uses a Burr Brown INA105 precision differential amplifier (Texas Instruments, Dallas, TX) and a Texas Instruments OPA4132 quad FET-input operational amplifier (Texas Instruments, Dallas, TX), provides 40 dB gain, and passes 0.2 Hz to 20 Hz. A 16-bit National Instruments 6036E NIDAQ PCMCIA card (National Instruments, Austin, TX) was used with a PC for digitization at 100-Hz sampling rate, and custom MATLAB software performs digital signal processing (DSP). The baseband board also includes power circuitry so that the board and the CMOS chip can be powered with a single battery. The signal conditioning board operates at ± 5 V and the CMOS chip operates at 3 V with an oscillator tuning voltage of 3.5 V. A Power-Sonic PS-628 rechargeable lead-acid battery (Powersonic Corporation, Redwood City, CA) was used to power the board.

The signal source is a voltage-controlled oscillator (VCO) that delivers a 1-dBm 2.2-GHz signal to the RF_{out} port, provides the LO, and consumes 40 mW. The external LO port (EXT LO) was terminated for the measurements since the internal oscillator was used for all measurements. The next block in the local oscillator (LO) path is a passive resistor-capacitor network (RCCR) that is used to split the LO signal into the I and Q channels, which have a 90° phase difference. In each receiver chain, the LO is amplified and converted from a single-ended to a differential signal with an active balun-amplifier (buffer). Each balun-amplifier dissipates 15 mW. The RF input signal is divided into the two receiver chains, and each has an active balun-amplifier for single to differential conversion. The double-balanced ring mixer is fully passive. Use of a balanced mixer avoids even-order distortion; this is especially important in a direct-conversion architecture, as even-order distortion creates interference at the baseband signal. Additionally, a passive mixer decreases $1/f$ noise that can be limiting in homodyne systems that have data near dc. This circuit draws a total of 100 mW.

The chip was fabricated with the Agere Systems 0.25- μ m CMOS process with 5 metal levels, including a 3- μ m thick top-level metal providing an inductor quality factor of 8-10.

The chip has a size of 4.3 mm by 3.8 mm, and is packaged in the Amkor exposed pad TQFP-48 package with a 7 mm by 7 mm body size.

6.3.1.3 Digital Signal Processing

The digital signal processing filters the signals to remove noise and to isolate the Doppler heart signal from the respiration signal, combines signals from different channels, determines the rate of the signal, and smooths the output rate. The system is illustrated in Figure 6.5. The first DSP step is to isolate the heart signal from the combined heart and respiration signals with a 400-tap Kaiser high pass filter with β of 6.5 and a cutoff of 0.6 Hz. The heart signals are then lowpass filtered to remove out-of-band noise with a 20-tap Kaiser filter having a β of 6.5 and a 20-Hz cutoff. The I and Q signals are then combined by projecting them onto the first principal component after principal component analysis. The delay introduced by the filters is corrected so the time scale is the same for all channels. The Doppler heart rate is calculated every 0.5 seconds; the signal in a 8-second Hamming window is autocorrelated, and the local maxima that would indicate a rate between 30 beats per minute and 120 beats per minute is used to calculate the heart rate. The heart rate from the electrocardiogram is determined by extracting the R waves using a wavelet-based algorithm and inverting the mean of the inter-beat interval in an 8 second window. The rates from both the ECG and the Doppler are then smoothed with an exponential filter having an α value of 0.93. The exponential filter is:

$$y(t) = (1 - \alpha)y(t - 1) + \alpha x(t) \quad (6.16)$$

where $x(t)$ is the input and $y(t)$ is the output of the filter.

The respiration is extracted from the combined heart and respiration signal. The respiration signal is lowpass filtered with a 50-tap 1.5-Hz cutoff filter to remove out-of-band noise. Then the I and Q signals are combined by projecting them onto the first principal component after principal components analysis. The respiration rate is found by autocorrelating the signal in an 18-second Hamming window, and finding the local maxima that indicates a rate between 4 and 30 breaths per minute. The same rate-finding technique is used for the chest and abdominal respiration straps, but the strap signals are combined

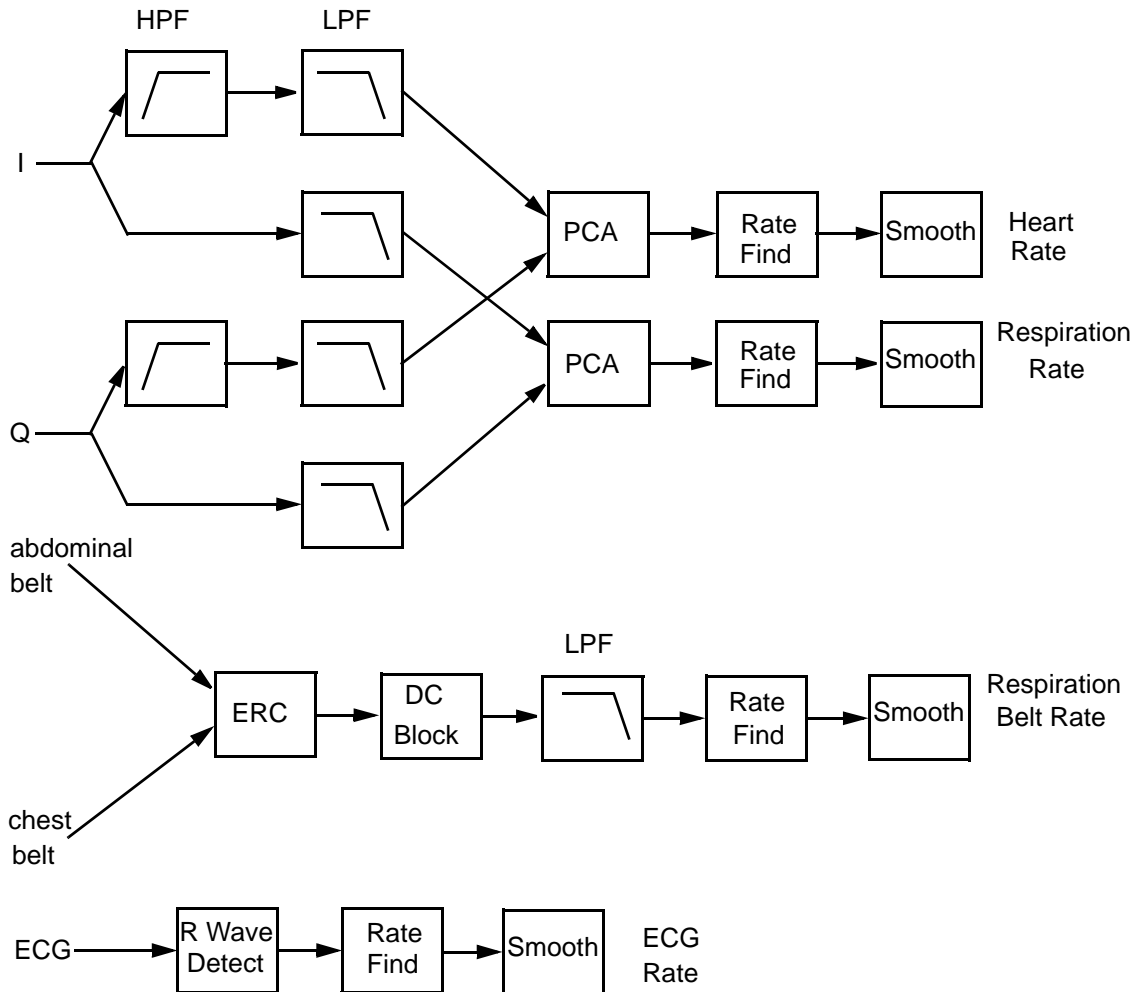


Figure 6.5. Signal processing block diagram. PCA represents principal components analysis, the technique used to combine the I and Q signals. ERC represents equal ratio combining, the technique used to combine the abdominal and chest respiratory effort belts. HPF indicates a highpass filter, LPF indicates a lowpass filter, DC Block indicates the removal of dc offset, “Rate Find” indicates a rate-finding step, “Smooth” indicates a smoothing of the rate, and “R Wave Detect” indicates that the timings of the ECG R waves are found.

with equal ratio combining rather than principal component analysis, are low-pass filtered after they are combined rather than before, and have their dc offset removed since they do not have dc-offset removal in the analog processing.

In communications applications, I and Q signals are often combined using an arctangent technique since they are 90° out of phase, or alternatively described as the sine and

cosine of the phase modulation. However, when the phase is demodulated to a baseband signal, as it is with the receiver architecture used in this system, there is significant data at dc. Because the dc value is also affected by mismatches on the chip, signal feedthrough from the transmitter to the receiver, and reflections from clutter, it is challenging to determine the dc value that is part of the data. Additionally, the large dc offsets make it impossible to amplify the signal to a value where both the heart and respiration signals can be digitized with sufficient resolution unless a 24-bit ADC is used. Therefore, the dc offset is removed in analog signal conditioning in this study, making arctangent combining an invalid option.

Since the arctangent approach is not valid, a data-driven approach is used. Principal component analysis is a method of transposing multi-dimensional data to a single dimension, suppressing redundant information and maximizing the variance in the data. First, any dc offset is removed from the data, and the covariance matrix between the I and Q channels is found. The I and Q data is then projected onto the eigenvector of the covariance matrix with the largest eigenvalue. Details on this technique can be found in Joliffe [188] and in Chapter 7.

Equal-ratio combining [181] involves adding the two sources of data after ensuring they are in phase. This diversity combining technique was used for the chest and abdominal straps.

6.3.1.4 Control Measurements

The control measurement for the heart rate is a three-lead ECG with LA and RA electrodes affixed to the left and right arms, and the LL electrode affixed to the left side of the abdomen. A Tektronix 412 ECG display and amplifier (Tektronix, Richardson, TX) was used for isolation and signal conditioning; its analog output was digitized simultaneously with the Doppler signal. Commercially available, FDA approved button-style ECG electrodes were used.

The control measurements for respiration were taken using Dymedix piezoelectric respiratory effort straps (Dymedix, Minneapolis, MN). The straps were connected to a signal conditioning circuit of instrumentation amplifiers.

6.3.1.5 Signal Delay

The delay from the RF output to the antenna and to the RF input was measured with a HP 8714C RF Network Analyzer. The cables, circulator, and antenna were kept in their experimental configuration, but removed from the RF circuit board. They were attached to the network analyzer, and the delay was measured at frequencies between 1 and 3 GHz. The delay in the spectral regions where the antenna does not transmit effectively was 5 ns. Since most of the signal is reflected at the antenna interface at these frequency regions, but is still in the effective range of the circulator, this value was taken to be the delay.

6.3.2 Human Subjects

Seven women and 15 men were measured in this study. The age of the subjects ranged from 19 to 67, with a mean age of 34. The body mass index of the subjects ranged from 18.3 to 31.4, with a mean BMI of 24.3. The average resting heart rate varied from 43.2 to 93.6 beats per minute, with a mean of 70.4 beats per minute, and the respiration rates varied from 4.8 to 21.0 breaths per minute with a mean of 12.8 breaths per minute. The subject data is listed in Table 6.1, and the methods used to make the measurements are described in the following section.

Table 6.1: Measured and Collected Subject Data. “Num” is the 4-digit subject number. “Age” and “Gen” are the subject’s age and gender as reported by the subject. “Ht” and “Wt” are the subject’s measured height in cm and weight in kg, and “BMI” is the subject’s body mass index, calculated as Wt/Ht^2 , with the weight in kg and the height in m. “CB,” “CD,” “WC,” and “CC” are the subject’s chest breadth, chest depth, waist circumference, and chest circumference, all measured at exhale. “HR” and “RR” are the subject’s average heart and respiration rates.

Num	Age	Gen	Ht [cm]	Wt [kg]	BMI [kg/m ²]	CB [cm]	CD [cm]	WC [cm]	CC [cm]	HR [bpm]	RR [rpm]
0353	30	M	178	98.3	31.0	32	23	103.5	102	69.9	20.8
1315	31	M	173	72.3	24.2	28	19	87.4	86.5	61.3	14.2
1738	26	F	152	44.6	19.3	22	15	63	68	73.5	16.5
2469	30	M	180	70.2	21.7	26	17	80	84	75.7	13.7
1436	28	M	176.5	64.9	20.8	25	18	70	82.5	68.0	10.8
2393	47	M	185.5	103.5	30.1	32	22	100.5	105	79.6	13.5
3343	29	F	170	53	18.3	24	16	66	68.5	75.7	12.0
3971	28	F	178	67	21.1	26	17	73.5	76.5	74.9	15.0
4062	31	M	166.5	82.7	29.8	30	19	95	96.5	45.7	12.6
4665	46	F	173	67.7	22.6	24	14	69	72	68.2	15.0
4729	28	M	165	70.1	25.7	20	19	84	90.5	64.7	12.7
4988	54	M	178	87.5	27.6	31	22	96	99.5	79.1	8.0
5617	30	M	170	68.8	23.8	28	20	84	91.5	62.1	9.9
6792	34	M	185	65.9	19.3	36	18	74	82	70.9	9.1
6238	31	M	188	94.7	26.8	30	20	96.5	97.5	76.5	4.8
7371	67	M	180	84	25.9	28	24	90	94	57.4	11.3
7683	35	F	162.5	68.9	26.1	25	17	75.5	82	69.7	11.4
8497	23	F	167.5	64	22.8	24	18	75.5	75	76.9	15.1
8980	35	F	162.5	55.8	21.1	25	16	18.5	70	81.0	12.1
9674	23	M	185.5	108	31.4	32	22	104	105	93.6	21.0
9831	44	M	188	95.7	27.1	30	21	93	96.5	43.2	10.7
9882	19	M	167.5	52.9	18.9	26	14	79	69	82.2	12.1
Avg	34.0		174.2	74.6	24.3	27.5	18.7	80.8	86.1	70.4	12.8
StdD	11.2		9.5	17.4	4.2	3.9	2.9	18.6	12.5	11.4	4.0

6.3.3 Measurements of Human Subjects

6.3.3.1 Weight

The subject's body weight was measured on a strain-gauge based digital scale with clothing on.

6.3.3.2 Chest Circumference

The chest circumferences were measured with a 0.7 cm wide measuring tape. The subject was instructed to stand erect, with his/her feet at shoulder width, and with the arms out enough to allow the passage of the tape around the chest. Once the tape was around the chest, the subject was instructed to lower his/her arms to their natural position at his/her side. The chest circumference was measured at the level of the bottom of the sternum, both at the end of a normal inspiration and at the end of a normal expiration [183].

6.3.3.3 Chest Breadth

The chest breadth was measured with Lafayette 01440 chest-depth calipers (Lafayette Instrument Co., Lafayette, IN). The subject was instructed to stand erect, with the feet at shoulder width and the arms far enough out to allow access to the measurement site with the calipers. The tips of the calipers were placed on the sixth ribs with the measurer's fingers beneath the caliper tips to prevent them from slipping into the intercostal spaces [196]. Very light pressure was applied and the chest breadth was measured at the end of a normal inspiration and at the end of a normal expiration.

6.3.3.4 Chest Depth

The chest depth was measured with Lafayette 01440 chest depth calipers (Lafayette Instrument Co., Lafayette, IN). The subject was instructed to stand erect, with the feet at shoulder width and the arms at the sides. One tip of the calipers was placed on the sternum in the midline at the level of the fourth costo-sternal junction [196]. The other tip was placed on the spinous process of the vertebra that is in the same horizontal plane. Mea-

surements were made at the end of a normal inspiration and at the end of a normal expiration.

6.3.3.5 Waist Circumference

Waist circumference was measured with a 0.7 cm wide measuring tape. The subject was instructed to stand erect with the abdomen relaxed, the arms at the sides, and the feet together. The tape was placed around the subject, in a horizontal plane and at the level of the natural waist or the narrowest part of the torso [183]. If the subject's waist was not well defined, the smallest horizontal circumference between the ribs and the iliac crest was measured [183]. Measurements were made at the end of a normal inspiration and at the end of a normal expiration, without the tape compressing the skin.

6.3.3.6 Body Mass Index

Body mass index (BMI) is used as a proxy for total body fat. This is the most commonly used estimate of body type, largely because weight and height are easy to measure, highly consistent, and require minimal expenditure on equipment. Its performance can be improved by allowing for age and gender, but not frame size [192]. The BMI does not separate the moderately obese from the muscular individual, nor does it take into account the changing composition with age [192]. Although some researches believe that a power other than two, or different powers for men and women, or different powers for different ages improves the accuracy of BMI as a measure of body fat [177, 192], a power of two is used for all subjects in this study, as is common in practice [191, 192].

A BMI below 18.5 is considered underweight, a BMI between 18.5 and 24.9 is considered normal, a BMI between 25.0 and 29.9 is considered overweight, and a BMI over 30 is considered obese [191].

6.3.4 Analysis of Human Subjects Data

6.3.4.1 Bland-Altman Analysis for Method Comparison

The Bland-Altman analysis technique for method comparison involves plotting the difference between the two methods' measurement values against the average of the two measurements. This plot is more informative than plotting the results of one measurement vs. the other measurement because the data is better spread out and it is easy to assess bias and variation of the measurements [178]. The standard measurement should not be considered error free, even when referred to as the "gold standard" [180], so it is important not to plot the difference against the "gold standard," to avoid introducing a bias into the measurement, as discussed in [179].

The mean difference is then an estimate of the average bias of one method relative to the other. Assuming the measurement error has a gaussian distribution about the bias, it is easy to calculate the 95% confidence intervals for the difference between the two methods of measurement. The bias, \bar{d} , is calculated as the mean of the difference between the two measurements. The standard deviation of the differences, s_d , is also calculated. For a gaussian distribution, the 95% confidence intervals are at $\bar{d} \pm 1.96s_d$ [180].

For Bland-Altman analysis, the sample size needs to be sufficiently large for the limits of agreement to be estimated well. The variance in the 95% confidence interval limits depends on the standard deviation of the difference between the methods and the sample size:

$$\frac{1.72s_d}{\sqrt{n}} \quad (6.17)$$

where n is the number of samples [180]. With 22 samples, the error is 0.37 times the standard deviation.

The Bland-Altman statistics are calculated for 60 seconds from each measurement, starting after 22 seconds, so that the filters and exponential average had time to load.

6.3.4.2 Signal-to-Noise Ratio

The signal-to-noise ratio of the heart signal is calculated from the power spectral density of the Doppler signal. The average rate of the ECG signal is determined to be the center of the signal, and the power within 10 beats per minute of the center is considered to be the signal power, with all power outside this window considered to be the noise power. The same technique is used for the respiration, but the signal is the power within 6 breaths-per-minute of the rate from the belts, and if the rate is below 6 breaths per minute, the minimum rate is 0.1 breaths per minute and the maximum rate is 12.1 breaths per minute.

6.3.4.3 Statistical Analysis: Correlation Coefficient

Since theory indicates that the signal-to-noise ratio is directly proportional to the cross sectional area, it is desirable to measure the relationship between the subject-size variables and the SNR at each range. This is done with the correlation coefficient and linear regression.

The correlation coefficient describes the degree of association between two random variables. The Pearson correlation coefficient, the correlation coefficient for a sample rather than the entire population, is calculated for variables X and Y , as:

$$r = \frac{\sum (X_i - \bar{X})(Y_i - \bar{Y})}{\sqrt{(\sum (X_i - \bar{X})^2)(\sum (Y_i - \bar{Y})^2)}} = \frac{\sum (X_i - \bar{X})(Y_i - \bar{Y})}{nS_xS_y}, \quad (6.18)$$

where n is the number of elements in both X and Y , and S_x and S_y are the standard deviations of X and Y , respectively [189]. The correlation coefficient is always between -1 and +1, with a value of 0 indicating no correlation and a value of ± 1 indicating that the two variables are proportional to each other, with the sign indicating whether the variables are directly proportional or inversely proportional.

The statistical significance of the correlation is assessed with the p-statistic. This statistic indicates the likelihood of randomly getting a correlation coefficient as large as the

observed value if there was actually no correlation between the values. For example, if the p-value is 0.03, that means that there is a 3% chance that the observed correlation would occur if the two variables were uncorrelated.

6.3.4.4 Statistical Analysis: Linear Regression

When measuring the size of a subject, it is expected that an increase in one dimension will indicate an increase in another dimension. Various measures of the size of a subject are expected to show dependencies; these dependencies are physiological properties and are expected to be present. Multicollinearity is a term used to indicate that nearly linear relationships exist between the explanatory variables, or a linear function of the variables is nearly equal to zero [193, 195]. When multicollinearity exists, precise estimation of the parameters for each variable is not possible [195], and using regression to identify the important variable is almost ensured to produce inadequate results [193].

When multicollinearity exists in a set of predictor variables, only a subset of the variables can be used. There is a large body of work on selection of these variables [187, 190], but no definitive answer on the best way to select the subset of variables, other than an exhaustive search of all permutations of variables [190]. Even with an exhaustive search it is not straightforward to choose a test for the “best” subset [187]. Principal components linear regression is often used when there are multicollinear variables, and while this analysis works well for prediction in some cases, it does not work well for determining parametric values for purposes of description [188].

Variables were selected for multiple linear regression using the principal components analysis technique described by Jolliffe [188]. Principal components analysis is performed on all variables, and the last principal component is associated with the variable that has the greatest projection onto it. That variable is eliminated, and principal components analysis is then performed on the remaining variables. This process is iterated until the desired number of variables is reached. This analysis resulted in the selection of height, waist circumference, and age for multiple linear regression with the SNR.

Single variable linear regression is performed on the variables and combinations of variables that were shown to be significantly correlated with the SNR for at least two ranges. Significant correlation is defined as $p \leq 0.10$, or 90% confidence.

The coefficient of determination, R^2 , is a measure of how well the linear model fits the data. It indicates how much of the variability is accounted for in the linear relationship and how much is just noise. For example, if the value for R^2 is 0.23, it means that 23% of the variation of the dependent variable is described by the linear relationship with the independent variable(s). For single-variable linear regression, this is the square of the correlation coefficient, r .

6.4 Results

6.4.1 Human Subjects Heart and Respiration Signals and Rates

The data collected from subject 4062 is shown in Figures 6.6 - 6.13. For each range, the 60-second traces that were used for Bland-Altman rate comparison are shown. These traces are the combined I and Q heart and respiration signals from the Doppler radar, the ECG signal, and the combined chest and abdomen respiratory effort straps. This subject was chosen because his low heart rate (average 46 beats per minute) makes the heart signal easier for the reader to view, and because the 31-year-old male's body shape and size were not at the extremes of this subject population in any dimension.

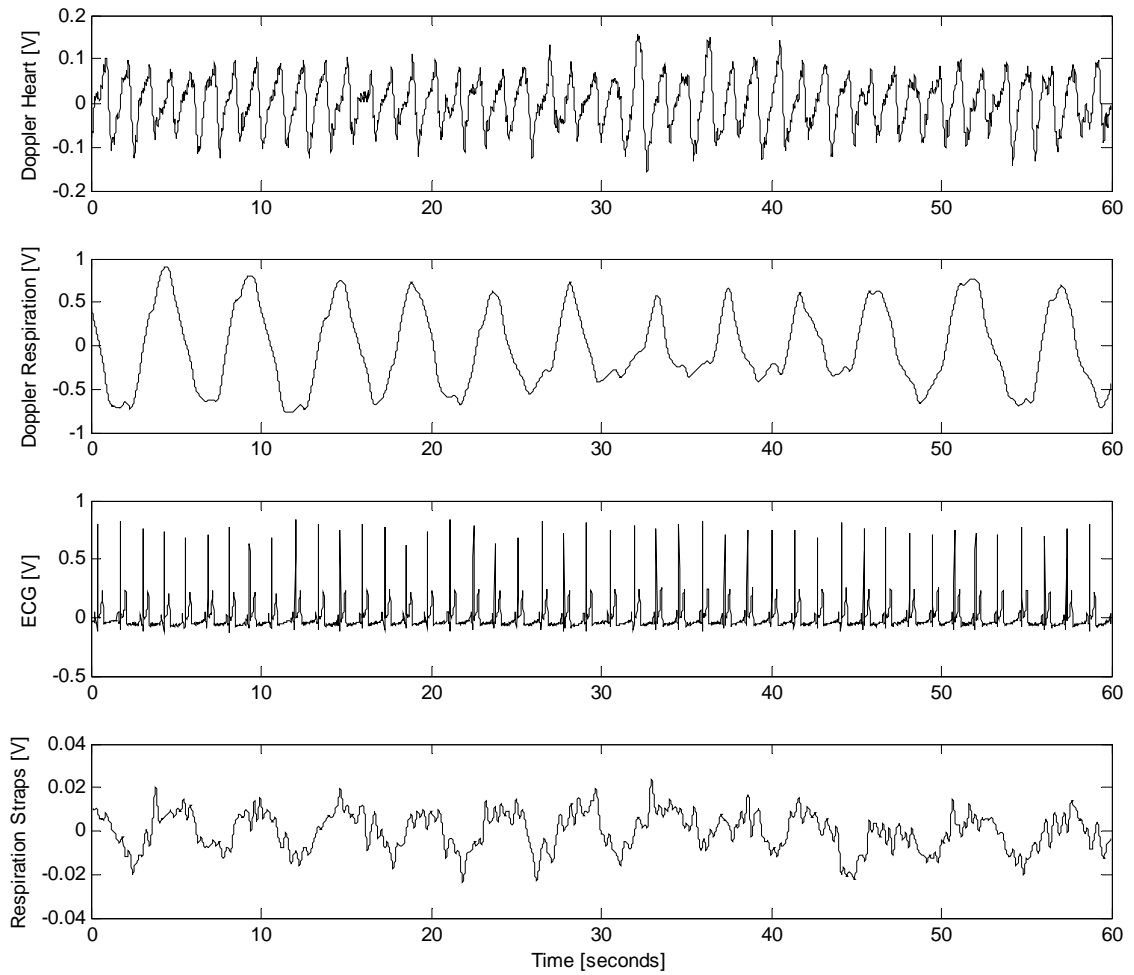


Figure 6.6. Data from Subject 4062 at 0.5 m. The top trace is the combined heart signal from the Doppler radar, the second trace is the combined respiration signal from the Doppler radar, the third trace is the ECG, and the bottom trace is the combined respiration signal from the straps.

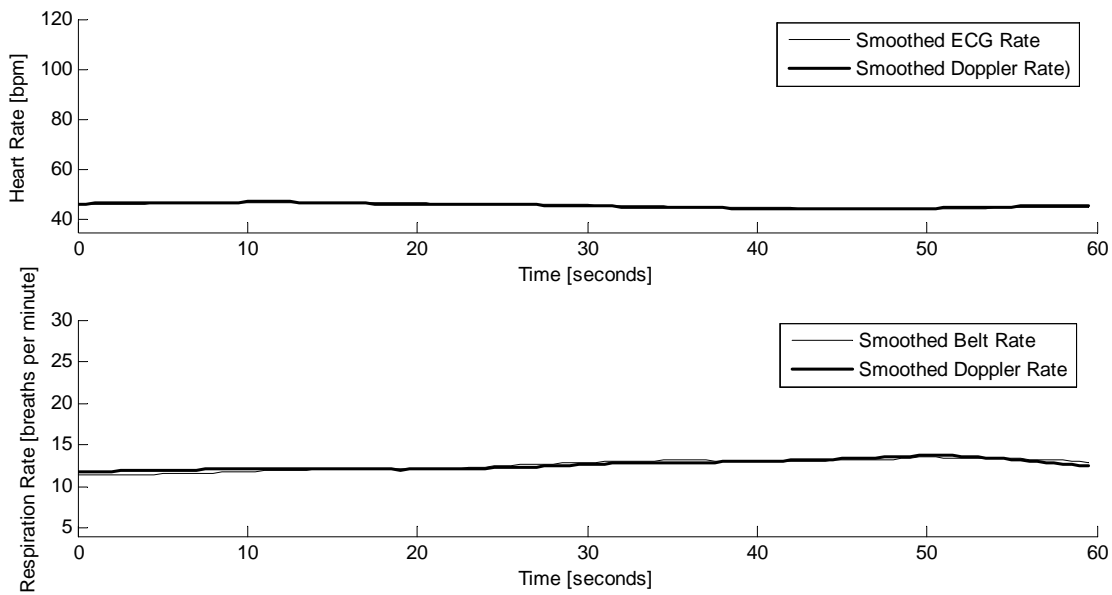


Figure 6.7. Heart and respiration rates from Subject 4062 at 0.5 m. The mean difference between the ECG heart rate and the Doppler heart rate was 0.030 beats per minute and the standard deviation of the difference was 0.292 beats per minute. The mean difference between the strap respiration rate and the Doppler respiration rate was 0.029 breaths per minute and the standard deviation of the difference was 0.263 breaths per minute.

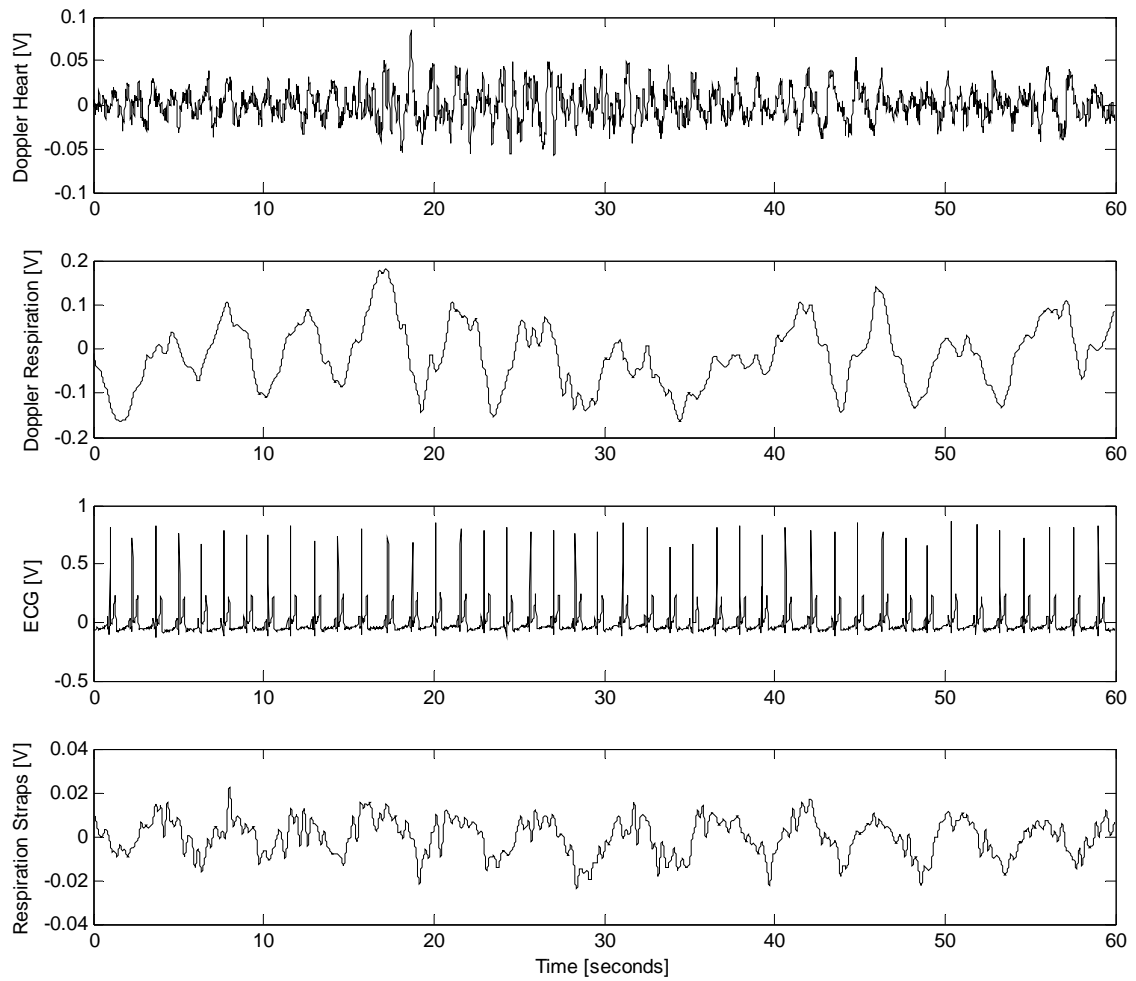


Figure 6.8. Data from Subject 4062 at 1.0 m. The top trace is the combined heart signal from the Doppler radar, the second trace is the combined respiration signal from the Doppler radar, the third trace is the ECG, and the bottom trace is the combined respiration signal from the straps.

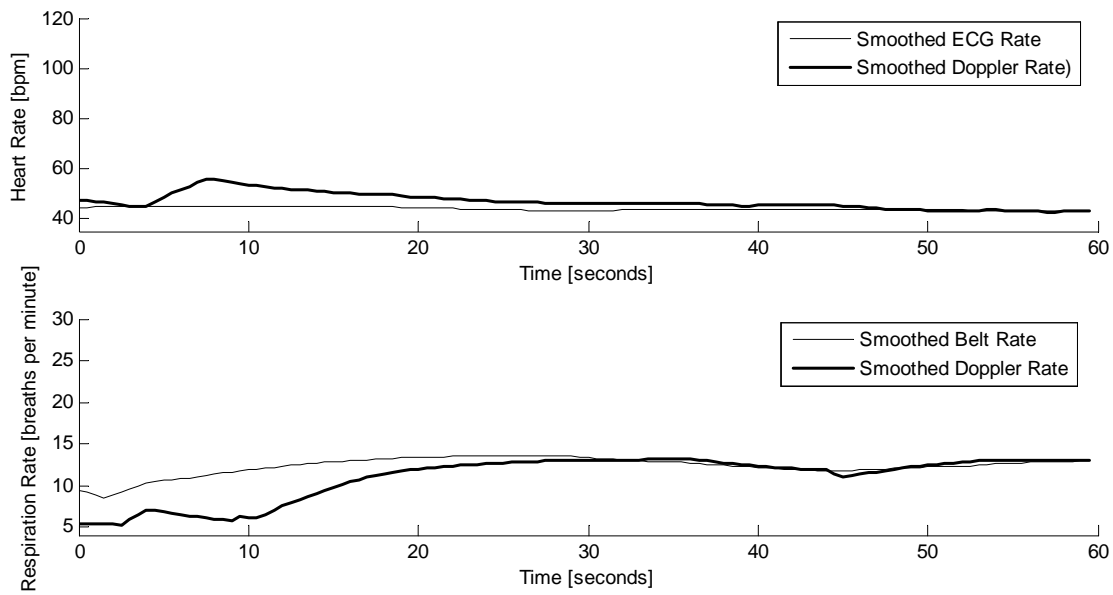


Figure 6.9. Heart and respiration rates from Subject 4062 at 1.0 m. The mean difference between the ECG heart rate and the Doppler heart rate was 2.61 beats per minute and the standard deviation of the difference was 2.195 beats per minute. The mean difference between the strap respiration rate and the Doppler respiration rate was -0.720 breaths per minute and the standard deviation of the difference was 1.769 breaths per minute.

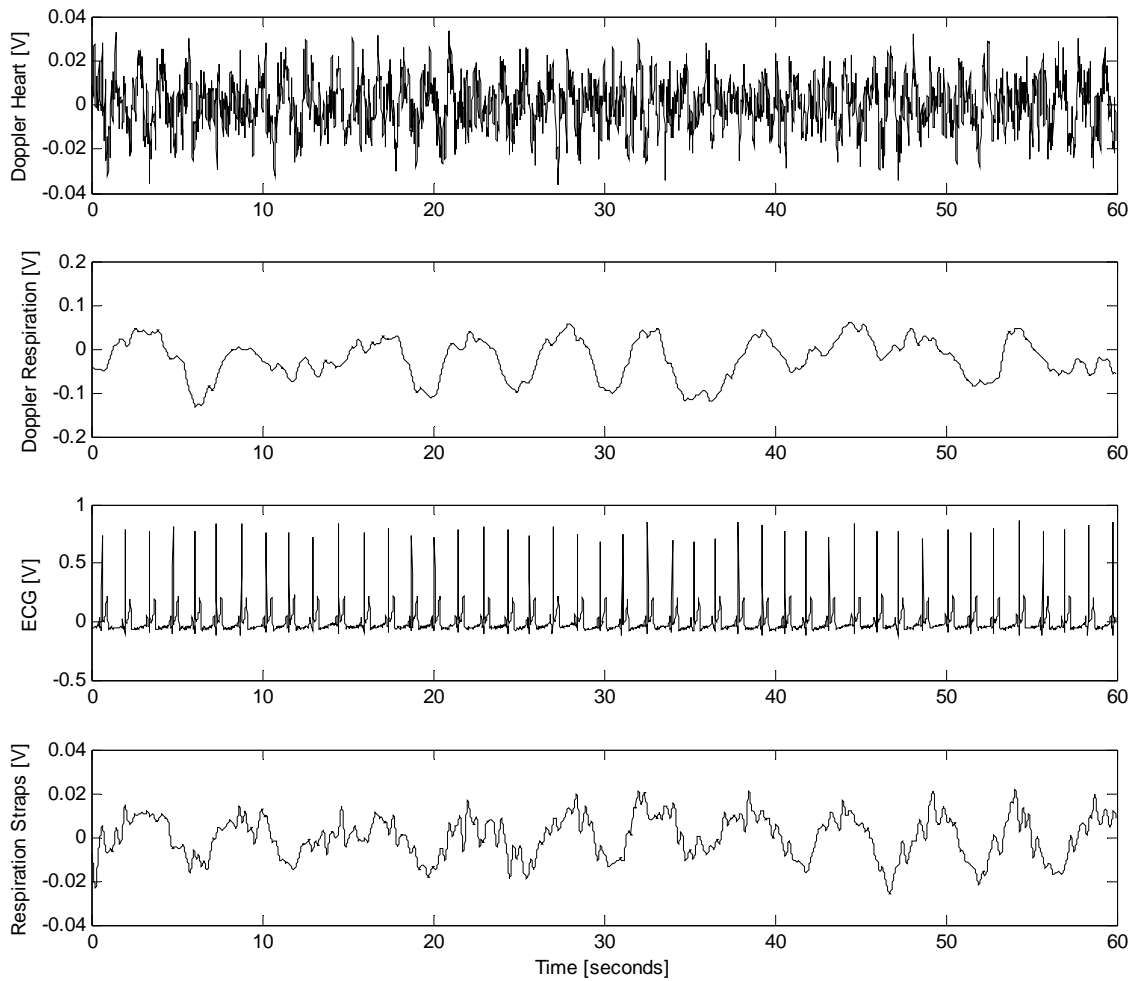


Figure 6.10. Data from Subject 4062 at 1.5 m. The top trace is the combined heart signal from the Doppler radar, the second trace is the combined respiration signal from the Doppler radar, the third trace is the ECG, and the bottom trace is the combined respiration signal from the straps.

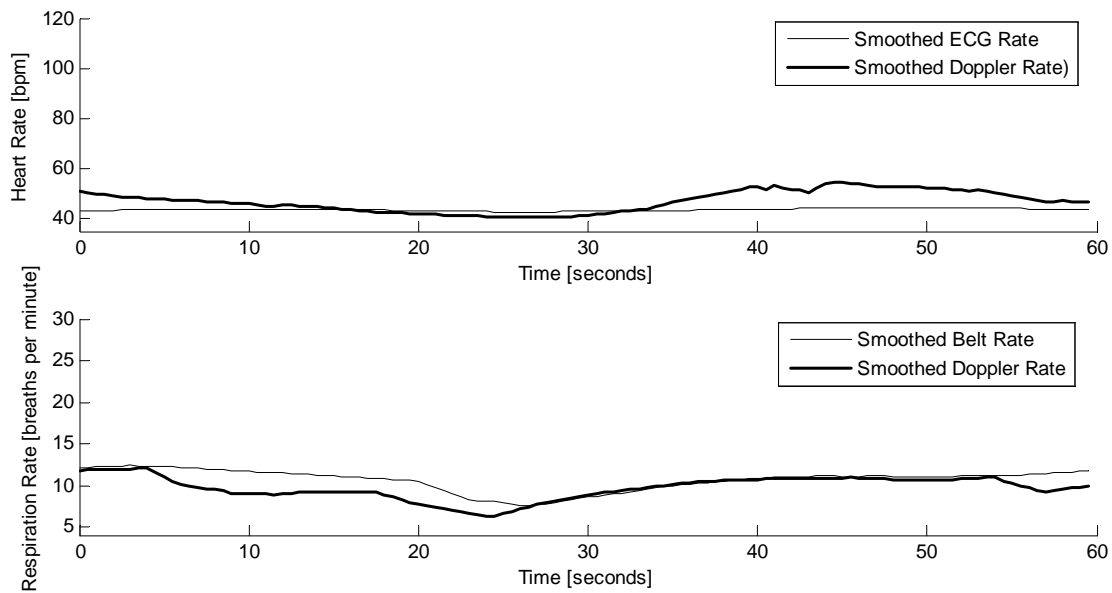


Figure 6.11. Heart and respiration rates from Subject 4062 at 1.5 m. The mean difference between the ECG heart rate and the Doppler heart rate was 0.821 beats per minute and the standard deviation of the difference was 1.925 beats per minute. The mean difference between the strap respiration rate and the Doppler respiration rate was -1.144 breaths per minute and the standard deviation of the difference was 1.722 breaths per minute.

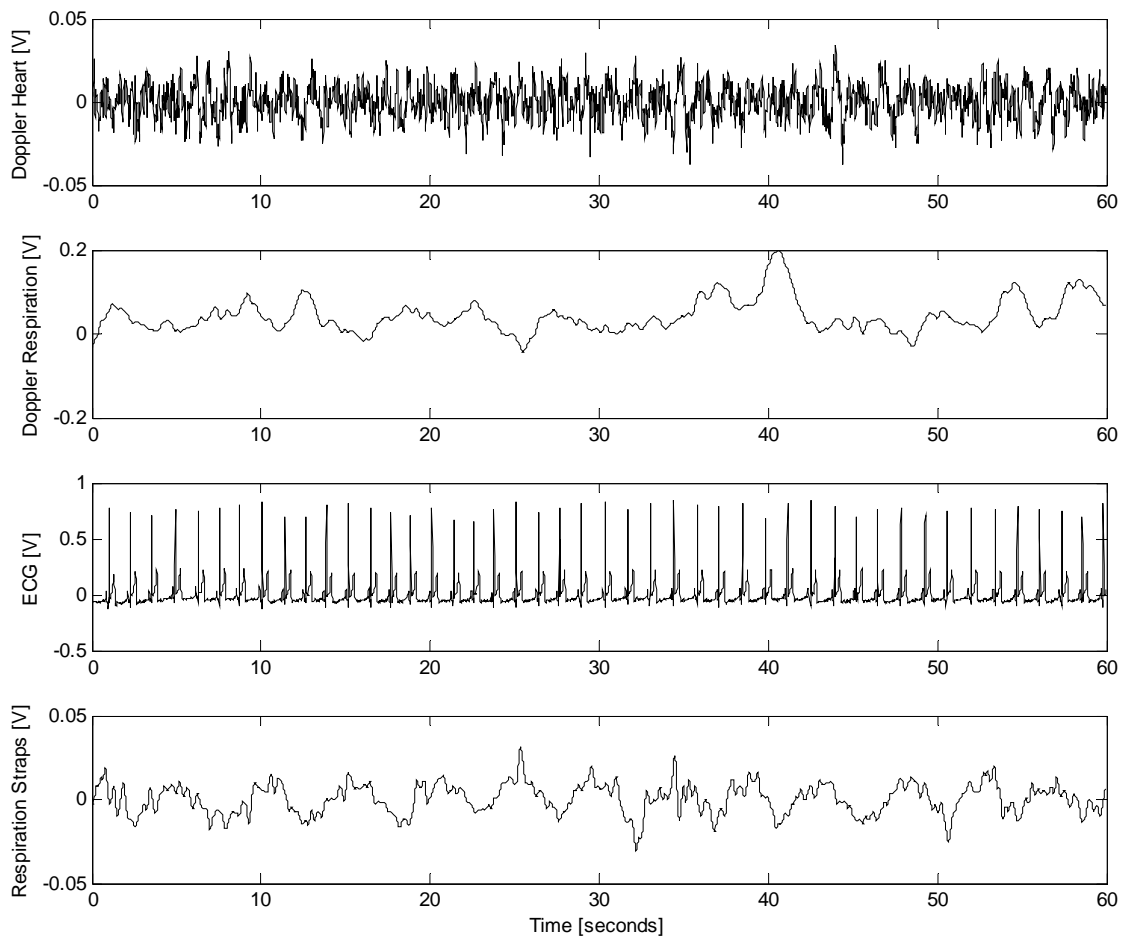


Figure 6.12. Data from Subject 4062 at 2.0 m. The top trace is the combined heart signal from the Doppler radar, the second trace is the combined respiration signal from the Doppler radar, the third trace is the ECG, and the bottom trace is the combined respiration signal from the straps.

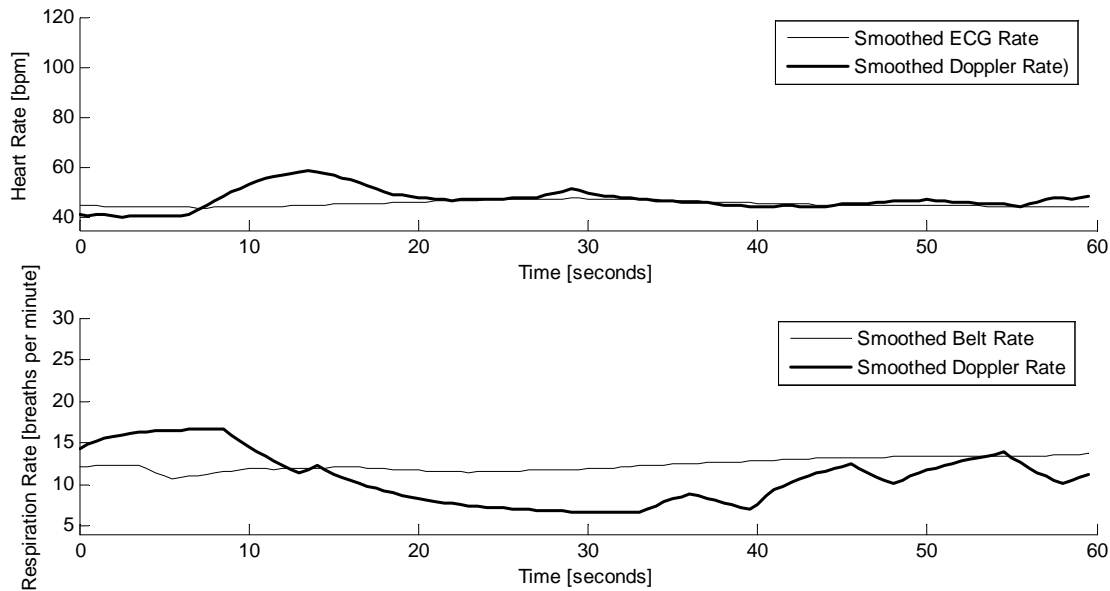


Figure 6.13. Heart and respiration rates from Subject 4062 at 2.0 m. The mean difference between the ECG heart rate and the Doppler heart rate was 0.786 beats per minutes and the standard deviation of the difference was 3.701 beats per minute. The mean difference between the strap respiration rate and the Doppler respiration rate was -0.306 breaths per minute and the standard deviation of the difference was 3.354 breaths per minute.

6.4.2 Overall Accuracy of Heart and Respiration Rates

The Bland-Altman plots shown in Figures 6.14 through 6.21 and statistics listed in Tables 6.2 and 6.3 show the heart and respiration rates measured for 22 subjects every half second over a 60 second interval. There are 120 rate measurements displayed per subject.

6.4.2.1 Heart Rate Accuracy

Bland-Altman plots are shown for all heart rate data collected at each range in this section. There are 120 points plotted for each of the 22 subjects; the rates were calculated every 0.5 seconds over a 60-second interval. The Bland-Altman graph plots the difference between the heart rates found with the Doppler system and the ECG vs. the mean of the rates. Table 6.2 shows the mean and standard deviation of the difference between the rates for each subject at each range.

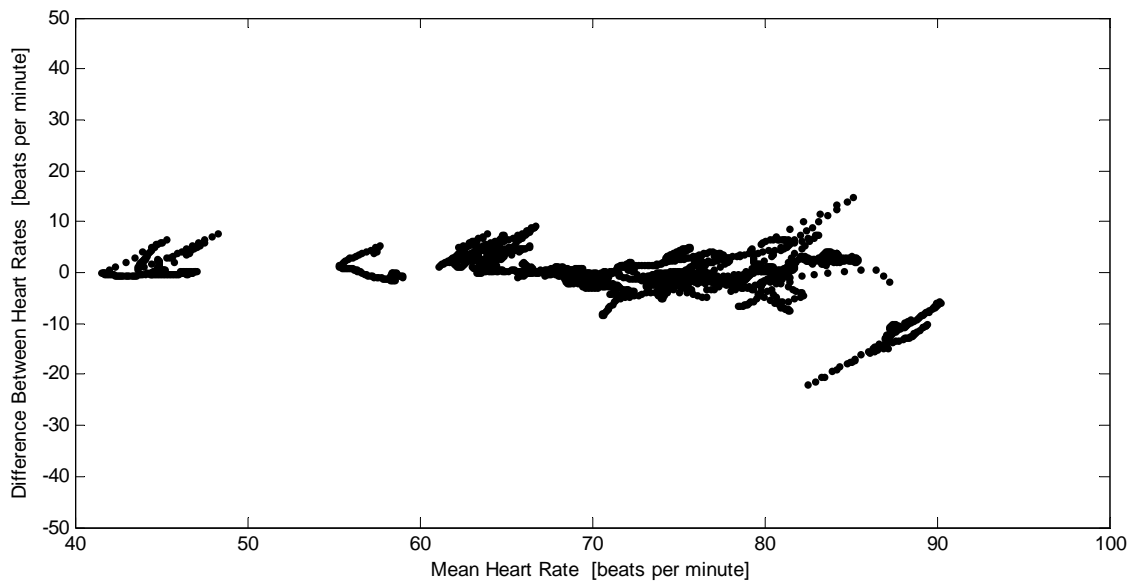


Figure 6.14. Bland-Altman plot of heart rate measured with Doppler radar at 0.5 m range and ECG, for all subjects.

At 0.5 m, the heart rate measurements from the combined radar signal are between 7.04 beats per minute above and 7.00 beats per minute below the rate measured with the ECG with 95% confidence. The difference between heart rates calculated with the combined radar signal and the ECG has a mean of 0.02 beats per minute and a standard deviation of 3.58 beats per minute.

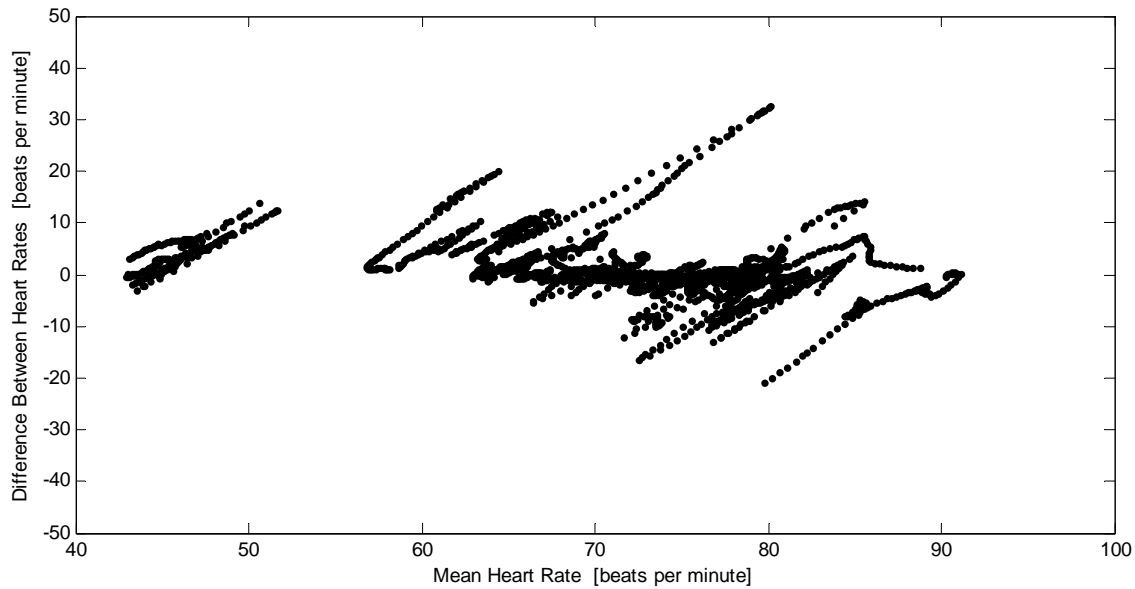


Figure 6.15. Bland-Altman plot of heart rate measured with Doppler radar at 1.0 m range and ECG for all subjects.

At 1.0 m, the heart rate measurements from the combined radar signal are between 11.18 beats per minute above and 9.59 beats per minute below the rate measured with the ECG with 95% confidence. The difference between heart rates calculated with the combined radar signal and the ECG has a mean of 0.80 beats per minute and a standard deviation of 5.30 beats per minute.

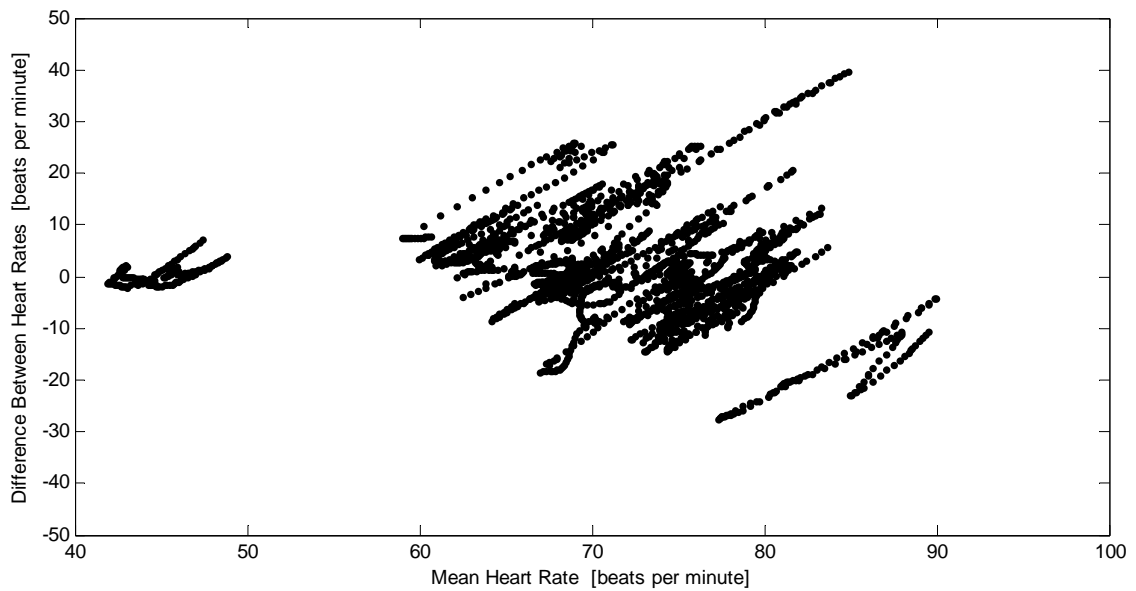


Figure 6.16. Bland-Altman plot of heart rate measured with Doppler radar at 1.5 m range and ECG for all subjects

At 1.5 m, the heart rate measurements from the combined radar signal are between 19.74 beats per minute above and 16.74 beats per minute below the rate measured with the ECG with 95% confidence. The difference between heart rates calculated with the combined radar signal and the ECG has mean of 1.50 beats per minute and a standard deviation of 9.31 beats per minute.

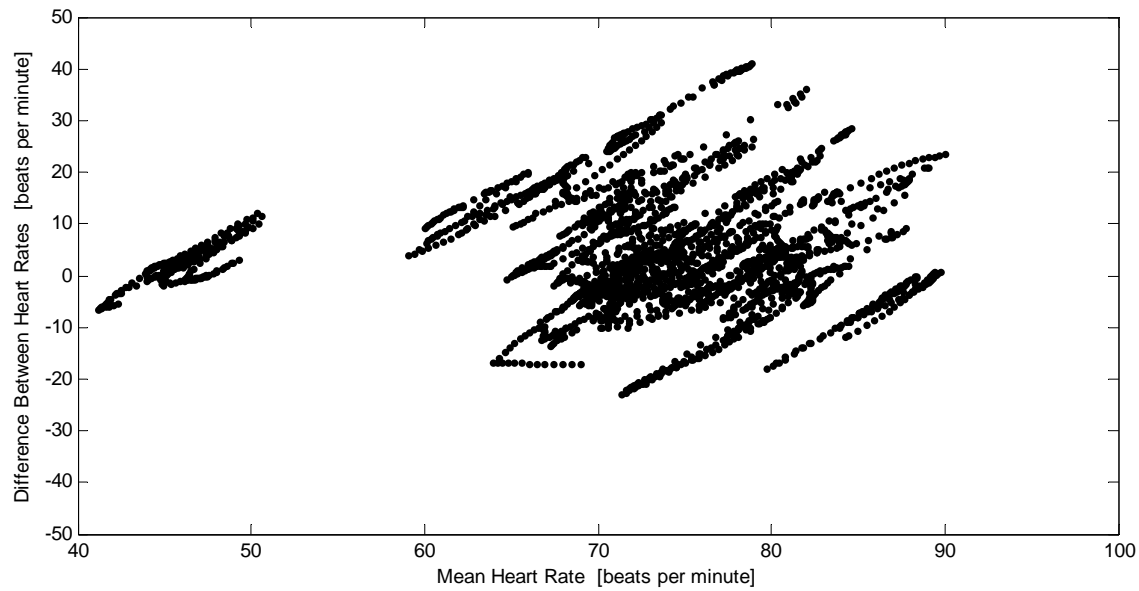


Figure 6.17. Bland-Altman plot of heart rate measured with Doppler radar at 2.0 m range and ECG for all subjects.

At 2.0 m, the heart rate measurements from the combined radar signal are between 25.90 beats per minute above and 16.15 beats per minute below the rate measured with the ECG with 95% confidence. The difference between heart rates calculated with the combined radar signal and the ECG has mean of 4.88 beats per minute and a standard deviation of 10.73 beats per minute.

Table 6.2: Bland-Altman Data for Each Subject's Heart Measurement. "Mean" indicates the mean of the difference between the heart rate found with the Doppler system and that found with the ECG. "Std dev" indicates the standard deviation of the difference between the rates. The units are beats per minute.

Subject Number	0.5 m		1.0 m		1.5 m		2.0 m	
	mean	std dev						
0353	-0.439	0.267	-0.299	0.676	0.299	2.368	1.884	4.867
1315	4.706	1.996	7.53	2.746	10.027	4.3322	14.881	5.0618
1738	3.061	1.065	1.586	0.927	5.306	7.132	14.070	7.539
2469	-1.174	1.429	-1.018	1.495	1.277	5.236	1.175	6.093
1436	0.0159	0.172	-0.299	0.323	1.641	2.485	0.863	5.727
2393	0.480	1.039	-4.510	4.060	-2.221	4.866	-2.158	2.082
3343	-2.235	2.001	-0.549	1.628	0.904	3.224	1.958	6.066
3971	-0.399	0.463	-0.264	0.298	1.042	1.142	3.997	8.894
4062	0.030	0.292	2.610	2.195	0.821	1.9253	0.786	3.701
4665	0.453	0.246	0.216	1.508	16.382	11.02	6.376	8.000
4729	0.7296	0.7858	10.494	10.088	4.275	2.1082	26.882	8.622
4988	-0.207	3.888	-0.947	1.416	-6.633	6.599	-8.407	5.025
5617	3.541	1.492	1.906	3.274	7.034	7.246	12.636	5.538
6792	-1.938	1.169	-0.644	1.295	1.285	3.124	1.361	1.361
6238	-1.330	0.769	-0.973	1.111	-2.482	7.237	5.482	9.011
7371	0.323	1.574	6.861	5.499	14.162	7.395	15.547	3.076
7683	0.485	0.654	1.088	1.287	14.216	7.137	15.180	8.161
8497	1.666	4.632	-1.227	7.565	-0.096	3.713	5.640	9.194
8980	-0.592	2.049	-5.185	3.790	-7.028	4.563	-8.719	5.881
9674	-11.43	3.761	-5.179	4.140	-17.63	6.295	-5.382	4.746
9831	1.848	2.126	4.730	3.931	0.0387	1.155	3.492	3.349
9882	2.849	0.680	3.176	1.673	-6.196	4.272	3.583	3.317

6.4.2.2 Respiration

As it was for the heart data in the previous section, this section shows the Bland-Altman plots in Figures 6.18 to 6.21 for all respiration data collected at each range, and lists Bland-Altman statistics for this data in Table 6.3. Each plot includes 120 points per subject, indicating the rates calculated each 0.5 second for 60 seconds. Table 6.3 shown the

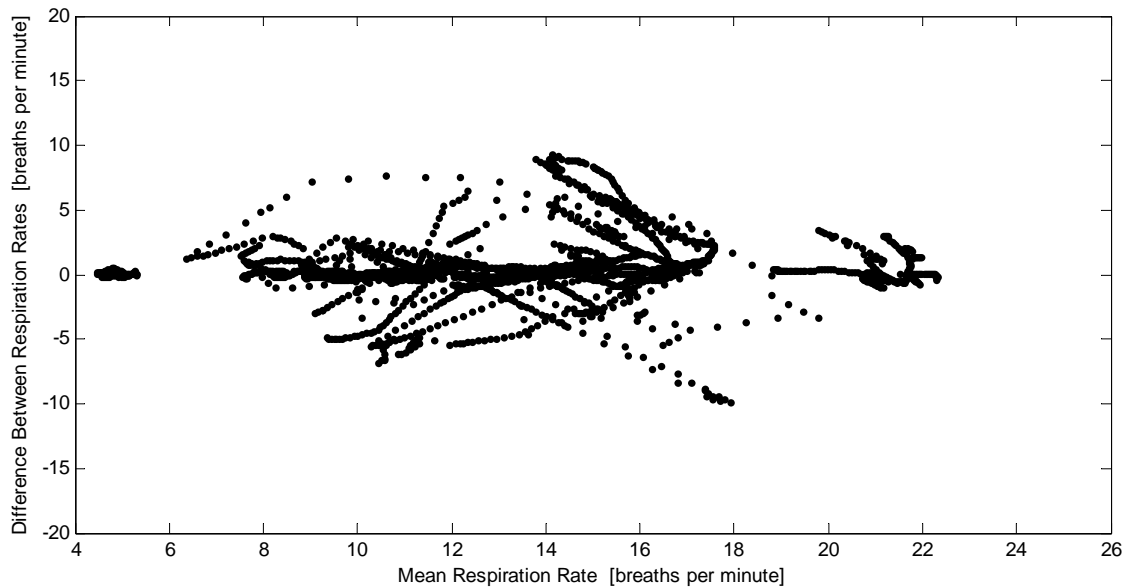


Figure 6.18. Bland-Altman plot of respiration rate measured with Doppler radar at 0.5 m range and respiratory effort belts for all subjects.

mean and standard deviation of the difference between the respiration rates found with the Doppler system and the respiratory effort belts.

At 0.5 m, the respiration rate measurements from the combined radar signal are between 4.75 breaths per minute above and -4.01 breaths per minute below the rate measured with the abdomen and chest straps with 95% confidence. The difference between respiration rates calculated with the combined radar signal and the abdomen and chest straps has a mean of 0.37 breaths per minute and a standard deviation of 2.23 breaths per minute.

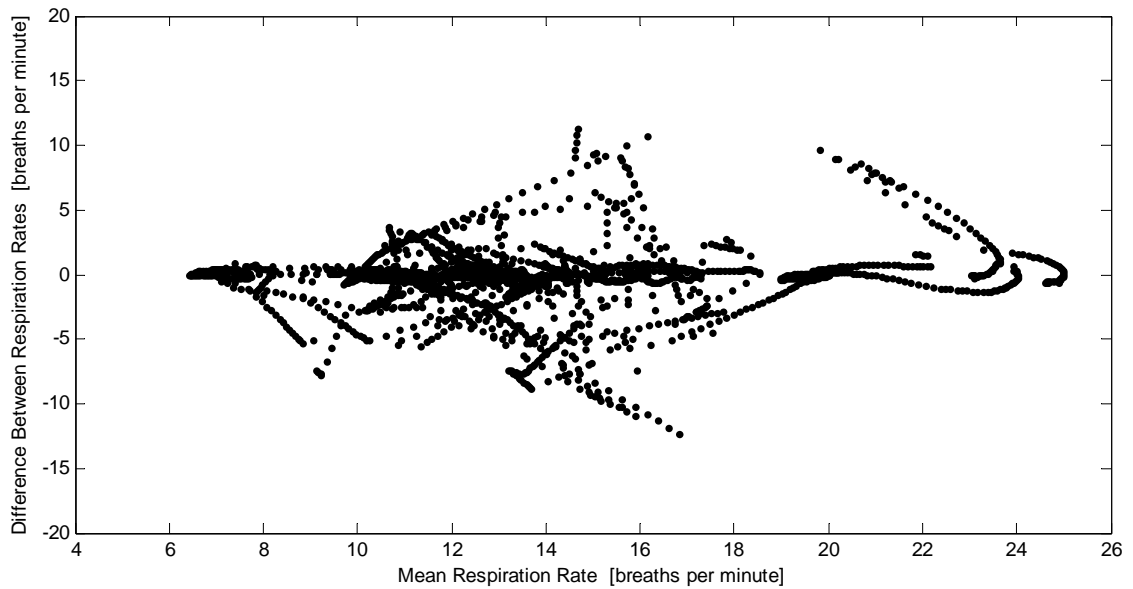


Figure 6.19. Bland-Altman plot of respiration rate measured with Doppler radar at 1.0 m range and respiratory effort belts for all subjects.

At 1.0 m, the respiration rate measurements from the combined radar signal are between 4.32 breaths per minute above and -4.78 breaths per minute below the rate measured with the abdomen and chest straps with 95% confidence. The difference between respiration rates calculated with the combined radar signal and the abdomen and chest straps has a mean of -0.23 breaths per minute and a standard deviation of 2.32 breaths per minute.

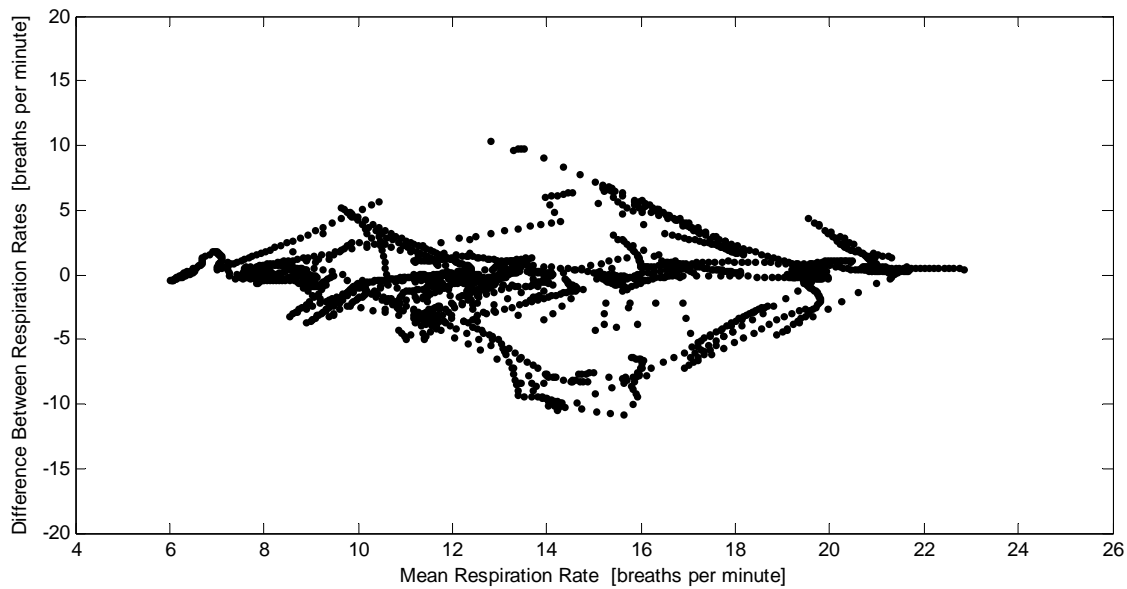


Figure 6.20. Bland-Altman plot of respiration rate measured with Doppler radar at 1.5 m range and respiratory effort belts for all subjects.

At 1.5 m, the respiration rate measurements from the combined radar signal are between 4.44 breaths per minute above and -5.06 breaths per minute below the rate measured with the abdomen and chest straps with 95% confidence. The difference between respiration rates calculated with the combined radar signal and the abdomen and chest straps has a mean of -0.31 breaths per minute and a standard deviation of 2.42 breaths per minute.

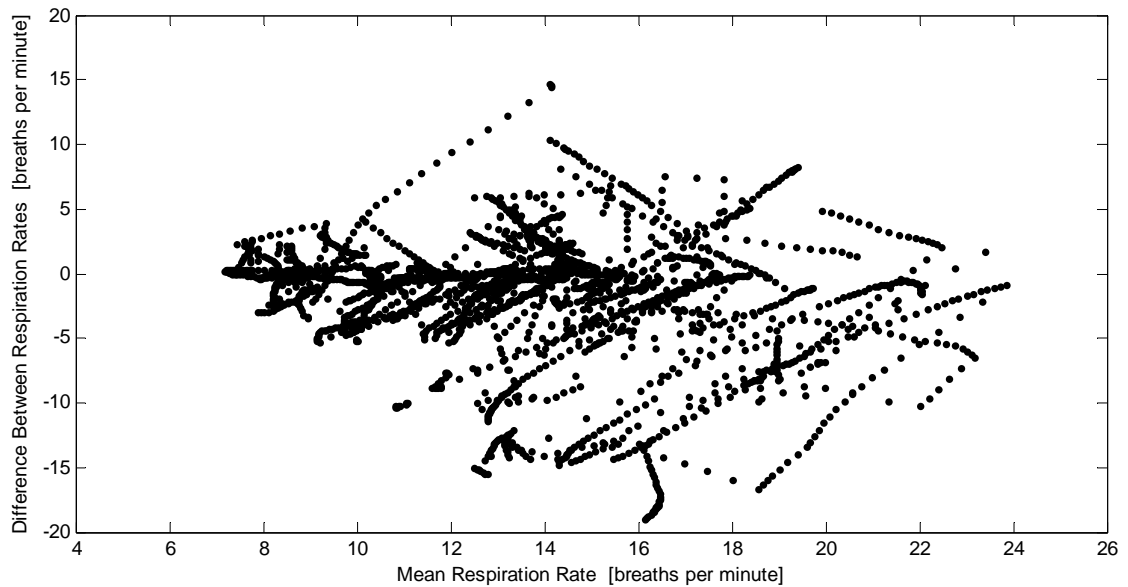


Figure 6.21. Bland-Altman plot of respiration rate measured with Doppler radar at 2.0 m range and respiratory effort belts for all subjects.

At 2.0 m, the respiration rate measurements from the combined radar signal are between 7.12 breaths per minute above and 10.53 breaths per minute below the rate measured with the abdomen and chest straps with 95% confidence. The difference between respiration rates calculated with the combined radar signal and the abdomen and chest straps has a mean of -1.70 breaths per minute and a standard deviation of 4.50 breaths per minute.

Table 6.3: Bland-Altman Data for Each Subject's Respiration Measurement. "Mean" indicates the mean of the difference between the respiration rate found with the Doppler system and that found with the respiratory effort belts. "Std dev" indicates the standard deviation of the difference between the rates. The units are breaths per minute.

Subject Number	0.5 m		1.0 m		1.5 m		2.0 m	
	mean	std dev						
0353	0.903	1.294	0.0159	0.673	1.134	0.950	-10.60	5.765
1315	4.073	1.741	-0.511	1.045	-2.085	2.253	-4.770	3.816
1738	-0.027	1.053	0.397	0.282	0.0320	0.362	-1.879	2.195
2469	1.2702	1.536	1.9721	1.524	1.6333	1.6606	5.2136	2.9964
1436	0.290	0.715	0.902	1.579	0.606	0.530	-0.389	1.793
2393	-1.283	1.837	-0.677	1.830	-1.450	1.601	-1.436	1.971
3343	5.171	3.117	-1.381	3.085	3.877	1.560	2.052	3.606
3971	-0.804	1.055	-0.180	0.374	-0.251	0.545	-1.920	1.883
4062	0.029	0.263	-0.720	1.769	-1.144	1.722	-0.306	3.354
4665	1.736	1.451	-0.071	0.551	-0.130	0.924	0.932	1.290
4729	0.340	0.409	0.0404	0.465	-0.324	0.894	-1.681	1.511
4988	0.266	0.430	0.155	0.377	0.770	0.887	1.773	3.643
5617	-0.050	0.206	-0.028	0.275	-1.130	0.994	-0.194	0.414
6792	0.050	0.149	0.039	0.191	-0.186	0.154	-0.045	0.414
6238	0.077	0.165	0.060	0.208	1.143	1.292	0.502	0.721
7371	-0.856	2.204	-0.832	1.735	-0.228	0.337	-0.435	0.545
7683	-0.050	0.231	0.330	0.920	-0.055	0.645	-2.213	1.440
8497	-1.997	2.706	1.123	4.374	1.391	2.662	-0.522	3.136
8980	0.728	0.761	-2.723	3.193	-3.490	3.469	1.898	7.739
9674	-0.051	0.333	1.966	2.923	0.862	0.581	-4.842	6.444
9831	0.213	0.494	0.602	0.995	-0.535	0.575	-0.698	0.925
9882	0.277	0.832	1.255	2.362	-0.015	0.286	1.025	2.428

6.4.3 Signal-to-Noise Ratio vs. Range

The signal-to-noise ratio was calculated for the heart and respiration traces for each subject at each range, and this data is shown in Table 6.4. The average signal-to-noise ratios at 0.5 m, 1.0 m, 1.5 m, and 2.0 m are shown for heart and respiration in Figure 6.22 and Figure 6.23, respectively.

Table 6.4: Doppler Signal-to-Noise Ratio for Each Subject's Heart and Respiration Measurements.

Subject Number	0.5 m		1.0 m		1.5 m		2.0 m	
	Heart	Resp	Heart	Resp	Heart	Resp	Heart	Resp
0353	0.94	20.00	0.91	12.91	0.18	6.95	0.16	0.34
1315	0.18	11.38	0.35	6.23	0.15	3.69	0.11	1.16
1738	1.07	2.87	0.58	4.83	0.09	2.48	0.09	0.58
2469	0.76	4.92	0.45	3.77	0.36	5.14	0.27	6.65
1436	1.79	47.55	0.75	7.87	0.21	15.24	0.19	4.89
2393	1.27	4.92	0.27	3.77	0.19	5.13	0.26	6.65
3343	0.83	2.59	0.39	1.48	0.28	1.37	0.11	1.40
3971	1.28	2.14	0.74	2.68	0.94	2.27	0.12	0.87
4062	2.88	21.15	0.61	4.20	0.47	5.08	0.33	2.68
4665	3.64	11.60	0.44	7.29	0.18	2.66	0.15	5.62
4729	0.86	7.37	0.20	7.88	0.19	5.81	0.07	2.42
4988	0.73	9.34	0.62	30.02	0.17	9.24	0.16	2.79
5617	0.41	29.16	0.26	16.68	0.05	4.02	0.18	18.65
6792	0.74	5.13	0.64	9.98	0.36	6.85	0.20	3.49
6238	0.89	29.16	0.44	16.68	0.12	1.30	0.20	18.65
7371	0.55	3.00	0.11	3.02	0.12	12.19	0.19	5.43
7683	0.81	15.6	0.54	12.97	0.17	6.65	0.09	2.95
8497	0.36	1.88	0.58	0.94	0.25	4.14	0.11	1.35
8980	0.48	2.88	0.32	0.89	0.17	0.73	0.15	0.55
9674	0.63	21.04	0.58	9.99	0.13	7.90	0.22	0.74
9831	0.60	1.83	0.17	7.02	0.31	3.54	0.19	3.06
9882	1.88	3.06	0.82	0.68	0.22	1.18	0.20	1.70
Average	1.07	11.75	0.49	7.81	0.24	5.16	0.17	4.21
Standard Deviation	0.83	11.93	0.22	6.92	0.18	3.64	0.06	5.07

The plots are shown with the theoretical signal-to-noise ratios calculated with equation (6.15) and displayed in Figure 6.1. Error bars represent the standard error, or the standard deviation divided by the square root of the number of data points. For the theoretical plots, the RCS-RMS motion product is 500 mm^4 for respiration and 2.25 mm^4 for the heart. The

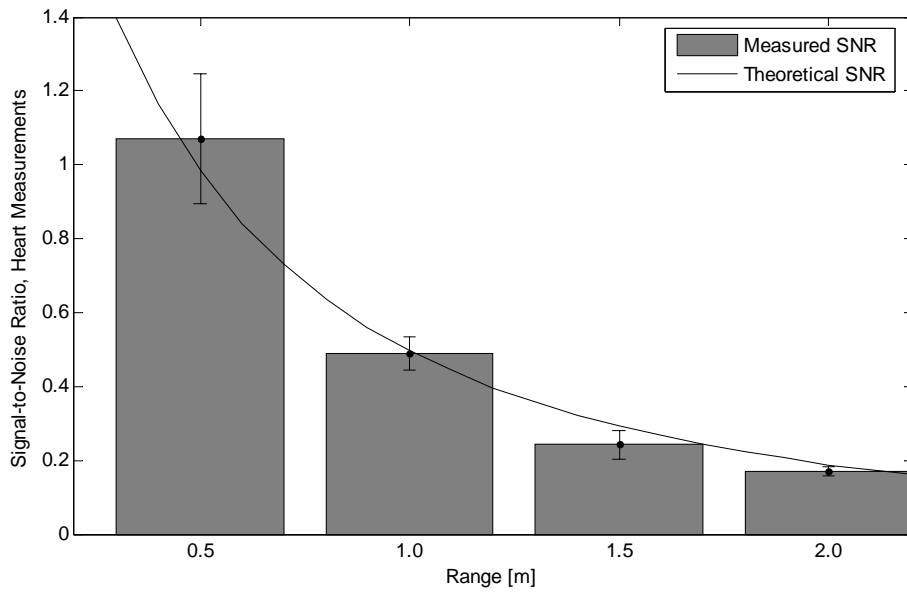


Figure 6.22. Measured and predicted signal-to-noise ratio vs. range for heart measurements.

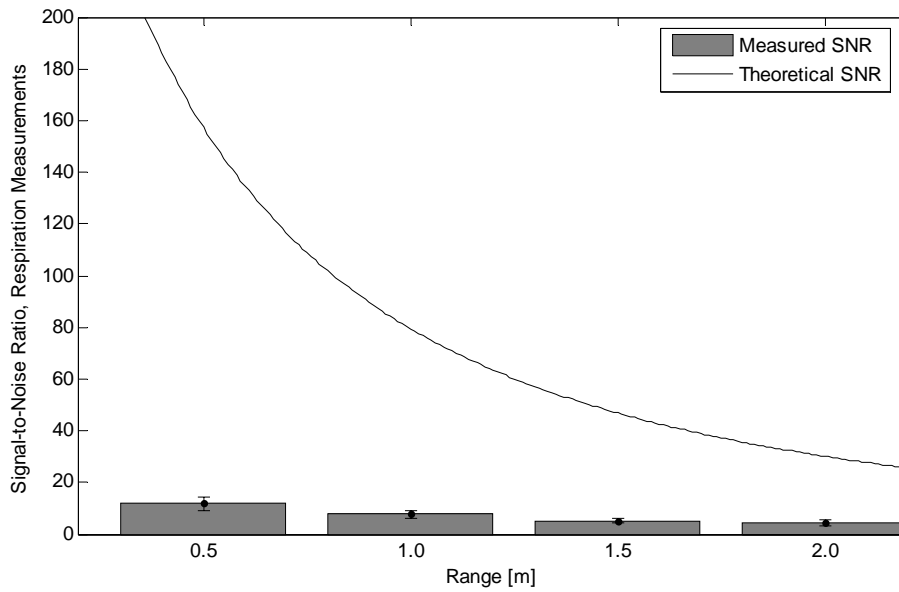


Figure 6.23. Measured and predicted signal-to-noise ratio vs. range for respiration measurements.

measured respiration SNR for does is far below the theoretical SNR. The best fit SNR will be shown in the discussion section.

6.4.4 Signal-to-Noise Ratio vs. Measured Parameters

6.4.4.1 SNR of Heart Measurements

The correlation coefficient was calculated between each measured parameter and the calculated heart SNR at each range. These values are displayed in Table 6.5. Since the values are linear and the radar cross section is an area, the correlation coefficient was also calculated between the products of the height and breadth or circumference parameters and the SNR at each range, as is also shown in Table 6.5. Also, for the same reason, correlation coefficients between the linear measurements and the square root of the heart SNR were calculated, and are shown in Table 6.6

Chest and waist circumference and chest breadth are significantly correlated with heart SNR only at the 2.0 m range. The correlation was higher when these variables were multiplied by the height. The only other significant correlations with heart SNR are age at 1.0 m range and chest depth at exhale with 0.5 m range. It is thought that a truly significant correlation between SNR and a parameter should occur at most or all ranges.

In this multiple regression analysis of age, height, and waist circumference, the models and their R^2 factors are as follows:

$$\text{SNR}(0.5 \text{ m}) = 3.00 + 0.0061 * \text{age} - 0.0098 * \text{height} - 0.0052 * \text{waist}; R^2 = 0.02$$

$$\text{SNR}(1.0 \text{ m}) = 0.51 - 0.0100 * \text{age} + 0.0019 * \text{height} - 0.0000 * \text{waist}; R^2 = 0.25$$

$$\text{SNR}(1.5 \text{ m}) = -0.64 - 0.0026 * \text{age} + 0.0085 * \text{height} - 0.0061 * \text{waist}; R^2 = 0.19$$

$$\text{SNR}(2.0 \text{ m}) = -0.36 - 0.0005 * \text{age} + 0.0022 * \text{height} + 0.0017 * \text{waist}; R^2 = 0.32$$

When scaled factors were regressed, the dominant variable was not consistent between the ranges.

Table 6.5: Statistical Correlation Between Physical Parameters and Doppler Heart Signal-to-Noise Ratios at the Different Ranges. The statistical correlation between the variables is the covariance of the two variables divided by the standard deviation of each variable. The measure 'r' is the correlation coefficient, and 'p' is the p-value for testing the hypothesis of no correlation. Each p-value is the probability of getting a correlation as large as the 'r' value randomly if the true correlation is zero. Correlations with p-values ≤ 0.10 , are in bold, indicating that there is at least 90% confidence in those correlations.

Parameter	Correlation between Heart SNR and Parameter							
	0.5 m		1.0 m		1.5 m		2.0 m	
	r	p	r	p	r	p	r	p
Age	0.02	0.94	-0.50	0.02	-0.16	0.47	0.14	0.53
BMI	-0.02	0.92	-0.11	0.62	-0.18	0.42	0.35	0.11
Height	-0.13	0.57	-0.09	0.69	0.15	0.51	0.50	0.02
Weight	-0.09	0.69	-0.13	0.56	-0.09	0.67	0.47	0.03
Chest Circumference, inhale	-0.13	0.55	-0.12	0.61	-0.21	0.35	0.51	0.02
Chest Circumference, exhale	-0.14	0.52	-0.12	0.61	-0.18	0.42	0.50	0.02
Waist Circumference, inhale	-0.11	0.62	-0.14	0.52	-0.23	0.31	0.50	0.02
Waist Circumference, exhale	-0.18	0.42	-0.13	0.57	-0.15	0.50	0.45	0.03
Chest Breadth, inhale	0.02	0.94	0.15	0.49	-0.05	0.82	0.60	0.00
Chest Breadth, exhale	-0.09	0.69	0.08	0.73	-0.05	0.83	0.61	0.00
Chest Depth, inhale	-0.34	0.13	-0.08	0.72	-0.26	0.24	0.31	0.16
Chest Depth, exhale	-0.40	0.06	-0.24	0.28	-0.19	0.38	0.29	0.19
Height x Chest Circumference, inhale	-0.15	0.50	-0.12	0.59	-0.13	0.56	0.54	0.01
Height x Chest Circumference, exhale	-0.16	0.48	-0.12	0.59	-0.11	0.62	0.54	0.01
Height x Waist Circumference, inhale	-0.13	0.54	-0.15	0.51	-0.16	0.48	0.53	0.01
Height x Waist Circumference, exhale	-0.19	0.39	-0.13	0.55	-0.10	0.66	0.49	0.02
Height x Chest Breadth, inhale	-0.04	0.85	0.07	0.74	0.00	0.99	0.60	0.00
Height x Chest Breadth, exhale	-0.12	0.60	0.02	0.93	0.00	0.99	0.61	0.00

Table 6.6: Statistical Correlation Between Physical Parameters and the Square Root of Doppler Heart Signal-to-Noise Ratios at the Different Ranges. The statistical correlation between the variables is the covariance of the two variables divided by the standard deviation of each variable. The measure 'r' is the correlation coefficient, and 'p' is the p-value for testing the hypothesis of no correlation. Each p-value is the probability of getting a correlation as large as the 'r' value randomly if the true correlation is zero. Correlations with p-values ≤ 0.10 , are in bold, indicating that there is at least 90% confidence in those correlations.

Parameter	Correlation between square root of Heart SNR and Parameter							
	0.5 m		1.0 m		1.5 m		2.0 m	
	r	p	r	p	r	p	r	p
Age	-0.01	0.97	-0.54	0.01	-0.16	0.49	0.17	0.45
BMI	-0.02	0.92	-0.11	0.62	-0.18	0.42	0.35	0.11
Height	-0.13	0.57	-0.09	0.69	0.15	0.51	0.50	0.02
Weight	-0.09	0.69	-0.13	0.56	-0.09	0.67	0.47	0.03
Chest Circumference, inhale	-0.11	0.62	-0.16	0.48	-0.20	0.37	0.52	0.01
Chest Circumference, exhale	-0.12	0.60	-0.16	0.49	-0.18	0.44	0.50	0.02
Waist Circumference, inhale	-0.18	0.42	-0.22	0.32	-0.22	0.32	0.50	0.02
Waist Circumference, exhale	-0.18	0.42	-0.16	0.47	-0.15	0.52	0.45	0.04
Chest Breadth, inhale	0.02	0.94	0.15	0.49	-0.05	0.82	0.60	0.00
Chest Breadth, exhale	-0.08	0.71	0.05	0.81	-0.05	0.81	0.65	0.00
Chest Depth, inhale	-0.34	0.13	-0.08	0.72	-0.26	0.24	0.31	0.16
Chest Depth, exhale	-0.40	0.06	-0.24	0.28	-0.19	0.38	0.29	0.19

6.4.4.2 SNR of Respiration Measurements

The correlation coefficient was calculated between each measured parameter and the calculated heart SNR at each range. These values are displayed in Table 6.7. Since the values are linear and the radar cross section is an area, the correlation coefficient was also calculated between products of the height and breadth or circumference parameters and the SNR at each range, as is also shown in Table 6.7. Also, for the same reason, correlation coefficients between the linear measurements and the square root of the heart SNR are calculated, and shown in Table 6.8

Respiration SNR is positively correlated with all the size-related variables. Chest circumference, waist circumference, and chest depth at inhale had statistically significant correlations with respiration SNR at 0.5 m, 1.0 m, and 1.5 m ranges. Chest circumference and chest depth at exhale had statistically significant correlations with respiration SNR at 1.0 m and 1.5 m ranges. BMI, weight, waist circumference at exhale, chest breadth and inhale and exhale had statistically significant correlations at 1.0 m only. Age had a statistically significant correlation at 1.5 m only. When the breadth and circumference parameters were multiplied by the height to estimate the chest area, the correlations between the parameters decreased from when the parameters were not multiplied by the height. However, the height-waist circumference product had significant correlation at 0.5 m, 1.0 m, and 1.5 m. When the linear measurements were compared with the square root of the SNR, the correlation coefficients were higher. No statistically significant correlations were found for respiration SNR at the 2.0 m range.

Scattergrams with linear regression for each range are shown with grouped bar graphs of the same data in Figures 6.24 to 6.27 for chest circumference, waist circumference, chest depth, and the waist circumference-height product. The trends may be more readily visible in grouped bar plots, so these are shown in addition to scattergrams.

In this multiple regression analysis of age, height, and waist circumference, the models found and their R^2 factors are as follows:

$$\text{SNR}(0.5 \text{ m}) = -8.56 - 0.41 * \text{age} - 0.062 * \text{height} + 0.53 * \text{waist}; R^2 = 0.30$$

$$\text{SNR}(1.0 \text{ m}) = -11.37 + 0.07 * \text{age} - 0.007 * \text{height} + 0.21 * \text{waist}; R^2 = 0.19$$

$$\text{SNR}(1.5 \text{ m}) = -5.21 + 0.08 * \text{age} - 0.007 * \text{height} + 0.11 * \text{waist}; R^2 = 0.25$$

$$\text{SNR}(2.0 \text{ m}) = -23.1 + 0.0003 * \text{age} + 0.1417 * \text{height} + 0.0315 * \text{waist}; R^2 = 0.10$$

When scaled versions of the parameters were used, the waist circumference was the primary factor and age the secondary factor at 0.5, 1.0, and 1.5 m. At 2.0 m, height was most important, followed by waist circumference. Waist circumference had a positive value for all ranges.

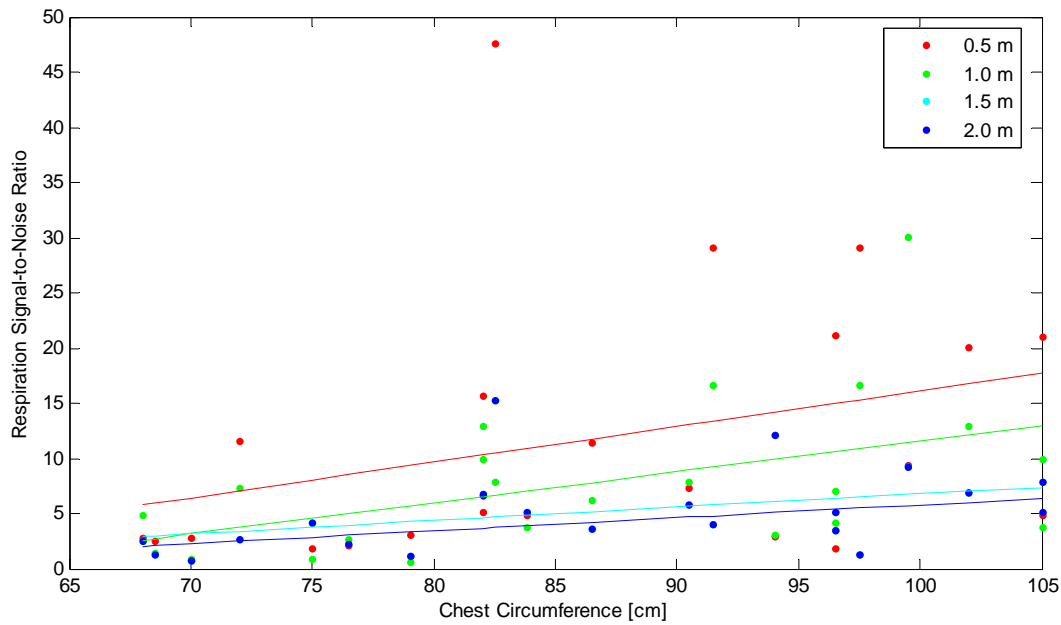
A grouped bar graph showing the variation of SNR with gender is shown in Figure 6.28. There is a statistically significant difference between the two groups, but this was primarily due to statistically significant size differences between the groups.

Table 6.7: Statistical Correlation Between Physical Parameters and Doppler Respiration Signal-to-Noise Ratios at the Different Ranges. The statistical correlation between the variables is the covariance of the two variables divided by the standard deviation of each variable. The measure 'r' is the correlation coefficient, and 'p' is the p-value for testing the hypothesis of no correlation. Each p-value is the probability of getting a correlation as large as the 'r' value randomly if the true correlation is zero. Correlations with p-values ≤ 0.10 , are in bold, indicating that there is at least 90% confidence in those correlations.

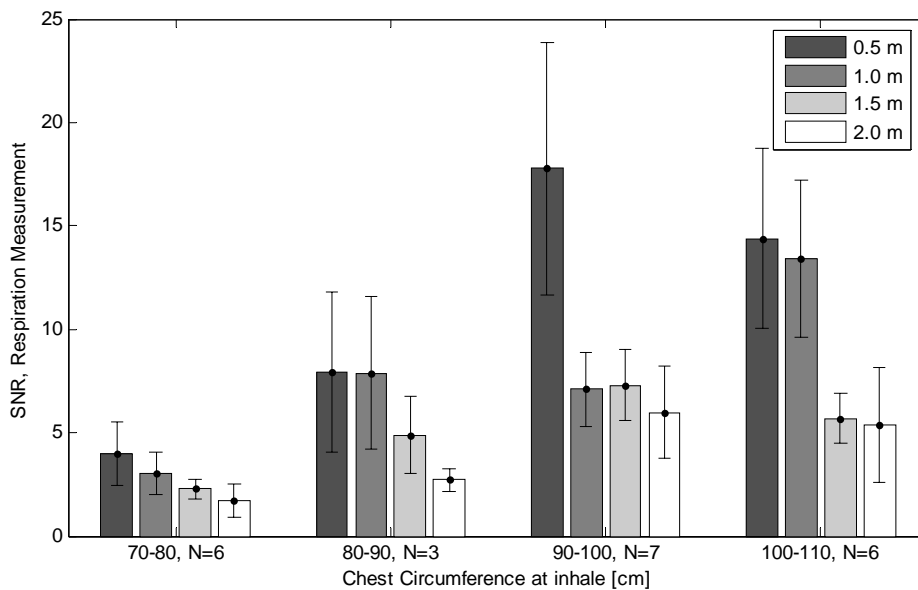
Parameter	Correlation between Respiration SNR and Parameter							
	0.5 m		1.0 m		1.5 m		2.0 m	
	r	p	r	p	r	p	r	p
Age	-0.20	0.37	0.25	0.26	0.36	0.10	0.12	0.60
BMI	0.26	0.24	0.40	0.07	0.29	0.20	0.09	0.69
Height	0.15	0.52	0.25	0.26	0.27	0.22	0.31	0.16
Weight	0.24	0.28	0.39	0.07	0.31	0.16	0.20	0.36
Chest Circumference, inhale	0.36	0.10	0.53	0.01	0.48	0.02	0.28	0.21
Chest Circumference, exhale	0.32	0.14	0.49	0.02	0.40	0.07	0.28	0.22
Waist Circumference, inhale	0.40	0.06	0.43	0.05	0.44	0.04	0.23	0.30
Waist Circumference, exhale	0.23	0.31	0.44	0.04	0.27	0.22	0.21	0.35
Chest Breadth, inhale	0.30	0.17	0.44	0.04	0.26	0.24	0.20	0.37
Chest Breadth, exhale	0.24	0.27	0.40	0.07	0.19	0.49	0.21	0.36
Chest Depth, inhale	0.40	0.07	0.55	0.01	0.67	0.00	0.23	0.30
Chest Depth, exhale	0.20	0.37	0.42	0.05	0.53	0.01	0.19	0.41
Height x Chest Circumference, inhale	0.31	0.15	0.49	0.02	0.44	0.04	0.31	0.16
Height x Chest Circumference, exhale	0.29	0.19	0.45	0.03	0.38	0.07	0.31	0.16
Height x Waist Circumference, inhale	0.36	0.10	0.42	0.05	0.43	0.05	0.27	0.21
Height x Waist Circumference, exhale	0.22	0.33	0.42	0.05	0.28	0.20	0.25	0.26
Height x Chest Breadth, inhale	0.27	0.23	0.40	0.06	0.28	0.21	0.25	0.26
Height x Chest Breadth, exhale	0.22	0.31	0.38	0.08	0.22	0.31	0.25	0.25

Table 6.8: Statistical Correlation Between Physical Parameters and the Square Root of Doppler Respiration Signal-to-Noise Ratios at the Different Ranges. The statistical correlation between the variables is the covariance of the two variables divided by the standard deviation of each variable. The measure 'r' is the correlation coefficient, and 'p' is the p-value for testing the hypothesis of no correlation. Each p-value is the probability of getting a correlation as large as the 'r' value randomly if the true correlation is zero. Correlations with p-values ≤ 0.10 , are in bold, indicating that there is at least 90% confidence in those correlations.

Parameter	Correlation between square root of Respiration SNR and Parameter							
	0.5 m		1.0 m		1.5 m		2.0 m	
	r	p	r	p	r	p	r	p
Age	-0.17	0.44	0.23	0.30	0.36	0.10	0.24	0.28
BMI	0.26	0.24	0.40	0.07	0.28	0.20	0.09	0.69
Height	0.15	0.52	0.25	0.26	0.27	0.22	0.31	0.16
Weight	0.24	0.28	0.39	0.07	0.31	0.16	0.20	0.37
Chest Circumference, inhale	0.42	0.05	0.57	0.01	0.54	0.01	0.31	0.16
Chest Circumference, exhale	0.40	0.07	0.54	0.01	0.47	0.03	0.29	0.20
Waist Circumference, inhale	0.45	0.03	0.46	0.03	0.47	0.03	0.23	0.30
Waist Circumference, exhale	0.32	0.15	0.28	0.02	0.36	0.10	0.19	0.40
Chest Breadth, inhale	0.30	0.17	0.44	0.04	0.26	0.24	0.20	0.37
Chest Breadth, exhale	0.30	0.17	0.39	0.07	0.23	0.31	0.18	0.43
Chest Depth, inhale	0.40	0.07	0.55	0.01	0.67	0.00	0.23	0.30
Chest Depth, exhale	0.20	0.37	0.42	0.05	0.52	0.01	0.19	0.41



a



b

Figure 6.24. a) Scattergram of signal-to-noise ratio vs. chest circumference with a linear regression model for each range. The model for 0.5 m is: $SNR = -16 + 32c$ with R^2 of 0.13. The model for 1.0 m is: $SNR = -17 + 28c$ with R^2 of 0.28. The model for 1.5 m is $SNR = -5.3 + 12c$ with R^2 of 0.22. The model for 2.0 m is: $SNR = -5.9 + 11c$ with R^2 of 0.078. (SNR indicates the signal-to-noise ratio and c indicates the circumference in centimeters.) The chest circumference was measured at a full inhale. b) Grouped bar graph for the same data.

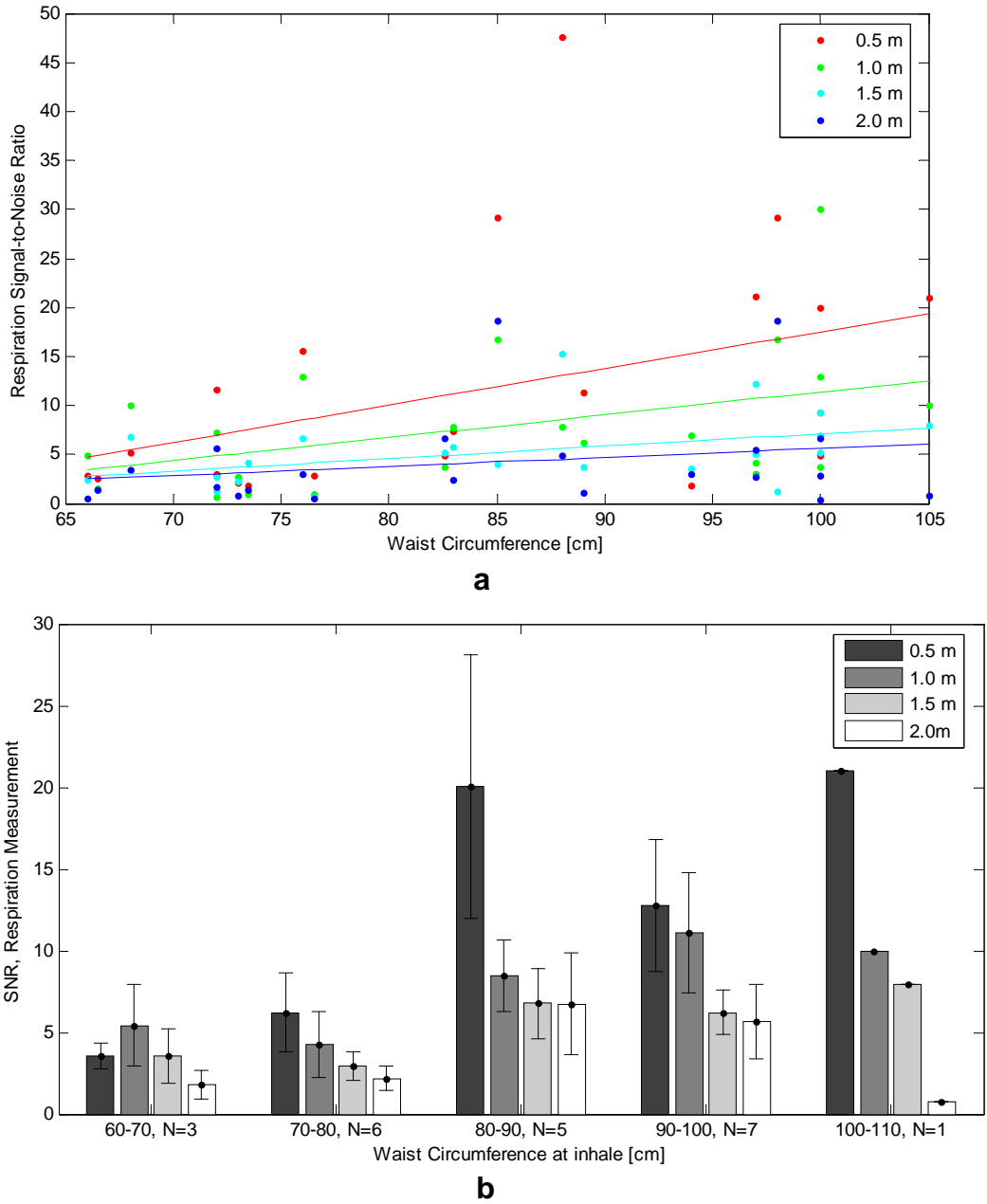
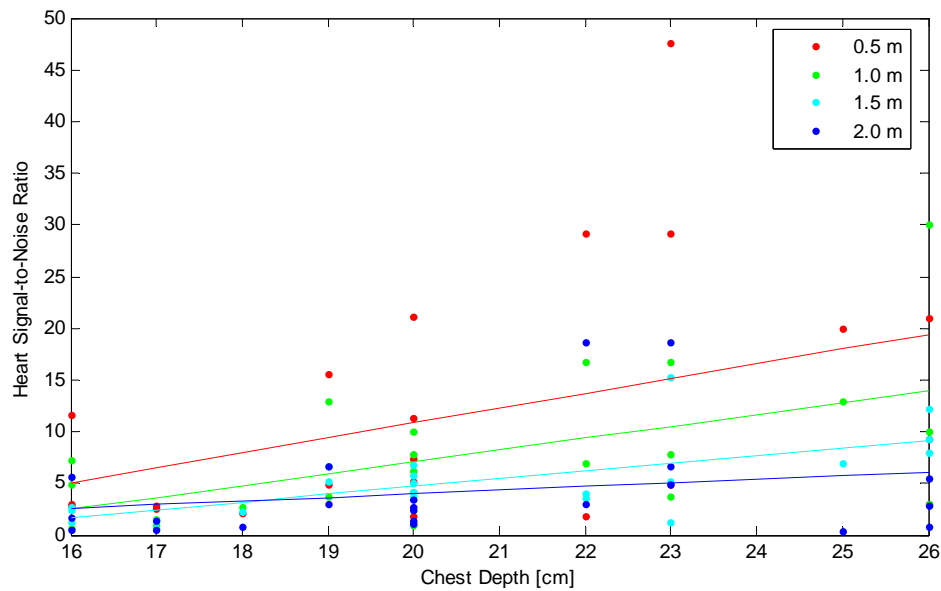
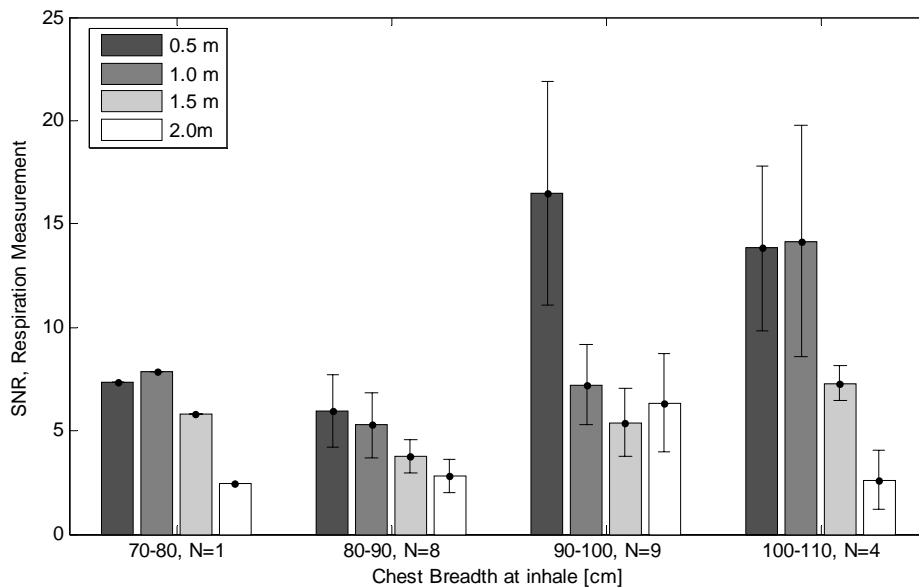


Figure 6.25. a) Scattergram of signal-to-noise ratio vs. waist circumference with a linear regression model for each range. The model for 0.5 m is: $SNR = -20 + 0.38c$ with R^2 of 0.16. The model for 1.0 m is: $SNR = -12 + 0.23c$ with R^2 of 0.18. The model for 1.5 m is $SNR = -5.6 + 0.13c$ with R^2 of 0.20. The model for 2.0 m is: $SNR = -3.6 + 0.092c$ with R^2 of 0.05. (SNR indicates the signal-to-noise ratio and c indicates the circumference in centimeters.) The waist circumference was measured at a full inhale. b) Grouped bar graph for the same data.

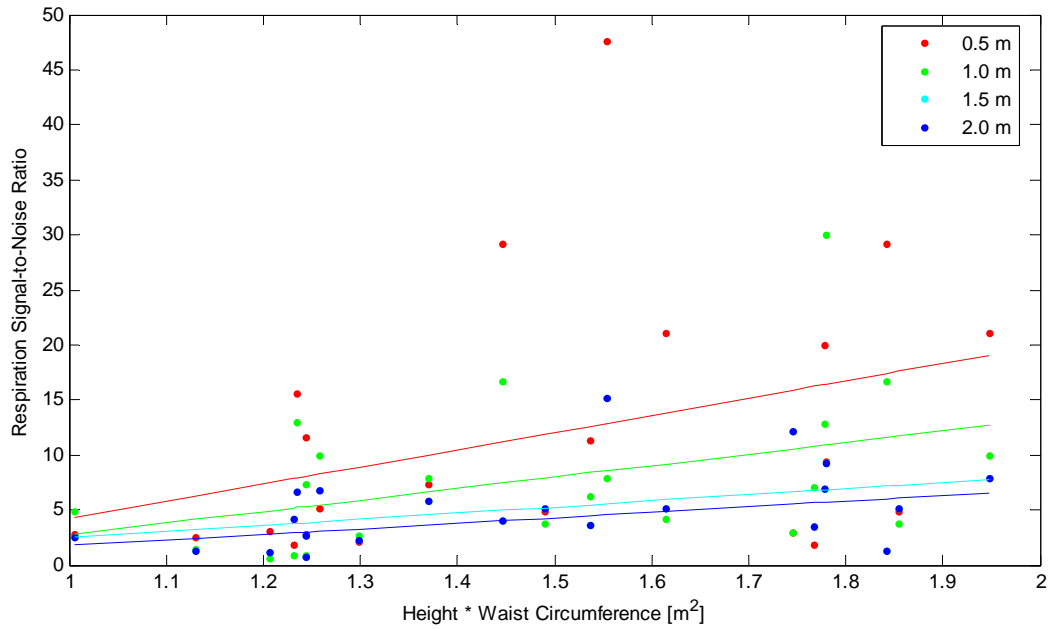


a

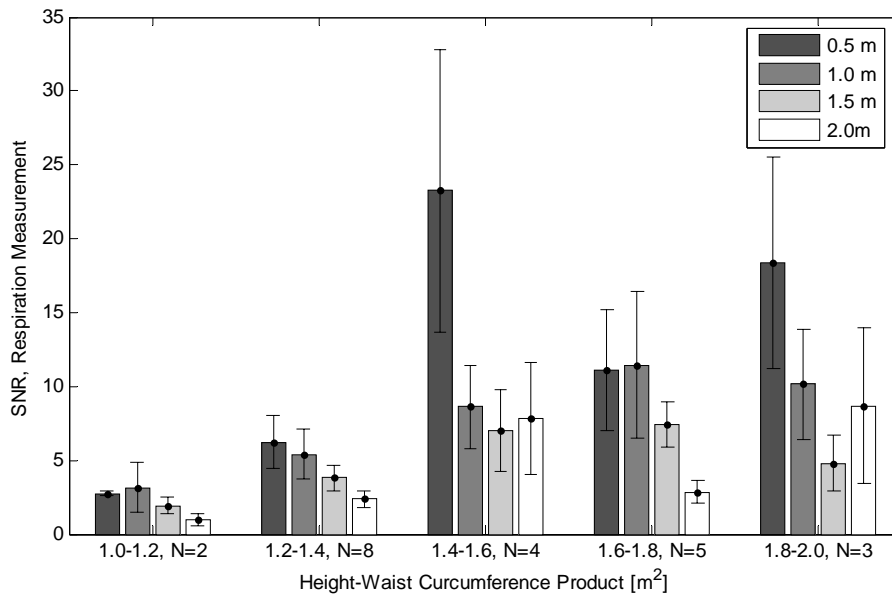


b

Figure 6.26. a) Scattergram of signal-to-noise ratio vs. chest depth with a linear regression model for each range. The model for 0.5 m is: $SNR = -17.83 + 1.43d$ with R^2 of 0.15. The model for 1.0 m is: $SNR = -15.87 + 1.15d$ with R^2 of 0.30. The model for 1.5 m is $SNR = -10.08 + 0.74d$ with R^2 of 0.45. The model for 2.0 m is: $SNR = -3.08 + 0.35d$ with R^2 of 0.053. (SNR indicates the signal-to-noise ratio and d indicates the chest depth in centimeters.) The chest depth was measured at a full inhale. b) Grouped bar graph for the same data.



a



b

Figure 6.27. a) Scattergram of signal-to-noise ratio vs. height-waist circumference product with a linear regression model for each range. The model for 0.5 m is: $SNR = -11 + 16x$ with R^2 of 0.13. The model for 1.0 m is: $SNR = -7.7 + 10x$ with R^2 of 0.17. The model for 1.5 m is $SNR = -3.2 + 5.6x$ with R^2 of 0.18. The model for 2.0 m is: $SNR = -3.2 + 5.1x$ with R^2 of 0.08. (SNR indicates the signal-to-noise ratio and x indicates the height-waist circumference produce in square meters.) The waist circumference was measured at inhale. b) Grouped bar graph for the same data.

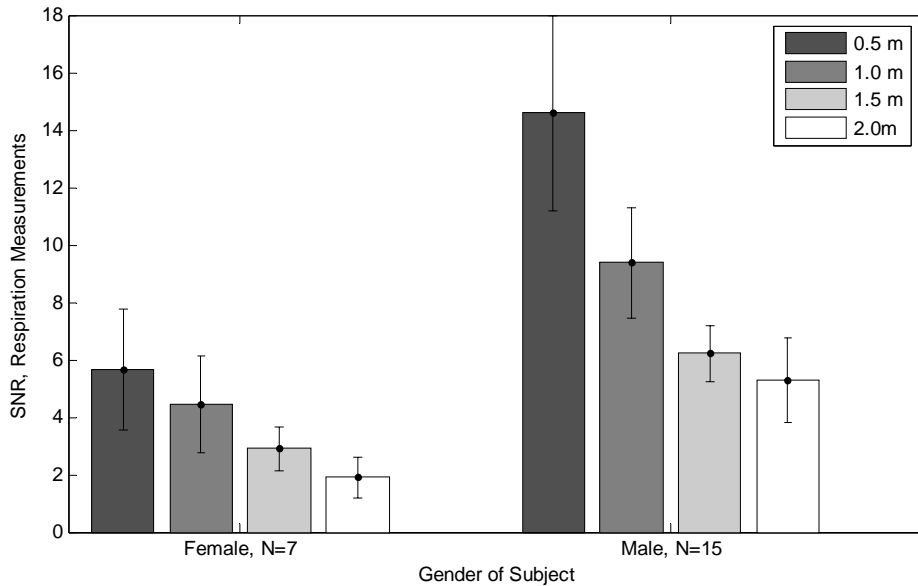


Figure 6.28. Variation of respiration signal-to-noise ratio with gender.

6.5 Discussion

6.5.1 Overall Heart and Respiration Rate Measurement Performance

The agreement between methods needs to be analyzed in the context of the application; how different the outputs of the two methods can be without causing difficulties is very application dependent. If the Doppler monitor is simply used to determine whether the subject has a normal or abnormal heart rate, a 5-10 beat per minute difference between that method and the electrocardiogram may not be problematic. However, if metabolic rate were being measured, the heart rate measured with the Doppler radar may need to be within one beat per minute of the rate measured with the electrocardiogram. Similarly, for the respiration, if only normal breathing rate vs. an abnormal breathing rate or breathing vs. not breathing is being measured, a 5 breath-per-minute error in the rate would be acceptable.

With the accuracy measured in this application, the current Doppler radar system could be used in applications where a normal vs. abnormal heart rate needs to be detected at ranges up to 1.0 m, but it is not sufficiently reliable for heart rate measurements at ranges beyond one meter. The respiration is reliable to 1.5 m, and becomes less reliable at 2.0 m.

The error was plotted vs. the SNR for all measurements in Figure 6.29. When the SNR is plotted in dB, there is an approximately linear relationship, so the accuracy is proportional to the log of the SNR. The model for heart accounts for 59% of the variation in heart, and the model for respiration accounts for 42% of the variation in respiration. This indicates that the SNR does affect the ability to detect heart and respiration rates. The accuracy was sometimes very good with an SNR as low as -1dB, but it was not consistently good until the SNR was greater than 10 dB. This indicates that improvements in the SNR will improve the accuracy for rate-finding. This also indicates that with better signal processing, the accuracy could be improved for signals with SNR as low as -1 dB.

Some subjects were less still than others, either fidgeting or twitching, and the detected motion interfered with the extraction of the heart and respiration rates. Subjects 4988, 8497, and 8980 had motion noted by the experiment administrator. This most likely further decreased the accuracy of these measurements.

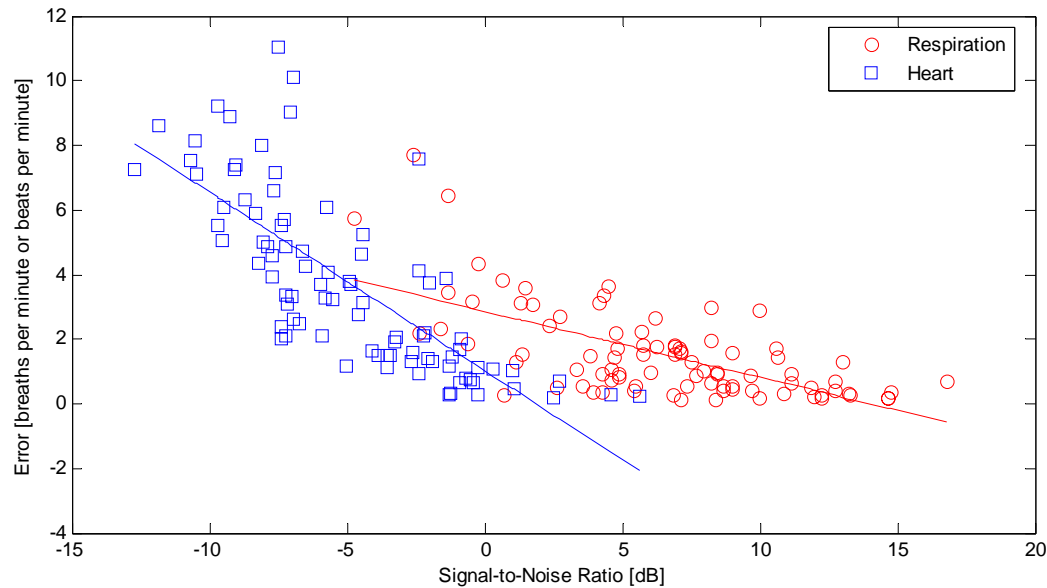


Figure 6.29. Scattergram of error vs. signal-to-noise ratio for heart and respiration. The error is defined as the standard deviation of the difference between the two measurements, and the signal-to-noise ratio is measured on the Doppler signal as described in Section 6.3.4.2. A linear regression is performed on the data; the model for the heart is $E=1.03 - 0.55 \cdot \text{SNR}$, with R^2 of 0.59. Model for respiration is $E= 2.86 - 0.20 \cdot \text{SNR}$, with R^2 of 0.42. In these models, E is the error and SNR is the measured signal-to-noise ratio.

6.5.2 Heart Signal-to-Noise Ratio - Discussion

Significant variation of the signal-to-noise ratio of the heart signal with any of the measured parameters was not detected. It was expected that age or BMI could affect the heart signal, as arterial compliance decreases with increasing age, and fat could attenuate the signal. However, no significant correlations between the heart signal-to-noise ratio and either BMI or age were seen. The only statistically significant correlation was between age and heart SNR at 1.0 m, but since significant correlation was not seen at the other ranges and because the sign of the correlation coefficient was not consistent at all ranges, age is not considered to be significantly correlated in general with heart SNR.

6.5.3 Respiration Signal-to-Noise Ratio - Discussion

Respiration was not expected to be significantly affected by age or by the body mass index, except as much as a larger body mass index leads to an increase in chest dimensions. There was significant variation with gender, as shown in Figure 6.28, but this variation could not be separated from that due to variations in thorax dimensions that are correlated with gender.

If the radar cross section-mean-squared motion product is set at 100 mm^4 to fit the data as closely as possible, the theoretical SNR is within the error bars from 1.0 m to 2.0 m, but not at 0.5 m, as shown in Figure 6.30. This indicates that the signal is behaving differently at close ranges than at long ranges, likely due to near-field effects. The SNR theory, based on the radar equation, assumes that the subject is in the far-field, or that the waves are planar when they reflect off the subject. However, this is not the case for respiration at 50 cm. The effects of near-field are discussed in Section 6.5.5. The best-fit radar cross section-mean-squared motion product of 100 mm^4 is only 44 times the heart RCS-RMS motion product. It was expected that this value would be about 1000 times, as the amount of motion from respiration was expected to be about 10 times greater than that for the heart, and the radar cross section for respiration was expected to be at least 10 times greater than that for the heart. The SNR is proportional to this value; the SNR for respiration was only about 10 times that of the SNR for heart, but it was expected to be at least 100 times the SNR for the heart. (A broader filter is used for respiration than for the heart, so there is more residual phase noise on the respiration signal than on the heart signal.)

One explanation is that some of the respiration signal may be cut out by the dc blocking filter, decreasing the respiration signal more than the heart signal. There was not a significant correlation between the SNR and the respiration rate. However, this dc-blocking filter has a 0.2-Hz cutoff - this corresponds to a 12 respirations per minute rate, and 9 of 22 the subjects had respiration rates at or below 12 respirations per minute. If the filter's attenuation of these signals is corrected for by dividing the SNR by the gain of the filter, as

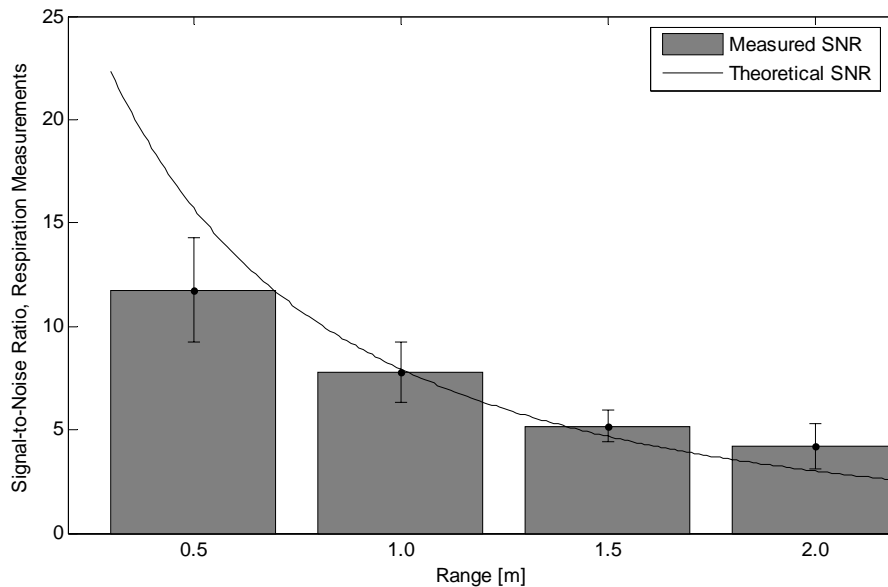


Figure 6.30. Respiration signal-to-noise ratio vs. range, with measured SNR and the theoretical SNR. The theoretical radar cross section-mean-squared motion product was decreased to a value of 100 mm^4 to match the data as closely as possible.

given in Appendix E, the average respiration SNR is increased by a factor of 2.5. This SNR plot is shown in Figure 6.31. Here, the best -fit value of the RCS-RMS motion is 250 mm^4 , 110 times that of the heart signal. The SNR at this point is about 30 times that of the heart signal.,

There are several additional potential explanations for the lower than expected ratio of respiration SNR to heart SNR. The respiratory effort belts that were used as the control were no more accurate than the Doppler measurement, so determining the signal frequency from the straps may be misleading. Second, it is possible that the respiratory effort straps may inhibit respiration, decreasing the total motion due to respiration and therefore the SNR, or that the subjects change their breathing pattern because they know that they're being measured [185]. Third, the frequency window used for the signal was 12 breaths per minute compared to a 20 beat-per-minute window for the heart, so slightly more noise bandwidth was included in the respiration measurements, which should decrease the SNR slightly. Fourth, only the fundamental signal is included in the signal portion of the measurement, and the harmonics are included in the noise. If the respiration signal has a

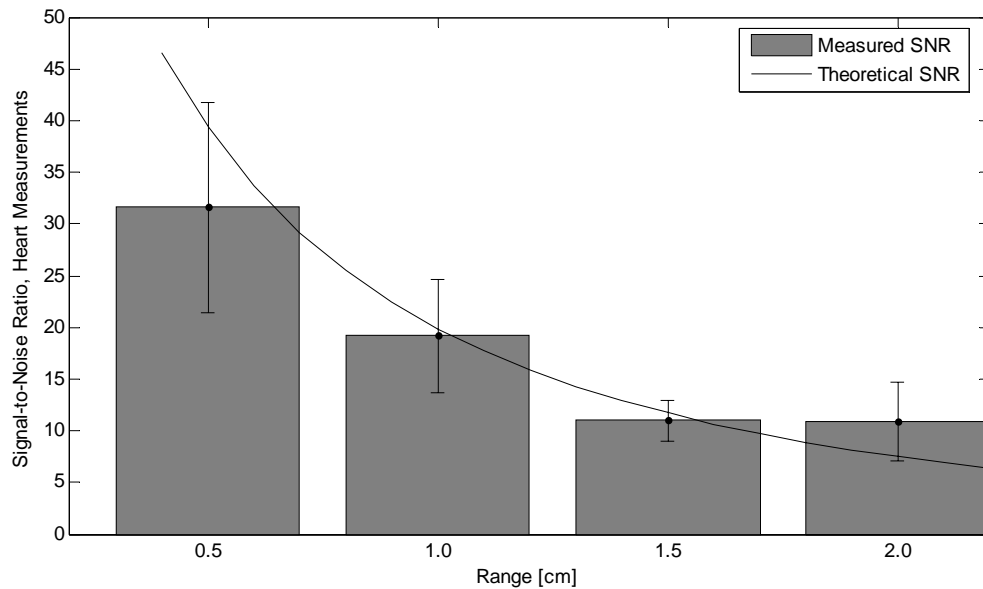


Figure 6.31. Respiration signal-to-noise ratio vs. range, with measured SNR, corrected for dc-blocking filter attenuation, and the theoretical SNR. The theoretical radar cross section-mean-squared motion product was set to a value of 250 mm^4 to match the data as closely as possible.

higher percentage of its energy in the harmonics than the heart does, this would degrade its SNR as measured for this experiment. Fifth, the heart signal is still present in the respiration measurements, so it contributes to the noise in the measurement. Sixth, if superficial pulses play a larger part in the detected motion than was expected, the signal could be over a larger area than expected. Seventh, the directivity may not be the same for the heart and respiration motion. If the directivity of the heart signals was significantly better than the respiration signals, the received heart signal power would be greater. It is also possible that the reflection at the superficial pulse sites is greater because the skin is over a blood-filled artery rather than over bone.

6.5.4 Variation of Signal-to-Noise Ratio with Range

6.5.4.1 Dominant Noise Source

If residual phase noise is dominant, the SNR is expected to be proportional to $(R + 0.75)^2 / R^4$, and if one of the other noise sources was dominant, the SNR is expected

to be proportional to $1/R^4$. The heart and respiration signal-to-noise ratio vs. range data shown in Figure 6.22 and Figure 6.30 matches much more closely with the residual phase noise model than the other noise source model, as was predicted.

6.5.4.2 Effects of Changes in the Radar Cross Section

The correlation coefficients are slightly higher when the linear measurements are compared with the square root of the SNR rather than with the SNR. This indicates that the total chest area is a factor in the radar cross sectional area for respiration, but it does not seem to be the only factor since the correlation coefficients are not above 0.6 and there is variation due to other sources. The SNR does increase with body size at all ranges. Many factors affect the SNR, so correlation coefficients near one were not expected. For example, an increase in chest area will not necessarily cause a directly proportional increase in the area that moves due to respiration. Also, the amount of motion may vary between individuals in a manner that is not proportional to chest area. Many factors other than the body size affect the SNR measured on an individual, including physiological differences, so a direct linear correlation is not expected.

6.5.5 Near-Field Antenna Effects

Figure 6.30 indicates that the respiration signal-to-noise ratio is not directly proportional to $(R + 0.75)^2/R^4$ as was predicted. Since the proportionality seems to be varying with range, and it affects the respiration signal and not the heart signal, it is expected that it is caused by antenna near-field effects. When a target is too close to the radar transmit and receive antenna, the power density does not fall off as $1/R^2$ and the antenna pattern varies with the range from the antenna, so that the antenna gain will be different from the specified far-field antenna pattern. This region is known as the near-field.

There are three regions of antenna patterns. The reactive near field is very close to the antenna; in this region the reactive components are large compared to the radiative components. The radiating near field is the intermediate area, where the radiation pattern depends on both distance and angle; this is the region that will be called the “near-field” in

this section. In the radiating far field, the relative amplitude and phase of components from different parts of the antenna does not vary with distance, and the field strength decays monotonically, inversely dependent on distance [194].

In the far-field region, the wave-front can be considered planar, and the rays are approximately parallel. In the near field the planar, parallel-ray approximation breaks down. The error in assuming the antenna is in far field is approximately [184]:

$$\varepsilon = \frac{D^2}{8R}, \quad (6.19)$$

where D is the largest dimension of the antenna or the target. and R is the range to the target. The radar equation, Equation 6.5, assumes far-field, so it is important to know how significant the error is. It is estimated that the far field starts when the range is greater than

$$R_{far-field} = \frac{2D^2}{\lambda}, \quad (6.20)$$

where D is the maximum dimension of the antenna or the scatterer, and λ is the wavelength. At this distance, the difference in the path length is $\lambda/16$; corresponding to a phase difference of 22.5 degrees.

At a range of 50 cm and a wavelength of 12.5 cm, the maximum target or antenna dimension using (6.20) is 17.7 cm. The smallest chest breadth of the 22 subjects in this study was 22 cm, and the average was 27 cm. Because Doppler radar measurement of heart and respiration rates measures only the moving part of the body, near-field considerations need to take into account the portion of the body that is moving. The area moving due to the heart beat and pulse is small compared to the range, while the area moving due to respiration may be large compared to the range in some cases.

The chest breadth of subjects ranged from 20 to 36 cm, and the average chest breadth at exhale was 27 cm. If the illumination at the chest is approximately a plane wave, the reflection off the chest can be assumed to be approximately uniform. If the reflection of the chest is uniform, Hansen's calculation of the E-field for a uniformly illuminated circular aperture can be used to estimate the near-field effects [186]. The electric field at a

distance R for a uniform circular aperture, at an angle θ from the axis, and a radius of length a , is:

$$E \approx \frac{-j\eta \cos\theta \cos\phi \exp\left(\frac{jka^2}{R}\right) \left[U_1\left(\frac{ka^2}{2R}, u\right) + jU_2\left(\frac{ka^2}{2R}, u\right) \right]}{\frac{ka^2}{R}} \quad [186] \quad (6.21)$$

where $U_n(w, u)$ is a Lommel function, which can be written as a Bessel series:

$$U_n(w, u) = \sum_{p=0}^{\infty} \frac{(-1)^p w^{n+2p} J_{n+2p}(u)}{u^{n+2p}} \quad [186]. \quad (6.22)$$

The gain reduction was calculated as the ratio of square the magnitude of the near-field E-field to the square of the magnitude of the far-field E-field. The far-field E-field is:

$$E_{far-field} \approx \frac{-j\eta \cos\theta \cos\phi J_1(u)}{2u}. \quad (6.23)$$

This gain reduction factor was multiplied by the theoretical signal when calculating the SNR, and the results are shown in Figure 6.32. For angles within 0.15 radians, or 8.6° of the axis, the near-field correction decreases the gain at 0.5 m by 1.0 dB and at 1.0 m by 0.25 dB. Although the uniformly illuminated circular aperture is only a rough estimate for the reflection from the chest due to respiration, this calculation indicates that near-field effects are likely the cause of the SNR not increasing as expected from 1.0 m to 0.5 m.

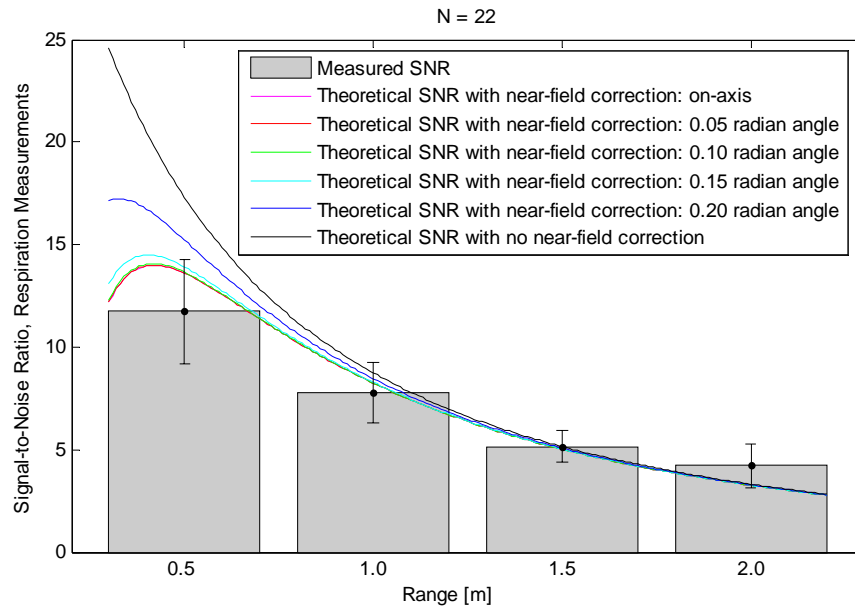


Figure 6.32. Theoretical SNR vs. range including near-field effects. The electric fields are calculated as if measured by a point source, with a 27-cm diameter uniformly illuminated circular antenna with a cosine distribution of electric field. At 0.5 m, there is a 1 dB reduction in gain, and at 1.0 m, there is a 0.25 dB reduction in gain. This calculation uses a RCS-RMS motion product of 100 mm^4 . (RCS indicates the radar cross sectional area.)

6.5.6 Radar Cross Section - Mean-Squared Motion Product

The estimated product of the radar cross section and the mean-squared motion can be derived from the measured signal-to-noise ratio and the theoretical signal-to-noise ratio. The best fitting values are 2.25 mm^4 for heart motion and 100 mm^4 for respiration; if the DC-blocking filter's attenuation of some of the respiration signal is corrected for, the best-fitting value for respiration is 250 mm^4 .

6.5.7 Potential Improvements

Two main areas where the system could be improved are indicated by this analysis. The SNR could be improved by decreasing the residual phase noise, and the accuracy could be improved by using more advanced signal processing so that the rates can be

found accurately at lower SNRs. The addition of a low-noise amplifier at the front end will not improve the SNR, as the limiting noise source is the residual phase noise.

One way to reduce the residual phase noise is to reduce the RF phase noise of the source. This could be accomplished by fabricating a chip with a technology other than CMOS for the oscillator, or by phase-locking the CMOS oscillator to a low phase noise reference. Another way to reduce the residual phase noise is to minimize the delay between the transmitter and the antenna and between the antenna and receiver. The 5-ns delay in this system is equivalent to a 75 cm increase in the range. If the circulator and antenna were placed on the same board as the radar chip, this delay could be reduced to as low as 1 ns, or an effective range of 15 cm. This 4 ns improvement would theoretically allow measurements to be made at 50 cm further with similar results.

The other area with opportunity for improvement is the signal processing. Some rate-finding systems use nonlinear smoothing algorithms that will discard outliers in the rate before averaging. Techniques other than autocorrelation, such as wavelet techniques could improve the rate-finding. Adaptive filtering to separate the heart signal from the respiration signal could provide more optimal filtering than the fixed filters used in this application. For example, two of the subjects had heart rates between 40 and 45 beats per minute, but none of the other subjects had heart rates below 60 beats per minute. A filter with a higher cutoff frequency could be used for the subjects with a higher heart rate, eliminating more noise and likely improving the rate-finding.

With a more advanced system, it may be possible to subtract motion such as fidgeting and twitching that interfere with extraction of heart and respiration rates. If these motions are not occurring regularly with periods in the range of those due to heart and respiration, they could be removed from the measurement, allowing improved detection of the heart and respiration signatures.

6.6 Conclusions

The Doppler radar system was effective at measuring heart rate up to a range of one meter and measuring respiration up to a range of 1.5 m. Putting the antenna and circulator on the same board as the radar chip could theoretically extend the range by 0.5 m. The current system is not accurate on a beat-to-beat basis as the electrocardiogram is, and this leaves much room for improvement in the signal processing, including a nonlinear smoothing algorithm that discards outliers. More advanced signal processing could greatly improve the accuracy of the system.

When near-field effects are taken into account for the respiration measurements, the SNR-range measurements were proportional to the theoretical SNR-range curves for both heart and respiration. It was expected that the SNR for respiration would be two orders of magnitude or more greater than the SNR for the heart, but it was closer to one order of magnitude. When the attenuation of some of the respiration signals by the dc-blocking filter is corrected for, the SNE for respiration is about 30 times that for heart. This information, and the derived mean-squared motion - radar cross section products for heart and respiration will be used for theoretical calculations for future designs.

The respiration SNR did, in general, increase with increasing chest area, but not in direct proportion as was expected. However, the area of the chest that moves with respiration is not necessarily directly proportional to the total chest area, and it is possible that the RMS motion due to respiration decreases with increasing chest area. It was found that the respiration SNR increased with the subject's weight, and it seems likely that larger subjects breathe a larger volume of air, and a larger change in the chest volume should result in a greater RCS-RMS motion product.

The heart SNR was not shown to negatively correlate with age as was expected due to arterial compliance reduction with age. This may have been because the greatest change in arterial compliance comes above age 50, and only two subjects over the age of 50 were included in this study. A study with a greater population over 50 would help to determine whether this effect is present as expected. The heart SNR was also expected to be nega-

tively correlated with the body mass index, since fat below the surface of the skin is expected to dampen motion to the surface.

This study has generally confirmed the SNR variation with range that was expected, and has given approximate estimates for the RCS-RMS motion product for heart and respiration that can be used in system sensitivity calculations when making changes to the system in the future. The Doppler radar heart and respiration rate system can be accurate with different body types and ages below 1 m, and changes have been recommended to extend the range and improve the accuracy for applications that require higher accuracy.

6.7 References

- [177] S. M. Bailey, "Theoretical considerations in the measurement and interpretation of change in adult dimensions," in Anthromorphic Assessment of Nutritional Status, (J. H. Himes, Ed.), New York: Wiley-Liss, 1991.
- [178] J. M. Bland and D. G. Altman, "Statistical methods for assessing agreement between two methods of clinical measurement," *Lancet*, vol. 1, no. 8476, pp. 307-310, 1986.
- [179] J. M. Bland and D. G. Altman, "Comparing methods of measurement: why plotting difference against standard method is misleading," *Lancet*, vol. 346, no. 8982, 1085-1087, 1995.
- [180] J. M. Bland and D. G. Altman, "Measuring agreement in method comparison studies," *Statistical Methods in Medical Research*, vol. 8, pp. 135-160, 1999.
- [181] D. G. Brennan, "Linear diversity combining techniques," *Proceedings of the IEEE*, vol. 47, pp. 1075-1102, 1959.
- [182] M. C. Budge, Jr. and M. P. Burt, "Range correlation effects on phase and amplitude noise," in *Proceedings of the IEEE Southeastcon*, 1993.
- [183] C. W. Callaway, W. C. Chumlea, C. Bouchard, J. H. Himes, T. G. Lohman, A. D. Martin, C. D. Mitchell, W. H. Mueller, A. F. Riche, and J. Wilmore, "Circumferences," in Anthromorphic Standardization Reference Manual (T. G. Lohman, A. F. Roche, and R. Martorell, Eds.), Champaign, IL: Human Kinetics Books, 1988.

- [184] Electronic Warfare and Radar Systems Engineering Handbook, Avionics Department of the Naval Air Warfare Center Weapons Division in 1992, document number TP 8347.
- [185] D. L. Gorgas, "Vital signs and patient monitoring techniques," in Clinical Procedures in Emergency Medicine: 4th ed., (J. R. Roberts and J. R. Hedges, Eds.), Philadelphia,: Saunders, 2004, pp. 3-28.
- [186] R. C. Hansen, "Aperture theory," in Microwave Scanning Antennas (R. C. Hansen, Ed.), New York: Academic Press, 1964.
- [187] R. R. Hocking, "A biometrics invited paper: The analysis and selection of variables in linear regression," *Biometrics*, vol. 32, no. 1, pp. 1-49, 1976.
- [188] I. T. Jolliffe, Principal Component Analysis, Secaucus, NJ: Springer-Verlag New York, Inc., 2002.
- [189] S. Michelson and T. Schofield, The Biostatistics Cookbook: The Most User-Friendly Guide for the Bio/Medical Scientist, New York: Kluwer Academic Publishers, 2002.
- [190] A. J. Miller, "Selection of subsets of regression variables," *Journal of the Royal Statistical Society, Series A (General)*, vol. 147, no. 3, pp. 389-425, 1984.
- [191] NHLBI Obesity Education Initiative, The Practical Guide: Identification, Evaluation, and Treatment of Overweight and Obesity in Adults, Bethesda, MD: National Institutes of Health, 2000. (NIH publication no. 00-4084)
- [192] N. G. Norgan, "Anthromorphic assessment of body fat and fatness," in Anthromorphic Assessment of Nutritional Status, (J. H. Himes, Ed.), New York: Wiley-Liss, 1991.
- [193] J. O. Rawlings, S. G. Pantula, and D. A. Dickey, Applied Regression Analysis: A Research Tool, Secaucus, NJ: Springer-Verlag New York, Inc., 1998.
- [194] A. W. Rudge, K. Milne, A. D. Oliver, and P. Knight, The Handbook of Antenna Design, vol. 1, London: Peter Peregrinus, 1982.
- [195] S. D. Silvey, "Multicollinearity and imprecise estimation," *Journal of the Royal Statistical Society, Series B (Methodological)*, vol. 31, no. 3, pp. 539-552, 1969.

- [196] J. H. Wilmore, R. A. Frisancho, C. C. Gordon, J. H. Himes, A. D. Martin, R. Martorell, and V. D. Seefeldt, "Body breadth equipment and measurement techniques," in Anthromorphic Standardization Reference Manual (T. G. Lohman, A. F. Roche, and R. Martorell, Eds.), Champaign, IL: Human Kinetics Books, 1988.

Chapter
7

Signal Processing

7.1 Introduction

In the Doppler radar cardiopulmonary motion monitoring system, the heartbeat and respiration signals are superimposed on each other. Because the chest moves a much greater distance due to breathing than it does due to the heart beating and a greater area of the chest moves for respiration, the amplitude of the respiration signal is typically about 100 times greater than that of the signal due to the heartbeat. Therefore, the respiration rate can be detected without filtering, but the heart signal must be isolated from the respiration signal to detect heart rate. Once the heart and respiration signals are separated, both need to be processed in order to determine heart and respiration rates, and for optimal accuracy, the stages before the rate determination should add minimal amounts of in-band noise. The processing should enable heart rate detection with precision to 0.5 beats per minute, or 0.008 Hz, and respiration rate detection with precision to 1 breath per minute, or 0.016 Hz. To accurately track changes in the rates, the rates should be determined with a time resolution of less than 10 seconds for the heart rate, and less than 20 seconds for the respiration rate.

The analog processing includes single-ended-to-differential conversion, dc blocking with a highpass filter with a 0.2-Hz cutoff, 40-dB gain and anti-alias lowpass filtering with a 22-Hz cutoff, and it is described in detail in Appendix E. Digitization must occur at a sample rate that is at least twice (and typically at least 2.5 times) the highest frequency component of the desired signal. For the heart signal, a 20-Hz cutoff leaves enough signal to identify the rate, but a 40 to 100-Hz cutoff leaves harmonics that are desirable when accurate beat times need to be measured for beat-to-beat variability studies. Therefore,

depending on the application, Doppler monitoring of heartbeat and respiration should have a sample rate of 50 to 250 Hz. A 100-Hz sample rate is used in this system. The analog-to-digital conversion is further described in Appendix I.

Digital signal processing (DSP) may include many functions that can be performed to condition the signal and determine its properties. Signal conditioning steps include filtering, removal of dc offsets, combining quadrature channels, and other techniques to enhance certain properties of the signal. Filtering can remove out-of-band noise and may be used to separate two signals that are at distinct frequencies, such as the heart and respiration signals. Removing dc offsets is readily performed in DSP; the average of all of the samples is subtracted from each of the samples. Digital signal conditioning sometimes also includes nonlinear pre-processing steps that help to emphasize the periodic portions of the signal. Many signal properties can be determined by DSP; the most important property in this application is the heart and respiration rates.

The heart and respiration signals are usually separated in frequency; as discussed in Chapter 3, the resting heart rate is generally between 0.83 and 1.5 Hz (50 and 90 beats per minute), while the resting respiration rate is generally between 0.15 and 0.4 Hz (9 and 24 breaths per minute). This means that the heart signal can usually be isolated from the respiration signal by a highpass filter with a pass-block transition between 0.83 and 0.40 Hz. However, the rates measured in the human subjects testing had a wider range, as described in Chapter 6, with heart rates varying from 43 to 94 beats per minute (0.7 to 1.6 Hz) and respiration rates varying from 5 to 21 breaths per minute (0.08 to 0.35 Hz). This requires a highpass filter with a transition between 0.70 Hz and 0.35 Hz to isolate the heart signal. Generally the heart and respiration rates track together - when a person exercises, as the heart rate rises, the respiration rate tends to rise, so it is unlikely that the heart and respiration fundamental signals will overlap. A sample of heart and respiration signals measured with the Doppler radar transceiver are shown in Figure 7.1. The heart signal was isolated with an analog high pass filter with a 1-Hz cutoff frequency. Signals are digitally filtered

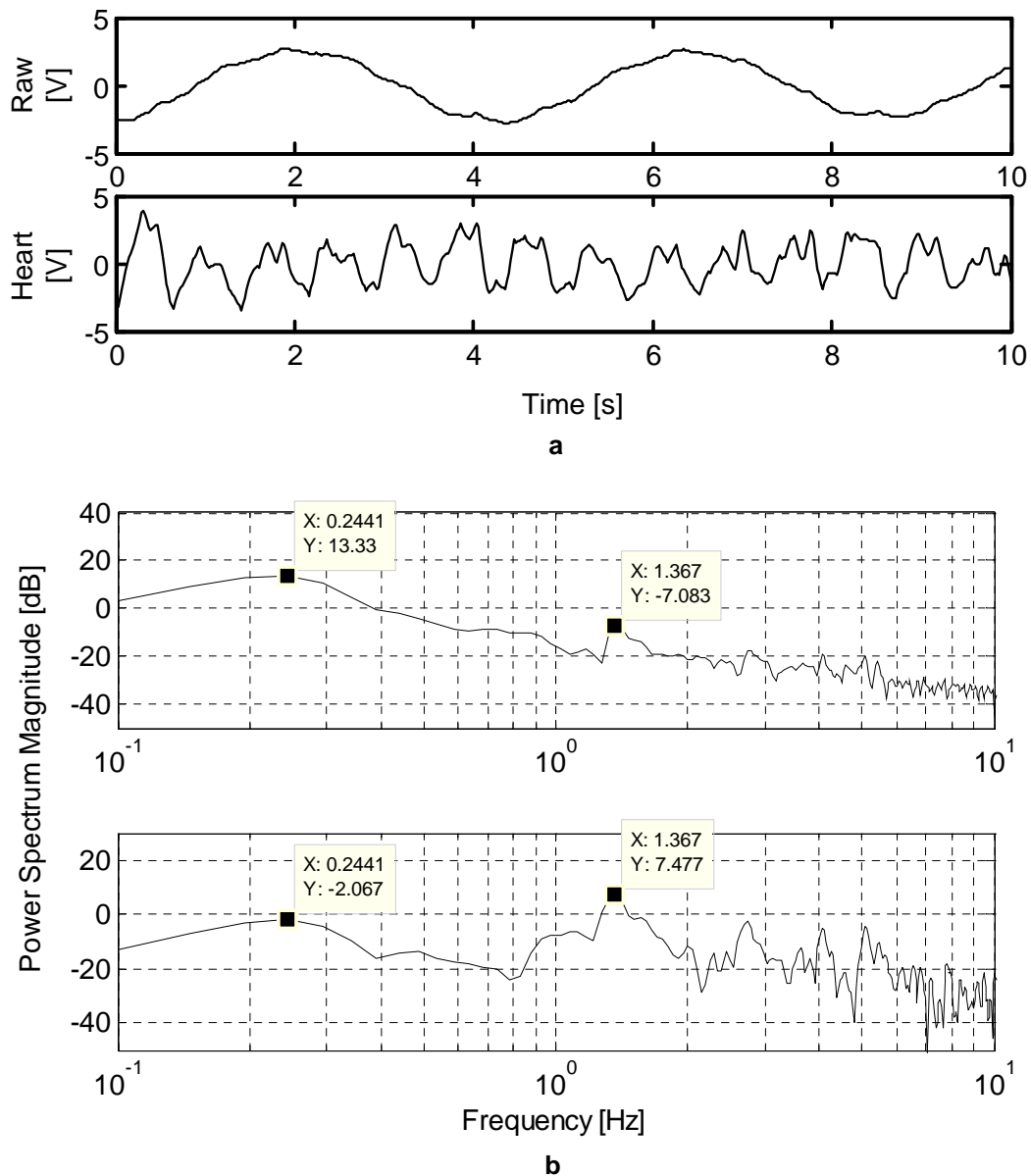


Figure 7.1: Sample heart and respiration traces measured with the hybrid radio at a 50 cm range shown in (a) the time domain and (b) the frequency domain. The heart signal was separated from the respiration signal with an analog highpass filter with a 1-Hz cutoff. The top trace in both the time and frequency domain representations is the superimposed heart and respiration signals, and the bottom trace is the isolated heart signal. Before filtering, the heart signal is approximately 20 dB below the respiration signal, and after the filter, it is about 10 dB above the respiration signal.

by weighting and summing present and past input and output samples of the filter to provide a filtered output sample.

As discussed in detail in Chapter 2, the use of a quadrature receiver rather than a single-chain receiver for Doppler monitoring of heart and respiration can greatly improve the measurement of heart and respiration signatures. If the better of the two channels is selected, the phase demodulation null points can be avoided. In this case, the dc offsets can be removed and a single-channel signal processing scheme can be used on the selected channel. A quadrature receiver also offers the possibility of direct phase demodulation to combine the I and Q signals. This was introduced in Chapter 2, Section 2.2.3, under the assumption of perfect phase and amplitude balance between the receiver chains. Appendix C discusses the problems encountered in the practical application of direct phase demodulation, also known as the arctangent technique, for combining I and Q signals, including dc offsets from sources other than the data, removal of dc offsets including that of the data, and phase and gain imbalance between the quadrature receiver chains. This appendix introduces the Gram-Schmidt technique for orthonormalization to combat the gain and phase imbalance, and analyzes the error introduced by removing dc offsets. Because of the error introduced with dc offsets, some data-driven combining approaches are also explored, including equal-ratio combining, maximum-ratio combining, and principal component analysis. All these techniques will be described, and their results will be compared for many data sets in this chapter.

The most important signal property to determine for Doppler cardiorespiratory monitoring is the rates of the heart and respiration signals. Three DSP approaches to rate-finding are the discrete Fourier transform (DFT), autocorrelation, and peak-finding. The DFT processes samples with an algorithm that shows the signal's frequency spectrum, the peak of which indicates the rate. Autocorrelation multiplies time-shifted samples of the signal together to emphasize periodic portions of the signal, and the period can be inverted to calculate the rate. Peak-finding is similar to the technique commonly used to find the heart rate from the ECG, where a peak is found for each beat and the average time between the peaks is inverted to calculate the rate. All these rate-finding methods are explored for the Doppler heart signal in this chapter. When finding the rate over time with the time-dependent Fourier transform (TDFT) or the short-time autocorrelation function

(STAF), the rate is calculated from a windowed subset of the samples that must contain at least two periods of the signal for accurate rate determination. Frequency variation within this interval cannot be detected, since the rate is determined for the entire interval. Therefore, longer intervals result in more accurate rate detection, but shorter intervals result in better the time resolution.

7.2 Background

7.2.1 Separating Heart and Respiration Signals

Since different windows are optimal for heart and respiration signals, they need to be separated before windowing and rate-finding. This can be accomplished with digital filters. When isolating the heart signature from the combined heart and respiration signature by its frequency, the simplest technique is a fixed-frequency highpass filter. This filter must attenuate the respiration signal at least 50 dB more than the heart signal. Digital filters multiply the input (and sometimes also the output) samples by the filter coefficients that are chosen to give a desired frequency response.

There are two main categories of fixed digital filters: finite impulse response and infinite impulse response. Finite impulse response (FIR) filters use current and past input samples only, so if a string of zeros is given, the output will eventually reach zero, regardless of the prior inputs. Infinite impulse response (IIR) filters have feedback, having sets of coefficients for previous input samples and for previous output samples. Since they depend on previous output samples, perturbations at the input can cause oscillations at the output, so even if the inputs transition to all zeros, it is possible that the output of the filter will not become zero; this is why this type of filter is called an ‘infinite’ impulse response. Because of this, it is important to design IIR filters so they are stable and do not oscillate.

The number of coefficients, or the filter order, and the values of those coefficients determine the filter’s properties. Properties in the frequency response include the cutoff frequency, the steepness of the transition between the passband and stopband, and the

amount of ripple in the passband and stopband. Time domain properties include the group delay - how much the signal is delayed in time - and the amount of ringing, or how long the filter has an output given a step or impulse at the input.

Group delay is the derivative of phase change between the filter input and output as a function of frequency. When group delay is constant over the passband, all of the frequency components of the filter input signal in that band are delayed by an equal amount of time before they reach the filter's output, so that no distortion is introduced to the signal. A linear phase response is important when the information is in the modulation of the signal, information is included in different frequency components of the signal, or if the signal harmonics are important. The phase shift of an FIR filter is linear within the passband if the filter has symmetrical coefficients, and the amount of group delay is determined by the filter order. Increasing the number of taps steepens the rolloff at the expense of greater group delay. An IIR filter typically has a nonlinear group delay, so that it can introduce distortion to the signal. In the Doppler system, the first harmonic of the heart signal is usually between 5 and 15 dB below the fundamental, and avoiding its distortion is important for signal shape, though is not always critical for rate-finding.

If an impulse or step is input into a filter with a long impulse response, a decaying sine wave is output; this is known as ringing. The steeper the transition from passband to stopband, the longer the impulse response and the greater the ringing. Minimizing ringing levels is important in systems with a mechanism for introduction of an impulse or step since recovery time depends on the level of ringing. In Doppler monitoring, motion of the subject or nearby objects can introduce an impulse, so a ringing time under 3-5 seconds is desired.

Ideally, the heart isolation high pass filter would pass a heart signal at 0.7 Hz while attenuating a respiration signal at 0.4 Hz by at least 50 dB, and introduce a group delay of less than 2 seconds that is flat over frequencies above 0.7 Hz. This would require a 250 dB/decade fall-off in the transition band with a cutoff at 0.83 Hz. This is not possible to achieve with an FIR filter, so requirements are set at a filter that has a 40-dB attenuation

by 0.35 Hz, which requires only a 133 dB/decade rolloff that can be achieved with a FIR filter with a group delay of 3 seconds.

An ideal filter in the frequency domain, with a step in frequency response, requires an infinite sinc function in the time domain. If the sinc function is multiplied by a window, it becomes finite in the time domain, as is necessary for digital signal processing. If the filter coefficient series is truncated to make it finite, there will be large ripples in the frequency domain since the filter frequency response is effectively multiplied by a sinc. Using non-rectangular windows can greatly decrease the passband and sideband ripple, but ripples cannot be completely avoided in practice since there will always be a finite number of coefficients. This is known as Gibb's Phenomenon: whenever an instantaneous discontinuity is represented by a Fourier series, there will be passband ripple [213].

The choice of a filter topology is a tradeoff between the steepness in the transition band, the amount of pass band ripple, and the sidelobe height. The Kaiser filter allows a parameter, β , to be used to trade off between the sidelobe height and steepness of response. Figure 7.2 shows 400-order Kaiser filters with β values of 2, 4, 6 and 8. As β is decreased, the transition between the passband and the stopband is steeper, but the sidelobe levels rise.

The longer the FIR filter, the steeper the transition between the passband and the stopband can be. Therefore, the minimum filter length is affected by the required stopband attenuation and the normalized transition bandwidth, or the distance between the passed and stopped frequencies. Increasing the filter order enables a steeper transition, so that the normalized transition bandwidth can be smaller and/or the stopband attenuation can be greater. In FIR filters, a greater filter order results in a longer group delay.

For the Doppler heart and respiration monitor, the heart signal can be isolated by filtering with a non-constant group delay filter. Because the harmonics may not align with the fundamental after this filter, a linear phase filter is preferable. However, if a nonlinear phase filter offers significant improvements in the signal processing, the non-constant group delay could be acceptable. For example, if the Doppler heart and respiration moni-

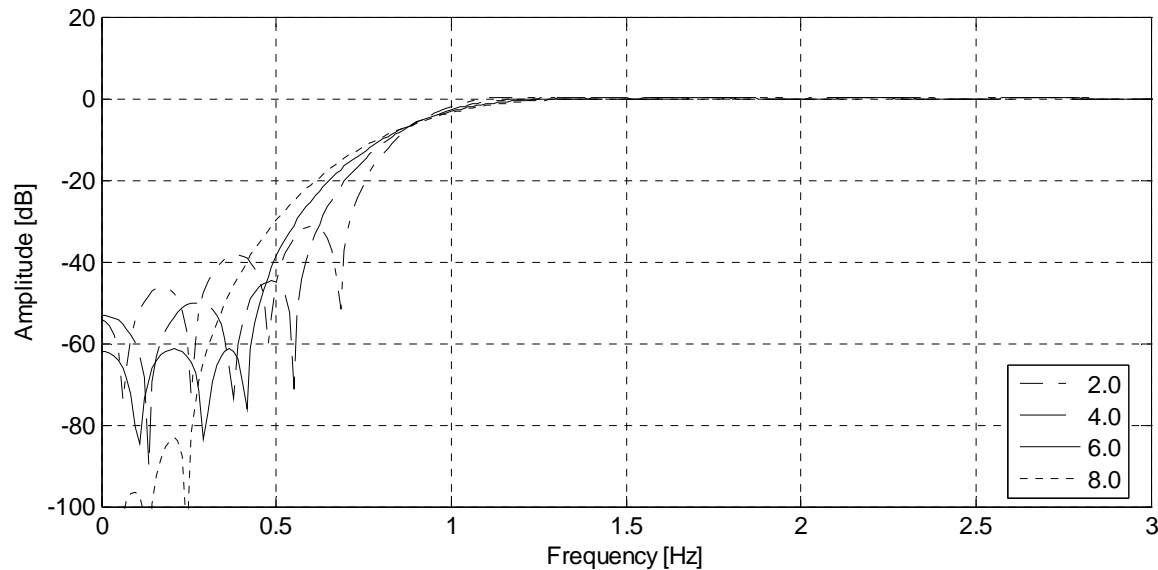


Figure 7.2: Comparison of 400-order Kaiser filters with cutoff of 0.9 Hz. The parameter β is varied between 2 and 8, trading off the steepness of the cutoff with the height of the sidelobes. The steeper the cutoff, the higher the sidelobes.

tor is used in a setting where the delay must be below a second, an IIR filter would be required to separate the heart and respiration signals. When a delay of 2 seconds or more is acceptable, an FIR filter is preferable. IIR filters have a nonlinear phase response but are very efficient, and they have less ripple and can have a much steeper rolloff than an FIR filter that requires the same number of multiplications.

7.2.2 Quadrature Theory

Direct conversion receivers typically use quadrature mixing to reconstitute down-converted signals, avoiding aliasing [197, 219]. Quadrature mixing is attractive for demodulating the chest displacement signal in Doppler cardiorespiratory monitoring because it avoids phase demodulation null points and it theoretically allows perfect phase demodulation.

The challenges inherent in the homodyne quadrature architecture - phase imbalance, gain imbalance, and dc offset - impede the combination of the I and Q channels to directly demodulate the phase using the arctangent technique. The gain and phase imbalance act as

a linear transformation on the I and Q components; the information is effectively collected on axes that are not normal and do not have the same scale. It is possible to correct for a known phase and amplitude imbalance using the Gram-Schmidt procedure to make two vectors orthonormal [204]. This method is insufficient in wideband systems where the phase imbalance varies with frequency, or in systems that need a high level of image cancellation that cannot be achieved with the residual imbalance from this method. However, the radar cardiorespiratory monitoring system is extremely narrow-band and the only image frequency is the reflection of the desired signal, so neither of these concerns are applicable.

The dc offset is typically 2 to 3 orders of magnitude larger than the signal amplitude, making it difficult to amplify the microvolt signals sufficiently for sufficiently high-resolution digitization with the 16-bit ADC used in this work without saturating either the amplifiers or with the analog-to-digital converters (ADCs). Removing the dc offset through filtering or subtraction before amplification avoids this problem, but leads to another: since the baseband signals have data at dc, when dc offsets are removed, a portion of the signal is removed, and this adversely affects direct phase demodulation, as is shown in Appendix C. This problem is strongly pronounced in this extremely narrow-band application, with respiration typically between 0.1 and 0.4 Hz, and heart typically between 0.83 and 1.5 Hz. The dc-blocking filter used in this work, described in Appendix E, is a high-pass filter with a 0.2-Hz cutoff.

Following is a general signal analysis of an imbalanced quadrature receiver used for Doppler radar cardiorespiratory monitoring. As shown in Chapter 2, the ideal baseband I and Q outputs are the cosine and sine, respectively, of a phase shift, $\theta(t)$, which consists of a constant phase-shift, θ , due to the nominal distance of the target summed with a time-varying phase shift proportional to the chest position, $x(t)$ and with a residual phase noise term, $\Delta\phi(t)$:

$$\theta(t) = \theta + \left(\frac{4\pi}{\lambda}\right)x(t) + \Delta\phi_N(t), \quad (7.1)$$

where

$$\Delta\phi_N(t) = \phi_N(t) - \phi_N\left(t - \frac{2d_0}{c}\right). \quad (7.2)$$

When only one of these channels is used to demodulate the phase, the value of the constant phase shift determines whether the signal is at an optimal phase demodulation point or at a null point. With no errors, the phase can be directly demodulated using the arctangent:

$$\theta'(t) = \operatorname{atan}\left(\frac{B_Q(t)}{B_I(t)}\right) = \operatorname{atan}\left(\frac{\sin(\theta(t))}{\cos(\theta(t))}\right) = \theta(t). \quad (7.3)$$

This phase demodulation approach works well when the phase between the two LO signals is exactly 90° , the amplitude of both LO signals and both RF signals are the same, there are no significant dc offsets due to sources other than the data, dc offsets from the data have not been removed, and baseband noise is not a significant factor. However, real systems have all of these non-idealities to some extent [207]. For this analysis, the amplitude error, A_E , is defined as the ratio of the amplitude of the Q channel RF signal to that of the I channel. The phase error, ϕ_E , is defined as the difference between the phases of the two LO signals minus 90° . The cumulative change in dc offset from the data's dc value on the I and Q channels are V_I and V_Q , respectively. A_R is the ratio of the amplitude of the RF input signal to the LO signal. With these non-idealities, the LO signals are

$$L_I(t) = \cos(2\pi ft + \phi_N(t)) \quad (7.4)$$

and

$$L_Q(t) = \sin(2\pi ft + \phi_N(t) + \phi_E). \quad (7.5)$$

The received signals are:

$$R_I(t) = A_R \cos\left(2\pi ft + \theta + \left(\frac{4\pi}{\lambda}\right)x(t) + \phi_N\left(t - \frac{2d_0}{c}\right)\right) \quad (7.6)$$

and

$$R_I(t) = A_R A_E \cos\left(2\pi f t + \theta + \left(\frac{4\pi}{\lambda}\right)x(t) + \phi_N\left(t - \frac{2d_0}{c}\right)\right). \quad (7.7)$$

After the received signal is mixed with the LO signals, the baseband signals are:

$$B_I(t) = V_I + A_R \cos(\theta(t)) \quad (7.8)$$

and

$$B_Q(t) = V_Q + A_R A_E \sin(\theta(t) + \phi_E). \quad (7.9)$$

7.2.3 Techniques for Combining Quadrature Channels

Five techniques for combining quadrature channels are described in this section. First, the arctangent technique for direct phase demodulation is introduced with the Gram-Schmidt orthonormalization technique. The theory of this technique and the problems associated with it are given in detail since this is the standard technique for combining I/Q data. Next, three diversity techniques for combining channels are introduced: selection diversity, equal ratio combining, and maximal ratio combining. These techniques traditionally are used when information is transmitted over multiple channels and not for quadrature channels, but are explored as alternatives to the arctangent method due to non-idealities in the direct-conversion quadrature receiver. Finally, principal component combining is introduced. This method projects the I and Q signals on a single best-fit vector to combine them.

7.2.3.1 Arctangent Technique for Combining Quadrature Channels

The arctangent technique takes advantage of the 90° phase difference between the I and Q signals, and combines the signals by taking the arctangent of the ratio of the Q signal to the I signal. When direct phase demodulation is used on the non-ideal outputs in (7.8) and (7.9), the calculated phase is:

$$\theta'(t) = \text{atan}\left(\frac{B_Q(t)}{B_I(t)}\right) = \text{atan}\left(\frac{V_Q + A_R A_E \sin(\theta(t) + \phi_e)}{V_I + A_R \cos(\theta(t))}\right). \quad (7.10)$$

With the non-idealities, the desired output, $\theta(t)$, is not straightforward to calculate. This does not lead straightforwardly to the desired output. Analysis of the errors introduced by the non-idealities in the signal are provided in Appendix C. Additionally, zero-crossings in the I signal, or the denominator, can cause divide-by-zero errors in the calculation, increasing the error with this technique. Dividing by values near zero on the I channel amplifies noise that occurs at those points on the Q channel more than noise at other points. If dc offsets are added to avoid zero-crossings, these errors are avoided, but the error due to dc offsets is increased.

The phase error, ε_ϕ , can be defined as the difference between the phase calculated with non-idealities and the ideal phase:

$$\varepsilon_\theta = \theta'(t) - \theta(t) = \operatorname{atan}\left(\frac{V_Q + A_R A_E \sin(\theta(t) + \phi_e)}{V_I + A_R \cos(\theta(t))}\right) - \theta(t). \quad (7.11)$$

The maximum error occurs at $\theta(t) = 0$, where

$$\varepsilon_{\theta, \max} = \operatorname{atan}\left(\frac{V_Q + A_R A_E \sin(\phi_e)}{V_I + A_R}\right) = \operatorname{atan}\left(\frac{\frac{V_Q}{A_R} + A_E \sin(\phi_e)}{1 + \frac{V_I}{A_R}}\right). \quad (G.12)$$

If ϕ_e is small, the small angle approximation yields:

$$\varepsilon_{\theta, \max} \approx \operatorname{atan}\left(\frac{V_Q + A_R A_E \phi_e}{V_I + A_R}\right) = \operatorname{atan}\left(\frac{\frac{V_Q}{A_R} + A_E \phi_e}{1 + \frac{V_I}{A_R}}\right). \quad (7.13)$$

If there are no unwanted dc offsets, the maximum error is:

$$\varepsilon_{\theta, \max} = \operatorname{atan}(A_E \sin(\phi_e)). \quad (7.14)$$

It is possible to correct for a known phase and amplitude imbalance using the Gram-Schmidt procedure to make two vectors orthonormal [204]. This procedure takes any two initial basis vectors, a_1 and a_2 and creates an orthonormal basis, with basis vec-

tors x_1 and x_2 . For this application, non-normal basis vectors B_I and B_Q are converted to the orthonormal basis vectors $B_{I,orth}$ and $B_{Q,orth}$. $B_{I,orth}$ is taken to be B_I , and then B_Q is converted to be orthonormal to $B_{I,orth}$, as described in detail in Appendix C, Section C.5.3. This operation is shown in matrix form in (7.15).

$$\begin{bmatrix} B_{I,orth} \\ B_{Q,orth} \end{bmatrix} = \begin{bmatrix} 1 & 0 \\ -\tan(\phi_e) & \frac{1}{A_e \cos(\phi_e)} \end{bmatrix} \begin{bmatrix} B_I \\ B_Q \end{bmatrix} \quad (7.15)$$

After the orthonormalization, the output after arctangent combining is

$$\theta'(t) = \text{atan} \left(\frac{V_Q + A_R \sin(\theta(t))}{V_I + A_R \cos(\theta(t))} \right). \quad (7.16)$$

If the amplitude and phase errors are measured correctly, the Gram-Schmidt technique will correct for them, but the Gram-Schmidt technique does not solve problems introduced by dc offsets.

7.2.3.2 Diversity Techniques for Combining Quadrature Channels

Diversity techniques are methods of combining signals sent over different channels. If the signals on the N different channels are:

$$f_j(t) = x_j(t) + n_j(t), \quad (7.17)$$

the output after signals are linearly combined with weights a_j determined by the diversity method is:

$$f(t) = \sum_{j=1}^N a_j f_j(t). \quad (7.18)$$

The three diversity techniques discussed here, selection diversity, equal gain diversity, and maximal ratio diversity, are three different methods for choosing the a_j values. These methods are traditionally used when a signal is transmitted over multiple different chan-

nels and a single result is desired. It is not traditionally used in I/Q processing, but is explored here because of the errors introduced by dc offsets in arctangent combining.

Selection diversity [199] selects the best of the noisy signals, based on the SNR. If

$$SNR_k \geq SNR_j, \quad j=1 \rightarrow n, \quad (7.19)$$

then

$$a_j = \begin{cases} 1, & j = k \\ 0, & j \neq k \end{cases}. \quad (7.20)$$

If the noise can be assumed to be the same on all channels, the amplitude can be used rather than the SNR, since the SNR is often challenging to calculate.

Equal ratio combining [199] (ERC) involves adding the two sources of data after ensuring they are in phase:

$$a_j = 1, \quad \text{all } j. \quad (7.21)$$

Equal ratio combining outperforms selection diversity if the noise is independent of the signal and additive, signals are locally coherent, the noise is locally incoherent, the local RMS signal values are statistically independent, and the RMS values of x_j are Rayleigh distributed [199]. These assumptions are not met in general for Doppler heart and respiration monitoring, so it is not clear whether ERC will outperform selection diversity.

Maximal ratio combining (MRC) weights each input channel based on its signal and noise power [199]:

$$a_j = \frac{x_j}{\sqrt{x_j^2 + n_j^2}}. \quad (7.22)$$

If the noise is the same on all channels, the weight is simply proportional to the signal power:

$$a_j = \frac{x_j}{\sqrt{x_j^2 + n_j^2}}. \quad (7.23)$$

Maximal ratio combining results in the maximum signal-to-noise ratio (SNR) realizable from any linear combination if the noise is additive to and independent of the signal,

signals are locally coherent, and the noise is locally incoherent [199]. This SNR is the sum of the individual SNRs:

$$SNR = \sum_{j=1}^N SNR_j \quad (7.24)$$

When these diversity combining techniques are used in Doppler monitoring of heart and respiration, they do not eliminate any phase noise or RF thermal noise, as these noise sources are the same for both signals. Since the baseband noise is different on the different signals, this technique can reduce the baseband noise.

The assumptions given by Brennan [199] for determining when maximal ratio combining is the optimal diversity technique are not fully valid for Doppler monitoring of heart and respiration. The signals are not necessarily in-phase; they may be in-phase or 180° out of phase; this is easy to correct for in the DSP. Also, depending on the phase relationship between the RF signal and the LO signal, one signal may have a larger squared component than the other. Since there is only one RF path, the RF signal power is the same for both channels, so that the baseband channels only differ in power due to gain imbalances between the signals and because of the differing phase relationship between the RF and the LO on the different channels. This means there is a correlation that should be predictable between the two channels.

7.2.3.3 Principal Component Combining of Quadrature Channels

Principal component analysis is a method of transposing multi-dimensional data to a single dimension, suppressing redundant information and maximizing the variance in the data. First, any dc offset is removed from the data. Then the covariance matrix between the I and Q channels is found. The I and Q data is then projected onto the eigenvector of the covariance matrix with the largest eigenvalue, also known as the principal component. Details on this technique can be found in Joliffe [210]. The principal component provides the best-fit line through the data, and the ratio of the associated eigenvalue to the sum of all eigenvalues indicates the percentage of the total data that is in the principal component.

Principal component combining has been explored by Liu [212], but is not a coherent combining technique so it cannot be used on many communications signals, and therefore does not have wide use in practice. It can, however, be used for the already demodulated signal to be combined in the Doppler system.

7.2.4 Windowing and Resolution

There are two definitions of frequency resolution: one is the accuracy with which the frequency of a signal can be detected and the other is the distance two signals need to be apart in order to be resolved as separate signals; the most relevant definition depends on the application. In Doppler heart and respiration rate monitoring the rate determination is critical and there are not multiple signals close in frequency-space, so that the accuracy at which the rate can be determined is most important. The required separation between the two signals to be resolved is important when the respiration harmonics are near to the heart signal in both amplitude and frequency. Heart rate detection should be accurate within 0.5 beats per minute, and respiration rate should be accurate within one breath per minute.

Windowing is important for rate calculations with both the short-time autocorrelation function and the short-time Fourier transforms. When a subset of samples is used to determine the rate over time, the truncation of the signal in the time domain results in leakage in the frequency domain. Shaping the signal by multiplying it by a non-rectangular window can improve DFT leakage while broadening the signal's spectral response. This decreases the ability to resolve closely spaced signals, but does not adversely affect the accuracy with which the rate can be determined. The time and frequency resolution of the short-time Fourier transform and the short-time autocorrelation function are greatly affected by the window length.

When data is simply truncated for time-dependent processing, the infinite data series is effectively multiplied by a rectangular (*rect*) function, creating a discontinuity in time at the beginning and at the end of the signal. While a constant voltage that lasts for infinite

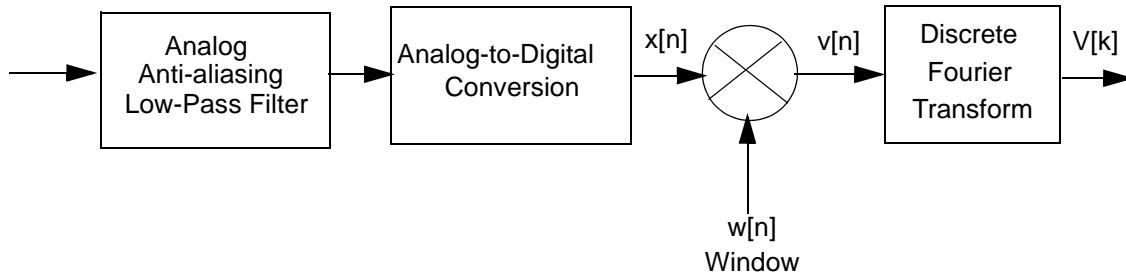


Figure 7.3: Sampling, windowing, and Fourier transformation of a signal.

time transforms to a delta function in frequency space, the rect function transforms to an infinite sinc function, leading to DFT leakage. The sinc function is effectively convolved with each sample in frequency space, causing a signal that should be in only one frequency bin to produce a non-zero value in other frequency bins. Using a non-rectangular window to truncate the signal can lessen or eliminate the discontinuity in time and can greatly decrease the DFT leakage. This window function, $w[n]$ is multiplied by the discrete signal $x[n]$ before the DFT is taken of the signal, as shown in Figure 7.3.

Discrete windows and their responses are thoroughly explored by F. J. Harris [209] and A. H. Nuttall [215]. The rectangular window, the triangular window, the Hanning window, and the Hamming window, each with a window length of 64, are shown in time and frequency space in Figure 7.4a and Figure 7.4b, respectively. In frequency space, the rectangular window has the narrowest main lobe, but has the highest sidelobes. The triangular window has the next narrowest main lobe, and the next highest sidelobes. The Hamming window has a slightly narrower main lobe than the Hanning window, and its sidelobes initially drop off the fastest, but do not decrease with increasing frequency. The Hanning sidelobes continue to decrease.

Non-rectangular window functions broaden the frequency response by a factor of about two [213], making it more difficult to distinguish between signals of similar amplitude that are also close in frequency [216]. However, windows help to detect a low-level signal near a high-level signal by minimizing the sidelobes of the high-level signal. Win-

dow selection is a trade-off between main lobe widening, first sidelobe levels, and how fast sidelobes decrease.

The more rapidly a signal changes its frequency characteristics, the shorter the window should be if the changes in frequency with time are to be resolved. As the window becomes shorter, the frequency resolution decreases, but the ability to resolve in time increases. The window length should be selected so that the spectral characteristics of the signal do not vary significantly over the length of the window [216].

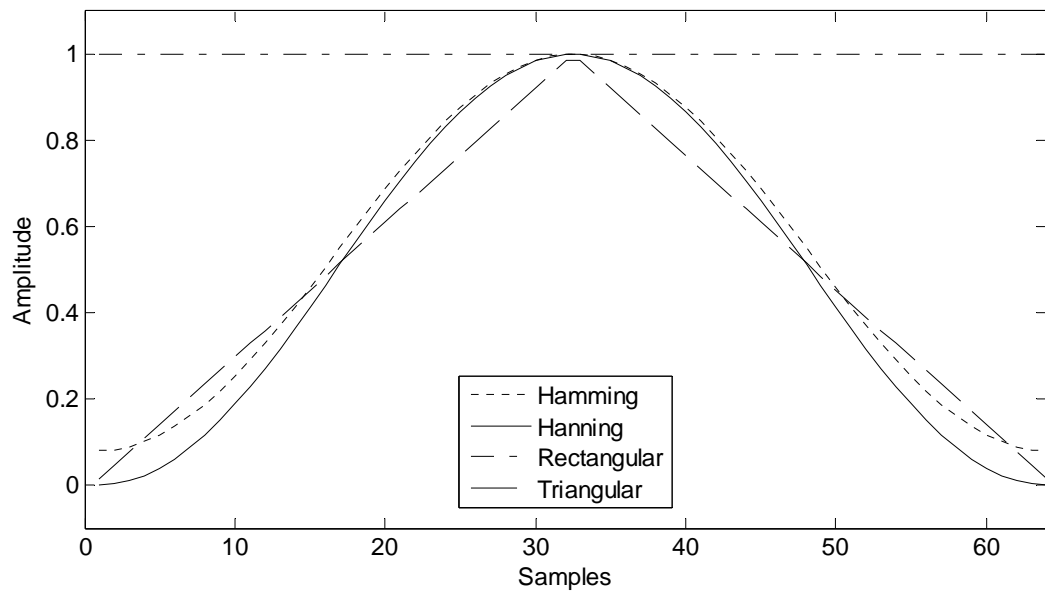
The bandwidth theorem states that the product of the effective duration, Δt , and the effective bandwidth, $\Delta\omega$, of a signal is greater than or equal to a constant, γ :

$$\Delta t \Delta \omega \geq \gamma, \quad (\text{G.25})$$

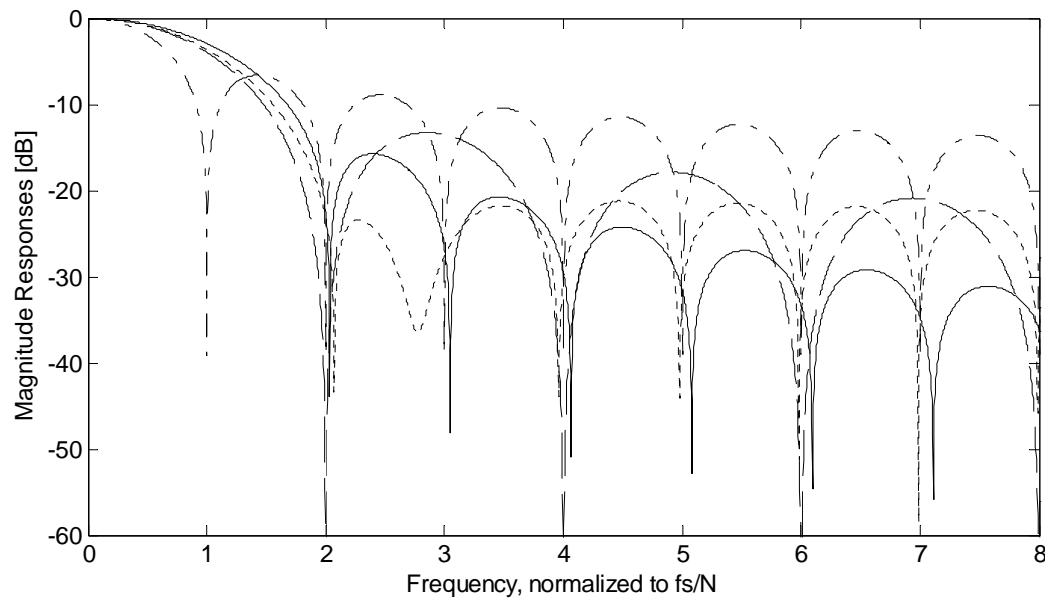
indicating that a function cannot have both arbitrarily small duration and arbitrarily small bandwidth [217]. This implies windowing signals increases their bandwidth, degrading the ability to distinguish between closely spaced signals. However, the frequency of a tone or the fundamental frequency of a signal can still be determined with arbitrarily good accuracy if it is sampled at least twice its bandwidth, as is described by the Nyquist theorem [216]. This resolution can be improved by increasing the number of DFT points through zero-padding.

7.2.4.1 Zero-padding

The Fourier transform of a signal has the same number of analysis points as the time-domain signal has samples. Appending the time-domain signal with zero-value samples increases the number of samples, providing ideal bandlimited interpolation of the signal spectrum [221]. Zero-padding does not improve the ability to resolve closely spaced signals when resolution is limited by the window's main lobe width [216], but the periodogram in frequency space can be better evaluated with more samples in frequency space [211] so that the peak of the signal can be better located. Zero-padding is important for the FFT, but it is not used in other rate-finding methods.



a



b

Figure 7.4: Comparison of rectangular, triangular, Hanning, and Hamming 64 sample window functions in a) time and b) frequency space. The frequency is normalized to f_s/N , where f_s is the sample frequency and N is the number of samples in the window.

7.2.5 Determining Heart Rate from Radar Heart-Motion Signature

Three methods to determine the heart rate from the Doppler radar signal are described: peak-finding, Fourier transform, and autocorrelation.

7.2.5.1 Peak-Finding

The rate of a periodic signal can be found by calculating the time of the peak of each period, and inverting the average period in a window to calculate the rate. This is the technique typically used for the electrocardiogram, which has a very strong peak at the R-wave in each peak. Although the Doppler heart signal peaks are not as well-defined as ECG R-wave peaks, this technique is explored. The signal is strongly lowpass filtered to remove peaks due to noise. This makes the peaks less sharp, so that they do not synchronize exactly with the ECG, but after averaging over several beats, the rate on a signal with good SNR should match the rate calculated from the ECG.

7.2.5.2 Fourier Transform

The Fourier transform is used extensively in signal processing to determine the frequency characteristics of a signal; when used for a sampled signal, the discrete Fourier transform (DFT) is used. With N time domain samples, the DFT determines the spectral content of the input at N equally spaced frequency bins. The frequencies at which the analysis is performed is determined by the sampling frequency, f_s , and N :

$$f_{analysis}(m) = \frac{mf_s}{N}, 0 \leq m \leq N. \quad (7.26)$$

The Fast Fourier Transform, or FFT, is a very efficient algorithm to compute the DFT when the number of input samples is an integral power of two, and it is the method commonly used to calculate the DFT. When a sample length is not an integer power of two, the sample is typically zero-padded to reach 2^n samples.

When the frequency response varies over time, as is the case with physiological signals, the time-dependent Fourier transform (TDFT), also known as the short-time Fourier

transform (STFT), must be used. This technique windows a portion of the signal, calculates the DFT of this portion, and then moves to another portion of the signal, calculating the DFT over time. The interval must be long enough to satisfy the desired FFT frequency resolution for the chosen sample rate. The total data collection time interval is N/f_s , and two signals must be at least f_s/N Hz apart to be detected. This cannot be improved by zero-padding.

Any dc offset should be subtracted before the DFT to eliminate a high-level 0-Hz component that will have a finite bandwidth and will obstruct signals near dc that are important when measuring heart and respiration.

7.2.5.3 Autocorrelation

The autocorrelation function is used to emphasize periodic patterns in a signal. In autocorrelation, the signal is multiplied by a version of itself shifted by a time delay, and the outputs are summed. This is performed over all possible time delays, the result is presented as a function of the time delay, and the output typically displays a prominent peak at the signal's fundamental period and at integer multiples of the fundamental period, but also displays peaks due to other frequencies in the signal, such as harmonics or modulations. The autocorrelation of a sampled signal, $x[n]$, is calculated as a function of sample delay, m , between the signal and a time-shifted version of itself, $x[n + m]$:

$$\phi_{xx}[m] = \lim_{N \rightarrow \infty} \left(\frac{1}{2N+1} \right) \sum_{n=-N}^N x[n]x[n+m] . \quad (7.27)$$

For a non-stationary signal, such as a physiological signal, the short-time autocorrelation function (STAF) must be computed; this operates on windowed segments of the signal and enables calculation of the period as it varies with time. The window causes the autocorrelation function to taper to zero with increasing time delay, emphasizing lower time delays over higher ones. Therefore, the window should contain between two and three periods of the fundamental frequency to ensure that the peak due to the fundamental

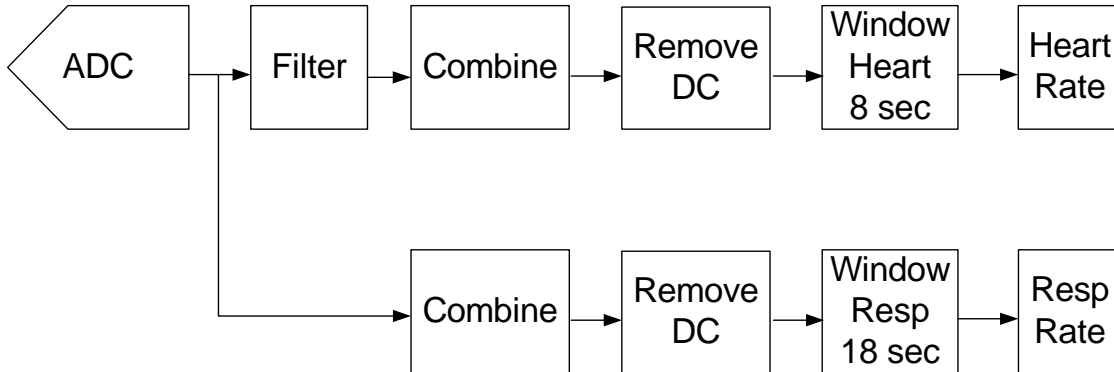


Figure 7.5: Digital signal processing flow.

frequency is not greatly attenuated by tapering [218]. The short-time autocorrelation can be defined as:

$$\phi_{xx, l}[m] = \frac{1}{N} \sum_{n=0}^{N-m-1} (x[n+l]w[n])(x[n+l+m]w[n+m]), \quad 0 \leq m \leq M_0 - 1, \quad (7.28)$$

where N is the section length in samples being analyzed, M_0 is the number of autocorrelation points to be computed, and l is the index of the starting sample in the frame [218]. This multiplies the windowed signal, $x[n+l]w[n]$, with a time-shifted version of itself, $x[n+l+m]w[n+m]$. This will be calculated for successive values of l so that the variation in the autocorrelation function over time can be evaluated.

7.3 Signal Processing Methods

After digitization, the physiological motion signal from the Doppler radar is split into the heart rate processing section and the respiration rate processing section, as shown in Figure 7.5. The heart signal is filtered to remove the fundamental of the respiration signal, the I and Q components are combined, the dc offset is removed by subtracting the mean, the signal is windowed, and then the heart rate is calculated. The respiration signal first has its I and Q components combined, then the dc offset is removed, and then it is windowed before the respiration rate is determined.

7.3.1 Separating Heart and Respiration with Digital FIR Filters

Because of the size of the harmonics of the heart signal, a relatively flat group delay over the fundamental and the first three harmonics is desired, and a delay of up to 3 seconds is acceptable, so that an FIR filter has been chosen for this experiment. The choice of filter order is a compromise between transition band steepness and group delay; at a 100 sample per second rate, a 600-order filter keeps the group delay at 3 seconds. A Kaiser filter with β set to 6.5 and a cutoff frequency of 0.65 Hz was selected. At 1 Hz, or 60 beats per minute, the amplitude is 0.0 dB, and at 0.83 Hz, or 50 beats per minute, the amplitude is 0.3 dB. At the high end of the respiration rates, 0.4 Hz, or 24 breaths per minute, the amplitude is -23.8 dB, and at 0.33 Hz, or 20 breaths per minute, the amplitude is -36 dB. At 0.265 Hz, or 15.9 breaths per minute, the amplitude is -60 dB, and below 0.258 Hz, or 15.5 breaths per minute, the amplitude is below -66 dB. This filter is shown in Figure 7.6. This filter has linear phase above 0.25 Hz, or 15 beats per minute, and its group delay is constant at 300 samples, or 3 seconds.

A 20-tap Kaiser lowpass filter with β of 6.5 and a 20-Hz cutoff is used after the high-pass filter. This filter decreases out-of-band noise that may interfere with the rate-finding. The frequency response of this filter is shown in Figure 7.7.

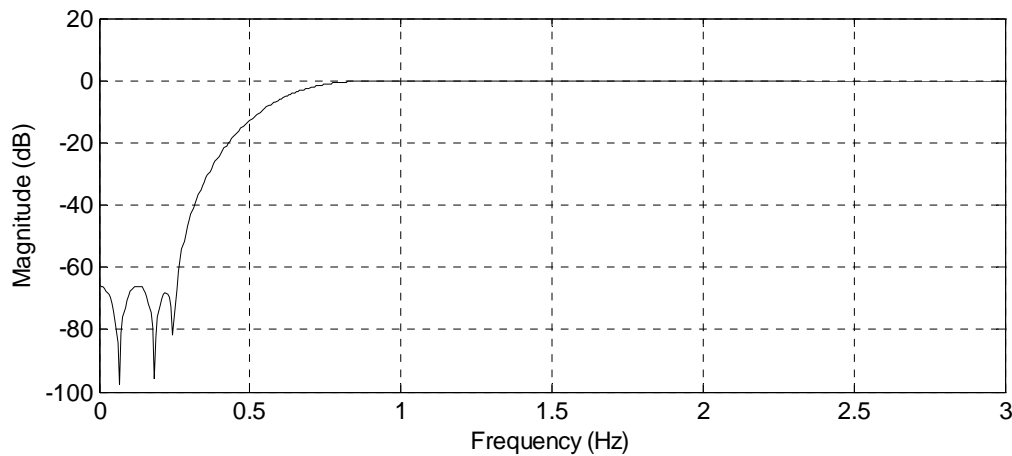


Figure 7.6: Frequency response of the digital filter used to isolate the heart signal from the respiration signal. For a 100 Hz sample rate, this 600-order Kaiser filter has the value of β set to 6.5 and a 3-dB cutoff frequency of 0.675 Hz, or 40.5 beats per minute. The amplitude is below 40 dB at frequencies below 0.315 Hz, or 18.9 breaths per minute, and below 60 dB at frequencies below 0.265 Hz, or 15.9 breaths per minute.

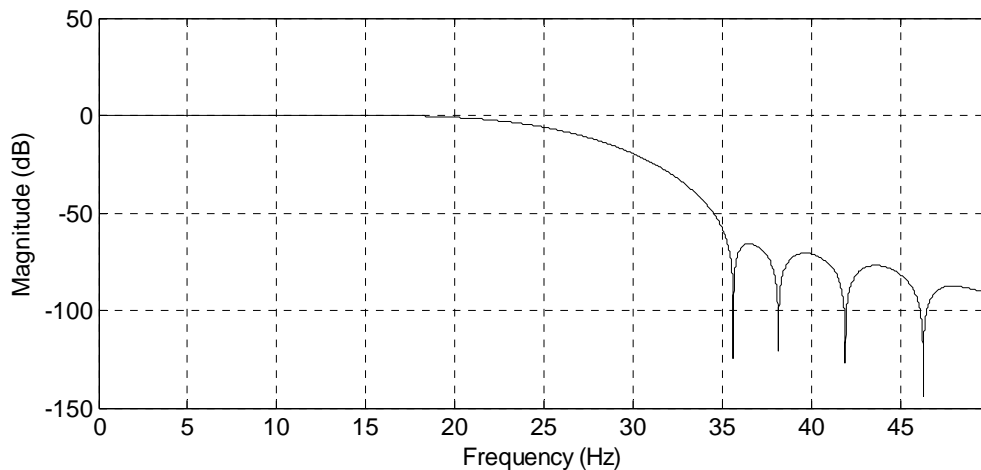


Figure 7.7: Frequency response of the digital filter used to decrease out-of-band noise. For a 100 Hz sample rate, this 20-order Kaiser filter has the value of β set to 6.5 and a 3-dB cutoff frequency of 20 Hz.

7.3.2 Comparison of Methods for Combining I and Q

Arctangent combining, selection combining, maximal ratio combining, equal ratio combining, and principal component combining were compared on all data sets measured in the human subjects testing, described in Chapter 6. The data collected from each subject at each range was processed using each combining technique, and the accuracy was deter-

mined via Bland-Altman statistics, and the SNR was calculated. The heart rate obtained with the Doppler system was compared with the rate obtained with the ECG, and the respiration rate obtained with the Doppler system was compared with the rate obtained with the respiratory effort belts. The accuracy and SNR calculated at each range were averaged for each method, so that the methods could be compared at each range.

The ECG rate is determined by calculating the times of the R-wave peaks, inverting the average of the inter-beat interval in a 8-second window. The rate from the respiratory effort belt is found by combining the abdominal and chest straps with equal-ratio combining followed by a 1-Hz low pass filter to remove out-of-band noise. The rate is calculated by inverting the maximum of the autocorrelated signal in a 18-second Hamming window. The respiration signal is then low-pass filtered with a 1-Hz low pass signal to remove out-of-band noise.

The heart signal is separated from the respiration signal using the Kaiser filter with β of 6.5 and a 0.65 Hz cutoff described in the previous section. The I and Q heart and respiration signals are then combined using each of the techniques. The delay introduced by the filters is corrected so that Doppler heart signals are synchronous with the ECG. The rate is calculated from each of the combined signals using autocorrelation in an 8-second window for the heart and a 18-second window for respiration. The measurement bias and the variance of the difference between the rate measured with the Doppler system and the control are calculated using the Bland-Altman technique, and the SNR is then calculated using the method described in Section 6.3.4.2.

The measurement is then repeated eliminating the data sets for which all methods have a Bland-Altman standard deviation greater than three beats per minute or three breaths per minute and/or a Bland-Altman bias with a magnitude greater than five beats per minute or five breaths per minute. Any differences between the results for the subset and for all data sets indicate that the results are being influenced by signals that are not accurately measuring the rate.

For arctangent combining, the I and Q signals are orthonormalized with the Gram-Schmidt technique, using a measured amplitude error of 2.66 and a measured phase error of 37° . The orthonormalized signals are then adjusted so that the minimum value of each is 0.1 to avoid errors at zero-crossings. Then signals are combined by taking the arctangent of the I signal divided by the Q signal.

For selection diversity the signal with the greatest root-mean-square amplitude is selected.

For equal ratio combining, the RMS amplitude of the sum of the two signals and the difference between the two signals is calculated. The combined signal with the greater RMS value is chosen; this technique is used to ensure that the signals are in-phase and not 180° out-of-phase.

For maximal ratio combining, it is assumed that the noise is the same on all channels since no straightforward technique to measure the noise has been determined. Each signal is multiplied by its RMS amplitude and the results are summed and differenced. The RMS amplitude of the sum and the difference of the scaled signals is calculated, and the combined signal with the greater RMS amplitude is used as the combined signal. This technique is used to ensure that the signals are in-phase and not 180° out-of-phase.

For the principal component combining, the covariance matrix of the I and Q signals is calculated. Its eigenvalues are calculated, and I and Q signals are projected onto the eigenvector associated with the maximum eigenvalue. This projected vector is used as the combined signal.

7.3.3 Comparison of Heart-Rate-Finding Methods

Peak-finding, autocorrelation, and Fourier transform methods of rate-finding are compared for the heart signals. The data collected from each subject at one range is processed using each heart-rate-finding technique with windows of 4 seconds, 8 seconds, 10 seconds, and 15 seconds. The heart rate accuracy is determined via Bland-Altman statistics,

comparing the heart rate found with the Doppler system using each rate-finding method with the heart rate found from the ECG in the same window.

For the peak-finding method, the data is low-pass filtered to eliminate as much noise as possible. An FIR filter with a 1-Hz pass frequency and a 3-Hz stop frequency, and a FIR with a 2-Hz pass frequency and a 1-Hz stop frequency were both used to determine which of the two gets better results. Then the peaks that are greater than zero and between two minima that are less than zero are taken to be beats. The average interval between the peaks in the window is inverted and smoothed with an exponential filter to determine the rate.

For the autocorrelation method, the signal is windowed with a Hamming window, the windowed signal is autocorrelated, and the peaks that indicate a period between 0.5 and 1.7 seconds, or a rate between 120 beats per minute and 35 beats per minute were used to indicate the signal period. The period is inverted, and the result is smoothed with an exponential filter.

For the Fourier transform method, the signal is windowed with a Hamming window, and the fast-Fourier transform with N of 16,384 is taken of the windowed data. The highest peak between 0.6 and 2 Hz is taken to be the heart frequency, and is multiplied by 60 and smoothed with an exponential filter to determine the rate.

7.3.3.1 Windowing

A Hamming window was selected because it minimizes sidelobes, so that the harmonics and residual harmonics from the respiration signal have sidelobes at least 20 dB below the signal. For the heart signal, different window lengths are explored with the various rate-finding methods. For the respiration signal, a 18-second window is used.

7.4 Results

7.4.1 Separating Heart and Respiration with a Digital FIR Filter

Data from two subjects is shown in the time domain and in the frequency domain in Figures 7.8 to 7.11. In each figure, the top trace is the digitized data before filtering, the middle trace is the signal after high-pass filtering to isolate the heart signal, and the bottom signal is the heart signal after low-pass filtering to remove out-of-band noise.

Data from subject 4062, a 31-year-old male with a heart rate of 45.7 beats per minute and a respiration rate of 12.6 beats per minute, is shown in Figures 7.8 and 7.9 to represent subjects with a low heart rate. With this low heart rate, the lowpass filter that removes out-of-band noise has a minimal effect, and only one harmonic of the heart signal is clearly visible. The 0.20-Hz respiration signal is attenuated by 65 dB and the 0.78-Hz heart signal is attenuated by 0.75 dB, so that the respiration signal that is originally 23 dB above the heart signal is 42 dB below the heart signal after the filter.

Data from subject 4665, a 46-year-old female with a heart rate of 68.2 beats per minute and a respiration rate of 15.0 breaths per minute is shown in Figures 7.10 and 7.11 to represent subjects with an average heart rate. With this heart rate, some noise reduction from the lowpass filter is visible in the time-domain signal. Two harmonics of the heart signal are clearly visible in the frequency spectrum. The 0.27-Hz respiration signal is attenuated by 52 dB and the 1.12-Hz heart signal is attenuated by 0.6 dB. This heart signal is 13.5 dB below the respiration signal, and after the high-pass filter, is 27.6 dB above the respiration signal.

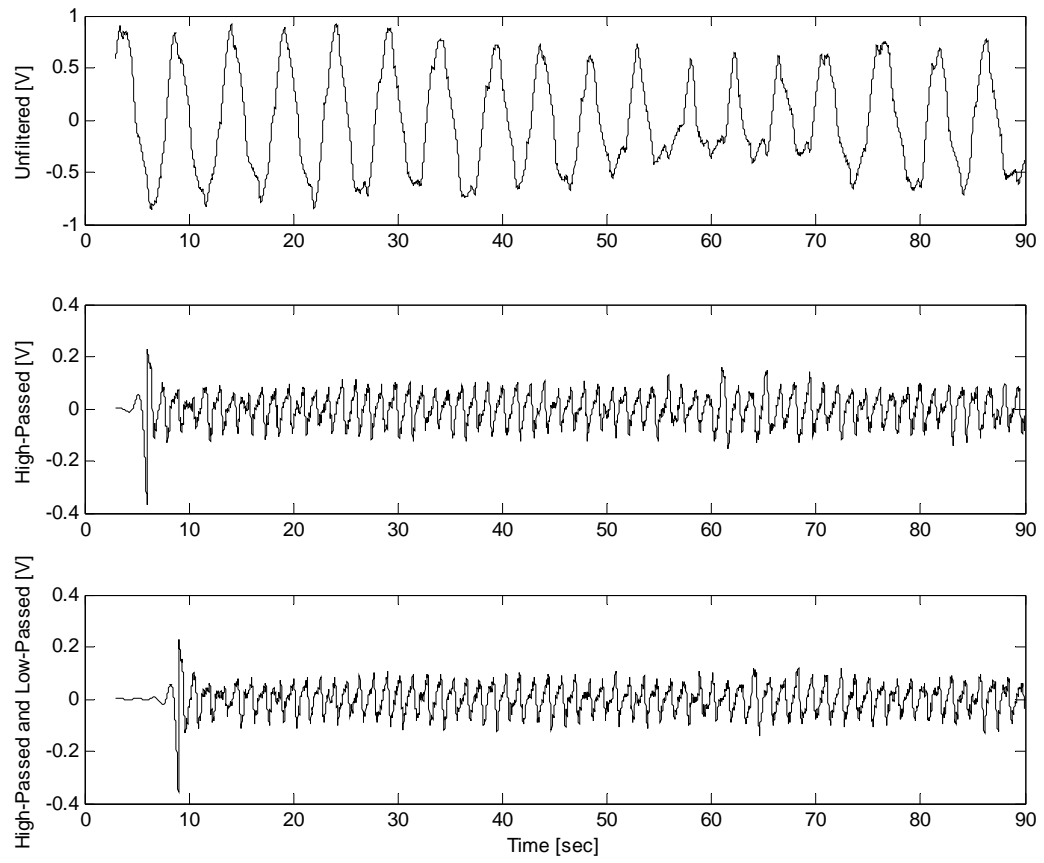


Figure 7.8: Time domain data from subject 4062 at a 50-cm range, before and after filtering.

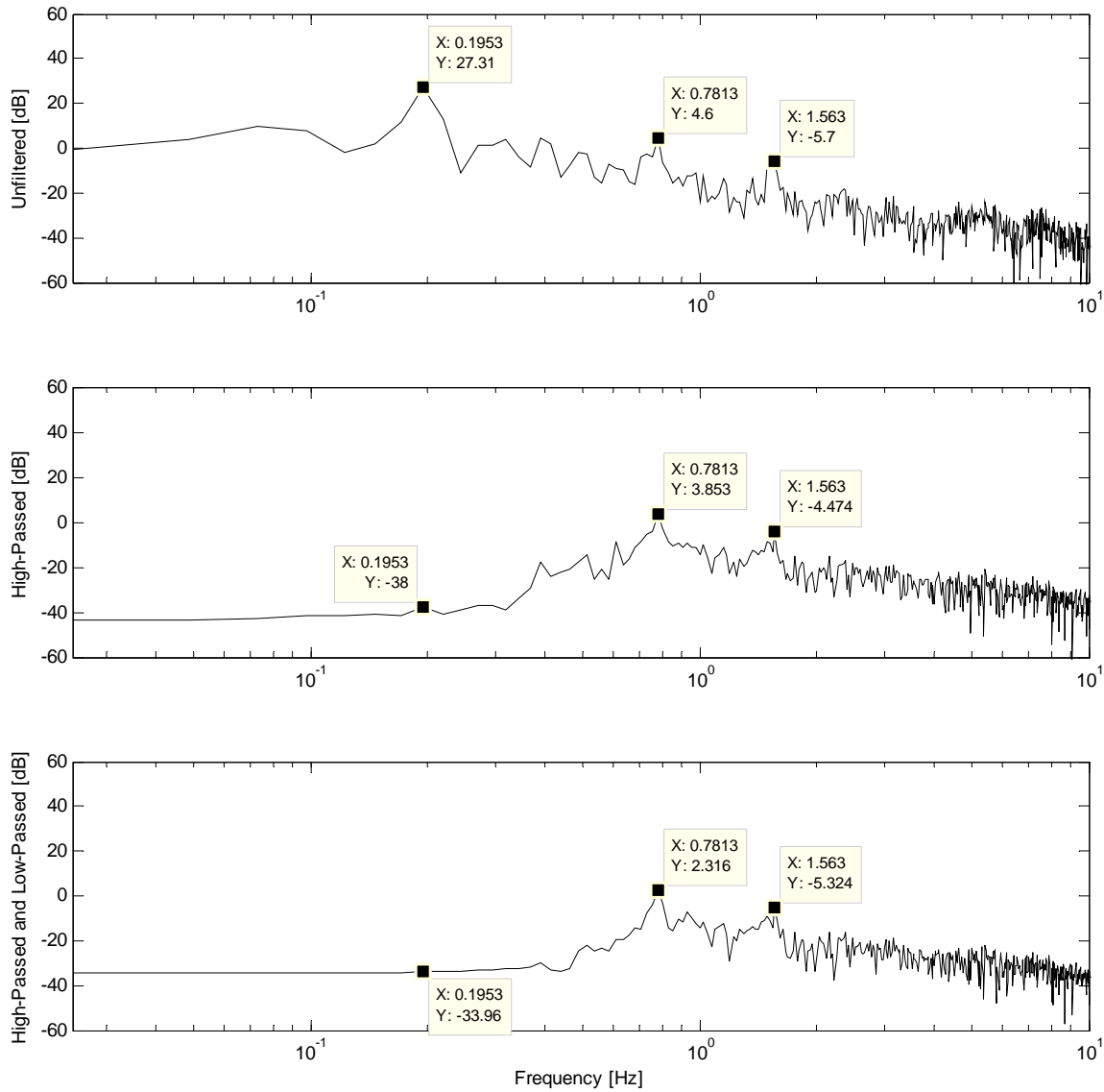


Figure 7.9: Frequency domain data from subject 4062 at a 50-cm range, before and after filtering. The respiration component is at 0.20 Hz, the heart fundamental is at 0.78 Hz, and the first harmonic of the heart signal is at 1.56 Hz.

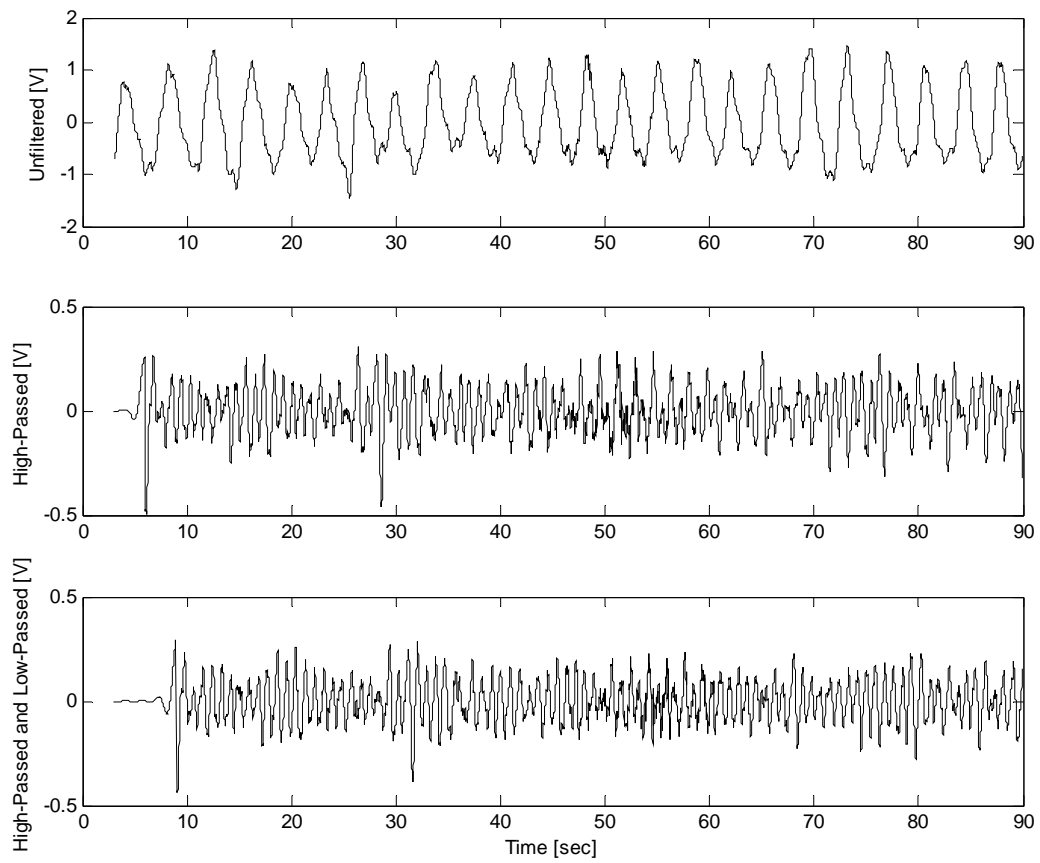


Figure 7.10: Time domain data from subject 4665 at a 50-cm range, before and after filtering.

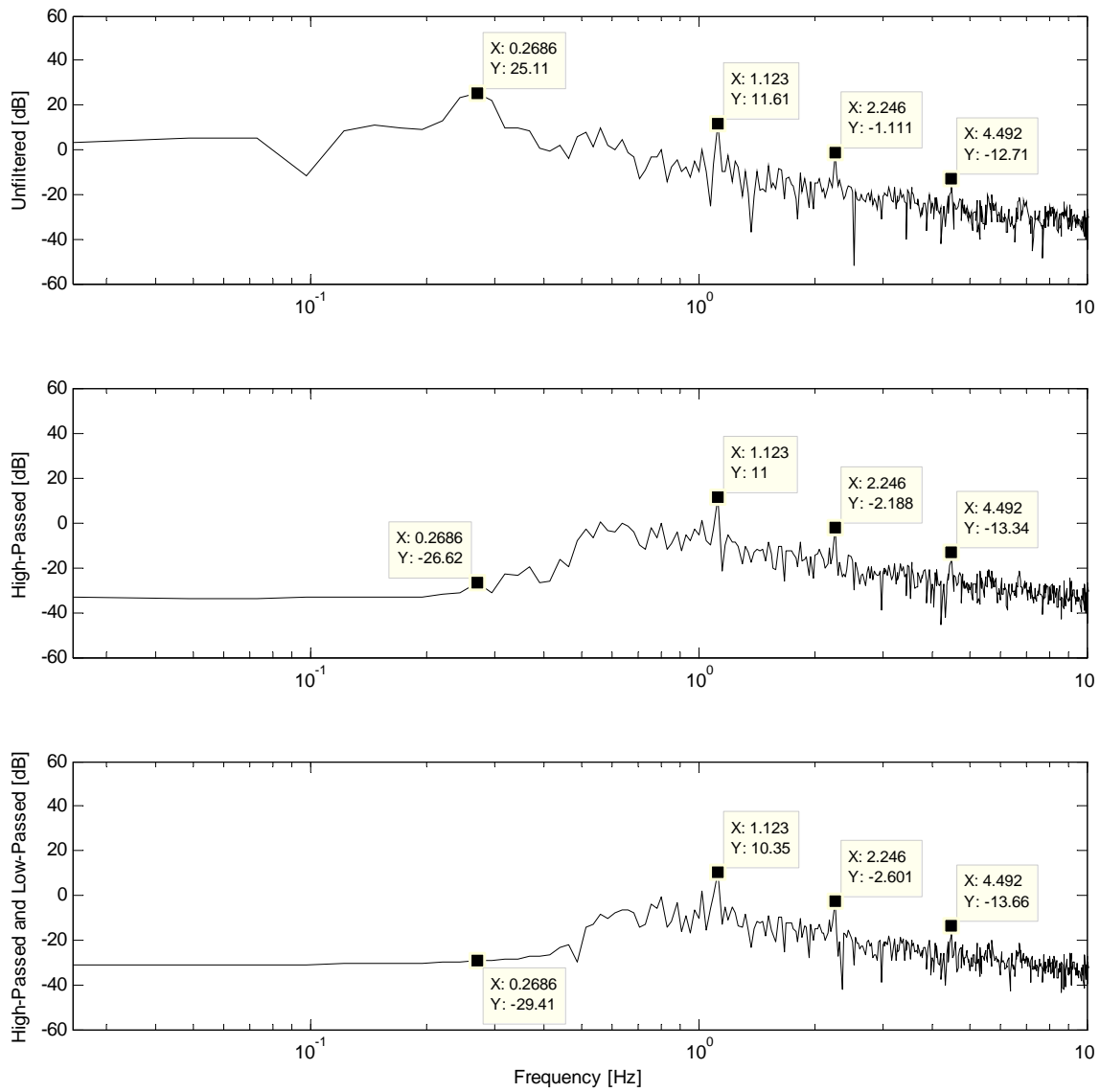


Figure 7.11: Frequency domain data from subject 4665 at a 50-cm range, before and after filtering. The respiration component is at 0.27 Hz, the fundamental of the heart signal is at 1.12 Hz, and harmonics of the heart signal are at 2.25 Hz and 4.49 Hz.

7.4.2 Combining Quadrature Channels

The five combining techniques are compared on all heart data sets, and are shown with the Bland-Altman statistics in Table 7.1 and with the SNR in Table 7.3. Then each data set with a Bland-Altman standard deviation greater than 3 beats per minute or a Bland-Altman bias magnitude of greater than 5 beats per minute is eliminated. The 2.0 m range is not used because only one sample had heart rate accuracy that met the criteria. The Bland-Altman statistics for these data sets are shown in Table 7.2 and the SNR results for these data sets are shown in Table 7.4.

For all heart data, principal components combining and arctangent combining give the best accuracy. Principal components combining seems to be better on the data at closer ranges. When the data set is limited to signals that have accuracy within three beats per minute and a bias under five beats per minute for at least one combining technique, principal components combining is the best.

Table 7.1: Bland-Altman Statistics for Comparison of Heart Rate Measured with the Doppler Radar System to that Measured with the ECG with Different Methods Used for Combining the I and Q Components of the Doppler Radar Signal. The mean of the difference between the rates from the Doppler and the ECG are the 'bias' and the standard deviation of the difference is 'std.' The numbers given are the average value of the statistics over 22 data sets at each range. The standard deviation is also given for the bias.

Combining Technique	Accuracy, heart signal [beats per minute], all 22 data sets							
	0.5 m		1.0 m		1.5 m		2.0 m	
	std	bias	std	bias	std	bias	std	bias
Arctangent Combining	1.75	0.23 ± 2.59	2.81	1.49 ± 4.57	4.69	2.96 ± 7.45	6.56	7.91 ± 9.97
Selection Diversity	2.55	1.10 ± 5.42	4.10	4.35 ± 8.19	6.50	7.44 ± 9.23	6.80	12.5 ± 9.87
Equal Ratio Combining	2.61	1.13 ± 5.51	4.10	4.41 ± 8.37	6.51	7.71 ± 9.42	7.00	13.00 ± 10.06
Maximal Ratio Combining	2.63	1.12 ± 5.46	4.06	4.29 ± 8.06	6.50	7.56 ± 9.26	6.82	12.89 ± 9.79
Principal Component Combining	1.63	0.21 ± 2.68	2.65	1.30 ± 4.39	4.87	2.56 ± 7.30	6.29	8.16 ± 10.17

Table 7.2: Bland-Altman Statistics for Comparison of Heart Rate Measured with the Doppler Radar System to that Measured with the ECG with Different Methods Used for Combining the I and Q Components of the Doppler Radar Signal on Subsets of the Data. The mean of the difference between the rates from the Doppler and the ECG are the 'bias' and the standard deviation of the difference is 'std.'

Combining Technique	Accuracy, heart signal [beats per minute], data subset					
	0.5 m, N=17		1.0 m, N=15		1.5 m, N=8	
	std	bias	std	bias	std	bias
Arctangent Combining	1.32	0.63 ±1.62	1.79	0.52 +/- 2.76	2.86	1.85 +/- 0.88
Selection Diversity	1.87	1.37 ± 3.84	3.23	2.17 +/- 3.98	6.20	5.97 +/- 4.22
Equal Ratio Combining	1.98	1.40 ± 4.10	3.15	2.28 +/- 4.16	6.06	5.98 +/- 3.90
Maximal Ratio Combining	1.96	1.35 ± 3.89	3.18	2.17 +/- 3.92	6.25	5.84 +/- 3.96
Principal Component Combining	1.20	0.68 ±1.56	1.65	0.36 +/- 2.63	2.59	1.76 +/- 0.72

The signal-to-noise ratio is similar for all combination methods except arctangent combining that has a lower SNR at 0.5 to 1.5 m, and a higher SNR at 2.0 m; this is the same with data subsets. The respiration SNR is similar for all diversity combining techniques, but is lower for the arctangent combining.

Table 7.3: Average Signal-to-Noise Ratio for Heart Signals with Each I/Q Combination Method at Each Range. The SNR is averaged over all 22 data sets, and the standard deviation is also provided.

Combining Technique	Signal-to-Noise Ratio, Heart Signal, all 22 data sets			
	0.5 m	1.0 m	1.5 m	2.0 m
Arctangent Combining	0.63 ± 0.52	0.31 ± 0.12	0.22 ± 0.12	0.20±0.08
Selection Diversity	1.02 ± 0.79	0.46 ± 0.21	0.25 ± 0.19	0.17 ±0.09
Equal Ratio Combining	1.01 ± 0.79	0.45 ± 0.20	0.24 ± 0.17	0.15 ±0.08
Maximal Ratio Combining	1.02 ± 0.79	0.46 ± 0.21	0.25 ± 0.18	0.16 ±0.08
Principal Component Combining	1.02 ± 0.79	0.46 ± 0.21	0.25 ± 0.19	0.16 ±0.08

Table 7.4: Average Signal-to-Noise Ratio for Heart Signals with Each I/Q Combination Method at Each Range on Subsets of the Data. The numbers given in the table are the average value of the statistics over N remaining data sets at each range, and the standard deviation is also provided.

Combining Technique	Signal-to-Noise Ratio, Heart Signal, data subsets		
	0.5 m, N=17	1.0 m, N=15	1.5 m, N=8
Arctangent Combining	0.70 ± 0.58	0.32 +/- 0.13	0.31 +/- 0.15
Selection Diversity	1.11 ± 0.88	0.54 +/- 0.18	0.39 +/- 0.25
Equal Ratio Combining	1.10 ± 0.87	0.52 +/- 0.16	0.37 +/- 0.22
Maximal Ratio Combining	1.12 ± 0.88	0.54 +/- 0.17	0.39 +/- 0.24
Principal Component Combining	1.12 ± 0.88	0.54 +/- 0.17	0.39 +/- 0.24

The five I/Q combination methods were also compared for the respiration signals, as shown in Tables 7.5 and 7.6. The respiration accuracy is similar for all combination methods. The SNR is also similar for all combination methods other than arctangent combining, which has a lower SNR at each range.

Table 7.5: Bland-Altman Statistics for Comparison of Respiration Rate Measured With the Doppler Radar System to that Measured with the Respiratory Effort Straps with Different Methods used for Combining the I and Q Components of the Doppler Radar Signal. The mean of the difference between the rates from the Doppler and the ECG are the 'bias' and the standard deviation of the difference is 'std.' The numbers given are the average value of the statistics over 22 data sets at each range. The standard deviation is also given for the bias.

Combining Technique	Accuracy, respiration signal [breaths per minute]							
	0.5 m		1.0 m		1.5 m		2.0 m	
	std	bias	std	bias	std	bias	std	bias
Arctangent Combining	1.28	0.40 ± 1.71	1.30	-0.41 ± 1.12	1.24	-0.16 ± 1.40	1.98	-1.26 ± 2.02
Selection Diversity	1.22	0.33 ± 1.79	1.34	-0.31 ± 1.04	1.15	-0.07 ± 1.37	2.05	-1.33 ± 2.03
Equal Ratio Combining	1.24	0.35 ± 1.76	1.33	-0.30 ± 1.04	1.13	-0.02 ± 1.37	1.92	-1.29 ± 2.10
Maximal Ratio Combining	1.23	0.33 ± 1.79	1.33	-0.31 ± 1.04	1.14	-0.04 ± 1.36	2.03	-1.32 ± 2.05
Principal Component Combining	1.22	0.33 ± 1.79	1.33	-0.31 ± 1.04	1.14	-0.04 ± 1.36	2.02	-1.32 ± 2.04

Table 7.6: Average Signal-to-Noise Ratio for Respiration Signals with Each I/Q Combination Method at Each Range. The SNR is averaged over all 22 data sets, and the standard deviation is also provided.

Combining Technique	Signal-to-Noise Ratio, Respiration Signal			
	0.5 m	1.0 m	1.5 m	2.0 m
Arctangent Combining	6.77 ± 6.12	6.22 ± 6.39	4.32 ± 2.76	4.84 ± 8.13
Selection Diversity	10.63 ± 11.84	8.71 ± 9.29	4.65 ± 3.19	6.42 ± 14.59
Equal Ratio Combining	10.67 ± 11.85	8.85 ± 9.71	4.70 ± 3.20	6.31 ± 13.97
Maximal Ratio Combining	10.64 ± 11.84	8.73 ± 9.35	4.66 ± 3.20	6.40 ± 14.47
Principal Component Combining	10.64 ± 11.84	8.73 ± 9.34	4.65 ± 3.20	6.40 ± 14.50

7.4.3 Heart Rate-Finding

Three different rate-finding techniques were used to calculate heart rates from the data collected in the human subjects study. Each of these techniques was applied with windows of 15 seconds, 10 seconds, 8 seconds, and 4 seconds. The Bland-Altman statistics comparing the heart rate found with the Doppler system using each rate-finding method and each window length to the rate found with the ECG are shown in Table 7.7. Then each data set with a Bland-Altman standard deviation greater than 3 beats per minute or a Bland-Altman bias magnitude of greater than 5 beats per minute is eliminated. The 2.0-m range is not used because only one sample had heart rate accuracy that met the criteria. The Bland-Altman statistics comparing the heart rate found with the Doppler signal with each rate-method technique and window length to the rate found with the ECG are shown in Table 7.8.

At 0.5 m, autocorrelation with any window length is better than any other method, and a longer window leads to better accuracy. At 1.0 m, peak-finding with a 1-Hz lowpass filter had similar accuracy numbers to autocorrelation, but a much larger bias. Autocorrelation is also the better method at this range, and again, a longer window results in better accuracy. The 1.5 to 2.0 m range is not possible to fairly judge since so much of the data had large biases. A limited data set must be used to judge this data.

With the limited data set, autocorrelation is best at all ranges, and longer windows result in better accuracy at 0.5 and 1.0 m. At 1.5 m range, a shorter window has lower variance but larger bias.

Table 7.7: Bland-Altman Statistics for Comparison of Heart Rate Measured with the Doppler Radar System to that Measured with the ECG with Different Methods Used for Rate-Finding of the Doppler Radar Signal. The mean of the difference between the rates from the Doppler and the ECG are the 'bias' and the standard deviation of the difference is 'std.' The numbers given are the average value of the statistics over 22 data sets at each range. The standard deviation is also given for the bias.

Rate-Finding Method	0.5 m		1.0 m		1.5 m		2.0 m	
	std	bias	std	bias	std	bias	std	bias
FFT, 15-second window	2.76	0.77 ± 4.34	4.47	3.37 ± 8.32	6.84	5.56 ± 9.74	7.90	11.45 ± 10.30
Autocorrelation, 15-second window	1.52	0.08 ± 2.64	2.62	0.60 ± 4.11	5.30	1.73 ± 7.07	6.31	7.95 ± 11.40
Peak-finding, 15-second window, 1-Hz pass	2.06	2.62 ± 6.17	2.72	4.87 ± 8.06	3.62	7.83 ± 8.13	3.46	9.83 ± 9.70
Peak-finding, 15-second window, 2-Hz pass	2.33	4.62 ± 6.98	3.01	8.90 ± 9.40	3.74	13.34 ± 9.52	3.55 56	16.20 ± 10.97
FFT, 10-second window	2.59	1.24 ± 5.39	4.30	4.09 ± 8.13	6.80	6.65 ± 9.63	6.93	12.31 ± 10.72
Autocorrelation, 10-second window	1.52	0.23 ± 2.76	2.68	0.95 ± 4.22	4.90	2.04 ± 7.22	6.28	8.05 ± 10.81
Peak-finding, 10-second window, 1-Hz pass	2.01	2.62 ± 6.13	2.71	4.85 ± 8.01	3.62	7.81 ± 8.14	3.50	9.80 ± 9.69
Peak-finding, 10-second window, 2-Hz pass	2.32	4.61 ± 6.92	3.00	8.89 ± 9.36	3.79	13.31 ± 9.52	3.59	16.17 ± 10.97
FFT, 8-second window	2.47	1.10 ± 5.37	4.14	4.36 ± 7.95	6.44	7.18 ± 9.00	6.56	12.73 ± 10.41
Autocorrelation, 8-second window	1.59	0.28 ± 2.81	2.78	1.25 ± 4.23	4.90	2.25 ± 7.60	6.04	8.08 ± 10.26
Peak-finding, 8-second win- dow, 1-Hz pass	1.98	2.62 ± 6.12	2.70	4.83 ± 8.00	3.64	7.77 ± 8.15	3.51	9.79 ± 9.69
Peak-finding, 8-second win- dow, 2-Hz pass	2.30	4.61 ± 6.91	3.00	8.87 ± 9.35	3.82	13.27 ± 9.53	3.62	16.16 ± 10.97
FFT, 4-second window	2.61	2.15 ± 6.50	3.89	5.87 ± 8.66	5.02	8.35 ± 8.44	5.40	13.32 ± 9.93
Autocorrelation, 4-second window	1.72	0.67 ± 3.50	2.84	2.40 ± 5.09	4.12	3.44 ± 7.32	5.15	8.21 ± 9.50
Peak-finding, 4-second win- dow, 1-Hz pass	1.91	2.55 ± 6.09	2.65	4.77 ± 7.99	3.65	7.68 ± 8.14	3.55	9.74 ± 9.66
Peak-finding, 4-second win- dow, 2-Hz pass	2.26	4.53 ± 6.88	3.01	8.81 ± 9.33	3.82	13.17 ± 9.51	3.70	16.10 ± 10.96

Table 7.8: Bland-Altman Statistics for Comparison of Heart Rate Measured with the Doppler Radar System to that Measured with the ECG with Different Methods Used to Determine the Heart Rate from the Doppler Radar Signal. The mean of the difference between the rates from the Doppler and the ECG are the 'bias' and the standard deviation of the difference is 'std.' Data sets with Bland-Altman standard deviation greater than 3 or bias magnitude greater than 5 for all combination techniques were eliminated. The numbers given in the table are the average value of the statistics over N remaining data sets at each range. The standard deviation is also given for the bias.

Rate-Finding Method	0.5 m, N=19		1.0 m, N=16		1.5 m, N=8	
	std	bias	std	bias	std	bias
FFT, 15-second window	1.80	0.60 ± 2.80	3.47	0.68 ± 4.09	4.69	4.12 ± 3.56
Autocorrelation, 15-second window	1.10	0.30 ± 1.93	1.69	-0.36 ± 2.32	2.61	0.78 ± 1.73
Peak-finding, 15-second window, 1-Hz pass	1.87	2.73 ± 5.37	2.71	2.27 ± 5.23	4.02	8.96 ± 5.40
Peak-finding, 15-second window, 2-Hz pass	2.12	4.34 ± 6.23	2.87	5.66 ± 6.31	4.03	14.75 ± 7.66
FFT, 10-second window	1.68	0.91 ± 3.30	3.50	1.33 ± 4.16	5.82	5.65 ± 3.68
Autocorrelation, 10-second window	1.06	0.48 ± 1.96	1.64	-0.28 ± 2.32	2.40	1.12 ± 1.38
Peak-finding, 10-second window, 1-Hz pass	1.80	2.74 ± 5.32	2.67	2.27 ± 5.22	3.94	8.94 ± 5.40
Peak-finding, 10-second window, 2-Hz pass	2.07	4.34 ± 6.19	2.85	5.66 ± 6.31	4.08	14.73 ± 7.65
FFT, 8-second window	1.78	1.06 ± 3.77	3.51	1.56 ± 3.88	5.92	6.43 ± 3.96
Autocorrelation, 8-second window	1.17	0.55 ± 1.92	1.71	-0.12 ± 2.30	2.28	1.33 ± 1.79
Peak-finding, 8-second window, 1-Hz pass	1.76	2.74 ± 5.31	2.65	2.25 ± 5.22	3.90	8.91 ± 5.40
Peak-finding, 8-second window, 2-Hz pass	2.04	4.34 ± 6.18	2.85	5.65 ± 6.32	4.09	14.70 ± 7.64
FFT, 4-second window	2.18	2.25 ± 5.09	3.37	2.76 ± 4.60	4.80	8.43 ± 4.26
Autocorrelation, 4-second window	1.46	1.02 ± 2.51	2.15	0.63 ± 2.72	2.81	2.74 ± 1.92
Peak-finding, 4-second window, 1-Hz pass	1.65	2.68 ± 5.29	2.59	2.19 ± 5.22	3.79	8.82 ± 5.43
Peak-finding, 4-second window, 2-Hz pass	1.98	4.27 ± 6.16	2.85	5.60 ± 6.30	4.07	14.61 ± 7.63

7.5 Discussion

7.5.1 Separating Heart and Respiration with Digital Filters

Because heart rates in the human subjects testing varied between 43 beats per minute and 93 beats per minute, the highest rate was over double the lowest rate; therefore, one fixed filter cannot be optimal for isolating both signals. The 600-tap Kaiser FIR filter used in this application works well given the constraints but has a 3-second group delay, causing changes in the heart rate to show up 3 seconds after they occur. The linear phase does not distort the signal at all.

If the group delay must be minimized for a given application and IIR filter could be better suited. It will distort the signal somewhat, but the fundamental is typically about 10 dB higher than the harmonics of the heart signal that the distortion should have only minor effects on rate-finding accuracy.

Adaptive signal processing could lead to a more optimal heart signal isolation [200, 203]. An adaptive filter can be used to cut out the signal component that has the highest power in the frequency spectrum. Thus the frequency of the respiration signal could be used to set the cutoff frequency of the heart-isolating filter. Self-tuning filters allow the filter cutoff frequency to vary with the heart and respiration rates so the filter does not have to be designed for the worst case [222 - 225]. This enables the use of a less complicated filter with better properties for the signal processing system. The tuning process simultaneously can be used to evaluate the rate of the signal since it tunes to the signal frequency. It is possible to use adaptive signal processing to remove harmonics of the respiration signal as well. This could avoid the harmonic of the respiration signal being misinterpreted as the heart signal.

7.5.2 Combining I and Q

Principal component combining has been found to be the best method for the combination of the I and Q channels when the dc offset is removed before they are digitized.

This method and arctangent combining with shifted dc levels both offered better performance than the traditional diversity techniques, and principal component combining is found to be slightly more accurate than arctangent combining. Principal component combining is a data-driven method, which means it does not require calibration as the arctangent technique with Gram-Schmidt orthonormalization does. If undesired dc offsets are removed without removing the dc offset from the data, arctangent combining may improve the accuracy of the signal.

7.5.3 Rate Finding

The optimal window length is found to be 8 seconds and the optimal method is found to be autocorrelation. The longer the window, in general, the better the signal matching. However, as the window gets longer, it takes longer for the measured rate to change with a change in the heart beat, and 8 seconds is determined to be the best compromise between performance and time resolution. Different methods were best on different data sets. On signals with a high heart SNR, the peak-finding method is typically the best method, but often all methods worked well on these signals. The autocorrelation typically is the best method on the signals with low SNR, and drawing accurate rates out of noisy data is the true challenge to the signal processing system.

It is possible to use multiple methods simultaneously to check whether changes in the rate are consistent between methods. Some non-linear signal processing in the rate-finding algorithm could further improve the accuracy. For example, ignoring sudden jumps in the rate when applying the exponential average could reduce errors in the rate.

If Doppler radar heart and respiration rate monitoring is used in a system where the heart signal has a higher SNR, a different rate-finding method may be optimal, but autocorrelation is the optimal method in the current system. Autocorrelation is also used for the respiration signal.

7.5.4 Advanced Signal-Processing Techniques

Several nonlinear methods can be used to flatten the autocorrelation spectrum, including center clipping and peak clipping [218]. Nonlinear preprocessing can be used to flatten the signal spectrum, increasing the amplitude of the harmonic components of the signal, and thereby enhancing the periodicity of the signal [218]. L. R. Rabiner discusses center clippers, peak clippers, and smoothers as used with autocorrelation to detect the fundamental frequency in [218]. Although these nonlinear preprocessing functions are not used in this work, they could be introduced in future work to improve the detection of the heart and respiration rates.

Wavelet signal processing avoids the trade-offs between time and frequency resolution, so heart and respiration rates could be detected simultaneously. Wavelet analysis inherently uses different resolutions for different frequencies, so it is possible that wavelet analysis could enable heart and respiration rate detection without separating the signals. Bendetto and Pfander [198] provide an overview of the use of wavelets for periodicity detection, and Rioul and Vetterli [220] provide a review and tutorial of wavelet signal processing.

Wavelets can also be used to remove noise in signals; de-noising is the attempt to reject noise by damping or thresholding in the wavelet domain. Donoho [206] presents a technique that reduces noise, achieving almost the best MSE while keeping the function at least as smooth as the original signal. This technique was adapted to images by Chang [202], to speech processing by Medina [214], and to EEG signals by Causevic [201]. This technique could be applied to heart and respiration signatures detected by Doppler radar to remove noise contributed by residual phase noise and baseband $1/f$ noise. Although traditional wavelet denoising [206] requires a SNR of at least 20 dB [205], Causevic et al. have proposed a technique to use denoising in weak biosignals [201].

7.6 Conclusions

The heart and respiration signals are separated digitally with an FIR filter, which is deemed to be superior to an IIR filter for this application. Although the IIR filter can have sharper cutoff with a shorter delay, the non-constant group delay distorts the signal enough that it should not be used unless a shorter group delay is mandatory for the application.

Principal component combining is found to be the best method to combine the I and Q signals after dc offsets have been removed. If a higher resolution analog-to-digital converter is used, dc offsets will not need to be removed. If dc offsets are not removed in analog processing, it may be possible to manipulate the dc value to make arctangent combining superior to principal component combining.

The Hamming window is selected for this application because it minimizes the close-in sidelobes, putting leakage from the respiration signal and its harmonics at least 20 dB below the signal. An 8-second window is chosen for the heart rate finding, as this allows time resolution sufficient to detect changes in the heart rate, but provides better accuracy than a shorter window. For the slowest heart rate of 43 beats per minute, this window includes over 5 heart beats. An 18-second window is chosen for respiration. For the slowest respiration rates, this window includes 1.5 breaths.

Autocorrelation is chosen as the most accurate rate-finding method for noisy signals. Pre-processing functions that enhance the periodicity of a signal may be used with the autocorrelation function in future versions of the digital signal processing algorithm to improve the rate-finding.

In this work, the heart and respiration signals are separated using fixed filters, then the I and Q signals are combined using the principal components combining technique. The heart rate is found by autocorrelating the signal windowed with an 8-second Hamming window, and the respiration rate is found by autocorrelating the signal windowed with an 18-second Hamming window. The rates are averaged with an exponential filter.

Further exploration in adaptive and wavelet signal processing could prove useful in this application, as both broaden the range of heart and respiration rates for which this application could be used by not requiring fixed filters or fixed windows, respectively. The simultaneous use of multiple rate-finding methods and the use non-linear techniques rather than the exponential average for determining if the rate measured is correct could decrease the occurrence of aberrations in the rate, and prevent one aberration from affecting the averaging for the length of the exponential averaging filter.

Additionally, it would be interesting to explore the use of a 24-bit ADC, eliminating the need for dc blocking in the analog signal processing stages. This would eliminate the need for a complicated stage that has a non-linear group delay and requires large capacitors, so that the baseband board could be smaller and more simple. This would also enable the subtraction of dc offsets that are consistent among all measurements made with a given measurement setup. Calibrating for these dc offsets and subtracting them from the data rather than high-pass filtering the signal would retain data at and near dc. When the data near dc is preserved, it is expected that the arctangent combining technique would not result in the errors seen when the dc offset is removed with filtering. This could result in more accurate phase demodulation.

7.7 References

- [197] A. Abidi, "Direct-conversion radio transceivers for digital communications," *IEEE Journal of Solid State Circuits*, vol. 30, no. 12, pp. 1399-1410, 1995.
- [198] J. J. Benedetto and G. E. Pfander, "Periodic wavelet transforms and periodicity detection," *SIAM Journal on Applied Mathematics*, vol. 62, no. 4, pp. 1329-1368, 2002.
- [199] D. G. Brennan, "Linear diversity combining techniques," *Proceedings of the IEEE*, vol. 47, pp. 1075-1102, 1959.
- [200] W. Byrne, P. Flynn, R. Zapp, and M. Siegel, "Adaptive filter processing in microwave remote heart monitors," *IEEE Transactions on Biomedical Engineering*, vol. BME-33, no. 7, pp. 717-722, 1986.

- [201] E. Causevic, R. E. Morley, M. V. Wickerhauser, and A. E. Jacquin, "Fast wavelet estimation of weak biosignals," *IEEE Transactions on Biomedical Engineering*, vol. 52, no. 6, pp. 1021-1032, 2005.
- [202] S. G. Chang, N. Yu, and M. Vetterli, "Adaptive wavelet thresholding for image denoising and compression," *IEEE Transactions on Image Processing*, vol. 9, no. 9, pp. 1532-1546, 2000.
- [203] H.-R. Chuang, Y.-F. Chen, and K.-M. Chen, "Automatic clutter-canceler for microwave life-detection systems," *IEEE Transactions of Instrumentation and Measurement*, vol. 40, no. 4, pp. 747-750, 1991.
- [204] F. E. Churchill, G. W. Ogar, B. J. Thompson, "The correction of I and Q errors in a coherent processor," *IEEE Transactions on Aerospace and Electronic Systems*, vol. AES-17, no. 1, pp. 131-137, 1981.
- [205] R. R. Coifman and M. V. Wickerhauser, "Adapted waveform 'de-noising' for medical signals and images," *IEEE Engineering in Medicine and Biology Magazine*, vol. 14, pp.578-586, 1995.
- [206] D. L. Donoho, "De-noising by soft-thresholding," *IEEE Transactions on Information Theory*, vol. 41, pp. 613-627, 1995.
- [207] S. J. Goldman, "Understanding the limits of quadrature detection," *Microwaves and RF*, vol. 178, no. 1, pp. 67-70, 1986.
- [208] L. J. Griffiths, "Rapid measurement of digital instantaneous frequency," *IEEE Transactions on Acoustics, Speech, and Signal Processing*, vol. ASSP-23, no. 2, pp. 2964-2972, 1975.
- [209] F. J. Harris, "On the use of windows for harmonic analysis with the discrete Fourier transform," *Proceedings of the IEEE*, vol. 66, no. 1, pp. 51-83, 1978.
- [210] I. T. Jolliffe, Principal Component Analysis, Seacaucus, NJ: Springer-Verlag New York, Inc., 2002.
- [211] S. Kay, "Spectral estimation," in Advanced Topics in Signal Processing, (J. S. Lim and A. V. Oppenheim, Eds.), Englewood Cliffs, New Jersey: Prentice Hall, 1988.
- [212] T.-H. Liu, "Principal component combining with differential detection for DPSK signals over Rayleigh fading channels," *IEEE Proceedings on Communications*, vol. 152, no. 6, pp. 1015-1020, 2005.
- [213] R. G. Lyons, Understanding Digital Signal Processing, Upper Saddle River, NJ: Prentice Hall PTR, 2001.

- [214] C. A. Medina, A. Alcaim, and J. A. Apolinario, "Wavelet denoising of speech using neural networks for threshold selection," *Electronics Letters*, vol. 39, no. 25, pp. 1869-1871, 2003.
- [215] A. H. Nuttall, "Some windows with very good sidelobe behavior," *IEEE Transactions on Acoustics, Speech, and Signal Processing*, vol. ASSP-29, no. 1, pp. 84-91, 1981.
- [216] A. V. Oppenheim and R. W. Schaffer, Discrete Time Signal Processing, Englewood Cliffs, New Jersey: Prentice Hall, 1989.
- [217] A. D. Poularikas, The Transforms Applications Handbook: 2nd ed., Boca Raton: CRC Press LLC, 2000.
- [218] L. R. Rabiner, "On the use of autocorrelation analysis for pitch detection," *IEEE Transactions on Acoustics, Speech, and Signal Processing*, vol. ASSP-25, no. 1, pp. 55-69, 1977.
- [219] B. Razavi, "Design considerations for direct-conversion receivers," *IEEE Transactions on Circuits and Systems*, vol. 44, no. 6, pp. 428-435, 1997.
- [220] O. Rioul and M. Vetterli, "Wavelets and signal processing," *IEEE Signal Processing Magazine*, vol. 8, no. 4, pp. 14-38, 1991.
- [221] J. O. Smith III, Mathematics of the Discrete Fourier Transform with Music and Audio Applications, W3K Publishing, 2003.
- [222] J. R. Treichler, "Transient and convergent behavior of the adaptive line enhancer," *IEEE Transactions on Acoustics, Speech, and Signal Processing*, vol. ASSP-27, no. 1, pp. 53-62, 1979.
- [223] B. Widrow and S. Stearns, Adaptive Signal Processing, New Jersey: Prentice Hall, 1985.
- [224] B. Widrow, J. R. Glover Jr., J. M. McCool, J. Kaunitz, C. S. Williams, R. H. Hearn, J. R. Zeidler, E. Dong Jr., and R.C. Goodlin, "Adaptive noise cancelling: principles and applications," *Proceedings of the IEEE*, vol. 63, no. 12, pp. 1692-1716, 1975.
- [225] J. R. Zeidler, E. H. Satorius, D. M. Chabries, and H. T. Wexler, "Adaptive enhancement of multiple sinusoids in uncorrelated noise," *IEEE Transactions on Acoustics, Speech, and Signal Processing*, vol. ASSP-26, no. 3, pp. 240-254, 1978.

Chapter
8

Summary, Outlook and Conclusions

Doppler radar monitoring provides a method to determine the heart and respiration rates of relatively still subjects without contact and through clothing or bedding. In some applications, this approach could eliminate the need for affixing electrodes to a subject's skin and wiring a subject to a monitor. The technology for this radar monitor has been miniaturized, with the radio transceiver fully integrated on a single CMOS chip. Because a monolithic design can be inexpensively mass-produced, this system could be applied to consumer markets for home monitoring of sleep-disordered infants and adults as well as the elderly and chronically ill. Additionally, if the electronics are inexpensive to manufacture, the incremental cost of adding additional transceivers is low, making it feasible to use multiple transceivers simultaneously to overcome problems such as motion artifacts and multiple subjects in the sensing area.

The feasibility of using a single CMOS chip for microwave Doppler radar monitoring of respiratory and heart motion has been demonstrated in this thesis. The transceiver chip, which operates in the 2.4-GHz ISM band, leveraged DCS-1800 cellular basestation CMOS subcircuit designs by using re-tuned versions in a different configuration to develop the radar transceiver. One free-running oscillator provides both the source for the transmitter and the LO for the receiver. The quadrature direct-conversion receiver uses two active-balun-amplifiers and a passive resistive ring mixer in each receiver chain. In this system, the dominant noise source is residual phase noise, and this noise limits the range from which heart and respiration rates can be accurately measured.

A method comparison study was performed with 22 human subjects to compare heart and respiration rates measured by the Doppler radar system at ranges from 0.5 m to 2.0 m to heart rates measured with a conventional ECG and respiration rates measured with respiratory effort belts. The heart rate was accurately measured at ranges up to one meter for most subjects, and the respiration was accurately measured at ranges up to 1.5 meters for most subjects. The data from the method comparison study was used to verify theoretical calculations of the variation of the signal-to-noise ratio with range, to determine that principal component analysis is the best of the five techniques evaluated to combine the quadrature channels after dc offsets are removed, and to determine that autocorrelation is the best of three methods evaluated for calculating the heart rate from the chest motion signature obtained with Doppler radar.

The use of CMOS fabrication technology makes the system potentially inexpensive to mass produce, but because CMOS transistors have high $1/f$ noise, it also means that the oscillator has high phase noise at the frequencies of interest, which are below ten Hz. The phase noise is reduced by the range correlation effect, but residual phase noise is the dominant noise source in the system when a CMOS transceiver is used. Range correlation theory shows that the total time delay between the transmitting and receiving the signal is the critical factor in determining the amount of residual phase noise - not just the target range or the transit time for the signal in the air, which determines the signal power. Therefore, minimizing delays between the oscillator and the antenna maximize the range for a given signal-to-noise ratio. Range correlation theory was experimentally verified for time delays applicable to Doppler radar monitoring of respiration and heartbeat in this thesis.

The noise sources, the variation of signal and noise powers with range, and how the noise sources affect system-level choices have been discussed in detail. The theoretical variation of the SNR with range was presented and the results from the human subjects testing showed that it falls off with range as predicted, confirming that residual phase noise is the dominant noise source.

There are three main areas for future work in single-chip Doppler radar cardiopulmonary monitoring. First, there are areas where the transceiver itself can be improved, both

the circuit design and potentially the architecture. Second, there is room for improvement in the signal processing; adaptive and wavelet signal processing could broaden the range of heart and respiration rates that could be measured, and they also could be used to eliminate some noise sources and perhaps some motion artifacts. Third, simultaneous operation of multiple transceivers with MIMO signal processing shows promise for separating signals from multiple subjects and for isolating physiological motion from other motions of the subject that are spatially separated from the heart and respiration motion.

A new version of the transceiver should explore possible improvements to the mixer, phase shifting network, and the voltage-controlled oscillator (VCO). With a direct-conversion receiver, $1/f$ noise and second-order intermodulation are important factors, and the mixer could be optimized for these values. The currently used resistive-capacitive phase shifting network has poor phase and amplitude balance in the integrated receiver; other phase shift networks should be explored to improve phase and amplitude balance. Finally, the VCO could be phase-locked to a low-phase-noise reference to reduce the residual phase noise and improve the SNR.

Additionally, if a new version of the transceiver is designed, a low intermediate-frequency architecture should be considered. Digitizing at the intermediate frequency would make analog signal conditioning, including dc offset removal and automatic gain control much more simple, and possibly integrable on the same chip as the radio. Removing the dc offset with a low-IF receiver would not result in a loss of data and it would remove mixer $1/f$ noise and second order intermodulation products issues. Finally, this architecture would allow more flexibility in the signal processing. This architecture is briefly discussed in Appendix F. Potential drawbacks with a low-IF transceiver include more stiff requirements on phase and amplitude balance, and a potential increase in residual phase noise from mixing the VCO signal with a digitally generated signal at a lower frequency.

The signal processing for isolating the heart signal from the respiration signal, and for determining the heart and respiration rates could be greatly improved. Either wavelet or adaptive signal processing for isolating the heart rate could broaden the range of heart and respiration rates that the system could detect for a given range with fixed filters. Wavelet

analysis avoids trade-offs between time and frequency resolution, and potentially eliminates the filtering step that separates the signals, allowing simultaneous detection of both rates. Adaptive filtering enables the cutoff frequency of the filter that isolates the heart signals to be tuned based on the frequency of the detected respiration signal. Nonlinear pre-processing of the signals before rate-finding has potential to enhance the periodicity of the signals, potentially improving the rate-finding. Wavelet denoising could reject noise at frequencies away from the signal frequencies without attenuating the signal's harmonics. Finally, in the rate-averaging step, some nonlinear methods could be used to determine when an outlier rate has been estimated, and eliminate it from the average, avoiding the propagation of an error in the rate for many subsequent measurements.

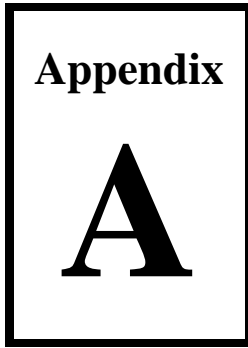
Finally, the simultaneous use of multiple transceivers with MIMO signal processing is promising for solving some of the problems that plague Doppler radar cardiorespiratory monitoring with current methods, such as the error that occurs when multiple persons are in the antenna illumination area, or the error when a part of the subject other than the chest is moving, creating motion artifacts, like the subject tapping his or her leg or twitching occasionally. This is a very interesting area for future research that should be explored, as solving these problems would open Doppler radar cardiorespiratory monitoring to a much broader set of potential applications, including emergency and triage situations and continuous monitoring of soldiers, first responders and astronauts.

Contributions of this thesis to the art and science of non-contact cardiorespiratory monitoring include the development of the first fully integrated CMOS radar transceivers, the first published experimental proof of the range correlation theory, a review of previous measurements of motion at the skin surface due to heartbeat and respiration, and a study comparing Doppler radar measurements of heart and respiration to standard measurements on over 20 subjects. Additionally, an estimated value for the product of the radar cross-section of the moving part of the chest and the amount of chest motion was determined for both heart and respiratory motion, enabling estimation of the SNR due to heart and respiration in future system-level analysis. Finally, principal components combining was shown to be the best method of five methods to combine quadrature channels if dc

offsets are removed in analog signal conditioning, and autocorrelation was shown to be the best of three techniques to determine heart rate from the Doppler radar heart signature.

The current version of the single-chip Doppler radar cardiorespiratory detection system can successfully measure heart rate up to one meter and respiration rates up to two meters in most subjects that have been instructed to sit still. The current system could be used to monitor sleeping or unconscious persons from a relatively close range, avoiding the need to apply electrodes in the correct position and to wire the subject to the monitor. The system can detect heart and respiration rates through clothing and bedding, so these rates can be monitored without the need for the subject to wear special clothing or to remove clothing from the subject, allowing a sleeping subject to sleep in normal conditions and allowing quicker access to and unconscious subject's vital signs.

Doppler radar cardiopulmonary monitoring offers a promising possibility of non-contact, through-clothing measurement of heart and respiration rates. A CMOS single-chip version of this technology offers a potentially inexpensive implementation that could extend applications to consumer home-monitoring products, and could enable the use of multiple transceivers to solve some system-level problems. Further advances in the circuit design, system design and signal processing can increase the range and quality of the rate-finding, broadening the potential application areas of this technology.



Medical Glossary

abdominal viscera - organs in the abdominal cavity

airway - tube connecting the external environment to the alveoli

alveoli - air containing sacs in the lungs where gas exchange occurs

anterior - the front

aorta - main trunk of the systemic arteries, carrying blood from the left side of the heart to the arteries of all limbs and organs except the lungs

aortic valve - passive heart valve between the left ventricle and the aorta that opens when left ventricular pressure is greater than aortic pressure, leading to ventricular ejection

apex - the pointed part at the lower end of the heart; the foremost part of the heart; in fit, young adults, the surface marking of the apex of the heart is the fifth left intercostal space

apexcardiogram - mechanical measurement of the chest wall motion due to heart at the point of maximal impulse relative to other parts of the chest.

arterial applanation tonometry - measurement of arterial pressure by measuring the force it takes to flatten a superficial artery

arteries - the muscular elastic tubes that form a branching system and that carry blood away from the heart to the cells, tissues and organs of the body

arterioles - the smallest of the arteries, that which feeds the capillaries

atrium - upper chamber of the heart, which stores blood from the veins and empties into the lower chamber. Plural is atria.

AV node (atrioventricular node) - A small mass of specialized cardiac muscle fibers located in the wall of the right atrium of the heart that receives heartbeat impulses from the sinoatrial node and directs them to the walls of the ventricles.

brachial artery - the main artery of the upper arm, superficial at the elbow

bundle of His - a bundle of modified heart muscle that transmits the cardiac impulse from the atrioventricular node to the ventricles causing them to contract

capillary - a microscopic blood vessel where fluid exchange between the blood and the tissue occurs

capnography - measurement of expired carbon dioxide

cardiokymograph - displacement cardiograph; a coil in a tuned oscillator is placed near to the chest wall; movement of the chest changes the coil's environment and therefore the oscillation frequency

carotid artery - either of two major arteries of the neck and head; branches from the aorta; superficial at the neck

depolarization - loss of the difference in charge between the inside and outside of the plasma membrane of a muscle or nerve cell due to a change in permeability and migration of sodium ions to the interior

diaphragm - the major muscle of respiration; the diaphragm is attached to the complete boundary of the thorax from which its dome extends up into the thoracic cavity, contacting the lower lobe of the lung.

dichrotic notch - small downward deflection in arterial pressure contour immediately following closure of the aortic valve and preceding the dichrotic wave; in the aorta it is sharper and is known as the incisura

distal - farthest from the origin

dorsalis pedis artery - the main artery of the foot superficial at the top of the foot

diastole - dilatation of the heart chambers, especially the ventricles, during which they fill with blood

exhale - to let out or force out the breath

- femoral artery** - the main artery of the thigh, supplying blood to the groin and lower extremity; superficial at the upper inner thigh
- heart** - chambered muscular organ that pumps blood received from the veins into the arteries, so that blood flows through the entire circulatory system
- impulse cardiogram** - mechanical measurement of the chest wall motion due to heart activity relative to the laboratory frame of reference
- incisura** - a downward notch in the curve recording aortic blood pressure that occurs between systole and diastole and is caused by backflow of blood for a short time before the aortic valve closes
- inhale** - to draw in the breath
- inferior vena cava** - largest vein in the human body, returns blood to the right atrium of the heart from bodily parts below the diaphragm
- interatrial septum** - the wall separating the right and left atria of the heart
- intercostal muscles** - muscles that connect adjacent ribs and costal cartilages.
- intercostal space** - the space between the ribs, numbered from top to bottom
- interventricular septum** - the wall separating the right and left ventricles of the heart
- isovolumetric contraction** - contraction of the heart while AV valves are closed, increasing the pressure on a constant blood volume in the heart
- kinetocardiogram** - see impulse cardiogram
- left atrium** - the left upper chamber of the heart that receives blood from the pulmonary veins
- left midclavicular line** - an imaginary line extending from the center of the left clavicle downward over the trunk parallel to the midline, often through the left nipple
- left ventricle** - the chamber on the left side of the heart that receives arterial blood from the left atrium and pumps it into the aorta
- lung** - organ of gas exchange in the thorax. The lung expands as the thoracic volume increases
- mechanocardiography** - measurement of the motion or vibration of the chest wall due to the heart beating

mid-clavicular line - an imaginary line from the midpoint of the clavicle, often through the nipple, dividing each side of the anterior chest into two parts

mitral valve - heart valve between left atrium and left ventricle

myocardium - muscular tissue of the heart

pacemaker cells - cells that control the heart rate by making electric impulses

parasternal - adjacent to the sternum

pericardium - the membranous sac filled with serous fluid that encloses the heart and the roots of the aorta and other large blood vessels

pleural sac - membrane enclosing a lung, connected to the lung, the thorax wall, and the diaphragm

point of maximal impulse (PMI) - the largest palpable impulse on the chest due to heart motion; in healthy young subjects, this is in the fourth or fifth intercostal spaces in the left mid-clavicular line

popliteal artery - continuation of the femoral artery that branches to supply the legs and feet; superficial at the back of the knee

posterior tibial artery - artery of the lower leg, superficial at the inner ankle

pulmonary - relating to, or affecting the lungs

pulmonary artery - artery that carries venous blood from the right ventricle of the heart to the lungs

pulmonary vein - vein that carries oxygenated blood from the lungs to the left atrium of the heart.

pulmonic valve - heart valve between the right ventricle and the pulmonary artery

Purkinje fibers - part of the impulse-conducting network of the heart; they rapidly transmit impulses from the atrioventricular node to the ventricles

radial artery - branch of the brachial artery beginning below the elbow and extending down the forearm around the wrist and into the palm; superficial at the wrist

repolarization - restoration of a polarized state across a membrane, as in a muscle fiber following contraction

right atrium - the right upper chamber of the heart that receives blood from the venae cavae

right ventricle - chamber on the right side of the heart that receives venous blood from the right atrium and forces it into the pulmonary artery

sinoatrial node (SA node) - small mass of specialized cardiac muscle fibers located in the posterior wall of the right atrium of the heart that acts as a pacemaker by generating at regular intervals the electric impulses of the heartbeat

sternum - the long flat bone in the middle of the thorax

superior vena cava - the second largest vein in the human body, returns blood to the right atrium of the heart from the upper half of the body

systole - contraction of the heart, especially of the ventricles, by which blood is driven through the aorta and pulmonary artery after each dilation or diastole

thorax - the part of the human body between the neck and the abdomen, bounded on the top by neck muscles and on the bottom by the diaphragm. The spinal column, ribs, and sternum form the thorax wall; displacement of either the rib cage or the diaphragm can change the volume of the thoracic cavity

tricuspid valve - heart valve between the right atrium and right ventricle

veins - any of the membranous tubes that form a branching system and carry blood to the heart

vena cava - either of two large veins by which the blood is returned to the right atrium of the heart: superior vena cava and inferior vena cava

ventricle - the lower chamber of the heart, which ejects blood into an artery.

ventricular ejection - when the aortic valve opens and blood from the left ventricle flows into the aorta

Appendix
B

Quadrature Mixing in Direct-Conversion Receivers

B.1 Introduction

Quadrature receivers are used in communications systems to decode phase-modulated information. Quadrature encoding and decoding are used in color television; its use allowed the color television signals to be backward compatible with the black and white televisions [233]. The amplitude still corresponded to the luminance, but the phase contained information about the color. Quadrature phase shift keying (QPSK) is a digital modulation scheme that requires coherent generation and demodulation, and it is commonly used in CDMA cellular signal encoding [232]. Quadrature receivers are also used in heterodyne image-rejection architectures. These avoid the need for front-end channel-select filtering at the RF frequency [236]. In direct conversion receivers, the image signal cannot be eliminated with filtering, because the image signal and desired signal are in the same frequency space, so that quadrature receivers are necessary with this architecture.

In radar, a quadrature receiver is used to develop a phase-coherent receiver. This enables obtaining a velocity vector rather than just a speed with the Doppler shift, which is important in both moving target indicator (MTI) and synthetic aperture radar (SAR) [240].

B.2 Complex Exponentials and Quadrature Mixing

While real signals' positive and negative frequency components are mirror images of each other, complex exponentials can have positive and negative frequencies that do not have the same frequency spectra. A detailed description of complex signals and negative frequency is given in Appendix C of [235], and a brief description is given here. Euler's equations define complex exponential phasors as:

$$e^{j\omega t} = \cos(\omega t) + j\sin(\omega t) \quad (2.1)$$

and

$$e^{(-j\omega t)} = \cos(\omega t) - j\sin(\omega t), \quad (2.2)$$

where $j = \sqrt{-1}$. The $\cos(\omega t)$ term describes the phasor's real component, while the $\sin(\omega t)$ term describes the phasor's component along the imaginary, or j axis. Euler's equations can be manipulated to show that

$$\sin(\omega t) = \frac{1}{2j}(e^{j\omega t} - e^{-j\omega t}) \quad (2.3)$$

and

$$\cos(\omega t) = \frac{1}{2}(e^{j\omega t} + e^{-j\omega t}). \quad (2.4)$$

These equations indicate that the cosine has equal positive components at $+\omega$ and $-\omega$, while the sine has a positive component at $+\omega$ and a negative component of equal magnitude at $-\omega$, as is shown in Figure B.1.

Additionally,

$$\sin(\theta) = \cos\left(\theta - \frac{\pi}{2}\right) \quad (2.5)$$

and

$$\cos(\theta) = -\sin\left(\theta - \frac{\pi}{2}\right). \quad (2.6)$$

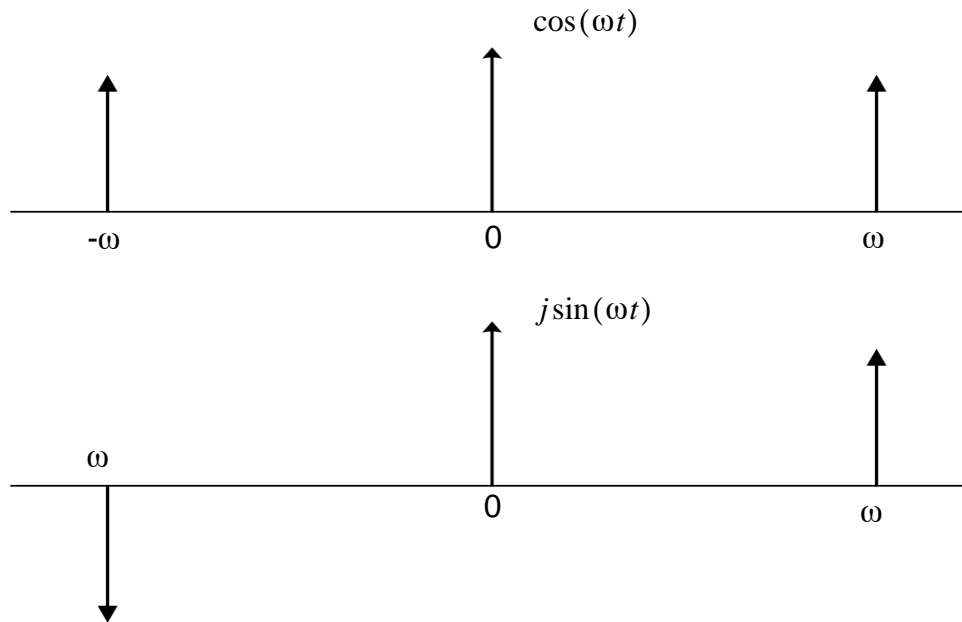


Figure B.1. Spectra of a real cosine signal and an imaginary sine signal when represented in complex notation.

Therefore, a delay in the time domain manifests itself as a phase shift in the frequency domain, and this delay can shift a sine wave to a cosine wave.

In quadrature processing, by convention, the real part of the spectrum is called the in-phase component, and the imaginary part of the spectrum is called the quadrature-phase component. Real signals, those signals that are real in the time domain, have positive and negative frequency components. The positive and negative frequency components of a real spectrum are symmetric about the zero-frequency point. However, the positive and negative frequency components of a quadrature, or imaginary, spectrum are complex conjugates of each other. Complex signals are a combination of in-phase and quadrature, or real and imaginary components.

A complex exponential, for example, $e^{-j2\pi f_{LO}t}$, has only a single frequency component, in this case at a negative frequency, $-f_{LO}$. Although the complex exponential is not real, it can be realized by multiplying the signal by both a sine and a cosine at the LO frequency, and then the two signals can be combined as in Euler's equation above [236]. This is illustrated in Figure B.2.

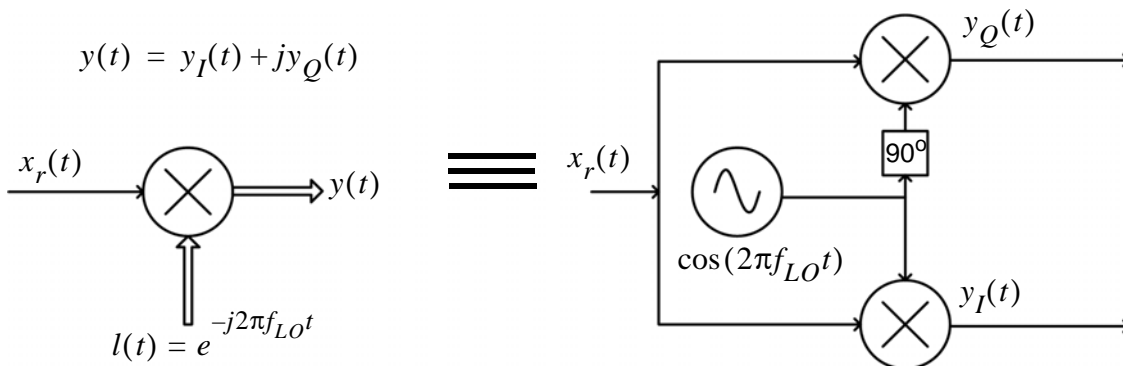


Figure B.2. For the real signal, $x_r(t)$, to be multiplied by a complex exponential with only a negative frequency component, $l(t)$, the signal must be split and mixed with local oscillator signals to determine the in-phase component, $y_I(t)$, and the quadrature component, $y_Q(t)$. The LO signal on the Q channel is delayed by 90° before mixing. The two components can be summed to create the output: $y(t) = y_I(t) + jy_Q(t)$.

B.3 Direct-Conversion Receivers

The architecture of a homodyne receiver is simpler than that of a heterodyne receiver. Since all the amplification and filtering is at baseband rather than at a higher intermediate frequency, direct conversion receivers use less power than heterodyne receivers, which is one of the main reasons for their popularity. Another advantage of a homodyne system is the lack of a need for the high-Q tunable bandpass filter; usually a broadband RF filter eliminates noise and distorting signals sufficiently to meet dynamic range requirements [228].

Each of these advantages have fueled interest in direct conversion receivers for communications applications and also apply to Doppler monitoring of heart and respiration motion. Additionally, the range correlation effect is maximized in a homodyne architecture where the same oscillator is used for transmitting and receiving, and no additional oscillators are needed that may also contribute phase noise.

B.3.1 Challenges with Direct Conversion Receivers

There are still several challenges with direct conversion receivers. The most serious problem experienced by direct conversion receivers is the generation of a dc offset in the baseband section following the mixer. This dc offset is usually larger than flicker or thermal noise and can be larger than the received signal itself, imposing a major adverse effect on the SNR [226]. The dc offset arises from many causes; the largest offset typically comes from a signal at the LO frequency that is not the desired signal. In communication receivers there is no transmitted signal, so that the offending offset is usually caused by LO coupling to the RF input port. This may happen by the LO signal exiting through the antenna, reflecting off an object, and returning to the receiver through the RF input port [226], or by the LO coupling to the RF input through the chip substrate, the bondwires, or the package leads. When this signal is mixed to baseband, it may cause a dc offset. Additionally, a large undesired interfering signal at the RF input can leak into the LO port of the mixer, causing additional down-conversion to dc [226]. The dc offset must be removed in order to avoid corrupting the signal or saturating baseband stages, either of which would decrease the SNR. The dc offset caused by a leaked signal reflecting off objects is time-varying, as are dc offsets from interferers. DC offsets through the package or the chip are not time-varying or vary slowly with time, so that they are easier to remove.

In a homodyne radar transceiver, the dc offset may come from all of these causes, as well as from others. The radar transceiver intentionally transmits a signal, unlike a communication receiver, so that undesired reflections (or clutter) reflect more signal back to the receiver than with unintentional LO transmission. If the transmitter and the receiver share an antenna, some of the transmitted signal may be reflected directly to the receiver. Also, the circulation between the transmitter and receiver may not provide sufficient isolation.

The first method to remove dc offset is with high-pass filtering of the signal. However, for most modulation schemes, this requires an extremely low frequency highpass filter (5-Hz or lower cutoff) [226]. This requires the use of prohibitively large capacitor values,

which are large and expensive (if available at all), cause phase distortion due to capacitive-resistive coupling, and cause long time-delays [226]. This is a viable solution when the signal has very little baseband energy near dc, so that higher cutoff frequencies can be used, thereby decreasing the size of the required capacitors [236]. For communications, there is a drive towards spectrally efficient dc-free modulation schemes that enable the ac-coupling method of dealing with dc offset problems. If the signal can be digitized with sufficient resolution without removing dc, dc offsets can be removed digitally: the baseband signal can be digitized and averaged over a time window, and a DAC can provide a dc value to be subtracted from the baseband signal [226]. The spectrum loss at dc depends on the time-constant of the averaging.

Another problem is flicker noise, which causes the SNR to be lower than at an IF where only the thermal noise is present. This is a particular problem in CMOS devices [236, 241].

Direct conversion receivers often have a problem with spurious LO leakage where part of the LO signal leaks to the antenna and transmits, causing a problem with FCC regulations [226]. This is not a problem in the Doppler radar, where the LO is also the transmitted signal.

Phase and gain errors in the quadrature signal generation can cause some problems. However, it is possible to use digital least-mean-square (LMS) adaptive algorithms at baseband to sense and compensate for phase and gain errors [226]. This gain and phase mismatch leads to imperfect complex mathematics. If it is not compensated for, the receiver's performance is deteriorated [236].

B.3.2 Direct Conversion Receivers Used in Radar Systems

Radar systems that use the same oscillator for transmitting and receiving are known as coherent radar systems [237]. Coherent systems alleviate requirements on oscillator phase noise [227]. Coherent radar signal processing techniques require that the receiver has knowledge of the phase of the transmitted signal, and this phase is used to extract informa-

tion from the received signal. The information is at least partially encoded in the difference between the phase of the received signal and the phase reference, and the information extraction typically takes place at baseband or a very low frequency [234]. The homodyne technique provides one obvious solution: multiply the received signal by the carrier to get the phase difference between the two signals [229].

Coherent system techniques allow target detection at weak signal levels lower than those detectable with non-coherent techniques [229]. When the dominant source of signal instability is the radar system oscillator that provides both transmitted and reference carrier signals, the requirements for the oscillator are decreased over an incoherent radar system [237].

When converting the signal to baseband, any signal that leaks directly from the transmitter to the receiver is converted to a dc offset, and reflections from clutter are converted to either dc offsets or very low-frequency noise. The baseband output can be filtered to remove dc offsets from the transmitted signal.

Converting to baseband folds the frequency spectrum, making incoming targets indistinguishable from outgoing targets. Additionally, sideband noise from both the positive and negative frequencies is folded into the baseband signal spectrum, resulting in a 3-dB decrease in the signal-to-noise ratio. However, a quadrature receiver can be used for single-sideband detection, which allows direction-sensitive detection [231] and avoids the decrease in the signal-to-noise ratio [239]. The quadrature detector is similar to that in Figure B.2. Approaching targets have a positive Doppler frequency shift, while receding targets have a negative Doppler frequency shift. After they are mixed to baseband in a quadrature receiver, single-sideband detection enables the determination of whether the frequency is positive or negative by assessing which channel lags the other by $\frac{\pi}{2}$ [231]. However, it is critical to maintain balance in the receiver chains to eliminate false targets [230].

B.4 Image Cancellation

B.4.1 Image Frequency

When a real RF signal is mixed with a real cosine signal, both its negative and positive frequency components are convolved with the negative and positive frequency impulses of the cosine wave. This results in components of the RF signal at $\pm(f_{RF} + f_{LO})$ and $\pm(f_{RF} - f_{LO})$, as shown in Figure B.3. Another signal, known as the image signal, is also translated to the intermediate frequency. This signal is centered at f_{IM} , where

$$(f_{RF} - f_{LO}) = (f_{LO} - f_{IM}) \quad (2.7)$$

or

$$f_{IM} = f_{RF} - 2f_{LO}. \quad (2.8)$$

Figure B.3 shows how the image signal is translated to the same intermediate frequency as the RF signal. If this signal is not sufficiently attenuated before mixing with the LO, it will overlap with the desired signal at the IF, causing interference that is difficult, if even possible, to remove.

B.4.2 Use of Quadrature Mixing in Image Cancellation

In a heterodyne receiver, the image frequency is two times the intermediate frequency from the radio frequency, as in (2.8). Since there are limits on the bandwidth of the RF band-pass filter, to keep the image channel outside the passband of the RF filter, the IF cannot be arbitrarily small. Filtering limitations typically limit the IF frequency to between 10 and 100 MHz, so that amplifying and filtering at this stage requires a relatively high power dissipation. Also, the high-quality IF filters usually require off-chip passive components that compose a large fraction of the size, weight, and cost of the receiver. With a higher IF, the requirements on the RF image rejection filter are relaxed, but the channel selection filters are typically either of lower quality or of greater expense.

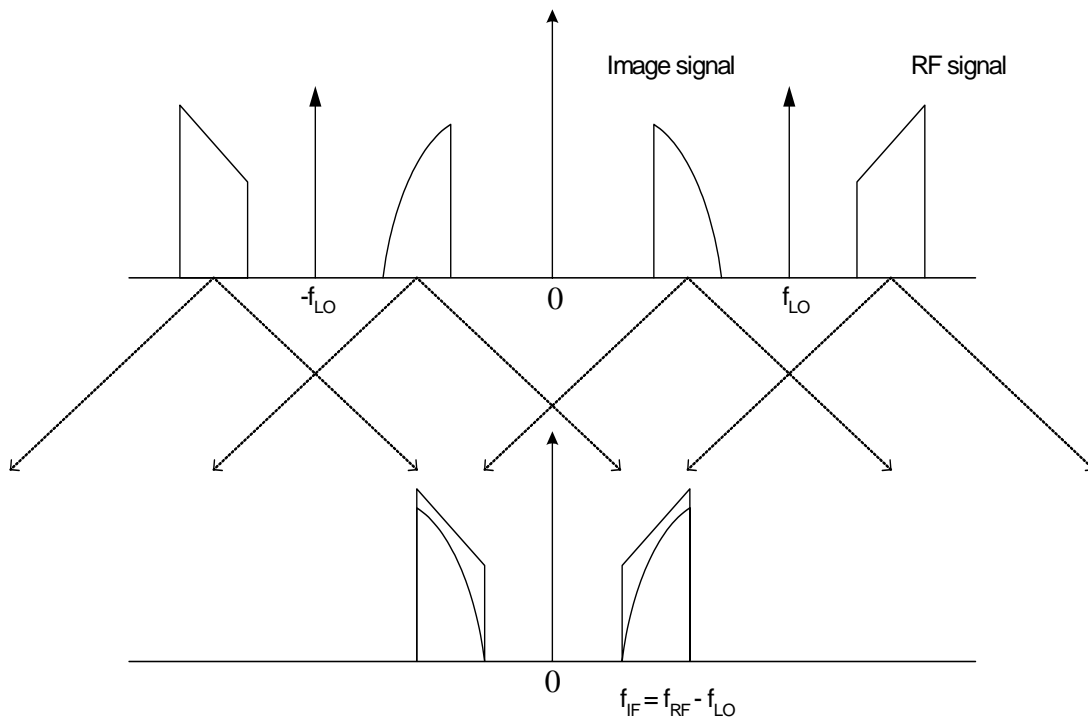


Figure B.3. RF and image signals in a heterodyne receiver. When a real signal is mixed with a real cosine signal, and the LO is not in the RF signal band, the RF signal and the image frequency are both mixed to the intermediate frequency. A pre-selection filter that attenuates the image signal must be used to obtain the desired signal without interference from the image. This often requires a high IF, since the image frequency is the RF frequency minus double the IF.

Therefore, the choice of IF is a trade-off between the image rejection and channel selection [236].

To relieve the requirements on the RF pre-select filter that attenuates the image signal, image signal cancellation schemes have been implemented. The function of image-reject architectures relies on mixing with a complex exponential rather than with a real sinusoid, as illustrated in Figure B.4. Although complex exponential signals cannot be created explicitly, cosine and sine signals can be combined to create complex exponential signals. Signal cancellation or image-rejection architectures downconvert the entire RF spectrum to the IF in two identical mixers driven by signals 90 degrees out of phase, or in quadrature. With appropriate signal processing, the image signal theoretically can be removed completely, which facilitates the use of a lower IF frequency.

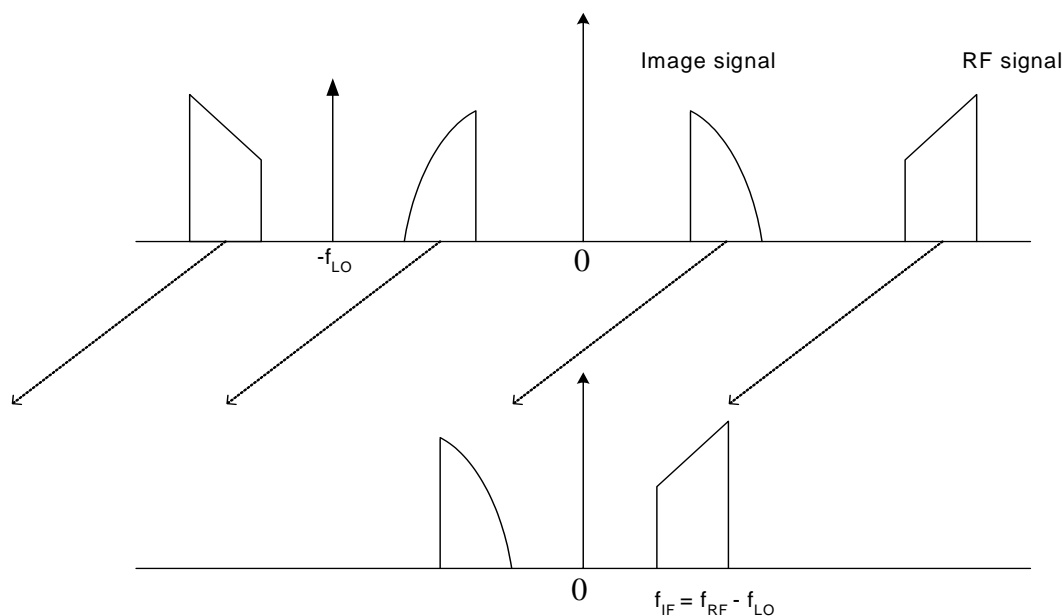


Figure B.4. RF and image signals in an image-reject architecture. When a real signal is mixed with a complex exponential, the RF and image signals continue to occupy separate places in the spectrum.

Two common image-reject architectures are shown in Figure B.5 and Figure B.6. Figure B.5 shows the Hartley image reject architecture, which uses single-sideband mixing. It mixes the RF input with quadrature outputs of the local oscillator, low-pass filters the results, and shifts one of the outputs by 90° before adding them together. With this architecture, when the input signal is equal to $A_{RF}\cos(2\pi f_{RF}t) + A_{IM}\cos(2\pi f_{IM}t)$ where f_{IM} is the image frequency, the output is $\frac{A_{RF}}{2}\cos(2\pi(f_{RF}-f_{LO})t)$. Mixing the input signal with the quadrature outputs creates the in-phase (I) and quadrature (Q) channels. Since the quadrature channel is in the imaginary plane, its negative frequency components are inverted. The 90° phase shift is the equivalent to multiplying by j , which inverts the negative frequencies again and brings the quadrature signal back to the in-phase plane. When the outputs of the two receiver chains are summed, the spectrum of the desired signal is positive in all cases, but the spectrum of the image is negative on the quadrature chain and positive on the in-phase chain, so that when added, the image disappears and the resulting output has the desired spectrum at both the positive and negative IF

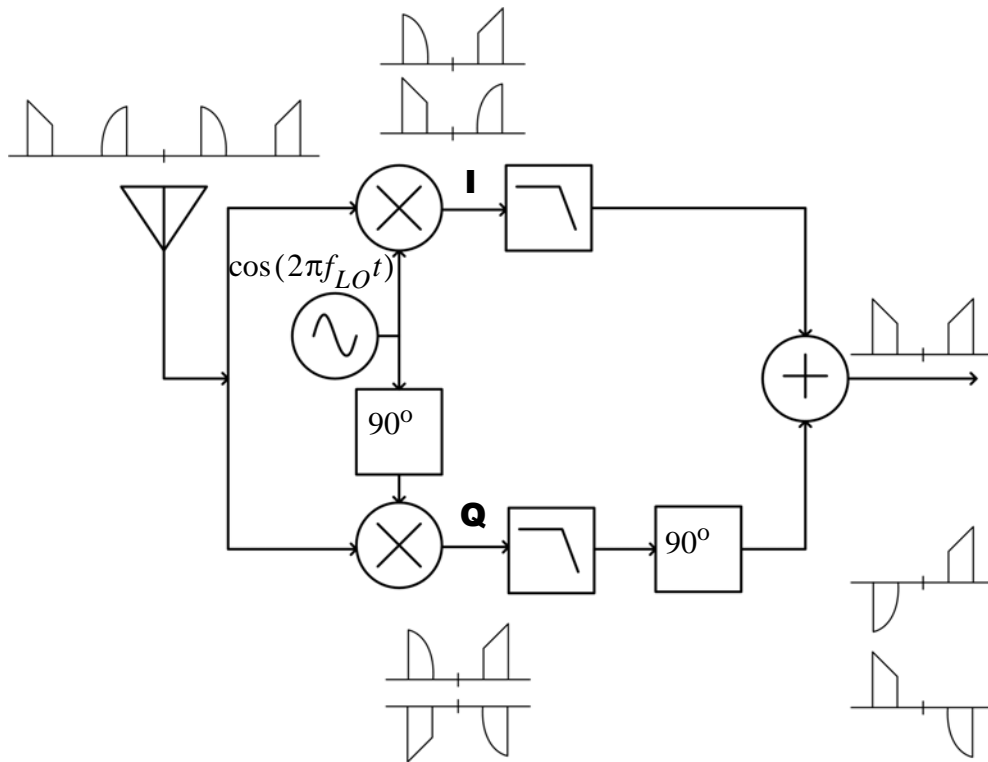


Figure B.5. Hartley heterodyne image rejection architecture. This design uses quadrature channels, with a 90° phase shift on the quadrature channel before the in-phase (I) and quadrature (Q) channels are summed, eliminating the image signal.

frequencies. A main drawback of this architecture is its sensitivity to mismatches, which typically limit its image rejection to 30 or 40 dB [238]. Additionally, achieving a 90° phase shift in the receiver chain requires a circuit that typically suffers from trade-offs between linearity, noise and power dissipation.

Figure B.6 presents the Weaver image-rejection architecture. To avoid the 90° phase shift in the receiver chain, an additional quadrature oscillator is used to provide the second phase shift. This second mixer downconverts the signals to baseband. Again, on the in-phase chain, all the signals are positive. The quadrature chain output has the image frequency positive and the desired signal negative. A subtraction of the two signals results in a baseband output with only the desired signal while cancelling the image signal. Similar

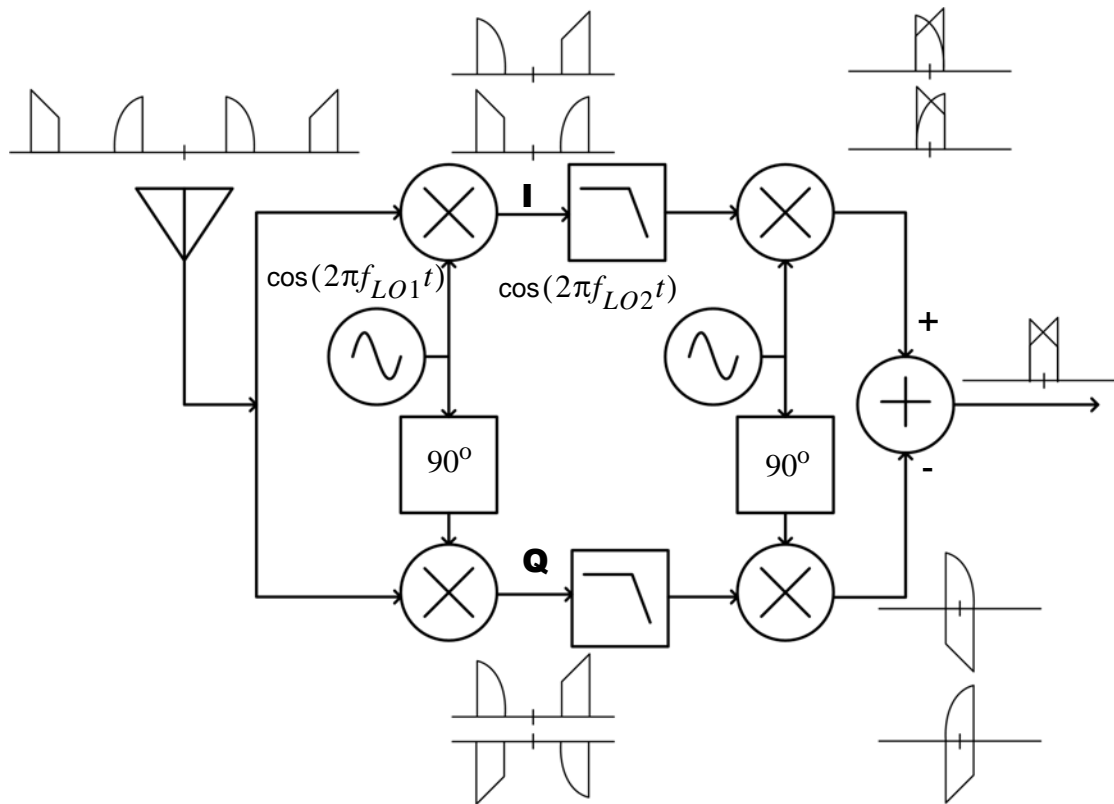


Figure B.6. Weaver heterodyne image rejection architecture. This design uses two downconversions to reach baseband, with a cosine LO used for the two downconversions on the in-phase (I) channel and a sine LO used for both downconversions on the quadrature channel. The two channels are summed to eliminate the image.

to the Hartley architecture, this architecture suffers from limitations due to mismatches in gain and phase between the two receiver chains [230].

B.4.3 Quadrature Mixing in Direct Conversion Receivers

When the IF signal is reduced to zero, the heterodyne receiver becomes a homodyne receiver, also known as a direct-conversion receiver or a zero-IF receiver. This architecture does not suffer from the image signal problem that the heterodyne receivers need to deal with, because the image frequency is the negative frequency component of the desired signal. However, as shown in Figure B.7, if the two sidebands of the RF spectrum are different, which they typically are, multiplying by a real sinusoid will irreversibly cor-

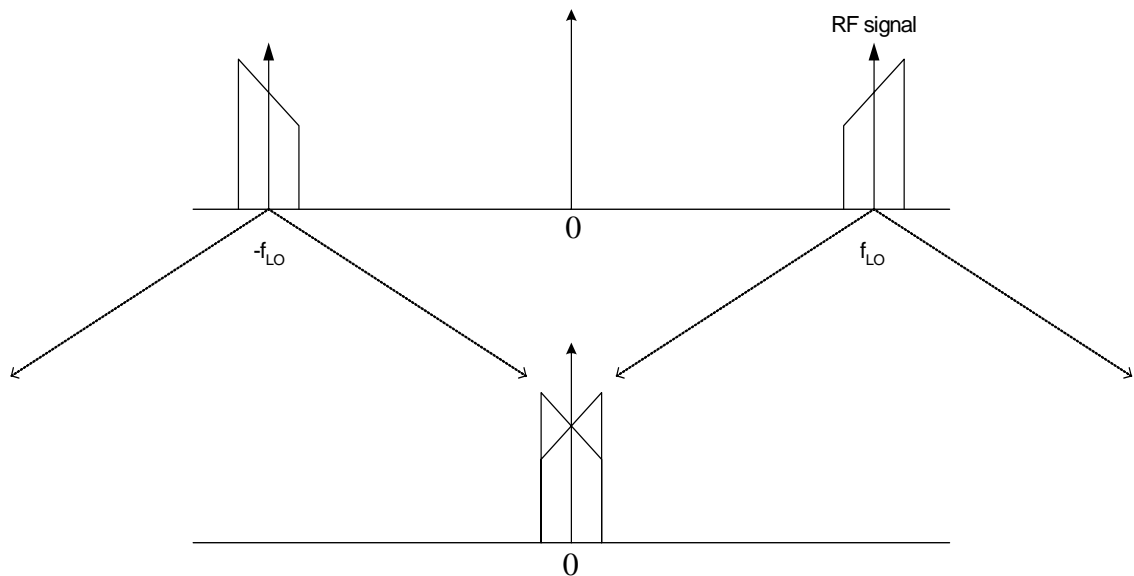


Figure B.7. Self-image problem with a direct-conversion receiver. If a quadrature receiver is not used, both the positive and negative frequency components are down-converted to baseband, where they can interfere with each other.

rupt the signal [226]. The signal corruption can be viewed as the negative frequency portion of the channel folding onto the positive frequency part of the channel. A quadrature receiver is typically used in homodyne receivers to avoid this problem, as shown in Figure B.7.

As with a heterodyne receiver, mixing with a complex exponential avoids the image problem, as shown in Figure B.8. As in heterodyne receivers, the precision to which the I and Q demodulation paths are matched determines how well the image signal can be suppressed. The specifications on image suppression are not as severe as they are for heterodyne receivers, because the amplitude of the image signal is known to be the same as the desired signal [228].

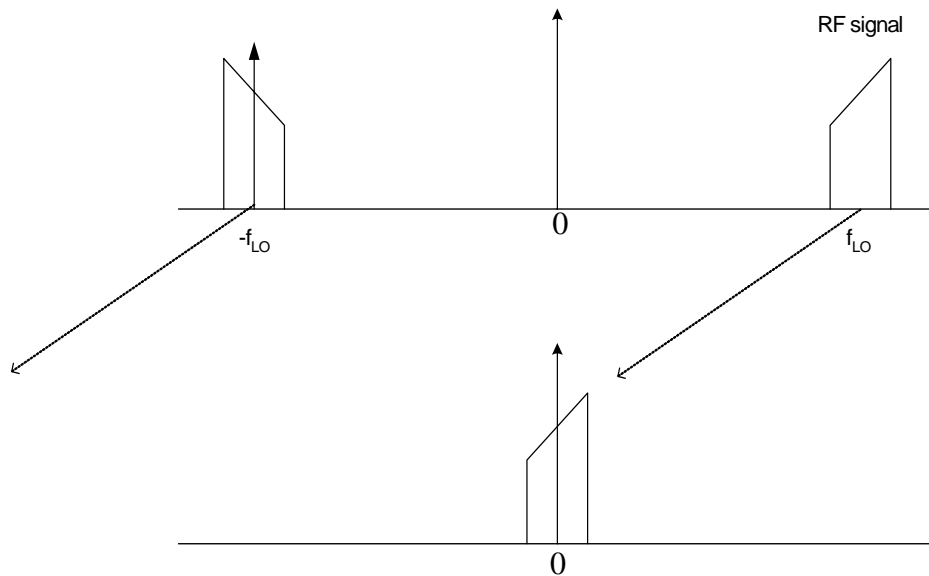
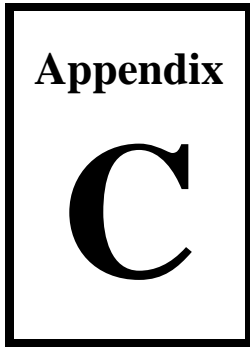


Figure B.8. Avoiding the self-image problem with a quadrature direct-conversion receiver. When the RF signal is mixed with a complex exponential, only the positive or the negative band is converted to baseband, avoiding the interference problem.

B.5 References

- [226] A. A. Abidi, "Direct-conversion radio transceivers for digital communications," *IEEE Journal of Solid State Circuits*, vol. 30, no. 12, pp. 1399-1410, 1995.
- [227] E. L. Christensen, S. N. Madsen, and N. Skou, "Review of the homodyne technique for coherent radar," in *Proceedings of the IEEE International Radar Conference*, 1990, pp. 159-163.
- [228] J. Crols and M. S. J. Steyaert, "Low-IF topologies for high performance analog front ends of fully integrated receivers," *IEEE Transactions on Circuits and Systems - II: Analog and Digital Signal Processing*, vol. 45, no. 3, pp. 269 - 282, 1998.
- [229] N. R. Gillespie, J. B. Higley, and N. MacKinnon, "The evolution and application of coherent radar systems," *IRE Transactions on Military Electronics*, vol. MIL-5, no. 2, pp. 131-139, 1961.
- [230] S. J. Goldman, "Understanding the limits of quadrature detection," *Microwaves & RF*, vol. 178, pp. 67-70, 1986.

- [231] H. P. Kalmus, "Direction sensitive Doppler device," *Proceedings of the IRE*, vol. 45, pp. 689-700, 1955.
- [232] Y. Jou, "Developments in third generation (3G) CDMA technology," in *Proceedings of the IEEE Sixth International Symposium on Spread Spectrum Techniques and Applications*, vol. 2, 2000, pp. 460-464.
- [233] B. P. Lathi, Modern Digital and Analog Communication Systems, New York: Oxford University Press, 1998.
- [234] J. P. Y. Lee, "Wideband I/Q demodulators: measurement technique and matching characteristics," *IEEE Proceedings on Radar, Sonar, and Navigation*, vol. 143, no. 5, pp. 300-306, 1996.
- [235] R. Lyon, Understanding Digital Signal Processing, Upper Saddle River, NJ: Prentice Hall, 2001.
- [236] S. Mirabbasi and K. Martin, "Classical and modern receiver architectures," *IEEE Communications Magazine*, vol. 38, no. 11, pp. 132 - 139, 2000.
- [237] R. S. Raven, "Requirements on master oscillators for coherent radar," *Proceedings of the IEEE*, vol. 54, no. 2, pp. 237-243, 1966.
- [238] B. Razavi, "Design considerations for direct-conversion receivers," *IEEE Transactions on Circuits and Systems - II: Analog and Digital Signal Processing*, vol. 44, no. 6, pp. 428 - 435, 1997.
- [239] W. K. Saunders, "CW and FM Radar," in Radar Handbook, 2nd ed., (M. I. Skolnik, Ed.). San Francisco: McGraw-Hill, Inc., 1990.
- [240] J. W. Taylor, Jr., "Receivers," in Radar Handbook, 2nd ed. (M. I. Skolnik, Ed.), San Francisco: McGraw-Hill, Inc., 1990, pp. 3.1-3.56.
- [241] H. Vermarien and E. van Vollenhoven, "The recording of heart vibrations: a problem of vibration measurement on soft tissue," *Medical and Biological Engineering and Computing*, vol. 22, pp. 168-178, 1984.



Direct Phase Demodulation and DC Offsets

C.1 Introduction

As discussed in detail in Chapter 2, the use of a quadrature receiver rather than a single-chain receiver for Doppler monitoring of heart and respiration can greatly improve the measurement of heart and respiration signatures. If the better of the two channels is selected, the phase-demodulation null points can be avoided. A quadrature receiver also offers the possibility of direct phase demodulation, as was introduced in Chapter 2 Section 2.2.3 under the assumption of perfect phase and amplitude balance between the receiver chains. This chapter discusses the problems encountered in the practical application of direct phase demodulation, including dc offsets and phase and gain imbalance. Phase imbalance occurs when the two LO signals are not exactly 90° out of phase, and gain imbalance occurs when the two RF signals do not have equal amplitude at the mixer. Another problem with direct phase demodulation is that the calculation of the phase requires taking the arctangent of the ratio of the Q channel to the I channel. Since the I channel is in the denominator, the ratio between the channels gets very large near the zero-crossings of the I-channel, amplifying noise on the Q channel in those areas.

In a homodyne transceiver, dc offsets occur due to several factors, including offsets inherent to the circuit, self-mixing, reflections from stationary objects, and dc values that are due to the phase relationship between the RF and LO signals and are actually part of

the data. When using a quadrature receiver in the direct demodulation mode, it is desirable to keep the portion of the dc offset due to the phase relationship between the signals, but not the other offsets. When using a single ended receiver or when selecting a single channel from a quadrature receiver, it is generally acceptable to remove the dc offset, which simplifies analog amplification and filtering.

The Gram-Schmidt technique for orthonormalization is introduced to combat the gain and phase imbalance. This technique uses a calibration of the gain and phase imbalance, and then applies a linear transformation to the I and Q signals to correct the gain and phase imbalance. This technique does not, however, correct for errors due to the zero-crossings or due to dc offsets.

C.2 Quadrature Receiver Theory

Direct-conversion receivers typically use quadrature mixing to reconstitute down-converted signals, avoiding aliasing [242], [245]. Quadrature mixing is attractive for demodulating the chest-displacement signal because it theoretically allows perfect phase demodulation. The challenges inherent in the homodyne quadrature architecture - phase imbalance, gain imbalance and dc offset - impede the combination of the I and Q channels to directly demodulate the phase. The gain and phase imbalance act as a linear transform on the I and Q components; the information is effectively collected on axes that are not normal and do not have the same scale. It is possible to correct for a known phase and amplitude imbalance using the Gram-Schmidt procedure to make two vectors orthonormal [243]. This method is insufficient in wideband systems where the phase imbalance varies with frequency, or in systems that need a high level of image cancellation. However, the Doppler radar system is extremely narrow-band and the only image frequency is the reflection of the desired signal, so neither of these concerns are applicable.

Following is a general signal analysis of an imbalanced quadrature receiver in a Doppler radar context, and methods of compensation with baseband digital signal processing. As shown in Chapter 2, the ideal baseband I and Q outputs are the cosine and sine, respec-

tively, of a constant phase-shift, θ , due to the nominal distance of the target summed with a time-varying phase shift proportional to the chest position, $x(t)$. When only one of these channels is used to demodulate the phase, the value of the constant phase shift determines whether the signal is at an optimal phase demodulation point or at a null point. With no errors, the phase can be directly demodulated using the arctangent:

$$\theta'(t) = \text{atan}\left(\frac{B_Q(t)}{B_I(t)}\right) = \text{atan}\left(\frac{\sin(\theta(t))}{\cos(\theta(t))}\right) = \theta(t) . \quad (\text{C.1})$$

The combined phase term is $\theta(t) = \theta + \left(\frac{4\pi}{\lambda}\right)x(t) + \Delta\phi_N(t)$, where $x(t)$ is the chest motion,

$$\theta = \frac{4\pi d_0}{\lambda} - \theta_0 \quad (\text{C.2})$$

is the constant phase shift and

$$\Delta\phi_N(t) = \phi_N(t) - \phi_N\left(t - \frac{2d_0}{c}\right) \quad (\text{C.3})$$

is the residual phase noise.

This phase demodulation works perfectly when the phase between the two LO signals is exactly 90° , the amplitude of both LO signals and both RF signals are the same, and there are no significant dc offsets due to sources other than the data. However, real systems have each of these non-idealities to some extent. For this analysis, the amplitude error, A_E , is defined as the ratio of the amplitude of the Q RF signal to that of the I RF signal. The phase error, ϕ_E , will be defined as the difference between the phases of the two LO signals minus 90° . The cumulative dc offsets on the I and Q channels are V_I and V_Q , respectively. A_R is the ratio of the amplitude of the RF input signal to the I chain LO signal.

With these non-idealities, the LO signals are

$$L_I(t) = \cos(2\pi ft + \phi_N(t)) \quad (\text{C.4})$$

and

$$L_Q(t) = \sin(2\pi ft + \phi_N(t) + \phi_E) . \quad (C.5)$$

The received signals are:

$$R_I(t) = A_R \cos(2\pi ft + \theta(t)) \quad (3.6)$$

and

$$R_I(t) = A_R A_E \cos(2\pi ft + \theta(t)) . \quad (3.7)$$

After the received signal is mixed with the LO signals, the baseband signals are:

$$B_I(t) = V_I + A_R \cos(\theta(t)) \quad (C.8)$$

and

$$B_Q(t) = V_Q + A_R A_E \sin(\theta(t) + \phi_E), \quad (C.9)$$

where V_I and V_Q are the dc offsets of the I and Q channels, respectively.

When direct phase demodulation is used on these outputs, the output is

$$\theta'(t) = \text{atan}\left(\frac{V_Q + A_R A_E \sin(\theta(t) + \phi_e)}{V_I + A_R \cos(\theta(t))}\right) \quad (C.10)$$

The phase error, ε_ϕ , can be defined as the difference between this phase, and the ideal phase:

$$\varepsilon_\theta = \theta'(t) - \theta(t) = \text{atan}\left(\frac{V_Q + A_R A_E \sin(\theta(t) + \phi_e)}{V_I + A_R \cos(\theta(t))}\right) - \theta(t). \quad (C.11)$$

The maximum error occurs at $\theta(t) = 0$, where

$$\varepsilon_{\theta, \max} = \text{atan}\left(\frac{V_Q + A_R A_E \sin(\phi_e)}{V_I + A_R}\right) = \text{atan}\left(\frac{\frac{V_Q}{A_R} + A_E \sin(\phi_e)}{1 + \frac{V_I}{A_R}}\right). \quad (C.12)$$

If ϕ_e is small, the small angle approximation yields:

$$\varepsilon_{\theta, max} \approx \text{atan}\left(\frac{V_Q + A_R A_E \phi_e}{V_I + A_R}\right) = \text{atan}\left(\frac{\frac{V_Q}{A_R} + A_E \phi_e}{1 + \frac{V_I}{A_R}}\right) \quad (\text{C.13})$$

If there are no unwanted dc offsets,

$$\varepsilon_{\theta, max, nodc} \approx \text{atan}(A_E \sin(\phi_e)) \quad (\text{C.14})$$

C.3 Causes of DC Offsets

In section Section C.3.1, the consequences of removing the dc offset due to the phase relationship are assessed. In Section C.3.2, the likelihood of the dc offset due to self-mixing being the same in the I and Q channels is discussed. If they are the same, it would be possible to remove this offset while leaving the offset due to the phase relationship. In section C.3.3, the magnitude of dc offsets due to stationary objects are assessed in relationship to the magnitude of the signal to determine whether they are negligible. However, it is difficult to remove the dc offset due to self-mixing while keeping the dc offset due to the phase relationship, as filtering methods simply remove all the dc offset.

C.3.1 DC Offset Due to Phase Relationships

The dc offset due to the phase relationships is important when combining the I and Q channels with the arctangent as in (C.1). When the two signals are in the optimum phase demodulation relationship, there is no dc offset, though the dc offset increases as the phase demodulation relationship becomes less optimal, reaching a maximum at the phase-demodulation null point. This dc offset is an important part of the phase relationship, and is therefore necessary to exactly obtain the phase by combining I and Q signals with the arctangent technique. The calculations below show the demodulated phase after the dc offset is removed. For simplicity in these calculations, the following substitutions are used:

$$p_0 = \theta + \frac{\pi}{4} \quad (\text{C.15})$$

$$dp(t) = \frac{4\pi x(t)}{\lambda} + \Delta\phi(t). \quad (\text{C.16})$$

With these substitutions, the I and Q signals at baseband are:

$$B_I(t) = A \cos(p_0 + p(t)) = A[\cos(p_0)\cos(p(t)) - \sin(p_0)\sin(p(t))] \quad (\text{C.17})$$

and

$$B_Q(t) = A \sin(p_0 + p(t)) = A[\sin(p_0)\cos(p(t)) + \cos(p_0)\sin(p(t))] . \quad (\text{C.18})$$

If $p(t) \ll 1$, ($x(t) \ll \lambda$), the small angle approximation can be applied and the baseband signals are approximately:

$$\begin{aligned} B_I(t) &= A[\cos(p_0)(1 - p^2(t)) - \sin(p_0)p(t)] \\ &\approx A[\cos(p_0) - \sin(p_0)p(t) - \cos(p_0)(p^2(t))] \end{aligned} \quad (\text{C.19})$$

and

$$\begin{aligned} B_Q(t) &= A[\sin(p_0)(1 - p^2(t)) + \cos(p_0)p(t)] \\ &\approx A[\sin(p_0) + \cos(p_0)p(t) - \sin(p_0)(p^2(t))] \end{aligned} \quad (\text{C.20})$$

The dc values are $D_I = A \cos(p_0)$ for the I channel and $D_Q = A \sin(p_0)$ for the Q channel.

C.3.2 DC Offset Due to Self-Mixing

DC offset due to self-mixing occurs when the RF output signal mixes with the LO, either through substrate coupling or from reflections at the antenna connection. This dc offset is undesirable, as it limits the dynamic range of the receiver without adding information about the target. One important question is how different the dc offsets are between the I and Q channels. If they are the same, it may be possible to remove this offset without removing the desirable dc offset due to the phase relationship.

The mixer conversion gain, referred to as A_C , is calculated as the ratio of the IF output power to the RF input power. Assuming the self-mixing signal is the LO or the transmitted signal (which are identical for these purposes) with a phase delay θ_{SM} and an amplitude A_{SM} , the baseband I signal is:

$$B_I = A_C A_{SM} \cos\left(2\pi ft + \frac{\pi}{4}\right) \cos(2\pi ft + \theta_{SM}) , \quad (C.21)$$

and after low pass filtering, the I channel dc offset is

$$B_{I,DC} = A_C A_{SM} \cos\left(\frac{\pi}{4} + \theta_{SM}\right) . \quad (C.22)$$

Similarly, the baseband Q signal is:

$$B_Q = A_C A_{SM} \sin\left(2\pi ft + \frac{\pi}{4}\right) \cos(2\pi ft + \theta_{SM}) , \quad (C.23)$$

and after low pass filtering, the Q channel dc offset is

$$B_{Q,DC} = A_C A_{SM} \sin\left(\frac{\pi}{4} + \theta_{SM}\right) . \quad (C.24)$$

If θ_{SM} is near zero, the offsets will be nearly identical, but if θ_{SM} is on the order of $\pi/4$ or greater, the offsets can become quite different. If self-mixing occurs through on-chip coupling, the value of θ_{SM} should be near zero. However, if it occurs through the antenna or coupler, the phase shift will be larger and may cause the offsets to be non-identical. The I and Q dc offsets are shown versus the phase delay in Figure C.1.

For coupling through the chip, the wavelength is about 62.5 mm, and for a 1 mm distance, $\theta_{SM-chip} \cong 0.10$ radians. For coupling through the board, the wavelength is similar and there is approximately an additional 30 mm of distance, which consists of a delay of $\theta_{SM-board} \cong 3.0$ radians. The coaxial cable to the antenna adds about 100 mm of round-trip distance, with a wavelength of about 108 mm, leading to $\theta_{SM-coax} \cong 5.8$ radians. There are additional delays due to the bondwires and package leads, as well as the connections between the leads. This analysis indicates that there are self-mixing delays from 0.1 to nearly 2π radians, so the I and Q dc offsets could be significantly different.

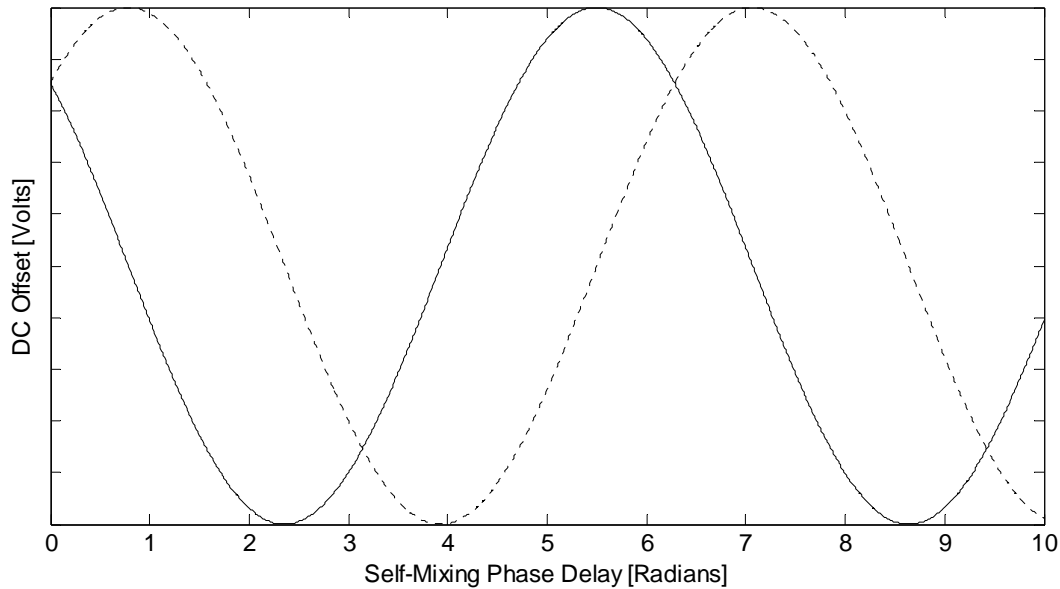


Figure C.1. The dc offset due to self-mixing vs. the phase delay in radians. The I signal's dc offset is the solid line, and the Q signal's dc offset is the dotted line.

If there are several self-mixing inputs at the RF input to the mixer, they interfere constructively and destructively before they are mixed to dc offsets at baseband. There will always be several self-mixing inputs, but they will often have different amplitudes, depending on how the signal is coupled from the output to the input.

C.3.3 DC Offset Due to Reflections from Stationary Objects

It is assumed that the signal hits much of the body that is not moving, as well as the bed or chair behind the subject, and that pulses have different waveforms at different locations on the body. Reflections from each of these sources will occur at a different distance from the transceiver, and each will have a different reflected amplitude. For simplicity, the following equations are described without including phase noise. The two pulses that are being measured have waveforms $x_0(t)$ and $x_1(t)$, are at distances d_0 and d_1 , and have received signal amplitudes A_0 and A_1 , respectively. The stationary part of the body and the bed behind the body are at distances d_2 and d_3 , with received signal amplitudes A_2 and A_3 , respectively, as shown in Figure C.2.

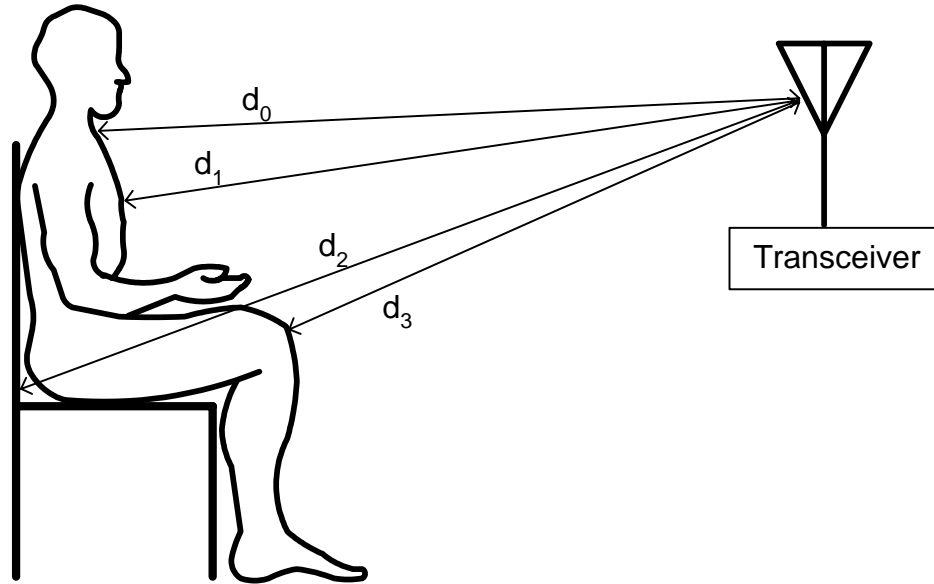


Figure C.2. Distances to moving and stationary parts of the subject and the chair.

$$R(t) = A_0 \cos\left(\omega t + \frac{d_0 + x_0(t)}{\lambda}\right) + A_1 \cos\left(\omega t + \frac{d_1 + x_1(t)}{\lambda}\right) + A_2 \cos\left(\omega t + \frac{d_2}{\lambda}\right) + A_3 \cos\left(\omega t + \frac{d_3}{\lambda}\right) \quad (\text{C.25})$$

When this is mixed with the LOs, the results are:

$$B_I(t) = A_0 \cos\left(\frac{x_0(t)}{\lambda} + \frac{d_0}{\lambda} - \frac{\pi}{4}\right) + A_1 \cos\left(\frac{x_1(t)}{\lambda} + \frac{d_1}{\lambda} - \frac{\pi}{4}\right) + D_I \quad (\text{C.26})$$

and

$$B_Q(t) = A_0 \sin\left(\frac{x_0(t)}{\lambda} + \frac{d_0}{\lambda} - \frac{\pi}{4}\right) + A_1 \sin\left(\frac{x_1(t)}{\lambda} + \frac{d_1}{\lambda} - \frac{\pi}{4}\right) + D_Q \quad (\text{C.27})$$

where the dc components from the stationary part of the body and the stationary background are represented by D_I and D_Q :

$$D_I = A_2 \cos\left(\frac{d_2}{\lambda} - \frac{\pi}{4}\right) + A_3 \cos\left(\frac{d_3}{\lambda} - \frac{\pi}{4}\right) \quad (\text{C.28})$$

and

$$D_Q = A_2 \sin\left(\frac{d_2}{\lambda} - \frac{\pi}{4}\right) + A_3 \sin\left(\frac{d_3}{\lambda} - \frac{\pi}{4}\right) \quad (\text{C.29})$$

If these dc offsets are not removed, it is difficult to directly demodulate the phase. Since the cross-sectional area that is not moving is much greater than the area that is moving, the A_2 and A_3 terms are expected to be much larger than the A_0 and A_1 terms, so that the dc offset due to this factor will be non-negligible. For this reason, it is necessary either to remove dc offsets before sampling or to have an analog-to-digital converter with high enough resolution to detect both the heart signal and the entire dc offset. If the dc is removed, either the phase can be demodulated using either I or Q, or the output will suffer the minor inaccuracies experienced when I and Q are combined after the dc offset is removed, as shown in Section C.4.

C.4 Effects of DC Offset Removal in a System with Signal Imbalance

In a homodyne transceiver, there are several causes of dc offsets. All receivers have some dc offset due to mismatch in the signal path between the mixer and I/Q inputs to the detector. All direct-conversion receivers have dc offsets due to imperfect isolation between the LO port and the RF input to the mixer; LO self-mixing will result in a dc value. Radar transceivers have additional self-mixing due to the non-idealities of the circulator and reflections at the antenna, as well as dc offsets due to reflections from clutter. The heart and respiration signals only come from the parts of the body that are moving; the surrounding environment and all the stationary parts of the body are considered to be clutter and contribute to the dc offset.

The dc offset is typically 2 to 3 orders of magnitude larger than the signal amplitude, which makes it difficult to amplify the microvolt signals sufficiently for high-resolution digitization without saturating the amplifiers or analog-to-digital converters (ADCs). Removing the dc offset through filtering or subtraction before amplification avoids this problem, but leads to another: since the baseband signals have data at dc, when removing

dc offsets, a portion of the signal is removed. This problem is strongly pronounced in this application, which is extremely narrow-band, with respiration rates typically between 0.1 and 0.4 Hz, and heart rates typically between 0.83 and 1.5 Hz.

When using a single-channel receiver, or when using a quadrature receiver in channel-selection mode, it is generally acceptable to remove the dc offset, which simplifies analog amplification and filtering. However, when directly demodulating the phase, as described in (C.1), it is desirable to keep the part of the dc offset caused by the phase relationship between the LO and the received signal, but not the dc offsets due to self-mixing and reflections from stationary objects. MATLAB simulations of the effect of removing the dc offset due to the phase relationship indicated that given a 0.5 mm peak-to-peak motion due to the heart and a 2 cm peak-to-peak motion due to respiration, the largest error due to removing the dc offset is 1%, as shown in the simulation in Section C.4.3.

C.4.1 Theory - Removal of DC without Phase and Amplitude Error

If the dc values calculated assuming $(x(t) \ll \lambda)$ in Section C.3.1 are removed before digitizing, the phase term is:

$$\theta'(t) = \operatorname{atan}\left(\frac{B_Q(t)}{B_I(t)}\right) = \operatorname{atan}\left(\frac{A \sin(p_0 + p(t)) - A \sin(p_0)}{A \cos(p_0 + p(t)) - A \cos(p_0)}\right) \quad (\text{C.30})$$

Using the $\sin(u) = \cos\left(u - \frac{\pi}{2}\right)$ trigonometric identity,

$$\theta'(t) = \operatorname{atan}\left(\frac{\cos\left(p_0 + p(t) - \frac{\pi}{2}\right) - \cos\left(p_0 - \frac{\pi}{2}\right)}{\cos(p_0 + p(t)) - \cos(p_0)}\right) \quad (\text{C.31})$$

Then, using the $\cos(u - v) - \cos(u + v) = 2 \sin(u) \sin(v)$ identity,

$$\theta'(t) = \operatorname{atan}\left(\frac{2 \sin\left(p_0 + \frac{p(t)}{2} - \frac{\pi}{2}\right) \sin\left(\frac{-p(t)}{2}\right)}{2 \sin\left(p_0 + \frac{p(t)}{2}\right) \sin\left(\frac{-p(t)}{2}\right)}\right) = \operatorname{atan}\left(\frac{-\cos\left(p_0 + \frac{p(t)}{2}\right)}{\sin\left(p_0 + \frac{p(t)}{2}\right)}\right) \quad (\text{C.32})$$

Using two tangent trigonometric identities, $(\sin(u))/(\cos(u)) = \tan(u)$ and $\tan(u + v) = (\tan(u) + \tan(v))/(1 - \tan(u)\tan(v))$, the phase can be calculated as:

$$\theta'(t) = \operatorname{atan}\left(\frac{-1}{\tan\left(p_0 + \frac{p(t)}{2}\right)}\right) = \operatorname{atan}\left(\frac{-1\left(1 - \tan(p_0)\tan\left(\frac{p(t)}{2}\right)\right)}{\tan(p_0) - \tan\left(\frac{p(t)}{2}\right)}\right) \quad (\text{C.33})$$

Dividing through by $\tan(p_0)$,

$$\theta'(t) = \operatorname{atan}\left(\frac{\left(\frac{-1}{\tan(p_0)}\right) + \tan\left(\frac{p(t)}{2}\right)}{1 + \tan\left(\frac{p(t)}{2}\right)\left(\frac{-1}{\tan(p_0)}\right)}\right). \quad (\text{C.34})$$

Then, using the $\operatorname{atan}((u + v)/(1 - uv)) = \operatorname{atan}(u) + \operatorname{atan}(v)$ identity,

$$\theta'(t) = \operatorname{atan}\left(\tan\left(\frac{p(t)}{2}\right)\right) + \operatorname{atan}\left(\frac{-1}{\tan(p_0)}\right) = \frac{p(t)}{2} + \operatorname{atan}\left(\frac{-1}{\tan(p_0)}\right) \quad (\text{C.35})$$

Substituting for p_0 and $p(t)$,

$$\theta'(t) = \frac{2\pi x(t)}{\lambda} + \frac{\Delta\phi(t)}{2} + \operatorname{atan}\left(\frac{-1}{\tan\left(\theta + \frac{\pi}{4}\right)}\right) \quad (\text{C.36})$$

The final term in (C.36) is a dc offset, and other than the dc offset, the $\theta'(t)$ term is proportional to the phase when the $(x(t) \ll \lambda)$ criteria is met. If the criterion is not met, the output is less straightforward.

C.4.2 Theory - Removal of DC with Phase and Amplitude Error

If the above equations are calculated including phase and amplitude imbalance, the I and Q signals at baseband are:

$$B_I(t) = A_R \cos(p_0 + p(t)) = A_R [\cos(p_0)\cos(p(t)) - \sin(p_0)\sin(p(t))] \quad (\text{C.37})$$

and

$$\begin{aligned} B_Q(t) &= A_R A_E \sin(p_0 + \phi_E + p(t)) \\ &= A_R A_E [\sin(p_0 + \phi_E) \cos(p(t)) + \cos(p_0 + \phi_E) \sin(p(t))] \end{aligned} \quad (C.38)$$

If $p(t) \ll 1$, which requires $(x(t) \ll \lambda)$ and small residual phase noise, the small angle approximation can be applied and the baseband signals are approximately:

$$\begin{aligned} B_I(t) &= A_R [\cos(p_0)(1 - p^2(t)) - \sin(p_0)p(t)] \\ &\approx A_R [\cos(p_0) - \sin(p_0)p(t) - \cos(p_0)(p^2(t))] \end{aligned} \quad (C.39)$$

and

$$\begin{aligned} B_Q(t) &= A_R A_E [\sin(p_0 + \phi_E)(1 - p^2(t)) + \cos(p_0 + \phi_E)p(t)] \\ &\approx A_R A_E [\sin(p_0 + \phi_E) + \cos(p_0 + \phi_E)p(t) - \sin(p_0 + \phi_E)(p^2(t))] \end{aligned} \quad (C.40)$$

The dc values caused by the phase relationship between the two signals are those without a $p(t)$ term: $D_I = A_R \cos(p_0)$ for the I channel and $D_Q = A_R A_E \sin(p_0 + \phi_E)$ for the Q channel. If these are subtracted from the baseband signals before they are summed, as would occur if all the dc offset was removed, the dc offsets in Section C.2 would be: $V_I = -D_I = -A_R \cos(p_0)$ and $V_Q = -D_Q = -A_R A_E \sin(p_0 + \phi_E)$. Therefore, when the dc offset is removed, the baseband signals are:

$$B_I(t) = A_R [\cos(p_0 + p(t)) - \cos(p_0)] = -2A_R \sin\left(p_0 + \frac{p(t)}{2}\right) \sin\left(\frac{p(t)}{2}\right) \quad (C.41)$$

and

$$\begin{aligned} B_Q(t) &= A_R A_E [\sin(p_0 + p(t) + \phi_E) - \sin(p_0 + \phi_E)] \\ &= 2A_R A_E \cos\left(p_0 + \phi_E + \frac{p(t)}{2}\right) \sin\left(\frac{p(t)}{2}\right) \end{aligned} \quad (C.42)$$

The directly demodulated phase is therefore:

$$\begin{aligned}
\theta'(t) &= \operatorname{atan} \left[\frac{-A_E \cos\left(p_0 + \phi_E + \frac{p(t)}{2}\right)}{\sin\left(p_0 + \frac{p(t)}{2}\right)} \right] \\
&= \operatorname{atan} \left[\frac{-A_E \left[\cos\left(p_0 + \frac{p(t)}{2}\right) \cos(\phi_E) - \sin\left(p_0 + \frac{p(t)}{2}\right) \sin(\phi_E) \right]}{\sin\left(p_0 + \frac{p(t)}{2}\right)} \right] \\
&= \operatorname{atan} \left[-A_E \left(\frac{-\sin\left(p_0 + \frac{p(t)}{2} - \frac{\pi}{2}\right)}{\cos\left(p_0 + \frac{p(t)}{2} - \frac{\pi}{2}\right)} \cos(\phi_E) - \sin(\phi_E) \right) \right] \\
&= \operatorname{atan} \left[A_E \left(\tan\left(p_0 + \frac{p(t)}{2} - \frac{\pi}{2}\right) \cos(\phi_E) + \sin(\phi_E) \right) \right]
\end{aligned} \tag{C.43}$$

If ϕ_e is small, the small angle approximation yields:

$$\theta'(t) = \operatorname{atan} \left[A_E \left((1 - \phi_E^2) \tan\left(p_0 + \frac{p(t)}{2} - \frac{\pi}{2}\right) + \phi_E \right) \right]. \tag{C.44}$$

C.4.3 Simulation of Effects of DC Removal

To illustrate the severity of the removal of dc, the baseband signals were modeled assuming that the chest movement due to respiration was a 5-cm sinusoid with a period of 5 seconds and that the movement due to heart was a 0.5-mm sinusoid with a period of 1.1 seconds. This was calculated with carrier frequencies of 2.4 GHz, 1.6 GHz, and 900 MHz, and with phase offset θ as in (C.2) with values of 0 , $\frac{\pi}{8}$, $\frac{\pi}{4}$, and $\frac{3\pi}{8}$. The dc offset is calculated as the mean over the measurement interval. The phase is calculated using the full signal, including the dc offset, and with the dc offset subtracted. The waveforms for the I and Q channel data, the phase calculated with the dc offset included, and the phase calculated with the dc offset removed are shown for a 2.4 GHz carrier in Figure C.3.

To determine the relative error between the signals, each of the output signals was scaled to match the chest motion signal with the minimum mean squared error. The scale values for each output are given in Table C.1. The chest motion signal was then scaled to have an amplitude of 1, and the output signals were each scaled by the same value. Then the normalized mean squared error (NMSE) between the scaled output signal and the scaled chest motion signal was calculated. This value is given in the plots, as well as in Table C.1.

The mean-squared error of the phase with the dc offset present is always lower than the error if the dc offset is removed. However, with the dc offset removed, the highest normalized mean squared error calculated was only 0.13%. Since these errors are so small, the cost of removing dc in phase demodulation is likely less than the benefits gained by increasing the signal's dynamic range through blocking the dc and amplifying the base-band signal.

When the Q signal is at a phase-demodulation null point ($\theta = \pi/4$), the mean squared error for that signal is very high because it is proportional to the square of the chest motion signal. The I signal at this value of θ is at the optimal phase demodulation point; it closely matches the chest motion signal. At values of $\theta = 0$ and $\pi/2$, the I and Q signals are both halfway between the optimal and the null phase demodulation points, so their errors are almost identical.

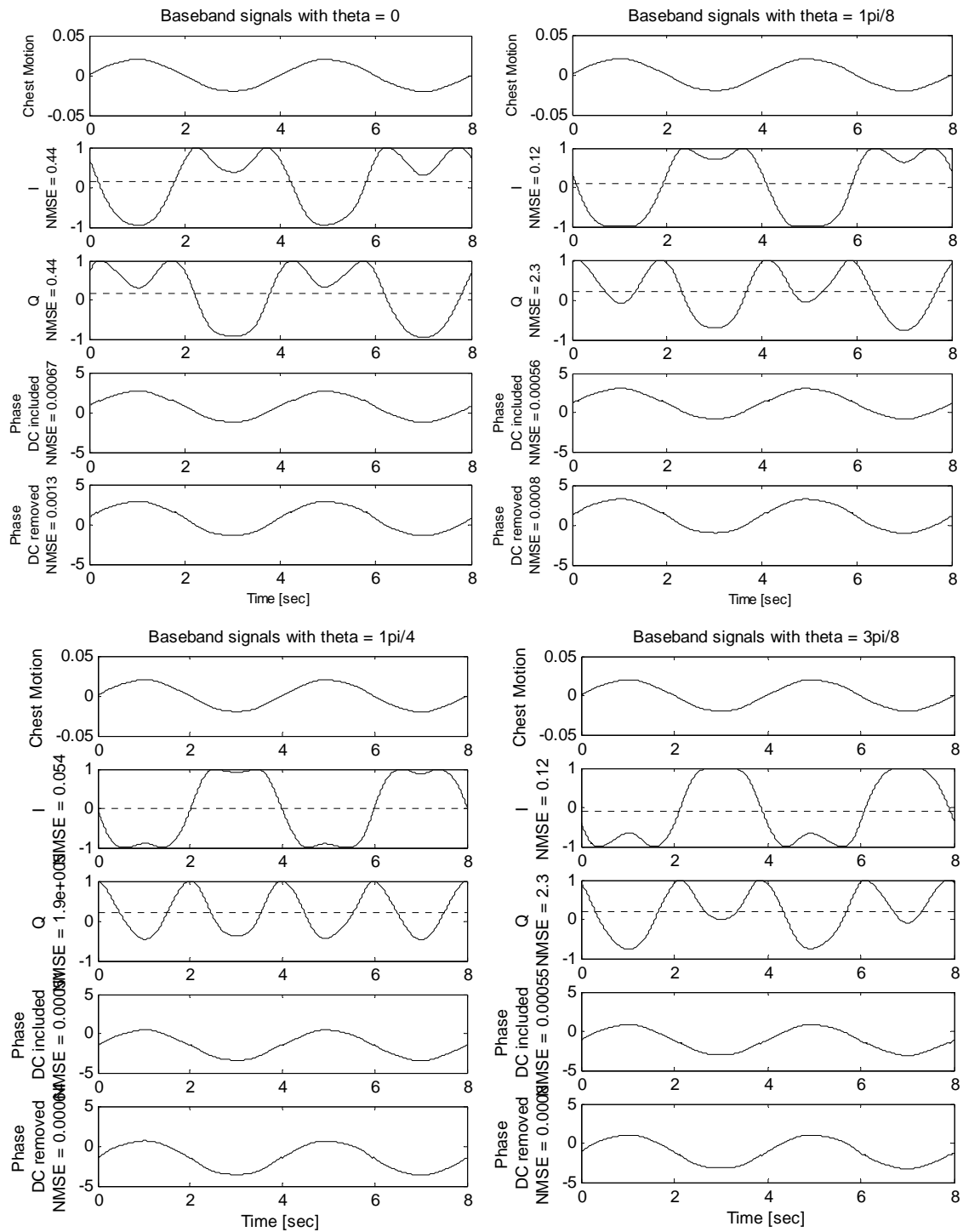


Figure C.3. Phases calculated with and without dc offset removed, for a 2.4 GHz carrier.

Table C.1: Weighting Values for Scaling Output Signals to Minimize Mean Squared Error Between the Outputs and the Chest Motion Signal.

Phase Shift (radians)	Weight				Normalized Mean-Squared Error (NMSE)			
	I	Q	Phase DC Present	Phase DC Removed	I	Q	Phase DC Present	Phase DC Removed
0π	-41	41	96	109	0.44	0.44	6.7e-4	1.3e-3
$\pi/8$	-53	22	96	108	0.12	2.3	5.6e-4	8.0e-4
$\pi/4$	-58	0.083	96	108	0.054	1.9e+5	5.1e-4	6.4e-4
$(3\pi)/8$	-53	-22	96	108	0.12	2.3	5.5e-4	8.0e-4

C.5 Effects of Signal Imbalance and Gram-Schmidt Technique

C.5.1 Causes of Phase and Amplitude Imbalance

Phase and amplitude imbalance between the two receiver chains are induced by the RCCR circuit and mismatches between RF components, baseband components, and the ADC in each receiver chain. A separate RCCR tester has a measured phase error of 3° and an amplitude imbalance of 3.3 dB. The overall phase difference between the I and Q channels was measured by using two signal generators as the external LO and the RF input, and looking at IF frequencies under 50 Hz. The voltage amplitude relationship between I and Q was measured by comparing the magnitude of the signals, and the autocorrelation of the two signals was used to determine their phase relationship. The measured amplitude error was 2.66 and the measured phase error was 37° .

C.5.2 Effects of Signal Imbalance

When direct phase demodulation is used, the magnitude with no DC offsets is:

$$B_{mag} = \sqrt{A_R^2 \cos\left[\theta + \frac{\pi}{4} + \frac{4\pi x(t)}{\lambda} + \Delta\phi(t)\right]^2 + A_R A_E \sin\left[\theta + \frac{4\pi x(t)}{\lambda} + \Delta\phi(t) + \phi_E\right]} \quad (\text{C.45})$$

If the unwanted dc offsets were completely removed, so $V_Q = V_I = 0$,

$$\theta'_{noDC}(t) = \text{atan}\left(\frac{A_E \sin(p(t) + \phi_e)}{\cos(p(t))}\right) \quad (\text{C.46})$$

If there are no dc offsets and no amplitude error, the only remaining error is the phase error,

$$\theta'_{phase\ error}(t) = \text{atan}\left(\frac{\sin(p(t) + \phi_e)}{\cos(p(t))}\right) \quad (\text{C.47})$$

C.5.3 Gram-Schmidt Technique for Orthonormalization

It is possible to correct for a known phase and amplitude imbalance using the Gram-Schmidt procedure to make two vectors orthonormal [243]. This procedure takes any two initial basis vectors, a_1 and a_2 and creates an orthonormal basis, with basis vectors x_1 and x_2 . For this application, non-normal basis vectors B_I and B_Q are converted to the orthonormal basis vectors $B_{I,orth}$ and $B_{Q,orth}$. $B_{I,orth}$ is taken to be B_I , and then B_Q is converted to be normal to $B_{I,orth}$:

$$B_{Q,orth}^{\sim} = B_Q - A_E \sin(\phi_E) B_{I,orth}, \quad (\text{C.48})$$

and is then normalized:

$$B_{Q,orth} = \frac{B_{Q,orth}^{\sim}}{A_E \cos(\phi_E)}. \quad (\text{C.49})$$

This operation is shown in matrix form in (C.50).

$$\begin{bmatrix} B_{I,orth} \\ B_{Q,orth} \end{bmatrix} = \begin{bmatrix} 1 & 0 \\ -\tan(\phi_e) & \frac{1}{A_e \cos(\phi_e)} \end{bmatrix} \begin{bmatrix} B_I \\ B_Q \end{bmatrix} \quad (\text{C.50})$$

If

$$\begin{bmatrix} B_I \\ B_Q \end{bmatrix} = \begin{bmatrix} A_R \cos(\theta(t)) \\ A_R A_E \sin(\theta(t) + \phi_E) \end{bmatrix}, \quad (\text{C.51})$$

then

$$\begin{bmatrix} B_{I, orth} \\ B_{Q, orth} \end{bmatrix} = \begin{bmatrix} A_R \cos(\theta(t)) \\ A_R \sin(\theta(t)) \end{bmatrix}. \quad (C.52)$$

C.5.4 Effects of DC Offset Removal on Gram-Schmidt Technique

If both the desired and unwanted dc offset are removed before the application of the Gram-Schmidt technique, no additional error is imparted into the data due to the use of the orthonormalization algorithm.

$$\begin{aligned} \begin{bmatrix} B_{I, orth}' \\ B_{Q, orth}' \end{bmatrix} &= \begin{bmatrix} 1 & 0 \\ -\tan(\phi_e) & \frac{1}{A_e \cos(\phi_e)} \end{bmatrix} \begin{bmatrix} A_R \cos(p_0 + p(t)) - A_R \cos(p_0) \\ A_R A_E \sin(p_0 + p(t) + \phi_E) - A_R A_E \sin(p_0) \end{bmatrix} \\ &= \begin{bmatrix} A_R \cos(p_0 + p(t)) - A_R \cos(p_0) \\ A_R \sin(p_0 + p(t)) - A_R \sin(p_0) \end{bmatrix} \end{aligned} \quad (C.53)$$

C.5.5 Effects of Residual Error on Gram-Schmidt Technique

If the phase and gain error estimate are not exact, some residual error remains after the application of the Gram-Schmidt algorithm. If the actual gain and phase error are A_E and ϕ_E and the values of the gain and phase error used in the Gram-Schmidt algorithm are $A_E + e_A$ and $\phi_E + e_\phi$, then

$$\begin{aligned}
& \begin{bmatrix} B_{I,orth}' \\ B_{Q,orth}' \end{bmatrix} \tag{C.54} \\
& = \begin{bmatrix} 1 & 0 \\ -\tan(\phi_E + e_\phi) & \frac{1}{(A_E + e_A)\cos(\phi_E + e_\phi)} \end{bmatrix} \begin{bmatrix} A_R \cos(p_0 + p(t)) - A_R \cos(p_0) \\ A_R A_E \sin(p_0 + p(t) + \phi_E) - A_R A_E \sin(p_0) \end{bmatrix}
\end{aligned}$$

The $B_{I,orth}$ vector is unaffected, but the $B_{Q,orth}$ vector is distorted. The A_R amplitude term has been set to 1 in the following calculations to simplify the equations.

$$\begin{aligned}
B_{Q,orth}' & = -\cos(p_0 + p(t))\tan(\phi_e + e_\phi) + \cos(p_0)\tan(\phi_e + e_\phi) \tag{C.55} \\
& + \left(\frac{A_E}{A_E + e_A} \right) \cdot \frac{\sin(p_0 + p(t))\cos(\phi_e)}{\cos(\phi_E + e_\phi)} + \left(\frac{A_E}{A_E + e_A} \right) \cdot \frac{\cos(p_0 + p(t))\sin(\phi_e)}{\cos(\phi_E + e_\phi)} \\
& - \left(\frac{A_E}{A_E + e_A} \right) \cdot \frac{\sin(p_0)\cos(\phi_e)}{\cos(\phi_E + e_\phi)} + \left(\frac{A_E}{A_E + e_A} \right) \cdot \frac{\cos(p_0)\sin(\phi_e)}{\cos(\phi_E + e_\phi)} \\
& = \left(\frac{A_E}{A_E + e_A} \right) \left(\frac{\cos(\phi_e)}{\cos(\phi_e)\cos(e_\phi) - \sin(\phi_e)\sin(e_\phi)} \right) [\sin(p_0 + p(t)) - \sin(p_0)] \\
& + \left(\tan(\phi_e + e_\phi) - \left(\frac{A_E}{A_E + e_A} \right) \frac{\sin(\phi_e)}{\cos(\phi_E + e_\phi)} \right) [\cos(p_0 + p(t)) - \cos(p_0)] \\
& = \left(\frac{A_E}{A_E + e_A} \right) \left(\frac{1}{\cos(e_\phi) - \tan(\phi_e)\sin(e_\phi)} \right) [\sin(p_0 + p(t)) - \sin(p_0)] \\
& + \left(\frac{(1 - (A_E/(A_E + e_A)))\tan(\phi_e) + \tan(e_\phi)}{1 - \tan(\phi_e)\tan(e_\phi)} \right) [\cos(p_0 + p(t)) - \cos(p_0)]
\end{aligned}$$

If $e_\phi \ll 1$, the small angle approximation gives:

$$\begin{aligned}
B_{Q,orth}' &= \left(\frac{A_E}{A_E + e_A} \right) \left(\frac{1}{1 - e_\phi \tan(\phi_e) - e_\phi^2} \right) [\sin(p_0 + p(t)) - \sin(p_0)] \\
&+ \frac{\left(\frac{e_A}{A_E + e_A} \right) (1 - e_\phi^2) \tan(\phi_e) + e_\phi}{1 - e_\phi \tan(\phi_e) - e_\phi^2} [\cos(p_0 + p(t)) - \cos(p_0)]
\end{aligned} \tag{C.56}$$

C.6 Effects of Zero Crossings

As is shown in Figure C.4, if the dc is removed and an additional offset is not added to avoid zero-crossings, the data spikes at the zero-crossings, making it impossible to view the trace. In the “shifted” traces, the dc values of the I and Q channels are shifted so the minimum value of each channel is 0.1 before the arctangent of the Q/I ratio is computed.

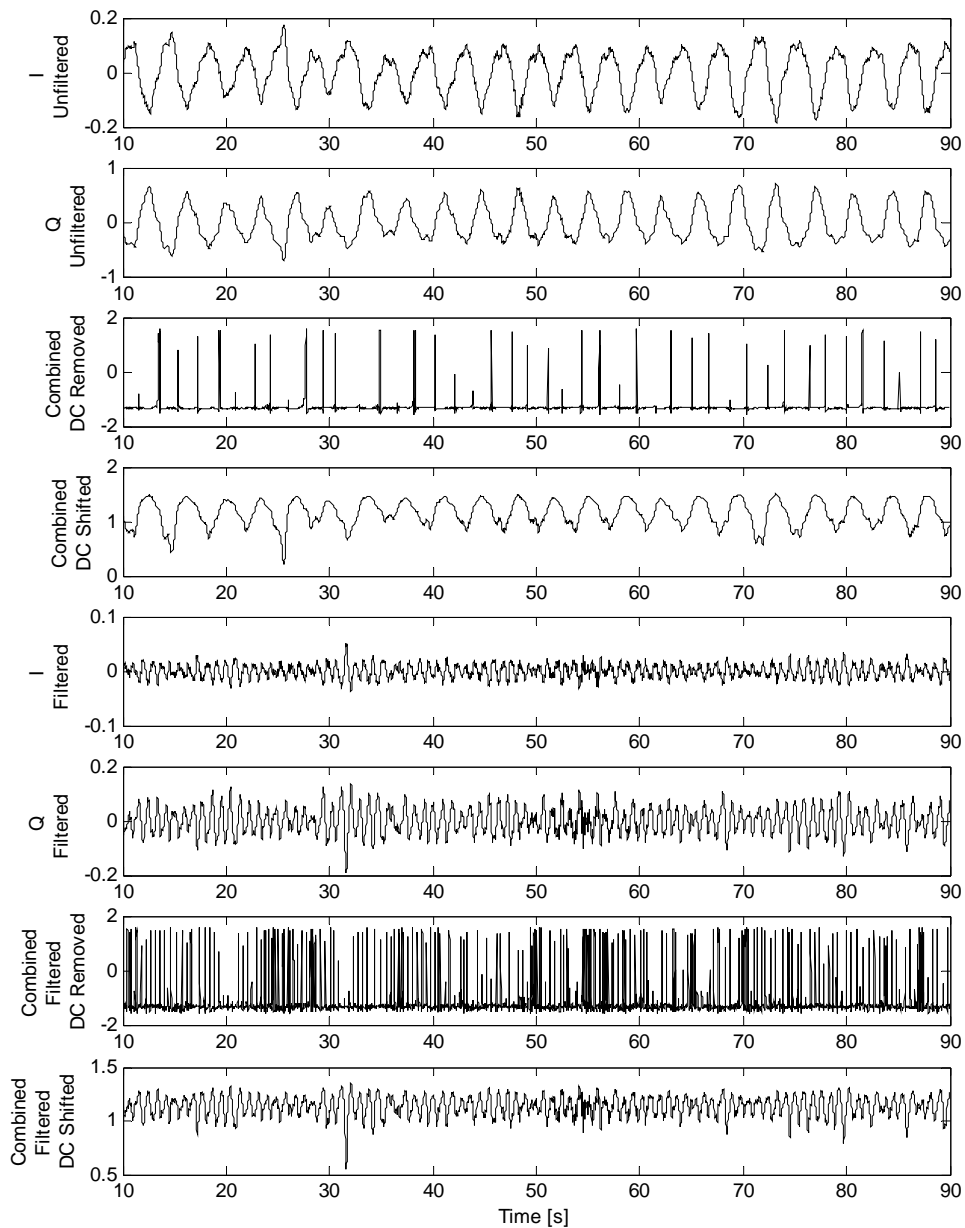


Figure C.4. Data from subject 4665, showing the I and Q channels, the combined channels using the arctangent technique after the dc offset was removed and the combined channels after the dc value was shifted to avoid zero-crossings. The top four traces are the respiration signal, and the bottom four traces are the heart signal.

C.7 Effects of Adding Offset to Avoid Zero Crossings

To determine how much error is produced by shifting the dc offset to avoid zero-crossings, the techniques were compared with simulated data. While removing the dc offset only slightly increased the normalized mean-squared error of the simulated signal, shifting the dc value resulted in a normalized mean-squared error as high as four orders of magnitude greater than the optimal phase demodulation. The simulated data is shown in Figure C.5 and in Table C.2.

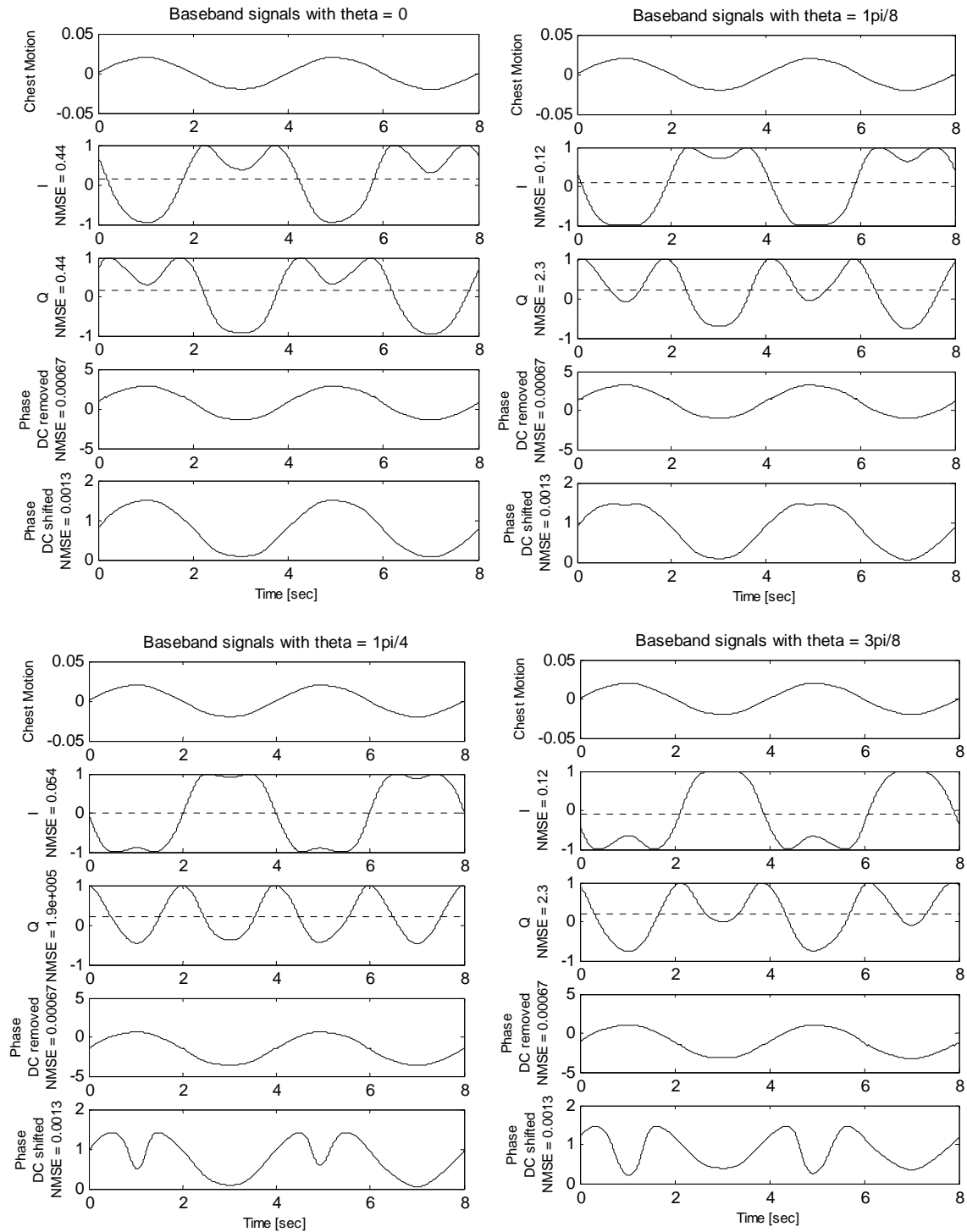


Figure C.5. Phases calculated with dc offset removed and with dc offset shifted to avoid zero-crossings, for a 2.4 GHz carrier.

Table C.2: Weighting Values for Scaling Output Signals to Minimize Mean Squared Error Between the Outputs and the Chest Motion Signal.

Phase Shift (radians)	Weight				Normalized Mean-Squared Error (NMSE)			
	I	Q	Phase dc present	Phase dc removed	I	Q	Phase dc removed	Phase dc shifted
0π	-41	41	109	37	0.44	0.44	1.3e-3	1.6e-3
$\pi/8$	-53	22	108	37	0.12	2.3	8.0e-4	0.010
$\pi/4$	-58	0.083	108	27	0.054	1.9e+5	6.4e-4	0.48
$(3\pi)/8$	-53	-22	108	11	0.12	2.3	8.0e-4	5.77

C.8 Conclusions

Some level of phase and amplitude imbalance is unavoidable in quadrature direct-conversion receivers, but these errors can be compensated for with Gram-Schmidt orthonormalization if the errors are known. DC offsets are also unavoidable in a direct-conversion radar receiver. Removal of the dc offsets causes only minor error in a noiseless system, but with noise the signal's zero-crossings can cause significant errors. If the signals are shifted to avoid zero-crossings, the error may become greatly increased at some RF-LO relationships. A low-IF transceiver will be considered in future versions of the transceiver to eliminate dc-offset concerns and to make baseband analog processing, especially the ADC and dc-offset removal, more straightforward.

C.9 References

- [242] A. Abidi, "Direct-conversion radio transceivers for digital communications," *IEEE Journal of Solid State Circuits*, vol. 30, no. 12, pp. 1399-1410, 1995.
- [243] F. E. Churchill, G. W. Ogar, B. J. Thompson, "The correction of I and Q errors in a coherent processor," *IEEE Transactions on Aerospace and Electronic Systems*, vol. AES-17, no. 1, pp. 131-137, 1981.
- [244] S. J. Goldman, "Understanding the limits of quadrature detection," *Microwaves and RF*, vol. 178, no. 1, pp. 67-70, 1986.

- [245] B. Razavi, "Design considerations for direct-conversion receivers," *IEEE Transactions on Circuits and Systems*, vol. 44, no. 6, pp. 428-435, 1997.

Appendix
D

Derivation of the Theoretical Signal-to-Noise Ratio

D.1 Introduction

The signal-to-noise ratio (SNR) is derived to assess the theoretical limits of the radar system, and to determine what factors affect the limits. The received power is determined by the radar equation, as described in Section D.2. This equation takes into account the range to the target, the transmitted power, the radar cross section, the antenna gain, the wavelength, and the range. The amount the signal is modulated is determined by the amount of physiological motion in the direction of the transceiver; Section D.3 describes how the amount of modulation is converted to baseband signal power. The amount of signal at baseband depends on received power and phase modulation. Noise sources include RF phase noise from the oscillator, environmental thermal noise, and baseband $1/f$ noise of the mixer and of the baseband signal conditioning circuits. The amount of noise at the mixer output from each of these sources is calculated in Section D.4. The variation of SNR with range, radar cross section, and the amount of physiological motion is explored in Section D.5. Section D.6 describes how operation in the near-field affects the antenna gain.

D.2 Radar Equation

The radar equation is used to estimate the received signal power in a radar system, helping to determine the system's theoretical limits. The estimated received power is based on the transmitted power, the range to the target, and the properties of the transmit antenna, the target, and the receive antenna. When measuring motion due to heart and respiration with a Doppler radar transceiver, in some cases the residual phase noise will be the limiting factor; otherwise the limiting factor will usually be receiver sensitivity and the received signal power.

To estimate the received signal power, it is necessary to determine how much power is lost and gained at various steps between the transmitter and the receiver. These losses and gains are discussed in this section, and they can be followed in Figure D.1 and Figure D.2. Greater detail on these steps can be found in [249] and [258].

To calculate the received power in a radar system, it is necessary to first calculate the transmitted power in the direction of the target. Antennas are generally measured in relation to an isotropic antenna that radiates uniformly in all directions. The power density, P_D , at any distance R from an isotropic antenna is the transmitted power, P_T , divided by the surface area of a sphere with radius R , $4\pi R^2$, with attenuation due to atmospheric absorption, given as $e^{-\alpha R}$ in each direction of propagation:

$$P_{D, isotropic} = \frac{P_T e^{-\alpha R}}{4\pi R^2}, \quad (\text{D.1})$$

in W/m^2 . The gain, G , of an antenna is the ratio of the power radiated toward the center of the target by that antenna to the power radiated in all directions by an isotropic antenna in that direction. The power radiated in the desired direction is known as the effective radiated power, ERP, and is equal to the gain multiplied by the transmitted power:

$$ERP = GP_T. \quad (\text{D.2})$$

The power density at a range R from a non-isotropic antenna is the ERP in that direction divided by the surface area of a sphere with radius R , with attenuation due to atmospheric absorption, α :

$$P_D = \frac{P_T G_T e^{-\alpha R}}{4\pi R^2} . \quad (\text{D.3})$$

The radar target intercepts a portion of the radiated power and reflects it, partially in the direction of the radar receiving antenna. The radar cross section, σ , is determined by the amount of power incident on the target that is re-radiated toward the antenna. The radar cross section is not the same as the physical cross section; it depends on the electrical properties of the material and its three dimensional shape, as described in Section D.2.1. The signal power reflected from the target is:

$$P_{\text{reflected}} = \frac{P_T G_T \sigma e^{-\alpha R}}{4\pi R^2} . \quad (\text{D.4})$$

This reflected signal then spreads out in space similarly to the transmitted signal. If the receiving antenna is co-located with the transmitting antenna, the power density just before the receiving antenna is the reflected power divided by the surface area of a sphere with radius R :

$$P_{D, \text{receiver}} = \frac{P_T G_T \sigma e^{-2\alpha R}}{(4\pi R^2)^2} . \quad (\text{D.5})$$

The receiving antenna is traditionally described by its effective area, $A_{e, R}$, which determines what portion of the radiated energy it can capture. The power received is equal to the power density at the antenna, multiplied by the effective capture area, A_e of the receiving antenna:

$$P_R = \frac{P_T G_T \sigma A_{e, R} e^{-2\alpha R}}{(4\pi R^2)^2} . \quad (\text{D.6})$$

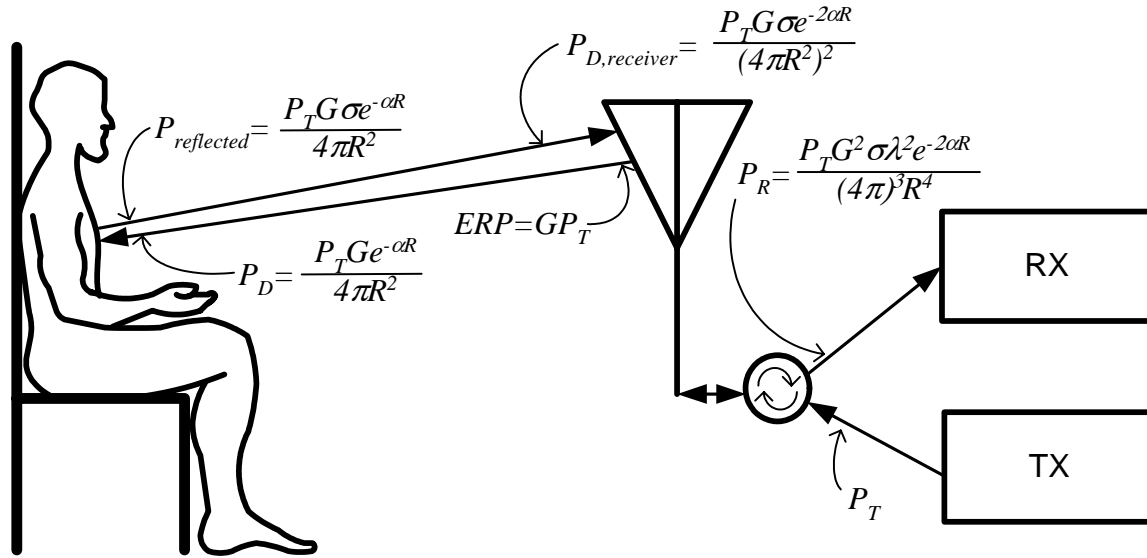


Figure D.1. Illustration of power, effective radiated power, and power density at various points in the Doppler radar system. P_T is the transmitted power, G is the antenna gain, R is the distance between the target and the antenna, α is the attenuation, σ is the radar cross section, and λ is the wavelength of the RF signal. These equations assume that the target and antenna are sized such that they are in the far-field at the range of measurement.

This equation can also be written in terms of the receiving antenna's gain. The relationship between the receiving antenna's gain and effective area is:

$$G_R = \frac{4\pi A_{e,R}}{\lambda^2}; \quad (\text{D.7})$$

when this is substituted into (D.6), the resulting expression for the received power is:

$$P_R = \frac{P_T G_T \sigma \lambda^2 G_R e^{-2\alpha R}}{(4\pi R^2)^2 (4\pi)} = \frac{P_T G_T G_R \sigma \lambda^2 e^{-2\alpha R}}{(4\pi)^3 R^4}. \quad (\text{D.8})$$

This final term is known as the radar equation. When the same antenna is used for transmitting and receiving, the gain is the same for both antennas, and the equation can be simplified to:

$$P_R = \frac{P_T G^2 \sigma \lambda^2 e^{-2\alpha R}}{(4\pi)^3 R^4}. \quad (\text{D.9})$$

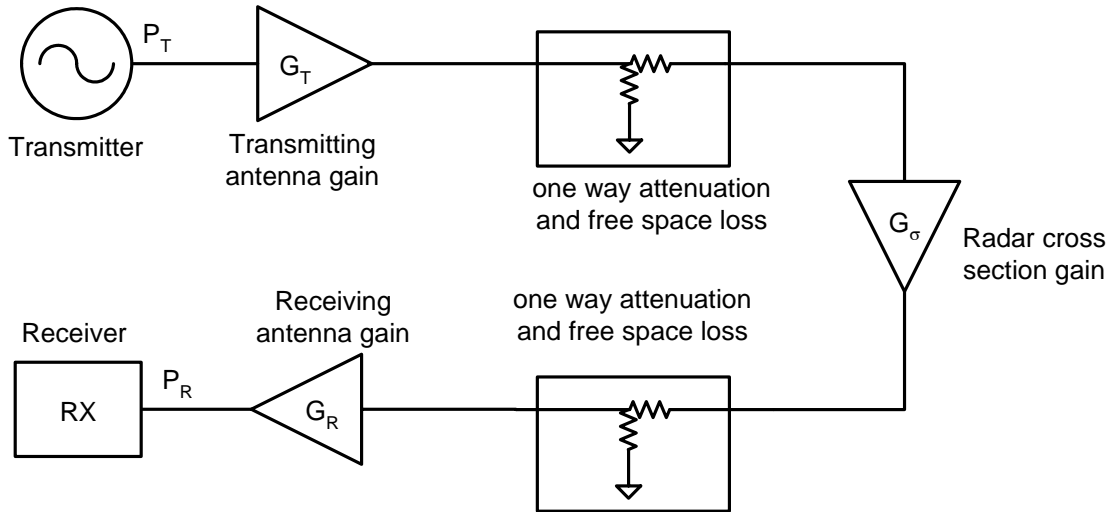


Figure D.2. Equivalent circuit representation of the radar equation, after [249].

However, for the distances used in this application, the attenuation term when operating through air has a negligible effect and can be dropped:

$$P_R = \frac{P_T G^2 \sigma \lambda^2}{(4\pi)^3 R^4}. \quad (\text{D.10})$$

An equivalent circuit representation of this equation is given in Figure D.2.

For radar monitoring of heart and respiration rate, the radar cross section is the only value that is not clearly defined. This will be discussed in more detail in the following section. The radar equation assumes that the target is in the antenna far field. This is not necessarily true for all cases, especially at very close ranges and for respiration, when the target is larger compared to the range than it is for the heart. The effects of being in the antenna near-field are discussed in Section D.6.

D.2.1 Radar Cross Section

The radar cross section (RCS) is a measure of how well the target reflects radar signals in the direction of the radar receiver. It can be described as the ratio of the strength of the reflected signal from the target to the reflected signal from a perfectly smooth and perfectly conducting sphere with a 1 m^2 cross-sectional area [249]. It is often described as:

$$\sigma = (\text{Projected cross section}) \times (\text{Reflectivity}) \times (\text{Directivity}) \quad (\text{D.11})$$

When measuring a person, calculation of the projected cross section requires including the whole person as well as the bed or chair on which they are sitting. If the entire person (as well as bed or chair) is not in the beam of the antenna, then only the illuminated portion should be considered. If this is the case, the target is in the near-field, as is discussed in Section D.6. However, for physiological motion measurement, the size of the area in motion determines the radar cross section; the stationary part of the body is considered to be clutter.

The reflectivity is the amount of the intercepted power that is reflected rather than absorbed. This is calculated based on the frequency of operation and the dielectric properties of the subject's skin and muscle in Section D.2.2.

The directivity is the ratio of the scattered power back towards the antenna to the power that would have back-scattered had the target been an isotropic radiator. This is difficult to calculate for this application, as it will depend on the individual's shape and their orientation with respect to the antenna.

The radar cross section of a sphere varies with its size in wavelengths. A sphere with a radius a has a circumference in wavelengths of:

$$ka = 2\pi\frac{a}{\lambda}, \quad (\text{D.12})$$

with $k = (2\pi)/\lambda$ [249]. The radar cross section exhibits a rapid rise in the region $0 < ka < 1$, known as the Rayleigh region. When $1 < ka < 10$, there is interference between creeping and specular waves. Specular waves are reflected from the front of the sphere, and creeping waves travel around the body and are reflected from the shadowed side. When the two types of waves are of similar sizes, they interfere constructively and destructively; the $ka < 10$ region is therefore known as the resonance region of the radar cross section. When $ka > 10$, the reflection is dominated by specular reflections; this is known as the optical region of the radar cross section. A plot relating the radar cross section to the area of the sphere is shown in Figure D.3 [249]. This relationship is often more

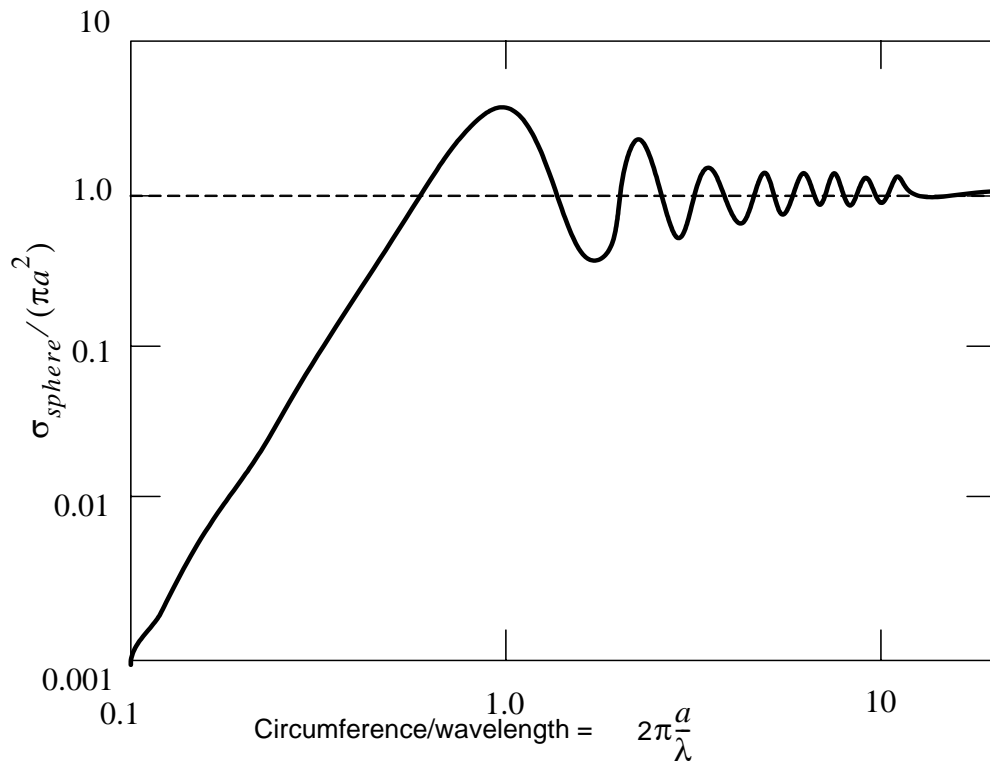


Figure D.3. Radar cross section of a perfectly conducting sphere as a function of its electrical size, ka . After [249].

complicated in a dielectric that is not perfectly conducting, because energy that enters the target may have multiple internal reflections before returning to the target.

For purposes of determining the power of the phase-modulated signal with heart and respiration information, the radar cross section depends on the fraction of the body that is moving. For residual phase noise and dc offset calculations, the entire person as well as the furniture behind them (or the portion that is illuminated by the antenna) should also be included. The area that is moving due to respiration may be the entire thorax, while the area due to the heart varies from less than a centimeter to a few centimeters. This means that for heart measurements, the target is in the Rayleigh region, while for respiration measurement, the target is in the resonance region of the radar cross section. At 2.4 GHz, the wavelength is 12.5 cm, so $ka \approx a / (2\text{cm})$. Since the radius of the area moving due to heart is expected to be below 2 cm, it is in the Rayleigh region. Since the radius of the area mov-

ing due to respiration is expected to be greater than 2 cm and less than 20 cm, the respiration RCS will be in the resonance region.

The radar cross section of humans was estimated by Schultz, et. al in 1954 by measuring a 200-pound man at five different frequencies with a CW Doppler radar [257]. The frequencies closest to those used in Doppler radar cardiopulmonary measurement were 1120 MHz and 2890 MHz. At 1120 MHz, the radar cross section varied from 0.28 to 0.88 square meters, while at 2890 MHz, the radar cross section varied from 0.20 to 0.72 square meters, depending on the aspect of the subject relative to the antenna and the antenna polarization. With the radar facing the front or back of the subject, at 1120MHz, the radar cross section was 0.72 m² for horizontal polarization and 0.88 m² for vertical polarization. At 2890 MHz, when facing the front, the radar cross section was 0.41 m² for horizontal polarization and 0.50 m² for vertical polarization, and when facing the back the RCS was 0.61 m² for horizontal polarization and 0.72 m² for vertical polarization.

Wu [262] computed the radar cross section of a human model using a muscle hemisphere head, a cylindrical neck, and a conical torso. He found that with horizontal polarization, the radar cross section was 15 dB $(RCS)/\lambda^2 < 28$ dB and with vertical polarization 0 dB $< (RCS)/\lambda^2 < 20$ dB, with RCS being the radar cross section and λ the wavelength. The variations again occur with the angle to the body. Facing the front of the body, Wu found $(RCS)/\lambda^2 \sim 14$ dB for both horizontal and vertical polarizations. At 2.4 GHz, this would indicate a radar cross sectional area of 0.39 m² closely agreeing with Schultz [257].

Although predictions and measurements of the Doppler signal from walking humans have been made [251, 260], they do not show measured values of the radar cross sections of each body part. Individuals can vary greatly in size, and therefore they will also vary greatly in radar cross section. Additionally, when determining the RCS for measurements of heart and respiration, it is necessary to determine the area of the body moving with pulse and breathing in the direction of the radar, which can also vary greatly from person to person.

D.2.2 Reflection and Absorption

The electrical properties of biological tissue affect how much of the signal is reflected and transmitted, both at the skin-air interface and at interfaces between different tissues within the body. Of the radiation that enters the body, the electrical properties determine how much of it is attenuated per unit distance, how much is transmitted to the next layer, and how much is reflected back towards the skin surface. Biological tissue is non-magnetic, therefore its permeability, μ , is nearly identical to that of free space. The dielectric constant, representing the material's permittivity ϵ , and the conductivity, σ , are the two electrical properties that primarily define the electrical characteristics of the biological tissue.

Using data from the parametric models from Gabriel and Gabriel [250], the transmission and reflection coefficients are graphed in Figure D.4. The intrinsic impedance of the materials, η , was calculated as

$$\eta = \frac{j\omega\mu}{\gamma}, \quad (\text{D.13})$$

where ω is the radial velocity, $2\pi f$, and γ is the propagation constant,

$$\gamma = j\omega \cdot \sqrt{\mu\epsilon} \cdot \sqrt{1 - \frac{j\sigma}{\omega\epsilon}}. \quad (\text{D.14})$$

The reflection coefficient, Γ , at the interface between free space and the material with intrinsic impedance η is:

$$\Gamma = \frac{\eta - \eta_0}{\eta + \eta_0}, \quad (\text{D.15})$$

where η_0 is the impedance of free space [247].

The transmission coefficient, T , at the same interface is:

$$T = 1 + \Gamma = \frac{2\eta}{\eta + \eta_0}. \quad (\text{D.16})$$

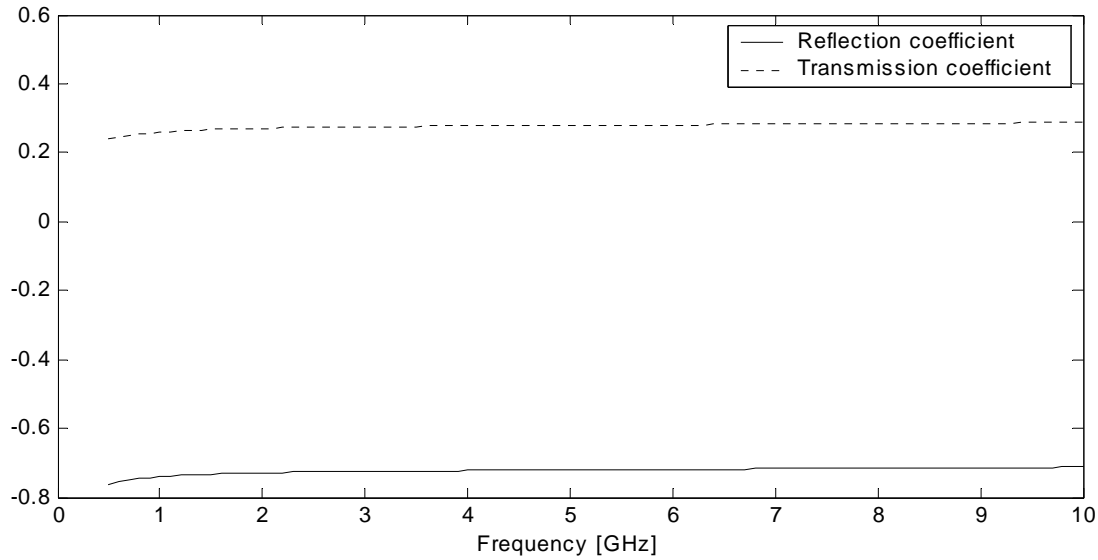


Figure D.4. Transmission and reflection coefficients for dry skin in air vs. frequency.

For the frequencies of interest, the reflection coefficient at the air-skin interface is approximately -0.71, while the transmission coefficient at the interface is approximately 0.29. The portion of the power that is reflected is equal to the square of the reflection coefficient [247]:

$$\frac{P_{refl}}{P_{inc}} = \Gamma^2. \quad (\text{D.17})$$

This means that 51% of the signal will be reflected at the skin/air interface.

The amount of the reflected signal due to internal reflections is shown in Figure D.5. Values of the intrinsic impedance and the attenuation coefficient of skin, fat, muscle, and heart at 2.4 GHz were taken from Gabriel and Gabriel [250], and the order of the tissues and their estimated thicknesses were taken from Gentili, et. al [252]. The reflectance, or the ratio of reflected power to incident power is:

$$\frac{P_{refl}}{P_{inc}} = \left| \frac{\eta_2 - \eta_1}{\eta_2 + \eta_1} \right|^2, \quad (\text{D.18})$$

and the transmittance is:

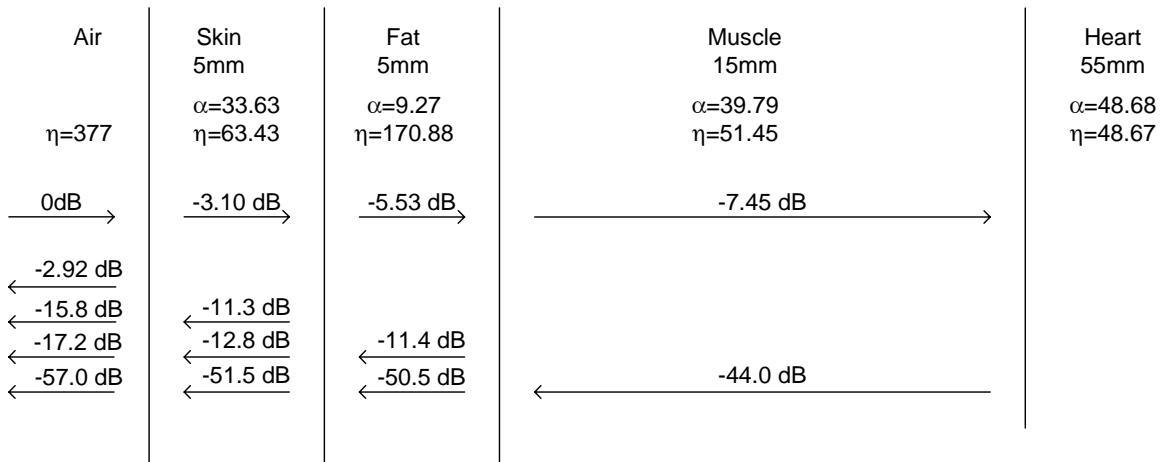


Figure D.5. Percentage of incident power reflecting from and transmitting through biological interfaces at 2.4GHz. The attenuation constant, α , and intrinsic impedance, η , of each material were taken from [250], and the thicknesses and the order of the materials were taken from [252].

$$\frac{P_{trans}}{P_{inc}} = 1 - \left| \frac{\eta_2 - \eta_1}{\eta_2 + \eta_1} \right|^2, \tag{D.19}$$

where η_1 is the intrinsic impedance of the material the incident wave is in, and η_2 is the intrinsic impedance of the scattering material [247]. The attenuation through each material was taken as:

$$P(z) = P(0)e^{-2\alpha z}, \tag{D.20}$$

where $P(0)$ is the power that enters the material, α is the attenuation constant of the material and z is the thickness of the material [247]. This indicates that about half of the incident power is reflected at the skin/air interface and that 91% of the total reflected signal is from the skin-air interface.

D.3 Phase-to-Amplitude Conversion

To determine the signal power at baseband, the received RF signal power, the receiver loss or gain, the mixer conversion loss or gain, and the amount of phase modulation must all be considered. The RF signal power can be determined with the radar equation, as

described in the previous section. The conversion of the phase-modulated signal to a base-band signal follows calculations used in communication phase-modulation link equations [255].

The signal at the LO input to the mixer is

$$L(t) = A_{LO} \cos(2\pi ft) , \quad (\text{D.21})$$

and the signal at the RF input to the mixer is

$$R(t) = A_{RF} \sqrt{G_{RX}} \cos(2\pi ft + \psi(t) + \theta) , \quad (\text{D.22})$$

where $\psi(t)$ is the phase modulation of the signal and θ is a constant relative phase shift between the two signals. A_{RF} and A_{LO} are the amplitudes of the signal and LO, and G_{RX} is the gain or loss between the antenna and the mixer's RF input. When the LO and RF signals are mixed, after low-pass filtering, the output is

$$B(t) = \sqrt{G_{CL} G_{RX}} A_{RF} \cos(\psi(t) + \theta) . \quad (\text{D.23})$$

G_{CL} is the conversion gain of the mixer (power gain), representing the ratio of the IF output power to the RF input power when signals are mixed.

The signal power at baseband is:

$$S_B = \frac{\overline{B^2(t)}}{Z} = \frac{G_{CL} G_{RX} A_{RF}^2 \overline{(\cos(\psi(t) + \theta))^2}}{Z} . \quad (\text{D.24})$$

To determine baseband signal power, the received power in (D.9) must be converted to the voltage amplitude at the RF input to the mixer, A_{RF} . The signal power at the input of the receiver is equal to the mean squared received voltage divided by the input impedance, Z :

$$P_R = \frac{\overline{R^2(t)}}{Z} . \quad (\text{D.25})$$

Since the RF signal is a phase-modulated sinusoid,

$$\overline{R^2(t)} = \frac{A_{RF}^2}{2} , \quad (\text{D.26})$$

and

$$A_{RF}^2 = 2P_R Z . \quad (D.27)$$

Plugging in (D.10) for P_R , the squared amplitude is:

$$A_{RF}^2 = \frac{2P_T G^2 \sigma \lambda^2 Z}{(4\pi)^3 R^4} . \quad (D.28)$$

Therefore, the baseband signal power is:

$$S_B = \frac{2P_T G_{CL} G_{RX} G^2 \sigma \lambda^2 \overline{(\cos(\psi(t) + \theta))^2}}{(4\pi)^3 R^4} . \quad (D.29)$$

For Doppler radar cardiopulmonary monitoring,

$$\psi(t) = \frac{4\pi}{\lambda} x(t) , \quad (D.30)$$

where $x(t)$ is the physiological motion in the direction of the antenna, so the power at the output of the mixer is:

$$S_B = \frac{2P_T G_{CL} G_{RX} G^2 \sigma \lambda^2 \overline{\left(\cos\left(\frac{4\pi}{\lambda} x(t) + \theta\right)\right)^2}}{(4\pi)^3 R^4} . \quad (D.31)$$

If the value of θ is such that the signal is at an optimal phase demodulation point, the small angle approximation applies and the baseband output is:

$$B(t) \approx \sqrt{G_{CL} G_{RX}} A_{RF} \frac{4\pi}{\lambda} x(t) , \quad (D.32)$$

and the signal power at baseband is

$$S_B = \frac{2P_T G_{CL} G_{RX} G^2 \sigma \overline{x^2(t)}}{4\pi R^4} . \quad (D.33)$$

D.4 Sources of Noise

There are three main sources of noise for the physiological signals: residual phase noise, downconverted RF additive white gaussian noise (AWGN) from the front end of the receiver, and baseband $1/f$ noise. These three noise sources are combined at baseband. Each of these sources at baseband must be calculated as the noise power due to each of these sources. These calculations are made at the output of the mixer, where the signal has been converted from a phase-modulated signal to a baseband amplitude signal and all the noise sources are additive.

D.4.1 Residual Phase Noise and Range Correlation

According to Budge and Burt [246], (D.34) can be used to calculate the baseband noise spectral density, $S_{\Delta\phi}(f_o)$, from the RF phase noise spectral density, $S_{\phi}(f_o)$, with the target at a given range, R , and offset frequency, f_o :

$$S_{\Delta\phi}(f_o) = 2S_{\phi}(f_o) \left[4 \sin^2 \left(2\pi \frac{Rf_o}{c} \right) \right], \quad (\text{D.34})$$

where c is the signal's propagation velocity. At values relevant for radar monitoring of heart and respiration, Rf_o/c is on the order of 10^{-9} , so the small angle approximation is valid, and residual phase noise causes the baseband noise spectrum to increase proportionally to the square of the target range, R , and the square of the offset frequency, f_o :

$$S_{\Delta\phi}(f_o) \approx 2S_{\phi}(f_o) \left[16\pi^2 \frac{R^2 f_o^2}{c^2} \right]. \quad (\text{D.35})$$

Since the ranges used for radar monitoring of heart and respiration are on the order of the equivalent ranges for time delays in the system, delays between the oscillator and the antenna and the antenna and the receiver need to be included in the range correlation equation:

$$S_{\Delta\phi}(f_o) \approx 2S_{\phi}(f_o) \left[16\pi^2 \frac{\left(R + \frac{ct_d}{2}\right)^2 f_o^2}{c^2} \right], \quad (\text{D.36})$$

where t_d is the time delay from the oscillator to the antenna summed with the delay from the antenna to the receiver.

Since the close-in phase noise has a -30 dB per decade slope, the phase noise can be defined by the phase noise at an arbitrary frequency f_1 :

$$S_{\phi}(f_o) = \frac{S_{\phi}(f_1)}{f_1^{-3}} \cdot f_o^{-3}. \quad (\text{D.37})$$

This is most easily defined at the 1 Hz intercept, $S_{\phi}(1)$:

$$S_{\phi}(f_o) = \frac{S_{\phi}(1)}{(1\text{Hz})^{-3}} f_o^{-3} = S_{\phi}(1) \cdot \left(\frac{f_o}{1\text{Hz}}\right)^{-3}. \quad (\text{D.38})$$

A model of residual phase noise can be found by using this result and the range correlation equation, (D.34):

$$\begin{aligned} S_{\Delta\phi}(f_o) &= 2 \left(S_{\phi}(1) \left(\frac{f_o}{1\text{Hz}}\right)^{-3} \right) \cdot \left[16 \left(\pi^2 \cdot \frac{\left(R + \frac{ct_d}{2}\right)^2 f_o^2}{c^2} \right) \right] \\ &= 32\pi^2 \left(\frac{\left(R + \frac{ct_d}{2}\right)^2}{c^2} \right) (1\text{Hz})^3 S_{\phi}(1) f_o^{-1} \end{aligned} \quad (\text{D.39})$$

The signal with phase noise at the transceiver's RF input is:

$$R_{PN}(t) = A_{RF, PN} \cos(2\pi ft + \phi(t - T)), \quad (\text{D.40})$$

where $A_{RF, PN}$ is the amplitude, f is the carrier frequency, and $\phi(t - T)$ is the phase noise of the signal. T indicates the time elapsed from when the signal left the transceiver to when it is received. The signal has a received power of:

$$P_{R,PN} = \frac{P_T G^2 \sigma_c \lambda^2}{(4\pi)^3 R^4} . \quad (D.41)$$

This is calculated from the radar equation (D.10), with σ_c the radar cross section of the clutter that reflects the signal with phase noise. The received phase noise power is equal to the mean square of its voltage divided by the input impedance, Z :

$$P_{R,PN} = \frac{\overline{R_{PN}^2(t)}}{Z} . \quad (D.42)$$

Therefore, the squared amplitude is:

$$A_{RF,PN}^2 = 2P_{R,PN}Z = \frac{2P_T G^2 \sigma_c Z \lambda^2}{(4\pi)^3 R^4} . \quad (D.43)$$

Since phase noise is a phase modulation, the baseband power can be calculated with the phase modulation link equation as it was for the phase-modulated signal in Section D.3., but the phase term at baseband is replaced with the residual phase noise term, $\Delta\phi(t)$, because the RF and LO phase noise are combined when the signals are mixed, as is explained in detail in Chapter 5. The baseband residual phase noise voltage is:

$$B_{RPN}(t) = \sqrt{G_{CL}G_{RX}} A_{RF,PN} \cos(\Delta\phi(t)) , \quad (D.44)$$

and the baseband residual phase noise power is:

$$N_{RPN,B} = \frac{\overline{B_{RPN}^2(t)}}{Z} = \frac{G_{CL}G_{RX} A_{RF,PN}^2 \overline{(\cos(\Delta\phi(t)))^2}}{Z} , \quad (D.45)$$

or

$$N_{RPN,B} = \frac{\overline{B_{RPN}^2(t)}}{Z} = \frac{2P_T G_{CL} G_{RX} G^2 \sigma_c \lambda^2 \overline{(\cos(\Delta\phi(t)))^2}}{(4\pi)^3 R^4} . \quad (D.46)$$

and applying the small-angle approximation,

$$N_{RPN, B} = \frac{\overline{B_{RPN}^2(t)}}{Z} = \frac{2P_T G_{CL} G_{RX} G^2 \sigma_c \lambda^2 \overline{(\Delta\phi(t))^2}}{(4\pi)^3 R^4}. \quad (D.47)$$

The mean squared residual phase noise in the time domain is the integral of the spectrum over the received frequencies:

$$\Delta\phi_{RMS}^2 = \int_{f_{min}}^{f_{max}} S_{\Delta\phi}(f_o) df_o, \quad (D.48)$$

where f_{max} is the highest frequency and f_{min} is the lowest frequency passed through the filters. Using the expression for $S_{\Delta\phi}(f_o)$ in (D.38), the mean squared residual phase noise can be expressed as:

$$\begin{aligned} \Delta\phi_{RMS}^2 &= 32\pi^2 (1Hz)^3 S_\phi(1) \frac{\left(R + \frac{ct_d}{2}\right)^2}{c^2} \int_{f_{min}}^{f_{max}} f_o^{-1} df_o \\ &= 32\pi^2 (1Hz)^3 S_\phi(1) \frac{\left(R + \frac{ct_d}{2}\right)^2}{c^2} \ln \left[\frac{f_{max}}{f_{min}} \right] \end{aligned} \quad (D.49)$$

This expression allows the baseband mean squared phase noise to be calculated from the RF phase noise, the range to the target, the transceiver time delay, and the selected filtering frequencies. The RMS noise is:

$$\Delta\phi_{RMS} = 4\sqrt{2}\pi \left(\frac{\left(R + \frac{ct_d}{2}\right)}{c} \right) \sqrt{S_\phi(1) \ln \left(\frac{f_{max}}{f_{min}} \right)}. \quad (D.50)$$

We can substitute this value into (D.47) to get an estimate of the residual phase noise with range, as follows:

$$N_{RPN, B} = \frac{P_T \sigma_c G_{antenna}^2 G_{RX} G_{CL}}{\pi f^2} S_\phi(1) \frac{\left(R + \frac{ct_d}{2}\right)}{R^4} \ln\left(\frac{f_{max}}{f_{min}}\right). \quad (D.51)$$

This value can be checked by assuming that with perfect phase demodulation, the residual phase noise signal-to-noise ratio will be the same as the ratio of the phase variation of the signal to that of the noise, multiplied by the ratio of the signal radar cross section to that of the clutter:

$$\left(\frac{S_0}{N_{RPN}}\right) = \left(\frac{\phi_{RMS, heart}}{\Delta\phi_{RMS}}\right)^2 \cdot \frac{\sigma}{\sigma_c} \quad (D.52)$$

or

$$\left(\frac{S_0}{N_{RPN}}\right) = \frac{\overline{\sigma x^2(t)} f^2}{2R^2 \sigma_c S_\phi(1) \ln\left(\frac{f_{max}}{f_{min}}\right)}. \quad (D.53)$$

If the signal power is scaled to be that calculated in (D.33), the noise power is:

$$N_{RPN, B} = \frac{P_T \sigma_c G_{antenna}^2 G_{RX} G_{CL}}{\pi f^2 R^2} S_\phi(1) \ln\left(\frac{f_{max}}{f_{min}}\right), \quad (D.54)$$

which matches the calculation in (D.51) except for the term for the transceiver time delay that was not included in this estimate.

D.4.2 Baseband 1/f Noise

In this application, $1/f$ noise from the mixer and from the baseband signal conditioning circuitry dominates the baseband noise spectrum. The $1/f$ baseband receiver noise can be approximated as:

$$N_{1/f, B} = \int_{f_{min}}^{f_{max}} P_{1/f}(1) f^{-1} df = P_{1/f}(1) \ln \left(\frac{f_{max}}{f_{min}} \right), \quad (D.55)$$

where $P_{1/f}(1)$ is the noise power in a 1-Hz bandwidth centered at 1 Hz.

D.4.3 RF Additive White Gaussian Noise

Since the information in Doppler radar cardio-respiratory sensing is encoded as a phase modulation, the RF SNR is not the same as the signal's SNR after it has been demodulated to baseband. The amplitude noise at RF affects the phase of the signal based on the percentage of phase modulation in addition to the RF SNR. The RF noise at the input is:

$$N_{RF, in} = NB, \quad (D.56)$$

where N is the white channel noise power spectral density and B is the receiver bandwidth.

Because the signal-to-noise ratio is being calculated after the mixer, the noise figure, receiver gain, and mixer conversion loss need to be included in the equations. The noise figure can be expressed as the ratio of the input signal-to-noise ratio to the output signal-to-noise ratio, or as the ratio for the noise output from the actual receiver to the noise output from an ideal receiver:

$$NF = \frac{\left(\frac{S}{N}\right)_{in}}{\left(\frac{S}{N}\right)_{out}} = \frac{N_{RF, out}}{G_{RX} G_{CL} N_{RF, in}}, \quad (D.57)$$

where G_{RX} is the gain of the receiver and G_{CL} is the mixer's conversion loss. The noise figure expresses the amount of noise added to the signal by the receiver. Therefore, the signal at the mixer output is:

$$S_B = G_{RX} G_{CL} (S_0)_{in}, \quad (D.58)$$

while the noise after the mixer is:

$$N_{RF,B} = G_{RX}G_{CL}(NF)N_{RF,in} = 2G_{CL}G_{RX}(NF)(NB) . \quad (D.59)$$

There is a factor of two because the thermal noise in the two sidebands is uncorrelated, so the noise power adds.

The dominant RF noise at the input to the receiver is thermal noise; thermal noise is zero-mean, has a gaussian distribution, and does not vary with frequency. This is additive to the RF signal. The thermal noise power is expressed by:

$$P_{N,thermal} = 4kTB , \quad (D.60)$$

where k is Boltzman's constant, T is the absolute temperature, and B is the bandwidth. Therefore, N can be substituted with $4kT$ in most cases. Therefore the total RF noise converted to baseband is:

$$N_{RF,B} = 8G_{CL}G_{RX}(NF)(kTB) . \quad (D.61)$$

D.5 Variation of Signal-to-Noise Ratio with Range and Radar Cross Section

The three main sources of noise, residual phase noise, downconverted RF additive white noise, and baseband $1/f$ noise, are combined at the mixer output after they have been converted to their values in baseband. Because the noise from the three sources is uncorrelated, the noise powers simply add. Therefore, the signal-to-noise ratio for the system is:

$$\frac{S_B}{N_B} = \frac{S_0}{N_{1/f,B} + N_{RF,B} + N_{RPN,B}} \quad (D.62)$$

This can be expanded to:

$$\left(\frac{S_B}{N_B} \right) =$$

$$\frac{P_T G^2 G_{RX} G_{CL} \sigma \overline{x^2(t)}}{2\pi R^4} \cdot \left(\frac{R + \frac{ct_d}{2}}{R^4} \right)^2 + 2G_R G_{CL} (NF)(NB) + \frac{P_T \sigma_c G^2 G_R G_{CL} S_\phi(1) \ln\left(\frac{f_{max}}{f_{min}}\right)}{\pi f^2} \cdot \left(\frac{R + \frac{ct_d}{2}}{R^4} \right)^2$$

(D.63)

This is equivalent to:

$$\left(\frac{S_B}{N_B} \right) = \frac{P_T G_{ant}^2 G_{RX} G_{CL} \overline{\sigma x^2(t)}}{2\pi(N_{1/f, B} + N_{RF, B})R^4 + 2\left(\frac{P_T \sigma_{clu} G_{ant}^2 G_{RX} G_{CL} S_\phi(1) \ln\left(\frac{f_{max}}{f_{min}}\right)}{f^2}\right)\left(R + \frac{ct_d}{2}\right)^2}$$

(D.64)

When residual phase noise is dominant, the signal-to-noise ratio will be proportional to $(R + 0.5ct_d)^{-2}$, and when either the baseband noise or the RF additive white gaussian noise is dominant, the signal-to-noise ratio will be proportional to R^{-4} . If one noise source is not dominant for all ranges, the residual phase noise will be dominant close to the target, and the baseband or RF noise will be dominant further from the target. The equation also indicates that the signal-to-noise ratio should be linear with the radar cross section of the target, and it should not affect the dominant type of noise. The radar cross section and the amount of motion for both heart and respiration is expected to vary from subject to subject, and likely also with orientation with respect to the antenna.

For this case, it was assumed that the signal is at the optimal phase demodulation point. This gives the best-case signal-to-noise calculation for a single-channel receiver. The output at the mixer will be filtered and amplified before it is digitized. For the quadrature receiver, if the signal is determined by choosing between the I and Q signals, the signal power and residual phase noise power would be cut in half. This would not affect the signal-to-noise ratio if residual phase noise is dominant, but does if either RF ampli-

tude noise or baseband $1/f$ noise is the dominant noise source. If the I and Q signals are combined, the baseband noise from the filtering and amplifying stages is added before the combination takes place. If residual phase noise is dominant, the SNR of the combined of I and Q signals will be similar to that of the single-channel receiver at the optimal phase demodulation point. If one of the other noise sources is dominant, the SNR would be a factor of two worse.

D.6 Near-Field vs. Far-Field Antenna Patterns

When a target is too close to the radar transmit and receive antenna, the power density does not fall off as $1/R^2$ and the antenna pattern varies with the range from the antenna, so that the antenna gain will be different from the specified far-field antenna pattern. This region is known as the near-field region.

There are three regions of antenna patterns.

1. Reactive near field: this is very close to the antenna; here, the reactive components are large compared to the radiative components
2. Radiating near field: the field is radiating, the radiation pattern depends on both distance and angle. This region is also known as the Fresnel region, and will be referred as the near-field in the following text.
3. Radiating far field: the relative amplitude and phase of components from different parts of the antenna does not vary with distance. The field strength decays monotonically, inversely dependent on distance. This region is also known as the Fraunhofer region [256].

In the far-field region, the wave-front can be considered planar, and the rays are approximately parallel. The near field is where the planar, parallel-ray approximation breaks down. The error in assuming the antenna is in far field is approximately [249]:

$$\epsilon = \frac{D^2}{8R}, \quad (\text{D.65})$$

where D is the largest dimension of the antenna and R is the range to the target. The radar equation, (D.10), assumes far-field, so it is important to know how significant the error is. For radar it is estimated that the far field starts when the range is greater than

$$R_{far-field} = \frac{2D^2}{\lambda}, \quad (D.66)$$

where D is the maximum dimension of the antenna or the scatterer, and λ is the wavelength. At this distance, the difference in the path length is $\lambda/16$; corresponding to a phase difference of 22.5 degrees.

At a range of 50 cm and a wavelength of 12.5 cm, the maximum target or antenna dimension using (D.66) is 17.7 cm. Because Doppler radar measurement of heart and respiration rates measures only the moving part of the body, near-field considerations need to take into account the portion of the body that is moving. The area moving due to the heart beat and pulse is small compared to the range, while the area moving due to respiration may be large compared to the range in some cases.

A description of the change in antenna pattern within the near-field is given in [248]:

As the observer moves nearer to the antenna under observation, two effects are noted. The main beam broadens, the nulls between the main lobes fill in, and the sidelobes are slightly raised. These effects become progressively more pronounced as the distance decreases until a point is reached at which the main beam tends to bifurcate into two beams, depending upon the aperture and aperture distribution.

Fields in patch and planar integrated antennas, such as that used in this study, typically have a cosine distribution in one direction and are uniform in the other direction [259, 261]. The near-field radiation pattern can be calculated for such a distribution [254]. If the electric field on the antenna is:

$$E(x, y) = \cos\left(\frac{\pi y}{b}\right), \quad (D.67)$$

the on-axis near field pattern is:

$$E_n(r, 0) = \hat{\theta} j e^{-jk r + j\left(\frac{\pi r \lambda}{4b^2}\right)} [C(u) - jS(u)] \{C(v) - C(w) - j[S(v) - S(w)]\} \quad (D.68)$$

where r is the distance from the antenna, b is the length of the antenna, λ is the wavelength in free space, and $k = \omega\sqrt{\mu_0\epsilon_0}$, ω is the radial frequency of the signal, μ_0 is the permeability of free space ϵ_0 is the permittivity of free space, and u , v , and w are parameters with:

$$u = \frac{a}{\sqrt{2r\lambda}}, \quad (\text{D.69})$$

$$w = \frac{-b}{\sqrt{2r\lambda}} + \frac{1}{b}\sqrt{\frac{r\lambda}{2}}, \quad (\text{D.70})$$

and

$$v = \frac{b}{\sqrt{2r\lambda}} + \frac{1}{b}\sqrt{\frac{r\lambda}{2}}. \quad (\text{D.71})$$

$C(x)$ and $S(x)$ are the standard Fresnel integrals:

$$C(x) = \int_0^x \cos\left(\frac{\pi t^2}{2}\right) dt \quad (\text{D.72})$$

and

$$S(x) = \int_0^x \sin\left(\frac{\pi t^2}{2}\right) dt. \quad (\text{D.73})$$

The derivation of this near-field pattern can be found in [254].

The axial gain is calculated as the ratio of the power density at near field to the power density at far field, multiplied by the gain at far field. This was calculated for a 10-cm square aperture with a cosinusoidal electromagnetic field distribution, as is shown in Figure D.6. The antenna used at this distribution is assumed to have this distribution. At 0.5 m, there is a 0.3 dB reduction in the gain as measured by a point source.

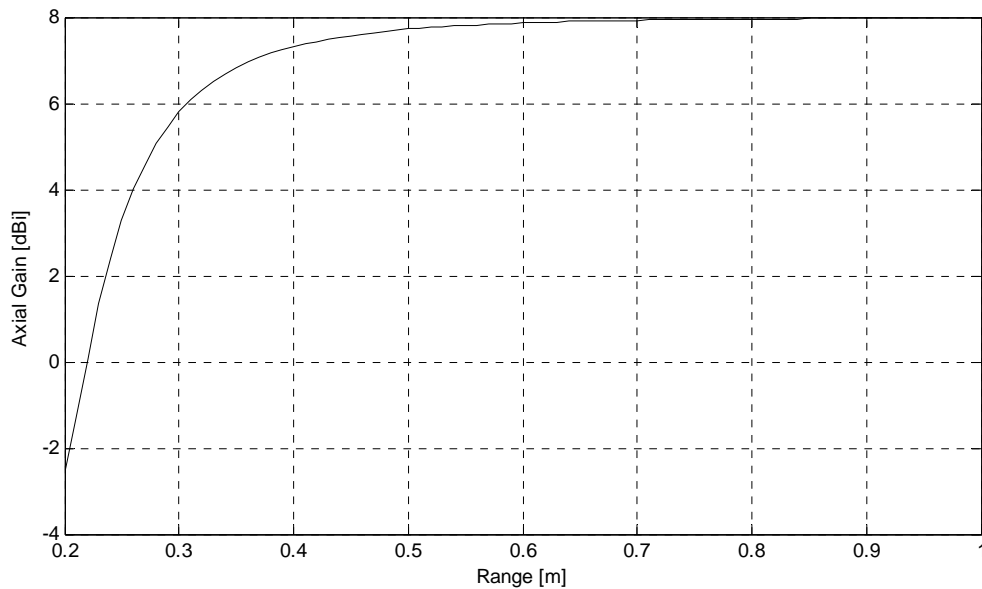


Figure D.6. Theoretical axial gain vs. range in the near-field for a 10 cm by 10 cm antenna with a cosine distribution of electric field. At 0.5 m, there is a 0.3 dB reduction in gain.

D.7 References

- [246] M. C. Budge, Jr. and M. P. Burt, "Range correlation effects on phase and amplitude noise," in *Proceedings of the IEEE Southeastcon*, 1993.
- [247] D. K. Cheng, *Field and Wave Electromagnetics*, Menlo Park, California: Addison-Wesley Publishing, 1992.
- [248] J. D. Dyson, "Measurement of near fields of antennas and scatterers," *IEEE Transactions on Antennas and Propagation*, vol. AP-21, no. 4, pp. 446-460, 1973.
- [249] *Electronic Warfare and Radar Systems Engineering Handbook*, Avionics Department of the Naval Air Warfare Center Weapons Division in 1992, document number TP 8347.
- [250] C. Gabriel and S. Gabriel: "Compilation of the Dielectric Properties of Body Tissues at RF and Microwave Frequencies", Internet document; URL: <http://www.brooks.af.mil/AFRL/HED/hedr/reports/dielectric/home.html> .

- [251] J. L. Geisheimer, E. Greneker, and W. Marshall, "A high-resolution Doppler model of human gait," *Proceedings of the SPIE: Radar Sensor Technology and Data Visualization*, vol. 4744, pp. 8-18, 2002.
- [252] G. B. Gentilli, V. Tesi, M. Linari, and M. Marsili, "A versatile microwave plethysmograph for the monitoring of physiological parameters," *IEEE Transactions on Biomedical Engineering*, vol. 49, no. 10, pp. 1204-1210, 2002.
- [253] R. C. Hansen, "Aperture theory," in *Microwave Scanning Antennas* (R. C. Hansen, Ed.), New York: Academic Press, 1964.
- [254] E. V. Jull, *Aperture Antennas and Diffraction Theory*, New York: Peter Peregrinus, 1981.
- [255] B. P. Lathi, *Modern Digital and Analog Communication Systems*, New York: Oxford University Press, 1998.
- [256] A. W. Rudge, K. Milne, A. D. Oliver, and P. Knight, *The Handbook of Antenna Design, Volume 1*, London: Peter Peregrinus, 1982.
- [257] F. V. Schultz, R. C. Burgener, and S. King, "Measurement of the radar cross section of a man," *Proceedings of the IRE*, vol. 46, pp. 476-481, 1958.
- [258] M. I. Skolnik, "An introduction to radar," in *Radar Handbook, 2nd ed.*, (M.I. Skolnik, Ed.), San Francisco: McGraw-Hill, Inc., 1990.
- [259] T. Taga, "Analysis of planar inverted-F antennas and antenna design for portable radio equipment," in *Analysis, Design, and Measurement of Small and Low-Profile Antennas* (K. Hirasawa and M. Haneishi, Eds.), Boston: Arctech House, 1992.
- [260] P. van Dorp and F. C. A. Groen, "Human walking estimation with radar," *IEEE Proceedings in Radar, Sonar, and Navigation*, vol. 150, no. 5, pp. 356-365, 2003.
- [261] R. Vaughn, J. B. Andersen, *Channels, Propagation, and Antennas for Mobile Communications*, London: Institution of Electrical Engineers, 2003.
- [262] T. Wu, "Radar cross section of arbitrarily shaped bodies of revolution," *Proceedings of the IEEE*, vol. 77, no. 5, pp. 735-740, 1989.

Appendix

E

Baseband Signal Conditioning

E.1 Introduction

Before a signal is digitized, it must be low-pass filtered to avoid having out-of-band interference alias onto the desired signal. The properties of the analog-to-digital converter (ADC) and the signal determine what other pre-processing steps are necessary. If the ADC's least-significant bit is too small to resolve the heart signal, the signal must be amplified to a level where the heart signal can be resolved. If the dc offset is sufficiently large that this level of amplification will saturate either the amplifier or the ADC, the dc offset must be removed, before or simultaneously with amplification. When the signal amplitude is significantly below the full-scale voltage of the ADC, the signal is typically amplified to near this level in order to take advantage of ADC's full resolution. When the signal's amplitude varies significantly over time and environment, a gain-controlled amplifier is typically used to fine-tune the signal's amplitude to keep it close to the full-scale voltage.

Initial measurements used Stanford Research Systems low-noise preamplifier components for the baseband filtering and amplification, but to put the entire Doppler heart and respiration measurement system in a small package, dedicated filter and amplification circuits must be used on a printed circuit board. These circuits must include amplification and anti-aliasing filtering, and dc blocking if the ADC resolution is insufficient without removing the dc. Since the system is designed to have the ADC connect to a PC running DSP software, separation of the heart and respiration rates will be performed digitally.

Also, the output of the radar circuit is differential, and conversion from differential to single-ended can happen either in the analog domain or the digital domain. If it occurs in the digital domain, fully differential filters and amplifiers must be used.

E.2 Background - Analog Signal Processing

Analog signal processing is also known as continuous signal processing: the analysis of physical processes that are continuous in time. Analog signal processing includes all the stages before the signal is sampled; this always includes anti-alias filtering, and may also include removal of dc offsets, amplification, variable gain amplification, and additional filtering stages. In Doppler heart and respiration rate measurement, additional filtering stages might include one to separate the heart and respiration signals, if that is done in analog signal processing.

E.2.1 Anti-Aliasing Filter

When a signal is sampled, it becomes periodic in frequency space, with a period equal to the sample frequency, f_s . If the sampled signal is not confined to a bandwidth less than half the sample rate, signals at higher frequencies will be folded onto lower frequency signal components; this is known as aliasing [265]. When sampling at a rate of f_s samples per second, it is impossible to distinguish between a sine wave of f Hz and one of $f + kf_s$ Hz if k is any positive or negative integer. Therefore, any signal energy located at a frequency $f + kf_s$ will be aliased to the in-band frequency f [265]. Aliasing will occur for signals at all frequencies above $f_s/2$ or below $-f_s/2$. This problem can be resolved with an analog low pass filter, with a cutoff frequency below $f_s/2$, known as an anti-aliasing filter [266]. In practice, sampling is typically performed at 2.5 to 4 times the signal bandwidth after anti-aliasing filtering. An analog anti-aliasing filter must be a low-pass filter with a cutoff frequency greater than the signal bandwidth, but less than half the sampling frequency.

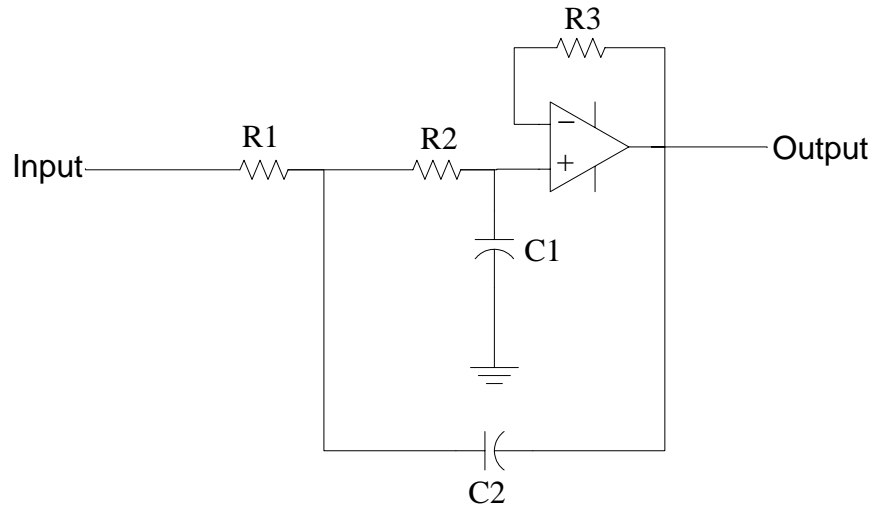


Figure E.1: Anti-aliasing Sallen-Key lowpass filter configuration.

A popular second-order active filter for anti-alias applications is the Sallen-Key filter. Passive second-order filters always have a quality factor (Q) of $1/2$, but a larger Q can be obtained if a positive feedback amplifier is included with the filter, as shown in the Sallen-Key design in Figure E.1 [263]. The filter topology can be qualitatively explained as follows. At frequencies low enough that the capacitors appear as open circuits, the signal is buffered to the output through the amplifier. At frequencies high enough that the capacitors act as short circuits, the signal is shunted to ground at the amplifier's input, so the amplifier's output is also zero. The cutoff frequency area occurs when the impedance of $C1$ and $C2$ is near that of $R1$ and $R2$. At this point, $C2$ provides positive feedback, improving the Q of the signal to provide a steeper cutoff than a passive filter would. This circuit has a linear group delay through the passband, minimizing pulse response overshoot. The cutoff frequency of the Sallen-Key filter in Figure E.1, f_c , is:

$$f_c = \frac{1}{2\pi\sqrt{R1R2C1C2}} \quad [263]. \quad (\text{E.1})$$

E.2.2 DC Blocking

In Doppler heart and respiration monitoring, if a 16-bit analog-to-digital converter to be used with the dedicated filter and amplification circuits, the dc offset needs to be

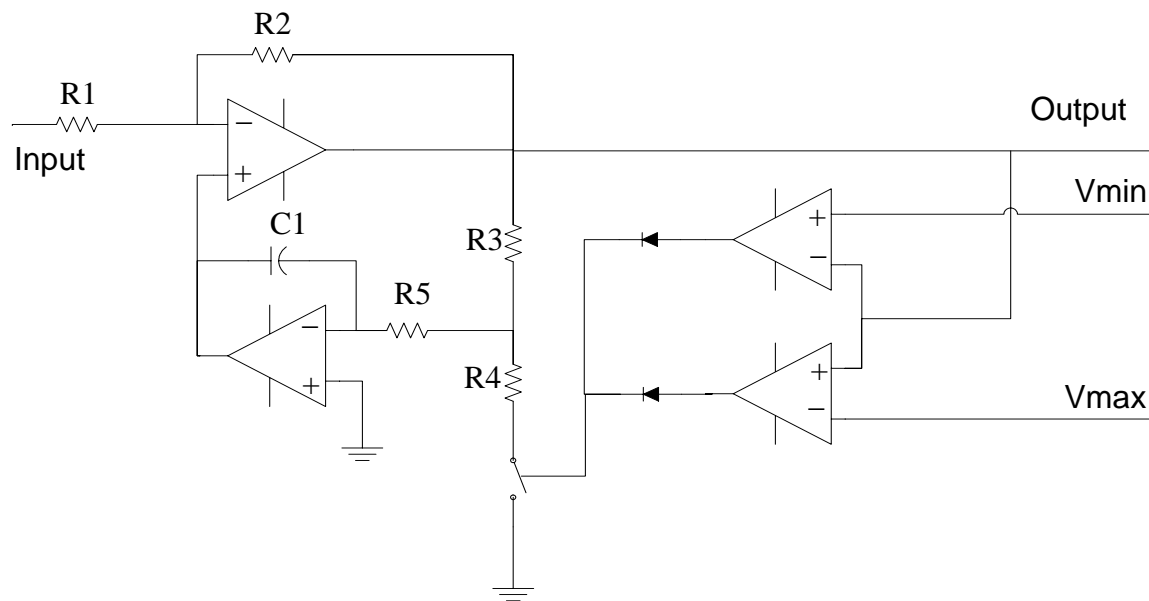


Figure E.2: DC block and amplification circuit.

removed in the analog stage so the signal can be digitized with sufficient resolution for the heart rate to be accurately detected. The dc blocking circuit needs to pass the 0.15-Hz respiration signal, and standard high-pass filter circuits designed for this specification require an extremely large capacitor and delay the signal significantly. A high-pass filter op-amp circuit recommended by R. D. Ricks that subtracts an integral of the signal to remove dc offset is shown in Figure E.2 [267]. This circuit also compares the signal with maximum and minimum reference levels to determine when the signal has too large a dc offset. When the signal is outside the boundaries, V_{\max} and V_{\min} , an analog switch is opened, shortening the time constant so the dc offset will be removed more quickly. This helps accommodate sudden changes in the dc offset, as might occur with changes in clutter or patient position in Doppler radar cardio-respiratory monitoring. When the signal returns within the boundaries, the switch closes, increasing the time constant, so the integration gives a more accurate representation of the dc offset, and does not remove as much of the respiration signal.

In Figure E.2, the resistors R1 and R2 determine the gain. The capacitor C1 and the resistors R3, R4, and R5 determine the time constants. The transfer function of this circuit when the switch is closed is:

$$\frac{V_{out}}{V_{in}} = (-G) \left[\frac{s}{s + (G + 1) \left(\frac{1}{C1 \left(R5 + R3 \left(1 + \frac{R5}{R4} \right) \right)} \right)} \right], \quad (E.2)$$

where the gain is

$$G = \frac{R2}{R1}. \quad (E.3)$$

From the transfer function, the time constant when the switch is closed can be calculated as:

$$\tau_{good} = \frac{C1 \left(R5 + R3 \left(1 + \frac{R5}{R4} \right) \right)}{(G + 1)}. \quad (E.4)$$

When the switch is open,

$$\frac{V_{out}}{V_{in}} = (-G) \left[\frac{s}{s + (G + 1) \left(\frac{1}{C1(R5 + R3)} \right)} \right] \quad (E.5)$$

and the time constant is

$$\tau_{out} = \frac{C1(R5 + R3)}{(G + 1)}. \quad (E.6)$$

For Doppler radar heart and respiration monitoring, capacitor C1 is chosen to be as large as is reasonable, based on size constraints. The two time constants, τ_{good} and τ_{out} are chosen so that when the signal is within the amplitude range, the circuit acts as a

high-pass circuit with a cutoff of 0.1 Hz, and when it is outside the amplitude range the cutoff is about 1 Hz. First the gain, the two time constants, and the capacitor value are selected. Resistor $R5$ is then calculated as:

$$R5 = \frac{\tau_{good}G}{C1}. \quad (E.7)$$

The value of resistor $R3$ can be selected to be equal to or smaller than $R5$. The resistor $R4$ is calculated as:

$$R4 = R3 \left(\frac{\tau_{out}}{\tau_{good}} \right). \quad (E.8)$$

The value of input resistor $R1$ is selected to determine the input impedance of the circuit, and the resistor $R2$ is determined based on the gain:

$$R2 = GR1. \quad (E.9)$$

E.2.3 Amplification

A typical signal is between 10 and 500 μV . To amplify this signal to the 5 V requires between 80 and 114 dB of amplification. DC offsets are typically in the 1 to 50 mV range, and if the dc offset is not removed, gain below 40 dB is required.

E.2.4 Automatic Gain Control

An automatic gain control circuit (AGC) is used to control the amplitude of a signal so it stays near the full-scale voltage of the ADC, maximizing the resolution of the signal, even as the input signal amplitude varies with time and the environment. Most AGC circuits rectify the output and integrate the rectified output to estimate amplitude, using this to control a variable gain amplifier. When the output is too large, the integrator output ramps up, decreasing the gain, and if the output is too small, the integrator output ramps down, increasing the net gain. The desired output level is set with a reference voltage. To integrate over several periods of respiration, as would be required for accurate gain con-

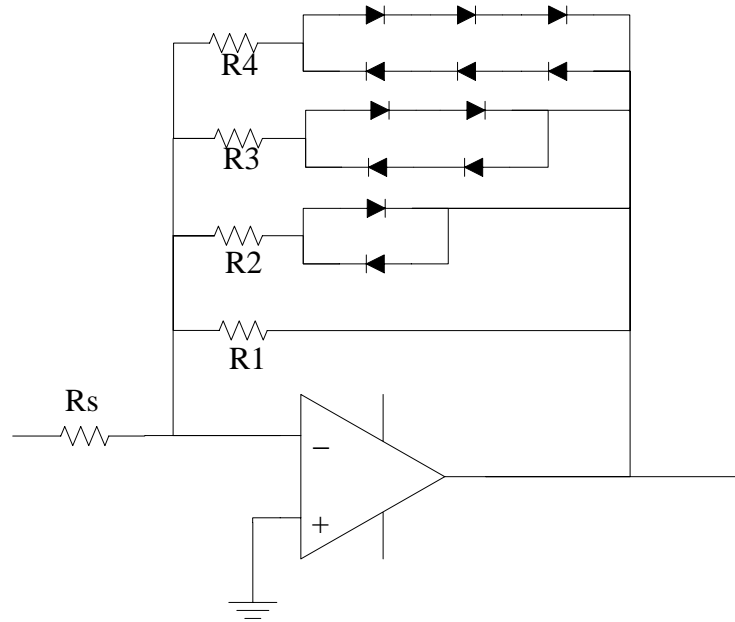


Figure E.3: Automatic gain control using diode voltage drops.

trol, an AGC designed with this topology for the Doppler monitor would require a time constant of at least 20 seconds, and therefore would need extremely large capacitors and the gain control would lag at least 10 seconds behind the amplitude.

R. D. Ricks recommended a circuit using diode voltage drops, as shown in Figure E.3 [268]. If the input signal amplitude is below one diode voltage drop, its gain is determined by one resistor, R1. If the input signal is bigger than one diode voltage drop, two resistors in parallel, R1 and R2, decrease the gain. If the signal is bigger than three diode voltage drops, three resistors, R1 - R3, in parallel further decrease the gain. The output voltage increases with the input voltage, but not linearly, and it is possible to select an input voltage at which the gain goes to zero by having a short rather than a resistor in series with the diodes. For this circuit, it is imperative that the fixed gain stage provides sufficient gain for the smallest input signals. The op-amps need to have rail-to-rail inputs and outputs and a FET input that does not have bias current compensation.

Because the heart signals are superimposed on different parts of the respiration signal, some are near the zero-crossing and others at the peak of the respiration signal. With this

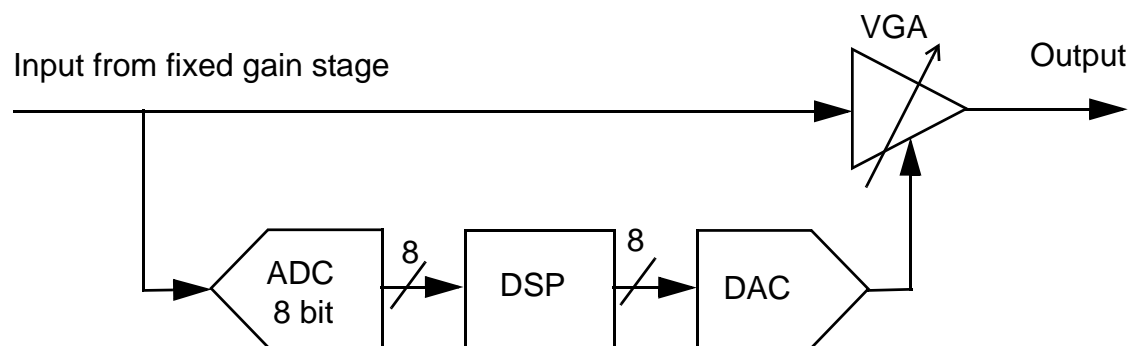


Figure E.4: An automatic gain control (AGC) circuit using an analog to digital converter (8-bit ADC) to coarsely digitize the signal, digital signal processing (DSP) to calculate the amplitude and desired gain, and a digital to analog converter (DAC) to convert the desired gain to a voltage that controls the variable-gain amplifier (VGA).

circuit, the heart beats near the zero-crossing would receive more gain than those at the peaks, so their amplitude would be modulated by the respiration signal. It would be desirable to have a circuit with a time constant greater than two respiration periods so the amplitude is averaged and the same amplification is applied to the entire period of the respiration signal. Additionally, the jumps in gain are not smooth, and this may adversely affect the output signal by adding harmonics.

A different AGC technique would be to digitize the signal with a coarse (possibly 8-bit) ADC to estimate the amplitude, then digitally calculate the desired gain value and use a digital-to-analog converter (DAC) coupled to a variable-gain amplifier to control the signal gain, as shown in Figure E.4. This approach to AGC could quickly alter the gain if it went outside of desired values, while providing flexibility in the time constant. The ADC would only need a 10 Hz sample rate to accurately digitize the respiration signal, and the number of periods over which it estimates the amplitude could vary with the respiration frequency.

A gain-control circuit was not included in the current design due to the challenges described in this section. In future designs, the digital gain-control will be implemented.

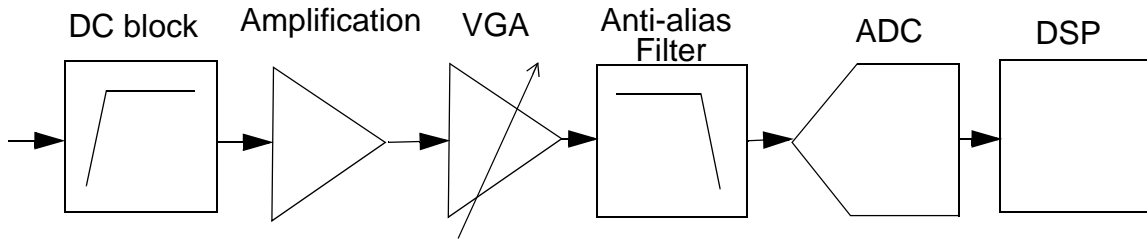


Figure E.5: Typical signal processing system. The dc portion of the signal is blocked before the fixed amplification. The variable gain amplifier (VGA) fine-tunes the amplification and the anti-alias filter removes out-of-band interference before the analog-to-digital converter (ADC) creates a digital signal for digital signal processing (DSP).

E.2.5 Combined Analog Signal Processing System

A typical signal conditioning system will first have the dc-blocking stage if it is required, because the dc offset limits the amount of amplification by saturating the amplifiers or the ADC when the gain is too great. This would be followed by fixed amplification that is placed at the beginning of the signal processing stage because the greater the signal magnitude, the less the effect of additive noise on the signal. Then the anti-aliasing filter and the gain-controlled amplifier would be added to prepare the signal for the analog-to-digital conversion. Once the signal is converted, digital signal processing appropriate for the application will be added. This signal flow is shown in Figure E.5.

E.3 Materials and Methods

E.3.1 SRS Preamplifier

The Stanford Research Systems SR560 low-noise voltage preamplifier was used in several experiments to provide dc blocking, amplification, and anti-aliasing filtering, and in some cases to separate heart and respiration signals. These boxes provide variable gain, from 1 to 50,000, can perform single-ended to differential conversion, can be ac or dc coupled, and have two configurable filters. The filters are first-order RC filters whose cutoff frequency and type (high pass or low pass) can be configured from the front panel. Filter

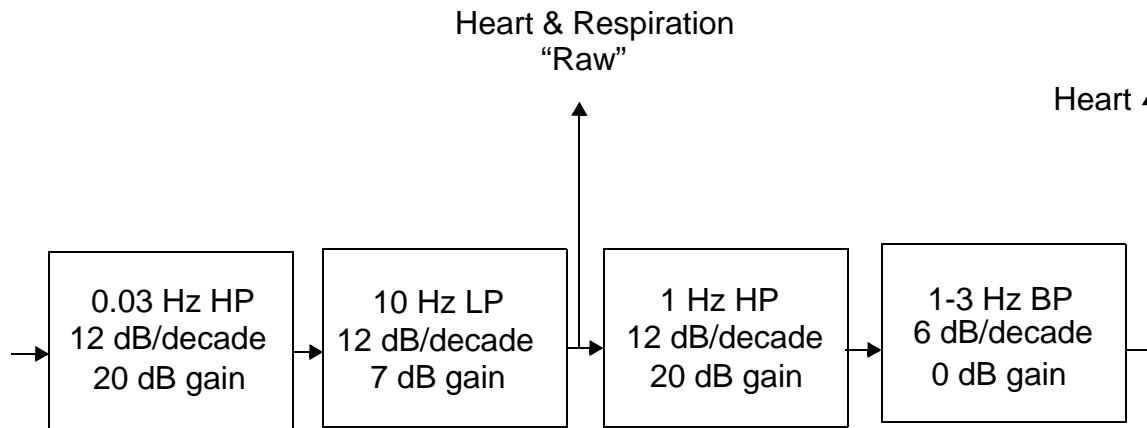


Figure E.6. Configuration of SR560 preamplifiers for single-channel measurements.

cutoff frequencies can be selected from 0.03 Hz to 1 MHz, and the filters have 6 dB/octave rolloff.

When the single-channel chips were tested, four SRS560 preamplifiers were used in the configuration shown in Figure E.6. The first was a 0.03-Hz high pass filter with a 12-dB/decade roll-off to block dc offset, with amplification of 20 dB. Then a 10-Hz low-pass filter with a 12-dB/decade roll-off was used for anti-aliasing and removal of out-of-band noise, and the signal was amplified 7 dB. The output of this signal was referred to as the “raw” signal; it contains both heart and respiration information. Two more SRS560 preamplifiers were used to isolate the heart signal. The signal went through a 1-Hz high pass filter with a 12-dB/decade roll off with 20-dB amplification followed by a 1-to-3-Hz band pass filter with 6-dB/decade roll-off.

When the quadrature transceiver was used with the SRS filter boxes, the heart signal was separated with digital filters rather than analog filters, and two SRS560 preamplifiers were used to prepare the raw signal by dc blocking, amplifying, and antialias filtering the signal. The first had a 0.1-Hz highpass filter with 12-dB/decade roll-off and 20-dB gain. The second was a 10 Hz lowpass filter with 13 dB gain. This configuration is illustrated in Figure E.7.



Figure E.7. Configuration of SR560 preamplifiers for quadrature measurements.

E.3.2 Custom Baseband Signal Conditioning Board

E.3.2.1 Anti-Aliasing Filter

The antialiasing filter was designed as a unity-gain Sallen-Key, low-pass linear-phase filter with a 20-Hz cutoff unity passband gain, as shown in Figure E.1 [263]. With the design values given in Table E.1, the theoretical cutoff frequency calculated with (E.1) is 22.5 Hz. The op-amps were Burr-Brown OPA4132 op-amps.

Table E.1: Actual Values Used in Sallen-Key Anti-Aliasing Filter, as in Figure E.1.

Component	Value
R1	500 k Ω
R2	500 k Ω
R3	20 k Ω
C1	10 nF
C2	20 nF

E.3.2.2 DC Blocking and Amplification Circuit

The dc blocking and amplification circuit discussed in Section E.2.2 was used in the dedicated analog signal processing circuitry. The final values used in this design are shown in Table E.2, with component names as shown in Figure E.2. The FET-input op-amp used was OPA4132; the comparator used was the Maxim MAX921.

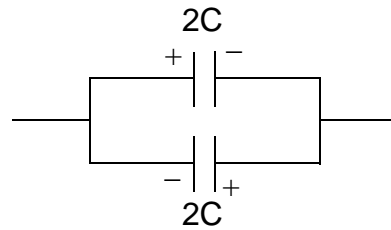


Figure E.8. Configuration of two polarized capacitors to equal one non-polarized capacitor [264].

Table E.2: Component Values for DC Block and Amplification Stage Shown in Figure E.2.

Component	Value - 40 dB gain	Value - 74 dB gain
R1	1 k Ω	1 k Ω
R2	100 k Ω	5.1 M Ω
R3	100 k Ω	2.499 M Ω
R4	20 k Ω	250 k Ω
R5	100 k Ω	5.1 M Ω
C1	100 μ F	100 μ F
τ_{out}	0.20 s	0.15 s
τ_{good}	0.70 s	1.15 s
G	100	5100

Initially the dc block circuit was designed only using non-polarized capacitors. However, Kovacs [264] suggested that using an electrolytic capacitor in this circuit is acceptable provided voltages across the capacitor remain below 700mV. If voltages are higher, electrolytic capacitors can be used in the configuration shown in Figure E.8. Using an electrolytic capacitor makes it possible to have a larger gain on the first stage, which makes the analog signal processing section more robust against noise.

E.3.2.3 Differential-to-Single-Ended Conversion

Differential-to-single ended conversion was achieved with the Burr Brown INA105 precision unity gain differential amplifier. This amplifier has common-mode rejection of

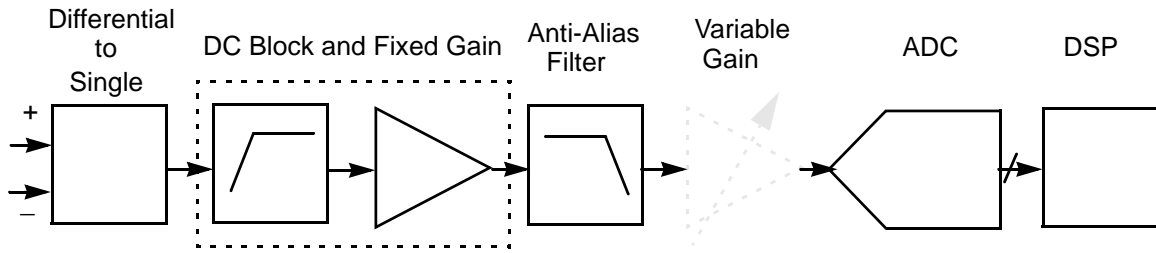


Figure E.9. The overall signal conditioning configuration includes differential-to-single-ended conversion, followed by the dc block and fixed-gain stage, followed by the anti-aliasing filter and sometimes a variable gain stage. After signal conditioning, the signal is digitized with an analog-to-digital converter (ADC) and further processed with digital signal processing (DSP).

100 dB below 1 kHz. Differential-to-single ended conversion was performed before the dc-blocking and gain stage because dc blocking requires the signal to be referenced to ground in a single-ended configuration.

E.3.2.4 Combined Configuration

Differential-to-single-ended conversion is performed before the dc blocking since the dc blocking circuit does not have a differential input. The dc blocking is performed simultaneously with the fixed gain so the dc offset does not limit the amount of gain. This stage is followed by the anti-alias filter, and, if included, the gain-control circuit. This conditioned signal is digitized and processed with digital signal processing, as shown in Figure E.9.

E.4 Results

E.4.1 Anti-aliasing Filtering

The simulated and actual frequency responses of the Sallen-Key anti-aliasing filter described in Section E.3.2.1 are shown in Figure E.10. The simulated cutoff frequency is 22.5 Hz, and the actual cutoff frequency was 21 Hz. This cutoff is sufficient for anti-aliasing for any sampling frequency above 50 Hz.

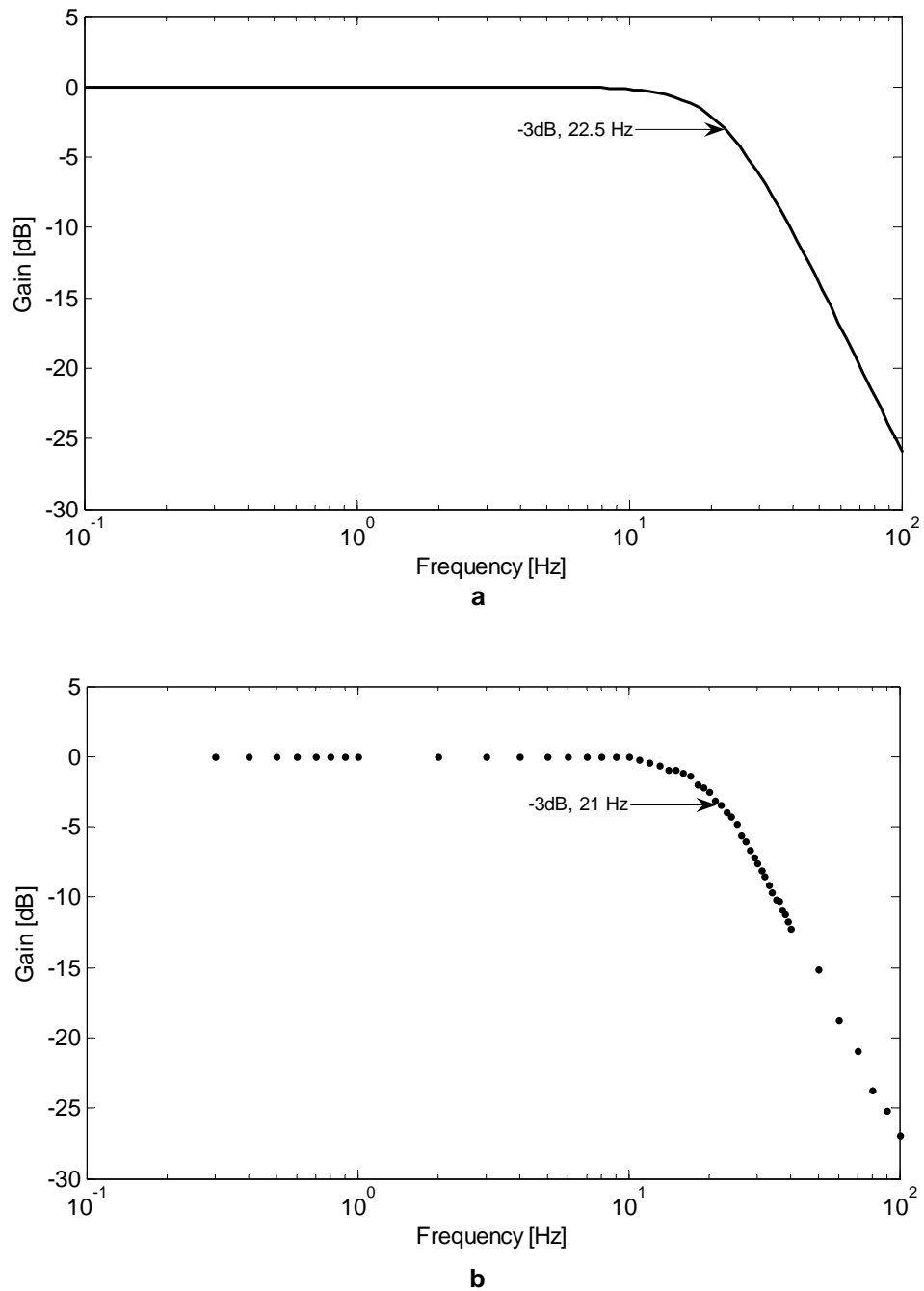


Figure E.10. Simulated (a) and actual (b) frequency response of the Sallen-Key antialiasing filter of Figure E.1 with the values given in Table E.1.

E.4.2 DC Blocking and Amplification

The dc blocking and amplification circuit discussed in Section E.3.2.2 The simulated frequency response is shown in Figure E.11. The dc-block cutoff frequency is 0.23 Hz when the switch is closed, and is 0.82-Hz when the switch is opened. The gain is 40 dB.

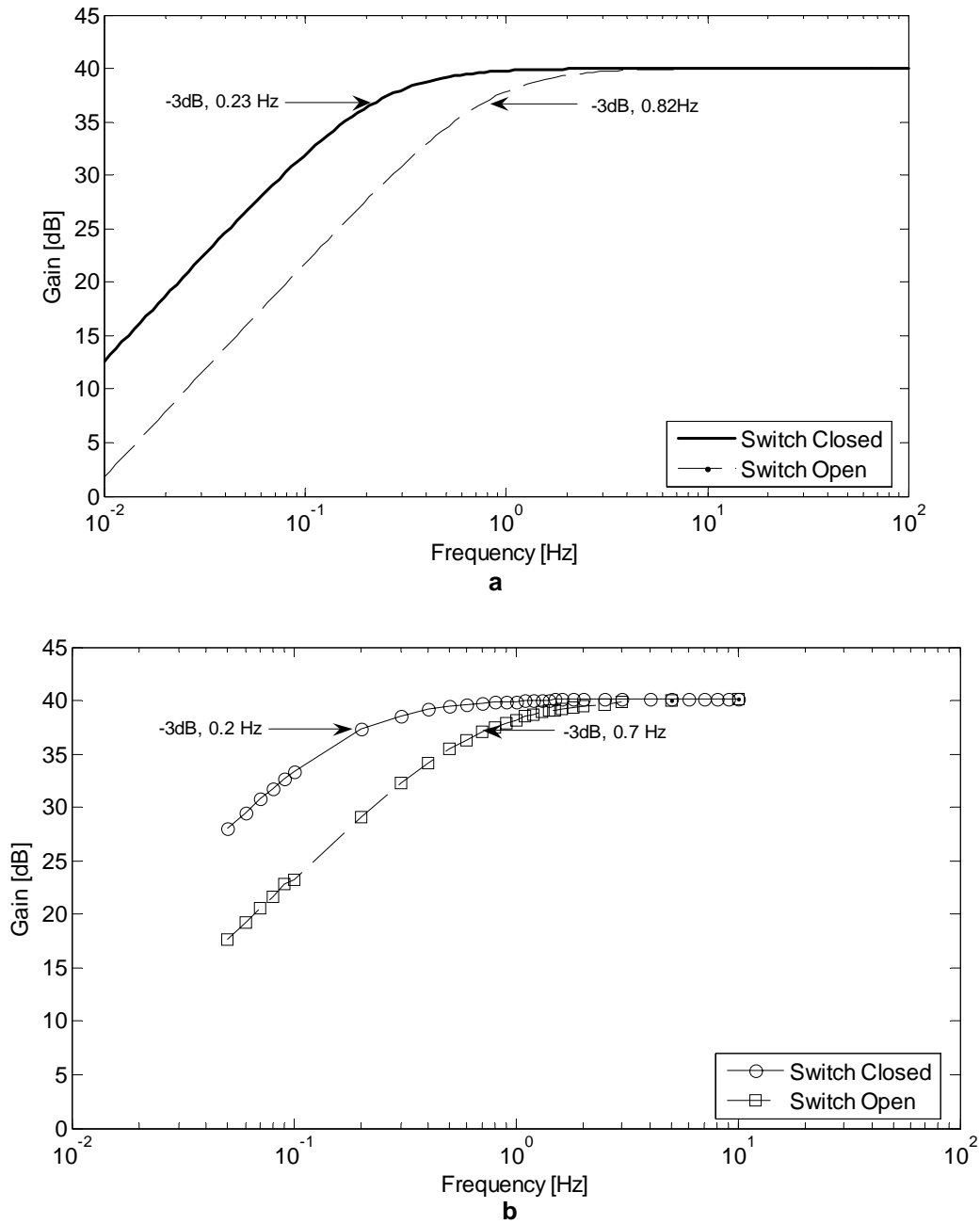


Figure E.11. Simulated (a) and measured (b) frequency response of the dc block and 40 dB amplification circuit.

E.5 Conclusions

It is desirable to minimize analog stages, because noise can be added until the point at which the signal is digitized. However, an analog anti-aliasing filter is required before digitization of the signal, and amplification of the signal to near the analog-to-digital converter's full scale voltage is required to utilize its full resolution. If dc offsets are large compared to the signal, either the resolution of the ADC must be sufficiently high to include the offset, or the dc offset must be removed. This system uses dc blocking, amplification, and anti-aliasing filtering to condition the signal prior to digitizing the signal with a 16-bit ADC. In a future iteration, an automatic gain control stage may be added to keep the amplification closer to the full-scale voltage as it varies over time.

The SRS filter boxes were used in initial measurements. Although the configuration of these boxes is easy to change, the boxes are too large to be used in field applications, so the custom printed-circuit board is used instead. The baseband board passes frequencies between 0.2 Hz and 21 Hz, or 0.7 Hz and 21 Hz if the signal is outside ± 1 V. The high-pass filter for dc-blocking removes at least half of the fundamental of the respiration signal of subjects with respiration rates that are at 12 Hz or below, and at least 20% of the fundamental of the respiration signal of subjects with respiration rates at 24 Hz, which included all of the subjects in the human subjects study. In future designs, it would be desirable to move the cutoff frequency to 0.015 Hz or below to avoid cutting off any of the respiration signal. It may also be possible in future versions of this device to use a 24-bit ADC and avoid removing the dc offset in analog signal processing. This would avoid the problem of cutting out the respiration fundamental altogether.

E.6 References

- [263] J. Karki, "Analysis of the Sallen-Key architecture," Texas Instruments, Application Report SLOA024B, September 2002.
- [264] G. T. A. Kovacs (private communication), 2004.

- [265] R. G. Lyons, Understanding Digital Signal Processing, Upper Saddle River, NJ: Prentice Hall PTR, 2001.
- [266] A. V. Oppenheim and R. W. Schaffer, Discrete Time Signal Processing, Englewood Cliffs, New Jersey: Prentice Hall, 1989.
- [267] R. D. Ricks (private communication), 2003.
- [268] R. D. Ricks (private communication), 2004.

Appendix

F

Low-IF Architecture

F.1 Low-IF Architecture for Doppler Radar Cardiopulmonary Monitoring

In Chapter 2, heterodyne and direct-conversion architectures for Doppler radar cardiopulmonary monitoring were explored. Another option is a low-intermediate-frequency (low-IF) architecture, a type of heterodyne architecture with an IF that is low enough to be digitized. When the signal is digitized at an IF, dc offsets and low frequency noise can easily be removed before digitization without any loss of information. However, when operating at typical IF frequencies in the MHz range, filters typically need to be discrete because of the large passive values they require. The filters can be avoided if quadrature downconversion paths are used in a heterodyne receiver, since all of the required information to separate the desired signal from interfering signals is present at the IF stage [272]. This architecture alleviates the dc offset problem, although it requires a higher-performance ADC than the direct-conversion architecture, and very good phase and amplitude balance are required to eliminate the interfering signals.

For a fully integrated Doppler radar cardiorespiratory monitoring system, it is important to use the same oscillator for both transmit and receive so that the residual phase noise is reduced sufficiently to be below the signal level by the range correlation effect. Therefore, the LO would have to be generated from the same noisy oscillator as the transmitted source mixed with a very stable oscillator at the intermediate frequency. The stable low-frequency signal could be generated digitally and converted to an analog signal to have very good precision, and two quadrature signals could be generated to ensure good phase and amplitude balance. When these signals are mixed, a mixing scheme similar to

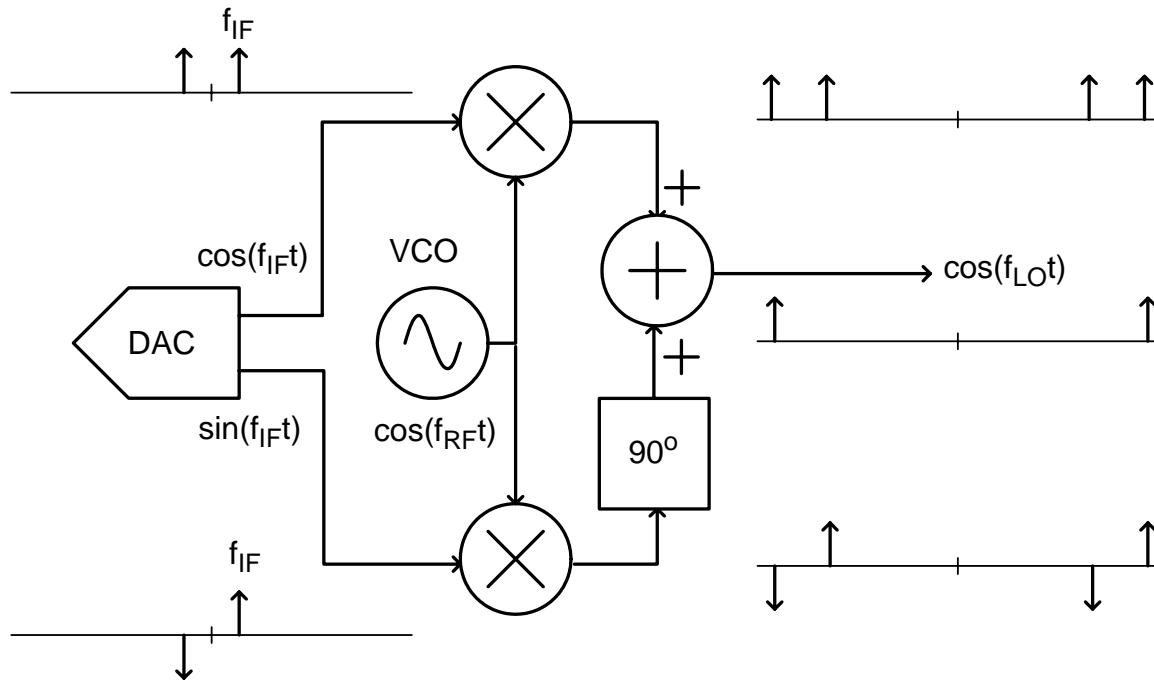


Figure F.1. Block diagram of the creation of the LO for a low-IF receiver for a next-generation Doppler radar cardiorespiratory monitoring system. The LO is the sum of the RF and IF frequencies.

an image-rejection architecture must be used to eliminate the sum of the RF and IF and keep only the difference for the LO. The block diagram of the LO creation circuit is shown in Figure F.1. The sine and cosine signals at the IF frequency are created digitally and converted to analog signals with a digital-to-analog converter (DAC). These signals are mixed with the RF signal from the VCO which is also the source for the transmitted signal. The RF signal mixed with the sine at the IF frequency undergoes a 90° phase shift to invert the negative frequency space, and then the two channels are summed to give a cosine at the LO frequency, the sum of the RF and IF frequencies.

The RF demodulation circuitry would be similar to that of the direct-conversion quadrature receivers used in this work, but the LO would be that created from the VCO signal and the IF signal rather than just the VCO signal. The general receiver architecture is shown in Figure F.2. The RF signal is split for the two receiver chains, with no phase difference. The LO is also split into two receiver chains, 90 degrees out of phase. After the RF and LO signals are mixed, the dc offset is removed from each receiver chain with a

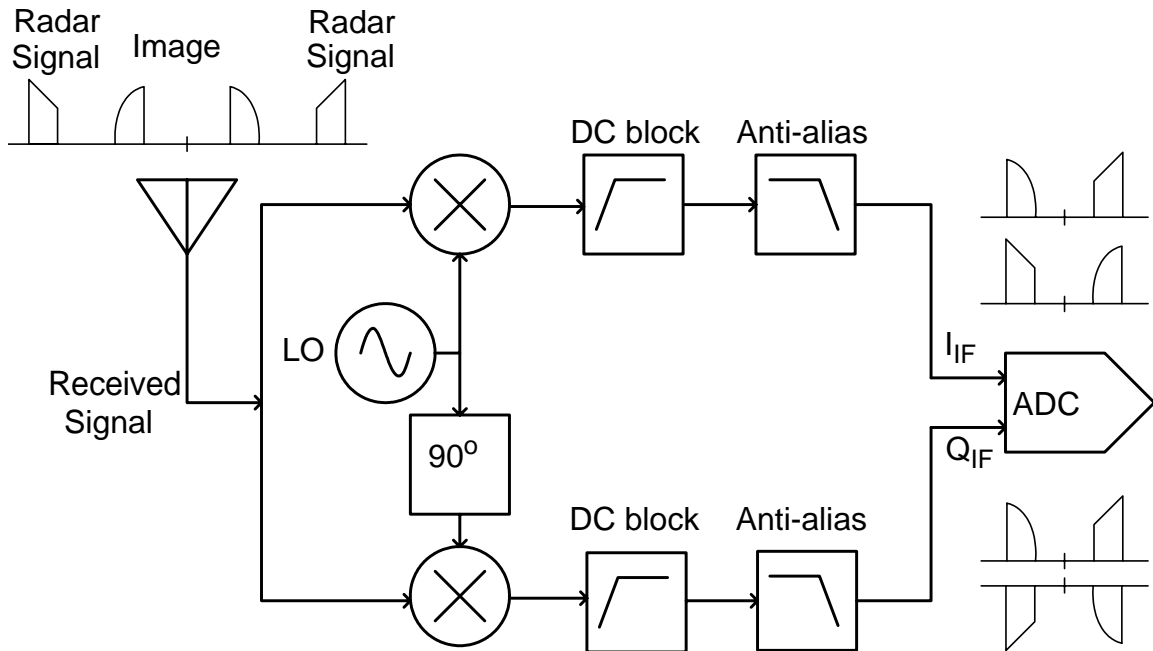


Figure F.2. Low-IF receiver architecture.

highpass filter and the signal is lowpass filtered for antialias filtering. Then the signals are digitized with the ADC.

The signal would be digitized at the intermediate frequency. The signal at the image frequency will still be present in the information, but it can be eliminated in digital processing to leave the I and Q signals, as shown in Figure F.3. The I and Q signals can then be combined using any of the schemes discussed in Chapter 7. It is possible that direct phase demodulation with the arctangent technique will be more effective with this receiver architecture since the dc offsets due to self-mixing and offsets can be removed without any loss of the signal. DC offsets due to the clutter will still be present after the signal is down-converted in DSP, however.

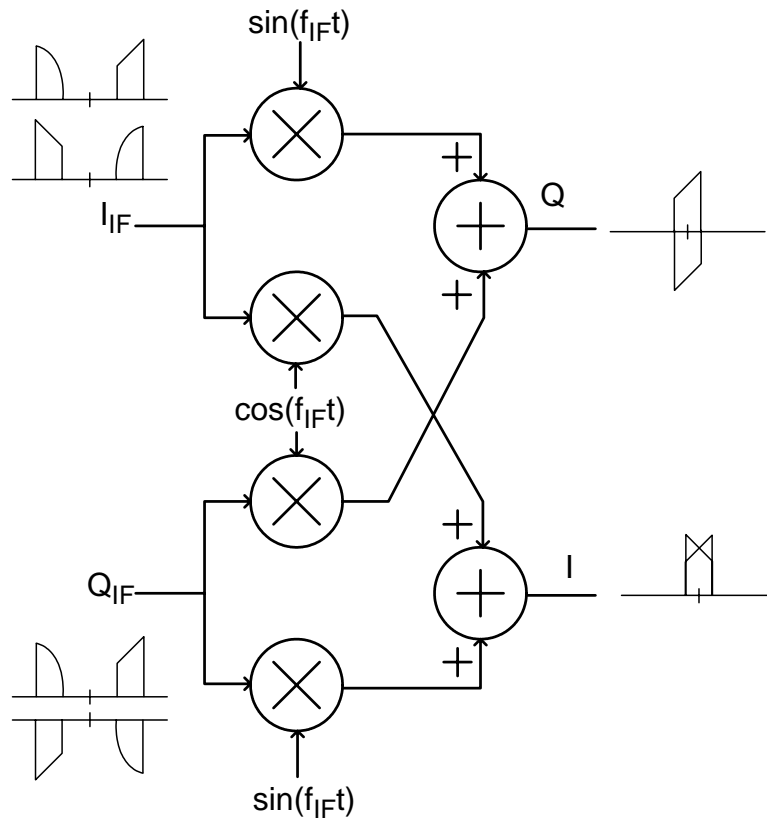


Figure F.3. Digital signal processing for low-IF architecture to give baseband I and Q signals.

With the direct-conversion receiver that is currently used, removing dc offsets also removes some information from the signal, and the signal can be affected by baseband $1/f$ noise. The baseband circuits that remove dc without cutting out too much of the respiration signal (as low as 0.08 Hz) require large capacitors and therefore can not be fully integrated on chip. Additionally, an automatic gain control with a time constant long enough that it is not affected by changes at the respiration rate requires such a long time constant that it would take at least 30 seconds to respond to a change in the amplitude, and therefore also would require large capacitors and not be possible to integrate on-chip. With a low-IF architecture, the cutoff for the dc-blocking filter would not need to be so steep, so that a smaller capacitor could be used and the time constant for the AGC could be much less than a second, improving response time and allowing smaller passives to be used. The signal conditioning could then be integrated on the same chip as the radar transceiver.

Additionally, removing dc would not remove any information, and there is more flexibility in the signal processing.

Potential problems with using the low-IF architecture are the requirements for very low phase and amplitude imbalance, and the risk in decreasing the range correlation effect by mixing to an IF rather than to baseband. The phase and amplitude balance in both the stages that create the LO and that downconvert the received RF signal need to be very good to completely eliminate the undesired signals. It may be necessary to use adaptive techniques to ensure gain and phase balance [270, 271, 273]. Since the signal that is mixed with the VCO signal to create the LO is created digitally, it should have very low phase noise, and therefore it should not significantly increase the residual phase noise at baseband.

The low-IF receiver could be a good option for the Doppler radar transceiver, as it solves several of the problems with the direct-conversion system. However, creating the LO from the VCO signal as described in this appendix would require two additional mixers, increasing the die size. The effects of using this architecture on the level of residual phase noise also need to be explored, and a reliable technique for ensuring good phase and amplitude balance needs to be researched. Once these issues are addressed, it should be clear whether a low-IF architecture is the right choice for Doppler radar cardiorespiratory monitoring.

F.2 References

- [269] J. Crols and M. S. J. Steyaert, "Low-IF topologies for high-performance analog front ends of fully integrated receivers," *IEEE Transactions on Circuits and Systems - II: Analog and Digital Signal Processing*, vol. 45, no. 3, pp. 269-282, 1998.
- [270] I. Elahi, K. Muhammad, and P. T. Balsara, "I/Q mismatch compensation using adaptive decorrelation in a low-IF receiver in 90-nm CMOS process," *IEEE Journal of Solid State Circuits*, vol. 41, no. 2, pp. 395-494, 2006.

- [271] A. Lohtia, P. A. Goud, and C. G. Englefield, "An adaptive digital technique for compensating for analog quadrature modulator/demodulator impairments," in *Proceedings of the IEEE Pacific Rim Conference on Communications, Computers, and Signal Processing*, 1993, pp. 447-450.
- [272] S. Mirabbasi and K. Martin, "Classical and modern receiver architectures," *IEEE Communications Magazine*, pp. 132-139, 2000.
- [273] L. Yu and W. M. Snelgrove, "A novel adaptive mismatch cancellation system for quadrature IF radio receivers," *IEEE Transactions on Circuits and Systems - II: Analog and Digital Signal Processing*, vol. 46, no. 6, pp. 789-801, 1999.

Appendix

G

Quantitative Measurements of Chest Wall Motion

G.1 Quantitative Measurements of Chest Wall Motion Due to Heartbeat

Table G.1: Quantitative Measurements of Chest Wall Motion Due to Heartbeat. All subjects are healthy unless otherwise specified.

Reference	Measurement Method	Subject(s)	Measurement Location	Position	Displacement [mm]
Aubert, et al [274]	Infrared Laser Displacement	N=5 21-40 year old males	Apex	lying in left lateral decubitus	0.6 ± 0.2
Berson and Pipberger, 1966 [275]	3-D Lamp-Photopotentiometer	N=3 male age 30-40	Apex	not specified	0.37 ± 0.41
Brandt, et al. [276]	Moiré Structured Lights	N=1 Young, healthy gender unspecified	Apex	left lateral supine position	1.7
Deliyannis, et al. [277]	Impulse Cardiogram	N=1 gender unspecified	Apex (PMI)	propped up in bed at an angle of about 45°	10
Gillam, et al. [278]	Impulse Cardiogram	N=20 14 males 6 females age 5 to 52 years	Left Parasternal Area, PMI	lying on a couch in a semi-recumbent position	3.6 (mean)

Table G.1: Quantitative Measurements of Chest Wall Motion Due to Heartbeat. All subjects are healthy unless otherwise specified.

Reference	Measurement Method	Subject(s)	Measurement Location	Position	Displacement [mm]
Ikegaya, et al. [279]	Calibrated Phonocardiographic Microphone	N=1 contact mass 100g	Apex	supine	0.05
		N=1 contact mass 200g	Apex	supine	0.08
Mohri, et al. [280]	Magnetic Displacement Sensor	N=1 22 year old male	Apex	not specified	0.21
Mohri, et al. [281]	Magnetic Displacement Sensor	N=1 22 year old male	Apex	not specified	0.035
		N=1 Overweight 22 year old male	Apex	not specified	0.012
Ramachandran and Singh [282]	Laser Speckle Interferometry	N=10 Varying build	Apex QRS		0.568 ± 0.11
			Apex P		0.372 ± 0.07
			Apex T		0.411 ± 0.04
		N=1 Cardiac Patient	Apex QRS		0.320
		N=10 Varying build	Aortic QRS		0.453 ± 0.11
			Aortic P		0.345 ± 0.8
			Aortic T		0.474 ± 0.08
			Right Ventricular QRS		0.423 ± 0.08
			Right Ventricular P		0.453 ± 0.07
			Right Ventricular T		0.418 ± 0.04

Table G.1: Quantitative Measurements of Chest Wall Motion Due to Heartbeat. All subjects are healthy unless otherwise specified.

Reference	Measurement Method	Subject(s)	Measurement Location	Position	Displacement [mm]
Ramachandran et al. [283]	Capacitance Transducer	N=5	Apex QRS	supine	0
			Apex P		0.005
			Apex T		0.04
			Aortic QRS		0.01
			Aortic P		0.005
			Aortic T		0.03
			Right Ventricular QRS		0.005
			Right Ventricular P		0
			Right Ventricular T		0
Ronaszeki et al. [284]	Linear Laser Displacement	N=1	Apex		1.2
Singh and Ramachandran [285]	Laser Speckle Interferometry (In Plane)	N=1 male	Apex QRS		0.09
			Apex P		0.05
			Apex T		0.07
			Aortic QRS		0.05
			Aortic P		0.04
			Aortic T		0.05
			Right Ventricular QRS		0.07
			Right Ventricular P		0.05
			Right Ventricular T		0.02

G.2 References

- [274] A. E. Aubert, L. Welkenhuysen, J. Montald, L. de Wolf, H. Geivers, J. Minten, H. Kesteloot, and H. Geest, "Laser method for recording displacement of the heart and chest wall," *Journal of Biomedical Engineering*, vol. 6, no. 2, pp. 134-140, 1984.
- [275] A. S. Berson and H. V. Pipberger, "Measurement of chest wall vibrations due to the activity of the heart," *Journal of Applied Physiology*, vol. 21, no. 2, pp. 370-374, 1966.
- [276] C. M. Brandt, H. Annoni, J. Harthong, J. M. Reiner, and R. Krauskhopff, "Evaluation of chest wall distortion related to cardiac activity by structured lights: A study of the apical impulse by the Moiré technique," *Acta Cardiologica*, vol. 41, no. 3, pp. 207-213, 1986.
- [277] A. A. Deliyannis, P. M. S. Gillam, J. P. D. Mounsey, and R. E. Steiner, "The cardiac impulse and the motion of the heart," *British Heart Journal*, vol. 26, pp. 396-411, 1964.
- [278] P. M. S. Gillam, A. A. Deliyannis, and J. P. D. Mounsey, "The left parasternal impulse," *British Heart Journal*, vol. 26, pp. 726-736, 1964.
- [279] K. Ikegaya, N. Suzumura, and T. Funada, "Absolute calibration of phonocardiographic microphones and measurements of chest wall vibration," *Medical and Biological Engineering and Computing*, vol. 9, no. 6, pp. 683-692, 1971.
- [280] K. Mohri, T. Jinnouchi, and K. Kawano, "Accurate mechanocardiogram sensors using amorphous star-shaped core multivibrator combined with a magnet," *IEEE Transactions on Magnetism*, vol. MAG-23, no.5, pp. 2212-2214, 1987.
- [281] K. Mohri, T. Kondo, H. Sugino, J. Yamasaki, and K. Yoshino, "Non-contact linear displacement sensors using amorphous-core multivibrators for mechanocardiography," *IEEE Transactions on Magnetism*, vol. MAG-21, no. 5, pp. 2071-2073, 1985.
- [282] G. Ramachandran and M. Singh, "Three-dimensional reconstruction of cardiac displacement patterns on the chest wall during the P, QRS, and T-segments of the ECG by laser speckle interferometry," *Medical and Biological Engineering and Computing*, vol. 27, no. 5, pp. 525-530, 1989.

- [283] G. Ramachandran, S. Swarnamani, and M. Singh, "Reconstruction of out-of-plane cardiac displacement patterns as observed on the chest wall during various phases of ECG by capacitance transducer," *IEEE Transactions on Biomedical Engineering*, vol. 38, no. 4, pp. 383-385, 1991.
- [284] A. Ronaszeki, A. E. Aubert, and H. de Geest, "Laser apexcardiogram in healthy young men: a comparative study with the conventional method," *Acta Cardiologica*, vol. 45, no. 3, pp. 203-210, 1990.
- [285] M. Singh and G. Ramachandran, "Reconstruction of sequential cardiac in-plane displacement patterns on the chest wall by laser speckle interferometry," *IEEE Transactions on Biomedical Engineering*, vol. 38, no. 5, pp. 483-489, 1991.

Appendix
H

Oscillator Phase Noise Theory

H.1 Introduction to Phase Noise

The ideal oscillator for a CW radar would be a perfect sinusoid, with amplitude A and frequency f , so that the signal, $s(t)$ is:

$$s(t) = A \sin(2\pi ft) . \quad (\text{H.1})$$

However, all real oscillators have noise, in both phase and amplitude, which makes the signal:

$$s(t) = (A + a(t)) \sin(2\pi ft + \phi(t)) , \quad (\text{H.2})$$

where $a(t)$ is the amplitude noise and $\phi(t)$ is the phase noise. The amplitude noise does not affect the signal at its zero crossing, and the phase noise does not affect the amplitude at the peaks. Since all practical oscillators have some type of amplitude limiting [286], the amplitude noise from the oscillator is usually negligible compared to the phase noise so that the signal is effectively:

$$s(t) = A \sin(2\pi ft + \phi(t)) . \quad (\text{H.3})$$

Frequency stability is the degree to which an oscillator produces the same frequency over time. All real sources have some variability in frequency. Fluctuations in frequency are due to spurious and phase noise. Spurious noise is caused by signals that modulate the signal frequency, and these appear as discrete components in spectral density plots. Phase noise is random, caused by thermal noise, shot noise, and flicker noise. A sample spectral

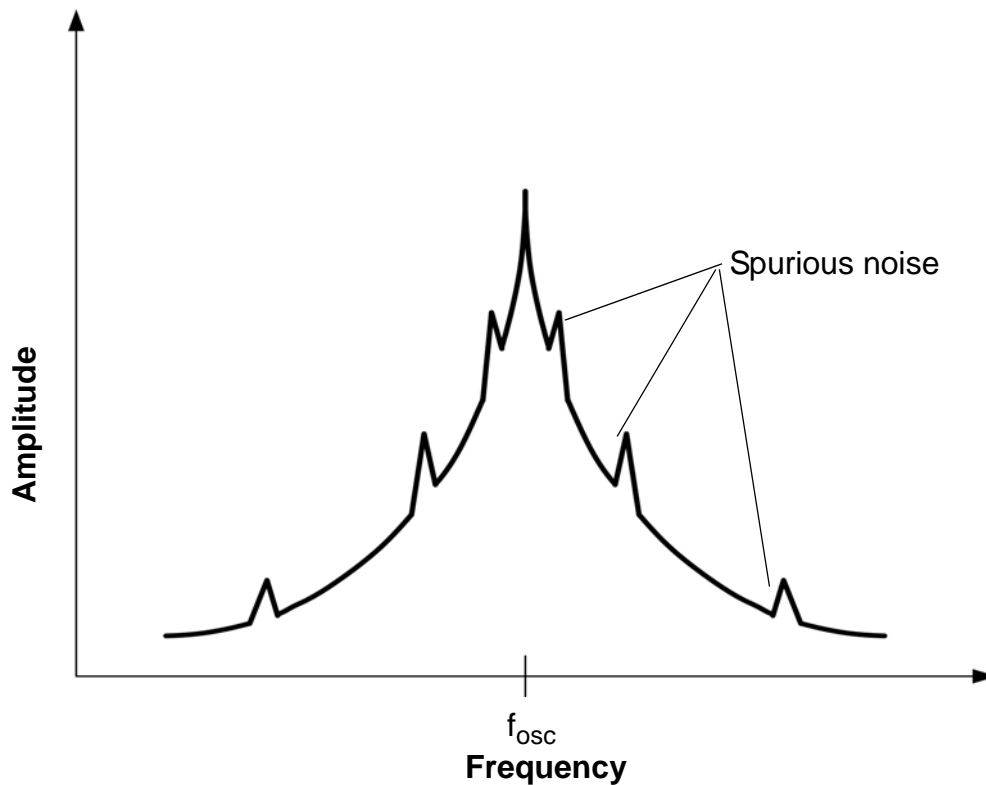


Figure H.1. RF sideband spectrum, including phase noise and spurious noise. The phase noise spectrum is symmetrical about the oscillation frequency, indicating that phase noise, and not amplitude noise, is dominant in this oscillator. The peaks in the spectrum are spurious noise, indicating modulation by other signals.

density plot is shown in Figure H.1. The ideal oscillator's spectrum would be a delta function at f_{osc} .

The signals in equations (H.1) and (H.3) are compared in the time domain in Figure H.2. In this figure, gaussian white noise with zero mean and a variance of 0.0625 was added to the phase of a 1-Hz sinusoid. Note that although the zero-crossings change, the amplitude of the signal does not vary.

All methods to quantify phase noise measure frequency or phase deviation of the source in either the frequency or the time domain. The most common measurement is spectral density of phase fluctuations per Hertz, $S_{\phi}(f_o)$. This describes the energy distribution as a continuous function in units of radian variance per unit bandwidth:

$$S_{\phi}(f_o) = \frac{\Delta\phi_{RMS}^2}{\text{bandwidth used to measure phase deviation}} = \frac{\text{rad}^2}{\text{Hz}} \quad (\text{H.4})$$

The spectral density is either given in units of $\frac{\text{radians}^2}{\text{Hz}}$ or in dB relative to 1 $\frac{\text{radian}^2}{\text{Hz}}$.

Another common measure of phase noise is the single sideband spectrum. This is the ratio of the power at an offset of f_o Hz from the carrier to the signal power, a measurement of the noise energy. As shown in Figure H.3, oscillator single sideband phase noise, $L_{\phi}(f_o)$, is defined as the ratio of the power in a 1-Hz bandwidth at an offset frequency f_o from the carrier frequency to the total carrier power.

$$L(f_o) = 10\log\left(\frac{\text{power density (in one sideband)}}{\text{total signal power}}\right) = 10\log\left(\frac{P_{ssb}}{P_s}\right) \quad (\text{H.5})$$

It is usually expressed in the units dBc/Hz (decibels below the carrier per Hertz) at a specific offset. Often round numbers such as 1 kHz, 10 kHz, or 1 MHz are used for the offset, with the actual number depending on what offset frequency is relevant for the application. However, when another frequency is important for the application, the specific frequency will be used; for example, the DCS1800 cellular basestation specification is given at 600 kHz.

(H.6)

When the total phase deviation is much less than a radian so that the small angle approximation applies, the relationship between the spectral density of phase fluctuations and the single-sideband phase noise is:

$$S_{\phi}(f_o) = 2L_{\phi}(f_o) \quad (\text{H.7})$$

However, at small offset frequencies on free-running noisy oscillators, the phase deviation can be near to or greater than a radian, and then this relation does not apply. In this case, the single sideband phase noise flattens, while the phase fluctuation spectral density can increase to over 0 dB/Hz. Phase noise over 0 dBc/Hz in noisy oscillators expresses that the carrier frequency is wandering over a frequency range, and the spectrum should flatten out when the small angle approximation no longer applies, indicating a wide spectral line due

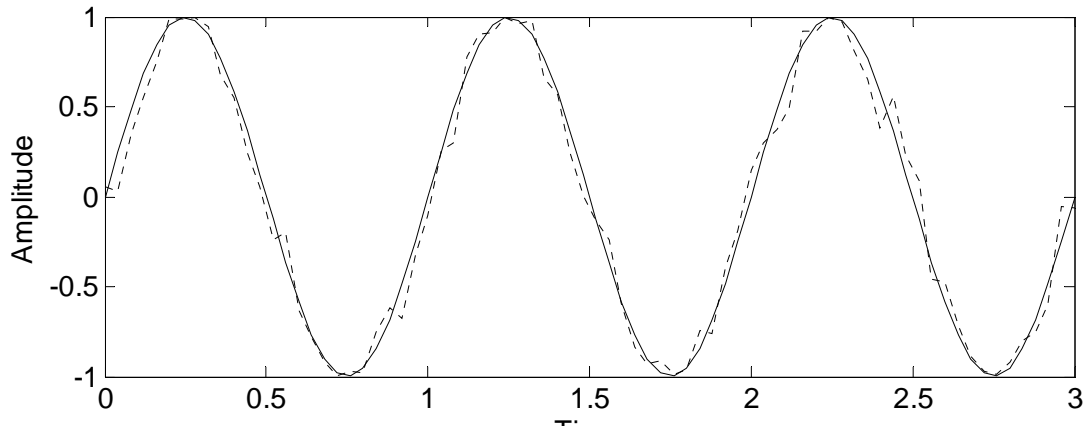


Figure H.2. Exaggerated depiction of phase noise in the time domain. The solid line is the perfect sinusoid in Equation H.1 and the dotted line is the sinusoid with phase noise in (H.3).

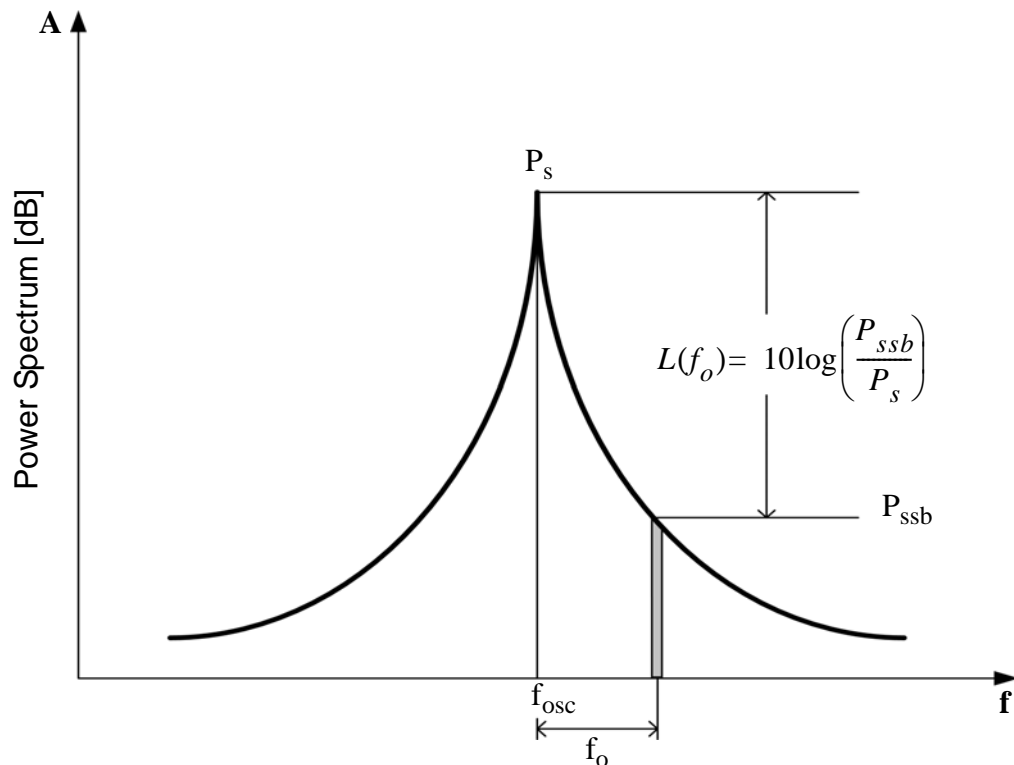


Figure H.3. Measurement of single-sideband phase noise, $L(f)$.

to frequency variation of the carrier. It is not correct to have a single-sideband phase noise value greater than 0 dBc/Hz, since the noise cannot be greater than the carrier. The carrier can be considered to have wider bandwidth.

The variation in the zero crossings is also sometimes referred to as jitter. Jitter is usually defined looking in the time domain at timing accuracy, while phase noise involves looking at the noise spectrum in the frequency domain

H.2 Sources of Oscillator Phase Noise

The noise-to-phase transfer function is linear and time-varying. The transfer function is linear because the oscillator phase disturbance is proportional to the resonator's amplitude disturbance. The time-varying nature of the relationship is shown by the response to an impulse at different points in the cycle. If the impulse occurs at a voltage maximum, the timing of zero-crossings (and therefore the phase) is not changed, but if the impulse occurs at any other time, the zero crossings change, and the amount they change depends on when the impulse occurs. Since the phase disturbance due to a noise impulse depends on when the impulse occurs, the noise-to-phase transfer function is time-varying, and the shape of the oscillation waveform affects how sensitive the oscillator's phase is to noise impulses [286]. The sensitivity of different waveforms to phase noise can be described through the impulse sensitivity function for the waveform, Γ [286].

Based on this theory, components of noise near integer multiples of the carrier frequency fold into noise near the carrier frequency, as described by Lee and Hajimiri [286]. White noise generates the $1/f_o^2$ portion of the phase noise:

$$L(f_o) = \left(10 \cdot \log \left(\frac{\overline{i_n^2} \Gamma_{RMS}^2}{2q_{max}^2 \cdot (2\pi f_o)^2} \right) \right), \quad (\text{H.8})$$

where $\overline{i_n^2}$ is the mean noise power, Δf_n is the noise bandwidth, q_{max} is the maximum charge displacement in the resonator, and f_o is the offset frequency from the carrier.

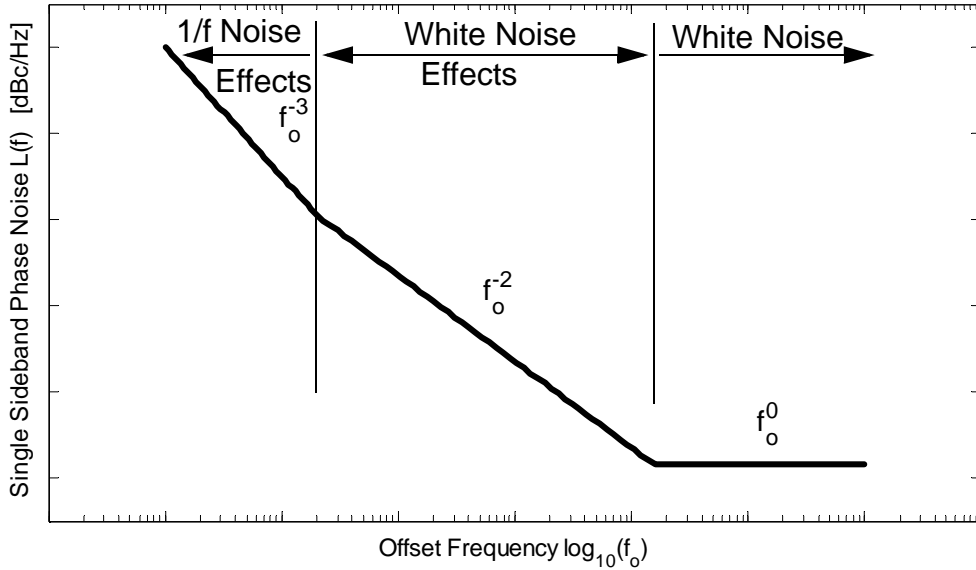


Figure H.4. Example phase noise spectrum: a typical phase noise spectrum will have a $1/f_o^3$ dependence close to the carrier, a $1/f_o^2$ dependence beyond that, and be flat farther from the carrier.

The $1/f_o^3$ portion of the phase noise is caused by $1/f$ noise at baseband:

$$L(f_o) = \left(10 \cdot \log \left(\frac{\frac{\overline{i_n^2}}{\Delta f_n} c_0^2}{8q_{max}^2 \cdot (2\pi f_o)^2} \cdot \frac{f_{1/f}}{f_o} \right) \right) \quad (\text{H.9})$$

Because phase noise is proportional to f_o^{-2} , as shown in (H.8), white noise near dc and other integer multiples of the carrier frequency is upconverted to the carrier with a $1/f_o^2$ slope, and (H.9) shows that $1/f$ noise near dc gets upconverted to the carrier, weighted by the coefficient c_0 , with a $1/f_o^3$ slope. White noise near the carrier remains at the same frequency. This typically leads to an oscillator phase noise spectrum with a $1/f_o^3$ dependence close to the carrier, a $1/f_o^2$ dependence beyond that, and flat at frequencies farther from the carrier [287]. This spectrum is shown in Figure H.4

Because Doppler monitoring of heart and respiration signals focuses on modulations on the order of 1 Hz from the carrier, the $1/f_o^3$ phase noise dependence is the only rele-

vant part of the spectra for this application. The phase noise with the $1/f_o^3$ slope is upconverted baseband $1/f$ noise at the transistor [286]. Since CMOS technology has notoriously poor $1/f$ noise performance, oscillators fabricated with this process have very high close-in phase noise.

H.3 References

- [286] T. H. Lee and A. Hajimiri, "Oscillator phase noise: A tutorial," *IEEE Journal of Solid State Circuits*, vol. 35, no. 3, pp. 326-336, 2000.
- [287] D. B. Leeson, "A simple model of feedback oscillator noise spectrum," *Proceedings of the IEEE*, vol. 54, pp. 329-330, 1966.

Appendix
I

Analog-to-Digital Conversion

I.1 Analog-to-Digital Converter Theory

The dynamic range of the ADC is the ratio of the maximum allowable input swing and the minimum input level that can be sampled with a specified accuracy. The dynamic range is limited by the threshold voltages of devices used in the circuit, the input-referred circuit noise, and the supply voltage [288]. The least significant bit (LSB) is the minimum change in input that causes a change in the output. The resolution is limited by the noise due to circuit noise, aperture jitter, comparator ambiguity, and device errors, and depending on the architecture, may be limited by the number of devices required. The resolution determines the amount of quantization noise; even in an ideal ADC, the conversion from continuous values to finite precision samples introduces some error.

The minimum change in input that causes a change in the output is known as the least significant bit (LSB), Δ , and is defined as [288]:

$$\Delta = \frac{V_{REF}}{2^m} = LSB . \quad (I.1)$$

where m is the number of bits, and V_{REF} is the input full-scale voltage. Since the resolution is limited, when the signal amplitude falls between two levels, quantization error is introduced. As the resolution increases the quantization error decreases. The effect of quantization noise is shown in the calculation of the signal-to-noise ratio of a full-scale

sinusoid in an ideal ADC. Assuming the signal voltage is randomly distributed, the quantization noise power, $\overline{\varepsilon_q^2}$ is [289]:

$$\overline{\varepsilon_q^2} = \frac{1}{\Delta} \cdot \int_{-\frac{\Delta}{2}}^{\frac{\Delta}{2}} \varepsilon_q^2 d\varepsilon_q = \frac{\Delta^2}{12} . \quad (\text{I.2})$$

If the analog input signal is a full-scale sinusoid, its total power is:

$$\frac{V_{REF}^2}{8} = \frac{2^{2m} \Delta^2}{8} , \quad (\text{I.3})$$

so the peak SNR for an ideal analog-to-digital converter is:

$$SNR_{peak} = \frac{(2^{2m} \Delta^2)/8}{\Delta^2/12} = \frac{3}{2} 2^{2m} . \quad (\text{I.4})$$

In decibels, the peak SNR of an ideal converter is [289]:

$$SNR_{peak} = 6.02m + 1.76 \text{ dB} . \quad (\text{I.5})$$

Non-ideal ADCs have additional nonlinearities and noise from thermal sources. Signal-to-noise ratio is the ratio of a full-scale sinusoid to the sinusoidal input for which the SNR would be 0 dB. This may be limited by thermal noise, quantization noise, or noise added by the ADC, and aperture jitter. The SNDR, signal-to-noise and distortion ratio, is the ratio of the signal power to the noise and harmonic power. This is limited by signal-to-noise ratio, nonlinearities, and charge injection. The effective number of bits, or ENOB, is defined as [289]:

$$ENOB = \frac{SNDR_{peak} - 1.76}{6.02} . \quad (\text{I.6})$$

I.2 Analog-to-Digital Conversion Requirements

Sigma-delta modulator ADCs with resolution up to 24 bits are commercially available operating at the sample rates required for Doppler radar monitoring of heart beats and respiration, between 50 Hz and 250 Hz. Sigma-delta modulator ADCs sample the analog signal at many times the Nyquist rate and use feedback to suppress quantization noise at low frequencies. Lower resolution Nyquist ADCs consume less power and require less processing computation, so using the lowest reasonable resolution is desired. In the measurements presented in this work, the signals were digitized with a digital oscilloscope or with a 16-bit National Instruments PCMCIA ADC card. The use of a 24-bit ADC eliminates the need for the challenging dc block filtering

The ADC requires sufficient resolution to accurately digitize the heart signal in the presence of the respiration signal and any dc offset that is not removed beforehand. If the ADC does not have sufficient resolution to digitize both the dc offset and the heart signal, the dc offset must be removed in analog signal processing prior to digitization. If the heart signal is two orders of magnitude smaller than the respiration signal and the dc offset is removed, the ADC should have at least 12 bits, providing 4096 digitization levels, to accurately digitize both signals. If the heart signal is three orders of magnitude smaller than the respiration signal, a 16-bit resolution will provide 65,536 levels, sufficient to digitize both signals. If the dc offset is 10 times greater than the respiration signal and therefore 10,000 times greater than the heart signal, an 18-bit ADC, providing over 260,000 levels, would provide accurate digitization of the heart signal. If the dc offset is 100 times or more greater than the respiration signal, it would be 100,000 times greater than the heart signal amplitude, a 20- or 24-bit ADC would be required, providing over one million levels of digitization. ADCs with resolution higher than 24 bits are not typically commercially available.

I.3 Analog-to-Digital Converters Used in Doppler Radar Physiological Measurement

The heart signature is typically 100 to 1000 times smaller than the respiration signal on which it is superimposed. The dc offset can be 100 times greater than the respiration signal. To accurately determine the heart rate, if only the heart rates is present and dc is removed, it should be measured with a minimum resolution of 4 bits. If both the heart and respiration signals are present and the dc offset is removed, a resolution of at least 14 bits is required. If both the heart and respiration rates are present and the dc offset is not removed, a resolution of at least 21 bits is required. Analog-to-digital converters are available with resolutions up to 24 bits at the required sampling frequencies in sigma-delta oversampled architectures, but not with USB or PCMCIA interfaces.

I.3.1 Digital Oscilloscope

In the measurements of the hybrid board, a HP Infinium oscilloscope was used with sampling rate of 50 samples/second and 8-bit resolution. In the measurements of the single-channel single-chip transceivers, the Tektronix 3014 digital oscilloscope with 9-bit resolution was used, which sampled at 25 samples/sec. For these measurements, the heart and respiration rates were separated with analog filters before digitization, so that the lower resolution digital signal did not pose a problem. When the Tektronix 3014 oscilloscope was used for the initial quadrature measurements, the analog filters had to be set to decrease the amplitude of the respiration signal to about 10 times that of the heart signal so that 8- and 9-bit digitization would be sufficient.

I.3.2 16-Bit ADC PCMCIA Card

The National Instruments NI-DAQ 6036E 16-bit ADC was used for measurements of the quadrature transceivers. This simultaneously digitizes 8 differential channels or 16 single-ended channels, so the I and Q channels as well as a reference can be simultaneously digitized. Custom Matlab code was written to display the digitized signal in real-time, and

can also display real-time data after digital signal processing. This data acquisition card can sample at rates up to 200 kS/second, so that the rates required for Doppler monitoring are not a problem. Because a 16-bit ADC was selected, dc offset had to be removed prior to digitization.

I.4 References

- [288] B. Razavi, Principles of Data Conversion System Design, New York: IEEE Press, 1995.
- [289] R. H. Walden, "Performance trends for analog-to-digital converters," IEEE Communications Magazine, pp. 96-101, February 1999.

